PHYSICAL CHEMISTRY

Volume 68, Number 10 October, 1964

38th National Colloid Symposium, *University of Texas, Austin, Texas, June 11-13, 1964*

Pulse Weight Distribution — Analysis DC & Other

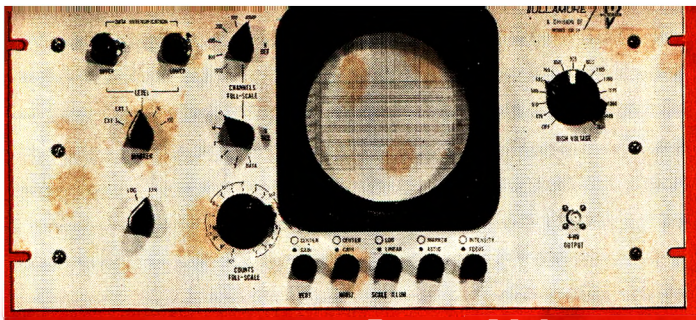

CRT DISPLAY

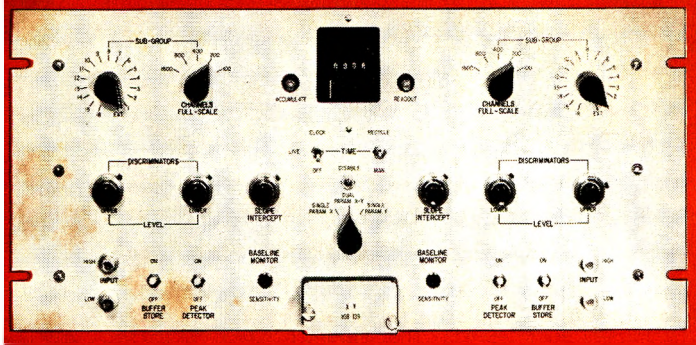

SINGLE OR DUAL ADC

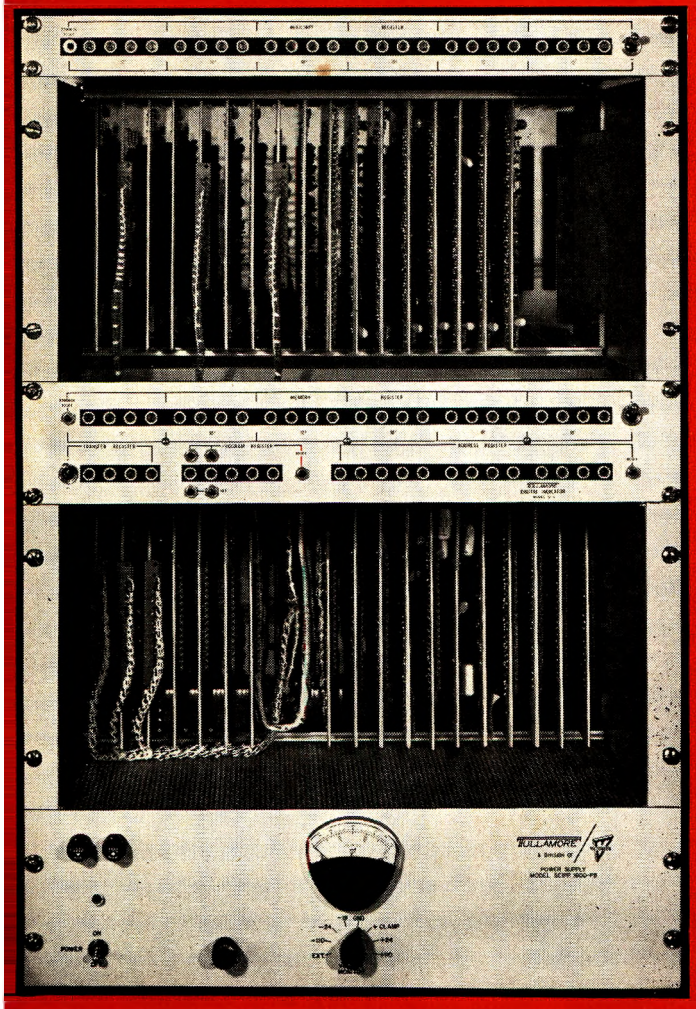

SCIPP 400/1600/10,000

VICTOREEN SCIPP SERIES
ON-LINE DATA-HANDLING

BASIC SCIPP SERIES COMPUTING INSTRUMENT*

400, 1600, 10,000 words (word length 10^6, decimal).

Patch program can be changed to meet virtually any requirement.

Built-in address and data register.

Random parallel access.

Serial and parallel outputs.

On-line data handling.

Memory subgrouping capability.

Display of memory (optional) is live, static, and static/live.

Full specifications on request.

GENERAL ADC FEATURES*

Single or dual units available.

8MC digitizing rate.

Independent or coincident operation.

10-Bit binary or 400/1600 BCD.

Analog function or pulse input ADC's.

Full specifications on request.

TULLAMORE / VICTOREEN

A DIVISION OF

THE VICTOREEN INSTRUMENT COMPANY

5857 West 95th Street • Oak Lawn, Illinois, U. S. A.

Full line of readout/readin accessories available.

*Field expandability from 400 to 1600 word, or 1600 two-parameter, operation—*exclusive with Victoreen.*

2248-A

NOTES

Important Notice to Authors

Professor Frederick T. Wall officially will assume the editorship of *The Journal of Physical Chemistry* effective January 1, 1965. New manuscripts submitted to *The Journal of Physical Chemistry* after December 1, 1964 should be sent directly to Professor Wall addressed as follows:

Dr. Frederick T. Wall, Editor, *The Journal of Physical Chemistry*
Department of Chemistry, University of California
Santa Barbara, California

THE JOURNAL OF
PHYSICAL CHEMISTRY

VOLUME 68, NUMBER 10 OCTOBER 15, 1964

Electric Monopole and Dipole Discreteness Effects in Adsorption

by J. Ross Macdonald and C. A. Barlow, Jr.

Central Research Laboratories, Texas Instruments Incorporated, Dallas, Texas 75222
(Received July 18, 1964)

Various consequences of element discreteness upon the electrical characteristics of adsorbed systems of monopoles and dipoles are discussed and methods for determining exact local potentials and fields in such systems are outlined in terms suitably general for wide application.

In the present paper we shall summarize some of the discreteness-of-charge effects accompanying adsorption and also describe some recent techniques for making exact discreteness-of-charge calculations possible. Before discussing any particular system, it is well to recognize that discreteness may produce a number of different effects: In particular, a given discrete array of monopoles or dipoles produces a potential which at almost any point differs from that produced by the continuous distribution of charges obtained by smearing the discrete entities over their plane. On the other hand, the potential averaged over a plane parallel to that of the array is equivalent to that obtained by smearing the discrete distribution in its plane. We see, therefore, that any property which depends on a more detailed behavior of the potential than merely the average will directly manifest discreteness effects. Examples of such properties relate to basic gas or liquid adsorption theory,[1-14] thermionic[14] and high field emission[15] characteristics, and electrode electrochemical kinetic properties.[16-18] Less obvious is the fact that discreteness will also indirectly influence the average potential. The manner in which this comes about is as follows. If the discrete array of elements is polarizable, either through orientation of permanent dipoles or creation of induced dipoles, the polarization depends on the local field acting to polarize the entity; this local field is the sum of the applied field and that arising from

(1) J. R. Macdonald and C. A. Barlow, Jr., Proceedings of the 1st Australian Conference on Electrochemistry, Sydney, Australia, Feb., 1963, to be published.

(2) A. N. Frumkin, *Phys. Z. Sowjetunion*, **4**, 256 (1933).

(3) O. Esin and B. Markov, *Zh. Fiz. Khim.*, **13**, 318 (1939); *Acta Fiz. Khim. URSS* **10**, 353 (1939).

(4) C. A. Barlow, Jr., and J. R. Macdonald, *J. Chem. Phys.*, **40**, 1535 (1964).

(5) O. Esin and V. Shikov, *Zh. Fiz. Khim.*, **17**, 236 (1943).

(6) D. C. Grahame, *Z. Elecktrochem.*, **62**, 264 (1958).

(7) S. Levine, G. M. Bell, and D. Calvert, *Can. J. Chem.*, **40**, 518 (1962).

(8) B. V. Ershler, *Zh. Fiz. Khim.*, **20**, 679 (1946).

(9) V. G. Levich, V. A. Kir'yanov, and V. S. Krylov, *Dokl. Akad. Nauk SSSR*, **135**, 1193 (1960); V. S. Krylov, *ibid.*, **144**, 356 (1962).

(10) R. J. Watts-Tobin, *Phil. Mag.*, **6**, 133 (1961).

(11) N. F. Mott and R. J. Watts-Tobin, *Electrochim. Acta*, **4**, 79 (1961).

(12) W. A. Steele and M. Ross *J. Chem. Phys.*, **35**, 850 (1961).

(13) W. Anderson and R. Parsons, *Proc. 2nd Intern. Congr. Surface Activity*, **3**, 450 (1957).

(14) A. J. Kennedy, *Advan. Energy Conversion*, **3**, 207 (1963).

(15) R. Gomer, *J. Chem. Phys.*, **21**, 1869 (1953).

(16) A. Aramata and P. Delahay, *J. Phys. Chem.*, **68**, 880 (1964).

the elements themselves. Since the latter contribution differs from the smeared (average) field, the net polarization and hence the effective dielectric constant of the array is a further property which could have been listed above as evincing discreteness-of-charge effects. The departure of the dielectric constant from the bulk value, which can be properly calculated only by taking full account of discreteness effects, has consequences[19-24] on the dependence of contact potentials or work functions upon adsorption and influences the differential capacitance of the electrical double layer in an electrolytic solution.[1,10,25-28]

In the present paper it is assumed that the adsorbed particles form a hexagonal array of spacing r_1 lying at the inner Helmholtz plane (IHP) and that one or the other of the following idealized situations prevails. Either there exist two equipotential planes, one on either side of the IHP which, like a hall of mirrors, produces an infinite set of images, or else one such plane exists (taken here to be the plane adsorbing electrode) and acts to produce single images of the adsorbed entities. In the former situation, appropriate to some degree to adsorption from electrolytes, one imaging plane is the electrode and the other is the outer Helmholtz plane (OHP), the plane of closest approach and maximum concentration for unadsorbed ions in the diffuse or Gouy layer[1,25,26,29-36] of the electrolyte. The inner or Stern layer[1,25,26,37] between the electrode and the OHP will be the primary region of interest in our discussion of the electrical double-layer problem, and for "unadsorbed electrolytes" will contain a monolayer of adsorbed solvent molecules taken here to be water.[1,25,26]

In earlier papers,[1,25,26] an effort was made to explain the differential capacitance data of Grahame[38] for aqueous NaF solutions at various temperatures, concentrations, and electrode charges. It was found that many of the features of the experimentally determined inner-layer differential capacitance could be explained without recourse to discreteness effects. In particular, the displacement of the point of maximum inner layer capacitance from the electrocapillary maximum potential (e.c.m.) could be ascribed to a natural orienting field at the electrode, of order 10^6 to 10^7 v./cm., which acts to align the water dipoles somewhat with the hydrogen toward the electrode. The fall-off of capacitance on either side of this maximum was accounted for by including dielectric saturation of the inner layer, and the eventual rise in capacitance at potentials further from the e.c.m. was explained by the compression of the inner layer under the large fields present therein. The actual values of capacitance were generally in excellent agreement with experiment over the varying potentials, temperatures, and concentrations, and, provided lack of association between water molecules was assumed, all best-fit parameters such as compressibility, thickness, dielectric saturation constant, etc., were in agreement with those to be expected based on bulk water values. In spite of the general success of this work, one feature of the data could not be explained: the rapidity of the final rise in capacitance at substantial anodic voltages.[38,39] This rise has been ascribed by various authors to adsorption, perhaps of OH^-,[40] perhaps of F^-,[26] perhaps of electrode "adatoms."[10,11] Parsons[18] suggests that an increased compressibility may be responsible. Although these explanations are possibly correct, the situation is far from clear. The point is that a reasonable fit to Grahame's data may be obtained without assuming adsorption other than the initial water monolayer simply by properly taking discreteness-of-charge into account and its effect upon the inner-layer dielectric constant.[1,41]

The procedure for obtaining the effective dielectric constant is roughly the following:

(17) A. N. Frumkin, *J. Electrochem. Soc.*, **107**, 461 (1960).

(18) R. Parsons, "Advances in Electrochemistry and Electrochemical Engineering," Vol. I, P. Delahay, Ed., Interscience, London, 1961.

(19) J. R. Macdonald and C. A. Barlow, Jr., *J. Chem. Phys.*, **39**, 412 (1963).

(20) J. K. Roberts, "Some Problems of Adsorption," Cambridge University Press, London, 1939.

(21) A. R. Miller, *Proc. Cambridge Phil. Soc.*, **42**, 292 (1946); "The Adsorption of Gases on Solids," Cambridge University Press, Cambridge, 1949, pp. 112, 113.

(22) J. H. de Boer, *Advan. Catalysis*, **8**, 118 (1956).

(23) I. Higuchi, T. Ree, and H. Eyring, *J. Am. Chem. Soc.*, **77**, 4969 (1955).

(24) G. E. Moore and H. W. Allison, *J. Chem. Phys.*, **23**, 1609 (1955).

(25) J. R. Macdonald, *ibid.*, **22**, 1857 (1954).

(26) J. R. Macdonald and C. A. Barlow, Jr., *ibid.*, **36**, 3062 (1962).

(27) R. Hansen, D. Kelsh, and D. H. Grantham, *J. Phys. Chem.*, **67**, 2316 (1963).

(28) N. F. Mott, R. Parsons, and R. J. Watts-Tobin, *Phil. Mag.*, **7** 483 (1962).

(29) G. Gouy, *J. Phys.*, **9**, 457 (1910).

(30) D. L. Chapman, *Phil. Mag.*, **25**, 475 (1913).

(31) R. H. Fowler, "Statistical Mechanics," 1st Ed., Cambridge University Press, London, 1929, pp. 282, 283.

(32) H. Müller, *Cold Spring Harbor Symp. Quant. Biol.*, **1**, 1 (1933).

(33) J. R. Macdonald and M. K. Brachman, *J. Chem. Phys.*, **22**, 1314 (1954).

(34) H. S. Frank and P. T. Thompson, *ibid.*, **31**, 1086 (1959).

(35) M. J. Sparnaay, *Rec. trav. chim.*, **77**, 872 (1958).

(36) H. Brodowsky and H. Strehlow, *Z. Elektrochem.*, **63**, 262 (1959).

(37) O. Stern, *ibid.*, **30**, 508 (1924).

(38) D. C. Grahame, *J. Am. Chem. Soc.*, **76**, 4819 (1954); **79**, 2093 (1957); **59**, 740 (1955).

(39) M. J. Austin and R. Parsons, *Proc. Chem. Soc.*, 239 (1961).

(40) N. Hackerman and P. V. Popat, "Capacity of the Electrical Double Layer and Adsorption at Polarized Pt Electrodes," Technical Report to the Office of Naval Research, 1958.

(41) J. R. Macdonald and C. A. Barlow, Jr., to be published.

1. Replace all permanent dipoles by their time averages, $\langle\mu\rangle$.

2. Find the local electric field $\mathcal{E}$ at the dipole sites arising from all other dipoles and induced polarization, the charges on the electrode, and the natural field.

3. Using an expression such as a Langevin function, obtain an implicit equation for $\langle\mu(\mathcal{E})\rangle$.

4. Write the electronic polarization $\mathcal{P}_1$ in terms of the local field.

5. Combine all previous steps to find the self-consistent values of $\mathcal{P}_1$, $\mathcal{E}$, and $\langle\mu\rangle$.

6. Express the final result in terms of an effective dielectric constant ϵ_{eff}.

If this program is carried out one obtains[19]

$$\mathcal{E} = \epsilon_{eff}^{-1}\{4\pi q - (3/4)^{3/4}\sigma N^{3/2}\langle\mu(\mathcal{E})\rangle\}$$

where $\epsilon_{eff} \equiv 1 + (3/4)^{3/4}\,\sigma\,\alpha\, dN^{1/2}$, $q \equiv$ electrode charge; $\alpha \equiv$ electronic polarizability, $\sigma \equiv 11.034$ for a hexagonal array, $d \equiv$ inner-layer thickness, and $N \equiv$ surface density of adsorbed particles. This equation has been solved numerically and, without attempting detailed fitting, leads to the qualitative agreement with Grahame's data mentioned before.

The same procedure may be used to determine the work function change arising from adsorption of ions in the single-imaging situation, provided one approximates the ion–image combination as an ideal dipole. Again, if one carries through the calculation, qualitative agreement with experiment is obtained for coverages θ sufficiently small (≤ 1) that such quantum effects as energy banding may be ignored. The detailed calculation which appears elsewhere[19] leads, under appropriate conditions, to the approximate result

$$\frac{\Delta V(\vartheta)}{\Delta V(1)} \cong \vartheta(1 - A)^{-1}(1 - \vartheta A)$$

where $\Delta V \equiv$ work function change, $\theta \equiv$ fractional coverage of surface by adions ($\theta = 1$ corresponds to a monolayer), $A \equiv 4\pi\alpha N_s/d_1$, $N_s \equiv$ maximum surface density of adions ($\theta = 1$), and $d_1 \equiv$ distance between electrode and adion centroid. For certain values of A the resulting behavior of $\Delta V(\theta)$ exhibits a maximum in the range $0 < \theta < 1$.

In order to calculate exact potentials and fields for discrete arrays, it is necessary to obtain somehow the sum of an infinite series of discrete Coulomb terms. This would present no problem were it not for the extraordinarily slow convergence encountered in either single or infinite image situations. The practical difficulties of obtaining exact results have led several authors[7,10,11,28] to seek approximate expressions, the accuracy of which is unfortunately not always particularly good; the present authors have proceeded in the other direction, to obtain more complicated but more rapidly convergent forms for the exact quantities. Comparison of the exact with various approximate results is published elsewhere.[4,42] The emphasis here will be in outlining the methods, which have been used before in different contexts and are applicable to a wide class of problems.

The simplest method for calculating lattice-sums of Coulomb terms is to multiply each Coulomb term in the series by an exponential convergence factor. Thus, $1/r \to 1/r \exp(-\delta r)$. The series is then evaluated for several values of δ and an extrapolation performed to ascertain the value for $\delta = 0$. Remark that a powerful method, the ϵ-algorithm,[43–45] exists for performing this extrapolation which is quite accurate and is discussed elsewhere.[45] The disadvantages of the above δ-method are that several calculations are necessary using different values for δ, some of which (near $\delta = 0$) are not very rapidly convergent; the closer one approaches in the computations to $\delta = 0$, the greater is the final accuracy but the longer is the required computer time. Furthermore, the requirement of a final extrapolation must be regarded as an additional disadvantage. Accordingly, this method has been used by the present authors primarily as a check on other methods or as the technique employed when others are unavailable.

A generally more satisfactory technique[4,46,47] is schematically described below for the three-dimensional (infinite-imaging) summation.

1. First write the sum to be evaluated, $\sum_k f(\mathbf{R}_k) \equiv S$, as $S = \int d^3R f(\mathbf{R}) \sum_k \delta(\mathbf{R} - \mathbf{R}_k)$, where $\mathbf{R}_k$ are the lattice points and $\delta(\mathbf{x})$ is the Dirac δ-function.

2. Next write the identity

$$S = \int d^3R \sum_k f(\mathbf{R})\Phi(\alpha\mathbf{R})\delta(\mathbf{R} - \mathbf{R}_k) + \int d^3R \sum_k f(\mathbf{R})\{1 - \Phi(\alpha\mathbf{R})\}\delta(\mathbf{R} - \mathbf{R}_k) \equiv S_1(\alpha) + S_2(\alpha)$$

where Φ is an arbitrary function which will be chosen conveniently and α is a parameter which also will be chosen conveniently. Note that $\partial S/\partial\alpha = 0$.

3. Writing the Fourier transform of $\{f(\mathbf{R})\Phi(\alpha\mathbf{R})\}$ as $G_\alpha(\lambda)$ and the Fourier transform of $\sum_k \delta(\mathbf{R} - \mathbf{R}_k)$ as $|\mathbf{a}_1\cdot\mathbf{a}_2 \times \mathbf{a}_3|^{-1} \sum_k \delta(\lambda - \lambda_k)$ where $\mathbf{a}_1$, $\mathbf{a}_2$, $\mathbf{a}_3$ are the

(42) C. A. Barlow, Jr., and J. R. Macdonald, *J. Chem. Phys.*, to be published.

(43) P. Wynn, *Math Tables Other Aids Computation*, **10**, 91 (1956).

(44) D. Shanks, *J. Math. Phys.*, **34**, 1 (1955).

(45) J. R. Macdonald, *J. Appl. Phys.*, to be published.

(46) F. W. de Wette, *Physica*, **23**, 309 (1957); **24**, 422, 1105 (1958).

(47) P. P. Ewald, *Ann. Phys.*, **54**, 519, 557 (1917).

basic lattice vectors and λ_k are the lattice points of the reciprocal lattice[46] ($\lambda_k \equiv |\mathbf{a}_1\cdot\mathbf{a}_2 \times \mathbf{a}_3|^{-1}\{k_1\mathbf{a}_2 \times \mathbf{a}_3 + k_2\mathbf{a}_3 \times \mathbf{a}_1 + k_3\mathbf{a}_1 \times \mathbf{a}_2\}$), make use of Parseval's theorem[48] to obtain

$$S_1 \equiv \int d^3\lambda G_\alpha(\lambda)\, \mathbf{a}_1\cdot\mathbf{a}_2 \times \mathbf{a}_3|^{-1} \sum_k \delta(\lambda - \lambda_k) = |\mathbf{a}_1\cdot\mathbf{a}_2 \times \mathbf{a}_3|^{-1} \sum_k G_\alpha(\lambda_k)$$

where $G_\alpha(\lambda) \equiv \int d^3R f(\mathbf{R})\Phi(\mathbf{R}) e^{2\pi i\lambda\cdot\mathbf{R}}$.

4. Choose $1 - \Phi$ to be a function which falls off as its argument increases and hence which speeds the convergence of S_2.

5. Choose α to minimize the total number of terms required for convergence of S. Large α results in rapid convergence of S_2 but slow convergence of S_1; small α interchanges these behaviors. An intermediate value may generally be chosen so as to optimize convergence.

6. Test to see that S remains invariant under changes in α. The above method has proven quite satisfactory, and generally the optimum value of α is of the order $[|\mathbf{a}_1\cdot\mathbf{a}_2 \times \mathbf{a}_3|]^{-1/3}$ with the required independence of the final result upon α providing a stringent test of the correctness of all computations. The function Φ actually used was the error function[49] in the work cited.[4]

The final technique[50] to be described here has proven generally to be the best one for summations occurring in practice. It results in an almost closed form expression for the potentials and fields, with the summations remaining frequently contributing negligible amounts to the final result. The vital steps of the method are sketched below.

1. Make use of the relation

$$x^{-n} = \frac{1}{\Gamma(n)} \int_0^\infty t^{n-1} e^{-xt}\, dt$$

to rewrite the terms of the lattice summation.

2. Introduce the substitution

$$\sum_{l=-\infty}^{\infty} \exp\{-(l + a)^2 t\} = (\pi/t)^{1/2} \times \sum_{s=-\infty}^{\infty} \exp\left\{-\frac{\pi^2 s^2}{t}\right\} \cos(2\pi a s)$$

3. Perform the integration using

$$\int_0^\infty t^{n-1/2} \exp\left\{-k^2 t - \frac{\pi^2 s^2}{t}\right\} dt = 2\left(\frac{\pi|s|}{k}\right)^{n-1/2} K_{n-1/2}(2\pi k|s|)$$

where K is the modified Bessel function.[49]

4. Execute remaining summations taking limits where special values require it.

The foregoing description is in terms sufficiently general to apply to a rather wide class of problems; however, the reader wishing an example of a specific application of the method may find such elsewhere.[42]

In summary, we have attempted to sketch some of the consequences of discreteness upon the basic electrical properties of adsorbed lattices. Whereas there has been little attempt here to explore all the secondary consequences of such electrical properties upon macroscopic measurables, clearly element discreteness has its impact upon a large number of surface phenomena. It is gratifying that all the methods outlined herein for exactly performing the pertinent calculations have always produced mutually consistent results.

(48) See, for example, P. Franklin, "A Treatise on Advanced Calculus," John Wiley and Sons, Inc., New York, N. Y., 1940, p. 492.

(49) See, for example, "The Bateman Manuscripts," A. Erdélyi, Ed., McGraw-Hill Book Co., Inc., New York, N. Y., 1954.

(50) B. M. E. van der Hoff and G. C. Benson, *Can. J. Phys.*, **31**, 1087 (1953).

Rates of Surface Migration of Physically Adsorbed Gases

by R. K. Smith[1] and A. B. Metzner

University of Delaware, Newark, Delaware *(Received March 18, 1964)*

A molecular model of the surface transport rate process is used to develop quantitative rate equations; these, containing one arbitrary parameter, are compared with experimental measurements of the surface migration rates of propane, butane, propylene, perfluoropropane, and dibromodifluoromethane over a wide range of pressures and a moderate range of temperatures on one solid surface, an alumina catalyst support. The agreement between the experimental results and the theoretical equations developed in this study shows an order-of-magnitude improvement over the prior art. As such, the results of this study support the theoretical model used. Further work, directed toward an understanding of the remaining parameter, would clearly be desirable in order to move more closely toward entirely *a priori* predictions of the transport rates or mobilities of adsorbed molecules.

Introduction

The mobility of adsorbed gases on solids has potential industrial importance in applications of heterogeneous catalysis, gaseous effusion processes, and in adsorption operations in which the intraparticle rates of mass transport are significant. Empirically, Carman[2] and a number of other workers[3-5] have shown surface migration or transport rates generally to be increasing functions of surface (adsorbate) concentration, at least under conditions of low surface coverage. This fact appears to be well established and thus invalidates the simple concept of a diffusion process having a constant diffusion coefficient and suggests strongly the presence of experimental aberrations in recent data[6] (on systems similar to those studied previously) which show, in a number of cases, more or less random variations of transport rate with surface adsorbate concentration.

Early predictions of surface transport rates have been shown to be inadequate, either theoretically or experimentally, by two very thorough reviews[2a,6] and thus will not be discussed further. The remaining prior art consists of a thorough but entirely empirical analysis,[5] an oversimplified theoretical approach,[7] and a semi-empirical equation[6] of the form

$$I_A = BRTx^2/p \qquad (1)$$

where I_A denotes the specific flux of the molecules of the adsorbed phase in mmoles/sec. cm. mm., R, T, and p the gas constant, temperature, and pressure, respectively, in consistent units, and x the surface concentration of the adsorbed transporting molecules in mmoles/g. of solid. B is an empirical, dimensional constant.

The validity of this expression may be demonstrated by means of logarithmic plots of the product $I_A p$ *vs.* x: data following this prediction would be located on a straight line having a slope of 2. For 18 out of a total of 20 sets of data available in sufficient detail to test this hypothesis[6,8-10] (including those of the investigators who proposed eq. 1) the slopes of such plots increase nonlinearly and usually rapidly

(1) Virginia Polytechnic Institute, Blacksburg, Va.

(2) (a) P. C. Carman, "Flow of Gases Through Porous Media," Academic Press, New York, N. Y., 1956, Chapter 5; (b) P. C. Carman and P. Malherbe, *Proc. Roy. Soc.* (London), **A203**, 165 (1950).

(3) G. Damköhler, *Z. physik. Chem.*, **A174**, 222 (1935).

(4) E. A. Flood, R. H. Tomlinson, and A. E. Leger, *Can. J. Chem.*, **30**, 389 (1952).

(5) L. O. Rutz and K. Kammermeyer, U. S. Atomic Energy Commission Report AECU-4328, "Flow Through Microporous Media-Vapor Transfer Through Barriers," 1958.

(6) E. R. Gilliland, R. F. Baddour, and J. L. Russell, *A.I.Ch.E. J.*, **4**, 90 (1958); see also J. L. Russell, Sc.D. Thesis, Massachusetts Institute of Technology, Cambridge, Mass., 1955.

(7) G. W. Sears, *J. Chem. Phys.*, **22**, 1252 (1954).

(8) P. C. Carman and F. A. Raal, *Proc. Roy. Soc.* (London), **A209**, 38 (1951).

(9) B. J. Muzzi, B.Ch.E. Thesis, University of Delaware, Newark, Del., 1963.

(10) R. K. Smith, M.Ch.E. Thesis, University of Delaware, Newark, Del., 1963.

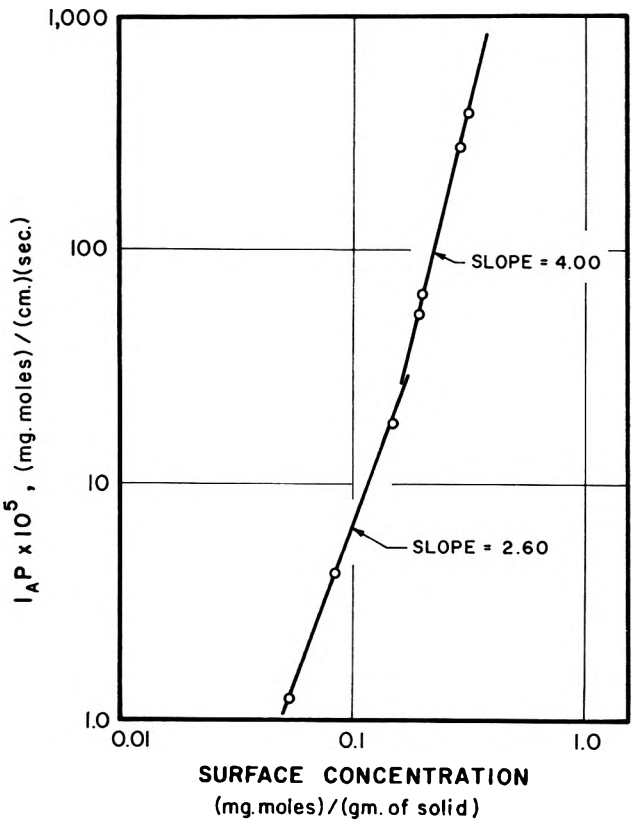

Figure 1. Dependence of surface transport rates on adsorbate concentration. Prior art (eq. 1) predicts a slope of 2.0, independent of surface concentration, on these coordinates. Data shown are for propylene at 50°.

with increasing surface concentration, x. A representative plot on such coordinates is shown in Fig. 1. Clearly, eq. 1 is not followed.

Theoretical

The following assumptions are employed in the development of the rate expression.

1. The surface of the solid is assumed to be heterogeneous energetically; as the molecules begin to adsorb they affix themselves first on areas of the surface with the lowest potential energies. Molecules thereafter adsorb onto the areas with the lowest energy level available. This assumption of energetic heterogeneity is believed to be completely valid for nearly all existing adsorbents[11,12]; that of alumina (which is of primary interest in the present study) has recently been studied in detail.[13]

2. By means of oscillations and collisions with the surface atoms, an adsorbed molecule may attain an activated state wherein its energy level is sufficient for it to become partially desorbed from the surface. Such a partially desorbed molecule "migrates" or "jumps" in random directions, expending its translational energy until it is completely readsorbed at another position of minimal surface energy.

3. While the molecules jump in completely random directions, gradients in either temperature or pressure will create a net transport rate of the adsorbed molecules.

4. The activation free energy for the migration process is determined primarily by that of the partial desorption step; this, in turn, is assumed to be proportional to that for complete desorption since both terms may be expected to be similarly dependent on the strength of adsorbate–adsorbent bonds.

Let λ denote the distance which a molecule traverses in jumping from one position on the surface to another. Consider a unit plane AB perpendicular to the direction of the net flux. The rate at which molecules undergo the partial desorption, which is postulated to be the rate-controlling step of the transport process, at plane AB, is defined as r_0 in mmoles/(cm.^{2} of surface area $\times$ sec.). Correspondingly, the rate a distance ξ to the right of AB (see Fig. 2) is, for small values of ξ

$$r_+ = r_0 + \frac{dr}{dz}\frac{\xi}{j} \qquad (2)$$

where z denotes distance from the plane AB and j is the tortuosity of the pore structure.

The rate of transport of molecules across plane AB which originally were adsorbed on the surface at distances between ξ and $\xi + d\xi$ from this plane is given by the product of the rate of partial desorption and the fraction of the desorbed molecules which move in a direction such that their motion results in their transport across plane AB. Assuming completely random motion, the fraction of the "jumps" which are useful is simply $2\theta/2\pi$, where 2θ represents the plane angle which includes those molecules oriented sufficiently toward the plane AB to cross it while jumping a distance equal to or less than λ_+, hence

$$\theta = \arccos(\xi/\lambda_+) \qquad (3)$$

Summing over all possible distances from which molecules may originate (0 to λ_+) the transport rate, from right to left, across plane AB is

$$\int_0^{\lambda_+} (r_0 + r'\xi/j)(\arccos \xi/\lambda_+)(s\rho/\pi)d\xi \qquad (4)$$

(11) See, for example, A. S. Joy, *Proc. 2nd Intern. Congr. Surface Activity*, 2, 54 (1957).

(12) D. M. Young and A. D. Crowell, "Physical Adsorption of Gases," Butterworths, Washington, D. C., 1962.

(13) S. J. Gregg and K. H. Wheatley, *Proc. 2nd Intern. Congr. Surface Activity*, 2, 102 (1957).

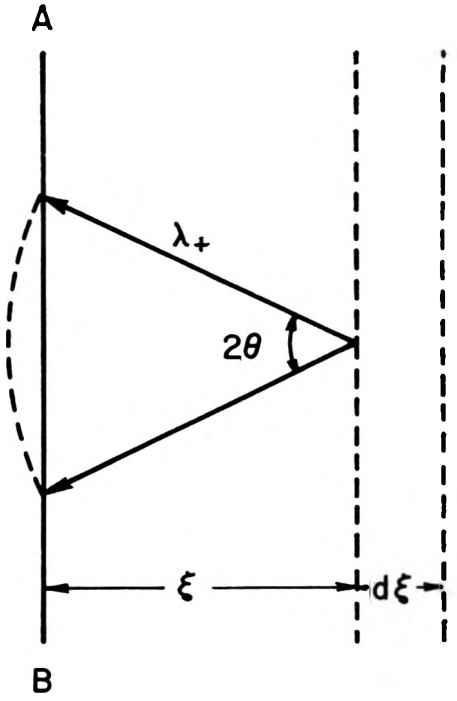

Figure 2. Model used to develop a theoretical transport rate expression.

where r' denotes dr/dz, s is the surface area per unit mass of adsorbent, and ρ is the bulk density of the solid. A similar relation may be written for the transport from left to right. Upon taking the difference between these equations one obtains, for the *net* transport rate in the positive z direction

$$\dot{N}_A = (s\rho/\pi)\left\{\int_0^{\lambda_-} [r - r'\xi/j][\arccos \xi/\lambda_-]d\xi - \int_0^{\lambda_+} [r + r'\xi/j][\arccos \xi/\lambda_+]d\xi\right\} \quad (5)$$

Defining the quantities λ_+ and λ_- as

$$\lambda_+ = \lambda + \lambda'(\lambda_+/2j)$$

and

$$\lambda_- = \lambda - \lambda'(\lambda_-/2j)$$

where λ' denotes $d\lambda/dz$, one obtains upon integration of eq. 5, after dropping all terms of second or higher order

$$\dot{N}_A = -\frac{s\rho}{\pi j}\left[r\lambda\lambda' + \frac{\pi}{4}r'\lambda^2\right] \quad (6)$$

Now, making the usual assumptions of the absolute rate theory,[14] one may write for the rate of partial desorption r

$$r = r(T,p) = \left(\frac{Q_1'}{Q}\right)\frac{kT}{k}\, x \exp(-\Delta F^*/RT) \quad (7)$$

where x denotes the concentration of the adsorbed species in mmoles/g. of adsorbent and the other terms have their usual significance.

The final result is obtained by differentiating eq. 7 to obtain r' and then substituting for both r and r' in eq. 6. To avoid loss of the significant results in straightforward but messy algebraic terms, it is perhaps convenient to consider isothermal and isopiestic processes separately. In the first instance, transport occurs as a result of a pressure or concentration gradient; in the latter instance, it occurs as a result of a temperature gradient. Choosing the isothermal case, to correspond to the conditions of the present experimental studies, and combining the temperature-independent terms, gives

$$r(T,p) = MxT \exp(-\Delta F^*/RT) \quad (8)$$

Now introducing the assumption that ΔF^* is directly proportional to ΔF, the free energy of desorption, and denoting ΔF by the usual logarithmic relationship one obtains

$$\exp(-\Delta F^*/RT) = (p/p^0)^a \quad (9)$$

where a denotes the proportionality constant.

One final assumption is now required. The distance λ which a molecule jumps will vary in some inverse manner with the number of sites and their relative strengths. With increased surface concentration, the molecule will have fewer sites to which it may jump. Furthermore, the intermolecular force fields originating at the surface of the solid would tend to be weaker as the sites with the lowest potential energies have largely become covered. Both of these factors would tend to cause λ, the average jumping distance, to increase with x, the surface concentration of the adsorbed molecules. Since the precise relationship of λ to x is unknown, the two-dimensional area, $\pi\lambda^2$, into which a molecule may jump from a point, is arbitrarily assumed to be directly proportional to the surface concentration. This assumption yields

$$\lambda = Lx^{1/2} \quad (10)$$

in which L is the proportionality constant, presumably a temperature-dependent quantity.

Combining eq. 8 and 9, taking derivatives of the resulting equation and of eq. 10 to define r' and λ', and substituting into eq. 6 yields, for *the isothermal case*

(14) S. Glasstone, K. J. Laidler, and H. Eyring, "Theory of Rate Processes," McGraw-Hill Book Co., Inc., New York, N. Y., 1941.

$$\dot{N}_A = \left[\frac{-s\rho L^2 MT}{\pi j p^0}\right]\left[\frac{x}{2}p^a\frac{\partial x}{\partial p} + \frac{\pi}{4}ax^2p^{a-1} + \frac{\pi}{4}xp^a\frac{\partial x}{\partial p}\right]\nabla p \quad (11)$$

Smith[10] has shown that the proportionality constant, a, may be taken as equal to unity in the case of the present data. This assumption implies that the partially desorbed molecule, under conditions of surface migration, is in fact very nearly completely desorbed. This gives

$$I_A = \frac{\dot{N}_A}{-\nabla p} = D\left[1.637xp\frac{\partial x}{\partial p} + x^2\right] \quad (12)$$

in which

$$D = \left(\frac{s\rho M}{4j}\right)\frac{L^2T}{p^0} \quad (13)$$

a parameter which must be defined experimentally and I_A denotes the permeability of the adsorbed gas. If the model used is valid, D will be found to be independent of pressure and surface concentration; the brackets in eq. 13 group the terms which are independent of temperature.

In summary, the basic postulates leading to eq. 12 and 13 are that the migrating molecules are nearly completely desorbed, that the rate-controlling step is this rate of partial desorption, and, implicitly, that the behavior of each molecule is independent of that of its neighbors. Additional specific assumptions involved in writing eq. 9 and 10 may readily be relaxed if required by experimental data on particular systems.

Experimental

The equipment and procedures used represented simple modifications of those employed by Villet and Wilhelm.[15] The porous solid chosen consisted of a single 0.95-cm. diameter pellet of a high alumina catalyst support, No. Al-1404T, manufactured by the Harshaw Chemical Co. According to information supplied by the manufacturer, this material has a surface area of 200 m.²/g. and a mean pore diameter of 90 Å. It was obtained in cylindrical form, machined to various convenient thicknesses, and fixed between two 0.546-l. reservoirs using a small amount of epoxy resin. Microscopic examination showed that the resin did not penetrate any significant portion of the pellet. A small pressure differential of the gas under study was placed across the pellet and pressure readings were taken as a function of time. In this manner, material balances could be made to check the internal consistency of the measurements and no doubt was left as to whether or not sufficient time had elapsed for decay of undesirable initial transients. The same technique provided for an excellent increase in precision of the results. The limiting factor was the accuracy of the pressure measurements; careful choice of operating conditions only reduced this to a few per cent, a wholly unacceptable level in view of the need to subtract the flux of nonadsorbed molecules (from the observed total flux) in order to obtain the quantity of interest. However, plotting the pressure–time data in both reservoirs and using the smoothed curves so obtained to ascertain the total fluxes resulted in measurements having greatly improved confidence limits: measurements of helium permeability over a 30-fold range of pressures gave a maximum deviation of only 0.1%. Nevertheless, even this level of accuracy leads to fairly large errors at low pressures when the adsorbed flux is small, 25% in one case and 10% in a number of other instances. Thus the confidence limits of the low pressure data points are quite large; fortunately, the adsorbed fluxes were found to increase rapidly with increasing pressure and the results are believed to be reliable except for a few data points at the very lowest pressures.

In addition to measurements using helium, the flux of nonadsorbed gases was also determined using nitrogen and argon to confirm the expected dependence of the gaseous permeability upon the square root of molecular weight. A correction to this calculated gaseous permeability was made to allow for constriction of the pores by the presence of adsorbed molecules. This latter correction, while employing fairly gross approximations to the true pore structure of the catalyst, was very small (0.600×10^{-6} mmole/sec. cm. mm. at a monolayer) and therefore not crucial. However, an independent study of pore constriction[16] has shown the model used for this process to conform to experimental fact with surprising accuracy.

The pressure drop across the pellet, during transport rate determinations, was kept small in comparison to the absolute pressure to enable the use of eq. 1 and 12 in differential form as shown. The necessary x–p equilibrium data (isotherm measurements) were made using a conventional quartz spring McBain-Bakr balance. These data were fit to polynomials of fifth degree, and the slopes of the isotherms ($\partial x/\partial p$ in eq. 12) were evaluated by differentiating the polynomial.

(15) R. H. Villet and R. H. Wilhelm, *Ind. Eng. Chem.*, **53**, 837 (1961).

(16) L. F. Brown, Ph.D. Thesis, University of Delaware, Newark, Del., 1963.

The original references[9,10] should be consulted for supplementary experimental details; tabulated results, including minor corrections to those presented in the theses, are available from the authors.

Results

Figure 3 compares the transport rates, as experimentally determined for one gas, with those calculated using the prior-art expression, eq. 1. The coincidence of the calculated and predicted values occurs at the pressure or concentration level at which the adjustable parameter, B, is fitted to the data, and neither this midpoint agreement nor the exact choice of the midpoint is of interest. The important point is that the predicted trends are clearly incorrect.

Figure 4 shows the comparison between the same data and eq. 12. Obviously, the equation fits extremely well, any deviations from the curve being of the same magnitude as the scatter in the data themselves. The small trend away from the curve at the highest fluxes occurs under conditions of surface coverage in excess of a monolayer. Under these conditions the model used, which assumes that each molecule moves independently of the others, would not be expected to apply.

The complete data of the present investigation are summarized in Table I. A significant fraction of the transport data for dibromodifluoromethane was obtained under conditions of surface coverage in excess of a monolayer; a comparison of the mean deviations listed shows clearly that eq. 12 does not apply under such conditions. A generally similar conclusion may be drawn from data obtained by Muzzi[9] using butane at 0° in which case all of the data were for surface concentrations in excess of a monolayer and, except for those points in the immediate vicinity of unimolecular surface coverage, the trends observed were not consistent with those predicted by eq. 12. With the exception of these data for surface concentrations in excess of a full unimolecular layer, the experimental results show, in no case, any systematic deviations from the predicted relationship. Even for those systems or conditions showing the largest mean deviations, the errors were found to be random, indicating experimental aberrations rather than some discrepancy between theory and experiment. The primary conclusion to be drawn from Table I is that the model proposed fits all of the data obtained at surface coverages below a full unimolecular layer, with an accuracy determined by the random scatter of the data, which is approximately 10%.[17]

Equation 13 for D may be rearranged to separate the known dependence on temperature and vapor pressure from the other terms

$$D = W^2L^2T/p^0;\ WL = \sqrt{Dp^0/T} \qquad (14)$$

in which $W^2 = s\rho M/4j$, a temperature-independent constant for each system.

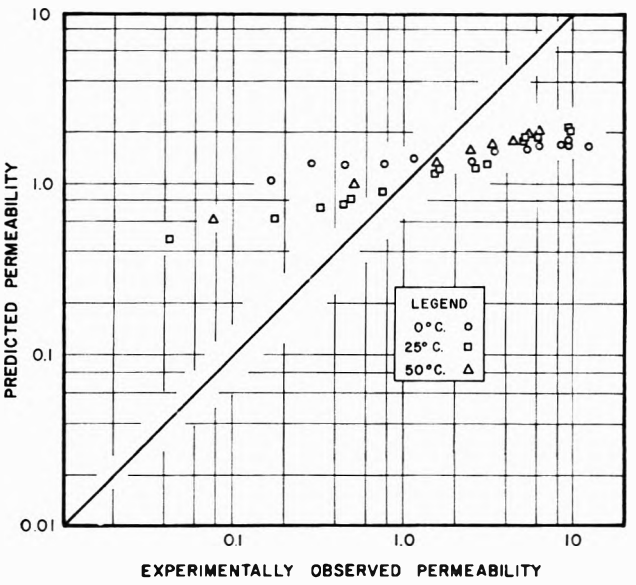

Figure 3. Comparison of experimentally observed transport rates with those predicted by eq. 1. Transport rates of the adsorbate expressed as permeabilities, $N_A/\nabla p$, mmoles/sec. cm. mm., multiplied by 10^6. Data for propane.

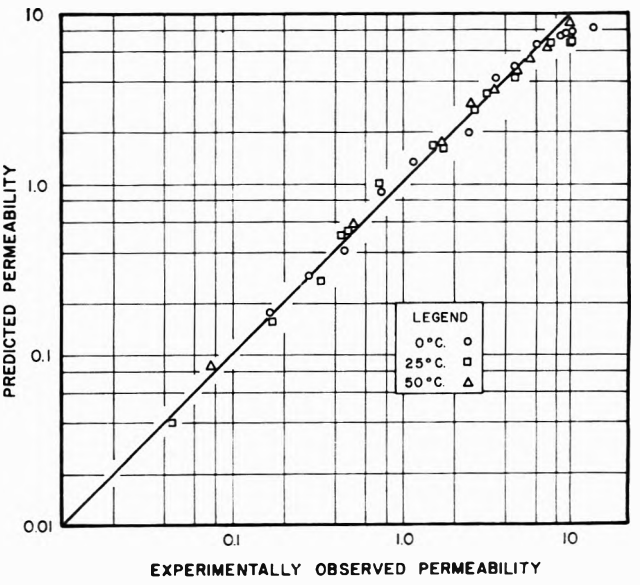

Figure 4. Comparison of transport rates of adsorbed molecules as predicted by eq. 12 with experimentally observed rates. Same data as shown in Fig. 3.

(17) In the case of the butane and dibromodifluoromethane measurements at low pressures, unusual experimental aberrations in a few of the results greatly increased the mean deviations. However, the mean deviation of all the data, even with these included, is still below 12%.

Table I

Gas	Temp., °C.	Pressure range, mm.	Surface concentration range, mmoles/g. of solid	Adsorbed permeability range × 10^6, mmoles/sec. cm. mm.	Mean deviations from eq. 1, %	Mean deviations from eq. 12, %
Propane	0	10.20–487.10	0.080–0.734	0.171–12.516	390.3	7.9
	25	9.95–604.00	0.038–0.600	0.042–9.913	446.0	4.9
	50	25.21–551.30	0.038–0.368	0.074–6.891	179.0	6.5
Propylene	0	18.70–364.70	0.120–0.530	0.439–8.652	110.2	9.2
	25	22.15–592.20	0.065–0.530	0.150–8.730	29.9	17.1
	50	42.50–557.40	0.065–0.340	0.303–6.399	108.5	8.9
	100	222.50–677.40	0.050–0.145	0.170–1.901	51.2	8.7
Butane[a]	25	74.50–587.20	0.214–0.974	0.180–0.974	50.5	17.8
Perfluoropropane	25	68.20–878.70	0.078–0.413	0.996–2.220	121.1	1.9
Dibromodifluoromethane (all data)	25	76.75–561.85	0.160–1.300	0.685–46.400	88.4	42.7
(Data below a monolayer)	25	76.75–365.00	0.160–0.650	0.685–8.070	83.7	12.8

[a] Data from thesis of Muzzi.[9]

Figure 5 depicts the term WL, as calculated from eq. 14 using the experimentally determined values of D, as a function of temperature.[18] This, in turn, reflects the temperature dependence of the mean "jumping distance," L, or λ (eq. 10). Since energy barrier effects have already been accounted for by eq. 7–9, one would expect L to be nearly independent of temperature in view of the comparatively small effects of temperature on intermolecular force parameters. Assuming the exponential temperature dependence suggested by Fig. 5, one does obtain, for the two hydrocarbons studied, a fairly low "activation energy" of 2.7 kcal./mole.

The experimental results are thus seen to confirm the primary arbitrary assumptions made in eq. 9 and 10 to a high degree, as well as the general model used. The variety of adsorbates used in the present study suggests some general applicability of the model in this respect, but further studies, employing other adsorbents, are clearly required. Turning to literature data which might be used to extend this test of the model was not very productive: only three sets of reliable data are available which include measurements of the isotherms and which are given in enough detail to enable reasonable estimates of all of the terms. Those of Rutz and Kammermeyer[5] are almost entirely restricted to surface coverages well in excess of a monolayer, and hence would not be expected to apply. The data published by Carman and Raal[8,19] on a wide variety of systems appear to follow the predicted trends at coverages below a monolayer, but a more precise statement is prohibited by the accuracy with which data points may be taken from the small scale figures.

Under conditions of a unimolecular surface coverage, the observed transport rates of the adsorbed molecules were generally about three times as great as the concomitant gaseous (Knudsen) diffusion rates. Obviously, these adsorbed transport rates may represent major contributions to the total flux, and are not negligible. From the viewpoint of potential applications to the behavior of transport-controlled solid catalyzed reactions, the data for propylene may be especially significant: the 100° data reveal that the transport rates in the adsorbed phase, at coverages of about a quarter of a monolayer, are of the same mag-

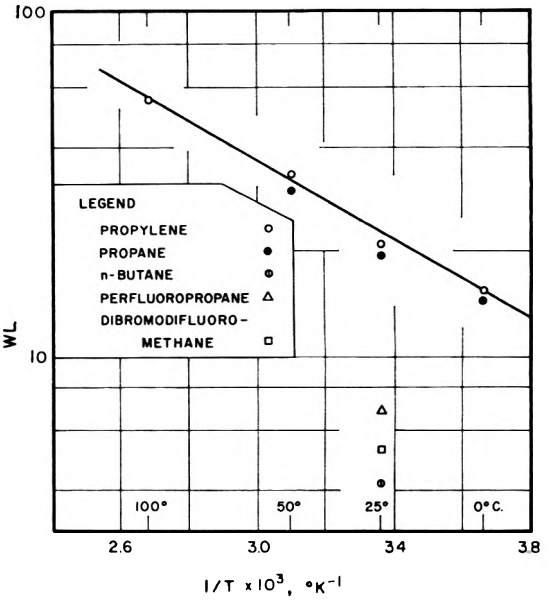

Figure 5. Temperature dependence and comparison of absolute values of the single arbitrary constant (eq. 14).

(18) The ordinate is expressed in units of g./(cm. sec. °K. mmoles)$^{1/2}$ multiplied by 10^3.

(19) P. C. Carman and F. A. Raal, *Trans. Faraday Soc.*, **50**, 842 (1954).

nitude as the flux of nonadsorbed molecules even at a temperature level slightly above the critical. Obviously, significant fluxes may be possible under the conditions used to carry out catalytic reactions; in this sense the present study complements recent data on adsorption equilibrium characteristics of hydrocarbons at high temperature levels.[20]

The *a priori* prediction of the transport rates in adsorbed layers requires an ability to predict the WL values of Fig. 5. These presumably vary in some inverse manner with the strength of the adsorbate–adsorbent bonds; recent studies of ethanol on alumina,[16] in which very strong bonds are formed, revealed no transport whatever of the adsorbed molecules. Thus, the differences among the several systems studied are as expected qualitatively; further studies are obviously necessary to determine the desired quantitative relationships.

Conclusions

The transport rates of adsorbed molecules through microporous solids such as employed in catalysis and adsorption operations are large and cannot be neglected (in comparison to concomitant Knudsen diffusion rates) under conditions of general interest, including temperature levels above the critical temperature of the adsorbate. In fact, in this study the surface transport rates exceeded those of Knudsen diffusion whenever the surface coverages exceeded about one-fourth to one-half of a unimolecular layer.

A model, based on the hypothesis of nearly complete desorption of the mobile molecules on the solid surface, followed by random "jumps" to nearby available surface sites, is shown to lead to an excellent prediction of the trends shown by the experimental results obtained using five different gases under the conditions of primary interest in catalysis, *i.e.*, less than unimolecular surface coverage. Further studies are required to determine the true generality of the proposed equations and to develop, if possible, means for the *a priori* prediction of the one arbitrary parameter of the model.

Acknowledgment. The authors wish to acknowledge with thanks the financial support of the National Science Foundation and of the Petroleum Research Fund of the American Chemical Society; the helpful assistance of their colleagues, J. A. Weaver and B. M. Muzzi; and the donation of the alumina catalyst support pellets by the Harshaw Chemical Company.

(20) P. E. Eberly, Jr., *J. Phys. Chem.*, **65**, 68 (1961); **66**, 312 (1962).

Surface Diffusion of Hydrogen on Carbon

by Andrew J. Robell, E. V. Ballou,

Lockheed Missiles & Space Company, Palo Alto, California

and Michel Boudart[1]

University of California, Berkeley, California *(Received March 18, 1964)*

The slow uptake of hydrogen on platinized carbon is due to activated diffusion of adsorbed hydrogen atoms away from platinum centers which chemisorb molecular hydrogen rapidly. The phenomenon has been studied both with hydrogen and deuterium, between 300 and 392°, from 30 to 60 cm. of pressure on carbon samples containing 0.2 and 1% platinum by weight.

Introduction

Physical adsorption of nitrogen is used routinely in the determination of the total surface area of porous adsorbents and catalysts. To determine the surface area of specific components, *e.g.*, metals dispersed on an oxide support, it is sometimes possible to use selective chemical adsorption. For instance, the surface area of platinum supported on alumina can be measured by means of chemisorption of hydrogen on the platinum component of the catalyst.[2]

In this particular example, the success of the method relies on the fact that hydrogen after adsorption on the platinum sites is apparently unable to migrate on the nonmetallic sites of the support so that, at selected temperatures and pressures, a one-to-one correspondence seems to prevail between exposed platinum atoms and adsorbed hydrogen atoms.

This condition was found to fail for a particular system studied in our laboratory. The total number of hydrogen atoms taken up by a platinum–carbon sample exceeded considerably the sum of two numbers: first, the number of hydrogen atoms taken up by the same weight of carbon sample in a separate measurement at identical pressure and temperature, and second, the number of hydrogen atoms equal to the total number of platinum atoms in the platinum–carbon sample.

Clearly, this observation suggests that a rather large fraction of the adsorbed atoms, after adsorption on the platinum sites, migrate to the carbon surface. A search of the literature revealed that the same phenomenon was reported in 1933 by Burstein, Lewin, and Petrow,[3] who proposed the same interpretation. However, this explanation was later contested by Roginskii.[4]

In order to elucidate the nature of the phenomenon further, it was decided to study systematically the adsorption of hydrogen on platinum supported on pure carbon. The effect of temperature, pressure, and amount of platinum on the rate of adsorption of hydrogen and deuterium on platinized carbon is reported and discussed in this work.

Experimental

The carbon selected was Spheron 6, a high purity channel black made by the Godfrey Cabot Corp., consisting of almost spherical nonporous particles, 150 Å. in radius, with a B.E.T. nitrogen surface area of 100 m.²/g. Samples containing 0.2 and 1.0 wt. % platinum were prepared by impregnation of the carbon with chloroplatinic acid.

The amount of hydrogen adsorbed as a function of time at a constant pressure and temperature was measured volumetrically in an apparatus of standard design. Hydrogen and deuterium were purified by diffusion through palladium. Samples contained in quartz cells were reduced in flowing hydrogen at 500°

(1) Stanford University, Stanford, Calif.

(2) L. Spenadel and M. Boudart, *J. Phys. Chem.*, **64**, 964 (1960).

(3) R. K. Burstein, P. Lewin, and S. Petrow, *Physik. Z.*, **4**, 197 (1933).

(4) S. Z. Roginskii, "Adsorption and Catalysis on Heterogeneous Surfaces," Moscow, 1948, p. 329.

and evacuated at 900° prior to and between the adsorption runs. Results are expressed as STP cm.³ of molecular hydrogen taken up per gram of sample.

After an adsorption run at 350°, gases were pumped out at temperature and analyzed: no more than 0.2% methane was found.

Results

A typical run is shown in Fig. 1. It is seen that the amount of hydrogen taken up after 50 min. exceeds by about 1 cm.³ the sum of two quantities: the amount taken up by the carbon sample without the metal and the amount corresponding to one hydrogen atom adsorbed for each platinum atom in the sample with the metal. This is the principal observation that was found in all the work described here. In what follows, we shall designate by "net adsorption" the amount adsorbed on a platinum carbon sample minus that adsorbed on the carbon blank alone.

The effect of pressure on the net adsorption is illustrated in Fig. 2. Such studies showed that the net amount adsorbed at a given time increases as the square root of the hydrogen pressure, p.

Net adsorption also increases with temperature (Fig. 3). From such data, an apparent activation energy, E, can be calculated. It is found to be about 8 kcal./mole (see Fig. 4).

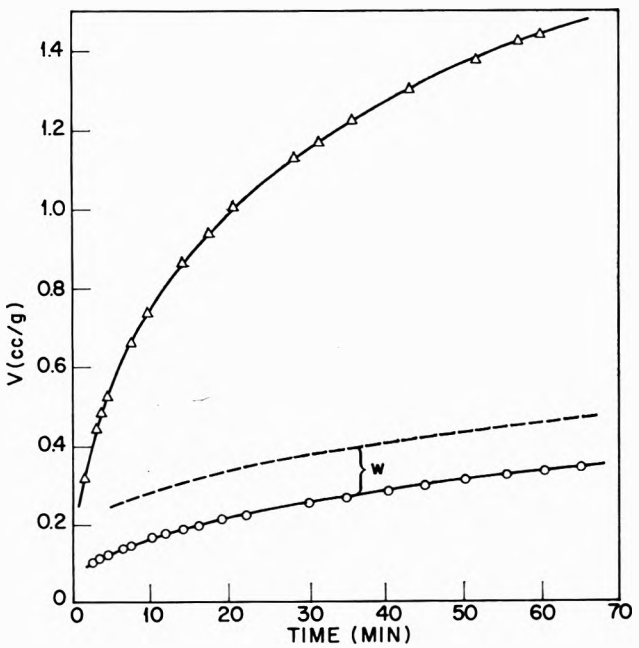

Figure 1. Volume (STP cm.³/g.) of hydrogen adsorbed as a function of time, at 350° and 60 cm.: O, Spheron 6; Δ, Spheron 6 + 0.2% Pt; w, adsorption of hydrogen corresponding to one hydrogen atom per platinum atom (calculated).

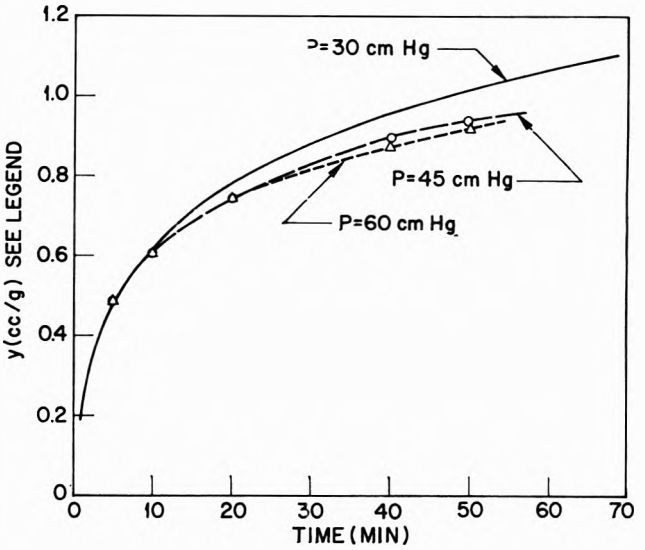

Figure 2. Effect of pressure on net adsorption of H_2: data at 300° on 1% Pt sample. Continuous curve, experimental values at 30 cm.; O, values at 45 cm. multiplied by $(30/45)^{1/2}$; Δ, values at 60 cm. multiplied by $(30/60)^{1/2}$.

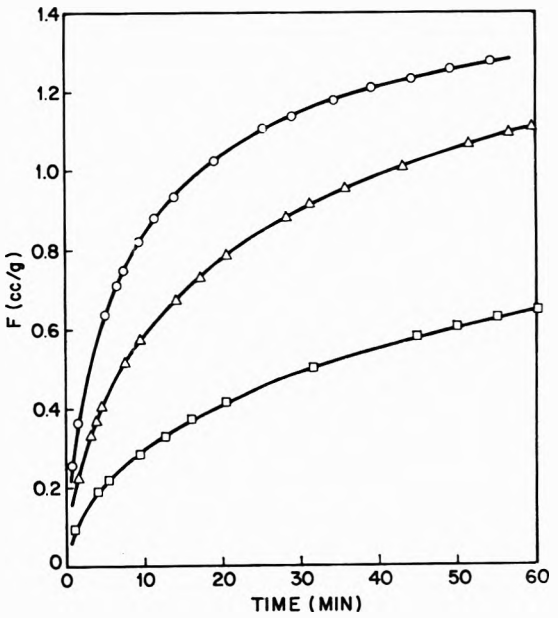

Figure 3. Effect of temperature on net adsorption of H_2: data at 60 cm. on 0.2% Pt sample: □, 300°; Δ, 350°; O, 392°.

Increasing the amount of platinum by a factor of five also increases the net adsorption by a factor of less than five (Fig. 5). At later times especially, the sample with the higher content of platinum exhibits an apparent saturation although the percentage of the total carbon surface which is covered by hydrogen does not

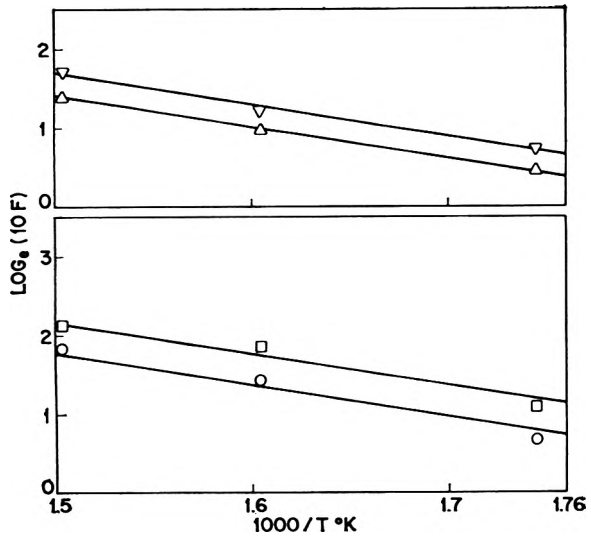

Figure 4. Determination of apparent activation energy E: values of net adsorption F of H_2 at various times t (min.) and pressures p (cm.): ▽, t = 10, p = 30; △, t = 5, p = 30; □, t = 10, p = 60; ○, t = 5, p = 60.

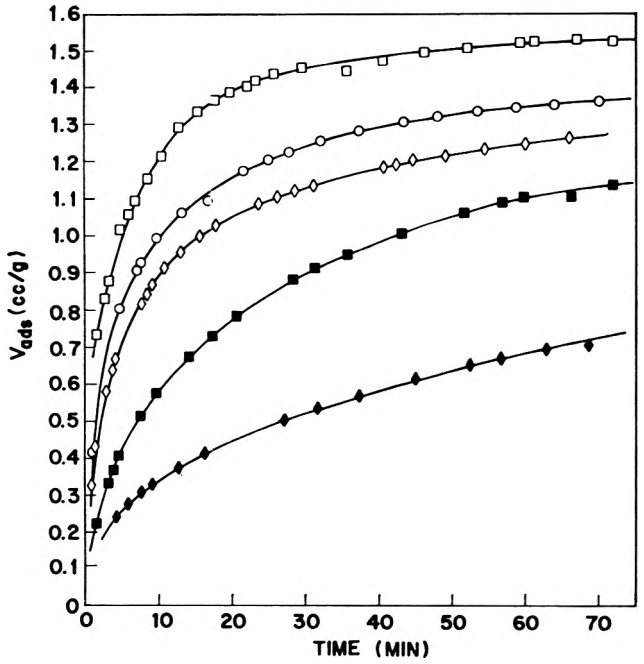

Figure 5. Effect of amount of platinum on net adsorption of H_2 at 350°. On 1% Pt: □, p = 60 cm.; ○, p = 45 cm.; ◇, p = 30 cm. On 0.2% Pt: ■, p = 60 cm.; ◆, p = 30 cm.

exceed about 1%. This apparent saturation becomes noticeable at high platinum contents, long times, and high temperatures and pressures, all favoring a large net adsorption.

Finally, the kinetic isotope effect shows distinctly that the nature of the net adsorption is different from

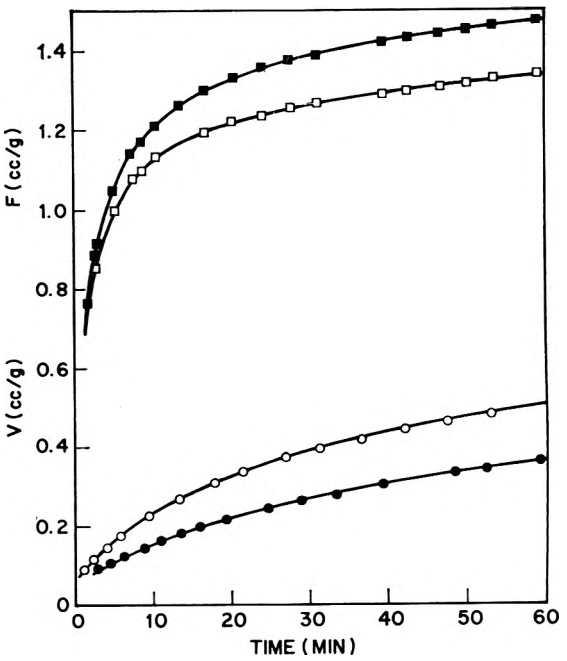

Figure 6. Kinetic isotope effect at 392° and 30 cm. Adsorption on carbon: ○, H_2; ●, D_2. Net adsorption on 1% Pt sample: □, H_2; ■, D_2.

that of direct adsorption on the carbon blank (Fig. 6). Indeed, hydrogen is adsorbed faster than deuterium on the pure carbon samples, but the reverse is true for the net adsorption on platinized carbon. Although these data do not warrant a detailed analysis, they are compatible[5] with the idea of activated adsorption of molecular hydrogen on pure carbon (with a normal kinetic isotope effect) and of activated diffusion of atomic hydrogen on the sample containing platinum (with an inverse kinetic isotope effect).

Discussion

All the data indicate that hydrogen molecules are adsorbed rapidly on platinum sites and then diffuse slowly away from them. It will now be assumed that the activated slow process is surface diffusion and not bulk diffusion. This assumption is supported by the apparent saturation occurring at relatively low values of surface coverage. This apparent saturation would be even more difficult to understand if the slow uptake were due to diffusion into the interior of the carbon particles. Furthermore, absorption of hydrogen in carbon has never been reported.

An attempt will now be made to explain the data quantitatively. Let us assume that the surface of carbon is covered with a certain number (n per gram)

(5) J. Bigeleisen, *J. Chem. Phys.*, 17, 675 (1949).

of identical active zones associated with the platinum centers. Each zone is covered with hydrogen atoms in equilibrium with gaseous molecular hydrogen. Let the surface concentration of hydrogen atoms on each zone be c_0 (number of atoms/cm.^{2}). The value of c_0 depends only on temperature and pressure and does not depend on time during an adsorption run.

It is already apparent that the rate of net adsorption will depend on pressure through c_0. It will be seen later that it must be proportional to c_0. Therefore (Fig. 2), c_0 must be proportional to $p^{1/2}$. This pressure dependence indicates dissociative adsorption in the low coverage region (Henry's law). But studies of adsorption of hydrogen on platinum[2] suggest that the surface of platinum ought to be almost completely covered with hydrogen at least at the lower temperature and higher pressure used in this work. Therefore, we are led to the hypothesis that the equilibrated zone serving as the source for surface diffusion consists of platinum centers surrounded by carbon centers. We now have to deal with a carbon zone in equilibrium with gaseous hydrogen, the rapid equilibration being brought about by the platinum centers.

The rapid equilibration also suggests that hydrogen atoms are rather freely mobile on the equilibrated carbon zone. By contrast, the rate of diffusion of hydrogen on the carbon surface surrounding the equilibrated carbon zone is very slow, as indicated by the data. This situation can be understood if the equilibrated carbon zone consists of basal planes of the graphite structure, whereas the surrounding carbon surface consists of more amorphous regions with a carbon–carbon distance more characteristic of the distance (3.4 Å.) between the basal planes in the graphite structure (Fig. 7).

Thus we shall assume that the jump distance, d, on the carbon surface surrounding the carbon equilibrated zone is equal to 3.4 Å. Now, for the coefficient D of activated surface diffusion, we use the Einstein type of expression

$$D = \frac{d^2}{4} \nu e^{-E_a/RT} \qquad (1)$$

where E_a (kcal./mole) is the activation energy for surface diffusion and ν is a frequency which, in the absence of further information, will be taken as equal to 10^{13} sec.$^{-1}$.

With this picture in mind, we can write down and solve the differential equation for surface diffusion away from a constant circular source of radius a. The solution adapted from the analogous problem for heat transfer[6] is shown in Fig. 8. In this doubly logarithmic plot, the abscissa is a dimensionless time

$$\tau = \frac{Dt}{a^2} \qquad (2)$$

The ordinate is a dimensionless amount of diffused particles at time t

$$\Phi' = \frac{2F'}{c_0 a} \qquad (3)$$

where F' is expressed in number of atoms having diffused at time t/cm. of source perimeter.

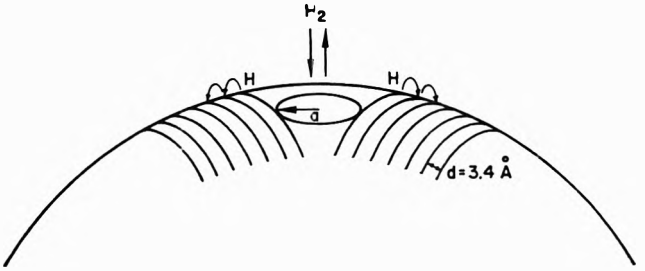

Figure 7. Equilibrated adsorption on zone of radius a followed by surface diffusion.

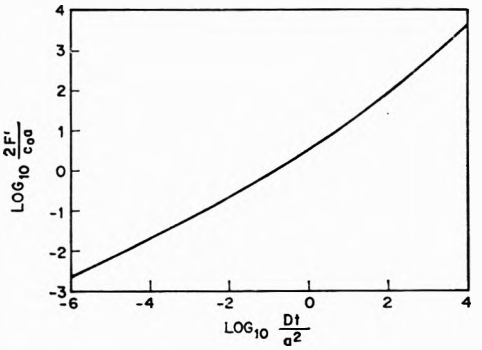

Figure 8. Solution of the diffusion equation; dimensionless plot of amount diffused *vs.* time.

As can be seen in Fig. 8, the relation between log Φ' and log τ is linear in a restricted interval of dimensionless times. The data obtained on the 0.2% Pt samples can also be represented in a doubly logarithmic plot (Fig. 9) and the logarithm of the net amount F taken up at time t is proportional to the logarithm of time t. The slope, at least at short times, not larger than 10 min., is 0.6. The corresponding region of interest in Fig. 8 is therefore that which can be approximated by a straight line of slope equal to 0.6. This happens for $-2 \lesssim \log \tau \lesssim 1.3$. In this region therefore

$$\log \Phi' = 0.6 \log \tau + \text{constant} \qquad (4)$$

(6) H. S. Carslaw and J. C. Jaeger, "Conduction of Heat in Solids," Oxford University Press, London, 1959.

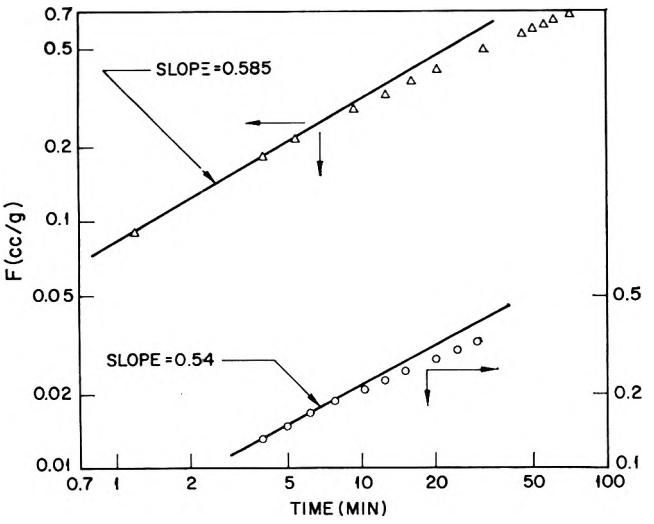

Figure 9. Net adsorption of H_2 at 300° on 0.2% Pt sample: △, p = 60 cm.; ○, p = 30 cm.

Since Φ' is proportional to F' and the latter is proportional to F, substitution of (2) and (3) into (4) gives

$$F \propto c_0 D^{0.6} \tag{5}$$

Thus, as stated earlier, the amount adsorbed at time t is proportional to c_0 and thus also to $p^{1/2}$ for adsorption with dissociation at small coverage. The value of c_0 depends exponentially on temperature

$$c_0 = c_0' \exp(q/2RT) \times p^{1/2} \tag{6}$$

where q is the exothermic heat of adsorption of hydrogen on the equilibrated zone, in kcal./mole.

From the measured temperature dependence of F, we get by substitution of (1) and (6) into (5)

$$E = 0.6E_a - 0.5q = 8 \text{ kcal./mole} \tag{7}$$

However, E_a and q are related. Indeed, the activation energy for surface diffusion is expected to be a certain fraction $\alpha (0 < \alpha < 1)$ of the strength s of the bond between the diffusing species and the surface

$$E_a = \alpha s \tag{8}$$

The heat of adsorption, q, is also related to s

$$q = 2s - 104.2 \tag{9}$$

where 104.2 stands for the dissociation energy of molecular hydrogen.

Substitution of (8) and (9) into (7) gives

$$0.6\alpha s + 52.1 - s = 8 \tag{10}$$

A choice has now to be made for α. This choice is in turn influenced by the assumed value of the radius a of the source. The latter will be taken to be equal to 10 Å. A smaller value would be meaningless. A larger value, say 50 or 100 Å., would lead to serious difficulties because the total area of equilibrated zones would correspond to a large amount of hydrogen taken up instantaneously. This is not observed.

Then, if $\log \tau = \log Dt/a^2$ must remain smaller than 1.3 for t = 10 min. and a = 10 Å., and if we use (1), we see that α must be larger than or equal to 0.58. We shall take α = 0.58 because larger values lead to correspondingly smaller values of the diffusivity, D, which in turn necessitate unreasonably large values of n, the number of diffusion sources, required to fit the data.

With α = 0.58, as will be seen, D already is quite small at the temperatures of the experiments. With this value, eq. 10 gives s = 67.7 kcal./mole.

Therefore, E_a = 39.2 kcal./mole from (8), and q = 31.2 kcal./mole from (9).

With E_a = 39.2 and the assumed value of the jump distance d = 3.4 Å., eq. 1 gives $D = 3.4 \times 10^{-19}$ and 5.8×10^{-17} cm.²/sec. at 300 and 392°, respectively.

Before adsorption curves can be calculated, two more parameters have to be chosen. One is the coefficient of proportionality c_0' in eq. 6. This will be chosen as large as possible because if it were small, a larger value of the number n of sources would be required to fit the data. The largest value of c_0' believed to be reasonable is that which gives $c_0 = 10^{15}$ at the experimental conditions of highest coverage, 300° and 60 cm. of pressure. This value of c_0 corresponds to 10% surface coverage on the equilibrated carbon zones and it is recalled that a condition of small coverage for these zones is required by the pressure dependence of the data.

The final parameter is n, the number of diffusion sources; it is a "scaling factor" and will be used to fit observed data. It is chosen equal to 3.16×10^{17} for the samples containing 0.2% platinum. This is a reasonable figure. Indeed, if platinum atoms were atomically dispersed on carbon, n would be equal to 6×10^{18}, but a large fraction of the metal was shown by X-ray diffraction to be present as particles of 80 Å. average diameter. The number of these, if all the platinum were accounted for by these particles, would be 2.8×10^{14}, a value about 1/1000 of that required if these crystals had to play the role of diffusion sources.

The assumed values are summarized in Table I. As discussed above, these values are suggested by the physical picture of the process. They are reasonable values and there is surprisingly little leeway in their choice as was emphasized during the discussion.

Table I: Assumed Values for the Calculation of Surface Diffusion

Quantity	Symbol	Value
Jump distance	d	3.41 Å.
Frequency	ν	10^{13} sec.$^{-1}$
Radius of diffusion source	a	10 Å.
Coefficient of proportionality	α	0.58
Adsorption at 300° and 60 cm.	c_0	10^{15} atoms/cm.^{2}
Number of diffusion sources	n	3.16×10^{17}

It can be seen from Table II that, with those values, a good agreement is obtained between calculated and experimental amounts of hydrogen adsorbed. In other words, the explanation in terms of surface diffusion can be quantitative. At higher temperatures and longer times, calculated values are systematically higher than experimental values. This effect of "saturation" has been mentioned earlier. It may be due to an interference or overlap between diffusion zones which have been assumed to be separated and independent.

Conclusion

Qualitatively and to a certain extent quantitatively, the uptake of hydrogen by platinized carbon can be interpreted successfully in terms of surface diffusion. Although it has been possible to propose a value of the surface diffusion coefficient, a quantitative treatment of the data is made very difficult by the number of parameters of the problem. Although there may be other cases where slow adsorption can be explained by surface diffusion from or to active centers, a quantitative explanation may prove even more difficult than for the very favorable case of platinized carbon considered in this investigation. In the determination of surface areas by selective chemisorption, the phenomenon may be quite troublesome.

Table II: Comparison between Calculated and Experimental Amounts of Hydrogen Diffusion on 0.2% Platinum Sample

Temp., °C.	Pressure, cm.	Time, min.	Amount of surface diffusion, cc. of H_2 (STP) Calcd.	Exptl.
300	60	5	0.15	0.21
		10	0.22	0.29
		50	0.59	0.60
	30	5	0.10	0.15
		10	0.15	0.21
		50	0.41	0.39
350	60	5	0.25	0.42
		10	0.35	0.58
		50	1.2	1.1
	30	5	0.18	0.26
		10	0.24	0.34
		50	0.87	0.64
392	60	5	0.49	0.63
		10	0.73	0.84
		50	2.5	1.3
	30	5	0.35	0.40
		10	0.52	0.55
		50	1.7	0.96 (est.)

Discussion

R. A. VAN NORDSTRAND (Sinclair Research Co., Houston). Have you studied the reversibility of this chemisorption? It seems that your mechanism consists of readily reversible steps, so that simply by dropping the hydrogen pressure to zero you should be able to desorb and follow the process using the same equations.

A. J. ROBELL. No, we have not studied the reverse process. The desorption kinetics would not be predicted by the same mathematical solution. The boundary conditions to the unsteady-state diffusion equation would be different; the source would be a two-dimensional field of varying concentration, and the sink a small area of essentially zero concentration.

We have noted that an instantaneous reduction in the hydrogen pressure during an adsorption run produces an immediate diminution in the rate of net adsorption, as predicted from our model.

J. W. E. COENENS (Unilever, Netherlands). In general I understand your wanting to "correct" your experimentally observed adsorption on platinum–carbon by subtracting the amount of gas adsorbed on carbon alone, but should it not be borne in mind that we are primarily concerned with the direct experimental observation, rather than with a subtraction of the two? This is especially important in the case of the kinetic isotope effect. You actually did appear to observe such an effect with carbon but you found no effect on the carbon-supported platinum. But it seems to me that you cannot say that the kinetic isotope effect is reversed, although your observation is still significant enough.

A. J. ROBELL. The experimental facts are as follows: on the carbon alone, hydrogen adsorbs faster than deuterium; on the platinized carbon, hydrogen and deuterium adsorb at essentially the same rate. Thus, "net" adsorption, as it is defined here, proceeds at a faster rate with deuterium than with hydrogen.

The point that I wish to bring out here with these observations is the following: the "normal" kinetic isotope effect, *i.e.*, the one in which hydrogen is faster than deuterium, observed in direct adsorption with carbon alone is not observed when platinum is dispersed on the carbon. This implies a different rate-controlling process.

Phase Transformations of Water in Porous Glass

by A. A. Antoniou[1]

Division of Applied Chemistry, National Research Council, Ottawa, Canada *(Received February 26, 1964)*

The system porous glass saturated with respect to water was studied in the temperature range +2 to −40°. Calorimetric measurements with simultaneous observations on length changes revealed that two kinds of transformations took place at different temperatures below the normal melting point of bulk water. The amount of water that did not transform when this system was cooled to about −40° is shown to correspond to approximately three monolayers. The experimental results suggest that the adsorbed water in porous glass even in the middle of the capillaries has a different state from that of bulk water, and it is concluded that the observed depression of the freezing point should be considered in terms of the different structure the adsorbate acquires from that of the bulk state.

Introduction

One of the interests of the Division of Building Research, National Research Council, Canada, is the action of frost in porous building materials, such as concrete, which is a consequence of the climatic conditions prevailing in this country. This problem is in essence the behavior of adsorbed water in porous materials at temperatures below the normal freezing point of bulk water. It is well known that the adsorbed water behaves differently from bulk water in that it shows a depression of its freezing point. Other adsorbates besides water also exhibit a similar behavior; such a study, therefore, could throw some light on the state of the adsorbed phase.

A variety of techniques have been used to study the phase changes occurring in the adsorbates: vapor pressure measurements,[2] dilatometric techniques,[3a] calorimetric methods,[3b,4] and observance of dielectric behavior.[5] In most of this work the depression of the freezing point below the normal one has been related to the existence of menisci, and thus the Kelvin equation has been used in combination with the Clausius–Clapeyron equation, pointing to a unique freezing point depending on the radius of the capillaries. The calorimetric methods used were based on the observance of the temperature change of the system under investigation, while a constant rate of heating was maintained. It is shown in the present work, however, that with this type of calorimetric method equilibrium conditions cannot be achieved.

Hodgson and McIntosh[6] studied the phase changes of water and benzene in porous glass at different degrees of saturation and found the existence of a range of temperatures at which water transforms from one state to another. At about −22° they observed an increase in volume when the system porous glass–water was cooled, and they concluded that a phase transformation occurs at about this temperature.

Since the system porous glass–water has been most extensively studied and since the results obtained by Hodgson and McIntosh were not conclusive, it was decided to study the same system, but at a state at which it is saturated with respect to water. Two parameters, length changes and heat measurements, have been measured, both at the same time. To the writer's knowledge simultaneous measurement of these two parameters has not been reported until now.

Two samples of porous glass have been studied. Although they belonged to the same batch of glass supplied by the Corning Glass Works, they exhibited different B.E.T. surface areas, and showed similarities as well as differences in their behavior. These are

(1) Formerly Inorganic Materials Section, Division of Building Research, National Research Council, Ottawa, Canada.

(2) B. R. Puri, Y. P. Myer, and D. D. Singh, *Trans. Faraday Soc.*, 53, 530 (1957).

(3) (a) I. D. Jones and R. A. Gortner, *J. Phys. Chem.*, 36, 387 (1932); (b) W. A. Patrick and W. A. Kemper, *ibid.*, 42, 369 (1938).

(4) Y. J. Iwakami, *J. Chem. Soc. Japan, Pure Chem. Sect.*, 80, 1094 (1959).

(5) I. Higuti and M. Shimizu, *J. Phys. Chem.*, 56, 198 (1952).

(6) C. Hodgson and R. McIntosh, *Can. J. Chem.*, 38, 958 (1960).

described and the information derived is discussed below.

Experimental

Calorimeter Assembly. The calorimeter used in this investigation is of an adiabatic type and is shown schematically in Fig. 1. It will be described in more detail later. The two principles upon which adiabatic calorimeters are constructed have been employed, *i.e.*, the space surrounding the container in which the sample under investigation is enclosed is evacuated and the container is surrounded by an adiabatic shield which is kept at all times at the same temperature as the calorimeter, within a few thousandths of a degree. The container in which the sample is placed will be referred to in this paper as "the calorimeter" and the shields, together with the calorimeter, "the calorimeter assembly." It is not strictly adiabatic because during measurements taken when heating the sample, the whole assembly had a constant rate of cooling. This was achieved by maintaining the temperature of the bath in which the calorimeter assembly is immersed, lower by 3° than the temperature of the calorimeter. This rate of cooling was found necessary because the process occurring during the heating of the sample is an endothermic one. The novel feature of this calorimeter is the incorporation of a window to allow length measurements to be taken together with heat measurements, using an extensometer which will be described later. The same calorimeter assembly but with a thermal shunt of copper turnings between the shield and the outer vessel was also used to measure heat capacities while cooling the sample.

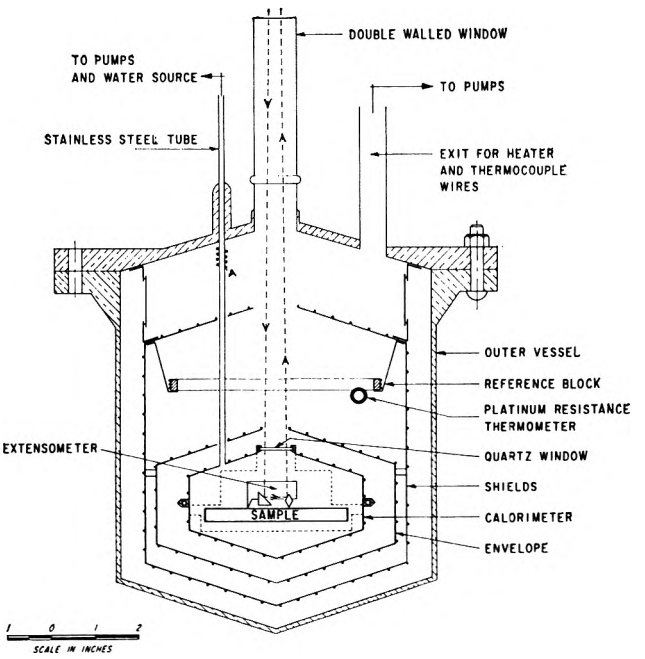

Figure 1. The calorimeter assembly.

The temperature was measured with a platinum resistance thermometer, capsule type, made by Leeds and Northrup Inc., No. 1531634, and was calibrated by the National Research Council, Canada. This capsule was attached thermally to the reference block. The resistance of the platinum resistance thermometer was measured with a G-2 Mueller bridge. The temperature difference between this block and the calorimeter was detected by a five-junction thermopile, which integrated the temperature of the surface of the calorimeter. This temperature difference was read by a Keithley millimicrovolt meter to 1×10^{-3}°.

The reference block where the platinum resistance thermometer is attached, the upper end "A" of the stainless steel tube, and the adiabatic shield were kept at the same temperature as the surface of the calorimeter within a few thousandths of a degree. This temperature control was achieved by a system of differential thermopiles, which transmitted the effects of any imbalance of temperature between the two surfaces concerned to a sensitive galvanometer, which in turn activated a system of phototubes and relays. The existing temperature difference was recorded and was integrated with respect to time, and the heat exchanged between the two surfaces was thus calculated. Between runs, the temperature of the upper part of the stainless steel tube was kept higher than that of the calorimeter to avoid cold spots; the temperature of the calorimeter was kept constant within 0.1° by proper adjustment of the bath temperature and that of the adiabatic shield.

Extensometer. The extensometer used in this investigation, called the Tuckerman gage, was manufactured by the American Instrument Co., Inc. Its construction is based on the principle of the optical lever and has approximate dimensions of 2.5 cm. × 1.3 cm. × 1.3 cm. It was attached firmly to the sample by a stainless steel spring.

The extensometer's sensitivity, $(\Delta l)/l$, is 4×10^{-6} as calibrated by the manufacturer. This was reduced by a factor of two through loss of clarity due to the calorimeter windows in the light path.

The thermal coefficient of expansion of the extensometer was determined by calibrating it against a copper–tellurium alloy bar whose thermal coefficient of expansion was measured by the National Research Council, Division of Applied Physics.

To ensure firm attachment of the extensometer to the sample, the surface of the sample was roughened where the extensometer came in contact with it. It is believed that no accidental displacement of the extensometer relative to the sample occurred during measurements, because readings were consistent when the temperature remained constant overnight or during longer periods of a few days. Furthermore, the information obtained does not show any erratic behavior.

Gravimetric Balance. The sample was saturated with respect to water in a McBain type quartz balance, which was suspended in a long glass tube tapered at the lower end a little above the position where the sample was suspended. The part of the tube where the sample was suspended was immersed in a cold bath. In order to maintain the same temperature inside the part of the tube where the sample was suspended as that of the outside cold bath, helium was introduced and a platinum foil in the shape of a frustrum of a cone was placed on the tapered sides of the tube. This cone prevented convection currents from the lower to the upper part of the gravimetric tube which was at room temperature. The temperature of the cold bath was regulated with a Precision temperature controller manufactured by the Bayley Instrument Co. As a refrigerant, precooled glycol solution was circulated in a copper coil placed in the outer part of the cold bath, which was filled with acetone. The bath could be removed so that a heater could be placed around the glass at the height where the sample rested, and the latter could be heated to about 300° in an oxygen atmosphere to burn out any contaminants. The cathetometer was manufactured by the Precision Tool and Instrument Co. Ltd.

To avoid contamination of the surface of porous glass with grease, the top of the gravimetric tube was sealed with a neoprene O-ring. Hoke valves were also used instead of stopcocks. The gravimetric assembly, together with the cold bath surrounding it, could be disconnected from the evacuating train and rolled into a cold room kept at −10° where the sample was demounted from the quartz balance and placed in the calorimeter.

The System Porous Glass–Water. The adsorbent was porous glass (Vycor brand) No. 7930 manufactured by the Corning Glass Works. It was 96% SiO_2 with 3% B_2O_3. The glass was first evacuated in the gravimetric apparatus to a pressure of 1×10^{-4} mm., and was treated with oxygen at about 300°. During this treatment the glass changed color to dark brown and became clear when the organic contaminants were burned off. The samples were cut out of 0.5-cm. thick porous glass plate. Their approximate dimensions were 8 cm. × 1 cm. × 0.5 cm. The adsorbate was distilled water, degassed by repeated freezing and melting.

The behavior of two samples of porous glass cut from the same batch, but not from the same plate, is reported. At saturation the first sample adsorbed 21 weight % of water; the second, 24%. The total amount of water adsorbed in the first sample was 1.53 g. and 1.82 g. in the second.

Precision and Accuracy of Calorimetric Results. The precision of the calorimetric measurements taken during heating was 0.3% of the total heat capacity of the calorimeter with porous glass saturated with respect to water. The heat capacity of the adsorbed water amounted to only 5% of the above amount, and therefore the precision with which the adsorbed water was measured was 6%. To determine the accuracy of these measurements the heat capacity of an amount of sodium chloride equivalent in calories to the amount of absorbed water present in the system was determined under similar conditions; these values were found to be 5% higher than the ones reported by Morrison, *et al.*[7]

Procedure

Saturation of the Porous Glass with Respect to Water. Calorimeter Assembly. The saturation of the porous glass took place in the gravimetric tube at a temperature just above 0° after it had been evacuated and heat treated at 300°. When the weight of the adsorbed water reached a constant value within $\pm 5 \times 10^{-4}$ g./g. of glass, saturation was taken to be complete.

To prevent distillation of the water from the sample when its temperature was lowered, helium was introduced into the gravimetric tube to a pressure of 25 mm. and the temperature of the bath was lowered to about −10° at a rate of less than 2°/hr. Separate experiments were carried out with other samples saturated with respect to water in which the temperature was lowered to −25°. The purpose of these experiments was to find out the conditions under which the temperature of the sample could be lowered without any appreciable loss of water. This was important because the sample in the calorimeter had to be cooled to −40°. It was found that when exchange gas was present at the above-mentioned pressure and the above rate of cooling was not exceeded, the weight of the sample remained constant within ±0.3%.

The transfer of the sample from the gravimetric tube to the calorimeter, the mounting of the extensometer, and the assembly of the calorimeter were done in a cold chamber kept at about −10°. It was considered acceptable to expose the sample to the atmos-

(7) J. A. Morrison and D. Patterson, *Trans. Faraday Soc.*, 52, 764 (1956).

phere at this temperature after it was saturated with water since diffusion of any gases into the adsorbate at this state would be extremely difficult. The assembled calorimeter was placed in its bath which was kept at $-10°$ and was connected to the evacuating train.

To remove the air from the calorimeter, it was evacuated to a pressure corresponding to a relative humidity of approximately 0.7. Resaturation of the sample took place at the triple point of water using a degassed water source at the same temperature. Saturation was considered complete when no more heat of adsorption was evolved, when the vapor pressure of the sample measured on a butyl phthalate manometer corresponded to the vapor pressure of the bulk water at $+0.01°$, and when no more length changes occurred. During this process, the calorimeter was kept at a temperature not lower than $+0.01°$ in order to ensure that no condensation of bulk water occurred in it. Also to avoid cold spots along the stainless steel tube, its upper part was kept warmer than the calorimeter. Finally, dry helium was passed into the calorimeter, which was isolated from the rest of the evacuating train by closing the valve situated immediately after the stainless steel tube.

Length Changes. These measurements were taken with the extensometer as described in the temperature range of $+20$ to $-40°$. The change of temperature after each measurement was less than 1°, especially when transformations were observed. The rate of change of temperature was less than 4°/day, and even smaller at the temperatures at which transformations were accompanied by evolution or absorption of heat.

Calorimetric Measurements Obtained When Heating the System. Calorimetric measurements obtained when heating the system were taken at increments of temperature of less than 1° and at a rate of less than 2°/day, especially in the transformation range of temperature. The temperature increase after a certain heat input was determined by extrapolating the fore and after drifts, to the middle of the heating period. Particular attention was given to the rate of cooling in order that the fore-period would be exactly the same as the after-period. The time required for the calorimeter to obtain this predetermined rate of cooling, after a heat input, was found to vary from a few minutes, when no transformations took place, up to more than 4 hr. when transformations occurred and for an increment of temperature of only 0.5°. The rate of cooling was of the order of 15×10^{-3}°/hr. During these measurements, the temperatures of the upper part of the stainless steel tube, reference block, and adiabatic shield were controlled and the heat exchanged was determined so that the necessary corrections could be applied to the heat capacity information. In most cases, these corrections were smaller than the accuracy of the measurements.

Calorimetric Measurements Obtained when Cooling the System. In order to detect the range of temperatures when evolution of heat takes place while cooling the system, use was made of the first-order rate law

$$\frac{dT}{dt} = K(T_{as} - T) = \frac{k}{C}(T_{as} - T) \qquad (1)$$

where T is the temperature of the calorimeter at time t, T_{as} is the temperature of the adiabatic shield, k is a cooling constant, C is the heat capacity of the system together with the calorimeter, and $K = k/C$. T_{as} was kept lower than T by about 0.8° and was of course different for each run. During the measurements it was kept constant within ± 0.02°. Besides employing the thermal shunt made of copper turnings it was also found necessary to increase the pressure to a fixed value in the space surrounding the calorimeter in order to increase the rate at which heat was removed from the calorimeter.

The K value in (1) was determined experimentally at a temperature above the normal melting point of water when no transformations take place. The heat capacity of the calorimeter and the system C was calculated from data already determined during the heating of the system, and thus the k value was obtained. This constant was used to obtain the heat capacity data in the temperature range where transformations take place. Between runs the temperature of the calorimeter was maintained constant within 0.02°.

Results

Length Changes. Figure 2 shows the behavior of the first sample during a temperature cycle from -40 to 0°. Repetition with the same sample gave essentially the same results after the water had been partly desorbed by degassing and the sample was resaturated according to the procedure mentioned above. Figure 3 shows the behavior of the second sample cut from the same batch of porous glass, but at temperatures extending from -40 to $+20°$.

These two samples are distinguished by different B.E.T. surface areas, 94.5 m.²/g. in the first and 82.5 m.²/g. in the second. Both samples showed essentially the same behavior during warming as well as during the cooling process. The four sections distinguishable in the cooling process and the four sections observed during the warming process will be dealt with separately.

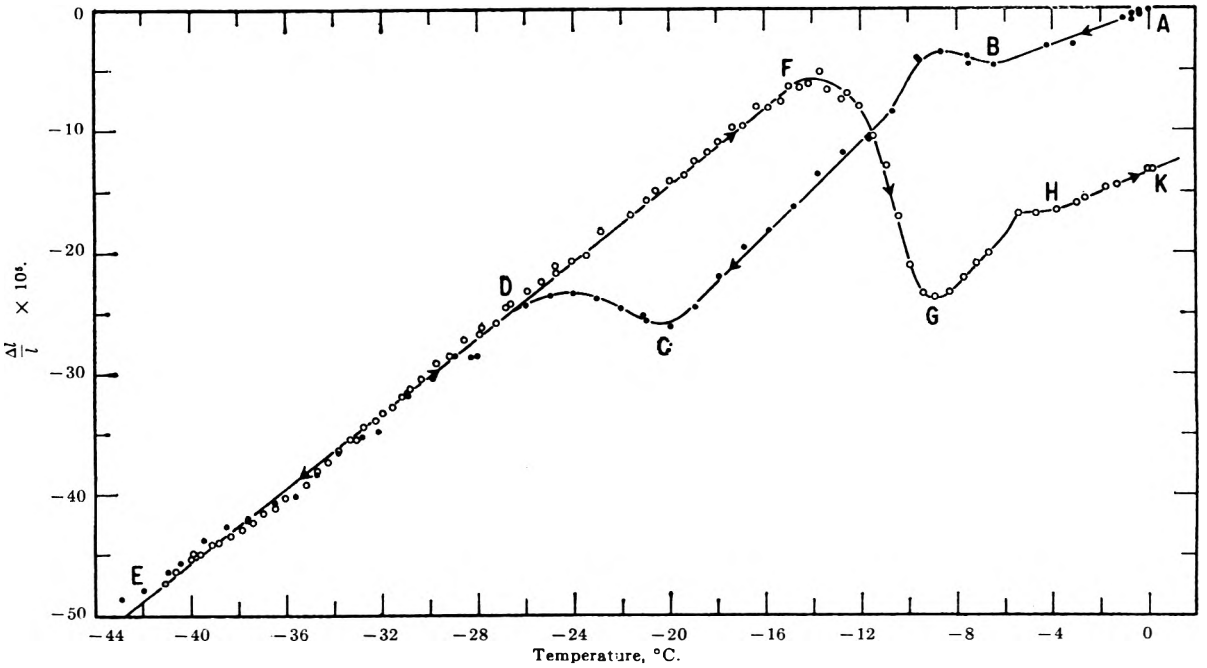

Figure 2. Porous glass saturated with respect to water, first sample. Length changes: ●, data obtained during cooling; O, data obtained during warming.

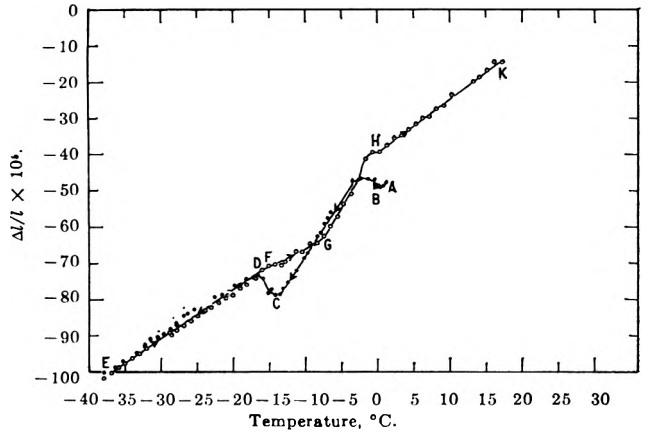

Figure 3. Porous glass saturated with respect to water, second sample. Length changes: ●, data obtained during cooling; O, data obtained during warming.

Section A–B. In Fig. 2 the sample contracts with a linear thermal coefficient of 7×10^{-6} deg.$^{-1}$ until it reaches $-7°$. In Fig. 3 measurements start just above 0° and the therma. coefficient cannot be determined. This cycle was repeated and a thermal coefficient of contraction of 5×10^{-6} deg.$^{-1}$ was found. These figures compare well with the linear thermal coefficient of expansion of porous glass evacuated with respect to water to a pressure of 1×10^{-4} mm., which was found to be 5×10^{-6} deg.$^{-1}$.

Section B–C. At approximately $-7°$ (Fig. 2) and at $-1°$ (Fig. 3) a small expansion occurs. This hump is not accidental. Litvan and McIntosh,[8] studying the behavior of porous glass partly saturated with respect to water by observing length changes, have noticed even more pronounced humps (expansions followed by contraction) in the same range of temperatures. The magnitude of these humps decreased with increasing water content the more saturated the porous glass was with respect to water. Following this small expansion the porous glass contracts with a higher linear coefficient of contraction, about three times the former value.

Section C–D. Between -20 and $-26°$ (Fig. 2) and between -14 and $-16°$ (Fig. 3), respectively, the two samples expand. The temperature range at which each sample expands was found to be reproducible when the temperature cycles were repeated. These expansions were studied for decrements of 0.5° or less and they were found to be gradual. In no case was a sudden expansion observed similar to the one which would be expected if a supercooled liquid transformed into a solid state.

Section D–E. The two samples contract below $-26°$ (Fig. 2) and below $-16°$ (Fig. 3), respectively, with a linear thermal coefficient of $15 \pm 1 \times 10^{-6}$ deg.$^{-1}$ in both cases.

Section E–F. Both samples expand when increasing the temperature from -40 to $-15°$ with approximately the same linear coefficient as for contraction.

(8) G. G. Litvan and R. McIntosh, *Can. J. Chem.*, 41, 3095 (1963).

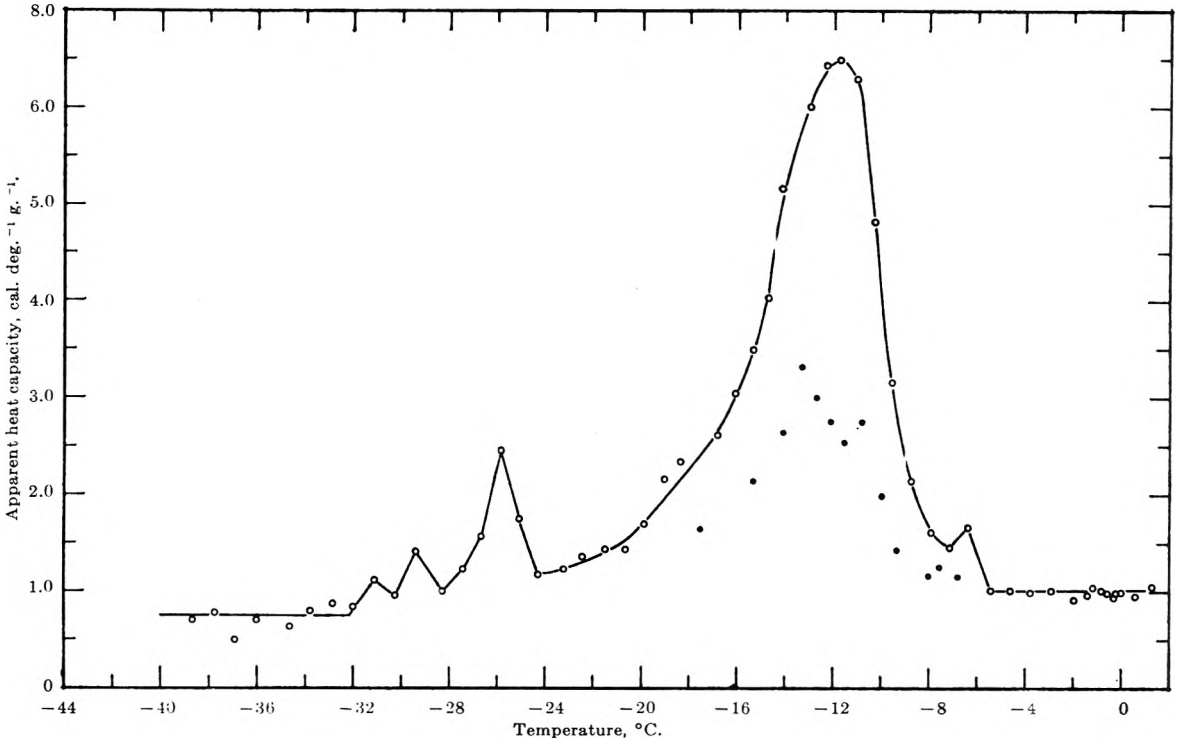

Figure 4. Porous glass saturated with respect to water, first sample. Apparent heat capacity of adsorbed water. For explanation of open and full circles refer to text.

Section F–G. A contraction is observed between −15 and −9° (Fig. 2) and a probable contraction superimposed on DG in Fig. 3 in the same temperature range. In the first case the absolute length of the sample after contraction was smaller than its length at the same temperature while cooling. In the second case, the contraction is more gradual, extends to a wider temperature range, and the absolute length of the sample after contraction is approximately the same as it was at the same temperature while cooling.

Section G–H. Upon further increase of temperature an expansion is observed (Fig. 2) for a short interval of temperatures up to −6° and for a wider range (Fig. 3) up to −1°. The slopes give 21×10^{-6} deg.$^{-1}$ for the first sample and 30×10^{-6} deg.$^{-1}$ for the second.

Section H–K. Above −5° (Fig. 2) and −1° (Fig. 3) the samples continue to expand but with a linear coefficient of expansion of 8×10^{-6} deg.$^{-1}$ in the first case and 15×10^{-6} deg.$^{-1}$ in the second.

Calorimetric Measurements Obtained when Heating the System. These were taken in the temperature range −38 to +2°. Three series of runs were obtained with the first sample of which the first one was of an exploratory nature; the other two were taken in more detail and accuracy and were accompanied by measurements of length changes. Nevertheless, all three depict the same general behavior, *i.e.*, an increase in the apparent heat capacity of the system in the same temperature range.

Figure 4 shows the observed "apparent heat capacities" for 1 g. of adsorbed water in porous glass, at saturation. The term apparent heat capacity is used because this quantity was calculated by subtracting from the total heat capacity observed, the heat capacity of the calorimeter and porous glass degassed to 1×10^{-4} mm. at room temperature. Under these conditions, of course, the glass was not completely degassed with respect to water.

Above −5° the points (open circles) fall on a straight line within the accuracy of measurements. It is reasonable to assume that no transformations take place in this region since the apparent heat capacity is constant and very close to unity. In all three sets of runs the heat capacity had leveled to this value at about −5°.

Between −32 and −5° the apparent heat capacity of the adsorbed water shows considerable variation and increase. There is a maximum at about −26° and another even more pronounced at about −12°. These two peaks were observed in the last two series of runs at the same temperatures.

Below −32° the heat capacities show values about a mean average of 0.8 cal. deg.$^{-1}$. Since the variation

is small, it is not known with certainty whether any transformations are involved in these temperatures.

The calorimetric results also show that the process of freezing and thawing is not reversible in the temperature range where transformations take place. This means that in performing a temperature cycle between two temperatures within the range -32 to $-5°$ the adsorbed water does not regain its initial state. This is seen in the calorimetric measurements during heating, by the smaller heat capacities when the initial temperature of the run was lower than the final temperature of the previous run by at least 0.1°. These measurements are shown in Fig. 4 by full circles. A similar observation has already been reported by Patrick and Kemper[3b] for the system silica and water. The specific heat of porous glass degassed with respect to water, as already mentioned, was found to be 0.16 cal. deg.$^{-1}$ at 0°.

Latent Heat of Transformation. It is assumed that, in the region of the increased apparent heat capacities, transformations take place and the increased value is due to the latent heat of transformation. The accompanying change in volume extending within this temperature range substantiates this assumption.

In order to determine the latent heat of transformation, the area under the curve between -32 and $-5°$ was calculated and the heat capacity of the adsorbed water and ice subtracted. The heat capacity of the ice and adsorbed water was determined by calculating the area under a straight line drawn between the heat capacity at $-5°$ and the heat capacity at $-32°$. This was considered a good approximation since the error involved would be very small compared with the number of calories representing the latent heat of transformation. Furthermore, the heat capacity of the "adsorbed ice" is not known. This area was found to represent 65.5 ± 0.5 cal. for 1.53 g. of adsorbed water in the two series of runs. In order to determine the amount of water which transformed from some sort of ice to some sort of liquid water, it is necessary to know the latent heat of fusion of "adsorbed ice" in porous glass at different temperatures. Such information is not available at present for water in porous glass or for other adsorbates. For this reason the value for the latent heat of fusion of bulk ice to bulk water was used and this was calculated at different temperatures by using eq. 2.[9]

$$\frac{d}{dT}\Delta H = \Delta C_p + \frac{\Delta H}{T} - \Delta H\left(\frac{\partial \ln \Delta V}{\partial T}\right)_p \quad (2)$$

As the last term on the right-hand side of eq. 2 was a very small quantity, it was omitted in the calculation. For the heat capacity of liquid water below 0° an extrapolated value was used and the heat capacity of bulk ice was also used for the "adsorbed ice."

The amount of water which transformed at each temperature was calculated by dividing the latent heat of transformation per increment of temperature, as determined experimentally, by the latent heat of fusion for the same temperature, calculated by the use of the eq. 2. The result is shown in Fig. 5. The amount of adsorbed water which transformed between -32 and $-5°$ is found thus to be about 55% of the total amount of adsorbed water. A simple calculation of the amount of water held by a monolayer in the porous glass reveals that, if the above assumptions are correct, the water which does not transform until $-40°$ is that held in approximately three monolayers on the surface of the porous glass.

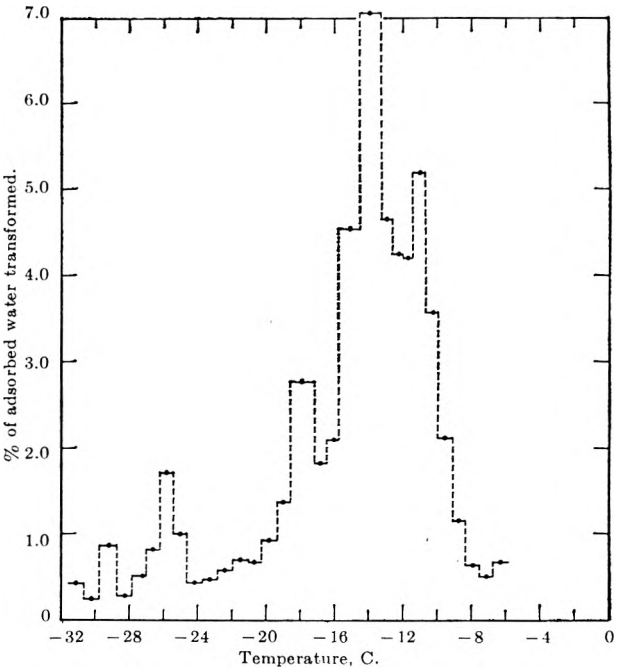

Figure 5. Porous glass saturated with respect to water, first sample. The per cent of adsorbed water transformed during heating per increment of temperature. Lines parallel to abscissa indicate temperature increment.

Calorimetric Measurements Obtained when Cooling the System. Figure 6 shows the calorimetric information obtained with the second sample when cooling the system. Only one series of runs was obtained and length measurements taken at the same time are shown in Fig. 3. They are the ones starting at +1.5° and ending at −38°. The heat data are reported in this case as the total apparent heat capacity

(9) E. A. Guggenheim, "Thermodynamics," 1959, p. 151.

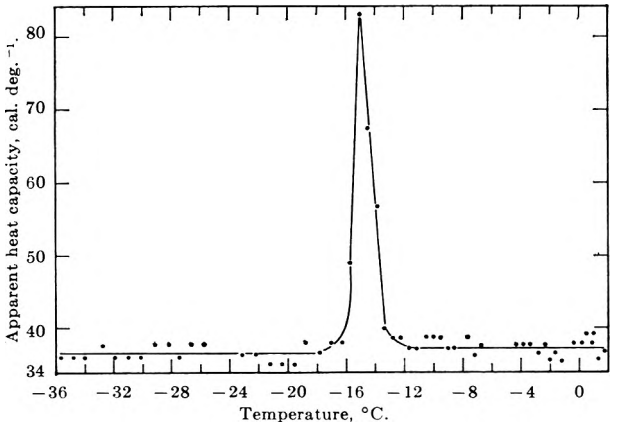

Figure 6. Porous glass saturated with respect to water, second sample. Apparent heat capacity of porous glass saturated with respect to water. The heat capacity of the calorimeter is included. Calorimetric data obtained during cooling.

of the system together with the calorimeter, because the accuracy is considerably lower than in the heating runs. It is seen that heat is evolved between −14 and −16° when at the same time the sample expands. No heat evolution which could be related to the latent heat of transformation is observed between 0 and −14° within the accuracy of these measurements. Again the area under the hump was calculated as before and this corresponded to an evolution of approximately 36 ± 5 cal./g. of adsorbed water. Water transformed was calculated as before using the $\Delta H(T)$ equation and it was found that 45 ± 7% of the adsorbed water was frozen.

Discussion

The phase transformations of water in porous glass have been observed during the process of cooling and heating in the temperature range from room temperature to −40° by observing length changes together with heat effects. This work shows that two kinds of transformations occur in this temperature region. The first one is not accompanied by a heat effect, occurs at temperatures just below the normal melting point of water, and becomes evident by the change of the linear coefficient of expansion. In this transformation the thermal coefficient of contraction or expansion passes through a maximum before returning to a normal value within a small range from 2 to 3°. Similar observations on the thermal coefficients have been observed for crystals which show a continuous transformation through a temperature range rather than a sharp transition. These transformations have been attributed to the coexistence of two different structures in the crystals.[10] Whether this explanation is a plausible one for the adsorbed water in porous glass remains to be seen.

The second kind of transformation occurs at lower temperatures than the one previously described, and extends over a range of temperatures. During freezing, the evolution of heat is accompanied by expansion; during thawing, there is an absorption of heat together with contraction. It is also observed that the length changes do not constitute the most reliable parameter for detecting phase changes occurring in porous materials. This is especially true during the thawing process. The same system, porous glass–water, but at relative humidities less than unity, has been studied by Hodgson and McIntosh[6] by observing the length changes with change of temperature. They showed that transformations occurred in a range of temperatures, and the general behavior of the system was the same as is reported here. The expansion during freezing was shown to occur at about −22°, but this temperature is not characteristic of this system as shown in the present paper. In addition, the first kind of transformations described above were not detected by them. Since there is no general agreement as to the nomenclature of the order or types of transformations,[10,11] and no information on compressibility for this system is available, no attempt is made here to classify these transformations.

Prediction of the Transition Temperature by the Kelvin Equation. The depression of the freezing point of the adsorbates has been attributed in the past to the different state the adsorbate acquires because of the existence of menisci. With this assumption, the Clausius–Clapeyron equation is combined with the Kelvin equation to yield the relationship[6]

$$\Delta T = 2T_f(\sigma_{lv}\bar{V}_l - \sigma_{sv}\bar{V}_s)/r\Delta H_{ls} \qquad (3)$$

Both the Clausius–Clapeyron and the Kelvin equations refer to a one-component system. Combination of the two equations presupposes the existence of equilibrium between vapor–liquid and solid. For a one-component system, there is only one temperature at which the three phases can coexist and this is the triple point of the macroscopic one-component system. If the adsorption forces do contribute in the freezing, in which case the situation is similar to the freezing of a macroscopic two-component system,[6] there is no term in eq. 3 to take care of the contribution of these forces. In addition, it has become certain that transformations occur within a range of temperatures.

Concluding Discussion. It is reasonable to assume

(10) A. R. Ubbelohde, *Quart. Rev.* (London), 11, 246 (1957).
(11) J. Jaffray, *Ann. Phys.* (N. Y.), 3, 5 (1948).

that the water that transforms during cooling or during warming of the sample is only the water found in the middle of the capillaries and not that adhering closely to the surface. This assumption is supported by the observations of Litvan and McIntosh[8] who studied the same system porous glass–water at different degrees of coverage by following length changes in the same temperature range as this work and they observed anomalies only at coverages higher than two monolayers. Morrison, Drain, and Dugdale[12] also observed increased heat capacities for the system nitrogen on titanium dioxide, again at coverages above the second monolayer. In addition, the observed differential heat of adsorption approaches very closely the heat of liquefaction after the completion of the second monolayer for most systems.

Further, it can be seen from the following observations that the water in the middle of the capillaries is not bulk water, *i.e.*, that it has properties different from bulk water. (1) The amount of water that transformed during heating above $-38°$, as calculated from the calorimetric results obtained during heating, amounts to 55% of the total adsorbed water in porous glass at saturation. This calculation shows that less than three monolayers of adsorbed water were unfrozen below $-38°$. A similar result is obtained from the calorimetric data of the cooling runs (within the accuracy of these results), for the amount of water frozen in the second sample.

On the other hand, the cubical expansion calculated from the observed linear expansion during cooling between -20 and $-26°$ in the first sample and -14 and $-16°$ in the second sample is 1.3×10^{-3} cm.^{3}/g. of adsorbed water, which would correspond to the approximate expansion of 0.014 g. of bulk liquid water when transformed into bulk ice. The observed contraction between -14 and $-9°$ in Fig. 3 during the heating runs will correspond to the melting again of 0.026 g. of bulk ice. Comparing these figures with those calculated from the calorimetric results, it is seen that the ratio of the amount of water transformed as calculated from the heating data to the amount transformed as calculated from the length changes is 40 in the first case and 20 in the second. Even though the assumptions which lead to this argument, *i.e.*, the calculation of ΔH as a function of temperature and the isotropic nature of the sample are not rigorous, the ratio observed is so high that it cannot invalidate the above argument. In addition, a Young's modulus of 1.5×10^{11} dynes cm.$^{-2}$ [13] shows that a pressure of only 40 atm. exerted by the adsorbed phase on the walls of the capillaries could produce the same volume expansion. For the water–ice transformation at these temperatures a pressure up to 2000 atm. is required. (2) The system porous glass saturated with respect to water shows a continuous contraction when the temperature is lowered from $+2$ to about $-7°$ (Fig. 2) with a thermal coefficient of contraction of approximately 6×10^{-6} deg.$^{-1}$ and with an even higher coefficient below $-7°$. When the temperature cycle shown in Fig. 3 was repeated, the sample again contracted from room temperature to about $-2°$ with the same thermal coefficient as shown in Fig. 2. These data are not shown in Fig. 3 for the sake of clarity.

It is seen, therefore, that in the first case the expansion should have been considerably greater if bulk water had been transformed into bulk ice. In the second case the system contracts from room temperature in a different pattern from that expected for bulk water, even in the supercooled state,[14] since no maximum in the density of the adsorbate is observed at $+4°$; and on the contrary the system exhibits a higher thermal coefficient of contraction below 0° at temperatures different in the two samples. It is obvious, therefore, that this state of water differs from that in the bulk state.

There is little doubt that the water adsorbed in the first two monolayers has a completely different structure from that of bulk water. Frohnsdorff and Kington[15] found that the apparent heat capacity of the intracrystalline water in zeolites at low water contents is 20 to 23 cal. deg.$^{-1}$ mole^{-1} at 27°, a value which is considerably greater than that of liquid bulk water. The heat capacity appeared to decrease with increasing water concentration. A possible explanation offered was that the two coordinated water molecules would have a greater vibrational and a greater "flapping" freedom (pendulum motion about surface) than the three or four coordinated molecules, and thus the heat capacity at low water concentrations would be expected to be greater than that of liquid water. Since, therefore, the first monolayers have a different structure than bulk water, and these will necessarily constitute the framework upon which further condensation from the gas phase takes place, it is possible that with further condensation the adsorbate assumes a different structure, a different epitaxy than it has in the bulk state. The conclusion is therefore reached that the change in freezing temperature of the adsorbed

(12) J. A. Morrison, L. E. Drain, and J. S. Dugdale, *Can. J. Chem.*, **30**, 890 (1952).

(13) Y. Kozirovski and M. Folman, *Trans. Faraday Soc.*, **58**, 2228 (1962).

(14) J. F. Mohler, *Phys. Rev.*, **35**, 236 (1912).

(15) G. F. C. Frohnsdorff and G. L. Kington, *Proc. Roy. Soc.* (London), **A274**, 469 (1958).

water should be related to the different structure of the water in porous glass. Similar considerations could, very likely, also hold for other adsorbates which exhibit anomalous behavior during cooling. Ubbelohde[16] has suggested that the depression of the freezing point of adsorbates might be associated with the different structure the adsorbent imposes on the adsorbate since there is a preferred orientation in the first monolayer. Perhaps his suggestion has not been sufficiently appreciated because of the lack of additional experimental evidence.

Table I summarizes the behavior of the two different samples of porous glass characterized by two different B.E.T. nitrogen areas. As the chemical composition

Table I: Differences Observed in the Two Samples

Sample	B.E.T. surface areas, $m.^2/g.$	Amount of water adsorbed at saturation, g./g.	Temp. at which linear thermal coefficient of contraction changes	Temp. range at which samples expand
First	94.5	0.21	−7°	−20 to −24°
Second	82.5	0.24	−1°	−14 to −16°

of the adsorbents and of the adsorbates is the same in both cases, the differences indicated in Table I should be attributed to the different geometry of the pores which results in the different structure of the water in the pores. If the melting temperature is a unique function of the structure of the water and the structure of the water is a unique function of the geometry of the pores, the distribution presented in Fig. 5 should represent a pore-size distribution of the sample. This is compared with the pore-size distribution, Fig. 7, calculated from the desorption part of the isotherm determined for the same sample of porous glass and calculated by using the Kelvin equation, which relates the relative vapor pressure to the radius of the capillary (meniscus). The derivation of the Kelvin equation assumes, nevertheless, that the adsorbate can be treated as bulk water under reduced pressure which is due to the existence of menisci. It is shown in this work that the adsorbate is not bulk water and that there is a series of domains, which are considered to be related to the different structure of the water. Under these circumstances the Kelvin equation should be used with caution. Comparison of Fig. 5 and 7 shows the different distribution one obtains in either case. The relation between the melting point and the radius of the capillary should be based on considerations of the structure of the adsorbate. Such a relationship

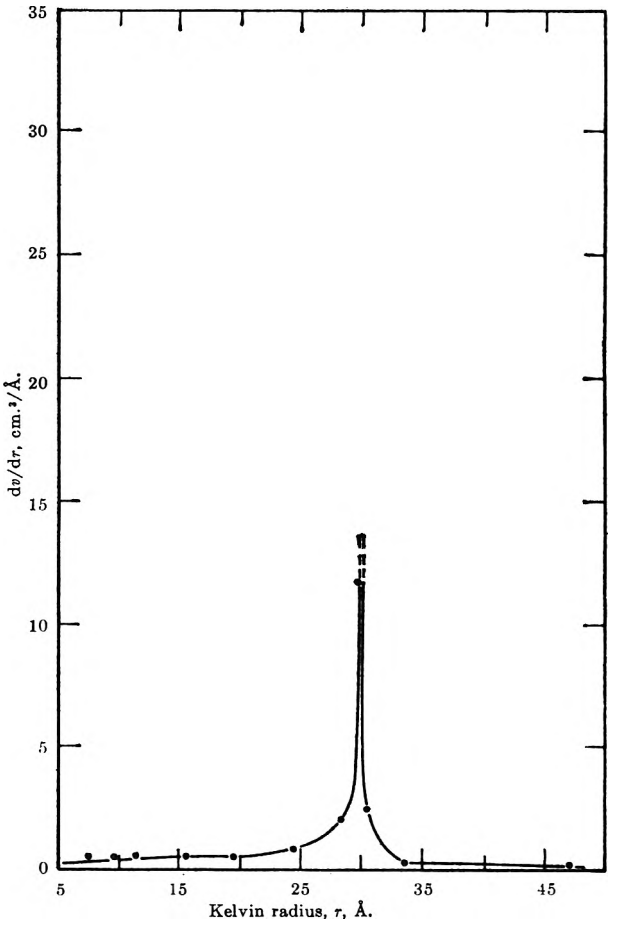

Figure 7. Porous glass saturated with respect to water, first sample. Pore-size distribution calculated from the desorption part of isotherm of same sample.

is not as yet known and in consequence the distribution represented in Fig. 5 cannot be expressed in terms of the radii of the capillaries. More work is required with samples bearing from less than one to more statistical monolayers.

Acknowledgments. The author wishes to thank Mr. P. J. Sereda for assistance offered during the course of this work, Dr. C. H. Amberg for helpful discussions, Mr. B. Hurley and Mr. W. Cheh for carrying out part of the experimental work and calculations, Mr. H. F. Slade for technical assistance, and Mr. D. Kulawic for obtaining the B.E.T. data.

Discussion

M. L. WHITE (Bell Telephone, Murray Hill). Did you obtain any time effects associated with length changes? That is, were there any supercooling effects that might explain some of the "humps" in your graphs?

(16) A. R. Ubbelohde, *Quart. Rev.* (London), **4**, 356 (1950).

A. ANTONIOU. The system was considered to have reached equilibrium only when the rates of change of temperature before and after heat input became identical. Observations on both the dimensional changes and the heat effects were made only at that stage. The time required to attain equilibrium was from 2 to 5 hr. for the range where the transformations took place, in contrast to about 15 min. when no transformations occurred. When the system expanded, the temperature was decreased as little as 0.2° and not more than three observations were taken in the course of 24 hr. The system did not show any sudden changes which could be attributed to supercooling. Under these conditions, one can assume to have reached an equilibrium state after each temperature change.

H. VAN OLPHEN (Shell Development Company, Houston). In the interpretation of your results, long-range effects of the surface on the structure of water are invoked, extending beyond one or two monolayers. My own belief is that a diffuse double layer is formed upon contacting the water with the glass. Therefore, any long-range effects might be discussed by taking into account the diffuse counterion atmosphere. Electroosmosis effects would indicate whether or not the presence of a double layer is important in this problem.

A. ANTONIOU. If we consider the capillaries to be some sort of tubes, we have to assume that this double layer should extend to their center, so that it would influence the properties of the adsorbate. This does not seem to me very likely. One would think that the diffuse double layer will extend only a few statistical monolayers away from the surface, so that the adsorbate in the middle of the capillaries will behave as in the bulk state, which is shown not to be the case. On the other hand, if the adsorbent is in the form of a network and the adsorbate fills the vacancies of this network, it may be that this double layer could extend throughout the bulk of the adsorbate. This would result again in a metastable condition for the adsorbate. Electroosmotic effects could possibly show the extent to which the diffuse double layer influences the orientation of the adsorbate.

T. MARTIN (Massachusetts Institute of Technology, Cambridge). In other systems there have been observations of rhythmic ice band structures. Do such structures have any bearing on your experiments?

A. ANTONIOU. It is doubtful whether one could distinguish ice bands in porous glass, as one can in macroscopic crystals, since the thickness of these bands in the adsorbate will have to be of molecular dimensions. It is apparent, though, that there is a series of domains which could be related to ice bands, though on a molecular scale.

A. C. HALL (Socony Mobil Oil Company, Dallas). In connection with Dr. Van Olphen's point as to the range of adsorption forces, I should like to draw attention to Deryaguin's work in which it was found that isotherms of polar adsorbates on high energy surfaces intercepted the adsorption ordinate whereas isotherms of nonpolar adsorbates did not, and to ask whether you expect to extend your experiments to nonpolar fluids.

A. ANTONIOU. The results which are reported certainly pose many questions which cannot be answered at the present time. Experiments with nonpolar fluids are under way at the Division of Building Research, National Research Council.

The Adsorption of Oxygen on Silver

by A. W. Czanderna

Union Carbide Corporation, Chemicals Division, South Charleston, West Virginia *(Received March 19, 1964)*

The rate of adsorption and desorption of oxygen on silver powder has been measured from −77 to 351° at an oxygen pressure of 10 torr employing a vacuum ultramicrobalance. The measurements were made on a silver surface on which both the total uptake and the rate of adsorption were reproducible at any temperature and pressure. Nominal activation energies of 3, 8, and 22 kcal./mole which were measured are believed to correspond to dissociative adsorption, molecular adsorption, and surface mobility of oxygen adatoms, respectively. Data on thermodesorption, vacuum desorption, and activation energy are combined to propose relative surface coverages of the various adsorption types.

Introduction

Silver, like many metals, undergoes both physical and chemical adsorption of gases. Numerous studies of the physical adsorption of gases on silver have been made.[1-3] Even more investigations have been reported on the rate of chemisorption of oxygen on silver.[1-8] The best chemisorption data show that[4-8] initially the rate of adsorption is very fast until the surface is covered or partly covered and then the rate decreases rapidly to saturation. Typical ranges of the activation energy reported for oxygen sorption on silver are 12–17,[2] 17–13,[2,6] 22,[4] and 27–29 kcal./mole.[4] The wide ranges in values probably result from calculations based on the adsorption at different surface coverages on different samples and at different pressures. There are numerous literature references concerned with other aspects of the interaction between oxygen and silver. Those which appear to have a bearing on the interpretation of the data presented below will be introduced when they are pertinent. However, in all cases of prior study of the adsorption of oxygen on silver, knowledge of surface coverages, reproducibility of chemisorption data, etc., have been somewhat incomplete.

For the experimental work, a vacuum beam ultramicrobalance was chosen to study the adsorption of oxygen on silver. This instrument permits the ambient pressure and temperature to be varied over wide limits making it possible to measure from the mass changes that occur: (a) the saturation uptake as a function of pressure and temperature, (b) the rate of adsorption and desorption, (c) the thermodesorption of adsorbed species, (d) the surface area, and (e) long-term mass changes in the sample. It is possible to determine the heat of adsorption[9] from (a) and the activation energy of adsorption[10] from (b). The desorption data of (b) cannot be used for the activation energy of desorption if powders or films are employed.[11] However, the desorption data of (b) and the data of (c), (d), and (e) provide important qualitative and historical information which are essential for assurance of reliability and reproducibility of the data.

Although a comprehensive study of oxygen on silver has been completed, only data relating to the rate of adsorption and desorption will be presented in this paper.

Experimental

Mass changes were determined with a pivot-type beam ultramicrobalance. A detailed description of the

(1) M. H. Armbruster, *J. Am. Chem. Soc.*, **64**, 2545 (1942).
(2) A. F. Benton, *ibid.*, **56**, 255 (1934).
(3) N. N. Kavtaradze, *Chem. Abstr.*, **17**, 325*b* (1957).
(4) W. W. Smeltzer, *Can. J. Chem.*, **34**, 1046 (1956).
(5) E. W. R. Steacie, *Proc. Roy. Soc.* (London), **A112**, 542 (1926).
(6) H. Taylor, *Z. physik. Chem. Bodenstein Festband*, 475 (1931).
(7) M. I. Temkin and N. V. Kulkova, *Dokl. Akad. Nauk SSSR*, **105**, 1021 (1955).
(8) J. N. Wilson, *et al.*, *Proc. Intern. Congr. Surface Activity, 2nd, London*, **2**, 299 (1957).
(9) B. M. W. Trapnell, "Chemisorption," Butterworths & Co., London, 1955, p. 44.
(10) B. N. W. Trapnell, *ibid.*, p. 49.
(11) B. M. W. Trapnell, *ibid.*, p. 79.

construction, operation, calibration, and limitations of the pivot-type balance has been given.[12] It was found helpful to modify the beam of the balance to facilitate automation. Details of this change will be published.[13]

Automation of the balance was based on the transducer method devised by Cochran[14] and more details of the automatic operation are available.[15] A schematic representation of the automatic operation is presented in Fig. 1.

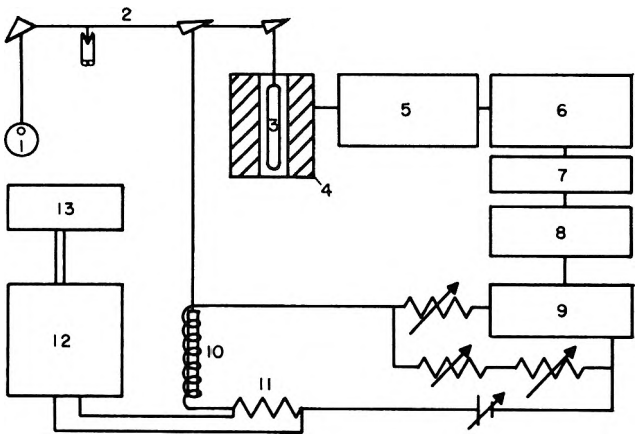

Figure 1. Block diagram of the apparatus: 1, sample container; 2, balance beam; 3, piano wire probe; 4, transducer; 5, translator; 6, amplifier; 7, servomotor; 8, servo speed changers; 9, Helipot 40 turn Model E; 10, compensation solenoid; 11, standard resistor; 12, bucking voltage; and 13, two-pen recorder.

With the automated balance employed in this study, the rate of oxygen adsorption could be followed after 20 sec., changes in mass of ± 0.1 to ± 0.2 μg. could be detected *in vacuo* or in the presence of the ambient gas, respectively, and changes in total sample mass of the order of 1 μg. could be monitored.

Vacuum in the system was produced with a two-stage mercury diffusion pump and mechanical forepump. Mercury vapor from the diffusion pump was condensed in a trap cooled with liquid nitrogen. The limiting pressure obtained in the balance housing with this system was 1×10^{-7} torr. Gas pressures in the gas-handling section of the vacuum system were read on a mercury manometer, a two-stage mercury McLeod gauge, or a thermocouple gauge. A pressure of 5×10^{-7} torr could be obtained in the gas-handling system when mercury vapor was condensed in a Dry Ice trap. Stainless steel bellows-type valves with Teflon gaskets were used in the gas-handling system between the sample chamber of the microbalance housing and the cold traps.

The gases used in this study were obtained from the following sources: oxygen was prepared by thermal decomposition of chemically pure potassium permanganate, dried with magnesium perchlorate, and stored in bulbs; nitrogen was prepared by the thermal decomposition of sodium azide; reagent grade hydrogen and carbon monoxide were obtained in 1-l. glass break-seal flasks from the Air Reduction Co.

The silver powder used was Fisher reagent grade, with a nominal purity of 99.97%. Major impurities included 0.02% sulfate and 0.005% chloride; minor metallic impurities were 0.002% lead, 0.001% copper, and 0.0005% iron. The silver powder was loaded into a spherical sample bulb, approximately 1 cm. in diameter, containing a 2–3-mm. diameter hole at the top and suspended from one side of the balance. A dummy bulb was suspended from the other side of the balance.

Two hinged tube furnaces (HeviDuty Type 70) were mounted about the sample bulb and dummy bulb. The voltage input into each furnace and hence its temperature was regulated by powerstats. The latter obtained power from a constant voltage regulator. In the absence of room temperature fluctuations, furnace temperatures were controlled to better than $\pm 1°$. The furnace temperatures were measured with calibrated ten-junction chromel–alumel thermocouples positioned between the furnace and balance leg, as near as possible to the sample and dummy bulbs. Prior to adsorption studies the actual sample temperature was determined as a function of the chromel–alumel thermopile temperature reading with a thermocouple placed inside the vacuum system. Thereafter, the thermopile e.m.f. was measured and the sample temperature obtained from this calibration curve.

Specialized techniques for determining the surface area from nitrogen adsorption at low temperatures have been described.[16] The difficulty encountered in obtaining the rate of adsorption because of thermomolecular flow forces at pressures of 0.001 to 20 torr has also been discussed.[17] Because of this difficulty,

(12) A. W. Czanderna and J. M. Honig, *Anal. Chem.*, 29, 1206 (1957).

(13) A. W. Czanderna, proceedings of a conference held in Pittsburgh, Pa., May, 1964, to be published in "Vacuum Microbalance Techniques," Vol. IV, Plenum Press, Inc., New York, N. Y.

(14) C. N. Cochran, "Vacuum Microbalance Techniques," Vol. I, Plenum Press, Inc., New York, N. Y., 1961, p. 23.

(15) A. W. Czanderna and H. Wieder, "Vacuum Microbalance Techniques," Vol. II, Plenum Press, Inc., New York, N. Y., 1962, pp. 151, 152.

(16) A. W. Czanderna and J. M. Honig, *J. Phys. Chem.*, 63, 620 (1959).

(17) A. W. Czanderna, "Vacuum Microbalance Techniques," Vol. I, Plenum Press, Inc., New York, N. Y., 1961, p. 129.

the oxygen adsorption and sample reduction were carried out at 10 torr to maximize the accuracy of the rate data.

Results

The purpose of the initial experiments was to establish a method of preparation of a silver surface that retained the highest possible surface area, that did not change in surface area, and possessed reproducible "chemisorption behavior" as a function of repeated adsorption reduction cycling. Both reproducibility of the rate of chemisorption and of the saturation uptake at the same temperature and pressure are included in the term "chemisorption behavior" and both must be the same if the sample surface reaches a stable configuration and is reproducibly cleaned by the reduction treatment. This requirement of the surface led to an exhaustive study of rearrangements that occur during adsorption–reduction cycling. Since the results of this study are to be published at a future date, some of the pertinent findings will be reported here.

Reproducible "chemisorption behavior" was obtained by cyclically outgassing, reducing, outgassing, and oxygenating as in Fig. 2. When the reducing gas was not hydrogen, one hydrogen treatment was necessary to remove adsorbed chloride ions. The first oxygen treatment removes sulfur as SO_2; the chloride departs as HCl.[18] Failure to employ a single hydrogen treatment prior to reduction with some other gas simply yields a surface that has reproducible "chemisorption behavior" at a lower level of mass uptake per unit mass of silver. This is consistent with recent findings.[19] Progressively larger amounts, of the order of 0.1% of the sample mass, were lost during outgassing a series of silver samples at progressively higher temperatures. A perfectly reproducible "chemisorption behavior" based on mass uptake per unit mass of silver at a given temperature and pressure could be achieved on different size aliquots of the silver samples when hydrogen, carbon monoxide, and other reducing gases were employed on the different samples.

The results presented below were obtained on a 0.515-g. aliquot of silver powder that was treated cyclically with carbon monoxide and oxygen at a pressure of 10 torr and a temperature of 360° to obtain reproducible "chemisorption behavior" at any arbitrary temperature below the reducing temperature. Before reaching constant mass, this sample lost 474 μg. by outgassing and 90 μg. by reduction in 16 complete cycles. The final surface area was 0.09 m.²/g. While the data presented below are explicitly for this sample, the author wishes to emphasize that these data have been reproduced for many other samples and that only one representative set is being presented to avoid cluttering the literature.

The Temperature Dependence of Oxygen Adsorption. The rate of oxygen adsorption on a reduced silver surface was measured from −77 to 350° at 10 torr. Typical adsorption data are shown in Fig. 3. As can be seen, the initial rate of adsorption was very rapid at all temperatures. The rate ultimately decreased until it was too slow to be measured. Above $\theta = 0.65$,[20] the rate was observed to decrease markedly with decreasing temperature to about 137°. At lower temperatures, the rate at coverages above $\theta = 0.65$ became constant or decreased slightly with decreasing temperatures.

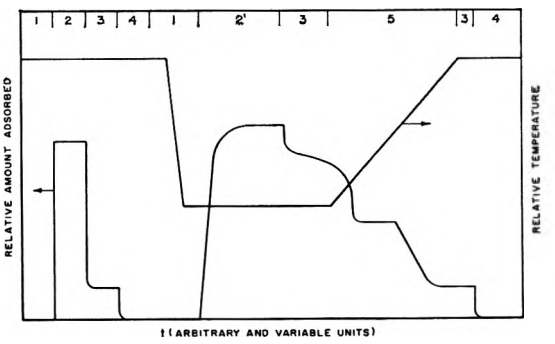

Figure 2. Typical adsorption–reduction cycles: 1, outgassing; 2 and 2′, oxygen adsorption; 3, oxygen desorption; 4, chemical reduction; and 5, thermodesorption. The rate and amount of oxygen adsorption (2 and 2′) could be reproduced for many months as long as the surface stabilization temperature was not appreciably exceeded.

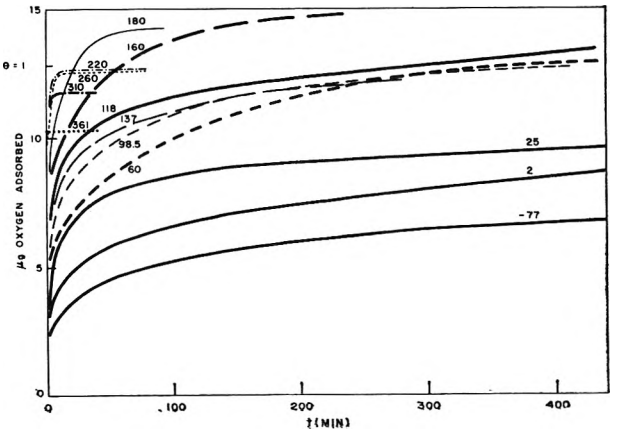

Figure 3. The adsorption of oxygen on reduced silver powder at various temperatures.

(18) A. W. Smith, unpublished results.

(19) R. G. Meisenheimer and R. N. Wilson, *J. Catalysis*, 1, 151 (1962).

The apparent activation energy for adsorption was obtained from Arrhenius plots at constant oxygen coverage θ of the data shown in Fig. 3. A typical plot for $\theta = 0.77$ is shown in Fig. 4. Plots similar to the one shown in Fig. 4 were obtained for θ-values from 0.23 to 1.07. The activation energies depend primarily on the temperature of oxygen adsorption and only slightly on the coverage as shown in Fig. 5. Three distinct ranges of activation energies were obtained. The activation energy range of 22–24 kcal./mole at temperatures above 150° and θ greater than 0.5 is in agreement with values most frequently quoted in the literature.[4] The lower activation energy ranges of 0–10 and 0–4 kcal./mole reveal quantitative changes in the oxygen adsorption that occur at about 100° and at about 25°. These changes, which are different from any previous findings, will be discussed in more detail below. The physical adsorption of oxygen on top of chemisorbed oxygen probably accounts for the decrease in the activation energies toward zero at increased coverage. This can be seen more explicitly in Fig. 6 from the adsorption of oxygen on silver at room temperature as a function of pressure. The cover-

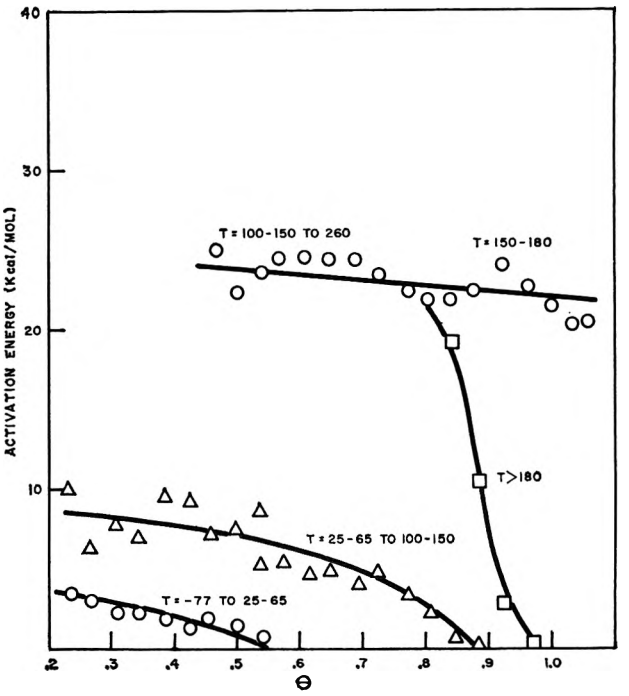

Figure 5. Activation energies for adsorption of oxygen on reduced silver and temperature ranges in which they are obtained.

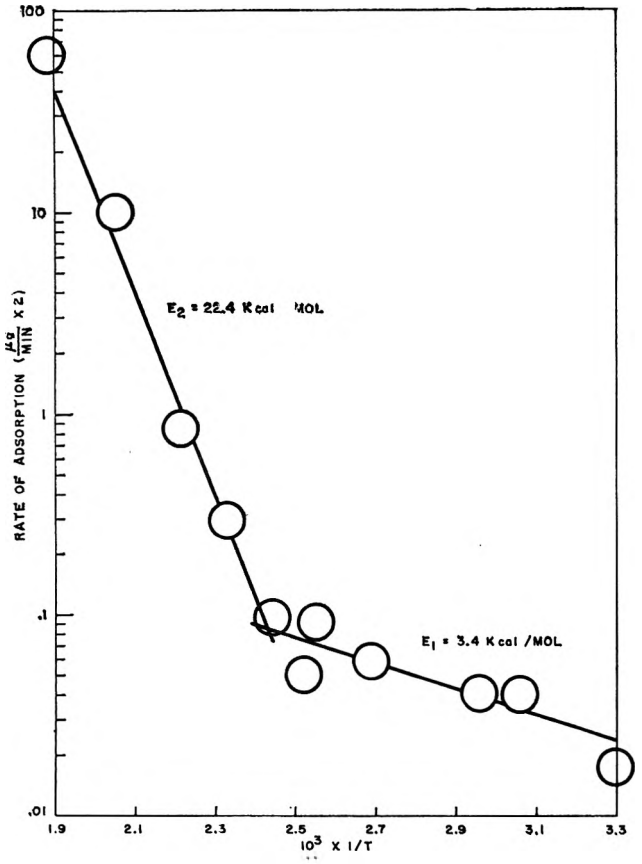

Figure 4. Arrhenius plot for $\theta = 0.77$ (ref. 20).

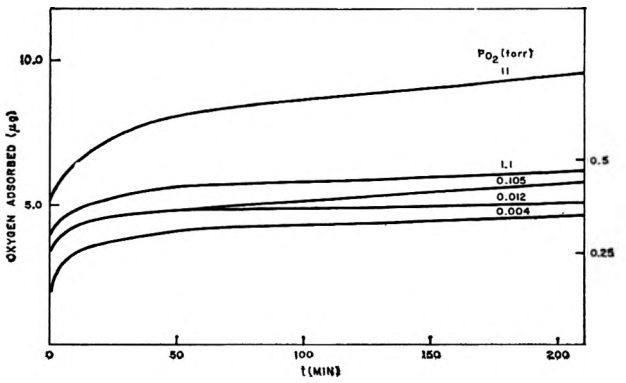

Figure 6. Oxygen adsorption on reduced silver at various oxygen pressures.

(20) In this report θ, the coverage of oxygen, is defined as the mass of oxygen adsorbed at any temperature divided by the mass of one monolayer of nitrogen adsorbed at 78°K. This convention was chosen in preference to mole ratios since the oxygen adsorption is not entirely molecular. Since it is generally believed that the adsorption is dissociative, the calculation of the true θ must assume a crystal face or set of faces, a mechanism for adsorption, and a ratio of molecular and atomic oxygen on the surface. Hence, θ as presented is actually $\psi(\theta)$ in terms of the usual adsorption nomenclature where ψ can be related to θ by proper selection of the variables mentioned above. Since the relationship between $\psi(\theta)$ and θ actually may be close to unity, the term θ will be used throughout this manuscript. Finally, $\theta = 0$ is an arbitrary reference point of a reproducible surface contamination which is in actuality $\theta = 0 + \theta'$. While the value of θ is unknown, θ' must be a constant since constant sample mass is ultimately achieved.

age or amount of oxygen adsorbed is nearly independent of pressure below 0.1 torr, but increases sharply at higher pressures. The pressure-independent coverage occurs up to $\theta = 0.3$, which is the same coverage where the activation energy falls toward zero. It can be readily seen from Fig. 5 how different investigators obtain activation energies ranging from 11 to 27 kcal./mole as indicated earlier. The oxygen adsorption isobar is shown in Fig. 7. At temperatures above 160°, a decrease in the saturation amount of adsorption is apparent. This indicates the rate of desorption is becoming more important than the adsorption rate at high coverages. At temperatures below 100°, the rate of adsorption is too slow to produce the maximum coverage permitted within the time allowed for the experiment.

The Rate of Desorption and Thermodesorption of Oxygen from Silver. It was found that most of the oxygen adsorbed at 350° could ultimately be removed simply by outgassing at the same temperature. After adsorbing oxygen at a series of lower temperatures (Fig. 3), the system was evacuated. The mass loss measured during evacuation at each temperature is plotted in Fig. 8. The rate of desorption below 160° and $\theta = 1.0$ is negligible, but above 200° it is quite rapid until low coverages are reached. The apparent activation energy for desorption was found to be about 25 kcal./mole for θ of 0.3 to 0.7. However, as was pointed out before, an activation energy calculated from the rate of desorption from powders cannot be exact. The true activation energy for desorption must be greater than 25 kcal./mole. When the rate of mass loss on outgassing at the adsorption temperature reached a negligible or zero rate, the furnace temperature was increased at a nearly constant rate to about

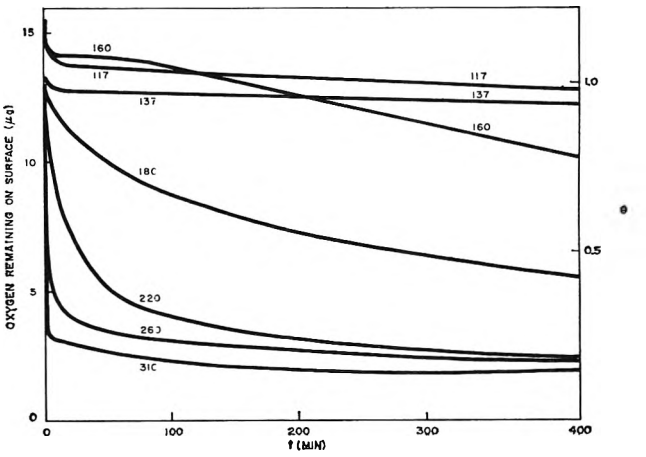

Figure 8. Desorption of oxygen from silver at various temperatures.

350°. This method was found particularly useful for adsorption temperatures below 140°, where the rate of desorption became negligible even at high coverages. A typical heating and mass loss curve is shown in Fig. 9. A curve similar to this was obtained after each subsequent oxygen adsorption. The break, A, in Fig. 9 appeared in all thermodesorption curves between 150 and 175° after adsorption at 140° or less and was independent of the heating rate. The drastic change in rate, B, occurred in all desorption and thermodesorption curves. Below 140°, there were always five distinct fractions of oxygen removed from the silver surface. These were: (1) a small fraction removed quickly at the adsorption temperature by evacuation alone; (2) a fraction which could be removed quickly by heating to 150–175° or by pumping for several days at lower temperatures; (3) a fraction which could be removed quickly by heating to 200–250° or by

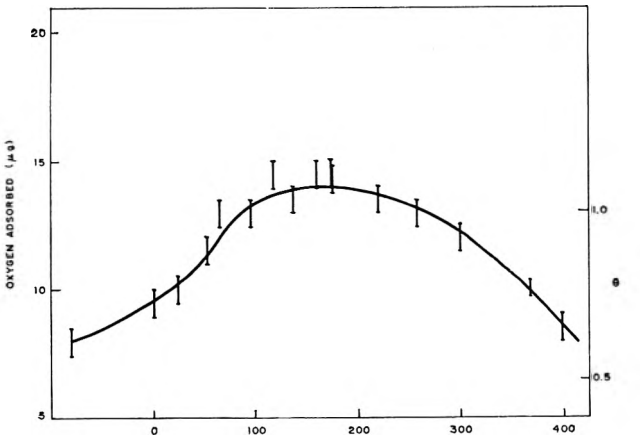

Figure 7. Oxygen adsorption isobar on reduced silver (P_{O_2} = 10 torr).

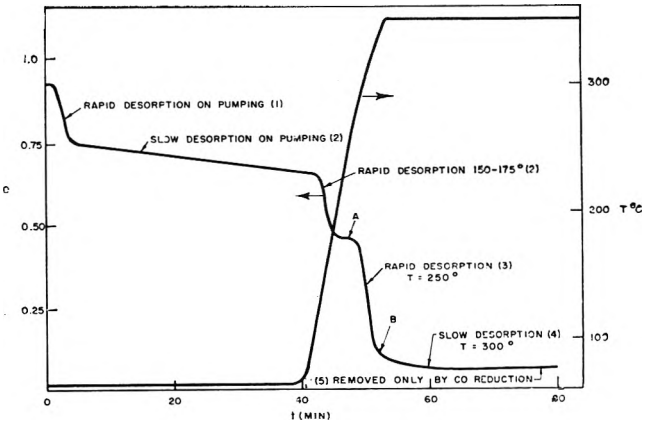

Figure 9. Desorption and thermodesorption of oxygen from silver after adsorption at 65°.

pumping at 160–200° for 24 hr. or more; (4) a fraction which could be removed by pumping at 350° for several hours; and (5) a fraction which required chemical reduction for its removal.

The five fractions obtained on desorption after adsorption at various temperatures are plotted as θ *vs.* the temperature of adsorption in Fig. 10. Above 150–170°, regions 1, 2, and 3 merge since differentiation between them is merely a rate effect. The ease with which oxygen can be removed from the surface is qualitatively associated with the strength of the bond formed between the oxygen and silver. Thus, in the progression from regions 1 to 5, the relative strength of the oxygen adsorbed is: (1) very weakly adsorbed oxygen, probably physically adsorbed; (2) weakly chemisorbed oxygen, possibly as charged molecules, $O_2^{\delta-}$; (3) chemisorbed oxygen, possibly as charged oxygen atoms, $O^{\delta-}$; (4) strongly chemisorbed oxygen which may be the same form as in fraction 3 but either placed far apart on the surface so that desorption as O_2 molecules is limited by the rate at which oxygen atoms can diffuse together, or partially submerged into the bulk silver lattice so the desorption rate is limited by the rate of their diffusion to the surface; (5) very tightly chemisorbed oxygen, probably on relatively high-index-plane adsorption sites.

Of particular interest in Fig. 10 is the increase in coverage of chemisorbed oxygen and the decrease in the amount of weakly chemisorbed material from 100 to 140° at θ of 0.5–1.0. The significance of the regions becomes more evident if the results obtained for the values of the activation energies are plotted as in Fig. 11. The numbers within this figure specify activation energies at various θ and T in kcal./mole. A variation in E with θ is indicated by the arrows between the numbers. The shaded regions indicate the θ and T

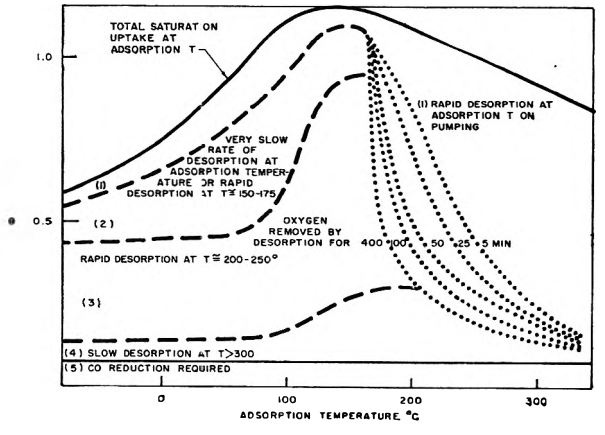

Figure 10. Composite of desorption and thermodesorption data.

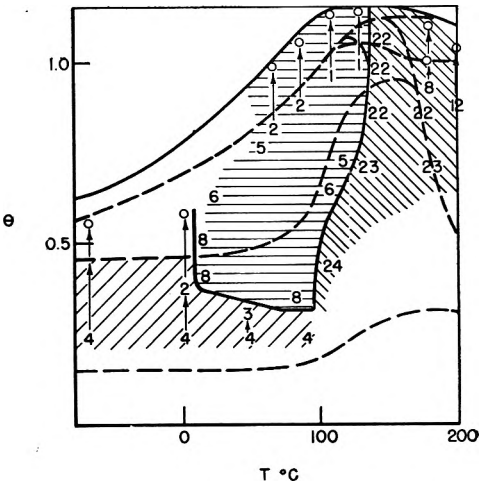

Figure 11. Comparison of activation energies of adsorption with thermodesorption and desorption "breaks."

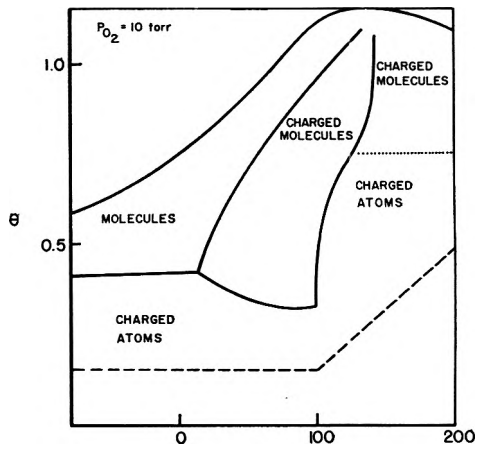

Figure 12. Species of oxygen probably adsorbed on silver at various coverages and temperatures.

where experimentally determined activation energies of adsorption have been obtained thus far. The broken lines define areas where different forms of oxygen exist as previously discussed. As can be seen, the regions where the activation energies are 3 and 22 kcal./mole coincide with the region where chemisorbed oxygen of type 3 and 4 occurs. The activation energy of about 8 kcal./mole coincides with the region where weakly chemisorbed oxygen (type 2) occurs. If the qualitative assignment of oxygen specified present from thermodesorption and desorption data is correct, then the species present at various coverages would be as shown in Fig. 12.

Discussion

In considering the forms of oxygen adsorbed on silver, the over-all adsorption mechanism might include all of the following steps.

$$O_2(g) \longrightarrow O_2(ads) \longrightarrow \begin{array}{l} O_2^{\delta-}(ads) \longrightarrow 2O^{\delta-}(ads) \longrightarrow 2O^{\delta-2}(ads) \\ \searrow \quad \nearrow \\ O_2^{\delta-2}(ads) \end{array} \quad (1)$$

Since it is not yet possible to distinguish $O_2^{\delta-}$ from $O_2^{\delta-2}$, the mechanism to be considered can be simplified to

$$O_2(g) \longrightarrow O_2(ads) \longrightarrow O_2^{\delta-}(ads) \longrightarrow 2O^{\delta-}(ads) \quad (2)$$

where the charges are assigned merely to indicate that the adsorbed species probably exist as ions, though of unspecified charge. It is known that some form of oxygen molecules and atoms must coexist on the surface from oxygen exchange work,[8,21] and that oxygen molecules are adsorbed and subsequently dissociate.

Thus, from this and eq. 2, it appears that only two different adsorption sites are required, *i.e.*, for charged oxygen atoms and charged oxygen molecules. The primary site for atom adsorption is envisioned to be the tetrahedral hole in an array of three silver atoms having face centered cubic packing. When neighboring clusters of this type are not available, oxygen must adsorb as a molecule, possibly by π-bonding. The multiple activation energies measured could result if there are, in addition, immobile and mobile forms of the charged atoms or in the clusters of silver atoms containing the charged atom. It is suspected from the data that there is a transition from immobility to mobility at about 100°. The adsorption below 100° could proceed by molecular adsorption followed by immediate dissociation into charged atoms which are immobile. This process has a negligible activation energy (3 kcal./mole) and continues as long as adjacent sites are available to accept the two charged oxygen atoms from each dissociated molecule. The random nature of the adsorption process prevents the surface from being completely covered by charged atoms because some silver atoms will become isolated in clusters of insufficient size and thereby become unable to dissociate oxygen molecules. Additional adsorption must then consist of charged oxygen molecules. This would correspond to a more highly activated process (8 kcal./mole). Above 100° the adsorbed charged oxygen atoms become mobile on the surface. Movement of the charged oxygen atoms would then allow formation of additional primary adsorption sites which facilitate additional molecular dissociation until the maximum number of charged atoms that can be held on the surface is reached. The highest activation energy (22–24 kcal./mole) is associated then with the movement of charged oxygen atoms on the surface to form additional primary adsorption sites. Coverage greater than the maximum charged atom concentration again would consist of weakly chemisorbed charged molecules—again possibly π-bonded and/or physically adsorbed oxygen molecules.

Conclusions

Activation energies of 3, 8, and 22 kcal./mole have been determined indicating that the nature of the oxygen adsorption on silver is more complex than previously reported. It is also shown that nearly all activation energy data obtained by other workers are obtainable if the proper temperature and surface coverage are chosen. A primary adsorption site consisting of an oxygen adatom in a tetrahedral hole has been proposed and that mobility or immobility of this adatom or site combined with dissociative oxygen adsorption can be used to explain the existence of three activation energies.

Acknowledgment. The author is grateful for the mass spectrometric measurements carried out by Dr. A. W. Smith. He also appreciates the numerous stimulating discussions of the results of this study with Dean Henry Eyring and Drs. F. G. Young, A. W. Smith, T. H. George, and P. O. Schissel. He is grateful for the extra careful manner in which Miss L. I. Forrest carried out the measurements. Finally, the author appreciates prepublication information released to him by Mr. C. N. Cochran.

Discussion

M. L. WHITE (Bell Telephone, Murray Hill). Do your results imply that silver does not oxidize in oxygen at temperatures up to 300°? Can silver be oxidized at any temperature, under these conditions?

A. W. CZANDERNA. These results show that at oxygen pressures of 10 torr or less and at temperatures below 350°, silver adsorbs about one monolayer of oxygen. There was no evidence from the mass data in this study that incorporation of oxygen above or below the silver surface occurred either by compound formation or by formation of a solid solution. There is no evidence from this study that silver can be oxidized at these oxygen pressures at any temperature. At higher temperatures, it is most likely that a solid solution of oxygen atoms in silver will be formed. The results here do not contradict the recent results of Menzel (E. Menzel and C. Menzel-Kopp, Preprints, International Conference on the Physics and Chemistry of Solid Surfaces, Brown University, June 21–26, 1964, p. LL-1), who showed that Ag_2O crystallites can be formed at oxygen pressures of 35 atm. and 250°, because of the thermodynamics of the reaction $Ag(s) + O_2(g) \rightleftharpoons Ag_2O(s)$.

(21) L. Ya. Margolis, *Izv. Akad Nauk SSSR, Otd. Khim. Nauk*, 21, 225 (1959).

J. H. DE BOER (The Hague, Netherlands). I quite agree with Dr. Czanderna wher he says that silver oxide cannot be made from silver layers ar d oxygen by a thermal method. My own experience before World War II, if I remember well, is that a glow discharge in dilute oxygen oxidizes a silver layer to Ag_2O, while a treatment with ozone results in the formation of higher silver oxides, probably a mixture of Ag_2O and AgO.

R. A. VAN NORDSTRAND (Sinclair Research, Houston). On what grounds did you decide that the oxygen prefers to adsorb onto a tetrahedral site?

A. W. CZANDERNA. As far as I know this possibility has not been considered before for the adsorption of oxygen on silver and certainly is entitled to further justification. The preference for the adsorption of oxygen at the tetrahedral hole forming a quasi-surface compound "Ag_3O" was reached as follows: oxygen adsorption at these temperatures is dissociative and has a low activation energy which is typical of many metals. Yet, it is apparent from the low temperature adsorption that the coverage of the surface with oxygen atoms is rate-limited. This is most probably because of a limited number of primary adsorption sites. It is not possible to account for the low coverage (θ = 0.45) at low temperatures unless at least three silver atoms are bound to one oxygen atom. In fact, if all the silver atoms of the surface are assumed to be close-packed (ref. 20 of the paper), uniform coverage with atom ions at θ = 0.45 (Fig. 10–12) would correspond to a true θ of 0.33 which would be the Ag_3O that has been proposed. While this quantitative agreement may be fortuitous, the assumptions made for the calculation do not appear to be wildly speculative because of the way the reproducible surface was prepared and the known repulsions of surface ions. Finally, oxygen atoms in Ag_2O occupy a position equivalent to the tetrahedral hole of three close-packed silver atoms, which means that this must be a preferred arrangement. The "Ag_3O" thus could also represent the simplest nucleus for the growth of Ag_2O on a silver surface when oxygen pressures are reached that make this thermodynamically feasible.

Molecular Orbital View of Chemisorbed Carbon Monoxide

by George Blyholder

Department of Chemistry, University of Arkansas, Fayetteville, Arkansas *(Received February 26, 1964)*

Carbon monoxide chemisorbed on metals is considered in the light of Hückel molecular orbitals for the metal–carbon–oxygen bonds. The Hückel molecular orbitals predict the existence of a partially filled π-molecular orbital which increases the metal–carbon bond strength but decreases the carbon–oxygen bond strength. In this model only effects in the π-bonding system are considered; *i.e.*, the σ-bonds are assumed constant. This model qualitatively explains: (1) the occurrence of several carbon–oxygen stretching frequencies in the infrared spectra of CO adsorbed on metals; (2) differences in spectra of CO adsorbed on evaporated and supported metals; (3) infrared band positions as a function of coverage; (4) the effect of adsorbing other gases in addition to previously chemisorbed CO; and (5) band shifts in going from adsorption on pure Ni to a Ni–Cu alloy.

Introduction

Recently, there has been accumulating a body of literature dealing with the infrared spectra of carbon monoxide adsorbed on metals. The carbon–oxygen stretching frequency for chemisorbed carbon monoxide has been observed from above 2100 cm.$^{-1}$ down to 1800 cm.$^{-1}$. As a variety of adsorption parameters are varied, the observed infrared bands shift their positions. For example, it has been observed that (1) the carbon–oxygen stretching frequency consistently shifts to higher wave numbers as the fractional surface coverage increases[1–4]; (2) the relative intensities of bands for carbon monoxide on evaporated and supported films are different[5,3]; (3) adsorption of

other gases after carbon monoxide shifts the observed band positions.[1] These and other phenomena have received scant explanation and certainly no over-all view of the nature of the metal–carbon–oxygen bonding system has been presented and used to attempt to explain or correlate these phenomena.

The principal structural conclusion drawn, first by Eischens and co-workers[2] and subsequently by other workers, from the observed spectra in the 5000 to 1400-cm.$^{-1}$ region was that bands above 2000 cm.$^{-1}$ represented a linear metal–carbon–oxygen system, while bands below about 1960 cm.$^{-1}$ were due to a bridge structure in which the carbon atom is bonded to two nickel atoms on the surface. These conclusions were based on a comparison to the spectra of a few carbonyls which give bands above 2000 cm.$^{-1}$ for linear metal–carbon–oxygen groups while $Fe_2(CO)_9$, which contains bridge carbonyl groups, gives a band[7] at 1828 cm.$^{-1}$. However, Cotton and Kraihanzel[8,9] have shown that in substituted carbonyls a linear metal–carbon oxygen system can have carbon–oxygen stretching frequencies down to 1800 cm.$^{-1}$. Thus the original correlation suggesting the bridge structure is not entirely valid. Recently, work in this laboratory has shown[6] that for carbon monoxide chemisorbed on nickel the infrared spectrum over the entire range from 5000 to 300 cm.$^{-1}$ does not support the bridge structure. If it is assumed, as we do, that all of the carbon monoxide is adsorbed in the linear structure, the problem of explaining the various carbon–oxygen stretching frequencies for the one structure remains.

It is proposed that a simple molecular orbital view of the nature of the metal–carbon–oxygen bond will go a long way in at least qualitatively explaining and correlating the observed band positions and the few observations that have been made on intensities.

Theory

The general molecular orbital approach to bonding in carbonyls as given by Orgel,[10,11] Ballhausen,[12] and Richardson[13] is adopted and herein adapted to chemisorbed carbon monoxide. The bonding in an isolated carbon monoxide molecule is regarded[14] as resulting from an sp_z-hybrid orbital of the carbon atom combining with the p_z-orbital of the oxygen to produce a σ-bond while the p_x- and p_y-orbitals of the carbon and oxygen atoms combine to produce two π-bonds. This leaves a lone pair of electrons on the oxygen 2s-orbital and a lone pair in a carbon sp_z-hybrid orbital, which can form a coordinate bond in a complex with a suitable acceptor orbital such as a d-orbital on a metal atom. This forms a σ-bond between the carbon atom and the metal atom. Since the formation of only this σ-bond puts a large formal negative charge on the central metal atom it is usually stated that back donation from a metal d-orbital to the antibonding π^*-molecular orbital on the carbon monoxide ligand occurs to remove this excess negative charge and stabilize the bond. This statement about the π-bonding between the metal and the ligand seems a bit misleading in that at first glance it implies the placement of electrons in a high energy antibonding orbital. However, formation of simple Hückel molecular orbitals indicates that the molecular orbitals into which these electrons go are lower in energy than the metal d-orbitals.

The π-molecular orbitals are formed by combining a metal d-orbital labeled X_1, carbon p-orbital labeled X_2, and an oxygen p-orbital labeled X_3. Following suggestions in Streitwieser[15] based on the electronegativities of the atoms involved, the integrals are assigned values $H_{11} = \alpha - \beta$, $H_{22} = \alpha$, $H_{33} = \alpha + \beta$, $H_{12} = \beta$, $H_{23} = \beta$. Solution of the secular equation gives energies $E_1 = \alpha + 1.7\beta$, $E_2 = \alpha$, and $E_3 = \alpha - 1.7\beta$ corresponding to wave functions $\psi_1 = 0.21X_1 + 0.58X_2 + 0.79X_3$, $\psi_2 = 0.58X_1 + 0.58X_2 - 0.58X_3$, and $\psi_3 = 0.76X_1 - 0.56X_2 + 0.20X_3$. Since α and β are both negative numbers, $E_1 < E_2 < E_3$. The wave function for the lowest orbital places most of the charge on the carbon and oxygen atoms and adds to the bond strengths for both the carbon–oxygen and metal–carbon bonds. However, the second orbital, whose energy indicates that it is lower in energy than a metal d-orbital, is bonding for the metal–carbon bond but antibonding for the carbon–oxygen bond, since the wave function has a node between the carbon and oxy-

(1) R. P. Eischens and W. A. Pliskin, *Advan. Catalysis*, **10**, 1 (1958).

(2) R. P. Eischens, S. A. Francis, and W. A. Pliskin, *J. Phys. Chem.*, **60**, 194 (1956).

(3) C. E. O'Neill and D. J. C. Yates, *ibid.*, **65**, 901 (1961).

(4) C. W. Garland, *ibid.*, **63**, 1423 (1959).

(5) L. D. Neff, M.S. Thesis, University of Arkansas, 1962.

(6) G. Blyholder, Paper I-38, Proceedings of the Third International Congress on Catalysis, Amsterdam, 1964, North-Holland Publishing Co., Amsterdam.

(7) R. K. Sheline and K. S. Pitzer, *J. Am. Chem. Soc.*, **72**, 1107 (1950).

(8) F. A. Cotton and C. S. Kraihanzel, *ibid.*, **84**, 4432 (1962).

(9) C. S. Kraihanzel and F. A. Cotton, *Inorg. Chem.*, **2**, 533 (1963).

(10) L. E. Orgel, "Transition Metal Chemistry," Methuen and Co. Ltd., London, 1959.

(11) L. E. Orgel, *Inorg. Chem.*, **1**, 25 (1962).

(12) C. J. Ballhausen, "Introduction to Ligand Field Theory," McGraw-Hill Book Co., Inc., New York, N. Y., 1962.

(13) J. W. Richardson, "Organometallic Chemistry," E. Zeiss, Ed., Reinhold Publishing Corp., New York, N. Y., 1960.

(14) C. A. Coulson, "Valence," Oxford, New York, N. Y., 1952.

(15) A. Streitwieser, Jr., "Molecular Orbital Theory for Organic Chemists," John Wiley and Sons, Inc., New York, N. Y., 1961.

gen atoms. A count of the electrons available indicates that this second π-molecular orbital would not be filled. In making this count, for example, for $Cr(CO)_6$, it is assumed that each ligand forms a low energy σ-bonding orbital which is filled and a σ^*-antibonding orbital which is empty. To aid in counting, the electrons may be assumed distinguishable and the electrons originally in the carbon lone-pair orbital are placed in the σ-bond. The π-orbitals labeled ψ_1, of which there are two for each ligand, one in the x-plane and one in the y-plane if the z-axis is the bonding axis, are all just filled by the electrons originally in the π-orbitals of the carbon monoxide ligands. This leaves the six electrons originally in the outer shell of the chromium atom to be spread out in the twelve ψ_2-orbitals. Thus there is competition among the ligands for electrons to put in these orbitals.

While this picture is greatly oversimplified it should be qualitatively correct and will be shown to explain a number of observations. Here the picture has been presented in terms of molecular orbitals extending only over the metal and one ligand rather than over the entire molecule as should be done for a symmetric case like $Cr(CO)_6$ because for the case of chemisorbed carbon monoxide, the octahedral symmetry is lost and only one carbon monoxide ligand will be dealt with. Further the σ- and π-bonds are assumed separable and all effects will be blamed entirely on the π-bonding. This means the problems to be treated will be limited to cases where one might reasonably expect the σ-bonding to remain approximately constant as an effect of a variable is observed.

One might wonder whether there is sufficient metal–carbon orbital overlap to produce orbitals like the Hückel orbitals calculated here. First, it is noted that even as the resonance integral H_{12}, which should be proportional to the overlap, is greatly decreased, the qualitative picture remains unchanged and the energy of ψ_2 remains below that of an electron in a metal d-orbital. A second and perhaps more convincing argument stems from a consideration of the observed carbon–oxygen stretching frequencies. If only a σ-bond is formed by the lone-pair electrons on the carbon atom, the carbon–oxygen stretching frequency for carbonyls would be expected to be very close to that of free carbon monoxide. In fact, this frequency is shifted to somewhat lower values. This is taken as an indication that π-bonding does occur with some charge occupying an orbital like ψ_2 which weakens the carbon–oxygen bond. Cotton and Kraihanzel[8,9] have shown that as carbon monoxide in hexacarbonyls is replaced with ligands which do not π-bond, the availability of electrons to go into π-orbitals of the remaining carbon monoxide ligands is increased with the result that the carbon–oxygen stretching frequencies are decreased. They observed frequencies down to 1800 cm.$^{-1}$.

It might also be expected that as the electronic charge available to go into orbital ψ_2 is increased, the extinction coefficient for the carbon–oxygen stretching band would change. Jones[16] has shown that as the extent of π-bonding increases, the extinction coefficient greatly increases for the carbon–nitrogen stretching band in a series of cyanide complexes which have bonding very similar to that in carbonyl compounds.

In applying the above considerations to chemisorption problems, a metal atom on the surface is regarded as the central atom in a complex with the surrounding metal atoms and the chemisorbed molecule as ligands. Here we do not have the high symmetry of the unsubstituted carbonyls. For the transition metals, the metal ligand atoms partially surrounding a particular surface metal atom will have available partially filled d-orbitals with appropriate symmetry to form π-bonds with the chosen surface atom and thereby compete with the adsorbed carbon monoxide for electrons from the adsorbent atom. The extent of the competition of the surrounding metal atoms for electrons which could go into a ψ_2 π-molecular orbital of the metal–carbon–oxygen system will determine the frequency and extinction coefficient for the carbon–oxygen stretching band of the adsorbed molecule. As an adsorbent atom occupies a position in different crystal faces or a position at an edge, corner, or dislocation, the number of surrounding metal atoms and hence the competition for electrons will vary.

Applications

1. Bands for CO on Ni. A Ni adsorbent atom in a 111 plane face or a 100 plane face has nine or eight surrounding Ni atoms, respectively. With this large number of ligands competing for electrons, the amount of electronic charge in the ψ_2 molecular orbitals of an adsorbed CO molecule would be expected to be small with the result that the C–O stretching frequency would be above 2000 cm.$^{-1}$ as in the unsubstituted carbonyls. However, for adsorbent atoms located at edges of planes, corners, and at dislocations, the number of surrounding nickel atoms can be around four, five, or six. On these sites the competition for electrons to go into the ψ_2 molecular orbitals of the metal–adsorbate system is materially reduced with the result that the C–O stretching band will occur at lower wave numbers. By analogy to the substituted carbonyls, the C–O

(16) L. H. Jones, *Inorg. Chem.*, 2, 777 (1963).

stretching frequency for these sites would be expected to be below 2000 cm.$^{-1}$ and perhaps down to 1800 cm.$^{-1}$. The spectra for CO on Ni usually show a band or bands around 2060 cm.$^{-1}$ and a broad band or bands around 1940 cm.$^{-1}$. According to this molecular orbital view, the bands above 2000 cm.$^{-1}$ are regarded as due to CO adsorbed on regular crystal faces where the adsorbent Ni atoms have a high coordination number while the bands around 1900 cm.$^{-1}$ represent CO adsorbed on sites where the Ni atoms have a somewhat lower coordination number. The low coordination number sites would be expected to be somewhat more variable and poorly defined by virtue of the extra freedom granted by the low coordination number when compared to the high coordination number sites. For this reason, it is expected and found that the low frequency bands are somewhat broader and more variable than the high frequency bands. The occurrence of several different bands in both regions is a result of there being a number of different types of sites that can produce bands in both regions. Also, as expected, there is a continuous variation of sites so that the bands in the two regions which seem to represent the largest number of sites overlap each other. It should be noted that all of this is on the basis of only one adsorbate structure, *i.e.*, a linear metal–carbon–oxygen system.

A word of caution is due on the subject of trying to determine with any degree of accuracy the relative number of surface sites of different types by comparing the intensities of the different C–O bands. As already mentioned, the extinction coefficient is expected to increase as the electronic charge in the ψ_2-orbital is increased. Since this effect is also used to explain the different frequencies, the extinction coefficient for the various bands is expected to increase as the frequency decreases. This has not been examined experimentally for chemisorbed CO, but if it occurs as predicted, the number of low coordination number sites could be considerably less than a casual glance at the spectra would suggest.

2. Supported and Evaporated Metals. The infrared spectra of CO adsorbed on silica-supported[5] and evaporated[6] Ni have been obtained in this laboratory. These spectra show the bands around 2060 cm.$^{-1}$ more intense than the band near 1900 cm.$^{-1}$ for the silica-supported samples while the reverse intensity pattern is observed for the evaporated samples. In producing the silica-supported Ni samples, the sample is heated for over 12 hr. at 400° in a stream of H_2. This should produce sintered, well-defined crystallites which have a maximum of plane faces exposed and a minimum of edge atoms, dislocations, and amorphous material. This is supported by electron micrograph studies of deBoer and Coenen[17] reported by Eischens. The adsorption sites on our silica-supported Ni should mostly be of the type to produce the high-frequency band. The evaporated metal is condensed in the vapor phase and the particles immediately quenched in oil. This would be expected to result in a more amorphous material with less well-crystallized particles. These particles should then have a larger proportion of sites which produce the low-frequency band. Thus this theory explains some of the differences we have observed in our samples.

A number of other reported spectra will now be commented on in the light of the arguments herein, but the conclusions are rather less clear. Eischens and workers[2,18] have reported spectra for CO chemisorbed on silica-supported nickel in some of which the low-frequency band is the more intense while in others the high frequency band is more intense. Their published reduction procedures are a bit uninformative, but apparently a batch reduction procedure with temperatures from 200 to 350° was used for unspecified lengths of time. Apparently, their samples were treated at lower temperatures for shorter times than ours and so would have less crystal growth and sintering occurring. This would produce more sites that give the low-frequency bands. Thus we could explain the variability in observed bands on the basis of sintering and crystal growth rather than the usual arguments about completeness of reduction. Eischens[19] and coworkers have also reported spectra for CO adsorbed on silica-supported Pt, evaporated Pt, and alumina-supported Pt with the high-frequency band at 2070, 2050, and 2050 cm.$^{-1}$, respectively. If these data are to be explained on the basis of the degree of crystallinity of the Pt, it would be stated that the evaporated and alumina-supported samples are a little less crystalline so that the ligand Pt atoms are less effective in competing for electrons in these samples with the result that the C–O frequency is lower. Following this line, the alumina-supported Pt has a larger low-frequency band and a broader high-frequency band than the silica-supported Pt sample. A lower crystallinity for the alumina sample is also supported by the statement of Eischens[2] that the alumina-supported Pt is more difficult to reduce than the silica-supported Pt. The evaporated Pt sample showed no low-frequency band but the intensity of the high-frequency band was low, so it is difficult to tell if one should have been observed.

(17) J. H. deBoer and J. W. E. Coenen, as reported in ref. 1, p. 15.

(18) R. P. Eischens, W. A. Pliskin, and S. A. Francis, *J. Chem. Phys.*, 22, 1786 (1954).

(19) R. P. Eischens, Acceptance Address for American Chemica Society Award in Petroleum Chemistry, San Francisco, Calif., 1958.

The shift in frequency with changing support could also be interpreted in terms of electron-donating properties of the support. If it is assumed that alumina donates electrons, this would shift the bands for the alumina sample to lower frequencies than for the silica sample. At the present time, there are no data available to assess the extent of such an electronic effect.

Yang and Garland[20] have observed that for CO adsorbed on alumina-supported Rh, sintering decreases the intensity of a band at 1925 cm.$^{-1}$. They stated that this fact is not consistent with the assignment of the 1925-cm.$^{-1}$ band to a simple bridge structure. This fact is consistent with the interpretation that sintering increases the degree of crystallinity and thereby decreases the number of sites giving the low-frequency band.

In a similar manner, the data of O'Neill and Yates[21] on the effect of using silica, alumina, or titania to support Ni for CO chemisorption studies can be discussed in terms of the degree of crystallinity of the supported Ni. They used a batch H_2 reduction treatment for only about 2 hr.

3. Band Position as a Function of Coverage. It has been observed that as the surface coverage increases, the frequencies of both the high- and low-frequency bands shift to higher values.[1-4] Two possible kinds of behavior can be predicted for the frequency as a function of coverage. One is that a particular band will simply shift its position to higher frequencies in a continuous manner as the coverage increases. The proposed model of the bonding explains this by noting that as the number of adsorbed molecules increases, the competition for the electrons of the surface atoms increases so that there is less charge available to put into each ψ_2-orbital with the consequence that the C–O frequencies increase.

A second kind of behavior is predicted if the types of sites are distinct and the adsorbed CO is mobile enough to find the sites which give the highest heat of adsorption. The heat of adsorption would be expected to be greatest on the low coordination number metal atom sites which give the lower frequency bands. Eischens[2] has indeed observed that the chemisorbed CO which gives the bands below 2000 cm.$^{-1}$ is the most tightly held. After the lowest energy type of site is filled, the next lowest type which will give a band at a higher frequency will be filled. The result will be a band with its maximum at a high frequency and one or more shoulders on the low-frequency side.

Actually, both kinds of behavior are observed. On nickel the second kind of behavior is usually observed although the separation of bands and designation of shoulders is sometimes a matter of personal taste. When chemisorbed CO is removed by pumping with or without heating, the bands are removed in just the reverse order in which they appear. This would seem to indicate that in the adsorption process the low energy sites are indeed occupied first.

4. Effect of Other Gases on Adsorbed CO Bands. The effect here is in terms of whether the added gas adsorbs with addition or removal of electrons from the metal substrate. If electrons are removed from the metal, the occupancy of the ψ_2-orbitals is reduced with consequent raising of the C–O frequency. Addition of electrons gives the opposite effect. Eischens and co-workers have shown that the chemisorption of O_2, which is expected to dissociate and form oxide ions on the surface, thereby removing electrons, shifts the bands for CO chemisorbed on Fe and on Cu to higher frequencies. This is in accord with the model of bonding proposed. Eischens and co-workers[1,19] have also shown that when H_2 is added to CO on Pt the C–O band is shifted to lower frequencies. From magnetic measurements[22] and electrical resistance data,[23] it is generally believed that adsorbed hydrogen contributes electrons to the metal. The observed shift in the C–O band is in accord with hydrogen contributing electrons to the metal.

Yates and Garland[24] have observed the effect of adsorbing mercury vapor on the bands of CO chemisorbed on Ni. They observed that adsorption of Hg first caused the disappearance of the low-frequency band. Here this band has been ascribed to a site in which the Ni atom has a low coordination number. That means that this site is the most exposed and gives the highest energy of interaction so the Hg might well be expected to displace CO from these sites first. They further observed that the high-frequency band was shifted to a lower frequency, the bond strength of the Ni–C bond increased for the remaining CO after the Hg adsorption, and the extinction coefficient for the remaining CO was greatly increased. The authors were unable to explain these results. Since Hg has its outer d-orbitals completely filled, it would be expected to contribute electrons to the Ni substrate upon adsorption. This would put more electrons into ψ_2-orbitals of the remaining CO groups with the observations just given following as a natural course.

5. $C^{12}O$ and $C^{13}O$ Desorption. Eischens, Francis,

(20) A. C. Yang and C. W. Garland, *J. Phys. Chem.*, **61**, 1504 (1957).

(21) C. E. O'Neill and D. J. C. Yates, *ibid.*, **65**, 901 (1961).

(22) P. W. Selwood, "Adsorption and Collective Paramagnetism," Academic Press, New York, N. Y., 1962.

(23) R. Suhrmann, *Z. Elektrochem.*, **60**, 804 (1956).

(24) J. T. Yates and C. W. Garland, *J. Phys. Chem.*, **65**, 617 (1961).

and Pliskin[2] observed that when a mixture of chemisorbed $C^{12}O$ and $C^{13}O$ is slowly desorbed by pumping and heating from a Pt surface, the intensity for the $C^{13}O$ band first increases and then decreases while the $C^{12}O$ band first decreases rapidly and then more slowly. They proposed to explain this result on the basis of dipole–dipole interaction of adjacent chemisorbed CO groups. An alternative explanation seems possible. On the basis of the model of bonding proposed here, the extinction coefficient for chemisorbed CO should increase as the coverage decreases. For slow desorption of $C^{12}O$ and $C^{13}O$ a kinetic isotope effect is expected with the lighter isotope coming off the surface faster. For the chemisorbed CO at almost complete coverage, the heat of adsorption is low and the isotope effect could be fairly large. If the rate at which $C^{13}O$ is being removed from the surface is less than the rate at which the extinction coefficient is being increased due mainly to $C^{12}O$ desorption, the intensity of the $C^{13}O$ band will initially increase. As CO is removed from the surface, the heat of adsorption for the CO increases so the activation energy for desorption increases, with the result that the difference in rate of desorption for $C^{12}O$ and $C^{13}O$ becomes less. As $C^{13}O$ is removed from the surface at more nearly the rate at which $C^{12}O$ desorbs, the intensity of the $C^{13}O$ band decreases even though the extinction coefficient may be increasing. The relative roles of dipole interaction and kinetic isotope effect in the observed phenomena do not seem to be readily determinable at present.

6. Band Position on Alloys. The only data giving the band position for CO on alloys that have been published are those of Eischens[25] for a 90% Ni–10% Cu alloy. Since Cu has its d-orbitals filled, it would be expected to donate electrons to the system which would put more charge in the ψ_2-orbitals with a consequent lowering of the C–O stretching frequency. The data of Eischens show the CO bands on the alloy to be very similar to those on pure Ni except that the alloy bands are indeed shifted to lower frequencies by about 40 $cm.^{-1}$.

In summary, the molecular orbital model of the metal–carbon–oxygen π-bonding system successfully qualitatively explains: (1) the occurrence of several carbon–oxygen stretching frequencies in the infrared spectra of CO adsorbed on metals; (2) differences in spectra of CO adsorbed on evaporated and supported metals; (3) infrared band positions as a function of coverage; (4) the effect of adsorbing other gases in addition to previously chemisorbed CO; and (5) band shifts in going from adsorption on pure Ni to a Ni–Cu alloy.

Acknowledgment. Acknowledgment is made to the donors of the Petroleum Research Fund, administered by the American Chemical Society, for partial support of this research.

Discussion

F. A. MATSON (University of Texas). The filling of the antibonding orbital should have a significant effect on the intensity of observed bands. Can such an effect be observed?

G. BLYHOLDER. I expect that such an effect could be observed, and, by analogy to the work of Jones (ref. 16 of the paper), it is expected to be a sizable effect.

E. HUTCHINSON (Stanford University, California). Would you expect that the effect of sintering on the geometry of a "central" atom is sufficiently pronounced to make it worthwhile to study the changes in the spectra of carbon monoxide adsorbed on evaporated or supported thin metal films as a function of time and temperature of sintering?

G. BLYHOLDER. Yes, and we expect to pursue this line of attack in the near future.

J. T. YATES, JR. (National Bureau of Standards, Washington, D. C.) (communicated). (1) Dr. Blyholder's view is that the spectrum of chemisorbed CO on Ni and other transition metals may be interpreted in terms of linear CO species adsorbed on metal atoms having various degrees of coordination with other metal atoms in the supported surface, the lower frequency bands being due to CO bonded to Ni atoms having less than the maximum number of neighbors. Although his theoretical deductions based on the spectra of substituted metal carbonyls may be qualitatively correct to some extent, he ignores a body of experimental data which supports the opposite point of view—namely, that both linear and bridged CO species are formed on crystalline Ni surfaces. Thus the work of Yates and Garland (*J. Phys. Chem.*, **65**, 617(1961)) established that *both* the low-frequency CO band centered at 1960 $cm.^{-1}$ and the band at 2035 $cm.^{-1}$ *increased* in relative intensity as the Ni crystallite average size was increased by increasing the percentage of Ni in the supported samples (as verified by X-ray line broadening studies). At the same time the relative intensity of the highest frequency band at 2080 $cm.^{-1}$ (which in my view is due to linear CO on dispersed Ni sites) decreased due to the decrease in the population of dispersed sites as the percentage of Ni was increased. Contrary to this, the Blyholder model would predict that the relative intensity of the 1960-$cm.^{-1}$ line would *decrease* as the number of fully coordinated Ni atoms in the surface was increased. Dr. Blyholder's argument is partially based on a comparison of spectra of CO on silica-supported Ni and Ni particles suspended in *oil*. Considerations of surface cleanliness in the case of the oil-suspended samples would seem to vitiate this comparison.

(2) It is suggested by Dr. Blyholder that a large kinetic isotope effect exists in the desorption of $C^{12}O^{16}$ and $C^{13}O^{16}$ and that this may explain the change in relative intensity of the two isotope bands during desorption from Pt as observed by Eischens. Calculations based on the classical mechanics of a linear three-body oscillator with end body of infinite mass (A. Adel, *Phys. Rev.*, **45**, 56(1934)) show that a change from $C^{12}O^{16}$ to $C^{13}O^{16}$ should result

(25) R. P. Eischens, *Z. Elektrochem.*, **60**, 782 (1956).

in a 2.3% decrease in the metal–carbon stretching frequency—a small effect. In addition, recent measurements (J. T. Yates, Jr., *J. Phys. Chem.*, **68**, 1245 (1964)) on Ni of the relative desorption kinetics of $C^{13}O^{16}$ and $C^{12}O^{18}$ have shown that to within ±2% (the experimental error) these two molecules desorb at the same rate. On this basis, then, Eischens' experimental results are better interpreted on the basis of an interactional effect, as he originally proposed.

(3) Finally, the recently observed oxygen exchange (see the article by Yates) between chemisorbed CO molecules on Ni suggests that *at high coverage* some adsorbed species exist where the oxygen end of the CO is associated with a Ni atom. It is presently open to question whether these species would be observable spectroscopically. These results suggest that CO chemisorption on transition metals may be more complicated than heretofore supposed.

G. BLYHOLDER. (1) My position is that while I have certainly *not* shown that the bridge form does not exist, I have shown that there is no evidence presently known that necessitates the postulation of a bridge species. The work of Drs. Yates and Garland shows only that as a large increase in the percentage of Ni in the supported samples is made, the number of crystallites large enough to give sharp X-ray lines increases. The X-ray work does not give information about particle size distributions or the relative numbers of different surface sites. Therefore, almost any change in the relative intensities of bands is consistent with their data in which the percentage Ni underwent large change. This leaves my interpretation not inconsistent with their data.

My interpretation is not partially based on a comparison of silica-supported Ni and oil-suspended Ni, but rather I argue that differences in the spectra of CO on these materials may be rationalized on the basis of my M.O. model.

(2) The difference in metal–carbon stretching frequencies in itself is not important. The important quantity in considering the relative rates of desorption of the different isotopic molecules is the ratio of the difference in zero point energies of the different isotopic molecules to the heat of adsorption. If this ratio is large at amost complete coverage, where the heat of adsorption may be very low, the rates for the different isotopic molecules may be rather different. At less than 95% coverage, where the heat of adsorption is large, the ratio is small and so the rates would be expected to be nearly equal, as suggested by Dr. Yates. Until data are available at essentially complete coverage I shall regard the question of explanations as open.

(3) In response to point 3, I can only repeat what I have said before, which is that infrared spectroscopy most readily gives information about the predominant surface species; and since catalytic reactions are known which involve only a very tiny fraction of the surface, any particular reaction may not involve the predominant surface species. I think that on general principles one can say that even at low coverages there will be some CO molecules adsorbed with structures different from the predominant ones.

Effects of Adsorption on Diffusion in Porous (Vycor) Glass[1]

by Robert L. Cleland, Jeffrey K. Brinck, and Richard K. Shaw

Department of Chemistry, Dartmouth College, Hanover, New Hampshire *(Received February 26, 1964)*

Apparent diffusion coefficients were measured in porous (Vycor) glass disks by an immersion method[2] as a function of composition and temperature for the C_6H_6–CCl_4 system. An estimate of the pore diffusion coefficient indicates that diffusion in pores of about 50 Å. diameter is somewhat, but not greatly, slower than free diffusion. A treatment of pore diffusion leads to expressions for diffusion coefficients in an interfacial region at the pore surface and in the bulk solution phase in the pore interior. When free diffusion is assumed to occur in the bulk phase, the surface diffusion coefficient is estimated to be one-third to one-half the free diffusion coefficient for an interfacial region thickness of 4 Å.

Introduction

Liquid diffusion coefficients may be determined with rather good accuracy by the disk immersion method described by Wall, Grieger, and Childers.[2a] The method involves the observation as a function of time of the weight W of a porous disk suspended in a bath liquid composed of two components having different densities. The porous disk initially contains a mixture of the same components differing in composition from the bath liquid. Solutions of the time-dependent differential equation for diffusion couched in a form adapted to this method have been given by Wall and co-workers for the case (i) that the diffusion coefficient D is independent of concentration,[2a] and (ii) that D depends in quadratic fashion on concentration.[2b] According to their results the coefficient D_0 corresponding to the composition of the bath liquid may be determined from the slope of a plot of the experimental data in the form log $(W - W_\infty)$ against time, where W_∞ is the weight of the immersed disk after equilibrium with the bath liquid is reached. The slope must be taken at times sufficiently long after the beginning of the experiment to permit neglect of transient terms occurring in the solutions of the equation.

The result does not depend on the shape of the porous body[3] nor on its internal pore geometry for pores which are sufficiently wide so that effects of the pore walls on the diffusion process are negligible. In the present work we have been interested in a case where such effects cannot be neglected. The disk immersion method is well suited to this case when the porous material is available as an immersible body of such dimensions that accurate determination of weight change during a reasonable time period is possible. The material studied was porous (Vycor) glass (hereafter termed simply porous glass), an intermediate in the manufacture of commercial Vycor glass, whose preparation and properties have been described by Nordberg.[4] The specific surface area of porous glass has been studied[5–8] with results consistent with an equivalent capillary model composed of capillaries approximately 50 Å. in diameter.

In their interpretation of anomalies in the flow behavior of paraffin hydrocarbons with respect to macroscopic viscosity, Debye and Cleland[9] postulated a flow mechanism which required introduction of a friction coefficient between a moving liquid layer and the pore boundary. An investigation of binary liquid diffusion in porous glass was carried out under the assumption

(1) This work was supported in part by a grant from the Research Corporation.

(2) (a) F. T. Wall, P. F. Grieger, and C. W. Childers, *J. Am. Chem. Soc.*, **74**, 3562 (1952); (b) F. T. Wall and R. C. Wendt, *J. Phys. Chem.*, **62**, 1581 (1958).

(3) F. Grün and C. Blatter, *J. Am. Chem. Soc.*, **80**, 3858 (1958).

(4) M. E. Nordberg, *J. Am. Ceram. Soc.*, **27**, 299 (1944).

(5) P. H. Emmett and M. Cines, *J. Phys. Colloid Chem.*, **51**, 1248 (1947).

(6) R. M. Barrer and J. A. Barrie, *Proc. Roy. Soc.* (London), **A213**, 250 (1952).

(7) H. Brumberger and P. Debye, *J. Phys. Chem.*, **61**, 1623 (1957).

(8) A. Ron, M. Folman, and O. Schnepp, *J. Chem. Phys.*, **36**, 2449 (1962).

(9) P. Debye and R. L. Cleland, *J. Appl. Phys.*, **30**, 843 (1959).

that this phenomenon would also be affected by such frictional interactions, an assumption which has been confirmed both by the present investigation and by a study of binary liquid flow in porous glass.[10] Values of D_{12}^*, the diffusion coefficient for free diffusion, are available as a function of temperature for the C_6H_6–CCl_4 system.[11] The density difference between the components made the latter system useful for our purposes. Apparent and estimated true pore diffusion coefficients of this liquid system as a function of composition at 10, 25, and 40° are presented in this work.

Experimental

The experimental method was described by Wall, Grieger, and Childers[2a] and has been reviewed in a recent laboratory manual.[12] Three similar disks of porous Vycor (supplied by Corning Glass Works), all 4.81 (±0.01) cm. in diameter had the following thicknesses: disk 2, 0.36 cm.; disk 3, 0.365 cm.; disk 4, 0.35 cm. (all ±0.005 cm.). The disks were all heated prior to use in air at 500° for at least 24 hr. to remove adsorbed organic matter. This treatment also causes some surface dehydration.[13] Before a diffusion experiment the disks were soaked in the desired initial mixture of C_6H_6 and CCl_4. This soaking procedure was normally an automatic result of the previous experiment. The soaking time was sufficiently long (usually 24 hr.) to assure attainment of equilibrium between pore liquid and bath liquid. Bath liquids were originally prepared volumetrically; the same liquid was reused in further experiments for which the same composition was required, evaporation losses being made up when necessary. Compositions were checked occasionally by pycnometry, but changes in volume fraction never exceeded 1%. This resulted from use of a large bath liquid volume (*ca.* 800 ml.) compared to pore volume (*ca.* 2 ml.) and use of successive experiments in which either larger or smaller concentrations of a given component were present in the pore liquid than in the bath. Bath liquids which were initially pure solvents were replaced when their composition approached 1% of the other component.

Experiments were conducted with the bath liquid contained in 1-l. erlenmeyer flasks clamped in a thermostated water bath. The disks were attached to fine copper wire by means of cadmium-plated steel clips. A loop in the wire was attached to the pan of an analytical balance. Two balances were used in this work, first a chain-equipped balance (Christian Becker Chain-o-matic) and later an analytical balance with optical scale (Mettler Model H15) fitted with a suspension for below-balance weighing. Both balances were supported over thermostated water baths by frameworks made of 2 × 4 in. wooden planks. To begin an experiment the porous glass disk was lifted out of the liquid in which it had soaked, was quickly wiped dry with a cotton towel, and was immediately dropped into the new bath liquid. The wire loop was attached to the balance pan and the bath flask was covered with a piece of heavy aluminum foil fitted with a slot to avoid touching the wire. The time was observed on an electric wall clock with a sweep second hand or, more conveniently, on a laboratory electric timer provided with digital indication of elapsed time to 0.01 min. (Lab-Line Model 1401). Readings were taken after about 0.5 hr. at 10- or 20-min. intervals either of time as weight balance was obtained (Chain-o-matic balance) or of weight at desired time intervals (Mettler balance). The Mettler balance proved to be particularly well suited to this experimental use. Weight readings were usually continued for about 4 hr. A value of W_∞ was obtained as the weight reading some 24 hr. after the beginning of the experiment. The readings of W_∞ in a given bath liquid appeared to increase by about 0.1 g. over the course of the first 2 weeks of use of a given disk, and then to become reproducible thereafter within 0.01 g. The bath liquid was stirred slightly by the motion of the suspended disk and this was supplemented occasionally by manual raising and dipping of the disk. The extra stirring did not appear to be necessary in view of good reproducibility of results in stirred and unstirred experiments. The reagents used in the bath liquids were reagent grade benzene and carbon tetrachloride (Mallinckrodt).

Results

For the description of their mixtures we shall designate benzene as component 1 and CCl_4 as component 2. Compositions will be expressed as volume fraction φ_i^0 or molar concentration c_i^0 (moles/cm.^{3}) when they refer to the bath liquid, and φ_i' or c_i' when they refer to the liquid in which the disk had initially been soaked.

The raw data obtained from the measurement of the weight W of the suspended disk (with suspension) and W_∞, the equilibrium weight after at least 24 hr., could be plotted in the form log $(W - W_\infty)$ against time t. An example of such a plot is given in Fig. 1. When

(10) R. L. Cleland, "Binary Liquid Flow in Porous (Vycor) Glass," to be published.

(11) C. S. Caldwell and A. L. Babb, *J. Phys. Chem.*, **60**, 51 (1956).

(12) D. P. Shoemaker and C. W. Garland, "Experiments in Physical Chemistry," McGraw-Hill Book Co., New York, N. Y., 1962, p. 150.

(13) R. L. Cleland, *J. Phys. Chem.*, **68**, 1432 (1964).

$\varphi_2' > \varphi_2^0$, the absolute magnitude of the slopes of such plots became steady after falling during the first 30 or 40 min. (at 25°). When $\varphi_2' < \varphi_2^0$, the slopes tended to decrease throughout. This behavior conforms to that predicted by the calculations of Wall and Wendt[2b] for the case that D decreases with increasing φ_2, as it does in this system.[14] The slopes were consequently corrected by the use of the calculations of these authors for the case that D varies quadratically with concentration. The parameters required for the correction procedure were obtained from a quadratic fit of the actual diffusion data.

In treating our data the steady uncorrected slopes were usually obtained with sufficient accuracy for $\varphi_2' > \varphi_2^0$ by direct calculation from the values of log $(W - W_\infty)$ and t without making the plot of Fig. 1. The correction procedure was applied to the slope thus obtained to provide a corrected slope m which corresponded theoretically to the apparent diffusion coefficient, D_{app}, at the composition of the bath liquid. The value of D_{app} was calculated from[2b]

$$D_{app} = -2.303\tau^2 m/\pi^2 \qquad (1)$$

where m is the value of $\lim_{t\to\infty}$ d log $(W - W_\infty)/dt$ obtained by correction of the experimental value of d log $(W - W_\infty)/dt$. The disk thickness τ is the only other experimental quantity required in the evaluation

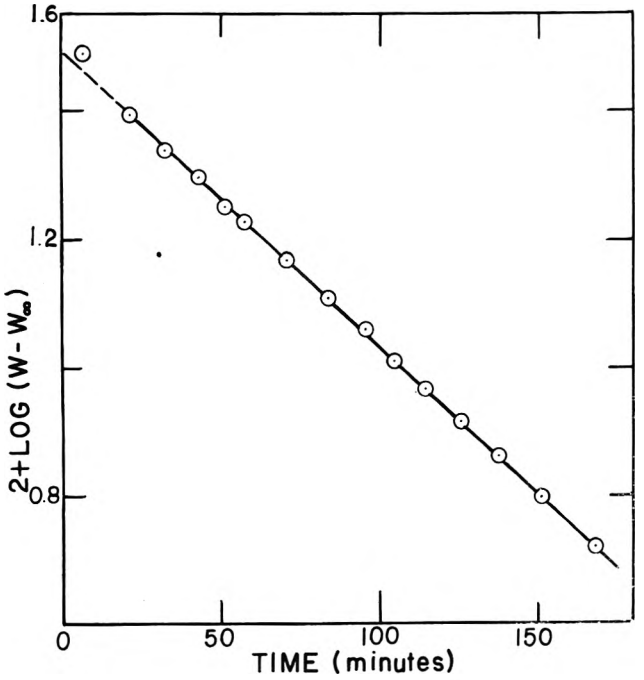

Figure 1. Plot for determination of d log $(W - W_\infty)/dt$. The data are for disk 4 at 25°, $\varphi_2' = 1.0$, $\varphi_2^0 = 0.75$.

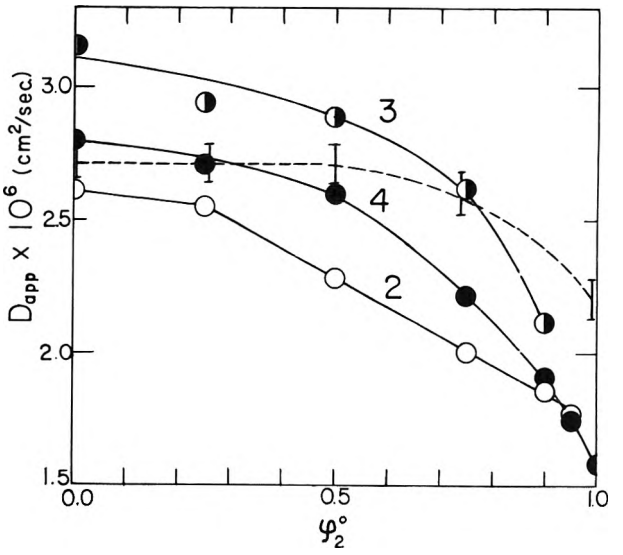

Figure 2. The apparent diffusion coefficient D_{app} for C_6H_6–CCl_4 in porous glass as a function of bath composition at 25°. Numbers indicate disk designations. The dashed line (vertical bar points) is a plot of D_{app} obtained from flow experiments with a porous glass membrane.[10]

of D_{app}. Values of D_{app} obtained at 25° for the three disks studied are shown in Fig. 2 as a function of composition. The deviation of values of the slope m from the mean for duplicate experiments was most often within 1% and seldom greater than 2% of the mean. Also shown in Fig. 2 are values of D_{app} estimated from flow experiments[10] in which a concentration gradient was applied between two cell compartments across a membrane. The diffusion was observed as a time rate of change of concentration in one cell compartment. Since the experimental technique in the flow case is different and the calculation of D_{app} involves an estimate of the cross-sectional area of membrane pores available for diffusion, the two methods give rather good agreement.

Treatment of Pore Diffusion

In order to estimate the magnitude of the supposed frictional effects of the boundaries of microscopic pores on ordinary liquid diffusion in the pore, a theoretical investigation of a simple capillary pore model was undertaken. We shall discuss in this section a single pore having a circular cross section of uniform diameter. Later (see Discussion) we shall suppose that the porous medium is composed of a set of such pores of equal diameter.

Diffusion in a pore may conveniently be treated as

(14) This statement corresponds to Fig. 1 in Wall and Wendt's paper. The sign of the coefficient β of these authors has evidently been reversed in their Fig. 2.

a frictional process in which the frictional forces exerted at any point on component i (per mole) by component j are assumed proportional to the product of c_j, the molar concentration of j, and the relative velocity $u_j - u_i$ of the two components at that point. When mechanical equilibrium exists in a macroscopic phase so that no net volume flow occurs, a force balance between $\nabla_T\bar{\mu}_i$, the gradient of the chemical potential (per mole) at constant temperature, and the sum of the frictional forces F_{ij} exerted by other components j may be written[15] for an isothermal system of n components

$$\nabla_T\bar{\mu}_i = \sum_{j=1}^{n} F_{ij} = -\sum_{j=1}^{n} R_{ij}c_j(u_i - u_j) \qquad (2a)$$

$$\nabla_T\bar{\mu}_i = \bar{V}_i\nabla p + \nabla_{T,p}\bar{\mu}_i \qquad (2b)$$

$$R_{ij} = R_{ji} \qquad (2c)$$

where the u_i are the local component velocities, $\bar{V}_i$ are partial molar volumes, ∇p is the pressure gradient, $\nabla_{T,p}\bar{\mu}_i$ are the chemical potential gradients at constant temperature and pressure, and the R_{ij} form a symmetric matrix of friction coefficients. In the absence of a pressure gradient eq. 2a–2c reduce to the diffusion equations discussed by Laity[16] as implicit in Onsager's treatment of diffusion.[17]

Treatments of diffusion in membranes in terms of eq. 2a–2c have been made for biological membranes by Kirkwood[18] and for ion-exchange membranes by Spiegler.[19] In these treatments the membrane was taken as a component of the diffusing system, while concentrations and velocities of the various components were supposed uniform over a membrane cross section. The membrane and the solution contained in it were, thus, treated as a single macroscopic phase. In our discussion we wish to include the possibility that concentrations and velocities may differ in the interfacial region at the pore surface from those in the bulk solution phase in a given pore cross section.

The model chosen to approximate the physical situation is illustrated in Fig. 3. The coordinate r represents radial distance from the pore center. The pore boundary situated at $r = a$ consists of the structural material of the membrane with any immobile adsorbed matter; the boundary is assumed smooth on a molecular scale. An interfacial film s, assumed to be of molecular thickness δ, forms an annular ring ($a - \delta < r < a$) adjacent to the pore boundary. The solution phase occupies the region of the pore cross section $r < a - \delta$. The model resembles that employed by Guggenheim[20] to discuss the thermodynamics of the interfacial region. We shall limit our discussion to the simple case for which the concentration c_i^* and the velocity u_i^* of each component are uniform throughout the

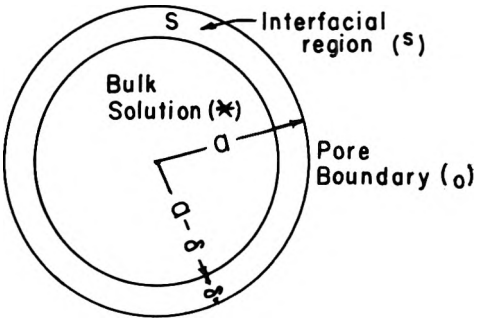

Figure 3. Diagram for model of capillary pore cross section.

solution phase portion of the cross section ($0 < r < a - \delta$), but may be different from the concentration c_i^s and the velocity u_i^s of that component in the interfacial region. The concentrations c_i^* may thus be taken to represent the concentrations of each component far enough from the pore boundary so that adsorption effects become negligible. Experimental evidence on adsorption from solution[21] supports the assumption that concentration effects occur only in a surface monolayer.

Although eq. 2a–2c are valid strictly only for a macroscopic phase, we shall assume their applicability to the solution phase of the microscopic pore, regardless of its dimensions. We shall also assume that a force balance similar to (2a) may be written for the interfacial region s. For this purpose the frictional forces on component i molecules in s may be divided into forces exerted by other molecules in (a) the solution phase and (b) the interfacial region, as well as forces exerted by (c) the pore boundary.

The principal contributions to the integrals[15] which express the coefficients R_{ij} in molecular terms come from nearest-neighbor interactions for relatively ideal nonelectrolyte solutions. In applying eq. 2a–2c in regions of molecular dimensions we shall make the approximation that the coefficients R_{ij} depend solely on nearest-neighbor interactions. As a further approximation the values of R_{ij} observed in the macroscopic solution will be assumed to represent frictional interactions between molecules in the interfacial region and their nearest neighbors when the latter are solution com-

(15) R. J. Bearman and J. G. Kirkwood, *J. Chem. Phys.*, 28, 136 (1956).

(16) R. W. Laity, *J. Phys. Chem.*, 63, 80 (1959).

(17) L. Onsager, *Ann. N. Y. Acad. Sci.*, 46, 241 (1945).

(18) J. G. Kirkwood, in "Ion Transport Across Membranes," H. T. Clarke, Ed., Academic Press, New York, N. Y., 1954, p. 119 ff.

(19) K. S. Spiegler, *Trans. Faraday Soc.*, 54, 1408 (1958).

(20) E. A. Guggenheim, *ibid.*, 41, 150 (1945).

(21) J. J. Kipling and D. A. Tester, *J. Chem. Soc.*, 4123 (1952).

ponents. This assumption ignores the possible effects on R_{ij} which may result from changes in orientation, distribution functions, intermolecular potentials, etc., due to the proximity of the pore boundary.

The frictional force F_{ij}^* exerted per mole of component i in region s by j molecules in the bulk solution phase and the force F_{ij}^s exerted by j molecules in the interfacial region may then be written in a form analogous to (2a)

$$F_{ij}^* = -R_{ij}z^*c_j^*(u_i^s - u_j^*)$$
$$F_{ij}^s = -R_{ij}z^sc_j^s(u_i^s - u_j^s)$$

The quantities z^* and z^s represent for a given molecule in s the fraction of its nearest neighbors which lie in the solution phase and in the interfacial region, respectively. These fractions are independent of which molecule in s is chosen when a random arrangement is assumed, on the average, in that part of its nearest-neighbor shell lying in a given region. We have also assumed arrangement of nearest neighbors on a lattice of equal-volume sites.

The frictional force F_{i0} exerted per mole of component i in region s by the pore boundary may be written

$$F_{i0} = -R_{i0}'(u_i^s - u_0)$$

where R_{i0}' is a boundary friction coefficient and u_0 is the velocity of the boundary. We shall set $u_0 = 0$, so that all component velocities are measured with respect to the pore boundary. For consistency with the previous approximation limiting contributions to R_{ij} to nearest-neighbor interactions, we shall neglect direct frictional interactions of the boundary with the bulk solution phase since these are assumed not to be in mutual contact.

The thermodynamic driving force $\nabla_T\bar{\mu}_1^s$ in the interfacial region may now be assumed equal to the sum of frictional forces exerted per mole of component i in that region. For example, for component 1 of a binary solution we write

$$\nabla_T\bar{\mu}_1^s = -R_{12}z^*c_2^*(u_1^s - u_2^*) - R_{11}z^*c_1^*(u_1^s - u_1^*) - R_{12}z^sc_2^s(u_1^s - u_2^s) - R_{10}'u_1^s$$

A similar equation may be written for component 2. Subtraction then gives

$$\nabla_T\bar{\mu}_1^s - \nabla_T\bar{\mu}_2^s = -R_{10}'u_1^s + R_{20}'u_2^s - R_{12}'(u_1^s - u_2^s) \quad (3)$$

$$R_{12}' = R_{12}(z^sc^s + z^*c^*),\ c^s = c_1^s + c_2^s,\ c^* = c_1^* + c_2^*$$

when we neglect, as a first approximation, the quantity $z^*[R_{11}c_1^*(u_1^s - u_1^*) - R_{22}c_2^*(u_2^s - u_2^*)]$, which represents the differences between frictional forces exerted per mole of component 1 in s by molecules of the same kind in the solution phase and those exerted in analogous fashion per mole of 2 in s. In the solution phase we have assumed the applicability of eq. 2a–2c, which implies neglect of this quantity for that phase as well. For the binary solution we then obtain

$$\nabla_T\bar{\mu}_1^* - \nabla_T\bar{\mu}_2^* = -R_{12}c^*(u_1^* - u_2^*) \quad (4)$$

In experiments of the kind described in this work the volume fluxes J_v^s and J_v^* in the interfacial region and the solution phase, respectively, may each be taken equal to zero. Thus

$$J_v^s = c_1^s\bar{V}_1^su_1^s + c_2^s\bar{V}_2^su_2^s = 0 \quad (5)$$

$$J_v^* = c_1^*\bar{V}_1^*u_1^* + c_2^*\bar{V}_2^*u_2^* = 0 \quad (6)$$

A relation between eq. 3 and 4 may be obtained by assuming that lateral equilibrium exists across a pore cross section in the sense that $\bar{\mu}_i$ is constant over the cross section. When $\nabla p = 0$, this assumption implies that $\nabla_{T,p}\bar{\mu}_i^* = \nabla_{T,p}\bar{\mu}_i^s$. The Gibbs-Duhem equation for the bulk solution phase may be written in the form

$$c_1^*\nabla_{T,p}\bar{\mu}_1 + c_2^*\nabla_{T,p}\bar{\mu}_2 = 0 \quad (7)$$

where we drop the superscript notation on $\bar{\mu}_i$. The differences occurring in (3) and (4) may then be written with use of (7)

$$\nabla_{T,p}\bar{\mu}_1 - \nabla_{T,p}\bar{\mu}_2 = (c^*/c_2^*)\nabla_{T,p}\bar{\mu}_1 \quad (8)$$

The molar flux J_1^s (moles cm.$^{-2}$ sec.$^{-1}$) $= c_1^su_1^s$ with respect to the pore boundary may be found from (3) and (5) and the flux $J_1^* = c_1^*u_1^*$ from (4) and (6) with use of (8) to give

$$J_1^s = -\frac{c_1^sc_2^s\bar{V}_2^s}{R_{12}' + \varphi_2^sR_{10}' + \varphi_1^sR_{20}'}\frac{c^*}{c_2^*}\nabla_{T,p}\bar{\mu}_1 = -D_s\nabla c_1^s$$
$$J_1^* = -\frac{c_1^*\bar{V}_2^*}{R_{12}}\nabla_{T,p}\bar{\mu}_1 = -D^*\nabla c_1^* \quad (9)$$

where $\varphi_i^s = c_i^s\bar{V}_i^s$, the volume fraction in region s. Diffusion coefficients D_s and D^* are defined formally in (9) for the interfacial region and the bulk solution, respectively.

The relation of these coefficients to experiment may be discussed as follows. Equation 1 was derived[2] for the case in which a concentration C in a porous disk was a function of the spatial coordinates and the time. If we neglect diffusion in the radial direction, C may be taken as a function of x and t, where x denotes the

direction normal to the circular face of the disk. A treatment analogous to that for the entire disk may be applied to a single pore, which is taken, for simplicity, to lie along the x-direction and to have a uniform cross section S of arbitrary shape. The ends of the pore lie at $x = -l/2$ and $x = l/2$, so that the origin lies at the midpoint of the pore. When the concentrations vary over the pore cross section because of selective adsorption forces, the diffusion equation $\partial c_1/\partial t = (\partial/\partial x)[D_p(\partial c_1/\partial x)]$ may be integrated over S to give

$$\frac{\partial \langle c_1\rangle(x,t)}{\partial t} = A^{-1}\int_S \frac{\partial}{\partial x}\left(D_p \frac{\partial c_1}{\partial x}\right) dS$$

$$\langle c_1\rangle = A^{-1}\int_S c_1\, dS \qquad (10)$$

where dS is an element of area and A is the total cross-sectional area of S. When the pore diffusion coefficient D_p is independent of position in the cross section (10) becomes

$$\partial\langle c_1\rangle(x,t)/\partial t = (\partial/\partial x)[D_p\partial\langle c_1\rangle(x,t)/\partial x] \qquad (11)$$

The boundary conditions for (11) are

$$\langle c_1\rangle(x,0) = \langle c_1'\rangle$$

$$\langle c_1\rangle(-l/2,t) = \langle c_1\rangle(l/2,t) = \langle c_1^0\rangle \qquad (12)$$

where $\langle c_1'\rangle$ and $\langle c_1^0\rangle$ are the pore-average concentrations corresponding to equilibrium with bath liquids of concentration c_1' and c_1^0, respectively. The concentration $\langle c_1\rangle$ of (11) and (12) is formally equivalent to the C used in the derivation of (1), and the corresponding solution is

$$D_p = -2.303 l^2 m/\pi^2 \qquad (13)$$

When D_p is not constant throughout S, a pore-average coefficient D_p may be defined by (11) in order to recover (13).

The flux equation corresponding to (11) is

$$J_1 = A^{-1}\int_S J_1\, dS = -D_p\nabla\langle c_1\rangle \qquad (14)$$

where J_1 is the average flux through S. Substitution of (9) into (14) with the assumption that the region s represents a fraction A_s/A and the bulk solution region a fraction A^*/A of the total cross-sectional area A ($= A_s + A^*$) of S leads to

$$-J_1 = \left(D_s \frac{dc_1^s}{dc_1^*}\frac{A_s}{A} + D^*\frac{A^*}{A}\right)\nabla c_1^* =$$

$$D_p\left(\frac{dc_1^s}{dc_1^*}\frac{A_s}{A} + \frac{A^*}{A}\right)\nabla c_1^* \qquad (15)$$

where c_1^* has been taken as the independent concentration variable.

Discussion

A tentative explanation of our experimental results may be offered on the basis of an assumption that the pore diffusion theory presented above describes the diffusion process in porous glass. Volume flow and diffusion in this material in the presence of pressure and concentration gradients have been discussed in terms of an equivalent capillary model.[9,10] A porous body is assumed in this model to be represented by a network of circular cylindrical capillaries of equal diameter whose average orientation may be specified by the geometric factor $\langle\cos\theta\rangle_{Av}$, which represents the ratio of macroscopic length to effective pore length in a given direction in the porous medium. The length l of (13) may be identified with the effective pore length $\langle l\rangle_{Av} = \tau/\langle\cos\theta\rangle_{Av}$ traversed over the macroscopic disk thickness τ. In this case x is taken as a coordinate whose direction is determined by the pore. Elimination of $l = \langle l\rangle_{Av}$ from (13) and comparison with (1) leads to

$$D_p = D_{app}/\langle\cos\theta\rangle_{Av}^2 \qquad (16)$$

An estimate of $\langle\cos\theta\rangle_{Av}^2$ in porous glass may be made on the basis of the equivalent capillary model by use of an expression derived[9] for molecular streaming (or Knudsen flow) of a gas through a porous membrane

$$B = qRT/A_m\bar{v}\gamma = 4\langle\cos\theta\rangle_{Av}^2\varphi^2/3\sigma \qquad (17)$$

where q is the molar gas flow rate, $\bar{v}$ the R.M.S. molecular velocity, γ the absolute magnitude of the capillary pressure gradient, A_m the mean membrane area, R the gas constant, T the absolute temperature, φ the volume fraction of voids, and σ the internal surface area to total volume ratio of the porous medium. A value of $\langle\cos\theta\rangle_{Av}^2$ may be estimated from the data of Barrer and Barrie[6] for gas flow through porous glass at temperatures sufficiently high so that B became constant and independent of the particular gas used. These authors gave $B = 1.0 \times 10^{-8}$ cm., $\varphi = 0.30$, and $\varphi/\sigma = 14.3 \times 10^{-8}$ cm., so that $\langle\cos\theta\rangle_{Av}^2$ is estimated from (17) to be 0.175. Debye and Cleland[9] gave $B = 0.89 \times 10^{-8}$ cm. and $\varphi = 0.30$ for another specimen of porous glass. With the value of φ/σ of Barrer and Barrie, these data give $\langle\cos\theta\rangle_{Av}^2 = 0.156$. A more probable value for σ is obtained from the specific surface area value[7,8] of 156 m.^{2}/g., which may be converted by the relation $\sigma = 156\rho_g(1-\varphi)$ to $\sigma = 2.4 \times 10^6$ cm.$^{-1}$ by use of the glass density $\rho_g = 2.18$ g./cm.^{3}. This value of σ and the data of Debye and Cleland lead to $\langle\cos\theta\rangle_{Av}^2 = 0.177$. For purposes of comparison, the value of $\langle\cos\theta\rangle_{Av}^2$ appropriate to random orientation of pore segments is 0.25. We remark that deviations of 10% or more may be expected for values of

$\langle \cos \theta \rangle_{Av}^2$ from one sample to another, and that it would be desirable to make an experimental determination of this quantity for each porous sample used in order to provide a more accurate test of flow theories.

Values of the coefficient D_p have been estimated from (16) with $\langle \cos \theta \rangle_{Av}^2$ taken equal to 0.176. The results are plotted in Fig. 4 as D_p/D_{12}^* for disk 4 at 25 and 40°. The points shown for 10° are those obtained with the assumption that experimental values of D_{app} obtained for disk 2 at 10° could be converted to those which would have been observed with disk 4 at this temperature by multiplication by the factor 1.11, which represents the average ratio of the 25° values of D_{app} for disk 4 to those for disk 2. The differences between the curves for different temperatures are not considered especially significant, since they are not much larger than experimental uncertainty. At high volume fraction φ_2^0 of CCl_4 the ratio D_p/D_{12}^* appears, however, to increase regularly with increasing temperature.

With due regard for variability with respect to porous specimen and uncertainty in the factor $\langle \cos \theta \rangle_{Av}^2$, which was not available for the individual disks used, the significant features of the data shown in Fig. 4 may be pointed out. First, diffusion in the C_6H_6–CCl_4 system is probably somewhat, although certainly not greatly, slower in pores of 50 Å. diameter than in free diffusion; second, retardation of diffusion appears to be considerably greater at high φ_2^0 than at low.

When the free diffusion coefficient D_{12}^* is defined in terms of a coordinate system fixed in the local liquid volume velocity J_v and the flux relation (constant T and p) $J_1 = -D_{12}^* \nabla c_1^*$, the coefficient R_{12} is given[16] by

$$R_{12} = RT/D_{12}^* c^* \qquad (18)$$

when solutions of 1 and 2 are ideal, a good approximation for the C_6H_6–CCl_4 system.[22] Substitution of (18) into the second equation of (9) and use of the identity

$$(\partial \bar{\mu}_1/\partial c_1^*)_{T,p} = RT/c_1^* c^* \bar{V}_2^* \qquad (19)$$

valid for ideal solutions, leads to $D^* = D_{12}^*$, as we expect in view of the assumptions made. Equation 15 then becomes

$$D_s/D_{12}^* = D_p/D_{12}^* + (D_p/D_{12}^* - 1) \times (A^*/A_s)/(dc_1^s/dc_1^*) \qquad (20)$$

The quantity (dc_1^s/dc_1^*) of (20) may be estimated at 25° from solution adsorption data[13] by use once again of the assumption that concentration effects of adsorption occur only in the surface region s. Estimated values are listed in Table I. Values of D_s/D_{12}^* calculated from the 25° data for disk 4 (given in Fig. 4) are plotted in Fig. 5 for $A^*/A_s = 1, 2, 2.5$, and 3.

The values of A^*/A_s employed may be converted to a film thickness δ of the region s in terms of a specific pore model. If the pore is assumed to be a circular cylinder of radius a, and the surface region to be a cylindrical annulus of outer radius a and inner radius $a - \delta$, $A^*/A_s = (a - \delta)^2/\delta(2a - \delta)$. The pore radius a is given by the equivalent capillary model as $a = 2\varphi/\sigma$; the values cited previously for φ and σ lead to a value of about 26 Å. for a. With this result the values of δ which correspond to each value of A^*/A_s chosen

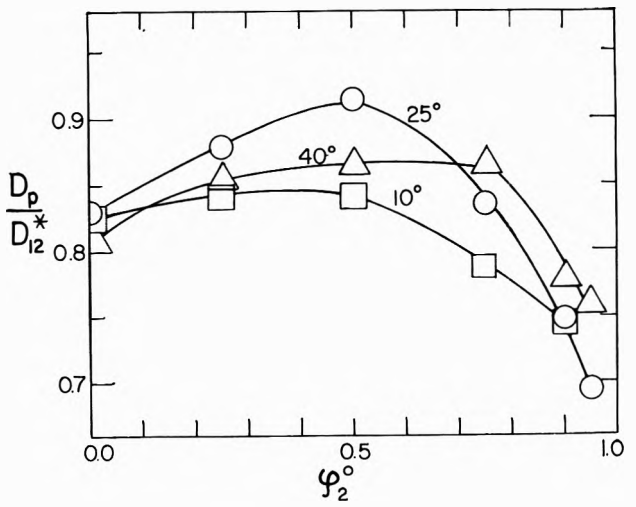

Figure 4. The ratio of the estimated pore diffusion coefficient D_p to the free diffusion coefficient D_{12}^* as a function of composition and temperature for C_6H_6–CCl_4 in porous glass. All data are based on disk 4. Points: □, 10°; ○, 25°; △, 40°.

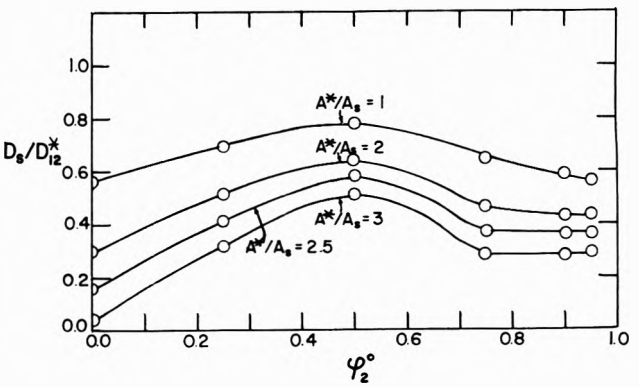

Figure 5. Estimated ratio D_s/D_{12}^* as a function of composition for C_6H_6–CCl_4 in porous glass (disk 4) at 25° for various values of A^*/A_s.

(22) G. Scatchard, S. E. Wood, and J. M. Mochel, *J. Am. Chem. Soc.*, 62, 712 (1940).

have been calculated as shown in Table I. A benzene monolayer on silica gel has been estimated[23] to have a thickness of about 4 Å., corresponding to $A^*/A_s = 2.5$.

The quantitative estimates of D_s/D_{12}^* provided by Fig. 5 are very rough in view of the crudeness of the equivalent capillary model, the somewhat arbitrary choice made for $\langle\cos\theta\rangle_{Av}^2$, the obvious differences (Fig. 2) in D_{app} for different porous specimens, and uncertainties in the quantity dc_1^s/dc_1^*. The conclusion that D_s/D_{12}^* is less than one seems justified, however. At $A^*/A_s = 2.5$ our estimate indicates that D_s values at most concentrations are of the order of one-third to one-half the free diffusion coefficient.

In order to discuss the friction coefficients of solution components with the boundary, it is convenient to define a "molecule" of the pore boundary as that amount of material occupying the average molecular volume in the solution, so that the "molar" concentration c_0 of boundary "molecules" is equal to c^*. The fraction z_0 which such "molecules" contribute to the nearest-neighbor shell of a molecule in the monolayer s would be estimated at $^1/_3$ for a close-packed lattice, as would the fractions z^s and z^*. We may write $R_{i0}' = R_{i0}z_ic_0$, where R_{i0} is a friction coefficient analogous to the R_{ij} in the interfacial region. We now substitute this definition of R_{i0} into the first equation of (9) and solve for D_s/D_{12}^* with use of (18) and (19) and the approximation $\bar{V}_2^s = \bar{V}_2^*$ to obtain

$$D_s/D_{12}^* = (h_s/k_s)/(dc_1^s/dc_1^*)$$
$$h_s = c_1^s c_2^s/c_1^* c_2^*$$
$$k_s = y_{12} + \varphi_2^s y_1 + \varphi_1^s y_2 \qquad (21)$$
$$y_{12} = z^* + z^s(c^s/c^*),\ y_i = R_{i0}z_0/R_{12}$$

The quantities h_s and dc_1^s/dc_1^* have been estimated in Table I from solution adsorption data[13] at 25°. The values of the parameter k_s given in Table I have been calculated at various A^*/A_s from (21) and the data of Fig. 5. It is interesting to note that the values of k_s so calculated, except at $\varphi_2^0 = 0$ for most A^*/A_s, are relatively independent of composition. The decrease in D_p/D_{12}^* at high φ_2^0 does not lead to high values of k_s. This decrease is thus evidently ascribable to concentration effects rather than to resistance effects. The term y_{12} in (21) should be concentration-independent, since the ratio c^s/c^* may be taken as unity to a good approximation. With our previous estimates of the z factors we then have $y_{12} = ^2/_3$, $3y_i = R_{i0}/R_{12}$.

The experimental values of y defined by

$$y = \varphi_2^s y_1 + \varphi_1^s y_2 = k_s - y_{12}$$

Table I: Estimation of Surface Diffusion Parameters[a]

φ_2^0	h_s	dc_1^s/dc_1^*		A^*/A_s = 1	2	2.5	3
				k_s			
0.00	0.78	0.64		2 2	4.1	7.6	39
0.25	0.81	0.64		1 8	2.5	3.1	4.0
0.50	0.94	0.64		1 9	2.3	2.5	2.9
0.75	1.30	0.9		2 2	3.1	3.9	5.1
0.90	1.91	1.6		2 0	2.7	3.3	4.3
0.95	2.46	2.3		1.9	2.5	3.0	3.6
			δ, Å.	7.6	4.8	4.0	3.5
			y	1 3	1.9	2.5	3.3

[a] Data are based on disk 4 at 25°.

given in Table I were obtained from an average value of k_s at all compositions, with the exception of the high values at $\varphi_2^0 = 0$. It is of interest in this connection that rough estimates of y_1 and y_2 can also be made from viscous flow data for the pure components. The estimates, based on a hydrodynamic treatment of a slipping film model,[9,10] which resembles in many respects the model used in this work, are $y_1 = 0\ 7$ and $y_2 = 0.8$ when A^*/A_s is taken to be 2.5. These estimates are subject to uncertainties similar to those in the present work. The values of the R_{i0} can thus be estimated to be from 2 to 10 times larger than R_{12}, the friction coefficient for the two liquid components.

The integrand of the integral expressions for the molecular friction coefficient[15] is proportional, among other things, to the gradient of intermolecular potential energy. We expect this gradient, equal in magnitude at a given point to the attractive force, to be greater at a given distance of separation for an i, 0 interaction ($i = 1, 2$) of an i molecule with a boundary (or 0) "molecule" than for an i, j interaction ($i, j = 1, 2$), when the boundary is a material which adsorbs positively. Our result is thus in qualitative agreement with theory.

Discussion

E. Hutchinson (Stanford University, California). You mentioned, in the informal discussion of your experiments, that diffusion experiments of this type are well suited to study in undergraduate physical chemistry laboratory courses. Would you care to comment on the conditions under which the experiments may be carried out in a reasonable length of time in such a course; *e.g.*, how long should one wait to get "infinite time" values?

(23) B. R. Smith and J. M. Thorp, *J. Phys. Chem.*, **67**, 2617 (1963).

R. L. CLELAND. This experiment has been used for 3 years in this department with good results following the instructions of Shoemaker and Garland (ref. 12 of the paper). According to these authors (p. 156) the need for values of W_∞ may be avoided by making weight determinations at equal time intervals of suitable duration and applying Guggenheim's method to the data. I believe that more accurate results would be obtained by determining W_∞ as we have done in this work. The latter procedure requires 4 to 6 hr., according to Shoemaker and Garland, when use is made of the porous disks that they recommend. I recognize the difficulty of adapting the latter time interval to undergraduate courses.

H. VAN OLPHEN (Shell Development Company, Houston). In diffusion processes in porous formations the tortuosity factor is probably different for the surface and the bulk diffusion paths. Would it not be desirable to consider possible interchange effects between bulk and surface layers? *Cf.* A. H. Bloksma, *J. Colloid Sci.*, **12**, 40 (1957).

R. L. CLELAND. In an actual pore the path is undoubtedly longer for diffusion in the surface layer than in the bulk phase. The pore and surface diffusion coefficients calculated on the assumption of a smooth pore surface are therefore underestimated somewhat in the present treatment. Interchange effects between the layers, representing radial diffusion processes, will smooth the concentration profile from that assumed here. The concept that adsorption affects concentration only in a monolayer requires a sharp concentration change at the interface between the layers, which is physically rather unrealistic. The calculation of diffusion coefficients will be affected to the extent that actual concentration gradients differ from those assumed here.

Physical Adsorption on Low Energy Solids. II. Adsorption of Nitrogen, Argon, Carbon Tetrafluoride, and Ethane on Polypropylene[1]

by Donald Graham

Research and Development Division, Organic Chemicals Department, Jackson Laboratory, E. I. du Pont de Nemours and Company, Wilmington, Delaware *(Received February 26, 1964)*

Nitrogen and argon are adsorbed on a solid hydrocarbon surface (polypropylene) as two-dimensional gases, nitrogen failing to show the supermobility previously observed on polytetrafluoroethylene (Teflon). Carbon tetrafluoride and ethane are adsorbed with some restriction of mobility, possibly due to their greater energies of self-interaction, the entropy changes in adsorption being intermediate between those associated with localization and with free mobility in two dimensions. Film pressures at a coverage representing one statistical monolayer are 12 to 14 ergs/cm.^{2} for nitrogen, argon, and ethane, but only 9 ergs/cm.^{2} for carbon tetrafluoride, reflecting its appreciably lower free energy of adsorption.

Introduction

An earlier paper[2] reported the adsorption of nonpolar gases on polytetrafluoroethylene, a solid characterized by the lowest surface energy of any solid readily available. The present investigation is concerned with the properties of nonpolar adsorbates on polypropylene —more particularly, with the adsorbate mobilities and the film pressures. The hydrocarbon polymers, of which polypropylene is one, are "low energy solids" but are more strongly bonded than the perfluorocarbon polymers. The surface energy of polytetrafluoroethylene has been estimated earlier as 56–69 ergs/cm.[2,3] but more recent extrapolation of measurements on related liquids indicates a value closer to 40 ergs/cm.^{2} and similarly, for the hydrocarbon plastics, about 50 ergs/cm.[2,4]

An isotherm for the adsorption of nitrogen on polyethylene reported earlier[5] yielded a linear B.E.T. plot and a reasonable value for the adsorbent surface area. This isotherm is essentially duplicated in the present study by the isotherm for adsorption of nitrogen on polypropylene, supporting consideration of the adsorbent properties of polypropylene as representative of those of the general class of hydrocarbon polymers.

Experimental

The polypropylene used as the adsorbent was a powdered sample supplied by Dr. L. F. Beste (Textile Fibers Department, E. I. du Pont de Nemours and Co., Inc., Wilmington, Del.), prepared by cracking a Hercules "Profax" resin in a hot mill to a weight-average molecular weight of 150,000 and a melt index of 24.1, precipitation from a solvent, and drying under vacuum. It is realized that the cracking process may have involved some oxidation, but this was not expected to have any appreciable effect on the adsorption of nonpolar molecules, an assumption supported by the similar behavior of the polyethylene adsorbent reported by Zettlemoyer, *et al.*[5]

The ethane used was obtained as Phillips research grade and was freed of noncondensible impurities by stripping under vacuum at liquid oxygen temperature.

All other materials were the same as used in the earlier paper[2] and the same equipment and methods of operations were employed.

Results and Discussion

Adsorption Data. As in the preceding paper, adsorption isotherms were obtained at two temperatures

(1) Contribution No. 368 from the Research and Development Division, Organic Chemicals Department, Jackson Laboratory, E. I. du Pont de Nemours and Co., Wilmington, Del.

(2) D. Graham, *J. Phys. Chem.*, 66, 1815 (1962).

(3) R. J. Good, L. A. Girifalco, and G. Kraus, *ibid.*, 62, 1418 (1958).

(4) Private communications from R. E. Johnson and R. H. Dettre.

(5) A. C. Zettlemoyer, A. Chand, and E. Gamble, *J. Am. Chem. Soc.*, 72, 2752 (1950).

Table I: Physical Constants of Adsorption Systems

	N_2	Ar	CF_4	CH_3CH_3
Latent heat of vaporization at I_{av} in cal./mole	1300	1580	3005	3487
T_1, °K.	77.4	77.5	139.5	184.6
T_2, °K.	90.2	90.2	144.9	189.8
T_{av}, °K.	83.8	83.9	142.2	187.2
Vapor pressures of adsorptive materials at the adsorption temperatures, in mm.				
$P_{0(1)}$ (at T_1)	762	210	500	761
$P_{0(2)}$ (at T_2)	2740	1024	745	1001
Capacity of monolayer (V_m) in ml. at STP/g. of adsorbent	23.30	27.40	17.65	16.45
Cross-sectional area per molecule in Å.^{2} (at T_{av})	16.6	14.1	21.9	23.5
Adsorbent surface area in m.^{2}/g.	103.4	103.4	103.4	103.4

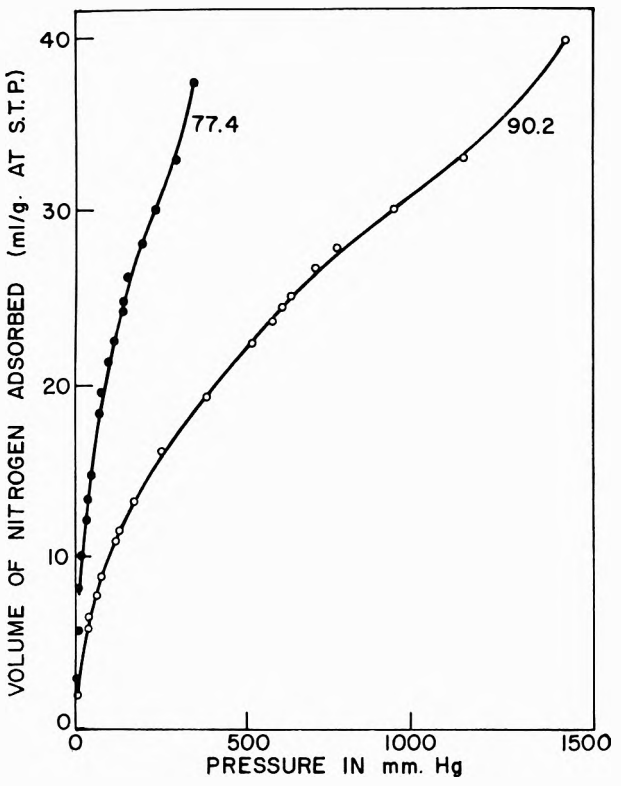

Figure 1. Adsorption of nitrogen on polypropylene at 77.4 and 90.2°K.

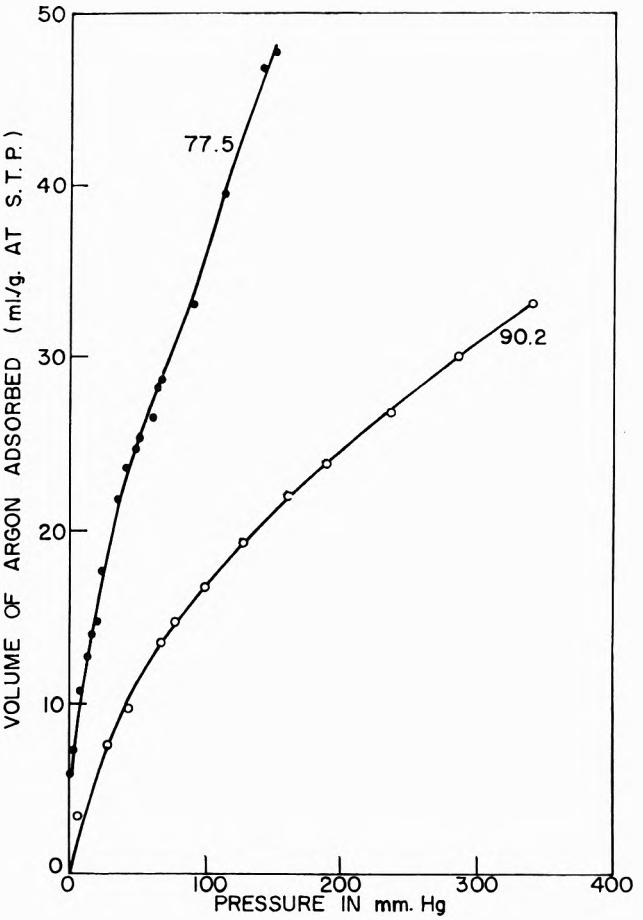

Figure 2. Adsorption of argon on polypropylene at 90.2 and 77.5°K.

near the boiling point of the adsorptive material for each system. Also, as before, values of σ (cross-sectional area of an adsorptive molecule) and θ (fractional coverage of the adsorbent surface) representing an average temperature were used in the heat and entropy calculations. The physical constants of the systems studied are given in Table I.

The adsorption isotherms for nitrogen, argon, carbon tetrafluoride, and ethane on polypropylene are shown in Fig. 1–4. In general form, the isotherms show no

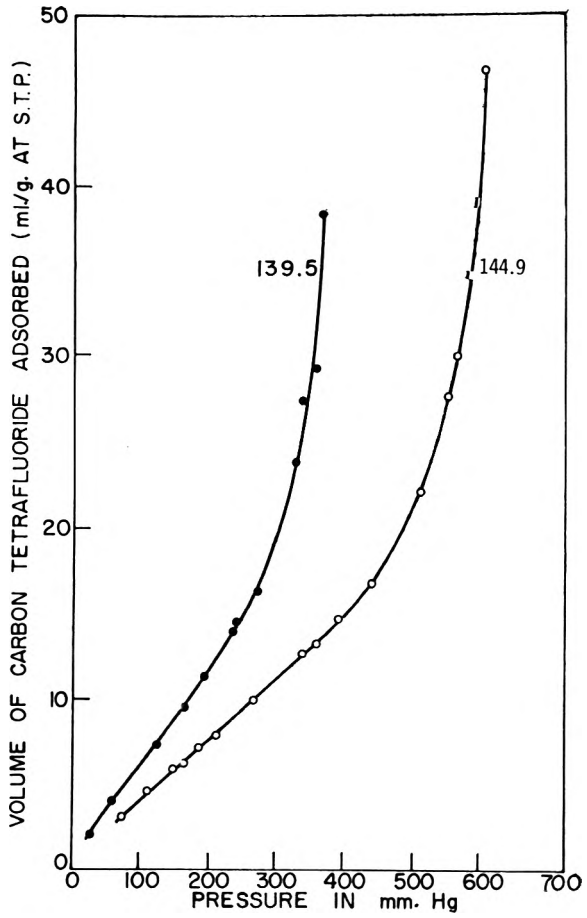

Figure 3. Adsorption of carbon tetrafluoride on polypropylene at 144.9 and 139.5°K.

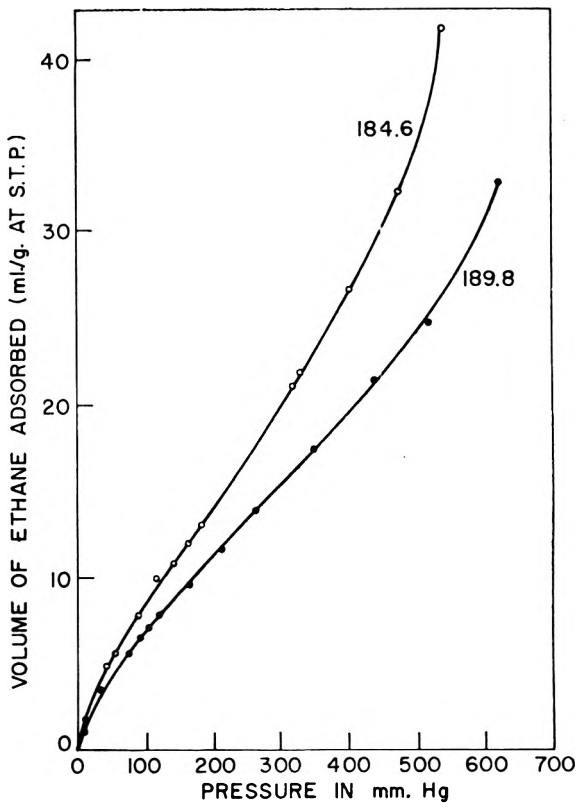

Figure 4. Adsorption of ethane on polypropylene at 184.6 and 189.8°K.

unusual characteristics, but in the adsorption of ethane there was a tendency for poorly reproducible hysteresis in the lower part of the isotherm. This may be due to microcapillaries or even to some penetration and swelling of the polymer. The lower part of the isotherm was not used in the thermodynamic calculations, as explained later, so this question was not pursued further.

Isosteric Heats of Adsorption. The isosteric heats of adsorption of each of the four adsorptive materials on polypropylene at temperatures near their respective boiling points were calculated by application of the Clausius–Clapeyron equation to the adsorption data. The results are plotted in Fig. 5. In every case, the initial high heats (usually ascribed to adsorbent heterogeneity) extend to unusually high coverage (near or exceeding $\theta = 0.5$). The same type of heat curve was reported by Zettlemoyer, *et al.*,[5] for the adsorption of nitrogen on polyethylene, suggesting that high surface heterogeneity may be characteristic of hydrocarbon plastics. Due to these high initial heats, the calculation of adsorption entropies was limited to coverages of $\theta = 0.5$ or greater.

It is also interesting to note that the polyatomic molecules, carbon tetrafluoride and ethane, are adsorbed with isosteric heats highly twice those for nitrogen and argon, in line with their stronger self-interaction as measured by the latent heats of condensation.

Argon is the only adsorbate showing isosteric heats close to or lower than the latent heat of condensation.

Adsorbate Mobility. As in the preceding paper, adsorbate mobility is evaluated in terms of standard differential entropies of adsorption calculated from the adsorption data and compared with those from theoretical, entropically ideal processes representing adsorption on fixed sites and as a mobile two-dimensional gas. The method of calculation and the notation employed are those proposed by de Boer and Kruyer.[6] The results are reported in Table II.

In each case, the observed loss of entropy is less than that which would occur if the adsorbate were localized. That is, $-\Delta S°_i$ (a combination of the experimentally observed entropy change with a configurational term)

(6) J. H. de Boer and S. Kruyer, *Proc. Konikl. Ned. Akad. Wetenschap.*, **B55**, 451 (1952).

Table II: Comparison of Observed Entropy Changes with Those of Idealized Models Representing Site Adsorption and Mobile Adsorption

				Std. diff. molar entropy of adsorption			
				Site adsorption		Mobile adsorption	
θ	$-\Delta H$, cal./mole	$-\Delta F$, cal./mole	$-\Delta S$	Expt. $-\Delta S°_i$	Theory ${}_gS°_{tr}$	Expt. $-\Delta S°_m$	Theory ${}_gS°_{tr} - {}_aS°_{tr}$
			Nitrogen				
0.5	1725	535	14.2	14.2	29.6	9.3	10.0
0.7	1740	417	15.8	14.1	29.6	10.2	10.0
0.9	1700	323	16.4	12.0	29.6	10.3	10.0
			Argon				
0.5	1600	428	13.9	13.8	31.7	8.9	10.7
0.7	1540	340	14.3	12.6	31.7	8.7	10.7
0.9	1520	259	15.0	10.6	31.7	8.9	10.7
			Carbon tetrafluoride				
0.5	3400	333	21.6	21.6	35.7	16.5	11.7
0.7	3510	224	23.1	21.4	35.7	17.3	11.7
0.9	3460	166	23.2	18.8	35.7	16.9	11.7
			Ethane				
0.5	4075	762	19.8	19.8	33.9	14.4	10.9
0.7	4110	582	21.1	19.4	33.9	15.0	10.9
0.9	4110	467	21.8	17.4	33.9	15.2	10.9

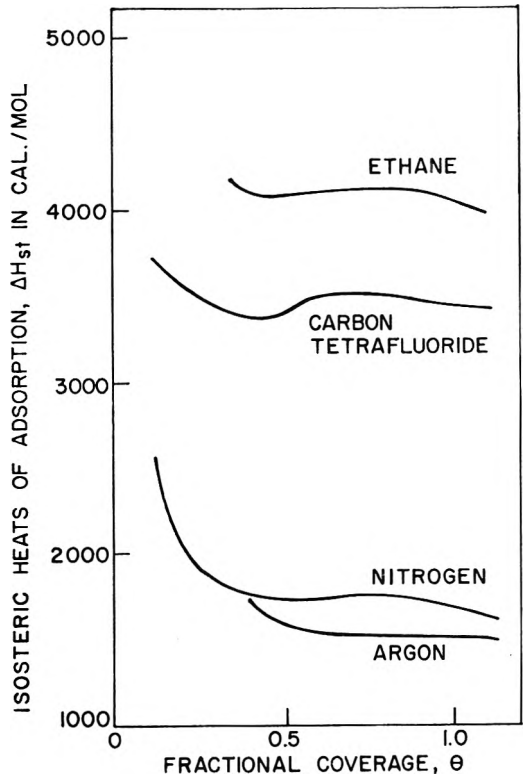

Figure 5. Isosteric heats of adsorption of nitrogen, argon, carbon tetrafluoride, and ethane on polypropylene.

is in every case much smaller than ${}_gS°_{tr}$ (the translational entropy of the adsorptive gas).

The test for mobile adsorption is a comparison of $-\Delta S°_m$ (a combination of the experimental entropy change with a measure of the area over which an adsorbed molecule is free to move at a specified coverage) with ${}_gS°_{tr} - {}_aS°_{tr}$ (the difference between the translational entropy of the adsorptive gas and that of the adsorbate as an ideal, mobile, two-dimensional gas, or the entropy change resulting from loss of one degree of translational freedom). Carbon tetrafluoride and ethane yield values of $-\Delta S°_m$ somewhat greater than the corresponding $({}_gS°_{tr} - {}_aS°_{tr})$ indicating that while not localized, their mobility is somewhat restricted. This result is in line with their larger heats of adsorption. In the case of nitrogen, the criteria for a mobile, two-dimensional gas are closely matched by the data. Argon, however, yields values of $-\Delta S°_m$ slightly smaller than the corresponding value of $({}_gS°_{tr} - {}_aS°_{tr})$. The loss of entropy in the adsorption process is thus slightly less than that representing one degree of translational freedom, indicating that argon retains some "supermobility," possibly as a vibration normal to the adsorbent surface. This "supermobility" is consistent with the observation, mentioned earlier, that the isosteric heat of adsorption of argon on polypropylene is slightly less than its latent heat of condensation.

Film Pressures. Film pressures, or changes in the surface free energy with adsorption, were calculated from the adsorption data for a coverage of one statistical monolayer by graphic integration of the Gibbs equation as has been described.[7]

The values obtained for nitrogen, argon, and ethane were 12, 13, and 14 ergs/cm.^{2}, respectively. In contrast, the film pressure of a statistical monolayer of carbon tetrafluoride was only 9 ergs/cm.^{2}, a value consistent with its lower free energy of adsorption.

Conclusions

Polypropylene adsorbs the nonpolar gases, nitrogen, argon, carbon tetrafluoride, and ethane, with small to moderate heats of adsorption, the low coverage results indicating extensive surface heterogeneity. Nitrogen and argon are adsorbed as mobile two-dimensional gases, argon retaining some "supermobility." The polyatomic gases, carbon tetrafluoride and ethane, were adsorbed with somewhat restricted mobility, but the film pressure of carbon tetrafluoride was lower than those of the other adsorbates, reflecting its lower free energy of adsorption.

Discussion

J. H. DE BOER (The Hague, Netherlands). In your introductory remarks you refer to the independent proof that 16.2 Å.^{2} is the right value to use for the molecular surface area of nitrogen, based on studies of the adsorption of iodine on carbon. It may be interesting to note that our recent work on the adsorption of lauric acid on alumina shows that one lauric acid molecule is adsorbed for every four oxygen atoms of the surface. This effect leads to a value of 26.9 Å.^{2} for a lauric acid molecule in this particular type of adsorption and confirms the value of 16.2 Å.^{2} for nitrogen.

P. K. ISAACS (W. R. Grace Company, Clarksville). Would a higher energy surface than polypropylene have less tendency to give rise to polymolecular layers? You seem to imply that polymolecular layers are peculiar to low energy surfaces below the saturation point.

D. GRAHAM. Physical adsorption at any coverage is favored by a high adsorbent surface energy. On a high energy surface, the first monolayer may be completed at a low relative pressure with multilayer deposition becoming appreciable as the vapor pressure of the adsorptive gas is approached. On a low energy solid adsorbent the first statistical monolayer retains considerable mobility and requires a higher relative pressure for its completion, tending to obscure the usual sigmoid inflection in the isotherm, *i.e.*, there is no well defined "point B"—see Fig. 1–4.

(7) W. D. Harkins, "The Physical Chemistry of Surface Films," Reinhold Publishing Corp., New York, N. Y., 1952, p. 211.

An Approach to a Theory of Monolayer Permeation by Gases

by Martin Blank[1]

Department of Physiology, College of Physicians and Surgeons, Columbia University, New York, New York
(Received February 28, 1964)

The permeability of a monolayer to gases is compared to that of thicker layers. The current theory explaining monolayer resistance, *i.e.*, the energy barrier theory, is also re-examined. This study introduces a new interpretation of monolayer resistance to permeation in terms of known properties of monolayers. The new model suggests that free spaces in the monolayer are available for permeation from: (1) the natural free area in a lattice, (2) the equilibrium fluctuations in monolayer density at a (gas molecule–monolayer) collision site, and (3) the work of expansion that the permeant molecule can perform against the monolayer forces. (This third factor turns out to be negligible.) From the entropy change associated with an expansion of a monolayer it is possible to estimate the probability of a given expansion. The monolayer resistance can then be derived if it is assumed that all local expansions which yield an area equal to or greater than the cross-sectional area of the permeant result in passage through the monolayer. There is qualitative agreement between the derived resistance and the measured one, but the derived value is much too small. The model is refined and brought into closer agreement with observations when two additional factors are considered: (1) gases that are present but at equilibrium (*e.g.*, air when water permeates) add to the measured resistance; and (2) the structure at a vacant site in a monolayer causes a reflection of most molecules that are attempting to permeate because their angle of approach to the hole results in a collision with a monolayer molecule.

I. Introduction

The effect of a monolayer on the transport of a gas across a gas–water interface is described in terms of a monolayer resistance, r (in sec./cm.). The total resistance to gas transport, p/U_t, is set equal to the sum of the monolayer resistance and the bulk phase resistance, p/U.

$$\frac{p}{U_t} = \frac{p}{U} + r \qquad (1)$$

where U_t equals transport rate of gas per unit time and area (cm.^{3}/cm.^{2}/sec.) when a monolayer is present, U equals transport rate in the absence of a monolayer, and p equals gas "pressure" in cm.^{3}/cm.^{3}. Equation 1 is a steady-state equation and it has been applied by La Mer and co-workers[2] to the steady-state transport of water through a monolayer. More recently, Blank[3] has studied the transport of other gases (CO_2, O_2, N_2O) under conditions that are not steady state but which allow an approximation to the steady state. The resistance (or its inverse, the permeability) of the monolayer to the various gases has been estimated. The variety of experimental procedures (monolayers in different surface phases, composed of various polar and nonpolar groups, with different gases permeating and at several temperatures) allow some general descriptions of the permeation process in monolayers. Table I compares the permeability of monolayers (about 30 Å. thick) to much thicker membranes (composed of synthetic polymers, for example, and microns or millimeters in thickness). These properties have been discussed at some length in a previous article.[3] Several of the assertions are supported by few experiments because the necessary measurements are dif-

(1) Supported by a Research Career Development Award (GM-K3-8158) and a Research Grant (GM-10101) from the U. S. Public Health Service.

(2) Specific references will be cited at appropriate points in the text. A bibliography can also be found in "Retardation of Evaporation by Monolayers," V. K. La Mer, Ed., Academic Press, New York, N. Y., 1962.

(3) M. Blank, *J. Phys. Chem.*, 66, 1911 (1962).

ficult to make in a variety of systems. Nevertheless, the statements summarize repeatable observations and represent the best available information regarding the permeability properties of monolayers.

Table I: Permeability of Interfacial Layers to Gases

Behavior of system	Thick membrane	Monolayer
1. Permeant obeys Fick's law for diffusion	Yes	No
a. Steady-state permeation rate proportional to pressure difference and area	Yes	Yes
b. Inversely proportional to barrier thickness	Yes	No
2. a. Temperature dependence of permeability constant gives activation energy of 5–15 kcal./mole	Yes	Yes
b. The activation energy varies with the barrier thickness	No	Yes
3. Size and shape of permeant molecule influence rate of permeation	Yes	Yes
4. Composition and physical state of barrier influence rate of permeation	Yes	Yes
5. Permeant obeys Henry's law for solution	Yes	No
6. Several gases permeate independently (excluding cases of chemical interaction)	Yes	No

There are several significant differences between macroscopic and monolayer processes. Some of the differences are reasonable: (a) (item 1) The inadequacy of Fick's law is to be expected when the size of the permeant approaches the thickness of the barrier. (b) (item 5) Since the monolayer has very little physical capacity for solute, we would not expect agreement with Henry's law. However, some of the differences imply that one is dealing with two qualitatively different phenomena. (c) (item 2b) The variation of the activation energy with the monolayer thickness implies a one-step, all-or-none process.[4] (d) (item 6) The extra resistance encountered when several gases permeate at the same time is indicative of a different mechanism.

The permeability of a monolayer has been described in terms of an extra energy barrier at the interface.[5] This theory has been used extensively to account for the observations and it has proved very useful in giving a quantitative description of the permeation process in terms of monolayer and permeant properties. The resistance

$$r = c \exp\left(\frac{E}{RT}\right) \qquad (2)$$

where c is a constant, E is the energy barrier, R is the gas constant, and T is absolute temperature. The form of eq. 2 can be derived from Boltzmann's equation where E is the energy necessary to penetrate the barrier and the exponential gives the fraction of molecules possessing this energy. E has been found to depend on the length of the hydrocarbon chain, the surface pressure, the cross-sectional area of the permeant, and some properties intrinsic to the monolayer (surface phase, compressibility, free surface area, and polar group). The relatively large number of properties that influence the energy barrier have made it difficult to visualize a unified physical mechanism for monolayer resistance.

The energy barrier formulation has also been unable to account for a number of observations. Briefly, some of the difficulties are: (a) The resistance is independent of the surface pressure, π_s, in the LC phase of fatty acids but not in other monolayers.[5b,6] (b) The energy barrier contribution per CH_2 group, E_{CH_2}, is greater for the LC phase than for the S phase of fatty acids. This is unusual because the S phase is more close-packed than the LC phase and E_{CH_2} increases as the average spacings between molecules decrease.[7] (c) For fatty acids about $^2/_3$ of E is attributed to the polar group,[5b] but oleic acid with the same polar group has no resistance,[8] and molecules with different groups (OH, OC_2H_5) have comparable resistances.[6] (d) Cholesterol monolayers at high π_s, are close-packed and have a low compressibility but, nevertheless, have immeasureably low resistance.[8,9] (e) The ability of two permeating species to interfere with each other is not considered by the theory.[10]

The complex dependence of the energy barrier on monolayer properties and the inability of the theory to account for some important findings have prompted the author to reconsider the process of monolayer permeation. This paper will suggest a new physical interpretation for the resistance due to a monolayer and attempt to arrive at an alternative to the energy barrier theory.

II. The Monolayer Resistance

A. Mechanism of Monolayer Permeation. For a gas molecule to pass "through" a monolayer, the two-dimensional lattice must contain a free space at least

(4) G. T. Barnes and V. K. La Mer in ref. 2, pp. 9–33.

(5) (a) I. Langmuir and D. Langmuir, *J. Phys. Chem.*, **31**, 1719 (1927); (b) R. J. Archer and V. K. La Mer, *ibid.*, **59**, 200 (1955).

(6) H. L. Rosano and V. K. La Mer, *ibid.*, **60**, 348 (1956).

(7) M. Blank and V. K. La Mer in ref. 2, pp. 59–66.

(8) F. Sebba and H. V. A. Briscoe, *J. Chem. Soc.*, 106 (1940).

(9) M. Blank and F. J. W. Roughton, *Trans. Faraday Soc.*, **56**, 1832 (1960).

(10) M. Blank, *J. Phys. Chem.*, **65**, 1698 (1961).

as large as the permeant. A free space can arise by three different mechanisms. (1) Monolayer molecules cannot pack together in a lattice without leaving free area. The free area per collision site, A_f, depends upon the size and shape of the monolayer molecules, the number of molecules per collision site, and the state of compression. (2) Since a colliding gas molecule will affect few monolayer molecules, there will be large fluctuations in monolayer density at any collision site. The fluctuations give rise to local expansions that increase the free area. (3) The penetrating molecule has kinetic energy which can do work against the surface forces in the monolayer. If all the kinetic energy ($^1/_2mv^2$) is utilized for expansion work ($\pi_s\Delta A$), the largest free space a gas molecule can form is $\Delta A = mv^2/2\pi_s$.

Let us consider the effects of these mechanisms in making holes available for gas permeation and attempt to calculate a monolayer "resistance." We shall assume that the permeation process is all-or-none, *i.e.*, either a gas molecule gets through in one shot when it collides or else it is reflected. The probability of permeating is, therefore, equivalent to the probability of the permeant finding or forming a hole of sufficient magnitude. We can consider the insoluble monolayer at the gas–water interface and the gas phase as equilibrium systems and the monolayer molecules as a hexagonal close-packed lattice (condensed phase). Equations valid for macroscopic systems will be used when necessary since the events discussed in terms of several molecules are repeated many times over the entire surface.

Let us assume that n, the number of molecules that are influenced by a collision, is equal to the number of molecules hit plus the nearest neighbors. n is 7 if a gas molecule hits a monolayer molecule head-on, 10 if it hits between two monolayer molecules, or 12 if it hits at the spaces between three monolayer molecules. The magnitude of n for an entire surface is obtained by averaging all values of n and weighting according to the fraction of monolayer area to which the value applies. Since this cannot be done unambiguously, we shall use an approximate value of n equal to 10. Although n for any collision is integral, the average over the whole surface is nonintegral. Furthermore, n changes with compression of a monolayer since the areas available for different kinds of collisions change.

B. Local Expansions in the Monolayer. The entire monolayer is at constant area, but as a result of normal molecular motions there are fluctuations in monolayer density in small regions of the monolayer. Let us estimate the probability of fluctuations in monolayer density at a collision site by assuming that n molecules undergo a change in the area (A) they occupy and that the rest of the monolayer acts as a reservoir for this process. For this system, which is at constant T, p, V, and n, the variation in the entropy due to a local expansion is

$$\Delta S = -\int \frac{\gamma dA}{T} \tag{3}$$

Since the surface pressure $\pi_s = \gamma_0 - \gamma$, where γ_0 equals the surface tension of pure water

$$\Delta S = -\frac{\gamma_0}{T}\Delta A + \frac{1}{T}\int \pi_s\, dA$$

The entropy change can be calculated on a per molecule basis, ΔS_m. For an LC or S monolayer at constant temperature and composition, the area per molecule, A_m, and π_s are related.

$$\pi_s = -k'A_m + k'' \tag{4}$$

where A_m is in Å.^{2}/molecule and k' and k'' are constants. Substituting for π_s and integrating between the equilibrium area per molecule, A_{eq}, and $A_{eq} + \Delta A_m$

$$\Delta S_m = -\frac{\gamma_0}{T}\Delta A_m + \frac{1}{T}\left[(-k'A_{eq} + k'')\Delta A_m - \frac{k'}{2}\Delta A_m^2\right]$$

For values of $\Delta A_m < 10\%\ A_{eq}$ we can neglect the ΔA_m^2 term. The final equation for the entropy change per molecule, therefore, is

$$\Delta S_m = -\frac{\gamma \Delta A_m}{T} \tag{5}$$

The entropy change at a collision site is nk_1 times eq. 5 where k_1 (2.39×10^{-24}) converts the ΔS into entropy units. We can set $n\Delta A_m = \Delta A$, the area change at a collision site.

The probability, W of observing a spontaneous *decrease* in entropy, ΔS is

$$W = W_0 \exp\left(\frac{\Delta S}{k}\right) \tag{6}$$

W_0 is the probability of the equilibrium state ($\Delta S = 0$), and k is the Boltzmann constant. Substituting for ΔS due to a local expansion at a collision site

$$W = W_0 \exp\left(-\frac{k_1\gamma\Delta A}{kT}\right) \tag{7}$$

The frequency distribution of fluctuations around the equilibrium area is not symmetric. However, it is

reasonable to assume that the bulk of the distribution is due to the small fluctuations immediately around A_{eq} and that these are symmetric. Therefore, we can evaluate W_0 by integrating eq. 7 over all values from $\Delta A = 0$ to $\Delta A = \infty$ and setting the integral equal to $^1/_2$. The result is

$$W_0 = \frac{k_1\gamma}{2kT} \tag{8}$$

Equation 7 gives the probability of an expansion, ΔA, at a collision site in a monolayer. The probability of passing through a monolayer is equivalent to the probability that a permeating molecule will encounter a hole equal to or larger than a_0, its cross-sectional area. Since the hole can arise from a local expansion (ΔA) or from the free area in the lattice (A_f), the condition for permeation is $a_0 \leqslant \Delta A + A_f$.

The probability of permeating the monolayer, W_p, if the available area is ΔA, is the probability of having $\Delta A \geqslant a_0 - A_f$.

$$W_p = \int_{a_0 - A_f}^{\infty} W_0 \exp\left(-\frac{k_1\gamma\Delta A}{kT}\right) d(\Delta A) \tag{9}$$

$$W_p = -\frac{W_0}{\left(\frac{k_1\gamma}{kT}\right)}\left[0 - \exp\left(-\frac{k_1\gamma[a_0 - A_f]}{kT}\right)\right]$$

Since $W_0 kT/k_1\gamma = {}^1/_2$, the probability of getting through the monolayer is

$$W_p = +\frac{1}{2}\exp\left(-\frac{k_1\gamma[a_0 - A_f]}{kT}\right) \tag{10}$$

C. Kinetic Energy of the Permeating Molecule. Let us now take into account the ability of the permeating molecule to expand the monolayer. The magnitude of the maximum expansion is given as $\Delta A = 10^{16}mv^2/2\pi_s$, where the factor 10^{16} converts ΔA into square angstroms. The condition for permeation is

$$a_0 \leqslant \Delta A + A_f + \frac{10^{16}mv^2}{2\pi_s} \tag{11}$$

and eq. 10 should read

$$W_p = \frac{1}{2}\exp\left(-\frac{k_1\gamma\left[a_0 - A_f - \frac{10^{16}mv^2}{2\pi_s}\right]}{kT}\right) \tag{12}$$

The distribution of one component of velocity (normal to a surface in one direction) is

$$\frac{dN}{N} = \left(\frac{2m}{\pi kT}\right)^{1/2}\exp\left(-\frac{mv^2}{2kT}\right)dv \tag{13}$$

dN/N is the fraction of molecules with a velocity between v and $v + dv$, or the probability that a molecule will have a velocity between v and $v + dv$. The joint probability I, that a gas molecule will have a given velocity (eq. 13) and that it will get through the monolayer if it has that velocity (eq. 12), is the product of the two individual probabilities.

$$I = \int^{\text{all } v} W_p\left(\frac{dN}{N}\right) \tag{14}$$

Substituting into eq. 14 and integrating between $v = 0$ and $v = \infty$.

$$I = \left(\frac{\pi_s}{\pi_s - 10^{16}k_1\gamma}\right)^{1/2}\left(\frac{1}{2}\right)\exp\left(-\frac{k_1\gamma[a_0 - A_f]}{kT}\right) \tag{15}$$

The first factor in eq. 15 is equal to unity since $\pi_s >> 10^{16}k_1\gamma$ (by about five orders of magnitude). Equation 15 reduces to eq. 10 and $I = W_p$. It appears that the permeating molecule does not affect the formation of a hole.

D. Derivation of the Resistance. I (or W_p) is the probability that a molecule will permeate when it collides with a monolayer. The number of molecules that strike 1 cm.^{2} of surface/sec.

$$N_1 = n_s\sqrt{\frac{RT}{2\pi M}} = n_sQ \tag{16}$$

n_s equals the number of molecules/cm.^{3} of gas, M equals the molecular weight, R equals the gas constant, and Q is set equal to the square root term. At equilibrium, the number of molecules entering or leaving a gas phase, the unidirectional flux, $U' = N_1\alpha$. α, the condensation coefficient, is the fraction of molecules that enters the liquid phase after striking the surface. When a monolayer is present, each unidirectional flux, $U_t' = N_1\alpha I$. (This assumes that the monolayer has not affected the condensation coefficient.)

If there is a concentration difference (Δn_s) across an interface, the *net* fluxes are $U = \alpha(\Delta n_s)Q$ and $U_t = \alpha(\Delta n_s')QI$. $\Delta n_s'$, the concentration difference across a monolayer, is smaller than Δn_s. Substituting for U and U_t into eq. 1

$$r = \frac{p}{\alpha Q}\left[\frac{1}{(\Delta n_s')I} - \frac{1}{(\Delta n_s)}\right]$$

Substituting for I

$$r = \frac{p}{\alpha Q}\left[\frac{1}{2(\Delta n_s')}\exp\left(\frac{k_1\gamma[a_0 - A_f]}{kT}\right) - \frac{1}{(\Delta n_s)}\right]$$

If

$$\frac{1}{2(\Delta n'_s)} \exp\left(\frac{k_1\gamma[a_0 - A_f]}{kT}\right) \gg \frac{1}{(\Delta n_s)} \quad (17)$$

then

$$r = \frac{p}{2\alpha(\Delta n'_s)Q} \exp\left(\frac{k_1\gamma[a_0 - A_f]}{kT}\right) \quad (18)$$

We can arrive directly at eq. 18 by setting the monolayer resistance equal to a driving force (p) divided by a net flux (U_t). This would avoid using eq. 1, which is defined in macroscopic terms. However, inequality 17 emphasizes our assumption that the total resistance is due to the monolayer, *i.e.*, the free surface has no effective resistance.

Equation 18 is an expression for the monolayer resistance to gas permeation. The pre-exponential term depends on properties of the permeant arising from gas kinetic theory. The exponential (energy barrier) term depends on equilibrium monolayer properties and on the size of the permeant. Comparing eq. 10 and 18, we see that the energy barrier is equivalent to the *probability* of permeating a monolayer. The measured energy barrier, obtained from the temperature dependence of r, is largely determined by the exponential term but the pre-exponential term is also a function of temperature.

III. Discussion

A. Properties of the Derived Resistance. According to the proposed model and in contrast to the energy barrier theory, the kinetic energy of a penetrating gas molecule does not contribute to monolayer permeation. A monolayer is permeable because, at equilibrium, spaces from the natural packing and from the density fluctuations are large enough for a permeant to pass through. Let us see how the monolayer resistance derived on the basis of this model can account for the properties of the observed resistance.

Consider first the resistance or energy barrier increment per CH_2 group in the hydrocarbon chain, E_{CH_2}. This can be attributed to two factors: (1) a smaller A_f because of the greater attraction between hydrocarbon chains and (2) smaller fluctuations in monolayer density because of an increase in mass and volume of the kinetic unit. For these reasons, we can expect the different values observed[5b] for E_{CH_2} in the LC and S surface phases. In the S state, the binding of fatty acid ions by calcium ions in the subphase decreases the density fluctuations and E_{CH_2} is lower than in the LC phase. (However, the S film still has a high resistance due to a large decrease in A_f.) The value of E_{CH_2} should also vary with the chain length since the first CH_2 group has a proportionally greater effect than a CH_2 group added to a longer chain. This would invalidate the linear extrapolation of resistance values to zero CH_2 groups and would explain the very high values found for for contribution of the polar group[5b] to the total energy barrier.

Let us consider now the dependence of $E \sim \gamma(a_0 - A_f)$ in eq. 18. Substituting for γ and multiplying through, we see that E, which depends on four terms

$$E \sim \underset{(1)}{\gamma_0 a_0} - \underset{(2)}{\gamma_0 A_f} - \underset{(3)}{\pi_s a_0} + \underset{(4)}{\pi_s A_f} \quad (19)$$

can account for a number of additional observations. (a) The monolayer lattice (*i.e.*, the number of molecules affected by a single collision and the free area per collision site) changes with surface pressure. For an increase in π_s, A_f decreases and in eq. 19 (1), the largest of the four terms, is constant, (2) decreases, (3) increases, and (4) probably increases. The large constant term (1) tends to minimize the variation in E. The terms (2) and (4) tend to increase E, while (3) tends to decrease E. If (3) is much greater than (2) + (4), E (or ln r) varies linearly with π_s as in the S phase of fatty acids. If the variation of (3) is equal to (2) + (4), ln r is independent of π_s as in the LC phase of fatty acid monolayers. (b) A comparison of monolayer permeation to two different gases (CO_2 and H_2O) indicates that the resistance depends on the cross-sectional area, a_0, of the molecules.[10] The agreement with eq. 19 is semiquantitative since the data do not warrant a more refined test. (c) The presence of a term that depends on A_f explains why some monolayers offer no detectable resistance even though they are incompressible and at high surface pressure (*e.g.*, cholesterol). The free area in such monolayers is much greater than in saturated fatty alcohols.[3] (d) In mixed monolayers, if the two components pack together to minimize A_f, the resistance is high. Since the surface isotherm indicates the nature of the packing and the value of A_f, it is possible to predict the resistance by comparing the partial areas of the components to the areas in one component monolayers. Recent work by Robbins and La Mer[11,12] on the incorporation of spreading solvents in monolayers supports this view. Further support comes from studies[13] on mixed monolayers of fatty alcohols which pack like a single component monolayer and where the resistance varies linearly with the mole fraction.

It appears that the proposed model can account for many qualitative observations on the resistance proper-

(11) V. K. La Mer and M. L. Robbins, *J. Phys. Chem.*, 62, 1291 (1958).
(12) M. L. Robbins and V. K. La Mer, *J. Colloid Sci.*, 15, 123 (1960).
(13) V. K. La Mer, L. A. G. Aylmore, and T. W. Healy, *J. Phys. Chem.*, 67, 2793 (1963).

ties of monolayers, including some properties that are not explained by the energy barrier theory. The quantitative predictions of eq. 18, however, lead to poor agreement when we substitute values and put r into the form of eq. 2. Approximate values for water permeating a close-packed monolayer (at 25°) are: $p = 0.03$, $\alpha = 10^{-2}$, $Q = 1.5 \times 10^{4}$ cm./sec., $\gamma = 50$ dynes/cm., $a_0 = 7$ Å.^{2}, and $A_f < 0.5$ Å.$^2 \sim 0$ (estimated for fatty alcohols). Using the equation $U_t = \alpha(\Delta n'_s)Q$ and the values given by Archer and La Mer,[5b] $(\Delta n'_s) = 2 \times 10^{12}$ molecules/cm.^{3}. (The maximum possible value is 8.4×10^{17}, when there is no backward flux.) Having the values for $(\Delta n'_s)$, k_1, and Avogadro's number, we arrive at

$$r \cong 10^{-16} \exp\left(\frac{500}{RT}\right) \qquad (20)$$

The pre-exponential factor is much lower than the measured[5] value of $c = 8 \times 10^{-11}$. The calculated $E \backsim 0.5$ kcal./mole is also much lower than the measured[5] value of 15 kcal./mole. In fact, the calculated value of E, which is on the order of RT, is not an energy barrier of any significance. However, the derivation of eq. 18 has neglected two aspects of monolayer resistance that can greatly increase the magnitude of r. They are: (1) the effect of a gas that is present but is not diffusing because it is at equilibrium and (2) the greater selectivity at a vacant site in a monolayer due to the angle at which the permeating molecule is moving relative to the hole. These two factors will now be considered.

B. Resistance Due to an Additional Gas at Equilibrium. The model for the process of water evaporation is a monolayer at a surface and water as both the liquid subphase and the gas phase. However, the real system also contains a high concentration of air (which we can assume is nitrogen). The N_2 molecules are in equilibrium between the gas and liquid phases and so must pass through the monolayer like the water vapor. Since N_2 remains at equilibrium during a transport of water, the unidirectional flux that is opposite to the net flux of water is effective in causing gas collisions that reduce the measured net flux. In the case of monolayer permeation by CO_2, where there is an equilibrium distribution of water, the observed net flux of CO_2 can be explained in terms of an additional resistance due to interference by water vapor.[10]

Let us estimate W_R, the probability that a water molecule, on moving through a monolayer, will collide with a gas molecule and be reflected. At equilibrium, H_2O and N_2 molecules move through the monolayer in both directions and for each gas the two rates are equal. The unidirectional fluxes for H_2O and N_2 are, respectively

$$(U'_t)_{H_2O} = {}^1/_2(\alpha n_s Q)_{H_2O} \exp(-Ka_{H_2O}) \qquad (21)$$

and

$$(U'_t)_{N_2} = {}^1/_2(\alpha n_s Q)_{N_2} \exp(-Ka_{N_2})$$

A_f has been neglected and $K = k_1\gamma/kT$. To a first approximation, W_R is equal to K_2 times the product of the simultaneous (and opposing) unidirectional fluxes of H_2O and N_2. (K_2 is a constant related to the frequency of binary collisions.) Therefore

$$W_R = K_2(U'_t)_{H_2O}(U'_t)_{N_2} \qquad (22)$$

When there is a net flux of water through the monolayer, we correct for the interference by nitrogen with an expression similar to eq. 22.

$$(U_t)_{H_2O}\ (\text{cor.}) = {}^1/_2[\alpha(\Delta n'_s)Q] \exp(-Ka_{H_2O}) \times [1 - K_2(U'_t)_{N_2}] \qquad (23)$$

The introduction of an effect due to the presence of gases changes certain aspects of our interpretation of monolayer permeation and of the techniques used to measure resistance. (a) If we use eq. 23 rather than eq. 10 to derive the monolayer resistance, the magnitude of r is significantly increased. (b) The last factor in eq. 23 indicates that the net flux of water should vary directly with the concentration of interfering gas (n_s of eq. 21). In the case of CO_2 permeation, where H_2O is the interfering gas, the monolayer resistance to CO_2 (proportional to the inverse of eq. 23) decreases in an approximately linear manner[10] with decreases in water concentration (vapor pressure). (c) In determining the magnitude of E by varying the temperature, the characteristics of the interfering gas must be considered. In CO_2 permeation, the water vapor pressure varies considerably with the temperature and greatly affects the measured value of E.[14] In water permeation the nitrogen concentration does not vary significantly with temperature. (d) If this mechanism is valid, the N_2 fluxes (assumed equal during water evaporation) must be unequal because of the asymmetric H_2O fluxes.

C. Geometric Considerations in Monolayer Permeation. All gas molecules that collide with the monolayer at a site where $a_0 \leqslant \Delta A + A_f$ were assumed to permeate. Actually the condition for permeation is more stringent because the vacant site is part of a structure and the gas molecule must approach the vacant site such that there will be no collision and reflection. In order to estimate this effect, let us assume that the vacant sites are right cylindrical holes of

(14) M. Blank in ref. 2, pp. 75–95.

transverse cross-sectional area ΔA and that the monolayer has a thickness. (In this section we shall ignore the effect of A_f.) Figure 1 is a diagram of the longitudinal cross section of a hole and θ is the maximum angle, relative to the axis of the hole, at which the gas molecule can approach and permeate.

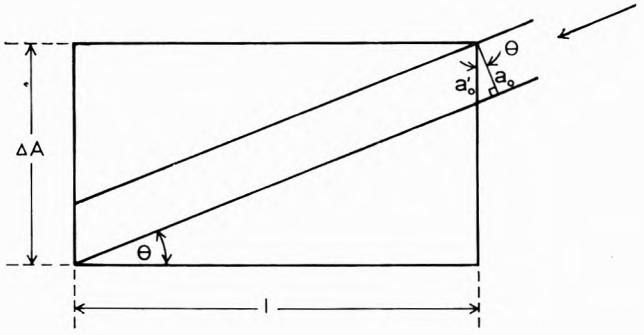

Figure 1. Longitudinal cross section of a right cylindrical hole in a monolayer showing the approach of a permeant molecule. The symbols are defined in the text.

$a'_0 = a_0 \sec\theta$, but since $\sec \cong 1$ for the small values of θ we need consider, we can set $a'_0 = a_0$. Therefore

$$\theta = \tan^{-1} \frac{2(\sqrt{\Delta A} - \sqrt{a_0})}{\sqrt{\pi} \times l} \qquad (24)$$

Assuming that all values of angle of collision are equally probable for the gas, the probability that a gas molecule will strike at an angle between 0 and θ is $2\theta/\pi$. The probability of getting through the monolayer, W_p, is therefore $2\theta/\pi$ times W of eq. 7. (The actual value of W_p is slightly different because one must average over all collisions on area ΔA. For example, if the gas molecule hits at dead center of ΔA the probability is θ/π. On the other hand, if one considers the possibility of reflection along the sides of the hole, the value could also be greater than estimated. The factor $2\theta/\pi$ is, therefore, a reasonable estimate of the probability of angular selection on the basis of the all-or-none assumption of section IIA.)

For small values of θ, $\tan^{-1}\theta \cong \theta$ and the probability of getting through the monolayer is

$$W_p = \int_{a_0}^{\infty} W_0 \exp(-K\Delta A) \times \left[\left(\frac{2}{\pi}\right) \frac{2(\sqrt{\Delta A} - \sqrt{a_0})}{\sqrt{\pi} \times l}\right] d(\Delta A) \qquad (25)$$

$$W_p = \frac{4W_0}{\pi^{3/2} l} \left[\int_{a_0}^{\infty} \sqrt{\Delta A} \exp(-K\Delta A)\, d(\Delta A) - \sqrt{a_0} \int_{a_0}^{\infty} \exp(-K\Delta A)\, d(\Delta A)\right] \qquad (26)$$

To evaluate the first integral of eq. 26 we set $y = \sqrt{\Delta A}$ and integrate by parts. This gives terms (1) and (2) of eq. 27. The second integral can be evaluated directly giving term (3) of eq. 27.

$$W_p = \frac{4W_0}{\pi^{3/2} l} \left[\underbrace{-\frac{1}{K} y \exp(-Ky^2)\Big|_y^{\infty}}_{(1)} + \underbrace{\frac{1}{K}\int_y^{\infty} \exp(-Ky^2)\, dy}_{(2)} + \underbrace{\frac{\sqrt{a_0}}{K} \exp(-Ka_0)}_{(3)}\right] \qquad (27)$$

Evaluating terms (1) and (3), we see that they are equal and cancel. The remaining term, (2), integrates to an error cofunction (erfc) term. Evaluating term (2) and substituting $W_0 = {}^1/_2 K$ we arrive at

$$W_p = I = \frac{1}{\pi l \sqrt{K}} \operatorname{erfc}(\sqrt{Ka_0}) \qquad (28)$$

Had we considered the effect of A_f, the last factor in eq. 28 would be $\operatorname{erfc}(\sqrt{K[a_0 - A_f]})$, a sensitive function of A_f.

W_p of eq. 28 is about four orders of magnitude lower than eq. 10. Since W_r determines the energy barrier term in eq. 18 and 20, the values of r and E are much higher than those given earlier and are comparable to the observed ones. (Inequality 17, leading to eq. 18, is apparently justified.) Since $K = k_1\gamma/kT$, the erfc term (when it includes the effect of A_f) contains the same terms as eq. 19. Therefore, the qualitative functional dependence of eq. 28 is quite similar to that of eq. 10. W_p is most sensitive to variations in the erfc term, but it also depends on the $\sqrt{K}$ and on the monolayer thickness. However, the dependence on monolayer thickness is complicated since γ and A_f also vary with l.

The particular shape (right cylinder) assumed for the spaces in the monolayer was used to demonstrate the great increase in the energy barrier that is due to geometrical selectivity. However, any shape or distribution of shapes would impose a greater resistance on the monolayer.

IV. Conclusion

This paper has attempted to demonstrate that the equilibrium properties of monolayers can be used to derive the monolayer resistance to permeation by gases. The model has considered the spaces in a two-dimensional lattice due to packing and fluctuations and the collisions with other gas molecules or with the walls of the free spaces. It has not considered the depend-

ence of A_f on ΔA or other such factors that are not expected to cause great differences in the general results. The monolayer resistance, derived on this basis, behaves qualitatively as expected and has a magnitude close to observed values. The proposed model, therefore, appears to offer a reasonable approach to a theory of monolayer permeability. Refinements may eventually lead to a better understanding of the diffusion process across very thin films and membranes.

Acknowledgments. The author thanks Dr. John Britten of this department for helpful discussions on several points in this paper and Miss Bess Denise Fried for typing assistance.

Critical Phenomena in Aqueous Solutions of Long-Chain Quaternary Salts. V. Temperature Studies of Hyamine 1622–Iodine Complex Systems

by Irving Cohen and Peter Economou[1]

Department of Chemistry, Polytechnic Institute of Brooklyn, Brooklyn, New York
(Received March 16, 1964)

The coacervating quaternary ammonium salt, Hyamine 1622, forms a complex with molecular iodine. In a previous study,[2] the micellar molecular weights and the charge properties of the homogeneous phase of this cationic soap system as a function of NaCl concentration and I_2 concentration at a fixed temperature were characterized from light scattering measurements. This paper extends this study to temperature effects in the Hyamine 1622–iodine complex system. Light scattering dissymmetries provided further evidence, previously deduced from viscosity, diffusion, and micelle molecular measurements, that the homogeneous phase exhibits a narrow electrolyte transition range (e.t.r.) in which, at low levels of NaCl concentration, a profound reorganization of the micelle occurs. The e.t.r. is relatively insensitive to small temperature changes in the system. For electrolyte concentrations in excess of the e.t.r., the micellar growth is an exponential function of the reciprocal of the absolute temperature of the system. A series of simple empirical equations has been developed which shows the functional relationships between the changes in micelle molecular weight with temperature changes, NaCl concentration changes, and changes in iodine content of the system. In a noniodinated system, the reduction of the temperature by 1° produced an increase in the micelle molecular weight equivalent to the increase in the micelle molecular weight produced by the addition of 5.7×10^{-3} mole of NaCl at a fixed temperature. Heats of micellization were calculated from the temperature coefficients of the critical micelle concentrations for selected systems. These calculations were confined to systems of low NaCl concentrations (0.06 *M*) where the micellar aggregation number does not change appreciably as a function of NaCl concentration.

Introduction

A number of dilute aqueous solutions of proteins,[2] polyelectrolytes,[3] and association colloids[4] behave as coacervates. The essential feature of coacervation phenomena is the spontaneous separation of a homogeneous macromolecular or macro-ion solution into two solution phases under a variety of conditions depending upon the nature of the solute species. A distinctive feature of dilute, aqueous two-solution-phase coacervate systems, as compared to two-phase systems, involving immiscible solvents or unmixing in a two-component system with the addition of a third component (*i.e.*, alcohol–H_2O–K_2CO_3) is the following situation.

The solvent component of the two phases in an aqueous coacervate system is the same chemical substance, H_2O. A colloidal solute particle migrating

(1) This work is submitted in partial fulfillment of the requirements for the degree of Doctor of Philosophy in Chemistry from the Polytechnic Institute of Brooklyn.

(2) D. G. Dervichian, *Trans. Faraday Soc.*, 18, 321 (1954).

(3) M. Eisenberg and G. R. Mohan, *J. Phys. Chem.*, 63, 671 (1959).

(4) I. Cohen and T. Vassiliades, *ibid.*, 65, 1774 (1961).

across the interface of a two-phase coacervate system finds itself in essentially the same environment on either side of the interface. From the point of view of composition, the difference between the two phases is a difference in solute concentration. Structurally, the two phases differ in that the colloidal solute of one phase (the equilibrium phase) is randomly oriented and the colloidal solute of the second phase (the coacervate phase) shows a great deal of order.[5] In all cases where coacervation has been observed, the solute species are geometrically anisotropic particles.

Coacervation is observed in some dilute soap solutions. This paper is one of a series concerned with coacervation in several long-chain quaternary salt solutions[4,5] in which two solution phases are formed with the addition of simple electrolytes such as NaCl, $NaNO_3$, and Na_2SO_4 to the homogeneous cationic soap solution. This phenomenon is classified as a form of simple coacervation involving a single micellar polyion species.

The quaternary ammonium salt, Hyamine 1622 (Hy), forms a coacervate with the addition of NaCl to a 1% solution of this cationic soap. In the salt-free solution and at low NaCl concentration (<0.07 *M*) the micelle molecular weights range between 12,500 and 25,000 at 30°. Coacervation is induced with the addition of 0.383 *M* NaCl at the same temperature. The micelle molecular weight at the onset of two-phase formation is in excess of 10^6. The purpose of the studies of the system is to characterize the onset of two-phase formation in terms of changes in the size, shape, and charge properties of the micellar solute induced by the addition of simple electrolytes to the aqueous micellar solution.

To date, the Hy–NaCl system has been studied at fixed temperatures. In addition, the Hy–iodine complex system has been studied.[5] Molecular iodine forms a complex with Hy. Small infusions of molecular iodine profoundly affect a number of properties of the micellar system. For an I_2/Hy(R) molecular ratio of 5×10^{-3}, the critical NaCl concentration necessary for two-phase formation is reduced by 0.02 *M* as compared to the iodine-free solution of the same soap concentration. A major effect of small iodine infusions is the reduction of the micellar ionization. Thus, Hy–I_2 complex formation provides a means of inducing small changes in the micellar ionization. The effects of these small changes in micellar ionization on the gross properties of the homogeneous phase have been studied.

These prior studies have established the following properties of the homogeneous phase of coacervating cationic soap systems: (a) at low electrolyte concentrations the degree of micellar ionization is critically suppressed; (b) the onset of coacervation is characterized by 10^2- to 5×10^2-fold growth of the micelles as compared to the micellar size in the electrolyte free solution; (c) intermediate between zero electrolyte and the critical electrolyte concentration, a narrow electrolyte transition range (e.t.r.) may be identified for each coacervating system at fixed temperature in which light scattering,[5] viscosity,[3] and diffusion[4] studies indicate an apparent transformation of the micellar species from an essentially isotropic to an anisotropic particle; and (d) the infusion of iodine into the Hy–NaCl system shifts the e.t.r. to lower NaCl concentrations.

The current investigation reported in this paper is concerned primarily with temperature effects in the Hy–I_2 complex system. Some light scattering dissymmetry data, not previously reported, are included in this study.

Experimental

A. Materials. The following materials were used in this investigation.

(1) Hyamine 1622, diisobutylphenoxyethoxyethyldimethylbenzylammonium chloride monohydrate, simply designated as Hy, is a commercial bactericide produced by Rohm and Haas Co. It was purified in the following manner. A quantity of Hy was dissolved in boiling acetone. The nearly saturated solution was filtered while hot and a few drops of distilled water were added to increase the solubility of the dissolved Hy. The filtrate was left to cool slowly and a crystalline product precipitated. The crystallization was repeated three times and the crystals were filtered, washed with diethyl ether, and dried in a vacuum desiccator for 24 hr.

(2) I_2 was obtained from Brothers Chemical Co. (resublimed, reagent, ACS) and was freshly sublimed before use in these experiments.

(3) NaCl was C.P. grade from Brothers Chemical Co.

(4) Molecular I_2 forms a complex with Hyamine 1622. The preparation of the Hy–I_2 complex has been described elsewhere.[5]

B. Light Scattering Measurements. Light scattering measurements were performed in a modified Brice–Phoenix photometer (Phoenix Precision Instrument Co.) using incident unpolarized monochromatic light of wave length 5460 Å. In this spectral region, Hy–I_2 complex absorption is minimal and does not interfere with light scattering measurements.[5]

(5) I. Cohen, P. Economou, and A. Libackyj, *J. Phys. Chem.*, **66**, 1829 (1962).

The instrument was modified to obtain temperature control by the use of an air bath surrounding the sample cell which does not interfere with the optical measurements. The temperature of the air was controlled by a thermistor temperature controller (direct dialing) and the YSI Thermistemp Model 71 manufactured by the Yellow Springs Instrument Co., Inc., was used. The main control dial is graduated to 0.5° and the fine adjustment vernier dial is graduated in ten divisions (0.05° each). Probes are sensitive to better than ±0.05° below 60° and better than ±0.1° above 60°. For the exact temperature measurement of the solution in the cell, a surface temperature probe was used with a time constant of 0.8 sec. The temperature of the circulating air was controlled by using an air temperature probe with a time constant of 2 min. in free, still air. The air was circulated by a pressure–vacuum motor-driven pump which has a free air delivery of 3.2 ft.^{3}/min. at 15 p.s.i. The air was filtered continuously with a compressed air, constant flow filter (E. H. Sargent and Co.) which has an average continuous service life of 240 hr. A Millipore filter of 1.2-μ pore size was used for additional filtration of the air. The air was dried by passing it through a trap at −60°. The upper cyclical part of the special cored cell table of the Brice–Phoenix photometer was cut off and replaced by a fritted stainless steel plate which allowed the air to pass through and surround the cell. The measurements were carried out in a cylindrical cell with solutions which had been filtered several times through a Millipore filter of 0.45-μ pore size, directly into the cell which had been repeatedly rinsed with filtered distilled water. The refractive index measurements (dn/dc) were measured with a Zeiss dipping refractometer, using light of 5820-Å. wave length. For soap concentration in excess of the c.m.c. (dn/dc) is independent of electrolyte concentration, iodine concentration, micellar size and shape, and temperature. The refractive index increment for the Hy–I_2–NaCl–H_2O systems is 0.1913 cm.^{3}/g.

The aggregation number, m, and the micellar charges, P, were derived from light scattering data by the methods developed by Hermans and Prins[6] and Mysels and Princen[7] which were modified by Anacker.[8] This method was described in a previous paper in this series.[5]

C. Critical Micelle Concentration. The critical micelle concentrations of the coacervating systems, HyCl–I_2–NaCl, used in this investigation were calculated graphically by using plots of the refractive indices (n) of the solutions *vs.* soap concentration in grams per cent. Straight lines were drawn through the points lying below and above the region in which a rapid change of slope was observed and the point of intersection was taken as the critical concentration for micelle formation.

D. Dissymmetries. The dissymmetries were obtained by observing the ratio of the scattering intensity of 45° to that at 135°. If the observed dissymmetry was greater than 1.2, it was subject to a correction for reflection of the primary beam at the exit window of the cell, as it is described in the Brice–Phoenix light scattering manual. If Z' is the apparent dissymmetry ratio, the corrected dissymmetry ratio Z is

$$Z = (Z' - r)/(1 - rZ') \qquad (1)$$

where r is the fraction of the primary beam reflected at the exit window. The value of r for the C-101 cell used is 0.039. None of the solutions investigated showed any appreciable depolarization and fluorescence effects.

Results and Discussion

Dissymmetries. The dissymmetries as a function of NaCl concentration are represented in Fig. 1 for the three systems: (a) $R = 0$; (b) $R = 2.0 \times 10^{-2}$; and (c) $R = 5.0 \times 10^{-2}$. At zero NaCl concentration, the dissymmetries are relatively high (1.24) and increase with increasing the HyCl–I_2 complex concentration to 1.33. With the initial addition of NaCl the dissymmetries decrease sharply approaching a value close to unity at low NaCl concentrations. A distinctive feature of all of the dissymmetry plots in the finding that at the NaCl concentration corresponding to the electrolyte transition region (e.t.r.) the dissymmetries are somewhat higher than the dissymmetries at contiguous lower and higher NaCl concentrations. Each of the dissymmetry curves has a characteristic bump. A possible explanation for this rise and fall in dissymmetry in the e.t.r. may be considered to be due to a greater polydisperse character of the micellar system in the e.t.r. than exist in the system on either side of the e.t.r. The dissymmetry data provide further evidence that the e.t.r. represents the electrolyte concentration region at which a profound reorganization of the micellar aggregate occurs. Supporting evidence for this view is provided by viscosity and diffusion data.[1] In addition, the dissymmetry data confirm a primary effect of Hy–I_2 complex formation, the shift of the e.t.r. to lower NaCl concentrations. For

(6) J. J. Hermans and W. Prins, *Proc. Konikl. Ned. Akad. Wetenschap.*, B59, 162 (1956).

(7) K. J. Mysels and L. H. Princen, *J. Colloid Sci.*, 12, 594 (1957).

(8) E. W. Anacker, *J. Phys. Chem.*, 62, 41 (1958).

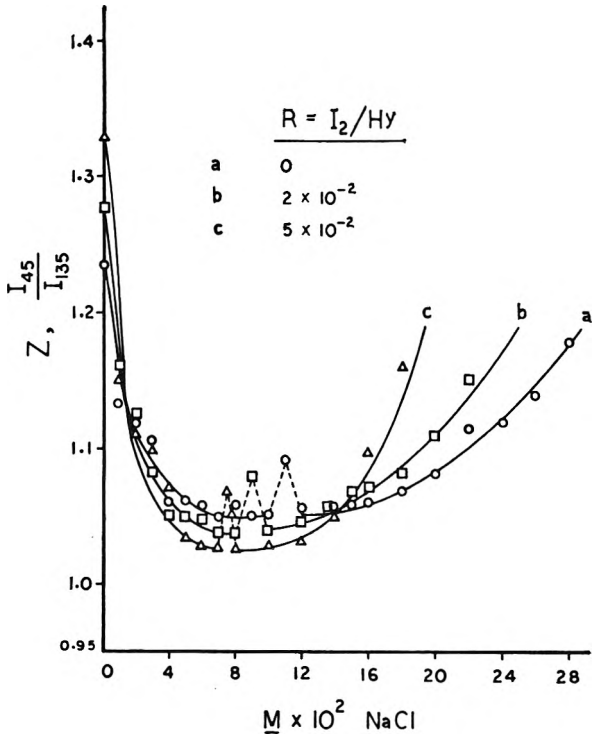

Figure 1. Light scattering dissymmetry data of Hyamine 1622–iodine complex at 30°: a, R = I_2/Hy = 0; b, R = 2×10^{-2}; c, $R = 5 \times 10^{-2}$.

NaCl concentrations in excess of the e.t.r., the dissymmetries rise, consistent with a growing anisotropic polyion solution particle.

Critical Micelle Concentration. The effect of the HyCl–I_2 complex concentration on the critical micelle concentration, at fixed NaCl concentrations and 30°, is shown in Fig. 2. The systems which have been studied are HyCl–I_2–NaCl: (a) R = I_2/Hy = 0; (b) $R = 0.5 \times 10^{-2}$; (c) $R = 1.0 \times 10^{-2}$; (d) $R = 2.0 \times 10^{-2}$; and (e) $R = 5.0 \times 10^{-2}$. The addition of I_2 to the system lowers the c.m.c. at fixed NaCl concentrations and fixed temperatures. The plot of log c.m.c. *vs.* R (the molecular ratio, I_2/Hy) shows a linear relationship. An examination of the slopes of several curves representing different NaCl concentration (0–0.6 M NaCl) shows that the effect of I_2 on the critical micelle concentration (slopes) is depressed by the addition of NaCl.

The c.m.c. dependence on electrolyte concentration is given by eq. 2,[9] and Fig. 3, shows such a dependence at fixed temperatures for the system $R = 2.0 \times 10^{-2}$.

$$\log (\text{c.m.c.}) = -Kg \log (\text{Ci}) + K \qquad (2)$$

where (Ci) is the counterion concentration and Kg and K are constants. The absolute values of these constants decrease with an increase in the HyCl–I_2 complex concentration. Also, the Kg values decrease with a decrease in the temperature, while the K values remain constant. The temperature dependence of the c.m.c. for the system Hy–I_2–NaCl ($R = 2.0 \times 10^{-2}$) is shown in Fig. 4, at fixed NaCl concentrations. Comparing Fig. 2, 3, and 4, it is apparent that iodine affects the c.m.c. in the opposite direction to that of the

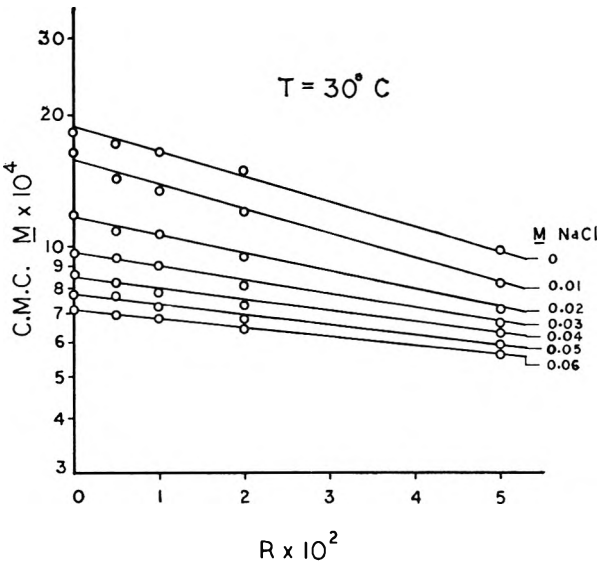

Figure 2. C.m.c. of Hyamine 1622–iodine complex as a function of iodine–Hyamine 1622 molecular ratio I_2/Hy(R) at fixed NaCl concentrations (0.00–0.06 M).

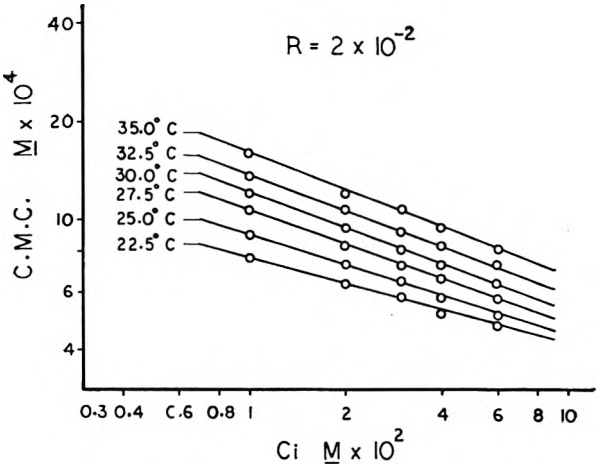

Figure 3. C.m.c. of Hyamine 1622–iodine complex ($R = 2 \times 10^{-2}$) as a function of counterion concentration at fixed temperatures (22.5–35.0°).

(9) M. L. Corrin and W. D. Harkins, *J. Am. Chem. Soc.*, 69, 683 (1947).

Table I: The Kg and K Values of Equation 2 [log (c.m.c.) = $-Kg$ log (Ci) + K] at Different Temperatures

Temp., °C.	$R = 2 \times 10^{-2}$		$R = 0$	
	Kg	K	Kg	K
22.5	−0.243	−3.5528	−0.368	−3.7447
25.0	−0.306	−3.5935	−0.403	−3.7545
27.5	−0.346	−3.6383	−0.441	−3.7447
30.0	−0.362	−3.6655	−0.471	−3.7328
32.5	−0.366	−3.6655	−0.505	−3.7212
35	−0.374	−3.6638	−0.562	−3.7447

temperature. Using the Stainsby and Alexander[10] expression

$$\Delta H_m = -RT^2 \, d \ln (\text{c.m.c.})/dT \qquad (3)$$

conventional heats of micellization for a number of systems were calculated and tabulated in Table II for $R = 0$ and $R = 2 \times 10^{-2}$. These calculations

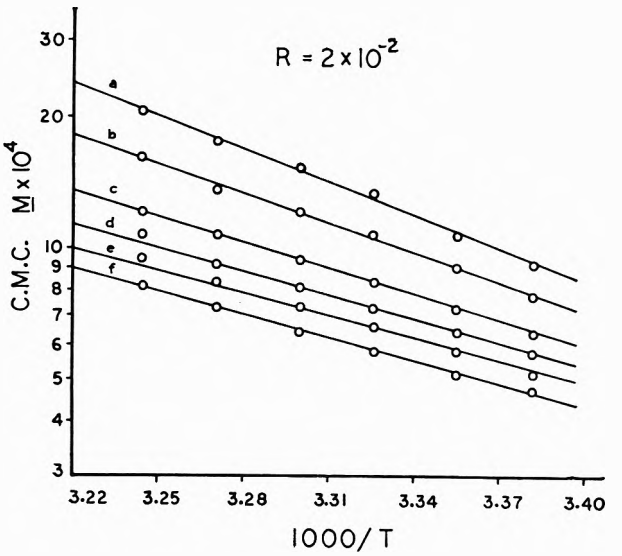

Figure 4. C.m.c. of Hyamine 1622–iodine complex ($R = 2 \times 10^{-2}$) as a function of the reciprocal of the absolute temperature at fixed NaCl concentrations: a, 0.0 M NaCl; b, 0.02 M NaCl; c, 0.03 M NaCl; d, 0.04 M NaCl; e, 0.05 M NaCl; f, 0.06 M NaCl.

were confined to systems of low NaCl concentration (0–0.06 M). In this region of NaCl concentration, the micellar aggregation number does not undergo large changes as a function of temperature. At the higher NaCl concentrations (in excess of the e.t.r.) the micellar aggregation number is quite sensitive to small temperature changes. The Stainsby and Alexander expression for ΔH_m assumes constant micellar activity for small temperature changes in the system, and hence is not applicable to the coacervating soap systems, to a reasonable degree of approximation, at the higher electrolyte concentrations.

Table II

Concn. of NaCl, M	$R = 0$ ΔH_m, kcal./mole	$R = 2 \times 10^{-2}$ ΔH_m, kcal./mole
0	14.19	11.67
0.01	13.05	10.38
0.02	11.12	9.01
0.03	9.57	8.21
0.04	8.97	8.16
0.05	8.60	8.12
0.06	8.30	8.08

Figure 5 represents the effect of HyCl–I_2 complex concentration on the micellar molecular weights at 30° and fixed NaCl concentrations (0.11–0.16 M NaCl). The slopes (d log M/dR) remain constant for a range of NaCl concentration (0.11–0.14 M) at 30°. For the 0.16 M NaCl curve, the slopes increase and this may be attributed to the contribution to the light scattering

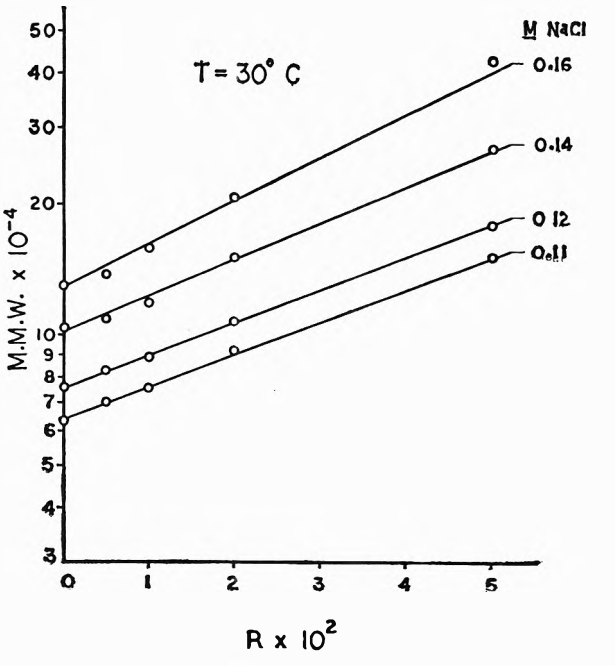

Figure 5. Micelle molecular weight (m.m.w.) of Hyamine 1622–iodine complex at fixed NaCl concentrations (0.11–0.16 M) at 30° as a function of the iodine–Hyamine molecular ratio (R).

(10) G. Stainsby and A. E. Alexander, *Trans. Faraday Soc.*, **46**, 587 (1950).

intensity of the critical opalescence. At lower temperatures, higher R values, and higher NaCl concentrations the systems are close to the critical point. The average slope (d log M/dR) has for the curves (0.11–0.14 M NaCl) a value of 6.55(k).

The temperature dependence of the micellar molecular weights (m.m.w.) of all iodinated and noniodinated systems at fixed NaCl concentration (0.11 M) is shown in Fig. 6. The slopes, d log M/d(1/T), remain constant at this NaCl concentration with an average value

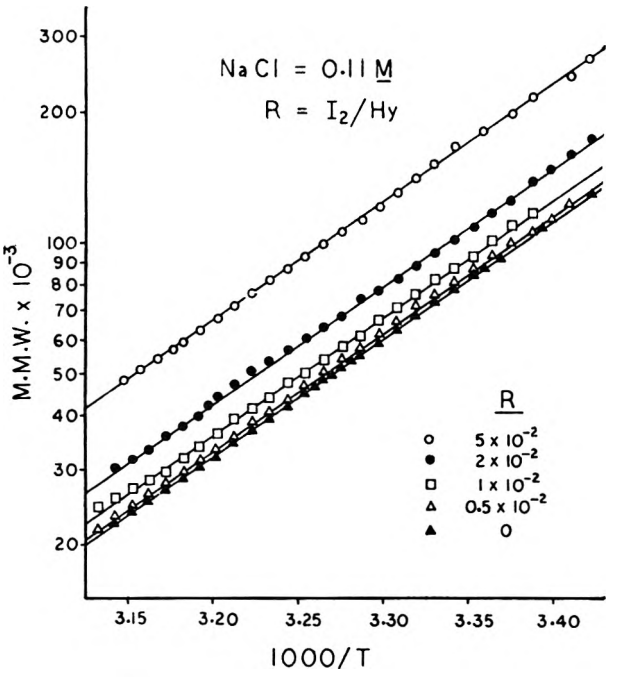

Figure 6. Micelle molecular weight of Hyamine 1622–iodine complex at fixed iodine–Hyamine molecular ratios (0.5 × 10^{-2} and 0.11 M NaCl) as a function of the reciprocal of the absolute temperature.

of 2.722 × 10^3. The temperature coefficient of the logarithm of the m.m.w., d log M/dT = −0.03035 (B). Previously,[5] it was shown that d log M/dC = K, where C is the NaCl molar concentration, depends on the value of R = I_2/Hy.

For R = 0, K'_0 = 5.32 and

$$K'_R = 5.43^{10R} \quad (4)$$

Dividing B by K'

$$(\text{d log } M/\text{d}T)_R/(\text{d log } M/\text{d}c)_R = (\text{d}c/\text{d}T)_R \quad (4')$$

$(\text{d}c/\text{d}T)_R$ represent the moles of NaCl required to change the micelle molecular weight at a fixed R value by an amount equivalent to that obtained by reducing the temperature of the micellar solution by 1°.

K'_R and $(\text{d}c/\text{d}T)_R$ values are tabulated in Table III.

Table III

R	K'_R	dc/dT, mole/deg
0	5.32	−5.7 × 10^{-3}
0.5 × 10^{-2}	5.60	−5.41 × 10^{-3}
1.0 × 10^{-2}	5.88	−5.16 × 10^{-3}
2.0 × 10^{-2}	6.43	−4.72 × 10^{-3}
5.0 × 10^{-2}	8.75	−3.46 × 10^{-3}

Figure 7 represents the logarithm of m.m.w. as a function of NaCl concentration in the range 0.08–0.18 M (R = 2.0 × 10^{-2}) at fixed temperatures. For each of these curves except for 0.08 M NaCl solution, micellar growth is indicated to be an exponential function of the NaCl concentration. The significance of this derivation in 0.08 M NaCl solutions of the m.m.w. from the logarithmic plots is that the systems are in the electrolyte transition region. The data presented in Fig. 7 would indicate that the electrolyte transition region is not temperature dependent.

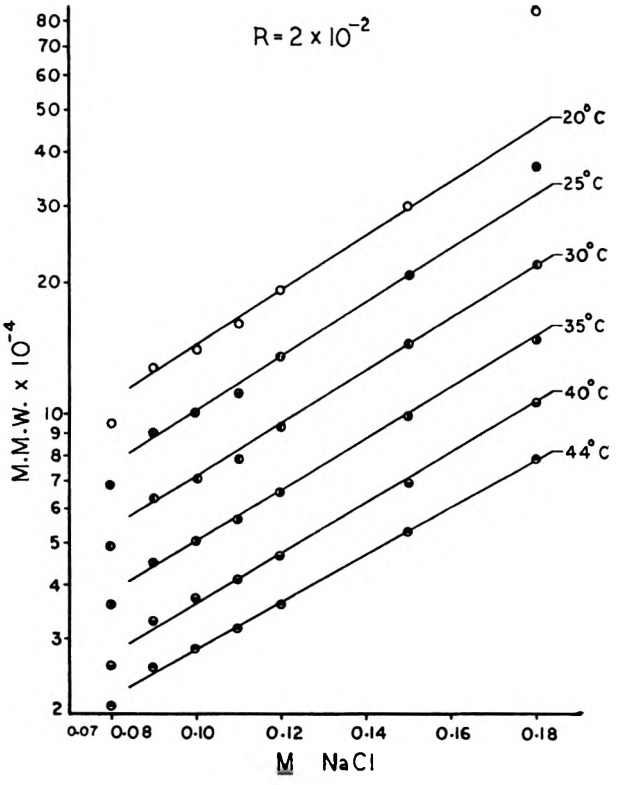

Figure 7. Micelle molecular weight of Hyamine 1622–iodine complex (R = 2 × 10^{-2}) as a function of NaCl concentration at fixed temperatures (20–40°).

The logarithm of micellar molecular weight as a function of $1/T$ at fixed NaCl concentrations is plotted for electrolyte concentration of 0–0.18 M NaCl for the $R = 2 \times 10^{-2}$ system, Fig. 8. The broken line curve represents the m.m.w. of 0.05 M NaCl solution showing no significant micellar growth as a function of decreasing temperature from 45 to 30°. The 0–0.04 M NaCl solutions show very small micellar growth for a wider temperature range (47–18°). The 0.06 M NaCl solution shows no micellar growth as the temperature is decreased from 45 to 37°. Between 37 and 20° the micelles grow appreciably and this growth is an exponential function of the reciprocal of the temperature. The rate of micellar growth as a function of $1/T$ increases as the NaCl concentration is increased to 0.08 M NaCl. For NaCl concentration in excess of 0.08 M (e.t.r.) the rate of micellar growth as a function of $1/T$ remains constant.

The effect of temperature on the ionization of the iodinated ($R = 2.0 \times 10^{-2}$) system has been studied. This effect is shown in Fig. 9. Lower temperatures produce effects similar to increasing the HyCl–I_2 complex[2] concentration. The same ionization maximum depression and the shift of the $(p/m)_{max}$ to lower NaCl concentrations produced by Hy–I_2 complexation are observed by lowering the temperature.

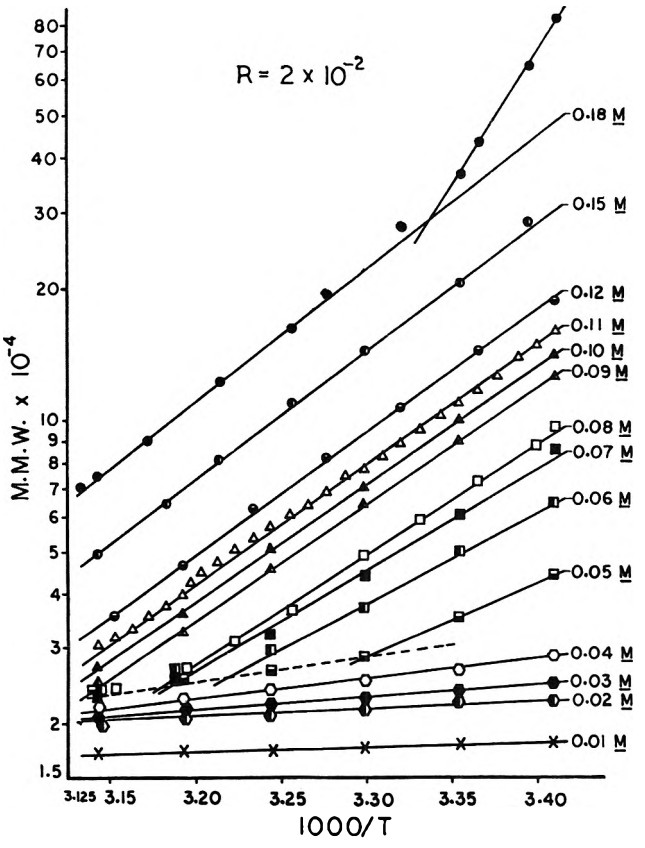

Figure 8. Micelle molecular weight of Hyamine 1622–iodine complex ($R = 2 \times 10^{-2}$) as a function of the reciprocal of the absolute temperature at fixed NaCl concentration (0.00–0.18 M).

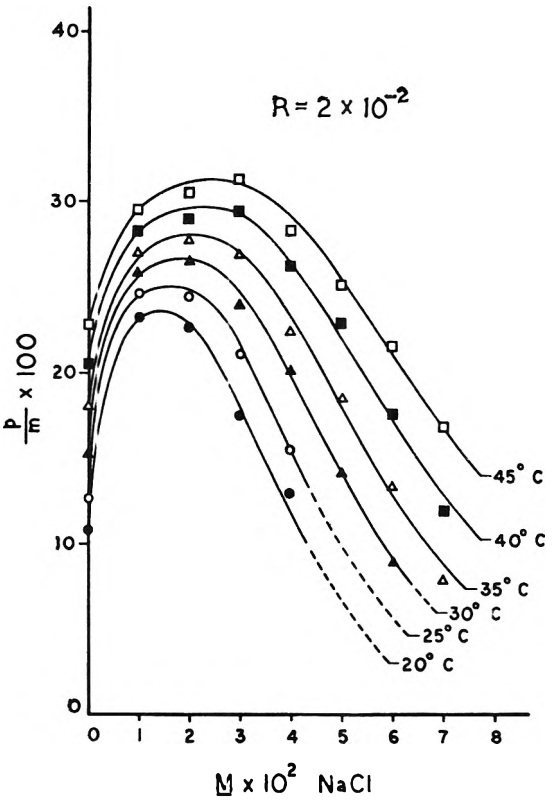

Figure 9. The ratio of micellar charges to micellar aggregation number (p/m) as a function of NaCl concentration for the Hyamine 1622–iodine complex ($R = 2 \times 10^{-2}$).

From the data in a previous study[5] and additional temperature data developed in this study, a number of empirical relationships may be derived which show the functional relationship between the micelle molecular weight and the temperature changes, NaCl concentration changes, and the I_2/Hy molecular ratio in the system.

Equation 5 is derived empirically from the temperature dependence of the logarithm of the micellar molecular weight.

$$(\log M)_{\substack{R=R\\T=T\\C=C}} = (\log M)_{\substack{R=R\\T=T_0\\C=C}} + B(T - T_0) \quad (5)$$

From the NaCl concentration dependence of log M

$$(\log M)_{\substack{R=0\\T=T_0\\C=C}} = (\log M)_{\substack{R=0\\T=T_0\\C=C_0}} + K'_0(C - C_0) \quad (6)$$

for a fixed R (I_2/Hy molecular ratio)

Table IV

$(\log M)_{\substack{R=0\\T=T_0\\C=C_0}}$	$(M)_{\substack{R=0\\T=T_0\\C=C_0}}$	$(C - C_0)$	R	$(T - T_0)$	$(M)_{R,T,C}$, calcd.	$(M)_{R,T,C}$, exptl.
5.87841	75,580	0.03	0	0	109,100	106,995
		0.04	0.5×10^{-2}	0	136,350	138,890
		0.03	0	3	86,500	81,845
		0	2.0×10^{-2}	2	87,800	82,180
		−0.03	2.0×10^{-2}	5	44,720	45,025
		0.10	0	0	250,300	244,000
		0.18	0	0	651,900	637,500
		0.12	0	0	318,000	310,500
		0.02	0.5×10^{-2}	0	105,000	109,170
		0.10	0.5×10^{-2}	0	287,100	286,530
		0	1.0×10^{-2}	0	87,990	88,810
		0.03	2.0×10^{-2}	0	158,800	143,600
		0.03	2.0×10^{-2}	4	120,100	108,840
		0.03	2.0×10^{-2}	8	90,800	81,000
		0	2.0×10^{-2}	6	67,300	62,655
		0	2.0×10^{-2}	−2	117,700	107,030
		−0.01	5.0×10^{-2}	−3	163,600	152,235
		−0.01	1.0×10^{-2}	0	66,970	65,810
		−0.01	1.0×10^{-2}	6	44,030	44,225

$$(\log M)_{\substack{R=R\\T=T_0\\C=C_0}} = (\log M)_{\substack{R=R\\T=T_0\\C=C}} + K'_0(C - C_0)^{10R} \quad (7)$$

By substitution of the second term of eq. 5 by its value from eq. 7 we get

$$(\log M)_{\substack{R=R\\C=C\\T=T}} = (\log M)_{\substack{R=R\\C=C_0\\T=T_0}} + K'_0{}^{10R}(C - C_0) + B(T - T_0) \quad (8)$$

From the R dependence of log M we obtain

$$(\log M)_{\substack{R=R\\T=T_0\\C=C_0}} = (\log M)_{\substack{R=0\\T=T_0\\C=C_0}} + kR \quad (9)$$

Then eq. 8 becomes

$$(\log M)_{\substack{R=R\\T=T\\C=C}} = (\log M)_{\substack{R=0\\T=T_0\\C=C_0}} + kR + B(T - T_0) + K'^{10R}(C - C_0) \quad (10)$$

substituting values for the constants, k, B, and K' from the data, or

$$(\log M)_{\substack{R=R\\T=T\\C=C}} = (\log M)_{\substack{R=0\\T=T_0\\C=C_0}} + 6.55R - 0.03035(T - T_0) + 5.32^{10R}(C - C_0) \quad (10')$$

Table IV gives the experimental values of m.m.w. for different values of R, T, and C and the values of m.m.w. calculated by using eq. 10′.

Conclusion

The data developed in this study of temperature effects upon the homogeneous phase of the Hy–I_2 complex–NaCl–H_2O cationic soap system are consistent with the qualitative micellar model previously proposed.[5] Initially, at soap concentrations in excess of the critical micelle concentration, the micelle is a relatively loose isotropic structure. The first small additions of NaCl to the system result in two effects which act upon the system in opposite directions: increased micellar ionization and the screening of intramicellar charge sites by the counterions added to the system. With further additions of NaCl, an effect is observed which is distinctive for coacervating soaps: a relatively sharp suppression of micellar ionization. The NaCl concentration region at which ionization suppression occurs is sensitive to temperature and Hy–iodine complex formation. The temperature-dependent micelle molecular weight data at fixed NaCl concentrations represented in Fig. 8 show the very different temperature-dependent behavior of the micellar system at low fixed NaCl concentrations as compared to the soap system at high fixed NaCl concentrations. A micellar transition is indicated in the data. The dissymmetry data, coupled with previous light scattering, viscosity, and diffusion data, show that the transition occurs in a narrow range of NaCl concentration designated the electrolyte transition region.

The proposed micellar model consistent with the

data is the following: at low levels of NaCl concentration the micelles grow to a limiting isotropic structure. The micellar ionization suppression and the counterion screening facilitate a progressively more efficient packing of the soap monomers in the micelle. The onset of the e.t.r. is the region of NaCl concentration corresponding to a saturated isotropic micellar structure. The e.t.r. represents the situation in which the intramicellar charge interactions are sufficiently damped so that the coulombic field associated with the micellar charge density no longer offers a constraint to the micellar shape. An apparent micellar reorganization occurs at the e.t.r. and with further additions of NaCl the micelles grow anisotropically. This growth proved to be an exponential function of the added NaCl. The studies of homogeneous dilute Hy soap solutions as a function of NaCl concentration, iodine complexation, and temperature have provided a detailed mapping of the transformation of the micelles of the soap system from relatively small isotropic aggregates to large anisotropic aggregates. This latter property of the micellar solute is an apparent necessary precondition for coacervation.

Acknowledgment. The authors wish to express their appreciation for support provided by the Department of Health, Education and Welfare, Public Health Service Grant GM-10845-05.

Discussion

R. CLELAND (Dartmouth College). E. F. Casassa and H. Eisenberg, *J. Phys. Chem.*, **64**, 753 (1960), pointed out that in order to obtain molecular weights from light scattering measurements in a three-component system by the use of the ordinary equations applicable to a two-component system it is necessary to measure dn/dc at osmotic equilibrium of the solutions with the proper "solvent" of low molecular weight compounds. In recent work with polyelectrolyte solutions (sodium hyaluronate–NaCl–H_2O) we have found that the value of dn/dc under conditions of osmotic equilibrium is about 25% lower than when measured at constant NaCl concentration, which causes a 60% increase in calculated molecular weights. Have you considered this effect on your molecular weight values?

I. COHEN. The major interest in this work has been the large changes in the micellar systems with small electrolyte increments. These large changes in the micellar system have been indicated by prior viscosity and diffusion studies as well as by the light scattering study reported here. We have been cognizant of the intensive discussion during the past several years of the proper interpretation of light scattering data obtained for association colloids. In the data presented in this study, the emphasis is on the relative molecular weights and not the absolute values of the micelle molecular weights.

P. K. ISAACS (W. R. Grace Company, Clarksville). (1) What, if any, is the effect of solubilized organic material on the coacervation by small, amounts of electrolyte?

(2) Have effects similar to those that you describe been observed on nonaqueous micellar systems?

I. COHEN. (1) Any additive to an aqueous coacervating micellar system that produces changes in the micellar charge density will affect the critical electrolyte concentration necessary for two phase formation. This is essentially our interpretation of the effects produced by small infusions of molecular iodine into the micellar system which we studied intensively.

(2) There have been reports of coacervation in mixed nonaqueous solutions of polymeric solutes. However, to date, these effects have not been reported for nonaqueous micellar systems.

Heats of Transition for Nematic Mesophases[1]

by Edward M. Barrall, II, Roger S. Porter, and Julian F. Johnson

California Research Corporation, Richmond, California *(Received February 17, 1964)*

Heats of transition have been measured for three pure compounds which exhibit a mesophase of the nematic type. The compounds are *p*-azoxyanisole, anisaldazine, and N-*p*-methoxybenzylidene-*p*-phenylazoaniline. Their liquid crystal or mesophase range is separated by first-order transitions from both a solid crystalline phase and an isotropic or true liquid state. Heats and temperatures for the two transitions of each purified compound were measured with an extensively calibrated custom-built differential thermograph. The nature of nematic mesophase transitions is discussed along with limited thermal data previously available on these compounds.

Nematic mesophases or liquid crystals represent a phase which is distinguishable from both a solid crystalline phase at lower temperatures and an isotropic or normal liquid phase at higher temperatures by first-order transitions.[2] Thermal data are rare for liquid crystals.[3] Definitive data are required for an insight into the field of order and flow of liquid crystals.

In this study, heats of transition for solid–nematic and nematic–isotropic states have been measured for three pure compounds which exhibit liquid crystal phases of the nematic type using differential thermal analysis (d.t.a.). The three compounds studied are *p*-azoxyanisole, anisaldazine, and N-*p*-methoxybenzylidene-*p*-phenylazoaniline. These compounds are hereafter referred to as PAA, AAD, and MBPA. The compound MBPA has been referred to as *p*-anisal-*p*-aminoazobenzene.[4] The source, structure, methods of purification, and compositional analyses for these three compounds have been previously described.[4] Published heat of transition data for PAA are evaluated in the light of these results. New heats of transition are reported herein for the other two compounds. The only previous information available is that the heat for the nematic–isotropic transition for MBPA is small, as estimated from double refraction near the transition.[5]

Calorimetric measurements for transition heats and temperatures of transition were made with an advanced-type differential thermograph. The design and calibration of this custom thermograph have been described recently.[6a,b] To achieve greatest precision and accuracy, different d.t.a. block designs and sample preparation procedures were used to measure transition temperature and heat absorption, respectively.

Experimental

Sample Preparation. Samples for the measurement of transition temperatures were prepared by diluting PAA, AAD, and MBPA with 500-mesh carborundum and grinding gently with a few drops of benzene. The carborundum had been purified as described previously.[7] The concentration of the liquid crystal compound was determined by extracting weighed aliquots of the dry carborundum mixture with chloroform and benzene and reweighing. Concentrations are shown in Table I. Samples for the determination of heats of transformation were prepared by precisely weighing about 10 mg. of the pure compound onto a 1-cm. square of aluminum foil. Foils were folded carefully to form small leakproof packets. Ammonium chloride, ammonium bromide, and NBS benzoic acid, prepared in the same way, were used to calibrate the apparatus

(1) Part IV of a series on order and flow of liquid crystals.

(2) P. L. Jain, J. C. Lee, and R. D. Spence, *J. Chem. Phys.*, **23**, 878 (1955).

(3) G. H. Brown and W. G. Shaw, *Chem. Rev.*, **57**, 1049 (1957).

(4) R. S. Porter and J. F. Johnson, *J. Appl. Phys.*, **34**, 51 (1963).

(5) V. N. Tsvetkov, *Acta Physicochim.* (USSR), **19**, 86 (1944).

(6) (a) E. M. Barrall, II, J. F. Gernert, R. S. Porter, and J. F. Johnson, *Anal. Chem.*, **35**, 1837 (1963); (b) E. M. Barrall, II, R. S. Porter, and J. F. Johnson, *ibid.*, **36**, 2172 (1964).

(7) E. M. Barrall, II, and L. B. Rogers, *ibid.*, **34**, 1101 (1962).

Table I: Thermographic Data on Three Liquid Crystal Compounds

Compound	Phase transition: Solid-nematic T_b[a]	Solid-nematic T_m	Solid-nematic T_e	Nematic-isotropic T_b	Nematic-isotropic T_m	Nematic-isotropic T_e	Compound concn. in d.t.a. tests: Wt. %	Compound wt., g.
PAA	113.50	117.60	125.02	133.30	133.85	136.72	10.25	0.0146
AAD	161.96	168.90	175.71	177.28	180.46	185.53	8.30	0.0143
MBPA	142.07	147.20	153.30	177.48	179.07	181.80	8.49	0.0188

[a] Temperatures indicate the beginning of the d.t.a. endotherm, T_b, the endothermal minimum, T_m, and the temperature, T_e, at which the recorder returned to the previously established base line for 4.7°/min. heating rate. Each temperature is the average of nine separate thermographic runs.

for calorimetry.[6b] The ammonium salts were Baker Analyzed reagent grade chemicals.

Procedure. All thermograms were recorded with the differential temperature signal as a function of sample temperature on an x–y recorder as described previously.[6,7] The sample temperature and the sample half of the differential temperature were measured with the same thermocouple.

Transition temperatures were measured with the thermocouples located in contact with, and in the center of, the 0.1-g. carborundum-diluted samples. The samples were contained in glass tubes. The block (block A) design has been described previously.[6b] Duplicate runs at four heating rates (4.7, 5.8, 11.4, and 12.7°/min.) showed no shift in the vertex of the endothermal minimum with heating rate.

Calibration. The temperature axis was calibrated with the melting points of NBS benzoic acid (m.p. 121.8°), salicylic acid (m.p. 158.3°), and potassium thiocyanate (m.p. 177.0°) diluted in the same manner as the samples in carborundum. The temperature at the minimum of the endotherms corresponded closely to the reported melting points.

The absolute temperature errors on the various portions of the thermographic endotherms were: beginning (T_b), ±0.09°, minimum (T_m), ±0.05°, and end (T_e), ±0.09°. The reason for this variation is the judgment which must be exercised in determining the beginning and end of the endotherm from peak shape. The location of the vertex is less dependent upon such judgments.

Runs at different heating rates were made on the same samples of PAA and AAD, since relocation of the samples during the melting process was not a problem with these materials. Sublimation of the MBPA melt necessitated the use of an identical, freshly weighed sample for each run in block A.

Calorimetry using block A suffers from large errors when samples of differing thermal conductivities and physical states are studied.[6b] Calorimetric measurements were therefore carried out in the block of different design (block B). Sample and calibration runs were carried out at the same heating rates as in block A. Block B produces peaks which are too broad for precise transition temperature measurements. The peak areas were determined by the automatic integration method.[8] Integration errors were limited to less than ±1.5%.

Ammonium bromide and chloride and benzoic acid were used in the calorimetric calibration since the transition temperatures bracket the temperature range of interest for the compounds studied. The temperatures and heats of solid–solid transition of ammonium chloride (183.1°, 1073 cal./mole) and ammonium bromide (137.2°, 882 cal./mole) have been determined by Arell.[9] The thermal data for the fusion of benzoic acid (121.8°, 33.9 cal./g.) have been tabulated by Rossini, *et al.*[10] The data obtained for these solid–liquid and solid–solid phase changes are found to fit the same calibration curve. This is consistent with the successful removal of extraneous sample variables by using block B.

The precision of the calorimetric studies was determined by running each sample and calibration three times and determining the standard deviation of the set.

Results

Transition Temperatures. Figure 1 shows representative differential thermograms for *p*-azoxyanisole (PAA), anisaldazine (AAD), and N-*p*-methoxybenzyli-

(8) K. W. Gardiner, R. F. Klaver, F. Baumann, and J. F. Johnson, "Gas Chromatography," Academic Press, New York, N. Y., 1962, p. 349.

(9) A. Arell, *Ann. Acad. Sci. Fennicae, Ser. A VI*, 57, 42 (1960).

(10) F. D. Rossini, D. D. Wagman, W. H. Evans, S. Levine, and I. Jaffe, "Selected Values of Chemical Thermodynamic Properties," National Bureau of Standards Circular 500, U. S. Government Printing Office, Washington, D. C., 1952.

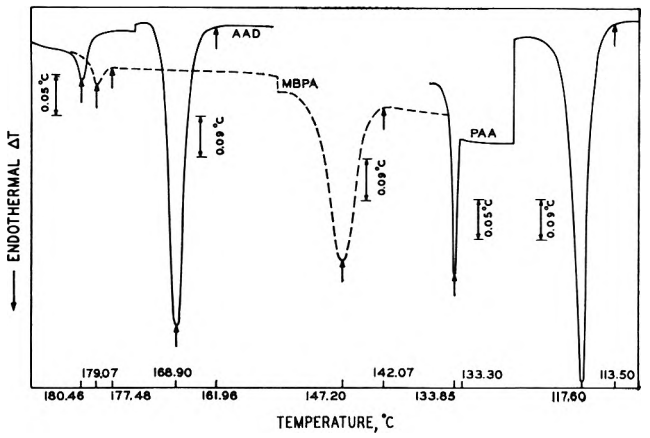

Figure 1. Thermographic traces of three liquid crystal compounds, block A: anisaldazine, AAD; N-*p*-methoxybenzylidene-*p*-phenylazoaniline, MBPA; *p*-azoxyanisole, PAA.

dene-*p*-phenylazoaniline (MBPA) at a heating rate of 4.7°/min. Table I gives the temperatures of the beginning, minimum, and end of the phase transition endotherms. These three temperatures define the thermographic characteristics for each mesophase transition.

Figure 2 shows thermograms for PAA at four heating rates. The location of the peaks on the temperature axis is not affected by heating rate. This is because of the choice of geometry for the d.t.a. system. In Fig. 2 the heat absorbed by the solid–nematic transition was 0.420 cal., and 0.0102 cal. for the nematic–isotropic transition of PAA. These results indicate that each transition may be considered a single event without a distinct pretransition caloric effect as has been reported.[11]

There is generally good agreement between the solid–nematic transition temperatures obtained from visual and d.t.a. measurements.[4] The visually observed nematic–isotropic transition is somewhat higher, 1–5°, than the vertex value but generally lower than the endotherm conclusion temperature as seen by d.t.a. This difference was seen by Martin and Müller.[11] The difference increases with decreasing heat of transition and, therefore, may be due in part to pretransition effects which are discussed below.

Transition Heats. Table II lists the results of the calorimetric studies carried out by d.t.a. on three liquid crystal compounds. These new calorimetric values for PAA agree excellently with the combined data obtained by Martin and Müller.[11] These values differ considerably, however, from an earlier extensive study of the nematic–isotropic transition for PAA.[12,13] Existing calorimetric values for PAA may be compared in Table III. There have been no previous reports for heats of transitions for the other two compounds.

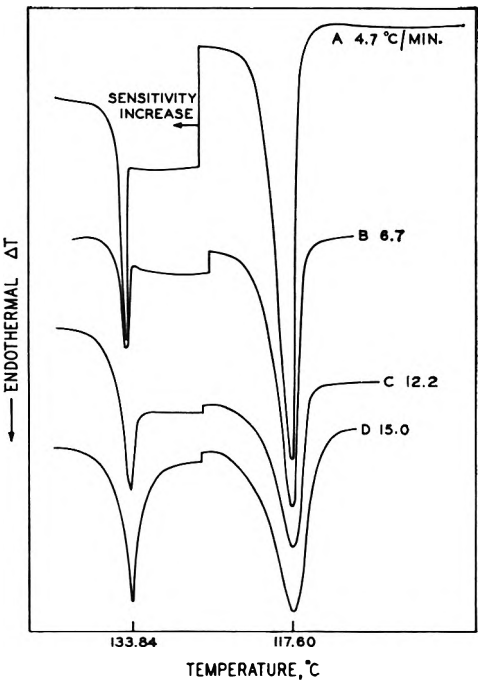

Figure 2. Thermographic trace of *p*-azoxyanisole at four heating rates, block A. A 0.0150-g. sample of PAA was thermographed at the indicated heating rates. The sensitivity on the ΔT axis for the 117.6° endotherm was: A, 0.09°/in.; B, 0.18°/in.; C, 0.36°/in.; D, 0.72°/in. The sensitivities for the 133.84° endotherm were: A, 0.05°/in.; B–D, 0.09°/in.

Table II: Heats of Transition for Three Liquid Crystal Compounds

Liquid crystal compound	Heat absorbed—phase transition— Solid–nematic, cal./g.	Nematic–isotopic, cal./g.
PAA	28.1 ± 0.9	0.68 ± 0.02
AAD	26.5 ± 0.5	0.59 ± 0.02
MBPA	25.9 ± 0.6	0.41 ± 0.02

High resolution nuclear magnetic resonance (n.m.r.) spectra obtained on these three compounds provide insight into nematic mesophase transitions.[14] In the high temperature isotropic state, spectra indicate normal liquid behavior. In the nematic state,

(11) H. Martin and F. H. Müller, *Kolloid-Z.*, **187**, 107 (1963).
(12) K. Kreutzer, *Ann. Physik*, (5) **33**, 192 (1938).
(13) K. Kreutzer and W. Kast, *Naturwiss.*, **25**, 233 (1937).
(14) R. S. Porter, unpublished results.

Table III: Thermal Data for Transitions of *p*-Azoxyanisole

Worker	Method	Solid–nematic		Nematic–isotropic	
		Temp., °C.	Heat, cal./g.	Temp., °C.	Heat, cal./g.
This work	D.t.a.	117.6	28.8	133.9	0.68
Schenck and Schneider and Buhner[a]	Ice calorimeter	...	29.8	132	0.68
Martin and Müller[b]	D.t.a.	117	28.2	(128) 132	0.69
Dekock[a]	Depression nematic–isotropic temperature	...	...	132	0.68
Hulett[a]	Clausius–Clapeyron pressure dependence	...	...	132	0.71
Kreutzer[c]	Ice calorimeter	...	...	131	1.79

[a] See R. Schenck, "Kristalline Flüssigkeiten," Leipzig, 1905, pp. 84–89. [b] See ref. 11. [c] See ref. 12 and 13.

n.m.r. spectra are much more complex and suggest that all aromatic protons are unique. This means that commonly flexible groups, such as methyl ethers, are free to rotate in the isotropic or true liquid state. In contrast, bonds in the nematic state must be fixed in nonrotating positions. These results are in accord with conclusions that molecules in nematic mesophases are packed such that they have freedom of rotation about one axis only, which is ordinarily the long axis.[15] The heat for nematic–isotropic transition thus involved energy for both molecular separation and internal rotation.

Discussion

Changes in physical properties have been observed at temperatures near first- as well as second-order transitions. Pretransition effects may be expected to be abnormally large in systems capable of forming liquid crystals.[16] By the theory of Frenkel, the largest pretransitions, *viz.*, heterophase fluctuations, are to be expected in cases where two phases differ but slightly from one another and where the heat of transition is small.[17] These features facilitate the formation of nuclei of one phase in another. Indeed, at a few degrees below nematic–isotropic transitions, a number of physical properties have been found to change rapidly with temperature, indicative of pretransition. These include density, specific heat, viscosity, dielectric constant, optical transparencies, and flow and magnetic birefringence.[16] There is also commonly a real discontinuity in these physical properties at nematic–isotropic transitions which is characteristic of first-order transitions.[4,18]

Precise density and magnetic and flow birefringence measurements also indicate pretransitions on the liquid side of the nematic–isotropic transformations.[4] Small aggregates have been found in the isotropic state of the nematic-forming compounds studied here.[5] The aggregates or molecular swarms contain tens to several hundred molecules and exist up to 5° above the nematic–isotropic transition. The fact that they are of such small dimensions is in good agreement with the apparent absence of aggregates in light scattering measurements on the isotropic state.[5]

By the theory of Frenkel, the extent of pretransition phenomena should be related to the heat of transition. Data on the three compounds studied here agree with this concept. The temperature range for pretransitions for the series increases with decreasing heat for the nematic–isotropic transition. This is revealed by viscosity data,[4,19] density data,[4] and by magnetic and flow birefringence measurements.[5]

Experimental evidence of several types clearly indicates pretransitions in liquid crystals. These effects appear adequately interpreted by Frenkel's heterophase fluctuation theory. Therefore, it seems unnecessary to separate the caloric effects due to so-called first-order and pretransition effects as has been done previously.[11]

Acknowledgment. The authors express appreciation to Messrs. D. Trujillo and A. R. Bruzzone for help with the experimental work.

Discussion

A. A. Antonioff (National Research Council, Ottawa). I wish to point out that in the system porous glass–water, also,

(15) R. Williams, *J. Chem. Phys.*, **39**, 384 (1963).

(16) W. A. Hoyer and A. W. Nolle, *ibid.*, **24**, 803 (1956).

(17) J. Frenkel, *Zh. Eksperim. i Teor. Fiz.*, **9**, 952 (1939), and "Kinetic Theory of Liquids," Clarendon Press, Oxford, 1946.

(18) E. Bauer and J. Bernamont, *J. Phys. Radium*, **7**, 19 (1936).

(19) R. S. Porter and J. F. Johnson, *J. Phys. Chem.*, **66**, 1826 (1962).

the phase transition for which becomes apparent as a change of the thermal coefficient of expansion, the value of this coefficient passes through a maximum.

R. S. PORTER. Effects both pre- and post- to the first-order transitions can likely be observed for a variety of systems and perhaps are only a matter of degree for many systems. Observations of these effects depend on the sensitivity of the measurement method, *e.g.*, heat capacity and specific volume, and on measurements at temperatures close to the transition. The inherent tendency for the test system to show such effects is, of course, important.

J. H. DE BOER (The Hague, Netherlands). Since entropy changes may—or rather should—give additional, or even primary information about these phase transitions, may I ask whether such entropy changes have been studied?

R. S. PORTER. Such a measurement is definitely desirable, particularly for liquid crystals, as the higher temperature nematic–isotropic transitions involve relatively large volume changes yet small latent heats, whereas just the reverse is true for lower solid–nematic transitions. Complete evaluation, of course, requires heat capacity data on the several phases which are not, as yet, available.

Solubilization of Polar Species by Micelle-Forming Soaps in a Nonpolar Solvent

by Samuel Kaufman

U. S. Naval Research Laboratory, Washington, D. C. 20390 *(Received February 26, 1964)*

The solubilization of diethyl ether, acetone, *n*-propylamine, and methyl acetate by sodium and magnesium dinonylnaphthalenesulfonates in toluene solution was studied by gas–liquid chromatography. Results are compared with data for the solubilization of methanol and acetic acid. Of the solubilizates studied, all were less extensively solubilized than methanol. Within the scope of the data, *n*-propylamine and acetic acid were solubilized approximately equally by the magnesium soap, but the sodium soap solubilized the acid more vigorously than the amine. The ether and ketone were only faintly solubilized and the ester occupied an intermediate position. The data are consistent with conclusions derived from earlier studies of micelle formation and solubilization by the same soaps. At very dilute concentrations of solubilizate, the cation of the soap controls the interaction, but with increasing concentrations, after the coordinating tendency of the cation is satisfied, the anion is the effective moiety. The relationship of solubilization to micelle formation is discussed.

Introduction

Solubilization is frequently considered a process wherein successive solubilizate molecules enter into and accumulate within persistent micelles, as in the solubilization of hydrocarbons by aqueous soap micelles.[1] Not all cases of solubilization conform to this pattern. The solubilization of methanol by both sulfonate and carboxylate soaps in toluene leads to the degeneration or disappearance of micelles[2]; water is known to expand zinc dinonylnaphthalenesulfonate micelles in benzene,[3] and no substantial difference is observed in the size or general nature of barium dinonylnaphthalenesulfonate micelles in benzene, whether solubilized Rhodamine B is present[3] or absent.[4] A

(1) M. E. L. McBain and E. Hutchinson, "Solubilization and Related Phenomena," Academic Press, New York, N. Y., 1955.

(2) S. Kaufman, *J. Colloid Sci.*, 17, 231 (1962).

(3) S. Kaufman and C. R. Singleterry, *ibid.*, 12, 465 (1957).

useful concept of solubilization imposes no restrictions upon the nature of the micelle or upon any changes it may undergo as solubilization commences and proceeds. Although this investigation did not include measurements of micelle size, the possibility of change in this and other properties of micelles with solubilization must be recognized. The term solubilization need not be restricted to species which are insoluble in the absence of the solubilizing agent; a soluble or insoluble species may be considered solubilized if it interacts with the solubilizing agent and both remain soluble thereafter. According to this concept, for any given stoichiometric concentration of solubilizate, its activity must be less in the presence of the solubilizing agent than in its absence, and the change in activity reflects the extent of solubilization.

The purpose of this investigation was to study the extent to which various classes of organic compounds are solubilized by micelle-forming soaps in a nonpolar solvent. Dinonylnaphthalenesulfonates in toluene solutions were used as solubilizing agents for diethyl ether, acetone, *n*-propylamine, and methyl acetate. By a gas–liquid chromatographic technique previously described,[2] saturated vapors over toluene solutions of the solubilizate with and without soap were analyzed. Quantitative inferences concerning solubilization were drawn from the observed changes in composition of the vapors caused by addition of soap to the solutions.

Experimental

Materials. The sodium and magnesium dinonylnaphthalenesulfonates (NaDNNS and $Mg(DNNS)_2$) were repetitively lyophilized and dried *in vacuo*. Details of their preparations have been described earlier.[2,5] Anhydrous ACS grade diethyl ether was percolated immediately before use through Linde Molecular Sieve 5A and activated alumina to remove traces of moisture and peroxides, respectively. Analysis of the percolate revealed no detectable quantity of either of these contaminants. The acetone was a spectrographic grade and was percolated immediately before use through Linde Molecular Sieve 5A and activated alumina to remove possible traces of water and acidic impurities. No detectable moisture was found in the percolate by gas chromatography. The most suitable of several lots of Eastman 1216 *n*-propylamine was selected on the basis of its gas chromatogram, which was free of extraneous peaks except for water, estimated at 1 part in 1000. Because of the satisfactory purity of this amine, and because of its tendency to develop impurities on attempts at further purification, it was used as received. The methyl acetate was Fisher Scientific Co. reagent grade M-203. This ester was percolated immediately before use through Linde Molecular Sieve 13X and activated alumina. The gas chromatogram of the percolate indicated no water, but about 4 parts methanol in 10,000 by volume. Any acidity present was assumed to be acetic acid. It was estimated from pH measurements that the ester–acid molar ratio was greater than 10^6:5. The method was validated by comparing results of titrations with those derived from pH measurements on untreated samples of the ester. The toluene has been described earlier.[2]

Procedure. Compositions of the vapors were studied with a Perkin-Elmer 154B fractometer. Details of method, procedure, and apparatus have been described.[2] Experimental modifications and features pertinent to the present measurements are reported here. To improve the base-line stability of chromatograms, the carrier-gas stream was split to provide independent channels for the reference and sample detectors. A capillary was interposed between the helium supply and the reference detector to moderate the flow of carrier gas in the reference channel. The flow meter monitoring the carrier-gas velocity was stabilized by moving it to the exit of the sample channel. Occasional trouble shooting was simplified by this change. The velocity of the carrier gas in the reference channel was not monitored, but was controlled by the inlet pressure and geometry of the channel so that it bore a fixed relationship to the velocity in the sample channel. The potential applied to the thermal conductivity bridge was 3.0 v. and the exit pressure was 0 p.s.i.g.

Columns were all 0.64 cm. o.d. and 1.83 m. long. Packings used were: Apiezon L, 20% w./w. on 60–80 mesh Gas Chrom P (I); Carbowax 400 (polyethylene glycol), 29% w./w. on 35–80 mesh Chromosorb Regular (II); Armeen SD, 20% w./w. on 60–80 mesh Gas Chrom P (III); and a composite column of 1 m. of I and 1 m. of II (I-II). For the study of the respective solubilizates, the column, operating temperature, inlet pressure, and carrier-gas flow rate were: for diethyl ether, I, 70°, 13.0 p.s.i.g., and 260 cc./min.; for acetone, I-II, 74°, 12 p.s.i.g., and 260 cc./min.; for *n*-propylamine, III, 64°, 12.0 p.s.i.g., and 160 cc./min.; and for methyl acetate, I, 54°, 12.2 p.s.i.g., and 110 cc./min.

Results and Discussion

The particular solubilizates used here were selected for their variety of representative functional groups

(4) T. F. Ford, S. Kaufman, and O. Nichols, paper presented at the 147th National Meeting of the American Chemical Society, Philadelphia, Pa., April, 1964.

(5) S. Kaufman, NRL Report No. 5639, U. S. Naval Research Laboratory, Washington, D. C. (1961).

and for their volatility, which suited them to the experimental method. Samples of saturated (25°) vapor over a series of toluene solutions of a given solubilizate were analyzed. The results were compared with those of a similar series of solutions containing known concentrations of soap. Differences between total solubilizate concentrations in the liquid at equal vapor compositions reflect the loss of activity of the solubilizate due to interaction with soap. The extent of this interaction, or solubilization, can therefore be calculated from the chromatographic data. Figures 1 and 2, respectively, for NaDNNS and $Mg(DNNS)_2$, display the data derived from the measurements. Included for comparison are data previously obtained for the solubilization of methanol[2] under strictly comparable conditions, and for acetic acid in benzene[6] under somewhat different conditions of soap concentration.[7]

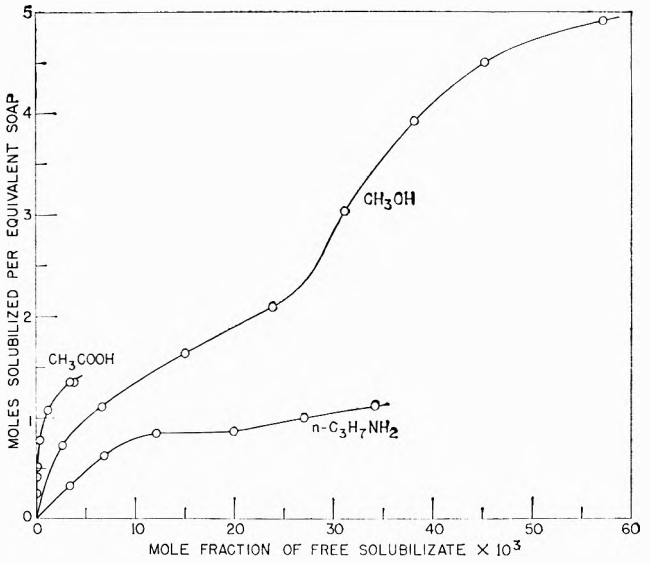

Figure 1. Solubilization of organic species by sodium dinonylnaphthalenesulfonate in toluene at 25°.

The abscissas are concentrations of unsolubilized solute remaining in equilibrium with that bound by the soap. The ordinates are ratios of bound solubilizate to soap present, in moles per equivalent or per gram-anion. Plotting in these coordinates maintains a practical comparability irrespective of cation valence if one is interested in the ultimate solubilization, but it distorts the impression obtained concerning the effect of the cation in the lower concentration range, which falls below 3 to 5 × 10^{-3} for these plots. Had the ordinates been plotted on the mole or gram-cation basis, they would be unchanged in Fig. 1, but doubled in Fig. 2.

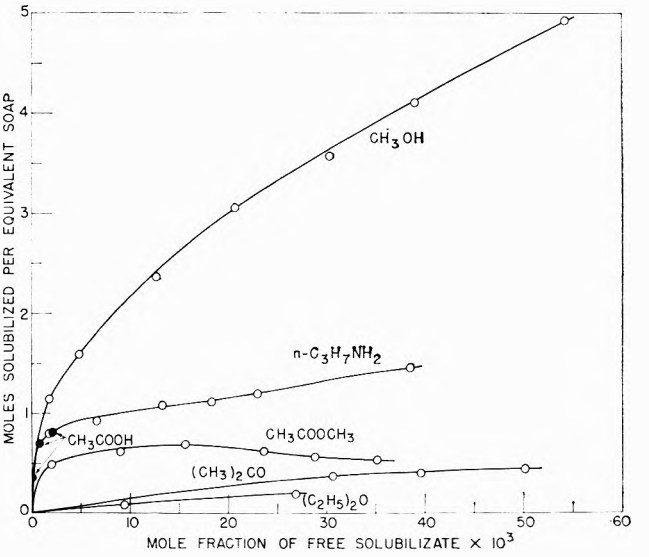

Figure 2. Solubilization of organic species by magnesium dinonylnaphthalenesulfonate in toluene at 25°.

Of the solutes shown in Fig. 2, methanol is most vigorously solubilized by $Mg(DNNS)_2$ once the initial stage is passed. Differentiation is not clear between the amine, acid, and alcohol in the very dilute region. For these three solubilizates it is concluded that in the initial stage nearly all the solute present is coordinated by the magnesium moiety of the soap because of the strong coordinating tendency of that cation. Discrimination between these solubilizates is consequently marginal or absent because nearly all the available solubilizate has interacted in each case. In Fig. 1 for NaDNNS there is a clear differentiation between these solubilizates because the more weakly coordinating sodium ion does not interact as vigorously. These data are consistent with earlier observations,[3] wherein it has been demonstrated that $Mg(DNNS)_2$ micelles are more firmly bound together than those of NaDNNS because of the charge-radius functions of the respective cations. In the upper concentration range, the ordinates and slopes both show that methanol is the most strongly and extensively solubilized of the solutes shown if acetic acid is excluded from consideration because of the limited data. This effect is attributed to the nature of the anion, common to both soaps. Coordination of amine with the cation appears to be the principal reason

(6) W. D. Bascom and C. R. Singleterry, *J. Colloid Sci.*, 13, 569 (1958).

(7) Concentrations of soap in the solutions studied here were 3.6 × 10^{-3} and 1.8 × 10^{-3} (mole fraction) for NaDNNS and $Mg(DNNS)_2$, respectively. Results are compared with benzene solutions of the same soaps whose concentrations were both 1.6 × 10^{-3} (mole fraction) in the acetic acid study. However, the functions plotted here reconcile these differences to a first approximation.

for its solubilization by both soaps, and a lesser interaction with the anion is indicated than for methanol, which is solubilized at higher concentrations by a hydrogen-bonding effect.

Acetone and diethyl ether are both very feebly bound by $Mg(DNNS)_2$, and although data are not available, it should be expected that NaDNNS would solubilize these compounds to a lesser extent than would $Mg(DNNS)_2$. It is probable that the ether and ketone both interact principally by coordination with the cation. The curve for methyl acetate suggests that the ester is solubilized exclusively by the cation. The initial slope distinctly differentiates the ester from the ether and ketone.

Discussion

E. HUTCHINSON (Stanford University, California). I quite agree with Mr. Kaufman's basic premise that the important thing to be observed about the classes of phenomena that generally go under the name of solubilization is that the thermodynamic activity of one component of a multicomponent system is reduced by the presence of another component—the solubilizer. Although we can discern, to be sure, many instances in which the solubilizing action can be traced to a mechanism which depends on the existence of micelles in or on which the solubilizate is attached, there is no good *a priori* reason to restrict the name solubilization to just that kind of action. From a thermodynamic viewpoint, one cannot distinguish between materials solubilized in micelles, materials adsorbed on the surface of particles, or, as in Mr. Kaufman's experiments, materials which appear to be strongly associated with the physically smaller portion of a long-chain salt.

On the Behavior of Some Glucosyl Alkylbenzenes and Glucosyl Alkanes

by Eric Hutchinson, Victor E. Sheaffer, and Fumikatsu Tokiwa

Department of Chemistry, Stanford University, Stanford, California *(Received January 28, 1964)*

An examination has been made of the surface properties and of some bulk colloid properties of a group of glucosyl alkanes and alkylbenzenes having the general formula $RC_6H_{11}O_6$, synthesized under conditions leading to products free of homologs. The lower members of the alkylbenzene series are surface-active but nonmicellar in aqueous solution, while higher members are both surface-active and micellar. A number of glucosyl alkanes were prepared but were found to be insufficiently soluble in water to permit extensive studies of their bulk properties.

Introduction

No matter whether the formation of micelles by an ionic surfactant is treated as a phase separation or as the equivalent mass-action association,[1] there is an inherent difficulty arising from the presence of charged particles. For example, representing micelle formation in sodium dodecyl sulfate (NaDDS) as

$$m\mathrm{Na}^+ + n\mathrm{DDS}^- \rightleftharpoons (\mathrm{Na}_m\mathrm{DDS}_n)^{m-n}$$

investigation of the properties of the micelles involves the determination of the two unknowns m and n. In contrast, the micellization of a nonionic compound X

$$m\mathrm{X} \rightleftharpoons (\mathrm{X}_m)$$

would appear to be much less complicated.

Attempts to extend the concepts of micellization, solubilization, and so on, derived from studies of ionic compounds, to nonionic compounds have, in the past, encountered difficulties arising mainly from the problem of obtaining pure nonionic materials. Thus, in the case of the glyceryl and glucosyl esters of fatty acids, the difficulties of preparing individual isomers are formidable, and in the case of polyethyleneglycol ethers one encounters considerable difficulty either in the synthesis of sharply defined compounds or in the fractionation of individual members from a homologous series arising from the usual industrial method of preparing such compounds.[2]

We have employed a synthetic method due to Hurd and Bonner[3] which produces clean preparations of well-defined glucosyl alkanes and alkylbenzenes and have succeeded, in the case of most of the compounds, in obtaining the α-isomer separately from the β-isomer. The syntheses will be reported in a separate publication.[4] Here it will suffice to indicate that the compounds in question have the structure

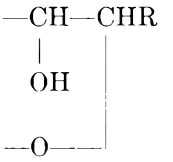

in which R is an alkyl or alkyl phenyl group attached to the anomeric center of the glucopyranose moiety. The starting material was in each case α-D-glucose, but in the course of the reaction some inversion occurs and the product initially contains both the α- and β-anomers, which can later be separated. Provided the reagents are free from homologs, the final product is pure in the sense that attachment of the R group occurs exclusively on the carbon atom indicated above.

A few variations on this reaction have been attempted, starting with xylose and glyceraldehyde, as indicated in the following list of compounds prepared: p-(β-D-glucosyl)toluene; p-(β-D-glucosyl)ethylbenzene; p-(β-D-glucosyl)propylbenzene; p-(β-D-glucosyl)butylbenzene; 1-(α- and β-D-glucosyl)hexane; 1-(α- and β-D-glucosyl)octane; 1-(α- and β-D-glucosyl)decane;

(1) K. Shinoda and E. Hutchinson, *J. Phys. Chem.*, **66**, 577 (1962).

(2) T. Nakagawa and K. Shinoda, "Colloidal Surfactants," Academic Press Inc., New York, N. Y., 1963, pp. 163–173.

(3) C. D. Hurd and W. A. Bonner, *J. Am. Chem. Soc.*, **67**, 1972 (1945).

(4) W. A. Bonner, V. E. Sheaffer, and E. Hutchinson, to be published.

1-(α- and β-D-glucosyl)dodecane; p-(α- and β-D-xylosyl)butylbenzene; and 1-(p-ethylphenyl)glycerol.

Physicochemical measurements have included surface tension, density, light scattering, ultrafiltration, freezing point depression, and a very limited number of solubilization studies. Most of the measurements have been made on the glucosyl alkylbenzenes, but surface tension studies have been made on all the compounds listed.

Experimental

1. Surface tension measurements on aqueous solutions of these compounds were, in the main, made by the drop-volume method, to which the corrections of Harkins and Brown[5] were applied. The drops were formed slowly on a tip, having a 0.204-cm. radius, attached to a micrometer syringe. Using drop-forming times of 5 min. or longer, no evidence of aging was found. A number of check measurements, using the du Nouy tensiometer method, showed no differences from the results of the drop-volume method.

2. Density measurements on the aqueous solutions were made using a pycnometer previously described.[6] Solutions were equilibrated in a thermostat at 25 ± 0.005°.

3. Light scattering measurements on the aqueous solutions were made on a Photo-Gonio-Diffusimetre instrument (Societe Francais d'Instruments de Controle et d'Analyse) in cylindrical cells, using unpolarized incident light of wave length 546 mμ. The instrument was standardized against a pure sample of benzene for which the reduced intensity was taken to be[7] 1.63×10^{-5}. Solutions were freed from dust, prior to study, by filtration through nitrocellulose membranes as described by Goring and Johnson.[8] Refractive index measurements were made using a Brice-Phoenix differential refractometer calibrated by means of potassium chloride solutions.

4. Ultrafiltration measurements on the aqueous solutions were carried out using nitrocellulose membranes previously described.[9] After quantitative dilution, the ultrafiltrate concentration was determined spectrophotometrically making use of the strong ultraviolet peak of the phenyl ring, in a Cary Model 14 instrument.

5. Freezing point depressions were measured by conventional methods, using a Beckmann thermometer.

6. Solubilization experiments with respect to propylene gas (Phillips Petroleum Co., 99.99% pure) were made by the method of Moore and Roaf.[10]

Results

Results for the surface tensions of the aqueous solutions at 25° are shown in Fig. 1–4, in which surface tension, σ, is plotted against the logarithm of the concentration of the nonionic compound. In the case of 1-(α-D-glucosyl)octane there appeared to be some indi-

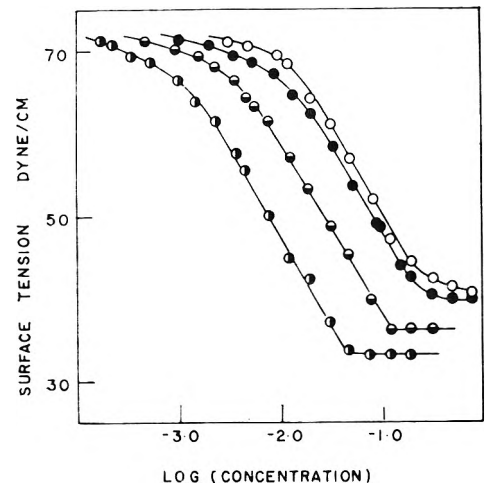

Figure 1. Graph of surface tension *vs.* log (concentration) for aqueous solutions of glucosyl alkylbenzenes at 25°. Concentrations are expressed in the units mole/l.: ○, p-(β-D-glucosyl)-toluene; ●, p-(β-D-glucosyl)ethylbenzene; ◒, p-(β-D-glucosyl)-propylbenzene; ◑, p-(β-D-glucosyl)butylbenzene.

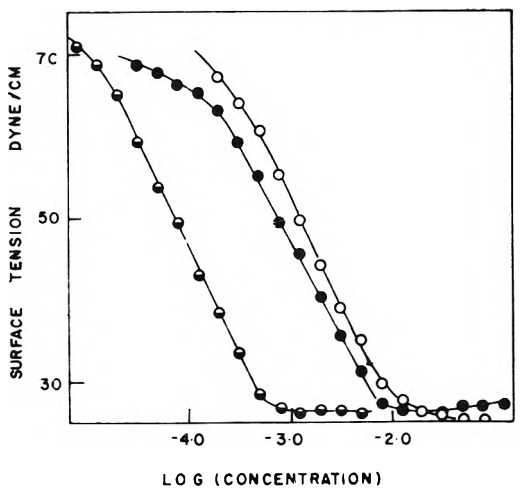

Figure 2. Graph of surface tension *vs.* log (concentration) for aqueous solutions of glucosyl alkanes at 25°. Concentrations are expressed in the units mole/l.: ○, α-D-glucosylhexane; ●, α-D-glucosyloctane; ◒, α-D-glucosyldodecane.

(5) W. D. Harkins and F. D. Brown, *J. Am. Chem Soc.*, **41**, 519 (1919).

(6) E. Hutchinson and C. S. Mosher, *J. Colloid Sci.*, 11, 352 (1956).

(7) C. I. Carr and B. H. Zimm, *J. Chem. Phys.*, **18**, 1616 (1950).

(8) D. A. I. Goring and P. Johnson, *J. Chem. Soc.*, 33 (1952).

(9) E. Hutchinson, *Z. physik. Chem.* (Frankfurt), 21, 38 (1959); E. Hutchinson and P. Shaffer, *ibid.*, 31, 397 (1962).

(10) B. Moore and H. E. Roaf, *Proc. Roy. Soc.* (London), **73**, 382 (1903).

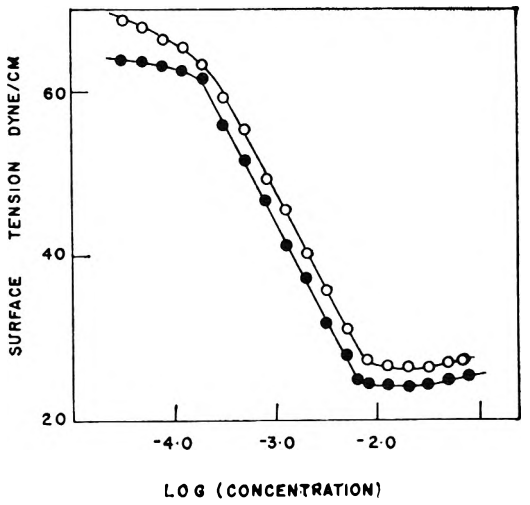

Figure 3. Graph showing the effect of temperature change on the surface tension of aqueous solutions of glucosyloctane: open circles, 25°; full circles, 50°.

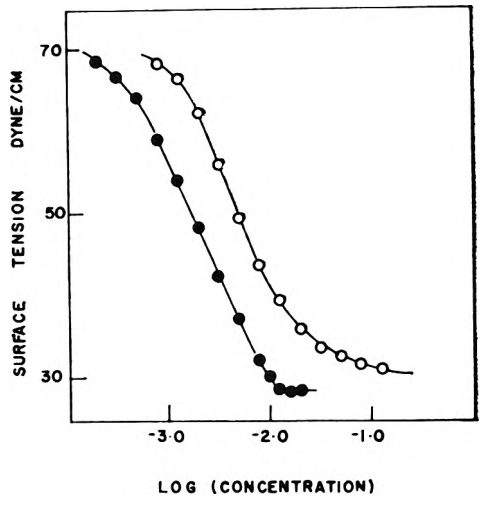

Figure 4. Graph of surface tension *vs.* log (concentration) for aqueous solutions of: open circles, 1-(*p*-ethylphenyl)glycerol; full circles, *p*-(β-D-xylosyl)butylbenzene.

cation of a minimum. Careful chromatographic and liquid–vapor chromatographic studies,[4] however, failed to detect any impurities in this material and failed, also, to remove the depression in the curve, which exceeded the estimated precision of the measurements.

Results for the densities and derived partial molal volumes of the glucosyl alkylbenzenes are given in Fig. 5–8. The graphs represent the best least-square plots over the appropriate linear ranges.

Results showing the reduced intensity, R_{90}, at right angles to the incident beam *vs.* concentration for *p*-(β-D-glucosyl)propylbenzene and -butylbenzene are given in Fig. 9. The corresponding conventional

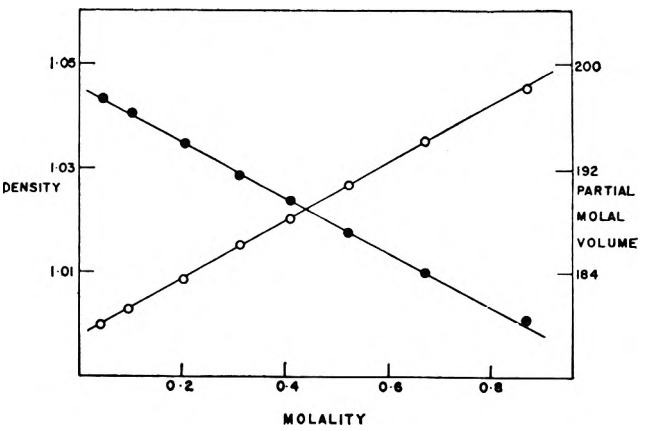

Figure 5. Graph showing: open circles, the densities; full circles, the partial molal volumes for aqueous solutions of glucosylethylbenzene at 25°. Left-hand ordinate refers to densities; right-hand ordinate refers to partial molal volumes.

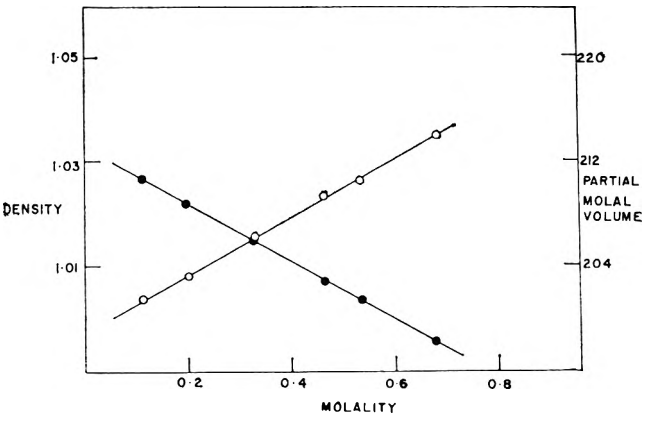

Figure 6. Graph showing: open circles, the densities; full circles, the partial molal volumes for aqueous solutions of glucosyltoluene at 25°. Left-hand ordinate refers to densities; right-hand ordinate refers to partial molal volumes.

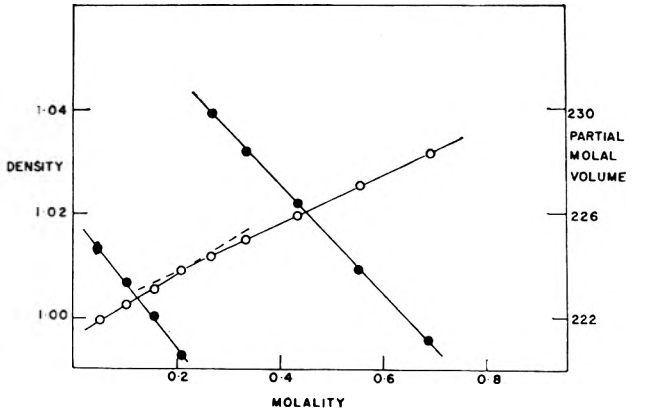

Figure 7. Graph showing: open circles, the densities; full circles, the partial molal volumes for aqueous solutions of glucosylpropylbenzene at 25°. Left-hand ordinate refers to densities; right-hand ordinate refers to partial molal volumes.

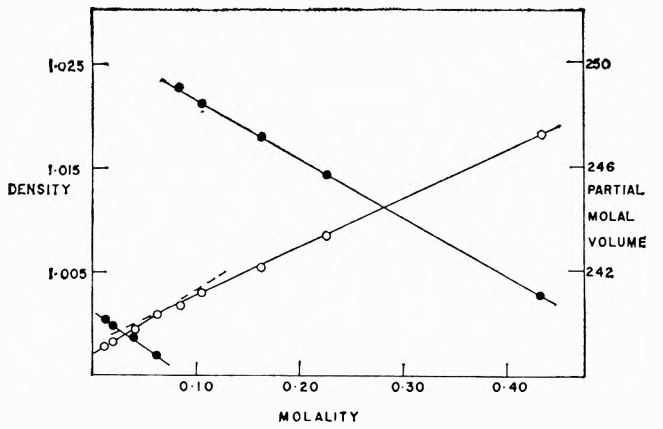

Figure 8. Graph showing: open circles, the densities; full circles, the partial molal volumes for aqueous solutions of glucosylbutylbenzene at 25°. Left-hand ordinate refers to densities; right-hand ordinate refers to partial molal volumes.

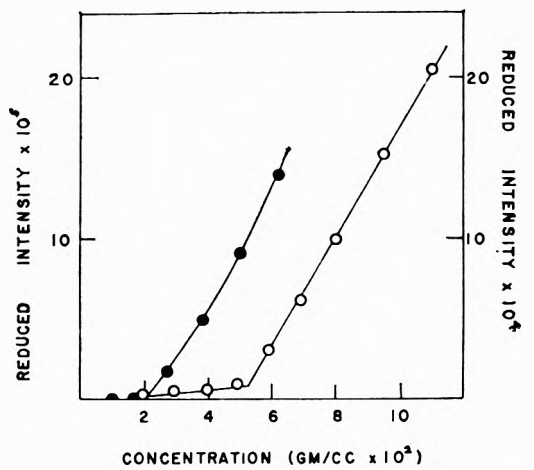

Figure 9. Graph showing the reduced intensity R_{90} as a function of concentration for aqueous solutions of p-(β-D-glucosyl)propylbenzene and -butylbenzene. Left-hand ordinate refers to glucosylpropylbenzene; right-hand ordinate refers to glucosylbutylbenzene.

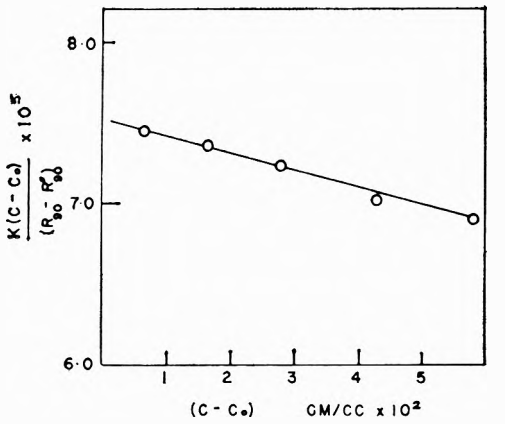

Figure 10. Graph showing the quantity $K(C - C_0)/(R_{90} - R_{90}°)$ as a function of concentration for aqueous solutions of glucosylpropylbenzene.

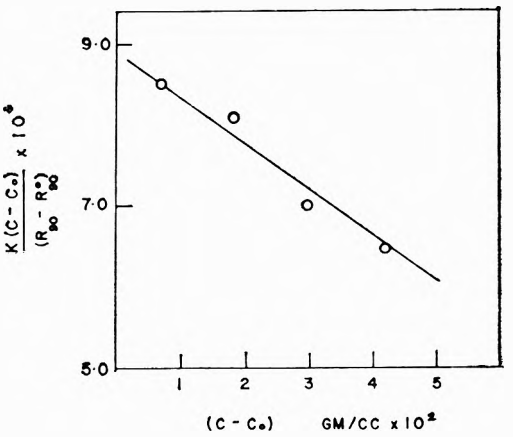

Figure 11. Graph showing the quantity $K(C - C_0)/(R_{90} - R_{90}°)$ as a function of concentration for aqueous solutions of glucosylbutylbenzene.

plots of $K(C - C_0)/(R_{90} - R_{90}°)$, where C and C_0 represent the concentration and critical concentration of the solute and R_{90} and $R_{90}°$ are the reduced intensity for the solution and pure water, respectively, are shown in Fig. 10 and 11. Dissymmetry ratios $I_{45°}/I_{135°}$, where I represents the scattered intensity, varied between 0.99 and 1.02 in most cases. Corresponding results for p-(β-D-glucosyl)toluene and -ethylbenzene have not been included. These latter results gave no indication of the presence of large aggregates in the solutions of these two compounds.

Results for the ultrafiltration experiments are shown in Fig. 12, in which the concentration of the ultrafiltrate is plotted against the concentration of the ultrafiltrand. The experiments were carried out at room temperature (20 ± 3°) under an average filtering pressure of 47 cm. Under these conditions, the rate of flow of pure water was approximately 10 ml./24 hr., whereas the rate of filtration of the solutions ranged from 3 to 6 ml./24 hr. To test that the behavior of the membranes was similar to that of earlier membranes,[9] a comparison was made of the ultrafiltration of p-(β-D-glucosyl)butylbenzene and sodium dodecyl sulfate solutions. For comparison the results are shown in Fig. 13, which suggests that the upward slope in ultrafiltrate concentration for the glucosylbutylbenzene is real and not due to leaks in the membranes.

Results for the freezing point depression in solutions of the glucosyl alkylbenzenes are shown in Fig. 14. Numerical data, including activity coefficients and osmotic coefficients, are given in Table I. The osmotic

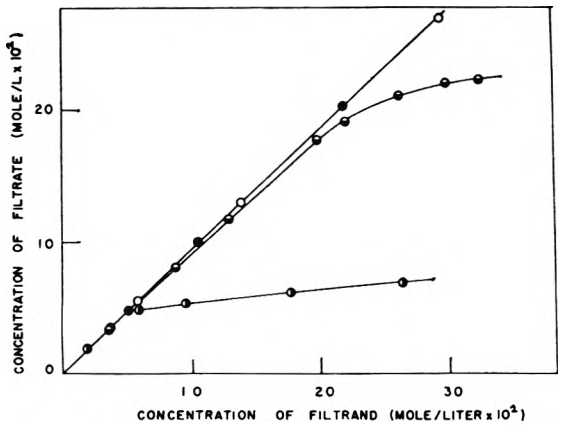

Figure 12. Graph showing the variation of the concentration of the ultrafiltrate varies with the concentration of the filtrand for aqueous solutions of glucosyl alkylbenzenes at room temperature. Filtering pressure 47 cm. ○, glucosyltoluene; ●, glucosylethylbenzene; ◑, glucosylpropylbenzene; ◒, glucosylbutylbenzene.

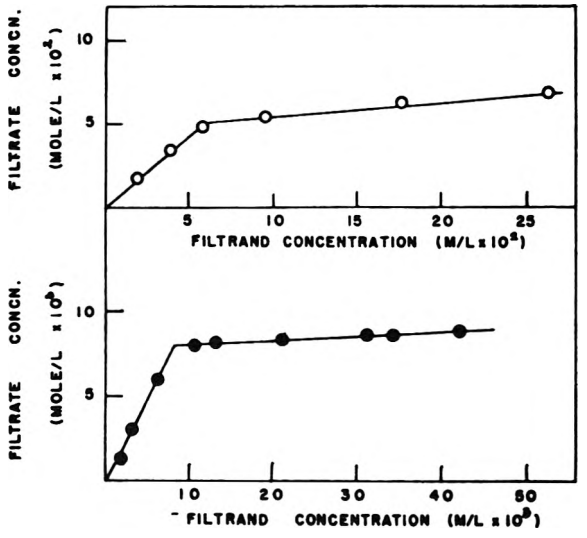

Figure 13. Graphs showing the comparison for the ultrafiltration of sodium dodecyl sulfate and glucosylbutylbenzene through the same membrane. Upper graph refers to glucosylbutylbenzene; lower graph refers to sodium dodecyl sulfate.

coefficient of the water, g_1, having been derived from the freezing point depression, the practical activity coefficient of the solute, γ, was calculated from the equation[11]

$$-\ln \gamma = (1 - g_1) + \int_0^m (1 - g_1)\, d \ln m$$

Results for the solubilization of propylene by solutions of *p*-(β-D-glucosyl)butylbenzene are given in Table II. C.m.c. values estimated from surface tension results are given in Table III.

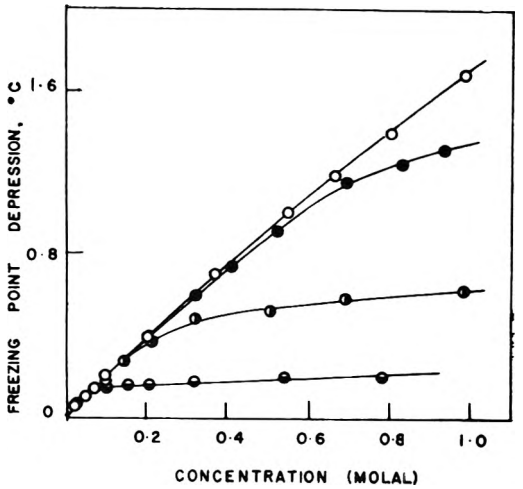

Figure 14. Graph showing the relation between freezing point depression and molal concentration for aqueous solutions of glucosyl alkylbenzenes: ○, glucosyltoluene; ●, glucosylethylbenzene; ◑, glucosylpropylbenzene; ◒, glucosylbutylbenzene.

Discussion

The first point to be noted is that in this class of compounds the solubility decreases rapidly as the size of the hydrocarbon moiety increases. Although we have not accurately measured the solubilities of these materials in water, the existence of turbidity in solutions of the glucosyloctane at about 1×10^{-1} mole l., and of the glucosyldodecane at about 6×10^{-3} mole/l., suggests that these solutions were saturated at room temperature. The octyl and dodecyl glucosides prepared by Shinoda, *et al.*,[12] which contain an additional oxygen atom in the form of an ether linkage, appear to be rather more soluble in water than their counterparts in our series of compounds. On the other hand, we have not found, to this point, in the case of the glucosyl hydrocarbons that are soluble in water, any indication of the cloud point effects commonly observed with glucosides and generally attributed, as in the case of polyethers, to the dehydration of the ethereal oxygen atoms.[13,14]

The onset of micellization is often taken to be reflected by the fairly abrupt change of slope in the surface tension–log (concentration) curve. In fact, the change of slope is frequently sharp enough that this

(11) E. A. Guggenheim, "Thermodynamics for Chemists and Physicists," North Holland Publishing Company, Amsterdam, 1949.

(12) K. Shinoda, T. Yamaguchi, and R. Hori, *Bull. Chem. Soc. Japan*, 34, 237 (1961).

(13) T. Nakagawa and K. Shinoda, "Colloidal Surfactants," Academic Press Inc., New York, N. Y., 1963, p. 129.

(14) P. H. Elworthy and C. B. Macfarlane, *J. Chem. Soc.*, 907 (1963).

Table I: Freezing Point Depression Results for Glucosyl Alkylbenzenes

Compound	Molality	Freezing point depression	Osmotic coefficient of water	Activity coefficient of solute
Glucosyl-toluene	0.0351	0.072	1.087	1.22
	0.0504	0.102	1.088	1.26
	0.102	0.204	1.074	1.32
	0.208	0.391	1.010	1.28
	0.374	0.690	0.991	1.26
	0.552	0.995	0.969	1.22
	0.669	1.185	0.953	1.20
	0.806	1.385	0.924	1.15
	0.987	1.680	0.915	1.13
Glucosyl-ethyl-benzene	0.0529	0.106	1.077	1.22
	0.107	0.210	1.055	1.26
	0.209	0.389	1.000	1.21
	0.325	0.593	0.980	1.18
	0.417	0.731	0.942	1.12
	0.533	0.911	0.919	1.07
	0.696	1.146	0.885	1.03
	0.830	1.235	0.880	0.916
	0.936	1.301	0.747	0.843
Glucosyl-propyl-benzene	0.0543	0.108	1.069	1.20
	0.100	0.193	1.038	1.22
	0.147	0.279	1.022	1.21
	0.206	0.373	0.974	1.16
	0.326	0.483	0.797	0.916
	0.507	0.520	0.551	0.622
	0.691	0.581	0.452	0.483
	0.980	0.621	0.341	0.349
Glucosyl-butyl-benzene	0.0368	0.072	1.053	1.12
	0.0745	0.138	0.993	1.11
	0.105	0.153	0.785	0.867
	0.159	0.160	0.541	0.588
	0.216	0.163	0.405	0.438
	0.323	0.183	0.304	0.305
	0.549	0.200	0.196	0.184
	0.783	0.213	0.146	0.131

Table II: Results for the Solubilization of Propylene by Solutions of Glucosylbutylbenzene[a]

Pressure of propylene, cm.	Moles of propylene/mole of glucosyl-butylbenzene
73.67	8.61×10^{-3}
73.32	6.13×10^{-3}
72.97	6.46×10^{-3}
72.61	5.70×10^{-3}
72.27	6.35×10^{-3}
71.97	6.51×10^{-3}
71.56	6.99×10^{-3}

[a] Temperature = 20.9°. Solution: 0.7501 g. of glucosyl-butylbenzene and 24.325 g. of water.

Table III: Values of the Critical Micelle Concentration, Surface Concentration, and Residual Area for Glucosyl Hydrocarbons

Compound	C.m.c., mole/l.	Surface concentration, mole/cm.^{2} $\times 10^{10}$	Residual area Å.^{2}/molecule
Glucosyltoluene	...	3.65	45.5
Glucosylethyl-benzene	(0.50)	3.61	46.0
Glucosylpropyl-benzene	0.13	3.66	45.4
Glucosylbutyl-benzene	0.05	3.77	44.0
Glucosylhexane	...	4.45	37.3
Glucosyloctane (25°)	0.0079	4.18	39.8
Glucosyloctane (50°)	0.0071	4.24	39.2
Glucosyldodecane	0.0006	4.51	36.8
Xylosylbutyl-benzene	0.011	4.61	36.0
Glycerylethyl-benzene	...	5.11	32.5

provides one method of measuring the critical micelle concentration (c.m.c.). The change of slope in the cases of glucosylpropylbenzene and glucosylbutylbenzene is comparable in sharpness to that observed with such ionic compounds as sodium dodecyl sulfate, and rather less so in the cases of glucosyloctane and glucosyldodecane. The curves for glucosyltoluene, glucosylethylbenzene, glucosylhexane, glycerylethylbenzene, and xylosylbutylbenzene show a more gradual change in slope in which real curvature at the knee of the curve is plainly visible. Similarly, micelle formation is also considered to be reflected in the fairly sharp changes in density and in the partial molal volume of the solute. Solubility considerations have so far limited our studies of density to the glucosyl alkylbenzenes, though more refined methods are currently enabling us to study the glucosyl alkanes. In the cases of glucosylpropylbenzene and glucosylbutylbenzene, the density–concentration plots appear to show the change of slope characteristic of micelle formation in ionic materials.[15,16] Any break in the cases of glucosyltoluene and glucosylethylbenzene appears to be ruled out by the fact that the mean square linear plots using all the results obtained extrapolate to a density for pure water consistent, within the limits of accuracy

(15) E. L. McBain and F. Hutchinson, "Solubilization," Academic Press Inc., New York, N. Y., 1955, p. 34.

(16) P. Mukerjee, *J. Phys. Chem.*, **66**, 1733 (1962).

of the experiments, with known values. For glucosylpropylbenzene and glucosylbutylbenzene, the change in partial molal volume reflected in the change of density is +10.3 and +10.7 ± 0.2 ml./mole, respectively. The increase in partial molal volume, here ascribed to micelle formation, is comparable to the effects observed in the sodium alkyl sulfates, potassium carboxylates, and dodecyl sulfonic acid.[16,17]

The presence of large aggregates, *e.g.*, micelles containing 30 or more units, can readily be demonstrated by light scattering methods, and in the cases of glucosylpropylbenzene and glucosylbutylbenzene, light scattering measurements clearly show the presence of large micelles. For glucosylpropylbenzene, the aggregation number appears to be about 47, while that for glucosylbutylbenzene is about 380; the corresponding micelle molecular weights are, respectively, 1.33×10^4 and 1.13×10^5. Light scattering measurements indicate the absence of large micelles in the cases of glucosyltoluene and glucosylethylbenzene at any of the concentrations studied. It will be noted that when the light scattering results are plotted according to the equation[18]

$$\frac{K(C - C_0)}{R_{90} - R_{90}^\circ} = \frac{1}{M} + 2A_2(C - C_0)$$

in which A_2 is the second virial coefficient, a negative value is found for A_2, the negative value being greater in the case of glucosylbutylbenzene than in the case of glucosylpropylbenzene. The value of A_2 is generally considered to be some measure of the solute–solvent interaction, being positive in "good" solvents and negative in "poor" solvents. Many micellar solutes yield positive values of A_2, but a number of cases reported for nonionic micellar solutes[19] show negative values, and studies of the effect of temperature change show that A_2 may change from positive to negative values as the temperature rises in solutions of polyethylene oxide ethers.[19] In the case of nonionic solutes the sign and magnitude of A_2 is a measure of the hydrophil–lipophil balance, and it will be noted that in solutions of glucosylbutylbenzene, for which A_2 has a larger negative value, the micellar molecular weight is much larger than in solutions of glucosylpropylbenzene. As yet we have not been able to study light scattering at a variety of temperatures to see whether A_2 undergoes a change of sign in these cases. Although the interpretation given above seems reasonable to us, on the basis of the evidence available, it may be remarked that Elworthy and Macfarlane[14] have interpreted the negative (and in some cases inconstant) slope of the $K(C - C_0)/R_{90} - R_{90}^\circ$ *vs.* $(C - C_0)$ plot in terms of a shifting equilibrium between smaller and larger micelles. The possibility of an equilibrium of that sort may have to be borne in mind in these cases also, as discussed below.

The action of an ultrafiltration membrane has been discussed, in earlier papers,[9] as providing a mechanical means of separating micelles from the monomer in equilibrium with them. As shown in Fig. 12 and 13, the behavior of these glucosyl alkylbenzenes in ultrafiltration differs somewhat from the behavior of sodium dodecyl sulfate. Glucosyltoluene and glucosylethylbenzene solutions pass through the ultrafilter without change of concentration, so that if association occurs in these solutions it can be fairly confidently asserted that the aggregates are smaller than about 10 to 20 monomers. Glucosylbutylbenzene solutions exhibit a quite sharp break at the c.m.c. but the concentration of the ultrafiltrate increases rather more rapidly with increasing filtrand concentration than is the case with sodium dodecyl sulfate.[9] Accordingly, if it may be assumed that the ultrafiltrate contains only monomers, at a concentration which represents equilibrium with the micelles in the filtrand, then this concentration is not as constant as would strictly be required if the formation of micelles were treated as a pseudo-phase separation.[1,20] The validity of the experiments appears to be satisfied by the control experiments using sodium dodecyl sulfate, which yielded results agreeing with those obtained earlier with a different batch of membranes, and the changing concentration in the ultrafiltrate can be accepted with some confidence.

The behavior of glucosylpropylbenzene is intermediate between that of the glucosylbutylbenzene and that of the two lowest homologs. There is a gradual change of slope in the region 0.20 to 0.30 mole/l. and a small, but measurable, difference in concentration between ultrafiltrate and filtrand above about 0.08 mole/l. The concentration at which this difference becomes quite marked, namely 0.20 mole/l., is to be compared with the value 0.13 mole/l. which appears to represent the c.m.c. as judged from the surface tension results. At the present time we have no way of knowing whether the ultrafiltrates contain only monomers, since light scattering is too insensitive to detect small aggregates in this region of concentration, and an answer to this question will have to await further studies.

(17) K. Shinoda, private communication; calculations based on densities reported by C. R. Bury and G. A. Parry, *J. Chem. Soc.*, 626 (1935), and others.

(18) P. Debye, *Ann. N. Y. Acad. Sci.*, 51, 575 (1949).

(19) T. Nakagawa, K. Kuriyama, and H. Inoue, 12th Symposium on Colloidal Chemistry, Chemical Society of Japan, 1959, p. 29.

(20) E. Hutchinson, A. Inaba, and L. G. Bailey, *Z. physik. Chem.* (Frankfurt), 5, 344 (1955).

Although, as indicated above, changes in the properties of the solutions are sufficiently pronounced in the cases of glucosylpropylbenzene and glucosylbutylbenzene that we can be reasonably sure that micelles are present in solutions of higher concentrations, and that we can assign at least approximate values for the c.m.c. of these systems, it appears from the results of the freezing point experiments that even in the case of glucosylethylbenzene there is an appreciable departure from ideality, suggesting association, at concentrations greater than about 0.4 mole/l. Even though these solutions do have freezing points indicating association at higher concentrations, they showed no diminution of concentration in the ultrafiltration experiments. It seems reasonable, by analogy with the higher homologs, to ascribe the deviation from ideality to association in this case also, but if true this implies that glucosylethylbenzene forms aggregates too small to be ultrafilterable. This conclusion is consistent with the considerable decrease in the size of the micelle in going from glucosylbutylbenzene to glucosylpropylbenzene.

A curious feature of all of the glucosyl alkylbenzene solutions is that in very dilute solutions the freezing point depressions are larger than for an ideal solute of the same concentration; that is, the osmotic coefficient of the water is greater than unity. Even making allowances for reasonable error in measuring the small freezing point depressions, it is hard to account for this feature. Elementary analysis of the solutes is sufficiently consistent with the assumed formula that the presence of nonionic solute impurities seems unlikely. Impurities cannot be ruled out entirely, however, since in one stage of the preparation[4] solutions of the compounds are passed through ion-exchange columns which may leave small traces of electrolyte in solution. We have established qualitatively (and are in the process of measuring accurately) the fact that the aqueous solutions of these compounds are poor, but definite, conductors. Resolution of this problem will have to await further study.

In a private communication, Dr. K. J. Mysels has raised with us the question of nomenclature in dealing with systems of this type. It seems evident that micelles, in the usual sense, are formed in solutions of glucosylpropylbenzene and glucosylbutylbenzene, and are absent, as far as we can tell, in any sense, in any of the solutions of glucosyltoluene studied here. However, in glucosylethylbenzene there is the suggestion, from freezing point depressions, that we have negative deviations from ideality consistent with the formation of small aggregates such as dimer, trimer, and so on. The question arises as to whether these are to be described as micelles and whether we can give the name critical micelle concentration (or region) to the concentration at which the formation of these species becomes appreciable. There seems to be no good reason why the terms should not be used in this situation as long as it is clearly understood that the term micelle is a flexible one.

In earlier papers[1,20] it has been argued that the formation of micelles has many of the characteristics of the appearance of a new phase in the system and that, although the treatment of micellization as an equilibrium described by the mass law is an equivalent treatment, the pseudo-phase change has some advantages for quantitative interpretation. The changes in properties in solutions of ionic micellar solutes, though not discontinuous, are relatively sharp, so that the term critical micelle concentration (rather than *region*) is not inappropriate. In the glucosyl hydrocarbons the changes are far more gradual than in ionic micellar solutions, probably owing to the more delicate balance of hydrophil–oleophil forces which results when an ionic hydrophil group is absent, and this type of material seems particularly well suited to a study of the region in which micellization begins. More detailed studies, particularly of the changes in thermodynamic properties such as heat of dilution, are now in progress.

All of the compounds prepared in this series possess considerable surface activity. We have applied the Gibbs adsorption equation to the surface tension results and obtain the values for the surface excess shown in Table III for concentrations corresponding to the linear portions of the σ–log (concentration) curves, which presumably apply to the close-packed adsorbed films.[12,21] The very limited number of experiments that we have so far carried out suggest that, with regard to solubilizing power, the glucosyl alkylbenzenes compare rather poorly with alkyl sulfates and carboxylates of the same general size of hydrocarbon chain, but insufficient evidence has been accumulated to justify any detailed conclusions on this point.

Acknowledgments. We gratefully acknowledge the support of the National Science Foundation, through Grant G-14168, and of the Kao Soap Co., Japan, for support to F. T.

(21) K. Shinoda, T. Yamanaka, and K. Kinoshita, *J. Phys. Chem.*, **63**, 648 (1959).

Interfacial Viscoelasticity of Poly-DL-alanine and Bovine Serum Albumin Monolayers[1]

by Kinsi Motomura

Department of Chemistry, Mount Sinai Hospital, New York, New York *(Received February 28, 1964)*

The ring torsion pendulum was devised to measure the viscoelasticity of monolayers at both air–water and benzene–water interfaces with the aid of the ring made from Teflon. The interfacial viscoelasticity of poly-DL-alanine and bovine serum albumin monolayers was measured at various areas. It was shown that poly-DL-alanine consists of an extended form in the monolayer and makes a brittle film due to strong intermolecular cohesive forces, among which hydrogen bonding plays an important role. Also, it was elucidated that bovine serum albumin molecules at the air–water interface assume a fairly round shape, but at the benzene–water interface a partially extended configuration in which some parts of the molecule behave like a synthetic polypeptide.

Introduction

The behavior of protein molecules in monolayers is insufficiently known to explain or interpret all experimental observations. In order to elucidate the surface behavior, many investigators have studied monolayers of synthetic polypeptides, which may be considered as protein analogs from the standpoint of chemical constitution; they measured surface pressure, potential, viscosity, and viscoelasticity at both air–water and oil–water interfaces.[2–5]

The macromolecular films are characterized by particular rheological properties. The rheological behavior of films might be satisfactorily described by mechanical models made up of an infinite number of Voigt models in series or Maxwell models in parallel as in three-dimensional rheology. Biswas and Haydon recently reported that they had analyzed the rheological behavior of adsorbed films under creep and stress relaxation in terms of mechanical models, for which retardation and relaxation spectra were obtained.[6] On the other hand, simple mechanical models are also useful to interpret the observed behavior of macromolecular films. Because of the advantage of easy construction and operation, several investigators used the torsion pendulum to determine for films under free oscillation the coefficients of viscosity and elasticity, which correspond to the dashpot and spring of the Voigt model, respectively.[7–9] Because of their remarkable viscoelastic behavior, the monolayer structure of macromolecules is broken so easily by oscillation that erroneous viscosity and elasticity data will be obtained. Motomura and Matuura showed that the behavior of linear polymer monolayers at air–water interface can be analyzed by a four-parameter model (Voigt model and Maxwell model in series) under the experimental condition that the monolayers are subjected to free deformation after the head of the torsion pendulum is twisted by a given angle at time zero.[10] They also showed that the structure of the monolayers is quite clearly revealed by combining the results of viscoelasticity with those of surface pressure.

(1) The experimental work was carried out with the support of Grant RG-04736 of the National Institute of Health.

(2) C. W. N. Cumper and A. E. Alexander, *Trans. Faraday Soc.*, **46**, 235 (1950).

(3) T. Isemura and K. Hamaguchi, *Bull. Chem. Soc. Japan*, **25**, 40 (1952); **26**, 425 (1953); **27**, 125, 339 (1954); T. Isemura and S. Ikeda, *ibid.*, **33**, 659 (1959); **34**, 137 (1960); T. Isemura and T. Yamashita, *ibid.*, **33**, 1 (1959).

(4) J. T. Davies, *Trans. Faraday Soc.*, **49**, 949 (1953); *Biochim. Biophys. Acta*, **11**, 165 (1953); *Biochem. J.*, **56**, 509 (1954).

(5) T. Tachibana and K. Inokuchi, *J. Colloid Sci.*, **8**, 341 (1953).

(6) B. Biswas and D. A. Haydon, *Proc. Roy. Soc.* (London), **A271**, 296, 317 (1963).

(7) A. A. Trapeznikov, *Dokl. Akad. Nauk SSSR*, **63**, 57 (1948).

(8) D. W. Criddle and A. L. Meader, *J. Appl. Phys.*, **26**, 838 (1955).

(9) N. W. Tschoegl, *J. Colloid Sci.*, **13**, 500 (1958); *Kolloid-Z.*, **181**, 19 (1962).

(10) K. Motomura and R. Matuura, *J. Colloid Sci.*, **18**, 295 (1963).

In the study of protein monolayers the measurements at the oil–water interface occupy an important part. Therefore, it is worthwhile to improve the above method to measure the viscoelasticity at the oil–water boundary. In this paper the viscoelasticity of poly-DL-alanine and bovine serum albumin (BSA) monolayers, which are formed by the same spreading technique, is measured at both air–water and oil–water interfaces, and the state and structure of BSA monolayer will be discussed.

Experimental

The ring torsion pendulum was used for measurements of surface viscoelasticity at both air–water and benzene–water interfaces. The apparatus was almost the same as one used for linear polymer monolayers except the ring which is made from Teflon and the shape of which is shown in Fig. 1. The radius of the ring R_1 was 1.05 cm.; a glass dish of radius R_2 = 4.33 cm. and

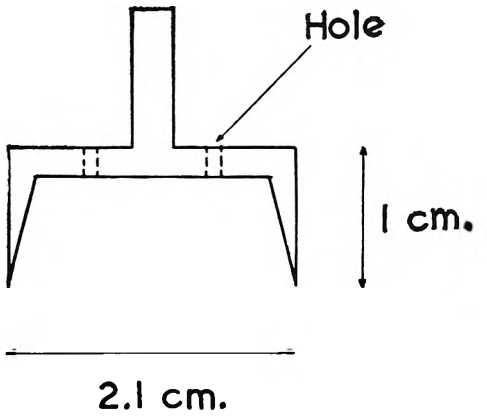

Figure 1. Teflon ring.

a polypropylene dish of radius R_2 = 4.70 cm. were used for measurements at the benzene–water and air-water interfaces, respectively. The torsion constant, κ, of the wire was 0.314 dyne cm. The experimental procedure was similar to that in the previous paper.[10] The solutions (0.03%) of poly-DL-alanine and BSA were spread with a micrometer syringe at a clean air–water boundary or at a benzene–water boundary under a benzene phase of *ca.* 0.3 cm. thickness: the Teflon ring was touched on the interface after the monolayers are left to stand for 30 min. After another 30 min., the shearing stress was applied on the monolayers by twisting the torsion head by a given angle ψ, and the following angular deformation of the film, θ, was observed. The increase in area due to the curvature of the interface near the wall of the glass dish was corrected by Thomas' equation.[11] The experiments were carried out at 24 ± 1°.

The deformation–time (θ/t) relation of monolayers was expressed in the previous article, where the derivatives may be found

$$\theta = \psi - A\exp\{-(\alpha - \beta)t\} - B\exp\{-(\alpha + \beta)t\} + D\sin(\epsilon t + F)\exp(-\delta t) \quad (1)$$

when the viscoelastic behavior is assumed to be representable by a four-parameter model. The damped oscillation term in eq. 1 is caused by the moment of inertia of the ring and is of little importance once the rigidity in films increases. The constants A, B, D, F, α, β, ϵ, and δ are related to the viscoelasticity, so that the spring E (elasticity) and dashpot η (viscosity) of the Maxwell model and the spring E_1 and dashpot η_1 of the Voigt model in the four-parameter model are evaluated by the following equations[10]

$$E = \frac{\kappa}{C}\frac{A + B}{\psi - A - B} \quad (2)$$

$$E_1 = 1\Big/\left(\frac{C}{\kappa}\frac{\psi - A}{A} - \frac{1}{E}\right) \quad (3)$$

$$\eta_1 = \frac{\kappa}{\kappa + CE}\frac{E + E_1 + (C/\kappa)EE_1}{2\alpha} \quad (4)$$

and

$$\eta = \frac{\kappa}{\kappa - CE}\frac{EE_1}{\eta_1}\frac{1}{\alpha^2 - \beta^2} \quad (5)$$

where

$$C = 4\pi\Big/\left(\frac{1}{R_1^2} - \frac{1}{R_2^2}\right)$$

The values of E and E_1 were calculated in dynes/cm. and those of η and η_1 in s.p. (surface poise, dynes sec./cm.).

Crystalline bovine serum albumin was obtained from Armour Pharmaceutical Company. Poly-DL-alanine, whose molecular weight is 6500, was supplied by Mann Research Laboratories. Both were spread from 60% isopropyl alcohol with sodium acetate added in a concentration of 0.5 *M*. Water, benzene, and isopropyl alcohol were triply distilled.

Results and Discussion

Poly-DL-alanine Monolayers at the Air–Water Interface. Poly-DL-alanine forms a so-called condensed film at the air–water interface.[4,12,13] Thus, in connection with

(11) A. G. Thomas, *Nature*, 179, 776 (1957).

(12) D. F. Cheesman and J. T. Davies, *Advan. Protein Chem.*, 9, 439 (1954).

(13) S. Ikeda, *Ann. Rept. Sci. Works, Fac. Sci., Osaka Univ.*, 10, 13 (1962).

the discussion in previous papers,[10,14] where it was clarified that synthetic linear polymers consist of an extended form in monolayers and that their viscoelastic behavior and surface pressure depend on the cohesive force between segments of the polymers, it is conceivable that the poly-DL-alanine monolayer will become viscoelastic at some areas. Indeed, the monolayer showed a viscoelastic behavior from fairly large areas downward, but it was so brittle that sufficient θ/t curves, required to calculate the viscoelasticity, could not be obtained above about 15 Å.²/residue.

The viscoelasticity of poly-DL-alanine monolayers at the air–water boundary is plotted against the area in Fig. 2. The smallest values observed are 2.8 dynes/cm., 4.2 dynes/cm., 1.2×10^3 s.p., and 6.5×10^3 s.p. for E, E_1, η_1, and η, respectively, which are unexpectedly large when compared with the corresponding values of polymethyl methacrylate (PMMA): 0.046 dyne/cm., 0.043 dyne/cm., 1.7 s.p., and 2.7 s.p. In Fig. 3 their difference is clearly shown. This

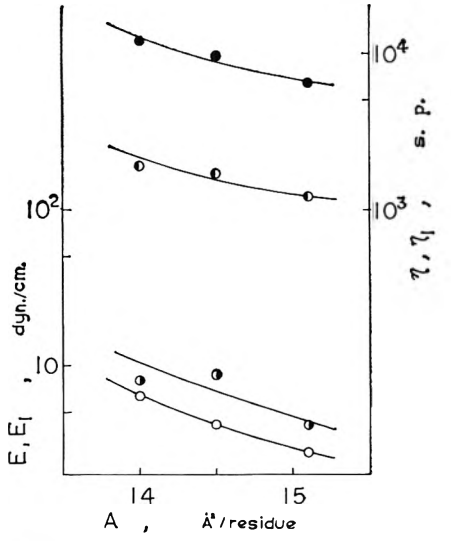

Figure 2. Viscoelasticity *vs.* area curve for poly-DL-alanine monolayer at the air–water interface: E (○), E_1 (◑), η_1 (◐), and η (●).

suggests that the intermolecular interaction of the former differs from that of the latter in which van der Waals and dipole moment interactions might play an important role. The poly-DL-alanine, on the other hand, resembles aluminum distearate in its surface viscoelastic behavior; for the aluminum distearate monolayer the viscoelasticity was measurable for large values only and E_1 was greater than E at all areas observed, as in Fig. 2.[15] The interaction between

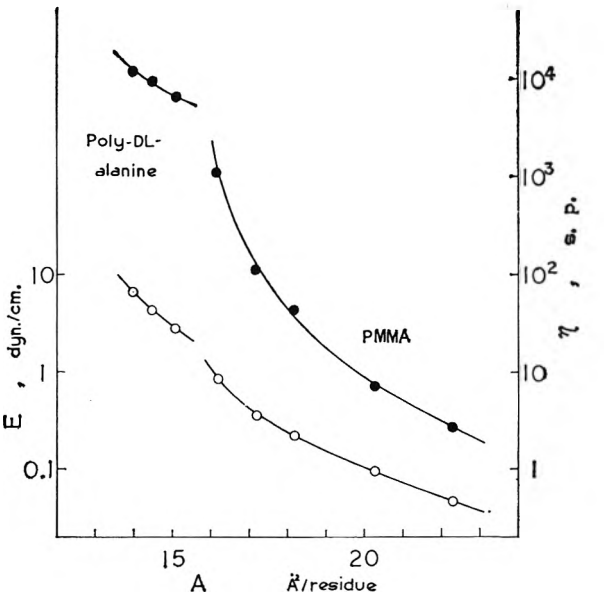

Figure 3. Comparison between E, η *vs.* area curves of poly-DL-alanine and PMMA monolayers at the air–water interface: E (○) and η (●).

segments of aluminum distearate, which has a linear polymer structure brought about by coordinate bonds, seems to be characterized by strong van der Waals forces and hydrogen bonding. In regard to the chemical structure of poly-DL-alanine it may, therefore, be said that the main intermolecular interaction takes place by van der Waals forces and hydrogen bonding between peptide groups.

Previous investigators found that polypeptide films show viscoelasticity,[5,6] and they emphasized the importance of hydrogen bond formation. Its importance in polypeptide monolayers was demonstrated by others on the basis of surface pressure and surface viscosity measurements.[13,16]

BSA Monolayers at the Air–Water Interface. Most protein monolayers at the air–water interface give condensed films such as that of poly-DL-alanine. If the protein molecules are completely unfolded, the monolayers will display viscoelasticity at areas larger than the close-packed state. The surface viscoelasticity of BSA was measured in the same way as for poly-DL-alanine, but viscoelastic behavior was not detected before the monolayer collapsed. Typical behavior was observed only at small areas and with poor reproducibility; *e.g.*, E = 0.43 dyne/cm., E_1 = 0.12 dyne/cm., η_1 = 13 s.p., and η = 37 s.p. at 0.56 m.²/mg.

(14) K. Motomura and R. Matuura, *J. Colloid Sci.*, **18**, 52 (1963).
(15) K. Motomura and R. Matuura, *Bull. Chem. Soc. Japan*, **35**, 289 (1962).
(16) E. Mishuck and F. R. Eirich, *J. Polymer Sci.*, **16**, 397 (1955).

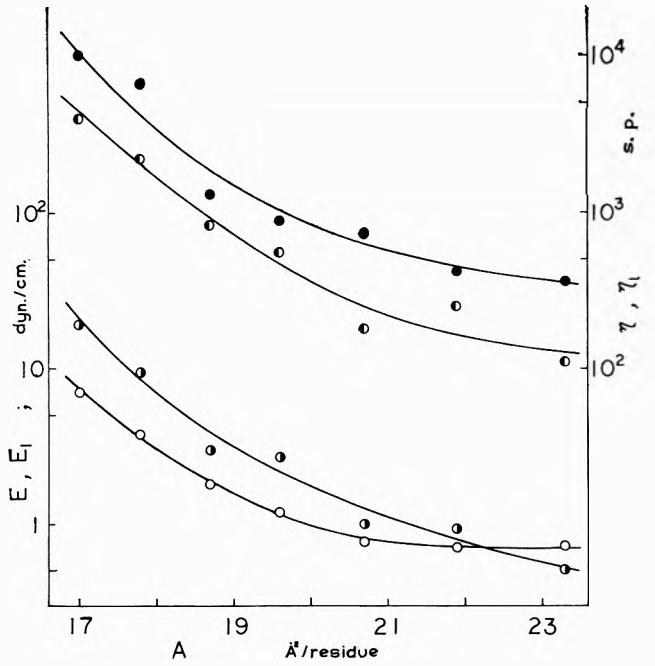

Figure 4. Viscoelasticity *vs.* area curve for poly-DL-alanine monolayer at the benzene–water interface: E (O), E_1 (◑), η_1 (◐), and η (●).

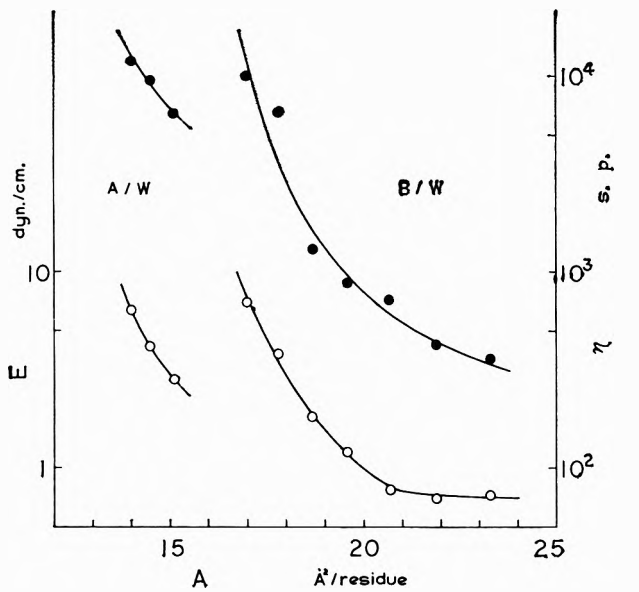

Figure 5. Comparison between poly-DL-alanine monolayer at the air–water and at the benzene–water interfaces: E (O) and η (●).

When this finding is compared with the value of poly-DL-alanine, a discrepancy is seen which we attribute to the difference of the molecular configurations in the monolayers. The BSA molecule has various kinds of side chains and moreover is known to have many (14–18) S–S linkages.[17,18] Thus, it is suggested that

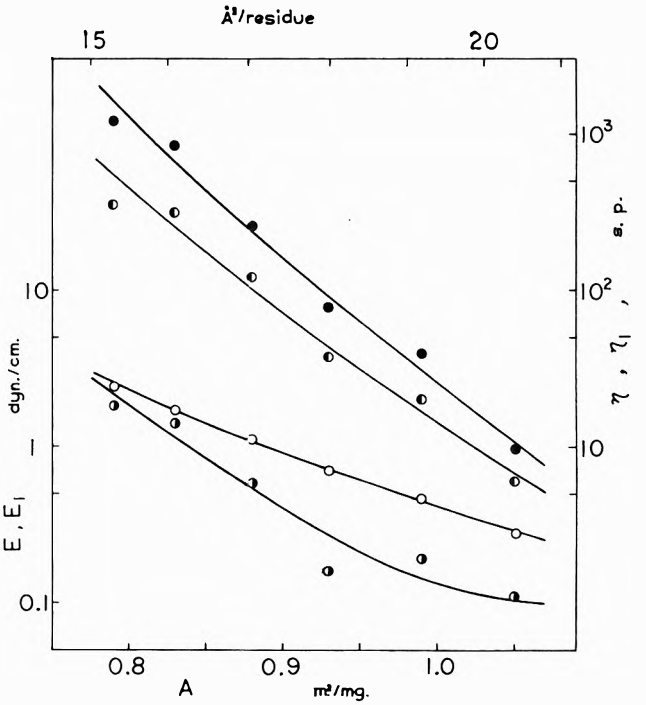

Figure 6. Viscoelasticity *vs.* area curve for BSA monolayer at the benzene–water interface: E (O), E_1 (◑), η_1 (◐), and η (●).

the molecule is unfolded. Hence, the peptide backbone would be brought into contact with the water surface over most of its length, but it may retain its spherical shape in two dimensions.

Poly-DL-alanine Monolayers at the Benzene–Water Interface. The cohesive force between the segments of synthetic polymers, for which the zero level of energy is defined as the energy of the polymer molecules at rest at infinite separation, is reduced at the oil–water interface; this permits the expansion of the monolayer and, as a matter of course, the increase of surface pressure. It is to be noticed at the same time that the presence of the oil phase strengthens the film structure as a whole. Therefore, it might be expected that the polymer monolayers at the oil–water boundary lose their stiffness in some measure and show a higher viscoelasticity over a wider range of the area.

Poly-DL-alanine monolayers at the benzene–water interface were hard but not as brittle as at the air–water interface. The smallest values of the measured viscoelasticity were quite small in comparison with those at the air–water boundary. Figure 4 shows the value of viscoelasticity *vs.* the area curve of poly-DL-alanine. Compared with the curve of PMMA monolayers, there seems to be a big difference between their

(17) D. F. Waugh, *Advan. Protein Chem.*, 9, 325 (1954).
(18) W. H. Hughes, Jr., *Proteins*, 2B, 663 (1954).

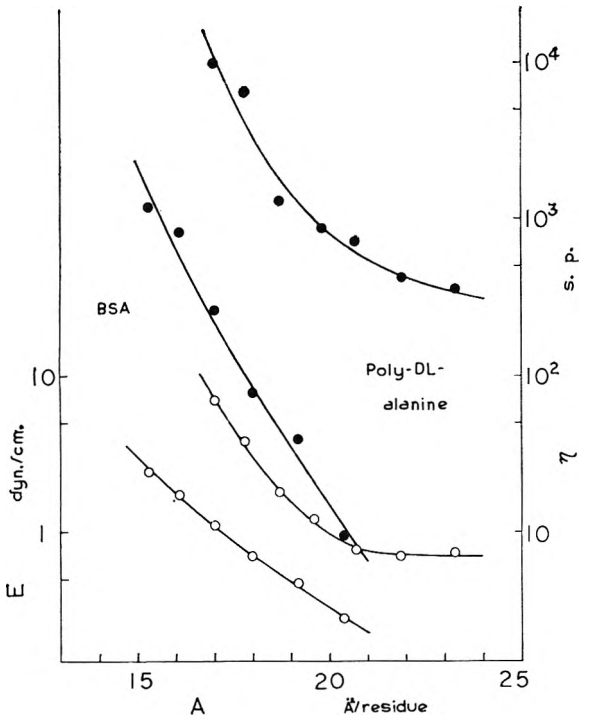

Figure 7. Comparison between E, η *vs.* area curves of BSA and poly-DL-alanine monolayers at the benzene–water interface: E (O) and η (●).

viscoelastic characteristics. This must be due to the part played by hydrogen bonding. Furthermore, we can see a difference between the viscoelastic behavior at the air–water and at the benzene–water interfaces. The difference of the variation of the E and η values with area is graphically shown in Fig. 5. This confirms that the benzene phase strengthens the film structure. The benzene phase appears to have a similar effect as plasticizers have in lowering the second-order transition point of polymers, when the increase of the surface viscoelasticity is left out of consideration.

BSA Monolayers at the Benzene–Water Interface. The viscoelastic behavior of BSA monolayers at the benzene–water boundary was found to be completely different from the behavior at the air–water interface and to bear a resemblance to those of synthetic polymer monolayers both at the benzene–water and air–water interfaces. The BSA exhibited viscoelasticity at areas larger than the close-packed area. The results are shown in Fig. 6, where the area is also expressed in Å.^{2}/residue on the assumption of the molecular weight and the number of residues of BSA being 66,000–69,000 and 588, respectively.[19]

It is noticeable that the values of E are higher than those of E_1 over all the areas in contrast to poly-DL-alanine. Moreover, the aspect of viscoelasticity *vs.* area is distinctly different between the BSA and the poly-DL-alanine monolayers. This may be ascribed to the decrease in the role of hydrogen bonding or to incomplete unfolding in the BSA monolayer. If the BSA molecule is completely unfolded, the monolayer will show higher viscoelasticity than poly-DL-alanine because of the greater length and the polar character of the side chains in BSA. As shown in Fig. 7, where the E and η values are plotted against the area, the BSA shows smaller values. This fact indicates that the molecules are extensively but not completely unfolded. It may, therefore, be concluded from these results that the BSA molecule is unfolded with the aid of benzene up to a partially extended configuration in which some parts of the molecule move around freely, like synthetic polypeptides, and other parts are prevented from extending by the side chains and S–S linkages.

Acknowledgment. The author wishes to thank Dr. Harry Sobotka for discussion and aid in the preparation of the manuscript.

Discussion

R. MANNHEIMER (Southwest Research Institute, San Antonio). Did you, in your experiments, carry out any measurements at a variety of angles, so as to investigate the effect of shear stress on your films?

K. MOTOMURA. No effect of shear stress upon the viscoelasticity of monolayers was observed in the few experiments carried out. However, since the viscoelasticity measurements were made over a narrow range of stresses, because of the stiffness of the monolayers, such effects cannot be positively ruled out.

W. WADE (University of Texas). Did you ever observe any time-dependent effects in your studies of the viscoelasticity of monolayers?

K. MOTOMURA. I observed time dependences of the viscoelasticity which varied somewhat according to the monolayer. After about 1 hr., however, the monolayers seemed to be stable.

(19) G. R. Tristram, *Proteins*, **1A**, 181 (1953).

Aerosol Studies by Light Scattering. III. Preparation and Particle Size Analysis of Sodium Chloride Aerosols of Narrow Size Distribution[1]

by W. F. Espenscheid,[2] E. Matijević, and M. Kerker

Department of Chemistry, Clarkson College of Technology, Potsdam, New York *(Received February 28, 1964)*

Sodium chloride aerosols in the submicron range and of narrow size distribution were produced with excellent reproducibility when nucleated with sodium fluoride nuclei in a high temperature generator. In contrast to crystalline sodium chloride, the particles produced by this method are spherical and show no sharp electron diffraction rings, indicating that they are mainly amorphous. The particle size distribution of the aerosols could be determined uniquely and with high precision and accuracy from light scattering data using the polarization ratio method described in detail previously. Two different wave lengths have been used. The agreement between these results and electron microscopy is very good. The effects of the flow rate of carrier gas, nuclei concentration, and generator furnace temperatures upon the aerosol size distribution were systematically investigated. With increasing flow rate at constant furnace temperatures the average particle size decreases. At constant flow rate the average particle size becomes larger with increasing furnace temperatures. Particle size also increases with dilution of nuclei.

Introduction

Sodium chloride aerosols have been prepared by several investigators using three different methods: (a) the aspirator technique,[3-8] (b) the hot wire generator,[9-11] and (c) evaporation or sublimation.[12-16] The particles obtained were usually cubes or irregularly shaped and of undetermined or wide size distributions. This paper describes the preparation of aerosols of sodium chloride consisting of solid *spherical* particles of narrow size distribution. Whereas, earlier, solid aerosols had been produced by self-nucleation,[17,18] here the aerosols are obtained by vapor condensation upon sodium fluoride nuclei. The particle size distribution is determined by the polarization ratio method[19-21] and confirmed by electron microscopy. These aerosols can be prepared reproducibly when appropriate precautions in operating the generator are taken. The dependence of the size distribution upon the generator conditions has been studied. The spherical aerosols produced by these methods do not show the electron diffraction rings that are characteristic of crystalline materials even in this range of particle size and appear to be mainly amorphous.

Experimental

Materials. Sodium chloride used for preparation of the aerosols was reagent grade, further purified by fourfold precipitation from saturated aqueous NaCl solutions using gaseous HCl. The purified salt was

(1) This investigation was supported in part by PHS Research Grant AP-0048 from The Division of Air Pollution of the Public Health Service.

(2) Part of a Ph.D. Thesis by W. F. Espenscheid.

(3) C. Orr, Jr., F. K. Hurd, W. P. Hendrix, and C. Junge, *J. Meteorol.*, 15, 240 (1958).

(4) C. Orr, Jr., F. K. Hurd, and W. J. Corbett, *J. Colloid Sci.*, 13, 472 (1958).

(5) T. T. Mercer, U. S. Atomic Energy Commission Report UR-474, (1957).

(6) C. F. Schadt and R. D. Cadle, *J. Colloid Sci.*, 12, 356 (1957), *J. Phys. Chem.*, 65, 1689 (1961).

(7) L. Dautrebande, German Patent 1,027,180 (April 3, 1958).

(8) F. Fanhoe, A. E. Lindroos, and R. J. Abelson, *Ind. Eng. Chem.*, 43, 1336 (1951).

(9) I. S. Yaffe and R. D. Cadle, *J. Phys. Chem.*, 62, 510 (1958).

(10) J. P. Lodge and B. J. Tufts, *J. Colloid Sci.*, 10, 256 (1955).

(11) D. Schiff, H. I. Schiff, and P. R. Gendron, *Can. J. Chem.*, 31, 1108 (1953).

(12) W. Walkenhorst and G. Zebel, German Patent 1,036,470 (August 14, 1958).

dried at 110° and roasted at 600° before use.[22] Sodium fluoride used for nucleation was Fisher certified reagent. Pure helium (Linde Co.), the carrier gas, was passed through a glass fritted filter of F grade before use.

Preparation of Sodium Chloride Aerosols. Sodium chloride aerosols were generated using the evaporation–sublimation technique either with self-nucleation[17,18,23] or heterogeneous nucleation. The heterogeneously nucleated aerosols were obtained by repeatedly evaporating and condensing NaCl upon NaF nuclei in a stream of helium. The generator equipment is schematically represented in Fig. 1. Three

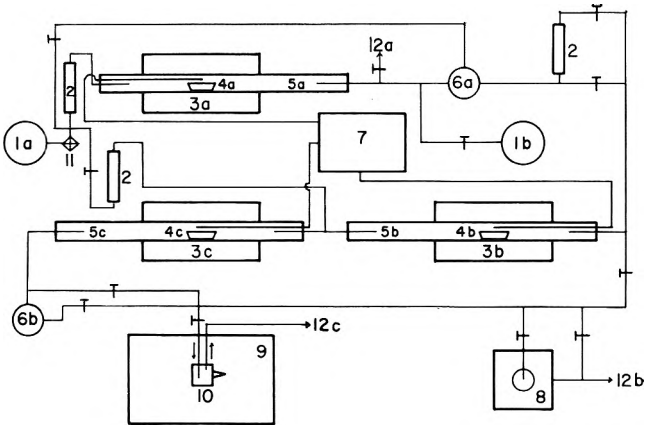

Figure 1. Schematic diagram of the aerosol generator: (1a,b) helium sources, (2) flow meters, (3a,b,c) combustion furnaces, (4a,b,c) combustion boats, (5a,b,c) combustion tubes, (6a,b) viewing chambers, (7) potentiometer, (8) thermopositor, (9) light scattering photometer, (10) light scattering cell, (11) gas filter, and (12a,b,c) exhausts.

heavy-duty hinged-type combustion furnaces (3a,b,c) were used to produce the aerosol in stages. The first (3a) served as a generator for NaF nuclei, the second (3b) produced a partially grown NaCl aerosol, and the third (3c) supplied additional NaCl vapor from which the final aerosol of narrow size distribution was formed. In the self-nucleation technique, the nucleator furnace and the first NaCl furnace were bypassed using only the last furnace (3c) containing NaCl. In the preparation of nucleated aerosols, solid NaF was placed in a combustion boat (4a) and kept at 850°, while NaCl was in combustion boats (4b and 4c) which were inserted into the second and third McDanel high temperature combustion tubes (5b,c). Under these conditions the NaF nuclei are too small either to show a detectable Tyndall cone (6a) or to be observed in an electron microscope (35 Å. resolution) even after a prolonged collection by thermal precipitation. The temperature was controlled using Variac resistors and measured with a chromel–alumel thermocouple in connection with a Wheelco portable potentiometer, series 300 (7). The aerosol formed could be observed in a three-neck flask which served as a viewing chamber (6b). The three furnaces correspond, in a way, to the nucleator, boiler, and reheater of the Sinclair–La Mer generator.[24] In this sense we consider this a "boiler" technique.

Collection of aerosol for the particle size distribution counts in the electron microscope was performed by thermal precipitation in a Model B thermopositor (American Instrument Co.) (8). Collection was made directly on collodion-coated electron microscope grids in the thermopositor chamber. The aerosols which had been collected on these grids were immediately examined by electron diffraction and photographed in the electron microscope. The grids were not shadowed before photography. An example of these spherical aerosols is given in Fig. 2. The uneven edges are caused by some evaporation due to heating in the electron beam. The particles appear quite smooth when the beam is first turned on and then they develop the serrations upon continued exposure.

If these spherical particles, collected upon an electron microscope grid, were exposed to normal room humidities for a short period of time they became cubic[10,11,14,18,25]; the smaller particles changed more rapidly than the larger as expected from the theoretical considerations of Orr, *et al.*[3,4] In order to prevent this transformation, the generator system was operated in an air-conditioned dehumidified room which also housed the electron microscope. The thermopositor

(13) D. M. Young and J. A. Morrison, *J. Sci. Instr.*, **31**, 90 (1954); F. W. Thompson, G. S. Rose, and J. A. Morrison, *ibid.*, **32**, 325 (1955).

(14) A. Craig and R. McIntosh, *Can. J. Chem.*, **30**, 448 (1952).

(15) K. Clusius and H. Meyer, *Z. Naturforsch.*, **6a**, 401 (1951).

(16) S. G. Lipsett, F. M. G. Johnson, and O. Maass, *J. Am. Chem. Soc.*, **49**, 925 (1927).

(17) E. Matijević, M. Kerker, and K. F. Schulz, *Discussions Faraday Soc.*, **30**, 178 (1960).

(18) E. Matijević, W. F. Espenscheid, and M. Kerker, *J. Colloid Sci.*, **18**, 91 (1963).

(19) M. Kerker, E. Daby, G. L. Cohen, J. P. Kratohvil, and E. Matijević, *J. Phys. Chem.*, **67**, 2105 (1963).

(20) M. Kerker, E. Matijević, W. F. Espenscheid, W. A. Farone, and S. Kitani, *J. Colloid Sci.*, **19**, 213 (1964).

(21) E. Matijević, S. Kitani, and M. Kerker, *ibid.*, **19**, 223 (1964).

(22) J. J. Betts and B. A. Pethica, *Trans. Faraday Soc.*, **52**, 1581 (1956).

(23) A. G. Keenan and J. M. Holmes, *J. Phys. Chem.*, **53**, 1309 (1949).

(24) D. Sinclair and V. K. La Mer, *Chem. Rev.*, **44**, 245 (1949).

(25) T. A. McLaughlan, R. S. Sennett, and G. D. Scott, *Can. J. Res.* **A28**, 530 (1950).

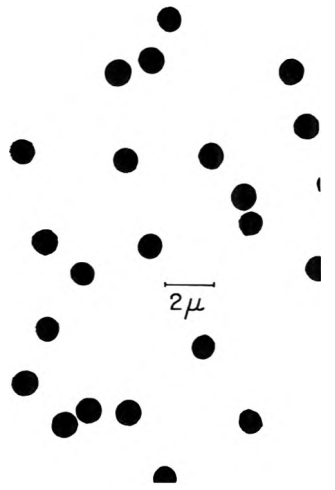

Figure 2. Electron micrograph of a nucleated sodium chloride aerosol: $t_1 = 755°$, $t_2 = 775°$, flow rate 1.0 l./min., 25% of nuclei, $\bar{\alpha}_{546} = 5.8$, $\sigma = 0.035$.

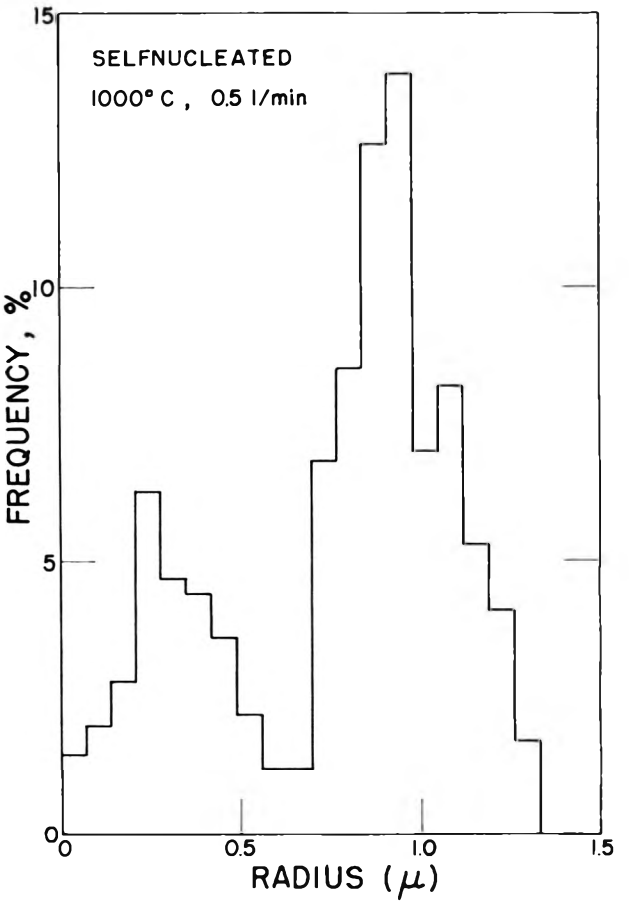

Figure 3. Bimodal frequency distribution of an aerosol obtained when nuclei are contaminated by impurities from thermocouple corrosion.

was placed adjacent to the microscope, and the grids were transported this short distance under a steady stream of dry helium. Under these conditions the particles remained spherical and when examined in the electron beam, they exhibited no sharp diffraction rings. On the other hand, if the same particles were exposed to moisture, they formed cubes which gave the sharp diffraction pattern characteristic of crystalline NaCl.

The reproducibility of the preparations made under apparently identical generator conditions for both self-nucleated and nucleated aerosols was, at first, quite poor. In the course of the experiments, several observations were made which finally led to procedures by which the aerosols could be prepared reproducibly, especially by the nucleation technique. First, it was observed that the thermocouples used in the furnaces corroded with time under the influence of NaCl vapor and consequently acted as a source of nuclei. This gave results varying between the extremes of homogeneous and heterogeneous nucleation, and frequently showed distinct signs of both processes occurring simultaneously. Figure 3 shows a bimodal distribution, obtained by electron microscopy, under these conditions. Accordingly, the temperatures of the furnaces were first carefully calibrated against the setting of a Powerstat variable transformer using a thermocouple. Then the thermocouple was removed and the furnaces operated in the absence of it. Temperatures were rechecked periodically in order to assure constancy.

In the nucleation method, it was observed that each time the combustion tube in the NaF nuclei generator was refilled with fresh NaF, the characteristics of the NaCl aerosols would change and fluctuate for long periods of time. However, after a few days of continuous operation of the nuclei generator, without any shutdown, reproducible aerosols were obtained. Because of this, the combustion boat was charged with NaF and the furnace was maintained continuously at the desired temperature until the supply of NaF was nearly exhausted. Since the nuclei generator was kept at a temperature almost 150° below the melting point of NaF, the loss due to evaporation was small and the nuclei generator could be operated for months between fillings.

For certain temperatures and flow rates, aerosols with moderately narrow size distribution could be prepared by heterogeneous nucleation with only two furnaces, one containing the NaF and the following one with the NaCl. However, in order to obtain narrow size distributions over a wide range of operating conditions, it was necessary to use three furnaces,

two of which contained NaCl as already described. If the last furnace did not also contain a charge of NaCl, hardly any aerosol was formed. In other words, it could not really operate on the principle of a reheater in the Sinclair–La Mer generator.[24]

One procedure which led to good results was as follows. Both furnaces containing the NaCl were set at 815°, a temperature above the melting point of NaCl (802°). The combustion boats with the NaCl were inserted, and this temperature was maintained over a 5-hr. period. After this, the temperatures of these furnaces were then individually reset to the desired temperature of the experiment and the entire generator allowed to equilibrate for a minimum of 10 hr. Then the flow of helium was started and maintained for at least 1 hr. before measurements were taken.

All measurements presented here, using the heterogeneous nucleation method, were taken on aerosols produced at temperatures *below* the melting point of NaCl by *sublimation* from solid NaCl and subsequent condensation upon the NaF nuclei. When the furnaces were operated *above* the melting point of NaCl, the particles tended to be considerably larger and of quite narrow size distribution, showing very brilliant higher order Tyndall spectra. However, the reproducibility with which these aerosols could be prepared was much poorer.

The influence of the temperature of each furnace upon the final aerosol size distribution was investigated in a systematic manner. In a series of experiments, the temperature of the first NaCl generator furnace was held constant while the second was varied over a range of temperatures. Once equilibrium had been reached at a given temperature of the second furnace, the conditions were kept constant during the aerosol collection and light scattering measurements. Several series of such experiments were carried out with the first furnace set at various temperatures. For each combination of furnace temperatures, the flow rate was varied during the course of a single experiment. This was possible because after a change of flow rate little time was required for equilibrium to be re-established.

Dilution of nuclei was accomplished by diverting a measured part of the nuclei into an exhaust (12a) and replenishing with the same amount of pure helium downstream from another gas cylinder. Thus, the same flow rate was maintained throughout the part of the generator containing NaCl, while varying the concentration of nuclei.

The flow rate was checked at several points of the assembly using Predictability flow meters. Table I shows the systematic manner in which the experimental conditions of the two furnace temperatures, the flow rate, and the concentration of the nuclei were varied.

Table I: Generator Conditions Used in the Preparation of NaCl Aerosols

First furnace temperature (t_1), °C.	Second furnace temperature (t_2), °C.	Flow rate, l./min.	Relative per cent nuclei
755	755	1.0	100, 75, 50, 25
		1.5	100
		2.0	100
755	775	1.0	100, 75, 50, 25
		1.5	100
		2.0	100
755	795	1.0	100, 75, 50, 25
		1.5	100
		2.0	100
775	755	1.0	100, 75, 50, 25
		1.5	100
		2.0	100
775	775	1.0	100, 75, 50, 25
		1.5	100
		2.0	100
775	795	1.0	100, 75, 50, 25
		1.5	100
		2.0	100
795	755	1.0	100, 75, 50, 25
		1.5	100
		2.0	100
795	775	1.0	100, 75, 50, 25
		1.5	100
		2.0	100
795	795	1.0	100, 75, 50, 25
		1.5	100
		2.0	100

Electron Microscopy. The particle size distribution and electron diffraction patterns of the aerosol samples were obtained with the aid of a Philips Model EM-75B electron microscope. This instrument has a resolution of 35 Å. The electron micrographs were projected for counting purposes and the size of several hundred particles was measured directly on the projection screen. Calibration was done with the aid of an electron micrograph of a carbon replica of a diffraction grating having 28,800 lines/in. Longer photographic exposures at low electron beam intensity were used in order to protect the particles from deformation in the electron beam.

Light Scattering Measurements. The light scattering measurements were carried out with a Brice-Phoenix

light scattering photometer 1000 Series, which was modified and adjusted as described previously.[26] The intensities of the vertically and horizontally polarized light were measured in a specially designed aerosol cell[17,21] at 5° intervals of θ, the angle between the directions of the incident and scattered beam, from 40 to 130°.

Computations. The polarization ratio, ρ, is the ratio of the intensity of the horizontally polarized component of the scattered light to that of the vertically polarized component. The theoretical intensity functions, i_1 and i_2, when multiplied by $\lambda^2/4\pi$, give the intensity of light scattered by a single spherical particle per unit solid angle at a particular angle of observation, θ. for a plane polarized incident beam of unit intensity whose electric vectors vibrate, respectively, perpendicularly and horizontally to the scattering plane. The calculation of the scattering functions for spherical particles[27] uses summations of Bessel functions with arguments (α) and $(m\alpha)$ where α is the usual dimensionless parameter given by

$$\alpha = \frac{2\pi a}{\lambda} \qquad (1)$$

The radius of the particle is a, λ is the wave length of light in the surrounding medium, and m is the relative refractive index of the particle compared to the medium. For a monochromatically illuminated region containing particles which scatter incoherently, the intensity of the two components of the light scattered at a particular angle, θ, is given by

$$I_1(\theta) = c\int i_1(\theta)f(\alpha)\mathrm{d}\alpha \qquad (2)$$

$$I_2(\theta) = c\int i_2(\theta)f(\alpha)\mathrm{d}\alpha \qquad (3)$$

and the polarization ratio for this angle, $\rho(\theta)$, is defined by

$$\rho(\theta) = I_2(\theta)/I_1(\theta) \qquad (4)$$

The polarization ratio method requires prior knowledge or an assumption of the form of the frequency distribution function, $f(\alpha)$. The distribution function which was assumed for these calculations was the logarithmically skewed distribution function used earlier.[20] The scattering functions were computed on the IBM 7090 digital computer for an array of the size distribution parameters $\bar{\alpha}$ and σ. The range covered was $\bar{\alpha}$ = 2.0 (0.1) 15.0 and σ 0.005 (0.005) 0.300. This was done for refractive index m = 1.51. Equations 2 and 3 were solved by numerical integration using intervals of 0.1 in α over a sufficiently broad range so that the integrand reached a limit. Here $\bar{\alpha}$ is the modal value of α for the logarithmic distribution and σ is related to the standard deviation. The computations were done for 5° intervals of θ from 40 to 130° and stored on punched cards. The final comparison between experimental data and theoretical calculations was carried out by an IBM 1620 digital computer as described earlier.[19,21]

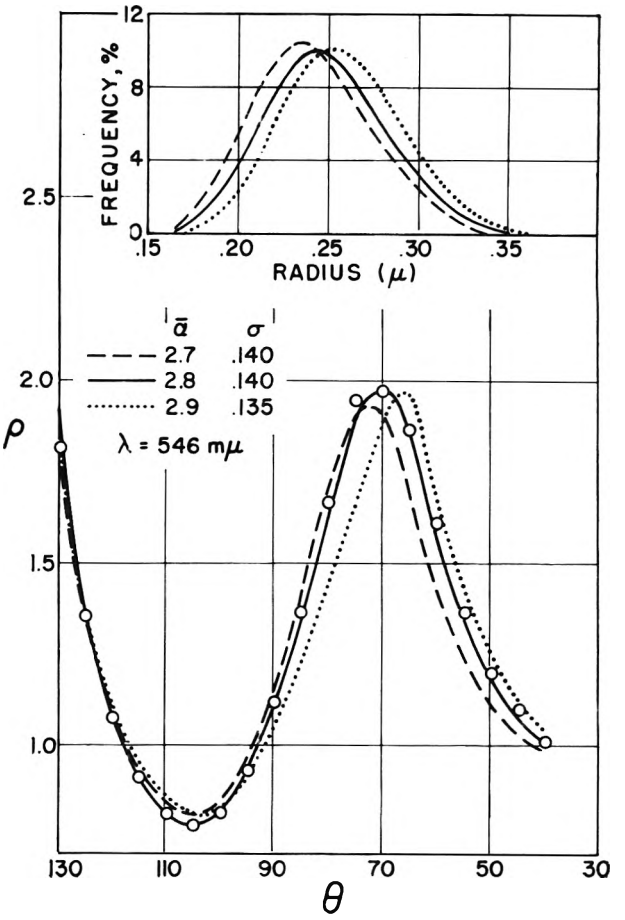

Figure 4. A comparison of experimental values (circles) of $\rho(\theta)$ with theoretical values (curves) corresponding to three sets of the size distribution parameters which best fit. Here the agreement is within 12% at each of the 19 angles θ = 40°(5°)130°. Each boiler furnace was at 775°, flow rate of 1.0 l./min., nucleated aerosol with 100% of nuclei used, and measurements taken with λ 546 mμ. Inset shows the corresponding frequency distribution curves.

An example of the comparison between the experimental values of ρ and the theoretical curves which agreed with it is shown in Fig. 4. For each of these theoretical curves, the agreement with the experimental data was within 12% at each of the 19 angles of observation. The corresponding size distribution curves

(26) M. Kerker and E. Matijević, *J. Opt. Soc. Am.*, **50**, 722 (1960).
(27) G. Mie, *Ann. Physik*, [4] **25**, 377 (1908).

are shown in the inset. There is little doubt that the distribution corresponds to $\bar{\alpha} = 2.8$ and $\sigma = 0.140$. The fact that the other two distributions, which are actually quite close to the one chosen, do not fit the experimental data as closely demonstrates the extreme sensitivity of this particular light scattering technique in elucidating the size distribution. The choice of the best fit was made on the basis of a minimum in the sum of the differences between the experimental and theoretical values and also a minimum in the sum of the squares of these differences.[21] This particular aerosol was produced by heterogeneous nucleation.

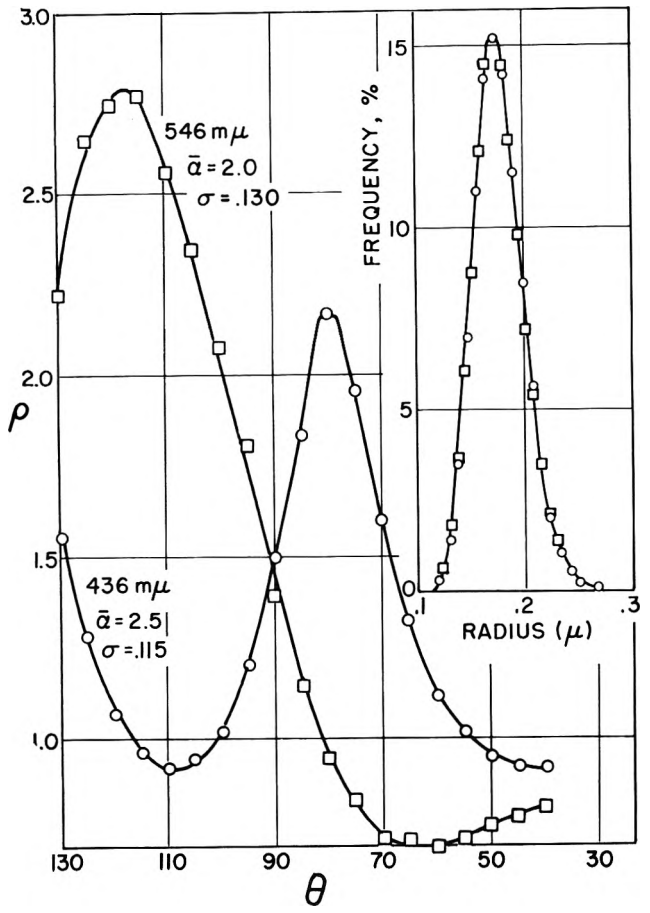

Figure 5. A comparison of experimental $\rho(\theta)$ *vs.* θ curves for the same aerosol measured at λ 546 mμ and λ 436 mμ. Both furnaces were at 775°, the flow rate was 1.0 l./min., and the NaF nuclei were not diluted. The inset shows the resulting frequency distributions obtained from each set of data. Circles (○) and squares (□) represent frequencies obtained from the blue and green light, respectively.

Since the size parameter α is dependent upon wave length, the values of $\bar{\alpha}$ should also change with the wave length of the light used in the measurements. Experiments were performed using two wave lengths: 436 mμ (blue) and 546 mμ (green). Figure 5 shows the experimental light scattering curves obtained on the same aerosol for these wave lengths and the calculated frequency distribution curves are presented in the inset. While the ρ–θ curves are considerably different, the calculated size distribution frequencies are in excellent agreement, again demonstrating the reliability of this method.

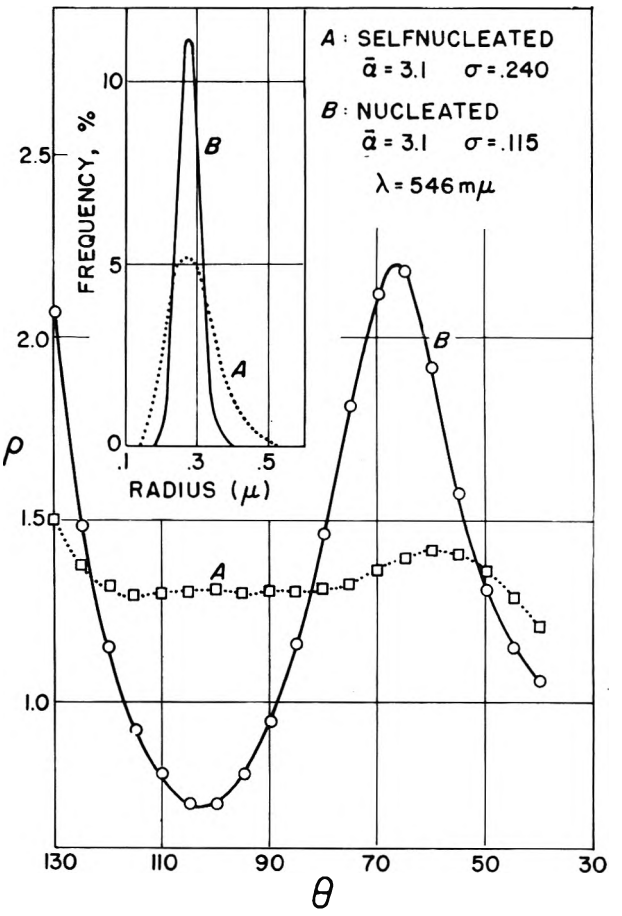

Figure 6. A comparison of $\rho(\theta)$ *vs.* θ and the corresponding frequency distributions for aerosols produced by self-nucleation and by heterogeneous nucleation. Self-nucleated aerosol (A): furnace at 835°, flow rate 1 l./min., wave length 546 mμ. Nucleated aerosol (B): furnace 3b, 775°, furnace 3c, 795°, flow rate 1.0 l./min., 100% of nuclei used, wave length 546 mμ.

Results

In general, aerosols produced by self-nucleation were of wider size distribution and showed less distinct higher order Tyndall spectra than aerosols of compa-

able average size that were produced by heterogeneous nucleation. Hence, the ρ *vs.* θ curves of these former aerosols showed less structure. An example of such a curve for a mean radius of 265 mμ is given in Fig. 6 (curve A). A typical ρ *vs.* θ curve for an aerosol of the same mean size which had been produced by heterogeneous nucleation is also shown in Fig. 6 (curve B). Even though the light scattering curves for the aerosol obtained by self-nucleation had very little structure, it was sufficiently characteristic to be analyzed by the polarization ratio method. The inset of Fig. 6 shows a comparison of the frequency distributions calculated from the light scattering curves for these aerosols of the same mean size produced by the two techniques.

A number of self-nucleated sols were prepared at various temperatures and at a constant flow rate of 1.0 l./min. These results are presented in Table II. Column three of Table II gives the $\bar{\alpha}$-values corresponding to the temperatures listed in column one and measured at the wave lengths given in column two. In column four all $\bar{\alpha}$-values were normalized to $\bar{\alpha}_{546}$ (*i.e.*, to $\bar{\alpha}$ at 546 mμ wave length) while the mean radii for the distributions are presented in column five, along with the averages of the mean radii obtained at each furnace temperature. These results show that with increasing temperature, the average particle size increases, similarly to what had been observed earlier with silver chloride aerosols.[17]

Table II: Size Distribution of Self-Nucleated Aerosols[a]

Furnace temp., °C.	Wavelength of measurements, mμ	Calculated size parameter, $\bar{\alpha}$	Normalized size parameter, $\bar{\alpha}_{546}$	Mean radius, mμ
835	546	3.1	3.1	269
	436	3.5	2.8	244
	436	4.0	3.2	278
	546	3.2	3.2	278
		Average = 267 ± 12 mμ		
850	436	4.5	3.6	313
875	546	5.0	5.0	436
	436	7.0	5.6	487
	436	6.5	5.2	452
		Average = 458 ± 19 mμ		
900	546	6.5	6.5	566
	436	8.5	6.8	592
	436	9.0	7.2	626
		Average = 595 ± 21 mμ		

[a] Flow rate of 1.0 l./min.

Aerosols produced by heterogeneous nucleation were of much narrower size distribution and exhibited brilliant higher order Tyndall spectra. These could be prepared quite reproducibly. The reproducibility is demonstrated in Table III which gives the results for several cases. Each run represents an independent experiment performed on a different day. In some cases (runs 1,2,3), several determinations of the size distribution were made in the course of a day's run. Both the stability of the output of the generator during a particular day and the reproducibility of its output on different days when operated under identical conditions

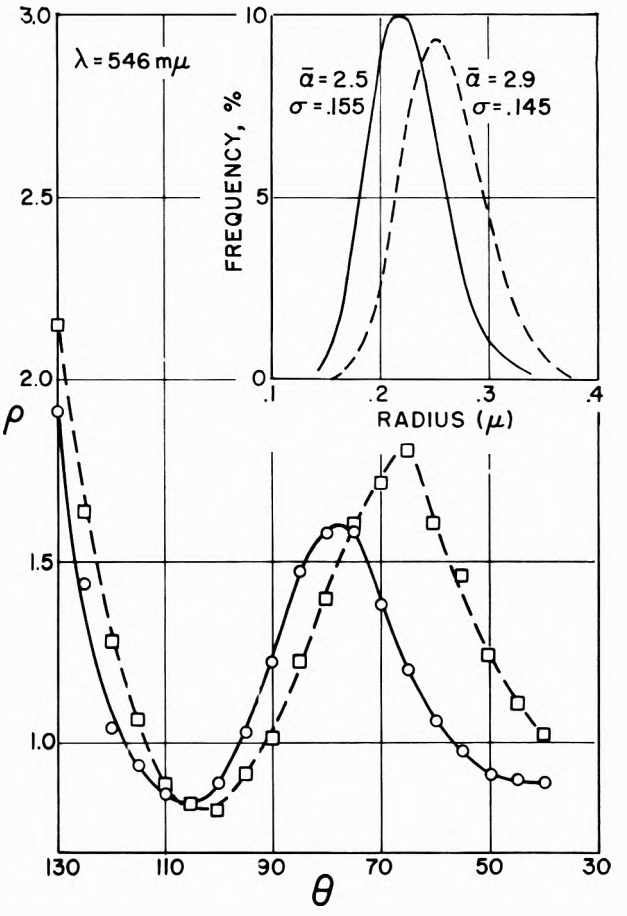

Figure 7. Comparison of the reproducibility of $\rho(\theta)$ *vs.* θ curves for aerosols prepared by heterogeneous nucleation. The two most divergent sets of data from a total of 13 experiments. Both furnaces at 775°, flow rate 1.0 l./min., 100% of nuclei. Light scattering data for 546 mμ wave length. Insert shows the corresponding frequency distributions.

are remarkable. The extreme limits of the ρ *vs.* θ curves for the first six runs and the two associated size distribution curves are shown in Fig. 7.

Results obtained when the generator furnace temperature was systematically changed (according to

Table III: Size Distribution of Nucleated Aerosols of NaCl[a]

Run no.	First furnace temp., °C.	Second furnace temp., °C.	Flow rate, l./min.	Relative per cent nuclei	$\bar{\alpha}_{546}$	σ_{546}	Mean radius, mμ
1	775	775	1.0	100	2.6	0.125	226
					2.6	.125	226
					2.6	.130	226
					2.7	.145	235
2	775	775	1.0	100	2.7	.150	235
					2.7	.140	235
					2.8	.140	243
3	775	775	1.0	100	2.7	.130	235
					2.7	.120	235
					2.7	.120	235
4	775	775	1.0	100	2.9	.145	252
5	775	775	1.0	100	2.5	.155	218
6	775	775	1.0	100	2.7	.110	235
				Average	2.68 ± 0.07	0.133 ± 0.012	233 ± 6 mμ
7	755	755	1.0	100	2.0	0.125	174
					2.0	.130	174
8	755	755	1.0	75	2.0	.125	174
					1.9	.140	165
9	755	755	1.0	50	2.9	.090	252
					2.7	.090	235
10	755	755	1.5	100	2.1	.100	183
					2.0	.120	174
11	755	775	1.5	100	2.4	.085	209
					2.3	.110	200
12	755	775	2.0	100	1.9	.115	165
					2.0	.110	174

[a] Measurements taken at 546 mμ wave length.

Table I) are presented in Fig. 8 and 9. Each curve in Fig. 8 represents the change of the average particle size if the flow rate and the temperature of the second furnace (t_2) were kept constant while varying the temperature of the first generator furnace (t_1). Different curves are shown for different flow rates and different temperatures of the second furnace. Thus, these curves give the relative influence of the first furnace upon the particle size of the NaCl aerosol. The average particle size does not vary much with increasing t_1 although the trend is toward larger sizes. For constant t_1 and t_2 the particle size becomes smaller with increasing flow rates in agreement with observations by others.[13] A similar effect of flow rate was found with liquid aerosols of octanoic acid.[21] Figure 9 is a similar plot which depicts the influence of the temperature change of the second generator furnace upon the mean particle diameter of the aerosol. In this case there is a marked increase in average particle size with temperature.

Experiments were also carried out under identical conditions of temperature and flow rate but with various relative nuclei concentrations of from 100–25% of the original concentration of nuclei. Dilution of nuclei produced much larger particles for a given set of generator conditions. This results in a more complex light scattering pattern. Examples of this change in light scattering curves are shown in Fig. 10 for 25, 50, and 100% of relative nuclei concentration. The inset of Fig. 10 shows the change in frequency distributions as a consequence of the nuclei dilution. Both generator furnaces were at 775° and flow rate 1.0 l./min.

This effect of the dilution of the nuclei was investigated over a range of generator conditions and the same

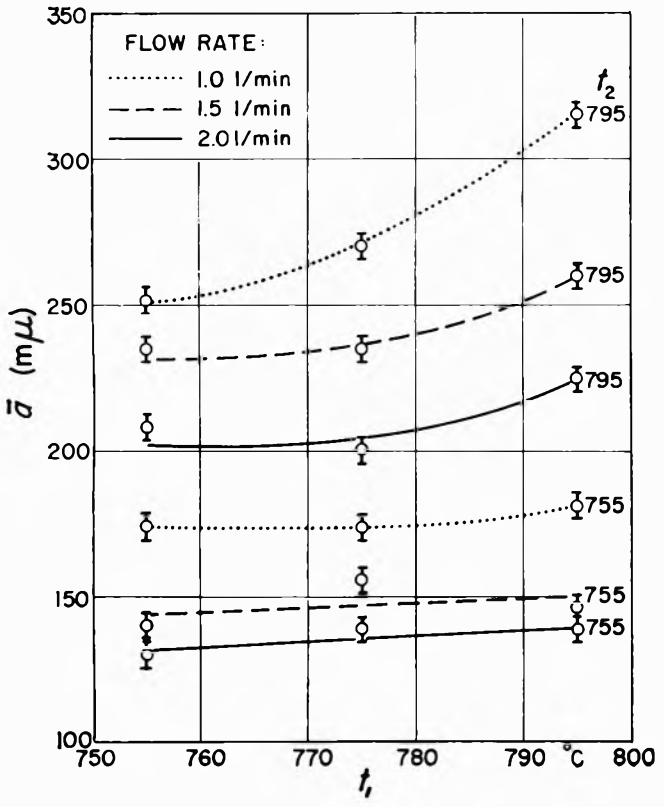

Figure 8. Effect of the temperature of the first furnace, t_1, upon the average radius at fixed values of the temperature of the second furnace, t_2, and of the flow rate. The NaF nuclei were undiluted in all cases.

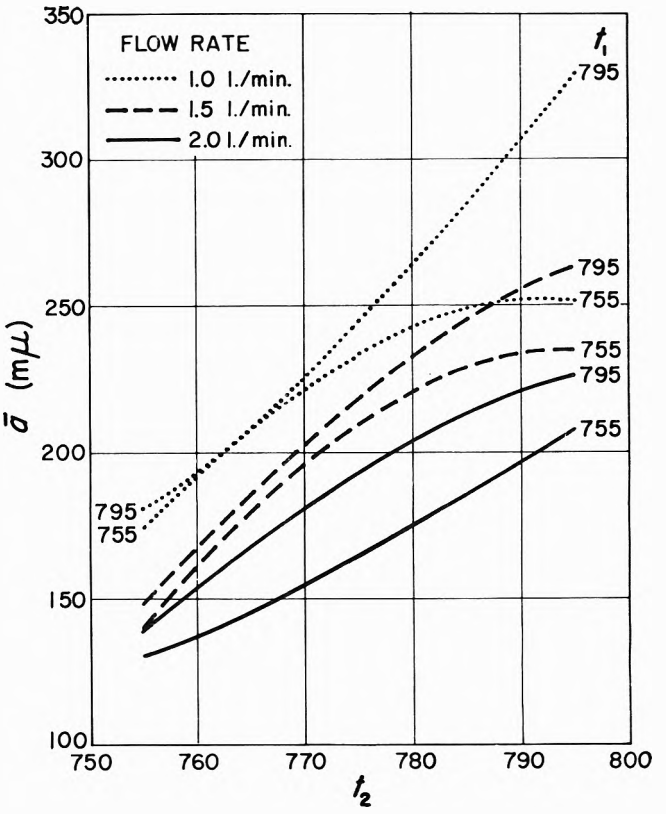

Figure 9. Effect of the temperature of the second furnace, t_2, upon the average radius at fixed values of the temperature of the first furnace, t_1, and of the flow rate. The NaF nuclei were undiluted in all cases.

general trend observed. Figure 11 gives a summary of the results. The estimated error associated with the determination of the mean size from light scattering (0.1α) is also shown.

Discussion

The fact that NaCl aerosols produced by this method are mainly amorphous was quite unexpected. This must be a result of the formation of the aerosols by the very rapid quenching of the NaCl vapor in the stream of dry carrier gas.

Since the particles are apparently "amorphous" NaCl, this leads to a question as to the proper refractive index (m) to use in calculating the theoretical light scattering functions. Actually, the light scattering functions appear to be less sensitive to the refractive index than to the size parameter, $\bar{\alpha}$. This was shown to be the case for sulfur sols for which small relative differences in refractive index (± 0.01) did not affect the polarization ratio markedly.[19] By the same token one would also expect that if the ρ–θ curves were extremely sensitive to m, there would be a variation in the frequency distributions calculated from light scattering data taken at different wave lengths because of the dispersion of m. This has not proven to be the case in these studies. Indeed there was excellent agreement between the frequency distributions calculated with wave lengths of 436 and 546 mμ (Fig. 5) for which the dispersion of m with wave length has been neglected.

The refractive indices of crystalline NaCl for 436 and 546 mμ wave lengths are 1.55 and 1.56, respectively. In order to assume an approximate value of m for the "amorphous" material of which the spherical particles are composed, an extrapolation of the density of liquid NaCl was made to 25° and used in the Gladstone–Dale[28] formula for the variation of m with density. On this basis an approximate value of 1.51 was assigned to m. That this choice is sufficiently accurate for this work is confirmed in the agreement between the theoretical and experimental ρ *vs.* θ curves and also in the agreement between frequency distribu-

(28) "The Microscopic Determination of the Nonopaque Minerals," 2nd Ed., U. S Geological Survey Bulletin 848, Washington, D. C., 1934.

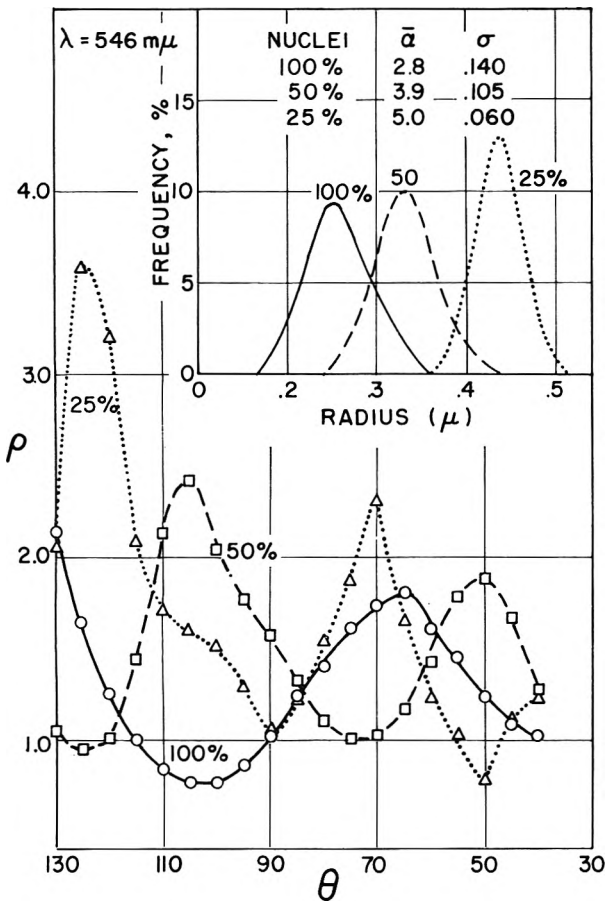

Figure 10. The effect of the nuclei concentration upon the light scattering and size distribution of sodium chloride aerosols. $t_1 = t_2 = 775°$; flow rate, 1.0 l./min.; wave length, 546 mμ.

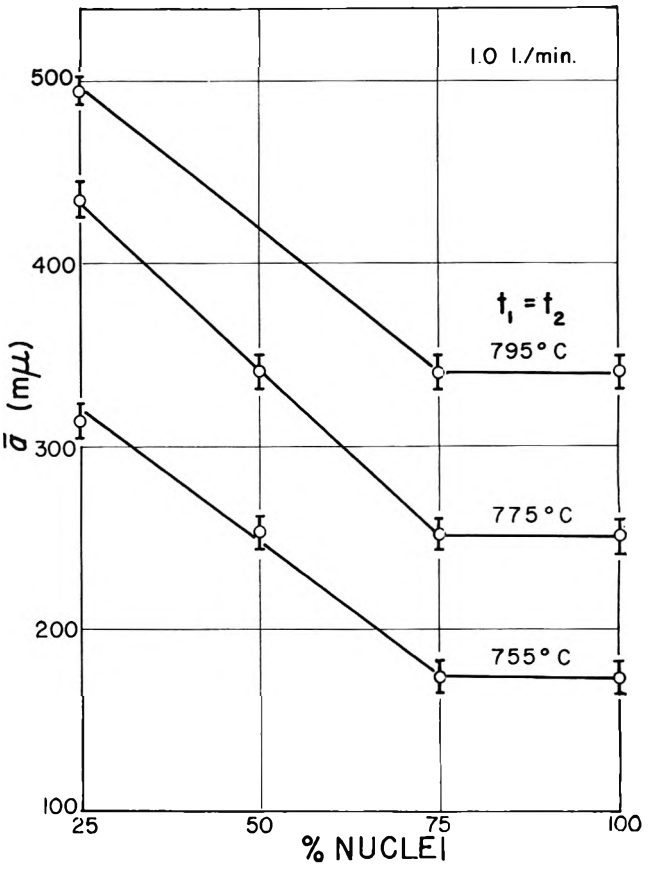

Figure 11. Change in average radius of sodium chloride aerosol particles as a function of nuclei concentration for varying furnace temperatures. Flow rate, 1.0 l./min.

tions from the light scattering data and the electron microscope histograms. As an example, a frequency distribution obtained by light scattering is shown in Fig. 12 along with the corresponding frequency histogram determined by electron microscopy (solid lines). This particular aerosol is the one shown in Fig. 2. There is approximately a 12% difference between the mode of the two distributions, but this is within the step width of the histogram or within the error associated with the electron microscopy. Such differences between electron microscopy and light scattering have been observed by others[29,30] and reflect the systematic error frequently obtained in electron microscope measurements. In order to show the excellent agreement between the shapes of the frequency distribution and the histogram, the former has been shifted until the modal diameters coincide (dotted line in Fig. 12).

For aerosols of narrow size distribution (unlike those which exhibit the bimodal character of the type shown in Fig. 3), one can assume that all of the aerosols production takes place by condensation upon the existing nuclei. The mass of vapor available for condensation depends upon the concentration of NaCl vapor in the helium stream. The aerosol size increases by increasing the temperature of the furnace as one would expect from vapor pressure considerations but not in a manner that can easily be predicted upon theoretical grounds. Craig and McIntosh[14] have shown by a mass balance for a similar generator that 20% of the NaCl evaporated is lost to the walls of the combustion tube. Two such generators in series make any rigorous theoretical treatment very difficult.

One might expect that many materials might serve as a source of nuclei in the production of aerosols by this technique. The exact nature of the NaF nuclei used here is not known. Most probably they are small solid embryos upon which the NaCl vapor can condense.[31] The helium entering the first furnace is at

(29) W. Heller and M. L. Wallach, *J. Phys. Chem.*, 67, 2577 (1963).
(30) G. Deželić and J. P. Kratohvil, *J. Colloid Sci.*, 16, 561 (1961).

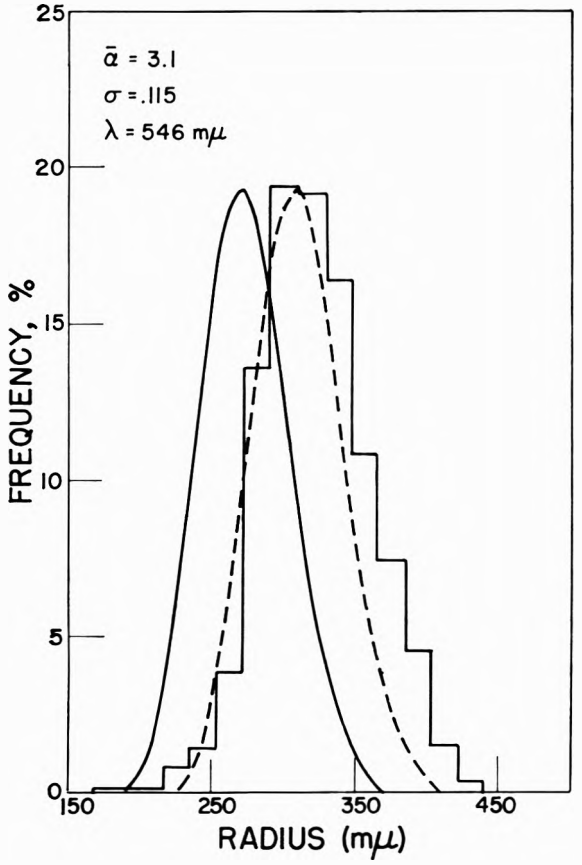

Figure 12. Comparison of particle size distributions obtained by light scattering and electron microscopy. First furnace temperature (3b) 775°, second (3c) 795°, flow rate 1.0 l./min., 100% of nuclei, wave length 546 mμ. Electron microscope histogram, 860 particles total count.

room temperature. As it passes over the boat containing the NaF the temperature of the helium is probably less than the temperatures of the boat or of the combustion tube wall. It is quite reasonable to expect that small particulate NaF nuclei form by sublimation from the boat and condensation in the cooler helium stream.

Although two furnaces containing NaCl were essential in order to produce aerosols of narrow size distribution reproducibly, introduction of still a third furnace in the series did not further improve the reproducibility nor provide an aerosol of still narrower size distribution. Since the average particle size of the final aerosol is considerably larger when two NaCl furnaces are employed as compared to aerosols produced using only one NaCl furnace at the same temperature, it is apparent that the aerosol grows in steps, particles produced in the first furnace growing further in the vapor of the second furnace.

As the flow rate of carrier gas is increased for a constant set of generator temperatures the particle size decreases. The ultimate particle size is determined by the number of nuclei, the NaCl vapor concentration, and the relative amount of NaCl lost by condensation to the walls. With a higher flow rate, it does seem reasonable that the vapor concentration of NaCl would be further removed from the equilibrium vapor pressure and that this lower value would give smaller particles. The number of NaF nuclei would not be affected to the same extent since its vapor pressure is so low that equilibrium may be established very rapidly.

As the number of nuclei is diluted under identical temperature and flow rate conditions, the average size increases. A given set of generator conditions should produce a constant mass or volume of vapor to condense upon these nuclei. If one neglects the loss of nuclei after dilution to the tube walls or by coagulation, one would then expect the average particle size to be inversely proportional to the cube root of the relative nuclei concentration. Table IV shows that

Table IV: Dependence of Aerosol Size upon Relative Nuclei Concentration at Various Temperatures[a]

Relative number of nuclei, N	755° Radius R, mμ	755° $R \times N^{1/3}$	775° Radius R, mμ	775° $R \times N^{1/3}$	795° Radius R, mμ	795° $R \times N^{1/3}$
1.00	174	174	252	252	340	340
0.75	174	158	252	229	340	308
0.50	252	200	340	270	...	...
0.25	312	196	433	273	496	313
Average		182 ± 9%		255 ± 7%		320 ± 4%

[a] Nucleated aerosols, 1.0 l./min. flow rate, $t_1 = t_2$, measurement taken at 546 mμ wave length.

the product of the modal radius times the cube root of the relative nuclei number is a constant within the experimental error of these experiments.[32]

Acknowledgment. We are greatly indebted to Mr. Charles Querfeld of the U. S. Army Electronics Re-

(31) V. A. Gordieyeff, *Arch. Ind. Health*, **14**, 471 (1956).

(32) NOTE ADDED IN PROOF.—It has come to our attention that the distribution function used in this and in our earlier work is not the usual logarithmic normal distribution but a new distribution function

$$p(\alpha) = [1/\sqrt{2\pi}\sigma_{L\alpha M}\rho^{\sigma_L^2/2}]e^{-(\ln \alpha - \ln \alpha_M)^2/2\sigma_L^2}$$

This distribution and its properties will be discussed by the present authors in a paper now in press in *J. Phys. Chem.*

search and Development Activity, White Sands, New Mexico, who arranged for the computations on the IBM 7090. We also wish to thank the Socony Mobil Oil Company, Inc., for a fellowship to W. F. E.

Discussion

J. H. de Boer (The Hague, Netherlands). You may well be congratulated on these beautiful results. May I ask whether you know what percentage of sodium fluoride is contained in the sodium chloride particles? Could the amount of sodium fluoride be large enough to be responsible for preventing crystallization?

M. Kerker. The percentage of NaF in the aerosol particles must be very small indeed. We have established that the NaF nuclei are considerably smaller than 35 Å. in diameter since this is the resolving power of our electron microscope. Accordingly, the NaF must comprise less than about 10^{-6} parts by volume. Furthermore, since the aerosols formed in the absence of nuclei were also amorphous, these traces of NaF could not account for the prevention of crystallinity.

R. J. Good (University of New York, Buffalo). Do you have any estimate of the maximum size of microcrystallite that might exist in these amorphous solids and yet escape detection by your electron diffraction studies?

M. Kerker. This information could not be obtained from our experiments.

J. W. E. Coenens (Unilever, Holland). Would it be difficult to prepare a quantity of, say, 500 mg. of these materials? Such materials might be ideal for dispersing metals to be used in infrared studies of adsorbed species on metal surfaces, provided they can be obtained in sufficient quantities.

M. Kerker. The total amount of material that can be prepared would depend on a combination of scaling up the equipment and the length of time one is willing to collect. With the present equipment for which the flow rate is 1 l./min. and the particle concentration about 10^4 to 10^5 particles/ml., it would take about 1 month to collect 0.5 g. of material.

M. T. Coltharp (University of Texas). Would you care to speculate on why the sodium fluoride leads to aerosol particles of uniform size whereas the self-nucleated aerosols have a much larger distribution of sizes?

M. Kerker. This is a typical result which has been generally experienced ever since Sinclair and La Mer developed the technique for generating monodisperse aerosols. In the presence of foreign nuclei, the vapor is condensed uniformly provided the rate of cooling is not too great. Otherwise, a degree of supersaturation is built up with subsequent homogeneous nucleation. In this case the supersaturation may be so high that it cannot be relieved entirely by growth to the existing nuclei, and as cooling proceeds there is fresh nucleation leading to a broad distribution in the final size spectrum.

A. W. Czanderna (Union Carbide, Charleston). Do you have information on the ratio of the density of your amorphous materials to the density of the crystalline solid?

M. Kerker. The ratio of the density of amorphous to crystalline NaCl used was 0.93. It should be emphasized that this was obtained by an extrapolation of the density of liquid NaCl as tabulated in the "International Critical Tables." However, as pointed out in the paper, the resulting uncertainty in the refractive index does not influence the light scattering analysis.

Corrections of Schlieren Data. I. Geometrical Effects of Light Bending and Refraction

by T. Foster Ford

U. S. Naval Research Laboratory, Washington, D. C. 20390

and Edwin F. Ford

2603 N. VanDorn Street, Alexandria, Virginia *(Received February 26, 1964)*

The bending of light in an ultracentrifuge or electrophoresis cell, combined with its refraction on passing through the second cell wall, results in tilting of schlieren patterns and consequent displacements of plots of the center line position against time. The displacement is small but well outside errors of measurement. Sedimentation coefficients and lag times, the time delay in separation of schlieren peaks from the meniscus, are affected. A geometrical optical analysis is presented for the two-collimating lens system used in the Spinco ultracentrifuge. Cell thickness is found to be an important factor in determining the schlieren center line displacement. When thick cells are used, the bending-refraction effect by itself might cause schlieren center lines to appear to separate from the meniscus even before centrifugation started. There is no effect on diffusion coefficients. The indicated corrections should not be used without also applying the equivalent level correction resulting from curvature of the light path in cells of finite thickness.

Introduction

Ultracentrifugal sedimentation velocity studies on barium dinonylnaphthalenesulfonate, with a micellar weight in benzene of about 8500,[1] developed special problems in the interpretation of schlieren patterns because the diffusion rate is large as compared with the sedimentation rate. The data, analyzed in the usual way, showed a distinct lag time in the separation of schlieren peaks from the meniscus. These lag times agreed well with theoretical lag times calculated by a formula given by Fujita and MacCosham.[2] However, Svensson has pointed out[3] that since the path of light entering a liquid column normal to a refractive index gradient is curved, an additional correction of the position of the sedimentation peak is required, and his estimate indicates a reduction of the observed lag time to the extent of 20% in our case.

It was, therefore, concluded that the Svensson curvature correction must be reviewed. If it were found valid, a search should be made for compensating errors. The review of the curvature correction is presented in part II of this report. The compensating error was found to be introduced by geometrical effects of light bending in the liquid plus further deviations due to refraction of the deflected light as it passes through the second cell wall. For the particular barium dinonylnaphthalenesulfonate data which prompted this study, the effect is opposite in sign and nearly equal in magnitude to that introduced by curvature.

Results

Qualitative Effects of Bending and Refraction. Figure 1 is a dimensionally distorted diagram of that part of the Spinco optical system between the cell and the plate, with the cylindrical lens omitted. It shows

(1) T. F. Ford, S. Kaufman, and O. D. Nichols, "Ultracentrifugal Studies of Barium Dinonylnaphthalenesulfonate–Benzene Systems. I. Sedimentation Velocity," presented at the Kendall Award Symposium, 147th National Meeting of the American Chemical Society, Philadelphia, Pa., April, 1964.

(2) (a) H. Fujita and V. J. MacCosham, *J. Chem. Phys.*, **30**, 291 (1959); (b) H. Fujita, "Mathematical Theory of Sedimentation Analysis," Academic Press, New York, N. Y., 1959, p. 87.

(3) H. Svensson, *Kolloid-Z.*, **90**, 141 (1940).

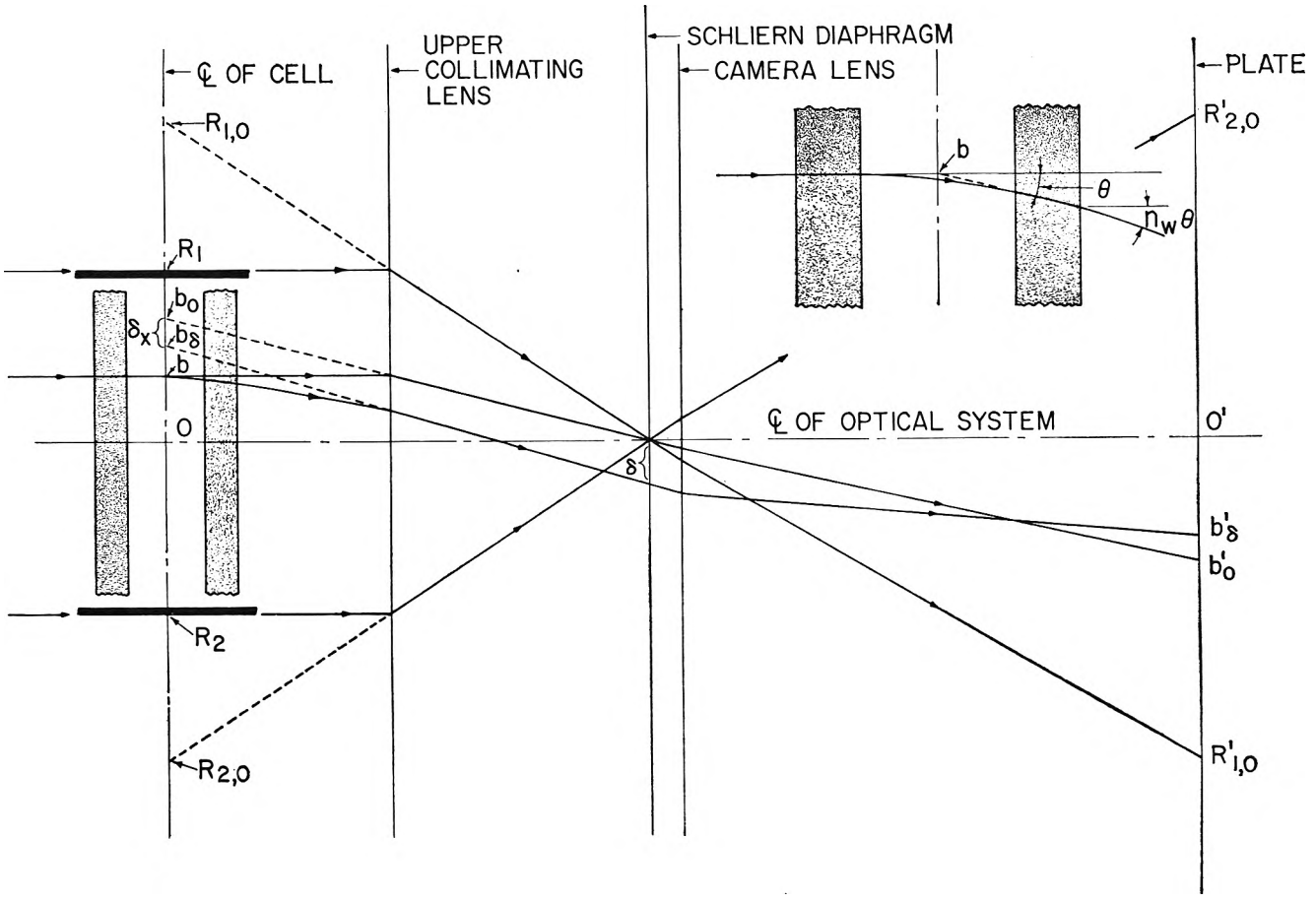

Figure 1. The principal part of the two-collimating lens schlieren optical system, omitting the cylindrical lens. The inserted diagram is a detail showing the path of a refractive index gradient-deflected ray through the cell only.

the paths of four rays. Two of these just graze the holes in the cell counterbalance and produce the upper and lower vacuum reference lines on the plate. These rays intersect the cell centerline at the points R_1 and R_2. One of the other two rays passes through the cell without any bending and intersects the cell center line at the point b; the last ray is bent in its passage through the cell, as would occur if a refractive index gradient were present.

We consider first the two reference rays and the one undeflected ray through the cell. The camera is focused on the cell center line, as is usual practice, and it records the virtual levels $R_{1,0}$, $R_{2,0}$, and b_0 for these rays. The respective image levels are $R'_{1,0}$, $R'_{2,0}$, and b'_0. The image distances between these camera-recorded points and the optical center line are $O'-R'_{1,0}$, $O'-R'_{2,0}$, and $O'-b'_0$, respectively. From similar triangles it is seen that these distances are in proportion to the real distances, $O-R_1$, $O-R_2$, and O–b (*cf.* Svensson, ref. 3). Therefore, if there were no bending, all levels in the cell would be proportionally recorded and would be correctly calculated using a proper magnification factor.

We now consider the ray which is bent. Reference must be made to the inserted diagram of Fig. 1, which shows the light path for this ray through the cell only. Here, for simplicity, the refractive index of the liquid is presumed to be equal to the refractive index of the material of the cell wall, n_w, as is nearly the case when the cell liquid is benzene. Thus, in this case, the only bending due to refraction occurs as the ray exits the cell wall, and the deflection inside the cell wall is equal to the deflection of the ray on exiting the liquid. To a first approximation, the path of the ray through the liquid is a parabola.[4] Therefore, the backward extension of the exit tangent intersects the center line of the cell on the entry level, or at b. Referring now again to the main figure, it is seen that in consequence of the total deflection of this ray the

(4) O. Lamm, *Nova Acta Reg. Soc. Sci. Upsaliensis*, 4, 10 (1937); T. Svedberg and K. O. Pedersen, "The Ultracentrifuge," The Clarendon Press, Oxford, 1940, p. 257 ff.

camera records the image position b'_δ, therefore the virtual position b_δ. The difference between b'_0 and b'_δ is the camera-recorded displacement of the entry level due to bending and refraction, and b_0–b_δ is the absolute virtual displacement.

Figure 1 was drawn by geometrical construction. Other, similar constructions drawn to scale show that the displacement may vary greatly with cell thickness. For thick cells it is reversed, so that b_δ appears to be above b_0 rather than below it.

Formulation. The correction for errors due to bending and to refraction can be formulated quantitatively. We refer to Fig. 2 and also to Fig. 3, which is an enlarged detail of Fig. 2. In these figures:

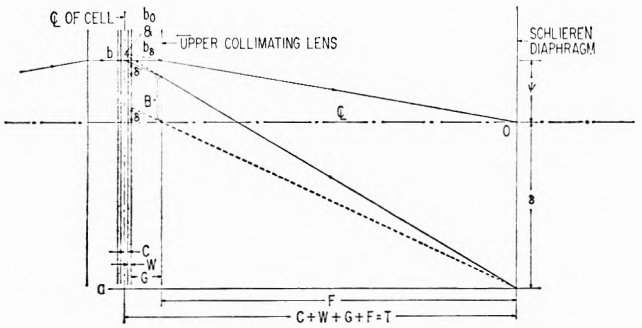

Figure 2. Diagram illustrating the bending and refraction correction for deflected rays.

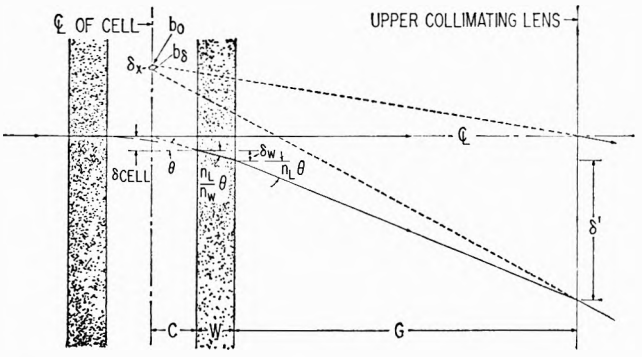

Figure 3. Detail of Fig. 2. Here δ_x is the bending and refraction correction.

ψ is the vertical distance between the entrance plane of a particular light ray, or sheet, and the center line of the optical system; δ is the observed vertical deviation of the light sheet at the schlieren diaphragm; δ' is the deviation of the light sheet between the camera side of the cell wall and the principal plane of the upper collimating lens; δ_w is the deviation of the light sheet in the cell wall; δ_{cell} is the deviation of the light sheet in the cell; F is the focal length of the upper collimating lens, *i.e.*, the optical lever arm; G is the distance from the cell wall, on the camera side, to the principal plane of the upper collimating lens; W is the thickness of the cell wall; and $C = {}^1/_2$ of the inside thickness of the cell.

We also introduce the term δ_x to designate the required refraction correction of x, in centrifuges, the distance from the center of rotation. We designate the refractive index of the liquid by n_1 and the refractive index of the material composing the cell walls by n_w.

We now note

$$\delta' = \frac{G}{F}\delta \tag{1}$$

$$\delta_w = \frac{W}{F}\delta\frac{1}{n_w} \tag{2}$$

$$\delta_{cell} = \frac{C}{F}\delta\frac{1}{n_L} \tag{3}$$

$$B = \psi - \delta' - \delta_w - \delta_{cell} \tag{4}$$

$$ab_0 = \delta + \psi\frac{T}{F};\quad ab_\delta = (\delta + B)\frac{T}{F}$$

where

$$T = C + W + G + F \tag{5}$$

Therefore

$$\delta_x = ab_0 - ab_\delta$$

$$= \delta + \psi\frac{T}{F} - \delta\frac{T}{F} - B\frac{T}{F} \tag{6}$$

Substituting (4) for B in (6), and remembering that $T = C + W + G + F$, we find

$$\delta_x = \delta - \delta\left(1 - \frac{G}{F} - \frac{W}{F}\frac{1}{n_w} - \frac{C}{F}\frac{1}{n_L}\right)\frac{T}{F} \tag{7}$$

It is seen from eq. 7 that (1) δ_x is positive when the combination of terms on the right is less than δ. In this case the cell level in question appears to the camera to be too far from the meniscus, or from the center of rotation. The quantity δ_x is therefore to be *subtracted* from the apparent x-value as recorded by the camera-schlieren lens system: (2) δ_x increases as the ratio T/F is increased.

We consider δ to be that portion of the total deviation due to the concentration gradient in the cell. In the absence of density gradients, preformed gradients, and cell distortion, as in electrophoresis, δ is the total deviation. In the ultracentrifuge it is that deviation given by the heights of schlieren ordinates above the

base line. The absolute value of this deviation may be calculated from the heights of the ordinates, the tracing/plate magnification factor, the cylindrical lens magnification factor, and the bar angle. In the Spinco optical system the maximum possible deviation giving complete resolution of patterns is set by obstacles in the light path, *e.g.*, the wire clips on the mirror mounting, and it may therefore be calculated from measurements on the apparatus with some accuracy. On a schlieren pattern maximum deviation is indicated by the appearance of a Toepler schlieren center line due to the extreme light sheets hitting the obstruction responsible. This maximum resolvable peak height once determined and the corresponding maximum deviation at the schlieren diaphragm, δ, known, deviations at other points on the pattern or on other patterns may be calculated by proportion, taking proper account of bar angles.

Numerical Calculations. Equation 7 is cumbersome because of the many symbols. It is better to make the calculations by steps. The following example, for a water system, is offered.

The dimensions to be used are those for our apparatus. A 1.2-cm. cell is assumed. The refractive index of the fused quartz walls is taken to be 1.467 for $\lambda = 0.434\ \mu$ at 25°; the refractive index of the solution, 1.34. We use the dimensions: $^1/_2$ of the cell thickness (C), 0.600 cm.; wall thickness (W), 0.500 cm.; wall to collimating lens (G), 4.531 cm.; optical arm (F), 48.504 cm. These dimensions give a total of 64.135 cm.

Referring directly to Fig. 2 and 3, without returning to the equations just derived, and using the preceding values, we find: $\delta' = 0.077458$; $\delta_w = 0.0058268$; $\delta_{cell} = 0.0076548$; $B = \psi - 0.090938$; $ab_0 = \delta + 1.09625\psi$; and $ab_\delta = (\delta + B)(1.09625)$; whence $\delta_x = ab_0 - ab_\delta = 0.00343\delta$; and $\delta_x/\delta_{cell} = 0.448$.

For our apparatus, the maximum total deviation at the schlieren diaphragm before appearance of a center line, as calculated from tracings using the cylindrical lens magnification factor, is about 1.80 cm. Actual measurements give about the same value. Of this 1.80 cm., 1.43 cm. is above the base line (at 59,780 r.p.m.). If we use this value, 1.43 cm., for δ we obtain: $\delta_{cell} = (0.007654)(1.43) = 0.01094$ cm.; and $\delta_x = (0.00343)(1.43) = 0.00490$ cm.

This absolute value for δ_x, the displacement of the camera-recorded x-value due to refraction, is about five times the possible precision of measurements. Actually, schlieren patterns are resolvable at deviations as much as 20% greater than that used above, and schlieren center lines may be found, by bisecting the Toepler schlieren line, at deviations as much as 100% greater. For such unresolved patterns the peak heights and therefore the deviations may be found by extrapolation of plots of the resolved peak heights against $1/\sqrt{\text{elapsed time}}$. Thus it is possible to calculate δ_x for such unresolved patterns. For these, then, we would find for the dimensions cited, $\delta_{cell} = 0.02188$ cm., and $\delta_x = 0.00980$ cm.

These values were calculated from actual data obtained on a bovine serum albumin solution, 1.22%, 59,780 r.p.m., at 25°. The pattern giving $\delta_x = 0.00980$ cm. was obtained 10.6 min. after starting the rotor; the pattern giving $\delta_x = 0.00490$ cm., was obtained 50 min. after starting the rotor. Resolvable patterns were obtained at intervals up to 154 min. after starting the rotor.

Correlations with Cell Thickness. Calculations such as those outlined above were made for all the cell thicknesses commonly employed in the Spinco ultracentrifuge, and also for an infinitely thin cell and for a cell completely filling the space between the collimating lenses. The other dimensions used were those given in the preceding section. These calculations were made for both benzene and water solutions. The refractive index of benzene is 1.5200, for $\lambda = 0.434\ \mu$, at 25°,[5] but to simplify the calculations it was assumed to be the same as that for quartz.

The values for $\delta_{x,\,max}$ and δ_x/δ_{cell} are plotted against cell thickness up to 4 cm. in Fig. 4. (For the hypothetical cell filling the space between the collimating, lenses, 10.26 cm., $\delta_x/\delta_{cell} = -0.407$ for benzene and -0.277 for water, and the δ_x-values are -0.0347 cm. and -0.0258 cm., respectively.) In the calculations of δ_x,

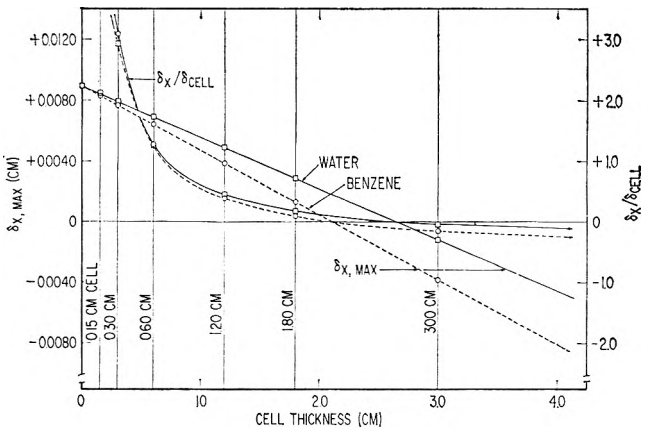

Figure 4. The variation of δ_x, and of the ratio of δ_x to the cell deviation, δ_{cell}, with cell thickness, for water and benzene systems.

(5) D. E. Gray, Coordinating Editor, "American Institute of Physics Handbook," McGraw-Hill Book Co., Inc., New York, N. Y., 1957, pp. 6-18.

the deviation at the schlieren diaphragm was assumed to be 1.43 cm. which, as noted above, is not the absolute maximum usable deviation.

Distortion of Gaussian Patterns. Figure 5 is a representation of the nature of the distortion of gaussian patterns due to light bending and refraction alone. The data for drawing this figure were obtained in the following manner.

We have chosen to use the 1.5-mm., 1.20-cm., and the hypothetical (10.26-cm.) cell, for which the maximum δ_x-values for completely resolvable patterns, for water solutions, are, respectively, +0.00846, +0.00490, and −0.02584 cm. We assume that the actual dc/dx *vs.* x distribution in the cell is gaussian. On the gaussian scale,[6] the peak of the curve is at 1.12838. At gaussian χ-values to the left and right of the center line of a gaussian curve the corresponding dc/dx, or H', values are given in tables of the error function.[7] For successive gaussian χ-values, we can, therefore, calculate the ordinate, H', as a fraction of the maximum peak height. The δ_x-values will be proportional to these fractions. It remains to convert these δ_x-values to the gaussian χ-scale. For this we take our particular experimental bovine serum albumin pattern for which, in a 1.20-cm. cell, δ_x = 0.00490 cm. For this pattern the actual distance between the two sides, $2u$, at the inflection level is 0.09035 cm. in absolute units, and it is 1.4142 on the gaussian χ-scale. Therefore, our δ_x-values, proportionated to the ordinates, must be multiplied by the factor 1.4142/0.09035, or 15.65. For any other cell thickness the factor is the same, because the width of the actual gaussian distribution in the cell is the same. The gaussian δ_x-values calculated in this way for several levels were algebraically added to the gaussian χ-values for the same levels, thus obtaining the patterns shown in Fig. 5. The theoretical gaussian curve is included for reference. These distorted patterns are those that would be recorded by the camera if the real distribution in the cell were gaussian, and if the refraction correction were the only correction to be considered. It is seen (Fig. 5) that the patterns for the 1.5-mm. cell and the 1.20-cm. cell are tilted to the right, and that the pattern for the hypothetical 10.26-cm. is tilted to the left. For an infinitely thin cell, the pattern is tilted farther to the right than for the 1.5-mm. cell in the ratio 0.00896/0.00846, or 1.06 (*cf.* Fig. 4).

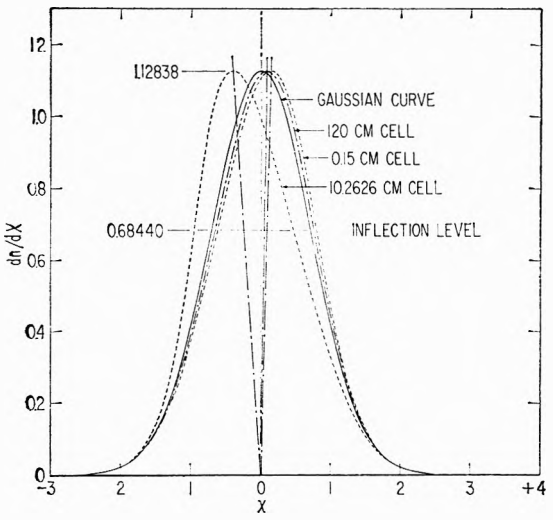

Figure 5. Theoretical distorted camera-recorded schlieren patterns compared with the gaussian pattern presumed to exist in the cell, for various cell thicknesses.

For each of these examples succeeding pictures in a time series would show decreasing displacements in proportion to the decreasing peak heights.

The schlieren center lines obtained by bisecting the patterns (Fig. 5) are straight lines, but they are not vertical. Therefore, a level of reference must be chosen, and x-values measured at this level. The apparent inflection level, for which the ordinate is 0.6065 times the peak height, is to be preferred for two reasons: (1) patterns are usually best defined in this region and precision of measurement greatest; (2) gaussian curves are almost linear at this level and for appreciable distances on both sides, which simplifies analytical calculations (*cf.* part II of this report).

Discussion

The bending and refraction correction of schlieren center lines has a very great effect on the time intercept of x–time plots and therefore on lag times. For thick cells such plots might intercept the meniscus apparently before the centrifuge was started, and the observed lag times could be negative.

The refraction correction by itself also has an effect on the slopes of x–time plots and therefore on s-values calculated from them. For the particular bovine serum albumin experiment cited the refraction-corrected $x_{inflection}$–time plot gives an s-value about 0.2% greater than that given by the uncorrected plot. For a 1.5-mm. cell this correction would be almost doubled. If the center line x-values at the peaks of the curves were used these corrections would be multi-

(6) In this report, and in the second part also, dimensions are frequently expressed in "gaussian units." In gaussian units the maximum ordinate of the normal distribution curve is always 1.12838 ($2/\sqrt{\pi}$), and the distance across the pattern at the inflection level, or at 0.6065 ($1/\sqrt{e}$) times the peak height, is always 1.4142 ($\sqrt{2}$).

(7) National Bureau of Standards, "Tables of the Error Function and its Derivative," Applied Mathematics Series, 41; The Superintendent of Documents, U. S. Government Printing Office, Washington 25, D. C., 1954.

plied by 1/0.6065, or 1.65, and for a 1.5-mm. cell the correction of s would be about +0.6%. It is emphasized, however, that if the δ_z correction be used it must not be used alone (*cf.* part II of this report).

The refraction correction has no effect on u-values, because at each level the patterns are displaced equally on the left and right and in the same direction. Peak heights are affected, but the areas under the patterns are also changed and in the same proportion. Therefore, there is no refraction effect on the values of diffusion constants calculated either from u-values or from peak heights and areas.

In the calculations given here, effects of centrifugal pressure gradients, preformed gradients, and cell distortion are presumed to be constant throughout any particular experiment and, therefore, are presumed to have no bearing on the δ_z-value to be used. This δ_z-value is calculated from the deviation caused by the concentration gradient, that is, from the height of the schlieren ordinate above the base line. When patterns are corrected to horizontal base lines as is common practice, all of these effects are combined as one and we have left a pattern describing the concentration gradient only. In electrophoresis, where density gradients and cell distortion are presumably absent, these matters need not be considered.

The numerical results given are for the Spinco ultracentrifuge optical system. For other optical systems, *e.g.*, electrophoresis, other dimensions would be required. The general formulation given would apply, however.

No account has been taken of nonhorizontal light entry, as would be encountered in a pressure-bowed cell or in a wedge-shaped cell or for optical systems employing only one collimating lens. If the light entry angle were constant in the x-direction, the resultant bending would be constant and would, therefore, be eliminated by the use of a blank-run base line.

For any particular optical system and a particular liquid medium, the refraction correction becomes zero at a definite cell thickness (*cf.* Fig. 4). For water systems in the Spinco apparatus, this occurs at a cell thickness of 2.7 cm.; for a benzene system, at 2.08 cm.

Corrections of Schlieren Data. II. The Equivalent Level

by T. Foster Ford

U. S. Naval Research Laboratory, Washington, D. C. 20390

and Edwin F. Ford

2603 N. VanDorn Street, Alexandria, Virginia *(Received February 26, 1964)*

The Lamm theory of light curvature, basic to interpretation of schlieren data, is strictly valid only for infinitely thin cells. Actually, a light ray traverses a finite x-coordinate interval in its passage through the cell. Thus a level must be selected which would be equivalent in effect to the finite interval actually traversed. Svensson has noted the effect and suggested a correction factor. The situation is considered here in more detail, both analytically and by numerical computational methods. The refractive index gradient distribution existing in the cell is assumed to be gaussian, and the schlieren pattern recorded by the camera is calculated and compared with the cell pattern. The curves are tilted toward the axis of rotation and are distorted. The displacement of the center line at any level is a little over $^1/_3$ the camera-recorded coordinate interval traversed. Peak heights are reduced, areas apparently preserved, and the horizontal distances across the pattern (u-values) are increased over the values at the same proportionate level on the original curve. Thus diffusion coefficients are increased, in extreme cases by many per cent. It is found that corrections of center lines may be expressed as functions of a single parameter. These corrections tend to cancel geometrical optical bending and refraction corrections for certain values of the parameter, but may in some cases, *e.g.*, thick cells, add to them.

Introduction

The schlieren optical systems employed in ultracentrifuges and in electrophoresis apparatus are based on the fact that when light enters a region where the refractive index varies with distance it is bent in the direction of increasing refractive index. It was pointed out by Svensson[1] that the camera-recorded deflection of the light ray (the angle θ in Fig. 1) is determined by the whole coordinate interval between the entrance and exit levels, *i.e.*, by the liquid wafer between A and B in Fig. 1. (It is to be noted that the camera-recorded entry level, C, is not necessarily the same as the real entry level, A, and that the camera-recorded cell deviation, δ_{cell}, is not necessarily equal to A minus B.) Svensson proposed to replace the liquid wafer actually traversed by a single level which would give the deflection observed. This we here call the equivalent level, the level D in Fig. 1. By approximate methods he deduced that the displacement of this equivalent level below the camera-recorded entry level, δ_E in Fig. 1, is about $^1/_3\delta_{cell}$. Little notice has been taken of this indicated correction of x-values, the distances of schlieren center lines from some point of reference, such as the center of rotation in ultracentrifugation.

The equivalent level correction of the schlieren center line is small in absolute units, but it may vary by roughly 50% in a time set of successive schlieren patterns (for bovine serum albumin, for example). This changing displacement results in tilting of x–time plots in such a direction that sedimentation coefficients calculated from the slopes of uncorrected plots are high, by as much as 1% or more. There are, however, two other important effects. First, uncorrected x–time plots are displaced along the time axis, and as a result the time intercept at the meniscus may be significantly affected. This time intercept deter-

(1) H. Svensson, *Kolloid-Z.*, **90**, 141 (1940).

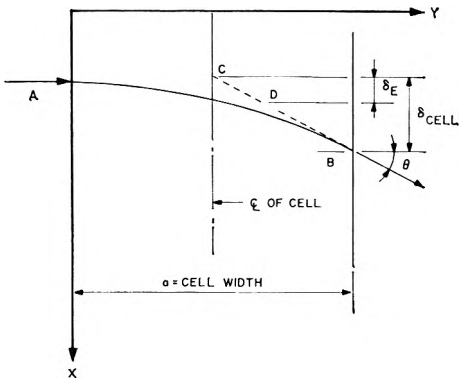

Figure 1. A slightly modified version of the diagram used by Svensson in his analysis of the effect of light curvature on the positions of schlieren center lines.

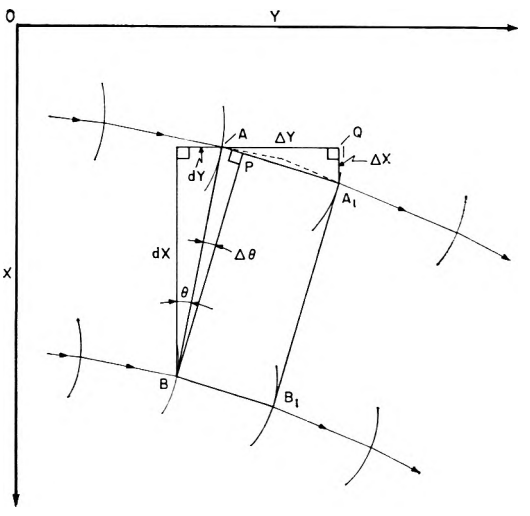

Figure 2. The diagram used by Lamm in the development of his theory of light curvature.

mines a lag time, or time delay in separation of the schlieren peak from the meniscus. The lag time has been shown to have a theoretical relationship to the sedimentation coefficient, s, the diffusion coefficient, D, and the angular velocity, ω.[2] Its accurate measurement could provide an independent measurement of D. Second, not only are schlieren patterns displaced by the effects of light curvature but they are also distorted. Maximum peak heights and 2σ-values (the horizontal distances across gaussian curves) are affected. When these are used for calculation of diffusion coefficients, errors resulting from neglect of curvature distortion may range from almost zero to many per cent in real cases.

For the above reasons we have found it necessary to re-examine the equivalent level correction, particularly in the light of the refraction–bending corrections discussed in part I of this report. We here present a new theoretical analysis of the effects of curvature on schlieren patterns, illustrative numerical examples for three systems (bovine serum albumin, barium dinonylnaphthalenesulfonate in benzene, and a hypothetical virus), and a generalized formulation of various corrections required for any reasonable combination of cell thickness and steepness of gaussian dc/dx *vs.* x-gradients.

Results

The Lamm Theory of Light Curvature. This theory[3] is basic to interpretation of schlieren patterns. The central, heavily outlined portion of Fig. 2 is identical with the diagram used by Lamm.[3b] Lamm's symbols are used on this figure, but the Svensson symbols of Fig. 1 will be adopted hereafter in this paper. Lamm's symbols A and B represent two points on the same wave surface. The refractive index at A is n and at B, $n + dn$. $\overline{AA_1}$ and $\overline{BB_1}$ represent the same optical path ΔL, *i.e.*, the distances traveled by the rays entering at A and B in equal times. Thus $\overline{AA_1} = \Delta L/n$ and $\overline{BB_1} = \Delta L/(n + dn)$. Therefore AP, which is equal to $\overline{AA_1} - \overline{BB_1}$, is equal to $\Delta L[1/n - 1/(n + dn)]$, or to $\Delta L[dn/(n^2 + ndn)]$, or, as an approximation, to $\Delta L d(n/n^2)$. By further geometrical reasoning based on this figure, and regarding the quantity $[(dn/dx)/n]$ as constant along a narrow pencil of light, Lamm obtains the equation

$$x - x_0 = a\theta_0 + {}^1/_2\left[\frac{dn/dx}{n}\right]a^2 \qquad (1)$$

where a is the cell thickness. When θ_0, the entering angle, is zero, this equation can be written

$$\Delta x = {}^1/_2\left[\frac{dn/dx}{n}\right]\overline{\Delta y^2} \qquad (2)$$

and from this it follows that

$$\frac{dx}{dy} = \left[\frac{dn/dx}{n}\right]y \qquad (3)$$

We omit the details of the derivation but include Fig. 2 because it is essential to this report.

With regard to the derivation, we note the following observations.

(1) Although in the integrations $[(dn/dx)/n]$ is considered to be constant, in the prior geometrical

(2) H. Fujita, "Mathematical Theory of Sedimentation Analysis," Academic Press, New York, N. Y., 1959, p. 87.

(3) (a) O. Lamm, *Nova Acta Reg. Soc. Sci. Upsaliensis*, **4**, 10 (1937); (b) T. Svedberg and K. O. Pedersen, "The Ultracentrifuge," The Clarendon Press, Oxford, 1940, p. 257 ff.

analysis only dn/dx is considered constant, and the assumption is that $n = n_0 + (dn/dx)\Delta x = n_0 + k\Delta x$.

(2) In consequence of this, eq. 1 and 2 are strictly applicable only for very small deviations, *i.e.*, for thin cells.

(3) According to the geometrical analysis, it is the relative light path, ΔL, rather than n which is actually considered to be a linear function of x. This is not Δy but $\Delta y/\cos\theta$, a correction which is ordinarily small but is real and to be remembered.

These observations are to be used in developing a method of numerical integration for constantly varying values of dn/dx.

Criterion of the Equivalent Level. It is seen that by Lamm's analysis, assuming $[(dn/dx)/n]$ to be constant, the bending is the same at all levels, the schlieren pattern is a horizontal straight line, and therefore no choice of an equivalent level is possible or necessary. Svensson[1] recognized this and therefore assumed $n = f(x)$. When this is done it is possible to choose for each ray that particular x-value for which the logarithmic derivative $[(dn/dx)/n]$ will give the deflection observed when substituted into formula 3. This we define as the equivalent level. Svensson's analysis is inexact, however, and serves as a first approximation only.

Analysis Based on the Fundamental Equation for Light Curvature. The general equation for the light path in an optically nonhomogeneous medium is[4]

$$\frac{d}{ds}\left(n\frac{\vec{dr}}{ds}\right) = \text{grad } n \qquad (4)$$

The most useful form of this equation in two-dimensional rectangular coordinates, measuring x and y in the directions used by Lamm, is

$$\frac{\partial n}{\partial y}\frac{dx}{dy} - \frac{\partial n}{\partial x} + \frac{n}{1+\left(\frac{dx}{dy}\right)^2}\frac{d^2x}{dy^2} = 0 \qquad (5)$$

We let $n = A + Bx + Cx^2 + \ldots$, and substitute this expression in (5) obtaining

$$(A + Bx + Cx^2)\frac{d^2x}{dy^2} = (B + 2Cx)\left\{1 + \frac{(dx)^2}{dy}\right\} \qquad (6)$$

An approximate solution of (6) for a ray entering horizontally at $x = 0$ is

$$x = \tfrac{1}{2}\frac{B}{A}y^2 + \left(\frac{1}{12}\frac{BC}{A^2} + \frac{1}{24}\frac{B^3}{A^3}\right)y^4 + \ldots \qquad (7)$$

This reduces to Lamm's equation (2) if the term in y is neglected. From (7) we obtain

$$\frac{dx}{dy} = \frac{B}{A}y + \left(\frac{1}{3}\frac{BC}{A^2} + \frac{1}{6}\frac{B^3}{A^3}\right)y^3 + \ldots \qquad (8)$$

For a cell of thickness a, the exit slope of the ray

$$\left[\frac{dx}{dy}\right]_a = \frac{B}{A}a + \left(\frac{1}{3}\frac{BC}{A^2} + \frac{1}{6}\frac{B^3}{A^3}\right)a^3 + \ldots \qquad (9)$$

and the exit height

$$[x]_a = \frac{1}{2}\frac{B}{A}a^2 + \left(\frac{1}{12}\frac{BC}{A^2} + \frac{1}{24}\frac{B^3}{A^3}\right)a^4 + \ldots \qquad (10)$$

The equation for the tangent to the ray at $y = a$ is

$$\frac{x - [x]_a}{y - a} = \left[\frac{dx}{dy}\right]_a \qquad (11)$$

On this tangent, at $a/2$, $[x_T]_{a/2} = [x]_a - a/2[dx/dy]_a$,[5] and using eq. 9 and 10 we obtain

$$[x_T]_{a/2} = -\left(\frac{1}{12}\frac{BC}{A^2} + \frac{1}{24}\frac{B^3}{A^3}\right)a^4 + \ldots \qquad (12)$$

In experiments, the height, x_0, at which the ray enters the cell is unknown but the exit tangent and the cell width are known. We choose an arbitrary origin for the x-axis We can measure $[x_T]_{a/2}$* (eq. 12) and $[dx/dy]_a$ (eq. 9) and we can extrapolate from $y = a/2$ to $y = a$ to obtain

$$[x_T]_a = [x]_a = \frac{1}{2}\frac{B}{A}a^2 + \left(\frac{1}{12}\frac{BC}{A^2} + \frac{1}{24}\frac{B^3}{A^3}\right)a^4 + \ldots \qquad (13)$$

If we apply the Lamm equation (3) to the observed exit deflection $[dx/dy]_a$, we find that the value of $(1/n)(dn/dx)$ deduced for this ray is

$$\left(\frac{1}{n}\frac{dn}{dx}\right)^* = \frac{1}{a}\left[\frac{dx}{dy}\right]_a = \frac{B}{A} + \left(\frac{1}{3}\frac{BC}{A^2} + \frac{1}{6}\frac{B^3}{A^3}\right)a^2 + \ldots \qquad (14)$$

We define the "equivalent level" x^* for this ray as that value of x at which

$$\frac{1}{n}\frac{dn}{dx} = \frac{B + 2Cx + \ldots}{A + Ex + Cx^2 \ldots} = \left(\frac{1}{n}\frac{dn}{dx}\right)^* \qquad (15)$$

From (15), after algebraic division, we find that

(4) M. Born and E. Wolf, "Principles of Optics," Pergamon Press, London, 1959, p. 121.

(5) To a close approximation, $[x_T]_{a/2}$ is the x-value recorded when the camera is focused on the center line of the cell.

$$\frac{B}{A} + \left(\frac{2C}{A} - \frac{B^2}{A^2}\right) x^* + \ldots = \frac{B}{A} + \left(\frac{1}{3}\frac{BC}{A^2} + \frac{1}{6}\frac{B^3}{A^3}\right) a^2 + \ldots \quad (16)$$

so that if the deviation of the ray is small we have

$$x^* = \frac{1}{6}\frac{B}{A} a^2 \times \frac{2AC + B^2}{2AC - B^2} + \ldots = \frac{1}{3}\frac{2AC + B^2}{2AC - B^2}\{[x]_a - [x_T]_{a/2}\} + \ldots \quad (17)$$

using (10) and (12).

The approximate formula (17) is adequate if the ray does not traverse too large a portion of the concentration gradient while passing through the cell. If this condition is satisfied, (17) shows that Svensson's "one-third" rule is a correct first approximation for the location of the equivalent level provided $2AC >> B^2$. This inequality will be satisfied for rays entering near the inflection points of gaussian dc/dx curves, but not for rays entering near the peaks since $C = 0$ at the peaks of the gaussian curves.

Real Cases. Figure 3 presents three refractive index gradient curves drawn to simulate patterns obtained with real systems. The height of the liquid column is assumed to be 1 cm. in each case. In terms of the width of the gaussian curve, this distance is variable as indicated. The width of the liquid wafer traversed by the ray exhibiting the maximum deflection is for illustrative purposes considered to be approximately constant in these three cases and is denoted in the figure by $\delta_{cell,\ max}$. Methods of calculating apparent cell deviations from camera-recorded deviations are given in the preceding paper.

It is clear from Fig. 3 that the range of dn/dx values traversed by a ray through the peak or at any other level on a gaussian curve may be very different for different schlieren patterns. Only for the very broadest patterns could dn/dx be considered constant at any average ordinate. It is noted, moreover, that there is a reversal of sign of $d(dn/dx)$ across the top. The purpose of these illustrative pictures is to show that the use of a linear function for n is severely limited, that a linear function for dn/dx is admissible near the inflection points in some cases, and that at some stage in the progressive sharpening of these curves even a polynomial function would become inadequate. If we wish to calculate light paths and equivalent levels with any degree of accuracy required, we must resort to numerical integrations using tables of the error function.

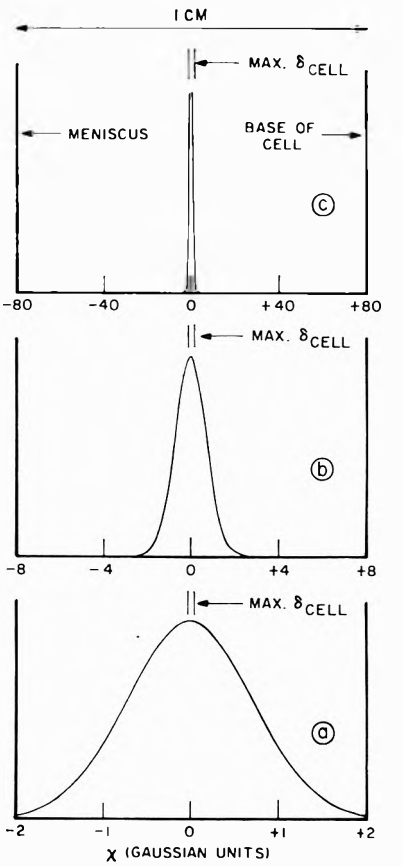

Figure 3. Three schlieren patterns covering roughly the range of physical interest. Pattern (a) is a real pattern, for barium dinonylnaphthalenesulfonate in benzene; pattern (b) is also a real pattern, for bovine serum albumin, but the scale of ordinates has been adjusted to make the maximum ordinate the same as that for BaDNNS; pattern (c) is a hypothetical pattern simulating a virus or a haemocyanin. Here max. δ_{cell} is the approximate maximum deviation of a light ray in its passage through a 1.20-cm. Spinco ultracentrifuge cell.

General Method of Successive Approximations. At this stage, reference should be made to Fig. 4, which is also to be discussed, in more detail, in the following section.

We assume that the real concentration distribution in the cell is gaussian. Therefore, at any desired level we can take dn/dx values, and their integrals, from tables of the error function.[6] We assume that the Lamm equation holds for an infinitely thin cell. We therefore divide the real cell into several successive thin or unit cells separated by imaginary partitions. (In Fig. 4 the construction is for five-unit cells, for the simulated virus model, and the dimensions shown are

(6) National Bureau of Standards, "Tables of the Error Function and its Derivative," Applied Mathematics Section 41, The Superintendent of Documents, U. S. Government Printing Office, Washington 25, D. C., 1954.

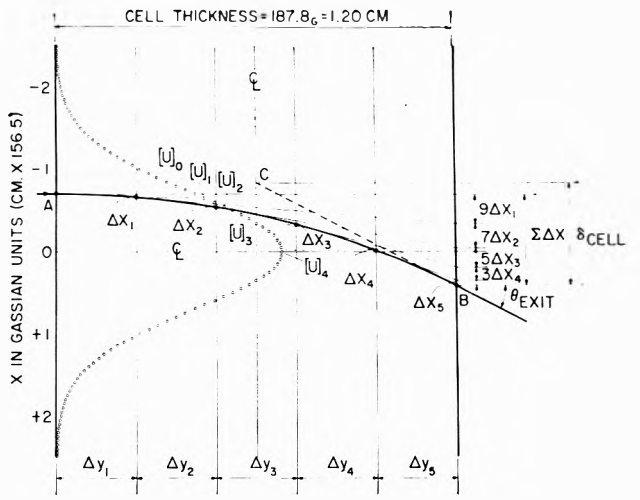

Figure 4. Diagram used in the development of a numerical integration method for the calculation of real light paths across liquid columns in schlieren optical systems. This model is for the simulated virus.

those used for that model, except that the scale of ordinate for the gaussian curve is arbitrary. The proportions of the fourth unit cell are exactly the same as used for the Lamm diagram, Fig. 2.) The direction of the entering ray for each unit cell is the same as the direction of the exit ray for the cell preceding. For each successive unit cell we apply the Lamm formula, using either Δy or ΔL which is equal to $\Delta y/\cos\theta$, and using that value for $[(dn/dx)/n]$ (the $[U]$-values of Fig. 4) appropriate to the entering level. Thus we obtain Δx_i which defines a new level and determines a new value for $[(dn/dx)/n]$. In this stepwise way we plot an approximate light path. By repeating this process for increasing numbers of unit cells we obtain a set of approximate total deviations and exit tangents. These values can then be plotted against the unit cell thicknesses and extrapolated to obtain values for an infinite number of thin cells. Thus we have the data required to plot real light paths and to calculate apparent levels as recorded by the camera. Using our data, we can trace the distorted patterns recorded by the camera. Using these, by graphical or analytical means, the required corrections of center lines and other corrections can be found by comparison with the original gaussian curve.

Although it is the distorted pattern which is observed, such data for a set of typical patterns are useful. The distorted patterns in most real cases will so closely resemble the correct patterns that corrections based on the dimensions of the distorted pattern will be in relative error by a lower order of magnitude.

Detailed Methods. Units. Since tables of the error function are to be used, it is convenient to express dimensions in gaussian units. We note that the peak height of a gaussian (dn/dx *vs.* x) curve is 1.12838; the inflection points are found at 0.68440, or 0.6065 times the peak height; the horizontal distance across the curve at the inflection, $2u_{infl}$, is 1.4142; and that the total area under the curve is 2.0.

We choose, for an example, the first completely resolvable schlieren pattern obtained for a 1.22% bovine serum albumin solution in the Spinco ultracentrifuge. The distance $2u_{0.6065}$ in the cell is 0.0904 cm. For a perfectly gaussian pattern $2u_{0.6065}$ is 1.4142 on the gaussian scale. Thus the conversion factor is 15.65. The cell thickness, 1.2 cm., is therefore 18.78. This, or some fraction of it, is Δy in the Lamm equation.

The refractive increment for bovine serum albumin is 0.001924 $n/$(g./100 ml.)[7] or, for our solution, 0.001935 $n/$(g./100 g.). At the time for this picture the concentration had been lowered by radial dilution to 1.119%. Therefore, the refractive index increase due to the solute is (1.119)(0.001935) or 0.002165. This we set equal to the area under a gaussian curve, 2.0. The refractive index of the solvent is 1.348. Thus, on the gaussian scale, the refractive index of the solvent is (1.348/0.002165)(2) or 1245. The refractive index of the solution at any χ-value along the gaussian curve is therefore 1245 plus the gaussian integral to that χ-value. Thus, once determining the solvent refractive index to be 1245, the logarithmic derivative $(dn/dx)/(n_{solv} + \Delta n)$ or $(dn/dx)/n_{soln}$ is readily determined using the gaussian tables.

Since y as used above is in gaussian χ-units, the Lamm equation gives the deviation $\Delta\chi$ in the same units. This deviation is proportional to and determines the displacement recorded by the inclined wire-cylindrical lens system; therefore, it determines the corresponding ordinate on the schlieren pattern. To convert these ordinates to the gaussian dn/dx scale, we calculate a theoretical deviation at the peak using the Lamm formula. Making $(dn/dx)/n = 1.12838\ 1246$, and making $\Delta y = 18.78$, we obtain $\chi = 0.15970$. To convert calculated deviations to the gaussian dn/dx scale we therefore multiply them by the factor 1.12838/0.15970, or 7.0658.

Summation of Increments. Referring to Fig. 4, it is seen that the extension of the ray exiting from each unit cell contributes to the final $\Sigma\Delta\chi$ by the deviation $\Delta\chi_i$ times $2N - 1$, where N is the total number of unit

(7) M. Halwer, G. C. Nutting, and B. A. Brice, *J. Am. Chem. Soc.*, **73**, 2786 (1951).

cells traversed. For each extended ray the sequence of increments is 1, 3, 5, 7, 9, 11, ...

Extrapolations. For rays entering near the inflection levels, quite accurate extrapolations are possible using approximate deviations and exit tangents for 1, 3, 5, and 9-unit cells. For rays crossing the tops of patterns the plots reverse and in such cases it may be necessary to use as many as 15-unit cells. Examples of extrapolation curves as well as other details of computational methods will be published elsewhere.[8]

Neglect of Cosines. Test calculations showed that neglect of the cosines in the Lamm equation does not introduce errors larger than 0.008% in $\Sigma\chi$-values nor larger than 0.015% in the exit tangents for the bovine serum albumin model. Cosines were therefore neglected.

Background Gradients. In electrophoresis, refractive index gradients due to pressure, and cell distortions due to pressure, need not be considered. In the ultracentrifuge at high speeds, these effects may be appreciable. They appear as an elevation of the base line above the vacuum reference lines. In our experiments at 59,780 r.p.m. in the Spinco ultracentrifuge, the ratio of this elevation to the first clearly resolved peak height is 0.261/1.128. Hence the maximum dn/dx to be used at this speed is 1.128 plus 0.261 or 1.389, and for any point on the curve the constant value 0.261 must be added to dn/dx. The effect is appreciable, and therefore calculations were carried through both with and without background gradients.

Results Obtained by Numerical Integration. We consider first a hypothetical model, simulating a virus, as an example of an extreme case, and then two models based on actual schlieren patterns, for bovine serum albumin and barium dinonylnaphthalenesulfonate in benzene (*cf.* Fig. 3).

Virus. Experimental details include: a 1.2-cm. cell; $2u_{0.6065}$ = 0.00904 cm.; gaussian cell thickness, 187.8; gaussian n_{solv} = 12,450; no background gradient.

Eleven rays were calculated by the method indicated. The rays differ markedly in curvature and in the position of the camera-recorded entry level, the level C of Fig. 1. For three rays, for example, near the left inflection level, near the top, and near the right inflection level, the ratios of the camera-recorded deviation, δ_{cell}, to the coordinate interval actually traversed are 1.207, 1.002, and 0.798, respectively. For the same rays the ratios δ_E/δ_{cell}, *cf.* Fig. 1, are 0.427, 0.097, and 0.200. Thus the deviations of the equivalent level from the camera-recorded level may vary radically for different rays of a single pattern, so that for single rays δ_E/δ_{cell} may be much greater or less than $^1/_3$. These ratios do not give the displacement of the schlieren center line, however. This is obtained by averaging the displacements on the two sides of the pattern at a single ordinate. This average we call δ_ϵ, and the ratio $\delta_\epsilon/\delta_{cell}$ does turn out to be close to $^1/_3$.

Figure 5 shows the camera-recorded, distorted pattern (in gaussian units, and greatly exaggerated in the χ-direction) for this model together with the gaussian pattern assumed actually to exist in the cell. The curve is tilted to the left and the peak height is reduced. Planimeter measurements indicate that the area is preserved. For each point δ_E is the horizontal χ-distance between the two curves.

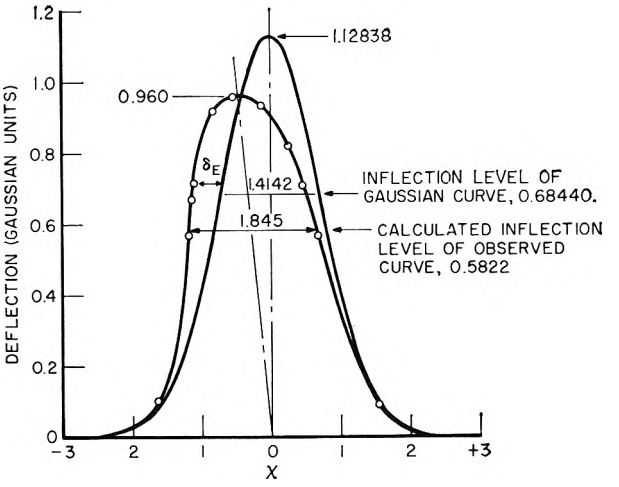

Figure 5. The theoretical camera-recorded schlieren pattern for the simulated virus in a 1.20-cm. cell, compared with the gaussian pattern assumed to exist in the cell. The scale of the abscissa is on the gaussian scale, here designated as χ-units. The pattern is greatly exaggerated in the χ-direction.

Since the displacement of the center line varies with the ordinate, it is necessary to choose a level at which to measure this center line. For reasons given elsewhere,[9] the apparent inflection level, 0.6065 times the apparent peak height, is chosen. We therefore redefine δ_ϵ as the displacement of the center line at the apparent inflection level. We also introduce the symbol G for the apparent peak height.

For this model we find: $\delta_\epsilon = 0.247\chi$, or 0.00158 cm.; $\delta_\epsilon/\delta_{cell}$ = 0.300; and $2u_{0.6065}$ = 1.845. Thus D, the diffusion coefficient, by the u^2 method, is $[(1.414)^2/(1.845)^2]D_{obsd}$ and the error in D_{obsd} is

(8) T. F. Ford, S. Kaufman, and O. D. Nichols, "Ultracentrifugal Studies of Dinonylnaphthalene Soaps. I. Sedimentation Velocity of the Barium Dinonylnaphthalenesulfonate Micelle in Benzene," U. S. Naval Research Laboratory, technical report.

(9) T. F. Ford and E. F. Ford, *J. Phys. Chem.*, **68**, 2843 (1964).

+70%; $G = 0.960$. If we assume the areas under the two curves to be equal, then D calculated by the peak height method is $[(0.960)^2/(1.128)^2]D_{obsd}$ and the error in D_{obsd} is +38%.

In the calculations for this model no background gradient was assumed because for such a large particle the centrifugal speed used would be low and therefore the density gradient and cell distortion would be negligible.

Bovine Serum Albumin. For this experiment, we used a 1.2-cm. cell; $2u_{0.6065} = 0.09035$ cm.; gaussian cell thickness, 18.78; gaussian $n_{solv} = 1245$.

The pattern for BSA is tilted to the left by a smaller but perceptible amount, *cf.* the curve $L = 0.5$ in Fig. 6. For this model, assuming no background gradient we find: $\delta_\epsilon = 0.0333\chi$, or 0.00215 cm.; $\delta_\epsilon/\delta_{cell} = 0.350$; and $2u_{0.6065} = 1.416$. Thus D_u is $[(1.4142)^2/(1.416)^2] \cdot D_{obsd}$ and the error is +0.3%; $G = 1.127$. Assuming the area to be preserved, D by the peak height method is in error by +0.25%.

If we assume a background gradient (of $0.261G$) we find: $\delta_\epsilon = 0.0456$, or 0.00292 cm.; $\delta_\epsilon/\delta_{cell} = 0.335$; $2u_{0.6065} = 1.421$; and the error in D_u is 1.0%.

Barium Dinonylnaphthalenesulfonate. Conditions included: a 1.2-cm. cell; $2u_{0.6065} = 0.3614$ cm.; gaussian cell thickness, 4.695; gaussian $n_{solv} = 311.25$. In this case the distortion of the pattern is almost imperceptible. Assuming no background gradient, we find: $\delta_\epsilon = 0.010\chi$, or 0.00247 cm.; $\delta_\epsilon/\delta_{cell} = 0.341$; $2u_{0.6065} = 1.415$; and the error in D_u is 0.05%, which is insignificant.

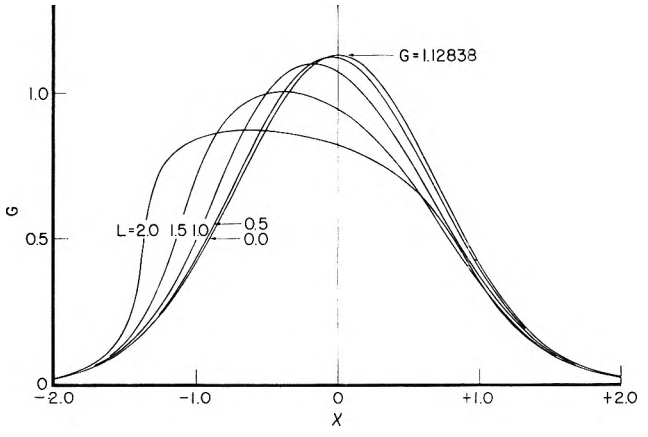

Figure 6. Computer simulation of camera-recorded schlieren patterns, compared with the gaussian pattern assumed to exist in the cell. The L-values are the values of a parameter used in the calculations

$$L = \left(\frac{\text{cell thickness in cm.}}{\text{gaussian inflection leg in cm.}}\right)\sqrt{\frac{\text{Total r.i. change due to concentration}}{\text{r.i. of the solution}}}$$

The dimensions shown are gaussian.

Generalized Results by Computer Calculations. It will be discerned from the foregoing discussion of numerical calculations that the distortion of a gaussian pattern on account of light curvature alone is a function of cell thickness, the distance across the pattern at any chosen level, *e.g.*, the apparent inflection level, and the ratio of the refractive index increment due to concentration to the refractive index of the solution at the particular level in question. However, we find that to a close approximation the various corrections may be calculated in terms of one dimensionless parameter.

We choose the parameter

$$L = \left(\frac{\text{cell thickness in cm.}}{\text{gaussian inflection leg in cm.}}\right)\sqrt{\frac{\text{total r.i. change due to concentration}}{\text{r.i. of the solution}}}$$

Using this parameter the problem was set up for computer calculations. Light rays were traced by a Runge-Kutta numerical integration scheme based on the basic differential eq. 5 for ray paths in a medium of variable refractive index, and the necessary data were obtained for the construction of theoretical camera-distorted patterns. A few patterns thus obtained, assuming no background gradient are shown in Fig. 6. Each of these curves is based on 21 points. Similar patterns were calculated adding our background gradient of 0.261. These patterns resemble the patterns of Fig. 6, except that the peaks are lower and the curves are distorted further toward the meniscus.

For the bovine serum albumin model calculated numerically, for example, $L = 0.532$. The machine-calculated pattern at $L = 0.532$ is superimposable on the pattern found by hand calculations. For the hypothetical virus pattern ($L = 1.68$) the machine curve corresponds almost exactly with that shown in Fig. 5.

Figure 7 shows the computer calculated changes with L, with and without a background gradient, of: (1) δ_ϵ, the displacement of the schlieren center line at the inflection level, in gaussian units; (2) G_{max}, the observed peak height, in gaussian units; and (3) $u_{0.6065}$, one-half the distance across the pattern at the apparent inflection level, again in gaussian units.

Discussion

The Parameter L. Figure 7 gives values for the camera-recorded maximum schlieren ordinate, G_{max}, the half-distance across the observed pattern at the apparent inflection level, $u_{0.6065}$, and the (negative) displacement of the center line at the apparent inflection level, δ_ϵ, all as functions of a single param-

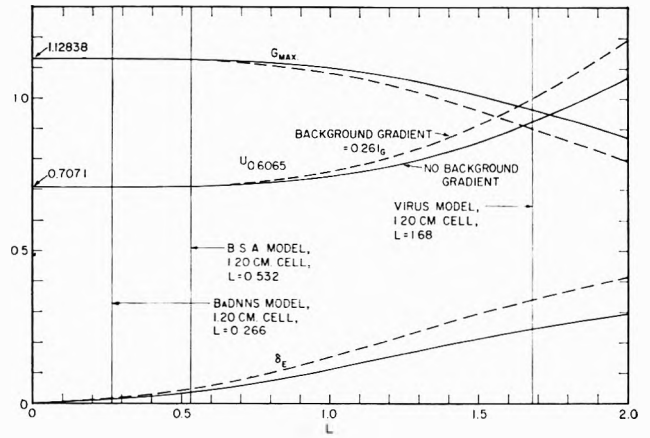

Figure 7. The variation with L of: the camera-recorded maximum ordinate, G; the half-distance across the observed pattern at the apparent inflection level, $u_{0.6065}$; and the negative displacement of the center line at the apparent inflection level, δ_ϵ. All values are shown in gaussian units. The values for $u_{0.6065}$ and δ_ϵ may be converted to centimeters by dividing by the factor $1.4142/2u_{0.6065,obsd.}$

eter, L. These values are for calculated schlieren patterns derived from an assumed gaussian pattern in the cell. They are in gaussian units. The values given for $u_{0.6065}$ and δ_ϵ may be converted to centimeters by dividing by the factor $1.4142/2u_{0.6065,obsd.}$ The parameter, L = (cell thickness in cm.)$(1/2u_{0.6065,obsd.})\cdot$ (total r.i. change due to concentration)$^{1/2}$(r.i. of solution)$^{-1/2}$. Since, relative to r.i._{concn}, r.i._{soln} may be considered practically constant, then for a fixed cell thickness, L is proportional to $(1/2u_{0.6065,obsd})$(total r.i. change due to concentration)$^{1/2}$, approximately. In any ordinary time set of successive sedimentation patterns, therefore, L will decrease with time, and the corrections indicated will be decreased for successive pictures.

Sedimentation Coefficients. For the correction of center line positions (x-values) the bending and refraction correction, δ_x, discussed in part I of this report, and the δ_ϵ correction considered here must both be used together. They may tend to cancel, or they may be additive.

As an example, results of calculations for a theoretically nonconcentration-dependent bovine serum albumin model are offered. Three cell thicknesses were assumed: 0.15, 1.20, and 3.0 cm. The net δ_x corrections over a 48-min. interval were +0.00133, +0.00074, and −0.00017 cm., respectively. Since the schlieren center line moved 0.194 cm. in this time, the indicated corrections of s-values, for δ_x alone, are +0.69, +0.38, and −0.09%. The corrections of s for δ_ϵ alone are +0.01, −0.26, and −1.07%. The total corrections are +0.70, +0.12, and −1.16%. Assuming a benzene system and the same constants the total correction, for the 3.0-cm. cell, is −1.38%.

Lag Times. The correct lag times are best found by plotting x-values, corrected as above, against time, and extrapolating to the meniscus. The time intercept less the equivalent starting time, separately determined, gives the corrected lag time. These corrections may be large and may even equal or exceed the true lag times.

Diffusion Coefficients. Since the δ_x correction has no effect on maximum ordinates nor on u-values, corrections of these values, and therefore of diffusion coefficients, can be found by use of Fig. 7 alone. Illustrations based on results of numerical integrations have been given in the text. It can be seen by reference to Fig. 7 that for $L < 0.05$, the corrections of D by either the peak height method or the u^2 method are negligible. At higher values of L the corrections rise rapidly, however. For $L = 1.68$, D_{obsd} by the peak height method, assuming an $0.261G$ background gradient (59,780 r.p.m. in our Spinco ultracentrifuge), is in error by +57% of the true value; by the u^2 method it is in error by +100% of the true value. These corrections apply to all schlieren measured diffusion coefficients as well as to those calculated from sedimentation velocity data.

Nonhorizontal Entry. No account has here been taken of original nonhorizontal entry of the light ray. Such entry may result from misalignment of the optical system or from pressure distortion of centrifuge cells at high speeds. The effect would be to increase the distortion of schlieren patterns.

Discussion

W. Wade (University of Texas). As far as general laboratory use of ultracentrifugation and other techniques using schlieren optics is concerned in most qualitative analysis, for what kinds of systems are your corrections most important?

T. F. Ford. Our corrections are, in general, most important for optical systems using thick cells, and for disperse systems giving steep schlieren patterns. The bending and refraction correction, δ_x, is, however, quite high for thin cells. It becomes zero at certain intermediate cell thicknesses, and is again high, but opposite in sign, for thick cells. This is shown by Fig. 4 of paper I.

The equivalent level corrections are functions of several variables, combined here into a single parameter L. For a particular disperse system, however, since concentration must be reduced in proportion as cell thickness is increased, L is approximately proportional to $\sqrt{\text{cell thickness}}$. The increasing net effect of cell thickness on the apparent value of the sedimentation coefficient, s,

is indicated by theoretical calculations given in the text for 0.15-cm, 1.2-cm, and 3.0-cm cells (paper II). For thicker cells the corrections would be much greater.

The effect of steepness of schlieren patterns is illustrated by the simulated virus model. Here the effect on s is not great because the diffusion rate is so low that the gaussian inflection leg does not change much during an ordinary sedimentation experiment; the x–time plot is not significantly tilted but only displaced along the time axis. The effect on the diffusion coefficient D is very great, however.

More detailed discussion of magnitudes, though desirable, would be too lengthy for inclusion here.

Evaporation and Condensation of Spherical Bodies in Noncontinuum Regimes

by James R. Brock

Department of Chemical Engineering, University of Texas, Austin, Texas *(Received February 17, 1964)*

The theory of the evaporation and condensation of spherical bodies is discussed for the slip-flow and free-molecule regimes. The value of the slip-flow density difference coefficient is discussed and the method of calculation in the slip-flow regime of evaporation and condensation rates of spherical bodies is outlined and illustrated with a simple example. Expressions for the evaporation and condensation rates in the free-molecule regime are given in detail for general dynamical states of the gas phase.

Introduction

The existence of noncontinuum effects in gas–liquid and gas–solid systems in which interphase mass transfer is occurring has been recognized for some time.[1-3] It seems useful to present a discussion of these effects consistent with the present understanding of noncontinuum phenomena.

It is the purpose here to present a description of noncontinuum effects for the evaporation and condensation of spherical bodies for the two dynamical regimes where exact calculation for the gas phase is possible: the slip-flow and free-molecule regimes.

For the slip-flow regime we will confine our explication to the quasi-steady evaporation or condensation of a stationary spherical liquid drop immersed in a quiescent, dilute binary gas mixture. The manner of extending the methods applied in this simple example to more general gas phase dynamical states is indicated.

In the free-molecule regime, evaporation and condensation rates of spherical bodies are discussed for general gas phase dynamical states for mass average velocity magnitudes which are small relative to mean molecular velocity magnitudes. The case of large mass average velocity magnitudes is also examined, but no account is taken of temperature, concentration, or velocity gradients in the gas.

Evaporation and Condensation in the Slip-Flow Regime

In noncontinuum problems it is convenient to divide, for computational purposes, the realm of definition of Knudsen number[4] $0 \leq (l/a) \leq \infty$ into three regimes which are termed slip-flow, $0 < (l/a) < \sim 0.25$[5,6]; transition, $0.25 < (l/a) < 10$; and free molecule, $(l/a) > 10$.

(1) N. A. Fuchs, *Phys. Z. Sowjet*, **6**, 225 (1934).

(2) R. S. Bradley, M. G. Evans, and R. W. Whytlaw-Gray, *Proc. Roy. Soc.* (London), **A186**, 368 (1946).

(3) P. G. Wright, *Proc. Roy. Soc.* (Edinburgh), **A66**, 65 (1962).

(4) Here l is the molecular mean free path and a is the radius of the spherical body.

(5) J. R. Brock, *J. Phys. Chem.*, **66**, 1763 (1962).

(6) D. Willis, KTH Aero TN 52, Royal Institute of Technology, Stockholm, Sweden, 1960.

The slip-flow regime covers that region of Knudsen number where one may apply the continuum equations of mass, momentum, and energy and account approximately for the noncontinuum effects through the introduction of slip-flow boundary conditions. This procedure, however, is found[5,6] to fail as (l/a) increases.

Before examining the slip-flow boundary conditions for problems of evaporation and condensation, let us regard the continuum treatment of a simple physical system already described above for the slip-flow regime.

Consider the quasi-steady evaporation or condensation of a stationary spherical liquid drop of component 2 of low vapor pressure immersed in a quiescent dilute binary gas consisting of component 2 in dilution and an insoluble component 1. We have for this physical system the continuum description of the condensation or evaporation

$$-D_{12}\frac{dn_2}{dr}4\pi r^2 = \Phi \qquad (1)$$

where D_{12} is the mutual diffusion coefficient, Φ the total rate of evaporation or condensation, n_2 the number density of 2, and r is the radial distance from the center of the sphere. The integrated expression in terms of the concentration of 2 at the sphere surface, $n_2(a)$, and at a large distance from the surface, $n_2(\infty)$, is

$$(\Phi/4\pi a^2) = D_{12}[n_2(a) - n_2(\infty)]a^{-1} \qquad (2)$$

which obviously fails for $a \to 0$.

Let us examine eq. 1 and its limitation in the slip-flow regime. Now well removed from the drop surface, we expect eq. 1 to apply, but as the drop surface is approached, the diffusional transport process deviates increasingly from the linear law. Indeed, at the drop surface one finds from a gas-kinetic analysis that the number density gradients become infinite.[7]

Previous students of this problem[1-3] have recognized that eq. 1 was not valid near the surface. Fuchs, in discussing the evaporation of spherical drops, introduced a distance Δ from the sphere surface; for $r > \Delta$, eq. 1 was taken to apply, and for $r < \Delta$, the vacuum evaporation rate was taken and both descriptions were matched at $r = \Delta$. No limitation of the validity of this procedure has been realized, although we will find here that in its previous applications it is identical with a slip-flow analysis. The Δ concept, while it may be applied in the slip-flow regime, $0 < (l/a) < \sim 0.25$ for the present simple one-dimensional physical system under consideration, is not capable of systematic extension to more complex physical systems. Through use of the usual slip-flow procedure, however, physical systems of arbitrary complexity may be discussed.

Now the slip-flow procedure states that we apply the continuum equation, eq. 1, to the problem of evaporation or condensation of the spherical drop and use a slip-flow boundary condition, which accounts for the fact that the value of the concentration at the surface is not that given by eq. 1, $n_2^c(a)$, but is a value determined by the solution of the Boltzmann equations for the two species near the surface. The state of a dilute binary gas system diffusing in the normal direction to a surface has been studied previously by the author[7] for a mixture of approximately equal molecular masses.

For the present physical system, the appropriate slip-flow boundary condition is analogous to the familiar velocity-slip and temperature-jump conditions. We may term this condition, by analogy, the density difference condition. The following general form is found for the density difference condition

$$n_i(a) - n_i^c(a) = c_{di}l\left(\frac{dn_i}{dr}\right)_{r=a} \qquad (3)$$

This equation expresses the difference between the density of i found at the surface under the assumption that the gradient (dn_i/dr) retains its value at some distance from the surface on extrapolation to the surface and the continuum value of the wall density from eq. 1; c_{di} is the density difference coefficient.

The coefficient c_{di} has been evaluated[7] through an approximate procedure using a linearized Boltzmann equation. For a dilute binary gas system of approximately equal molecular masses, c_{d2} may be shown to be

$$c_{d2} = \left(\frac{1 - 0.43\sigma_2}{\sigma_2}\right)2.40 \qquad (4)$$

where it is taken that[8] $D_{12} = 1.204\mu/\rho$, $\mu = 0.499\rho\bar{c}l$, which is exact for mechanically similar molecules. The coefficient σ_2 has the definition

$$\sigma_2 = \frac{N_2^-(a) - N_2^+(a)}{N_2^-(a) - N_{2eq}^+(a)} \qquad (5)$$

where $N_2^-(a)$ and $N_2^+(a)$ are, respectively, the actual fluxes toward and away from the surface. N_{2eq}^+ represents the value of the outward flux if all molecules 2 left in equilibrium with the surface. Thus a value $\sigma_2 = 1$ means all molecules 2 leaving the surface are in equilibrium with the surface. A value $\sigma_2 = 0$ indicates no incident molecule is adsorbed by the surface but is specularly reflected.

(7) J. R. Brock, *J. Catalysis*, 2, 248 (1963).

(8) S. Chapman and T. G. Cowling, "Mathematical Theory of Non-Uniform Gases," Cambridge University Press, London and New York, 1951.

A semimacroscopic derivation gives an expression for c_{di} with no restriction on the molecular masses for a binary system undergoing equimolar counter diffusion at a surface

$$c_{di} = \left(\frac{2 - \sigma_i}{\sigma_i}\right) \frac{2D_{12}}{\bar{c}_i l} \tag{6}$$

where $\bar{c}_i$ is the mean molecular velocity of i of the binary mixture and l is the over-all molecular mean free path for the mixture. The density differences for the two components are simply related for this case

$$n_1 - n_1^c = -\frac{\sigma_2 \bar{c}_2}{\sigma_1 \bar{c}_1}(n_2 - n_2^c) + \frac{(\sigma_1 - \sigma_2)}{\sigma_1 \bar{c}_1} 2D_{12} \frac{dn_2}{dr}$$

Combining eq. 1 and 3 we obtain the total rate of evaporation or condensation in the slip-flow regime

$$\Phi = \frac{4\pi D_{12} a[n_2^c(a) - n_2(\infty)]}{1 + c_{d2}\left(\frac{l}{a}\right)} \tag{7}$$

Under the assumption that for the continuum regime there is interfacial equilibrium, then $n_2^c(a) = n_{2eq}(a)$.

For practical application of the density difference boundary condition, the problems of calculation of reliable values of c_{di} are such that at present one must regard c_{di} as an empirical constant to be determined from experiment. Note that even where exact calculation for the gas phase for a particular molecular model has been carried out, eq. 4, the surface adsorption coefficient σ_2 has an empirical introduction. No *a priori* methods are at present available for the calculation of such coefficients, although evaporation and condensation rates are well known to be influenced strongly by the surface state.

The rate of evaporation or condensation of a spherical body in a binary gaseous system with general dynamical states of the gas phase may be described approximately in the slip-flow regime through application of the continuum mass, momentum, and energy equations together with the full set of slip-flow boundary conditions at the surface as given by eq. 3 for the density difference and as given previously by the author[9,10] for the temperature-jump and velocity-slip. Thus, given the set of slip-flow boundary conditions, the slip-flow description of the evaporation and condensation of spherical bodies becomes, usually, a trivial extension of the continuum description.

As a simple illustration of the application of additional slip-flow boundary conditions, let us examine here the question of the temperature of the drop (which will determine the value n_2^c) when cooling or heating of the drop occurs owing to evaporation or condensation. We assume there is no average velocity in the gas as before.

At the quasi-steady condition we have for the conduction heat flux

$$-\lambda_f \frac{dT_f}{dr} 4\pi r^2 = \Phi\eta_2 \tag{8}$$

where λ_f is the gas phase thermal conductivity, $\Phi\eta_2$ is the total heat flow, and η_2 is the heat of vaporization or condensation of 2. We have in addition the following relation for slip-flow between the drop temperature, T_s, and the gas temperature, T_f, at the surface

$$T_f - T_s = c_t l \left(\frac{dT_f}{dr}\right)_{r=a} \tag{9}$$

where c_t is the temperature-jump coefficient. Combining eq. 8 and 9 and integrating, we obtain for the total heat flow

$$\Phi\eta_2 = \frac{4\pi\lambda_f a[T_s - T_f(\infty)]}{1 + c_t\left(\frac{l}{a}\right)} \tag{10}$$

Hence T_s is the temperature at which $n_2^c(a)$ is to be evaluated for the drop of pure 2.

However, when the heat flow by radiation is important, this contribution must be accounted

$$\Phi\eta_2 = \frac{4\pi\lambda_f a[T_s - T_f(\infty)]}{1 + c_t\left(\frac{l}{a}\right)} + R \tag{11}$$

Of course, the form of R must depend on the conditions surrounding the drop In the simplest case of the effectively infinite body of gas with containment surfaces at $T_f(\infty)$ in radiant equilibrium with and surrounding the droplet at T_s, we have for R

$$R = 4\pi a^2 \sigma[\epsilon_s T_s^4 - \alpha_s T_f^4(\infty)] \tag{12}$$

where ϵ_s and α_s are the radiation emissivity and absorptivity coefficients for the drop and σ is the Stefan-Boltzmann constant.

Equations 7 and 12 give the total rate of condensation or evaporation in terms of the surface properties of the drop and the concentration of 2 well removed from the surface. With the noted restrictions on the state of the gas phase and known values of c_{d2}, c_t, ϵ_s, and α_s, these two equations will be found to describe approximately the evaporation and condensation of the spherical drop for $0 < (l/a) < \sim 0.25$.

(9) J. R. Brock, *J. Colloid Sci.*, **17**, 768 (1962).

(10) J. R. Brock, *ibid.*, **18** 489 (1963).

The extension of these considerations to multi-component gas systems is easily performed. Inasmuch as no new factors are introduced for multi-component systems, they will not be considered in detail here.

Evaporation and Condensation in the Transition Regime

For the transition regime $0.25 < (l/a) < 10$, no simple description of evaporation or condensation is available. For all physical systems involving the transfer of mass, momentum, and energy, no general methods have been found as yet for the transition regime.

Evaporation and Condensation in the Free-Molecule Regime

In the discussion of the slip-flow regime above, it is to be noted that the spherical body has a paramount influence on the state of the surrounding gas and it is, therefore, not possible to specify an arbitrary state for the gas.

For the free-molecule regime, $(l/a) > 10$, the simplification appears that the spherical body is so small that it does not affect the state of the surrounding gas. Hence the effect of arbitrary states of the gas on the evaporation or condensation may be accounted quite easily in this regime.

We shall present here, principally for completeness of the discussion, expressions for evaporation and condensation rates in the free-molecule regime. Some of the results are interesting in their implication in the problem of droplet growth in the atmosphere.

Consider the region of a dilute binary gas mixture surrounding a rigid spherical body where, for generality, both components of the mixture are evaporating or condensing. It will be assumed that the velocity of advance or regression of the surface owing to evaporation or condensation is negligible relative to the mean molecular velocity. Also, it will be assumed that the surface properties of the spherical body have no angular dependence.

In the region of the body, the state of the gas is specified by assigning number densities, n_i^-, temperature, T^-, mass velocity, $\vec{q}$, and gradients, ∇n_i, ∇T^-, $\nabla \vec{q}$. It will be taken that the over-all gas density is such that all fluxes in the gas may be accounted by expressions linear in the gradients. A reference coordinate system is taken fixed in the spherical body.

With the specification above, the distribution functions, f_i^-, for the gas surrounding the spherical body have the form

$$f_i^- = f_i^{(0)-}\{1 - \vec{A}_i \cdot \nabla \ln T - \vec{D}_i \cdot \vec{d}_{12} - \vec{\vec{B}}_i : \nabla \vec{q}\} \quad (13)$$

where $f_i^{(0)-} = n_i^-(\beta_i^-/\pi)^{3/2} \exp[-\beta_i^-\{(v_i - q)^2\}]$, $\beta_i^- = (m_i/2kT^-)$, and $\vec{v}_i$ is the molecular velocity vector of species i. The functions $\vec{A}_i$, $\vec{D}_i$, $\vec{\vec{B}}_i$ are defined and discussed elsewhere[9,10] to the level of approximation chosen here.

For the molecular flux calculations, the distribution functions, f_i^+, for the molecules leaving the surface are defined by

$$f_i^+ = \sigma_i f_i^{(0)+} + (1 - \sigma_i) f_i^- \quad (14)$$

where σ_i is previously defined and

$$f_i^{(0)+} = n_i^+ \left(\frac{\beta_i^+}{\pi}\right)^{3/2} \exp[-\beta_i^+ v_i^2] \qquad \beta_i^+ = (m_i/2kT^+) \quad (15)$$

The total rate of evaporation or condensation of the spherical body is given by the expression

$$\Phi = \sum_{i=1}^{2} \Phi_i = \sum_i \int_s d\vec{S}\vec{n} \cdot \sum_{\pm} \int_{\pm} \vec{v}_i f_i^{\pm} dv_i \quad (16)$$

where

$$\int_{\pm} \equiv \text{sign } (\vec{n} \cdot \vec{v}_i) \int_{-\infty}^{\infty} \int_{-\infty}^{\infty} \int_0^{\text{sign } (\vec{n} \cdot \vec{v}_i)}$$

and $\vec{n}$ is the unit surface normal. It is apparent that the calculations which follow may be readily extended to convex bodies of otherwise arbitrary shape.

A simplification in the calculation of Φ is found with the restriction

$$2\beta_i \vec{v}_i \cdot \vec{q} \ll 1 \quad (17)$$

that is, when the magnitude of the mass average velocity is small relative to that of the mean molecular velocity. For this approximation we obtain for the over-all rate of evaporation the following expression from eq. 13, 15, and 16.

$$\Phi = \Phi_1 + \Phi_2 = 2\pi a^2 \left\{ \sum_{i=1}^{2} \sigma_i \left[n_i^+ \left(\frac{2kT^+}{\pi m_i}\right)^{1/2} - n_i^- \left(\frac{2kT^-}{\pi m_i}\right)^{1/2} \right] + \sum_{i=1}^{2} \frac{8}{3} \sigma_i (2\pi m k T^-)^{-1/2} \rho - D_{12} \vec{q} \cdot \nabla \omega_i - \sum_{i=1}^{2} \sigma_i \frac{2}{\pi^{1/2}} \frac{n_i a_i}{T} \vec{q} \cdot \nabla T \right\} \quad (18)$$

where $\omega_i = \rho_i/\rho$ is the mass fraction of i. For the situation where the thermal conductivity, λ, of the mixture does not vary appreciably from that of each pure component, the last term on the right may be written

$$\Sigma\sigma_i \frac{2}{\pi^{1/2}} \frac{n_i a_i}{T} \vec{q}\cdot\nabla T = -\left[\sigma_1 n_1 + \sigma_2 n_2 \left(\frac{m_2}{m_1}\right)^{1/2}\right] \frac{8\lambda}{5\pi n} \frac{1}{kT\left(\frac{2kT}{\pi m_i}\right)^{1/2}} \vec{q}\cdot\nabla T$$

An order of magnitude calculation reveals that the last two terms on the right of eq. 18 are of negligible order except for extremely large density and temperature gradients. Contributions of inertial terms have previously been disregarded as of order q^2.

An interesting feature of eq. 18 is that there are no contributions to the net flux of first order in $\vec{q}$ or the gradients. Thus for small relative $|\vec{q}|$ and gradients the evaporation and condensation rates in the free-molecule regime are completely specified, as will be seen, for the gas phase by n_i^- and T^-. The only effect to first order in $\vec{q}$ is the indirect one of changing the local environment n_i^-, T^- of the body.

Equation 18, however, is not completely determinate; n_i^- and T^- (as well as $\vec{q}$, $\nabla\omega_i$, and ∇T) are regarded as specified. However n_i^+ and T^+ are not arbitrary but have values prescribed by eq. 18 and the over-all heat flux, $\Phi\eta$ of the evaporating or condensing body. With the approximation of eq. 17 we have for $\Phi\eta$, neglecting contributions proportional to $\vec{q}\cdot\nabla\omega_i$, $\vec{q}\cdot\nabla T$ *and assuming only translatory communicable energy*

$$\Phi\eta = \sum_{i=1}^{2} \Phi_i\eta_i = 4\pi a^2 \sum_i \tau_i \left[n_i^+ kT^+ \left(\frac{2kT^+}{\pi m_i}\right)^{1/2} - n_i^- kT^- \left(\frac{2kT^-}{\pi m_i}\right)^{1/2}\right] + R \quad (19)$$

where η_i is the heat of vaporization or condensation of species i and τ_i is the thermal accommodation coefficient[9] of species i. R, as in eq. 11, represents the contribution to the over-all heat flow by radiative processes. The particular form of R will depend on a more complete specification of the body environment. In terms of present notation for the environmental assumption discussed in eq. 12, R has the form, by way of example

$$R = 4\pi a^2\sigma[\epsilon_s(T^+)^4 - \alpha_s(T_\infty)^4] \quad (20)$$

Equations 18 and 19 now form a determinate set for Φ. For a given binary composition x_i^s of the body surface, $n_i^+ = n_i^+(T^+, x_i^s)$ and the relation is assumed to be the appropriate equilibrium one for the surface. T^+ is, of course, determined by eq. 18 and 19 in terms of the various independent parameters in the equations.

If one of the components of the binary gas system does not undergo condensation or evaporation on adsorption by the surface, then eq. 18 and 19 must be modified. Let 1 be the inert component. Then we have (neglecting the last two terms on the right of eq. 18)

$$\Phi_1 = 0$$

giving the specific relation for n_1^+

$$n_1^+ = n_1^-(T^-/T^+)^{1/2} \quad (21)$$

to be applied in eq. 19 for the over-all heat flow. n_2^+ is assumed specified as before as the value corresponding to the equilibrium vapor pressure. Thus Φ is completely determined in the instance where one of the components of the binary system is inert by eq. 18, 19, and 21.

We may consider the condensation and evaporation rates more generally by relaxing the assumption of eq. 17. In this case we obtain contributions to Φ of all orders in $\vec{q}$. The effect of including all orders of $\vec{q}$ seems of principal importance and we shall confine ourselves to this consideration and regard contributions involving the gradients as of negligible order. The inclusion of the gradients would be quite simple.

With this view, on relaxing the assumption of eq. 17 we obtain for Φ

$$\Phi = 2\pi a^2 \sum_{i=1}^{2} \sigma_i \left[n_i^+ \left(\frac{2kT^+}{\pi m_i}\right)^{1/2} - n_i^- \left(\frac{2kT^-}{\pi m_i}\right)^{1/2} \times \{(1+\beta_i^- q^2)E_0(\beta_i^- q^2) - \beta_i^- q^2 E_2(\beta_i^- q^2)\}\right] \quad (22)$$

where

$$E_n(\beta_i^- q^2) \equiv \int_0^1 d\xi \xi^n e^{-\beta_i^- q^2 \xi^2} = -\frac{1}{2\beta_i^- q^2}\{e^{-\beta_i^- q^2} - (n-1)E_{n-2}(\beta_i^- q^2)\}; \quad n = 2, 4, 6, \cdots$$

$$E_0(\beta_i^- q^2) = \left(\frac{\tau}{\beta_i^-}\right)^{1/2} \frac{1}{2|\vec{q}|} \operatorname{erf}\{(\beta_i^-)^{1/2}|\vec{q}|\} \times \operatorname{erf}\{(\beta_i^-)^{1/2}|\vec{q}|\} = \frac{2}{\pi^{1/2}} \int_0^{(\beta_i^-)^{1/2}|\vec{q}|} d\xi e^{-\xi^2}$$

and are tabulated functions.

For the over-all heat flow we obtain

$$\Phi\eta = \sum_{i=1}^{2} \Phi_i\eta_i = 4\pi a^2 \sum_i \tau_i \left[n_i^+ kT^+ \left(\frac{2kT^+}{\pi m_i}\right)^{1/2} - n_i^- kT^- \left(\frac{2kT^-}{\pi m_i}\right)^{1/2} \left\{\left(\frac{\beta_i^- q^2}{2} + 1\right) E_0(\beta_i^- q^2) + \frac{\pi^{1/2}}{4}\left(\beta_i^- q^2 + \frac{5}{2}\right)\beta_i^- q^2 [E_0(\beta_i^- q^2) - E_2(\beta_i^- q^2)]\right\}\right] \quad (23)$$

For two condensing or evaporating components, eq. 22 and 23, as in the linear case, form a determinate

set for Φ. For an inert component, 1, for example, the additional condition, $\Phi_1 = 0$, together with eq. 22 and 23 completely determine Φ.

The extension of these results to multicomponent systems is readily performed. No new basic results are introduced. Accounting for an angular dependence of the surface properties of the spherical body presents no difficulty if this dependence can be specified. So long as the shape of the body remains convex, for a given time-dependent change in shape whose rate is small relative to the mean molecular velocity eq. 18 and 19 or 22 and 23 are easily modified, but no new basic considerations are introduced. The results presented here may be considered as adequate to describe evaporation or condensation of a collection of spherical bodies in the free-molecule regime so long as the distance, d, between the surfaces of the various bodies is such that $(l/d) \backsim 0$.

Conclusions

If the condensed surface properties are known, evaporation and condensation rates for a spherical body for completely general gas phase dynamical states may be calculated in the slip-flow, $0 < (l/a) < \sim 0.25$, and free-molecule, $(l/a) > 10$, regimes with the methods outlined here. Methods for calculation of evaporation and condensation rates are under study at present for the transition regime, $0.25 < (l/a) < 10$.

The major uncertainty in these various evaporation and condensation calculations, as has long been recognized in continuum calculations, is the prediction of the condensed surface properties, such as σ_i and τ_i. These surface properties are of greater importance in noncontinuum than in continuum considerations and hence are perhaps more easily studied experimentally for the free-molecule regime. Further experimental determinations of surface properties are needed, but equally important is the development of *a priori* methods for prediction of surface properties.

Acknowledgment. The author wishes to thank Prof. P. G. Wright, Queen's College, Dundee, for calling the author's attention to this problem, and the National Science Foundation for support through Grant G19432.

Free-Molecule Drag on Evaporating or Condensing Spheres

by James R. Brock

Department of Chemical Engineering, The University of Texas, Austin, Texas *(Received February 17, 1964)*

The free-molecule drag on evaporating or condensing spheres is discussed. A gas–surface interaction parameter specifying the fraction of impinging molecules adsorbing on a surface but not undergoing condensation is introduced. The evaluation of this parameter from experimental free-molecule drag measurements is proposed.

Introduction

The problem of calculating the free-molecule drag on various bodies has received attention by several investigators.[1-3] The theory seems to be in fair agreement with the existing experimental data, although one finds here the ubiquitous difficulty of the specification of the gas–surface interaction.

In connection with a part of an accompanying paper in which the free-molecule evaporation or condensation of spherical bodies is investigated, a question has arisen concerning the free-molecule drag on such spherical bodies. Accordingly, we consider here the

(1) L. Waldmann, *Z. Naturforsch.*, **14a**, 589 (1959).
(2) M. Heineman, *Commun. Pure Appl. Math.*, **1**, 259 (1948).
(3) P. S. Epstein, *Phys. Rev.*, **23**, 710 (1924).

free-molecule drag on an evaporating or condensing sphere in a gas mixture whose state is specified by number densities, n_i^-, temperature, T^-, and mass velocity, $\vec{q}$. It will be noted in the discussion that appropriate experimental free-molecule drag measurements can be used to obtain fundamental information on the condensation process at a surface.

Free-Molecule Drag Description

For calculation of the free-molecule drag, we require the velocity distribution functions at the sphere surface for impinging molecules, f_i^-, and emitted molecules, f_i^+.

The function f_i^- for the physical system specified above is simply

$$f_i^- = n_i^- \left(\frac{\beta_i^-}{\pi}\right)^{3/2} \exp[-\beta_i^-\{(\vec{v}_i - \vec{q})^2\}] \quad (1)$$

where $\beta_i^- = m_i/kT^-$.

The function f_i^+ is determined from a knowledge of the gas molecule–surface interaction. The simple one-parameter specification of this interaction given in the accompanying paper is not, however, sufficient for the drag calculation.

For the drag calculation we introduce a parameter δ_i which is the total fraction of incoming molecules of species i adsorbed by the surface. By adsorbed molecule we mean here that the molecule achieves the temperature of the surface. We could introduce an additional parameter to distinguish between momentum and energy accommodation; such a procedure will receive later, brief consideration. The fraction $(1 - \delta_i)$ is assumed specularly reflected from the surface. Of the fraction δ_i we further distinguish fractions α_i adsorbed but not undergoing condensation and $(1 - \alpha_i)$ adsorbed and condensing.

Thus an absolute condensation coefficient, γ_i, is, in terms of δ_i and α_i

$$\gamma_i = \delta_i(1 - \alpha_i)$$

and we have no possibility of learning anything experimentally concerning δ_i and α_i individually from measurements of condensation and evaporation rates alone. We shall see here, however, that drag measurements make possible the determination of δ_i and α_i when only one component of a gas mixture is undergoing condensation at a surface.

f_i^+, then, has the form

$$f_i^+ = \delta_i\alpha_i\bar{f}_i^{(0)+} + \delta_i(1 - \alpha_i)\bar{\bar{f}}_i^{(0)+} + (1 - \delta_i)f_i^-(\vec{v}_i') \quad (2)$$

where

$$\bar{f}_i^{(0)+} = \bar{n}_i^+ \left(\frac{\beta_i^+}{\pi}\right)^{3/2} \exp(-\beta_i^+ v_i^2) \quad (3)$$

$$\bar{\bar{f}}_i^{(0)+} = \bar{\bar{n}}_i \left(\frac{\beta_i^+}{\pi}\right)^{3/2} \exp(-\beta_i^+ v_i^2) \quad (4)$$

$$\vec{v}_i' = \vec{v}_i - 2\vec{n}(\vec{n}\cdot\vec{v}_i\cdot) \quad (5)$$

and $\vec{n}$ is the outwardly directed surface normal.

Further, we require that

$$n_i^+ = \bar{n}_i^+ + \bar{\bar{n}}_i^+$$

where

$$\bar{\bar{n}}_i^+ = \bar{\bar{n}}_i^+(T^+, x_j^s) \qquad j = 1, 2, \ldots \nu - 1 \quad (6)$$

which is taken as the appropriate thermodynamic relation for the surface composition. T^+ may be calculated as described in the accompanying paper from the over-all evaporation or condensation equations. n_i^+ is calculated from the requirement

$$\vec{n}\cdot\left\{\int_+ \vec{v}_i \bar{f}_i^{(0)+}\, dv_i + \int_- \vec{v}_i f_i^-\, dv_i\right\} = 0 \quad (7)$$

$$\int_\pm \equiv \text{sign}\,(\vec{n}\cdot\vec{v}_i) \int_{-\infty}^{\infty}\int_{-\infty}^{\infty}\int_0^{\text{sign}(\vec{n}\cdot\vec{v}_i)\infty}$$

The free-molecule drag, $\vec{\Delta}$, on the evaporating or condensing sphere is given by the expression

$$\vec{\Delta} = -\sum_i \left\{\int_s dS\vec{n}\cdot\sum_\pm \int_\pm m_i\vec{v}_i\vec{v}_i f_i^\pm\, dv_i\right\} \quad (8)$$

Applying eq. 1 and 2 in eq. 8 we obtain the following expression for $\vec{\Delta}$

$$\vec{\Delta} = \sum_i 2a^2 n_i^-(2\pi m_i kT^-)^{1/2}[(1 + \beta_i^- q^2)E_0(\beta_i^- q^2) + E_2(\beta_i^- q^2) - \beta_i^- q^2 E_4(\beta_i^- q^2) + \delta_i\left\{\frac{1}{2}E_0(\beta_i^- q^2) - \frac{3}{2}\left(1 + \frac{2}{3}\beta_i^- q^2\right)E_2(\beta_i^- q^2) - \frac{1}{2}\beta_i^- q^2 E_4(\beta_i^- q^2)\right\} + \frac{2}{3}\delta_i\alpha_i\frac{\pi}{4}\left(\frac{T^+}{T^-}\right)^{1/2}]\vec{q} \quad (9)$$

$$E_n(\beta_i^- q^2) \equiv \int_0^1 d\xi\, \xi^n e^{-\beta_i^- q^2\xi^2}$$

which becomes for $1 >> \beta_i^-\vec{v}_i\cdot\vec{q}$

$$\vec{\Delta} = \sum_i \frac{8}{3}a^2 n_i^-(2\pi m_i kT^-)^{1/2} \times \left[1 + \delta_i\alpha_i\frac{\pi}{8}\left(\frac{T^+}{T^-}\right)^{1/2}\right]\vec{q} \quad (10)$$

Discussion

It may be seen then that appropriate experimental measurements on evaporating or condensing spheres

can be used to determine the two parameters δ_i and α_i. The experiments would be of the following form. For convenience we consider a drop of a pure substance j in a gas mixture of none or more noncondensing species and j. The condensation coefficient, $\sigma_j = \delta_j(1 - \alpha_j)$, is determined from the over-all evaporation or condensation rate as given in the accompanying paper. From drag measurements without j in the gas, in the instance of noncondensing gases, the δ_i ($\alpha_i = 1$), $i \neq j$, are determined from eq. 9 or 10. Finally, drag measurements with j present would then determine $\delta_j\alpha_j$. Thus from these measurements δ_j and α_j are separately determinable.

Aside from the experimental difficulty, there is some uncertainty in this described method. We have not distinguished momentum and energy accommodation. In the previous paper in calculating the total heat flow to an evaporating or condensing sphere, the molecules were assumed to have only translational communicable energy, aside from the latent condensation or evaporation energy. For such molecules it does not appear necessary to distinguish between momentum and energy accommodation. However, for polyatomic molecules with other forms of communicable energy, such a division may be in order. We might then say that of the fraction $\delta_i\alpha_i$ a fraction $\delta_i\alpha_i\epsilon_i$ achieves momentum accommodation alone and a fraction $\delta_i\alpha_i(1 - \epsilon_i)$ momentum and energy accommodation.

On introduction of the parameter ϵ_i, eq. 9 would have the form

$$\vec{\Delta} = \sum_i 2a^2 n_i^- (2\pi m_i k T^-)^{1/2} \Big[(1 + \beta_i^- q^2) E_0(\beta_i^- q^2) + E_2(\beta_i^- q^2) - \beta_i^- q^2 E_4(\beta_i^- q^2) + \delta_i \Big\{ \frac{1}{2} E_0(\beta_i^- q^2) - \frac{3}{2}\left(1 + \frac{2}{3}\beta_i^- q^2\right) E_2(\beta_i^- q^2) - \frac{1}{2}\beta_i^- q^2 E_4(\beta_i^- q^2) \Big\} + \frac{2}{3}\delta_i\alpha_i\epsilon_i \frac{\pi}{4}\left(\frac{T^+}{T^-}\right)^{1/2} + \frac{2}{3}\delta_i\alpha_i(1 - \epsilon_i)\frac{\pi}{4} \Big] \hat{q} \quad (11)$$

In view of the empirical nature of δ_i, α_i, ϵ_i and also of even the question of the correctness of describing the gas–surface interaction by such parameters, the validity of this further division is in need of examination.

However, it does seem of interest to have some measure, even empirically, of the fraction of those molecules striking the surface which are adsorbed but do not undergo condensation. Careful free-molecule measurements on evaporating or condensing bodies, as suggested here, could be made to yield such information.

We make the additional observation that analogous considerations could be applied, for example, to a sphere on whose surface a catalytic reaction occurs. From free-molecule drag measurements on such a sphere one could determine some measure of the fraction of impinging reactant molecules which are adsorbed but do not undergo reaction.

Acknowledgment. The author wishes to thank the National Science Foundation for support through Grant G19432.

Liquid–Liquid Phase Separation in Alkali Metal–Ammonia Solutions. I. Lithium, Potassium, Rubidium, with New Data on Sodium

by Paul D. Schettler, Jr., and Andrew Patterson, Jr.

Contribution No. 1724 from the Sterling Chemistry Laboratory, Yale University, New Haven, Connecticut
(Received July 30, 1963)

Phase diagrams are presented for the liquid–liquid phase separation of lithium and potassium solutions in liquid ammonia. Solutions of lithium separate into two phases at temperatures below −63.5° in the range of concentration between approximately 0.02 and 0.09 g.-atom of lithium/mole of ammonia. Separation of potassium solutions is observed below −70° in the range of concentration including approximately 0.02 and 0.07 g.-atom of potassium/mole of ammonia. Solutions of rubidium in liquid ammonia have not been observed to separate into two phases at temperatures above the freezing point of ammonia and at concentrations including those at which lithium, sodium, and potassium do so. Visual observations of the phenomenon of phase separation are reported which explain previous anomalous results in solutions of this type. Data on phase separation in sodium–ammonia solutions at previously unreported temperatures and concentrations are included as well.

It is commonly stated that one of the characteristics of alkali metal–liquid ammonia solutions is to exhibit separation into two immiscible liquid phases. This statement appears to be based principally on the behavior of sodium–ammonia solutions, for which phase diagrams have been reported and on which extensive studies have been made.[1-3] On more careful examination of the literature, however, one finds the evidence for phase separation among solutions of the other alkali metals uncertain and contradictory. Thus, Hodgins and Flood report visual observations and resistivity measurements as evidence for phase separation in lithium solutions,[4] pointing out that Kraus and Johnson[5] had already given convincing evidence of the separation from vapor pressure–concentration measurements, and amending the statement of Birch and MacDonald,[6] who stated that lithium–ammonia solutions do not show phase separation, to read "liquid–liquid phase separation above −78° is exhibited by all alkali metal solutions except *cesium* . . ." in view of Hodgins' extensive work on cesium[7] and brief tests on lithium.[4] However, it is not possible to construct any more than a guess at a phase diagram from the data available on lithium solutions.[4,5,8] The data on potassium are even more fragmentary, there being no report of visual observation of phase separation, although vapor pressure and warming curve data[6] suggest that it may occur. Observations of phase separation have been made in potassium solutions to which potassium iodide has been added, in a temperature range of −31 to −35°.[9] In spite of what is implied by Hodgins and Flood's statement quoted above,[4] there is no report of any determination on rubidium.

(1) C. A. Kraus and W. W. Lucasse, *J. Am. Chem. Soc.*, **44**, 1949 (1922).

(2) O. Ruff and J. Zedner, *Ber.*, **41**, 1948 (1908).

(3) R. A. Ogg, Report to the Office of Naval Research, Physics Branch, 1947, included results for lithium and potassium. The work has not been published. Also, the dissertation of D. E. Loeffler, Stanford University, 1949, includes similar material. M. J. Sienko has disclosed these results at Lille, France, Colloque Weyl, June, 1963.

(4) J. W. Hodgins and E. A. Flood, *Can. J. Res.*, **27B**, 874 (1949).

(5) C. A. Kraus and W. C. Johnson, *J. Am. Chem. Soc.*, **47**, 731 (1925).

(6) A. J. Birch and D. K. C. MacDonald, *Trans. Faraday Soc.*, **44**, 735 (1948).

(7) J. W. Hodgins, *Can. J. Res.*, **27B**, 861 (1949).

(8) P. R. Marshall and H. Hunt, *J. Phys. Chem.*, **60**, 732 (1956).

(9) D. D. Cubicciotti, *ibid.*, **53**, 1302 (1949).

The present paper reports measurements on solutions of lithium, potassium, and rubidium in liquid ammonia, and some additional data on sodium.[10] Extreme care has been taken to prepare solutions free of materials other than the alkali metal and ammonia, both to assure the stability and long life of the solutions and to exclude additional components which have a profound effect on the temperature and concentration ranges in which phase separation is observed.[10]

Experimental

Two rather different means of determining the phase diagram have been used. The method most often used by other investigators to ascertain whether phase separation has occurred is to measure the conductance of a solution as the temperature is changed and to await a jump in the measured quantity.[1] With the intention only of making some preliminary measurements on potassium, we undertook to use a straightforward visual observation of phase separation. From these visual observations, we concluded that (for potassium at least) uncertainties in conductance measurements may well have been due to the peculiar surface tension behavior of these solutions and especially to the manner of phase separation. The phase separation studies on potassium have, therefore, been made entirely visually, as will be described. In the case of solutions of lithium, a more refined measurement technique which separates the two phases and permits analysis of both phases has been employed.[10] In all cases, the distillation of ammonia and alkali metals has been conducted in a high vacuum system from which undesired contaminants have been rigorously excluded and in which, apart from the component being distilled, a vacuum in excess of 10^{-6} torr is maintained. All glassware which came in contact with the metal, liquid ammonia, or the finished solution was cleaned prior to use by successive treatment in alcoholic potassium hydroxide solution, fuming nitric acid–concentrated sulfuric acid mixture, and distilled water followed by drying in an oven.

For the measurements on potassium the apparatus in Fig. 1 was employed. The tube A was evacuated to 10^{-6} torr, heated at 300° overnight, and previously prepared potassium metal (Mallinckrodt 6692) was triple distilled from a measured length of capillary through a succession of sausage-shaped tubes into tube A. Triple-distilled ammonia, dried over sodium, was distilled into tube A, following which the tube was sealed and separated from the vacuum system. The separated tube was kept at −196° until it was needed, and then inserted in a short length of rubber tubing which was attached to a longer length of Pyrex tubing

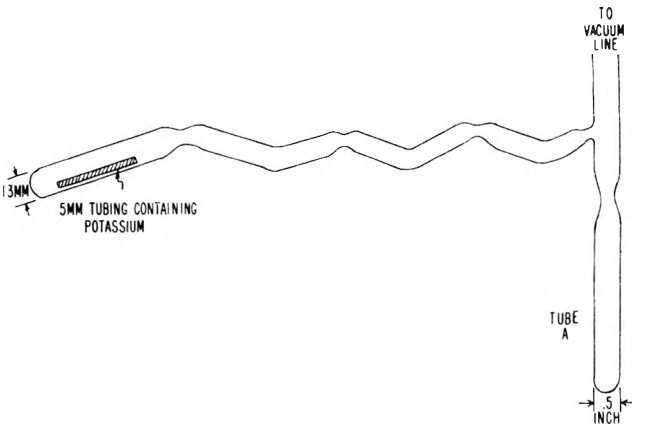

Figure 1. Schematic diagram of glass apparatus used for preparation of potassium–ammonia sample.

of the same diameter as tube A for a handle. The sealed tube and handle were immersed in a thermostat made from a dewar flask containing 4 l. of cold ethanol stirred by a mechanical stirrer. The temperatures were measured by short-range alcohol thermometers calibrated to better than 0.1° against a platinum resistance thermometer. The tube was shaken periodically, and times up to 10 min. allowed for attainment of equilibrium before the tube was removed momentarily from the bath for inspection to see if one or two phases existed. If two phases were found, a higher temperature was tried; if only one, a lower temperature. When the approximate temperature of phase separation was found, it was fixed more precisely by picking temperatures alternately slightly above it and then below it. The maximum temperature of phase separation was judged to have been found when it was boxed in as described by at least two points 0.1° apart and with several points no more than a few tenths of a degree above and below this temperature such that all those above showed only one phase, and all those below, two phases. To eliminate errors caused by the experimenter subjectively anticipating the temperature reading, the thermometer was not read until after the one- or two-phase observation was made. Of about 350 individual readings, only three were inconsistent. This lends assurance to the visual observation of phase separation.

Temperature control was achieved by adding to the alcohol bath small amounts of powdered Dry Ice through a wire strainer at about 30-sec. intervals, varying the amount of Dry Ice added and the intervals between addition as dictated by the rate of deviation of the thermometer from the desired temperature.

(10) P. D. Schettler, Jr., and A. Patterson, Jr., *J. Phys. Chem.*, **68**, 2870 (1964).

Temperatures could be kept constant to within ±0.05° for any necessary length of time.

After measurements on one tube were completed, it was weighed and frozen in liquid nitrogen. Reaction of the potassium with the ammonia could then conveniently be checked by using a Oudin coil leak tester; in nearly every tube prepared, and for all those reported here, the characteristic pale, dirty green electrical discharge in ammonia vapor was still clearly visible, indicating that very little, if any, decomposition had taken place, with attendant hydrogen evolution. The tubes were then opened, the ammonia allowed to evaporate into a stream of nitrogen gas, the contents oxidized in air, and the residue titrated to the carbonate end point with standard acid. The ammonia was determined by difference in weight between the full and empty tube. The reproducibility of temperature measurement was such that the most probable cause of scatter of the points (see Results) is difficulty with the analysis. Further, nearly half the tubes exploded at some point during the air oxidation, so the method was discarded for a more satisfactory one described below.

For the measurements on lithium, a different piece of glassware was used, except for measurements at the critical point, where the method used above was employed, though with a more elaborate thermostat.[10] The glass apparatus, Fig. 1, ref. 10, has also been used in phase separation studies of sodium–liquid ammonia with and without added sodium iodide.[10] It allowed the separation and sampling of the two phases in an inert atmosphere and at a precisely controlled and measured temperature. Lithium (K and K Laboratories, 99.9% pure) wire was measured off and the contaminating coating removed with a paint scraper under heptane which had previously been dried with sodium and swept free of nitrogen by passing argon through it. The bright, freshly scraped, and still wet piece of lithium was then quickly transferred to the preparation bulb which had already been filled with argon and the remaining heptane removed in a stream of argon. The apparatus, already attached to the vacuum system, was immediately sealed and evacuated for an extended period. Ammonia, previously purified, was then added in the amount desired while the preparation bulb was cooled in Dry Ice–alcohol, followed by the addition of purified helium at about 650 torr pressure. The apparatus was then sealed from the vacuum system and removed to a low temperature thermostat controlled to 0.01° or better. The detailed operation of the apparatus is described elsewhere.[10] Briefly, by inverting the apparatus and lowering a float, separate samples of the two phases were obtained. Since the two phases could be separated at a measured temperature, duplicate determinations are possible for the points lying below the consolute temperature. The separated tubes were frozen in liquid nitrogen, opened, the ammonia evaporated by a stream of carbon dioxide-free helium, and the lithium decomposed in a stream of water vapor. Conductivity water was then added, a protective atmosphere of butane placed in the titration flask, and a straightforward acid–base titration conducted. The end point was determined with a differential electrode or acid–base indicator. The entire procedure was much more satisfactory than that used for potassium. The amount of ammonia was determined, as before, from the weight of the sealed tube before and after opening.

For the preparation of rubidium metal, rubidium chloride (K and K Laboratories, 99.8%) was reduced by calcium metal filings in the side tube shown in Fig. 1. At temperatures near the softening point of Pyrex glass, reaction of an intimate mixture of powdered calcium and rubidium chloride took place in less than an hour. Flame photometric analyses of the residue indicated about 94% yield of the rubidium. The mixture had to be degassed with great caution in advance of the distillation, this being facilitated by placing the entire apparatus (similar to Fig. 1) inside a controlled oven. In one determination a Faraday tube arrangement was used in place of tube A so that a range of concentrations and temperatures could quickly be surveyed with one preparation of solution.

Results

The determinations are shown in Table I and are plotted, together with data for sodium,[1] in Fig. 2. To the data on sodium we have added points which result from other studies on sodium–ammonia solutions as noted in the legend. The two points at −75° are extrapolated a slight distance from a measured concentration of sodium iodide to zero sodium iodide.[10] The two points at −55.5° are direct determinations.[10] For lithium the consolute temperature is −63.5 ± 0.2° and the consolate composition is 0.0451 ± 0.005 g.-atom of lithium/mole of ammonia. For potassium the consolute temperature is −70.0 ± 0.4° and the consolute composition is 0.0455 ± 0.005 g.-atom of potassium/mole of ammonia. In our determinations on rubidium, a tube was prepared and analyzed to contain 0.0545 g.-atom of rubidium/mole of ammonia; although this concentration is close to that for phase separation in lithium, sodium, and potassium, we were unable to detect liquid–liquid phase separation at any temperature above that at which the ammonia froze, approximately −78°. In the preparation made with a

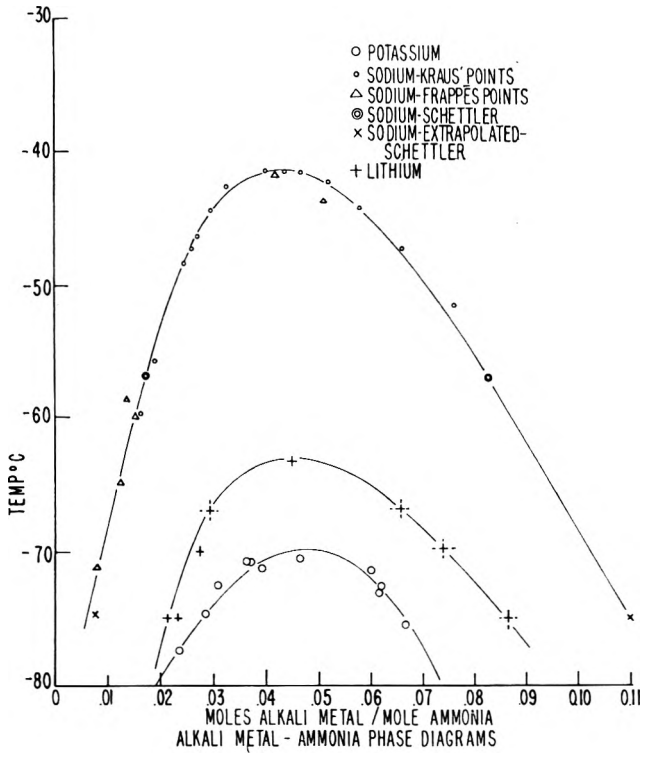

Figure 2. Plot of phase data for lithium and potassium, with Kraus's data for sodium (small circles). The data of Frappé ("Phenomenes de transports electriques dans les solutions sodium–ammoniac liquide," D. E. S. Lille, 1958) are shown as triangles. Data of Schettler (ref. 10) shown as × (−75°) are extrapolated from finite to zero concentration of sodium iodide; those shown as concentric circles (−56.5°) are actual determinations on sodium. Lithium data shown as extended crosses are double points indistinguishable on the scale of the graph.

Faraday tube, we were unable to detect phase separation within a range of concentration including 0.02 to 0.10 g.-atom of rubidium/mole of ammonia and temperatures above the freezing point of the ammonia. From these experiments we conclude that phase separation for rubidium in all probability does not exist, and that a miscibility gap, if any, is too small and too close to the freezing point of the solution to be detected by visual means, which as we shall describe below is the most sensitive test we have been able to devise.

Discussion

When we attempted to repeat some of the observations reported by other workers we soon found that phase separation is much more easily observed in a tube of diameter relatively small compared to the depth of solution in it, while in a spherical bulb it is quite commonly not visible at all. Kraus[1] relates that his method for sodium was restricted to certain

Table I: Temperature of Initial Separation as a Function of Concentration

Temp. of initial separation	Conen — Mole ratio	Conen — m
	Lithium in liquid ammonia	
−75.00	0.02337	1.372
−75.00	0.02611	1.533
−70.00	0.02786	1.635
−67.00	0.02979	1.749
−67.00	0.02966	1.741
−63.51[a]	...	...
−63.31[a]	0.04509	2.648
−67.00	0.06580	3.868
−67.00	0.06611	3.882
−70.00	0.07472	4.3875
−70.00	0.07497	4.402
−75.00	0.08576	5.036
−75.00	0.08614	5.058
	Potassium in liquid ammonia	
−77.5	0.0239	1.403
−74.8	0.0284	1.668
−72.7	0.0308	1.8086
−71.2	0.0389	2.284
−70.9	0.0370	2.173
−70.6	0.0365	2.143
−70.6	0.0465	2.730
−71.4	0.0598	3.511
−72.6	0.0620	3.641
−73.2	0.0614	3.605
−75.5	0.0667	3.917
	Sodium in liquid ammonia	
−56.5	0.08212	4.822
−56.5	0.08180	4.803
−56.5	0.01734	1.018
−56.5	0.01698	0.997
−75.0[b]	0.008	0.4
−75.0[b]	0.11	6.4

[a] These samples were determined by the visual method as with potassium. [b] These data were extrapolated from finite concentration of sodium iodide to zero sodium iodide. See ref. 10.

ranges of concentration and temperature. In particular, he obtained small irregularities around the consolute temperature and large deviations at temperatures more than 20° below the consolute point. Our observations suggest that the reason for these difficulties lies in the surface-wetting and surface tension characteristics of the solutions. It thus appears desirable to recount some of our qualitative observations.

In what follows, the comments are equally applicable to lithium, sodium, and potassium. The less dense, concentrated metallic phase has a bronze luster with a reddish violet appearance, more so when the solution

is concentrated or saturated and when the solution is viewed directly on its surface rather than in contact with the glass tube. The more dense, dilute phase has the typical inky blue color. The contrast between the two phases is greatest at lower temperatures, and becomes progressively less sure as one moves toward the consolute temperature. When the composition is near this temperature, but two phases are present, the blue phase is observed to adhere to the glass and to "wet" it more effectively than does the concentrated phase. When a tube was withdrawn from the cold bath a two-phase solution would look as if it were composed completely of dilute phase, but within a few seconds the layer of dilute solution would slide down the glass sides revealing two phases. No doubt this phenomenon is the source of reports that there is no visible difference between phases, and one can anticipate it would cause trouble in resistance measurements to determine the presence of two phases. With solutions high in total metal content, the first droplet of dilute phase would form, not at the bottom of the tube, but as a ring just under the surface of the concentrated phase where it met the glass tube, at the edge of the meniscus.

When the solutions are frozen to liquid nitrogen temperature, the lithium solution retains its bronzy appearance, while the others become blue-gray crystalline masses.

The behavior of rubidium requires special comment. In the Faraday tube arrangement, the concentration could be varied conveniently over a range of fivefold, from 0.02 to 0.1 g.-atom of rubidium/mole of ammonia. The temperature was varied from that of Dry Ice in alcohol upward several degrees through use of an intermediate thermostat of liquid ammonia. The more concentrated solutions were bronzy, the more dilute blue. At no time was an interface observed which signified phase separation. Distilled portions of the ammonia solvent were prone to freeze on the walls of the tube mixed with the blue, dilute solution and then to melt and run down suddenly on warming a fraction of a degree, thus giving an appearance not unlike that described for phase separation in the other solutions at higher temperatures. This behavior never gave rise to a clear-cut phase boundary. On this evidence, we have concluded that with the most sensitive means of observation at our disposal, phase separation is not seen in rubidium–ammonia solutions above the temperature at which the ammonia freezes.

Acknowledgment. We are particularly indebted to M. le Chanoine Gérard Lepoutre, who assisted in much of this work, criticized it, and suggested the visual method for determining the potassium diagram. We thank also the National Science Foundation for their support.

Liquid–Liquid Phase Separation in Alkali Metal–Ammonia Solutions. II. Sodium with Added Sodium Iodide

by Paul D. Schettler, Jr.,[1] and Andrew Patterson, Jr.

Contribution No. 1741 from the Sterling Chemistry Laboratory, Yale University, New Haven, Connecticut
(Received August 5, 1963)

Results are presented for the effect on the phase separation of solutions of sodium in liquid ammonia of adding varying amounts of sodium iodide. The measurements were performed at −33.35, −56.50, and −75.00°. Apparatus is described which makes possible the convenient preparation and separation of these solutions under conditions guaranteeing their long life and freedom from undesired impurities, plus the analysis of both phases for all components. The results are discussed.

Introduction

Studies by Cubicciotti[2a] and Sienko[2b] have indicated a marked effect on the temperature of phase separation of the addition of small amounts of salt in the systems $Na–NH_3–NaI$ and $K–NH_3–KI$. The work of these authors showed that the addition of the iodide decreased the metal concentration in the dilute phase of the two-phase solutions, and that the preponderance of the salt appeared in the dilute phase. The tendency of metal–ammonia solutions to decompose under any but the most extreme conditions of chemical purity and rigorous exclusion of catalytically active materials, plus the large effect of the added salt, and in all probability of any products of decomposition, prompted us to undertake a study of the phase separation in sodium–liquid ammonia solutions with added sodium iodide which is reported in this paper, with the intention of improving the manipulative details to permit analysis of both phases for all components and to permit performance of all operations under high vacuum with precise temperature control. In addition to accomplishing these goals, with an accompanying increase in precision of the data, we have covered a wider range of concentrations of the components and of temperature in the study than has heretofore been reported.

Experimental

In Fig. 1 is shown a diagram of the glass apparatus used, incorporating several desirable features. It can be evacuated and baked out at high temperature; all distillations and separations can be conducted in an inert atmosphere or under high vacuum; it is semi-automatic in its function, and effects a complete and clear-cut separation of the two phases; the solutions can be removed for analysis of all components. The operation of the device can best be discussed after a brief description of its preparation. Tube D was made from 0.25-in. medium-wall Pyrex tubing. The section at K was made in two stages so that the very end was extremely thin. The tiny glass ball at the end is important for two reasons: it makes accidental breaking of the tip easily detectable, and it appears to make the tip easier to break at will. At the opposite end, a constriction as small as practicable was left at L and the tube sealed to a vacuum system inside an oven. After thorough bake out, it was filled with purified helium to about 250 torr and sealed off. Glass-enclosed magnet F was immediately attached. The remainder of the apparatus was then assembled. All glass used was cleaned by soaking in potassium hydroxide in ethanol, rinsing in water, soaking in a mixture of concentrated nitric and sulfuric acids, rinsing in distilled water, and drying in an oven. The object shown in bulb C is a magnetic stirrer. When completed, the device was sealed to a high vacuum system

(1) This paper is taken in part from a dissertation submitted to the Graduate School, Yale University, in partial fulfillment of the requirements of the Ph.D. degree, September, 1963.

(2) (a) D. D. Cubicciotti, *J. Phys. Chem.*, 53, 1302 (1949); (b) M. J Sienko, *J. Am. Chem. Soc.*, 71, 2707 (1949).

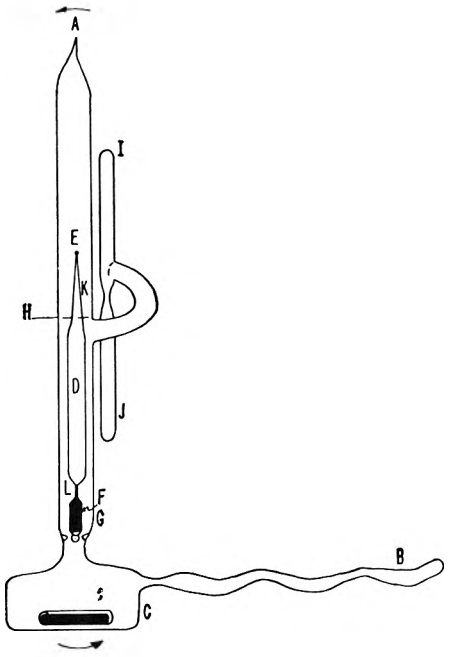

Figure 1. Schematic diagram of glass apparatus used for preparation of three-component solutions of sodium, sodium iodide, and liquid ammonia. The same device has been used for lithium–ammonia solutions. See ref. 3.

at A inside a controlled oven, but with the distillation tube for the alkali metal, B, protruding outside into the room. The vacuum system had arrangements for triple distillation, drying, and measuring of the ammonia. A weighed sample of sodium iodide (Mallinckrodt A.R.) was placed directly in bulb C, when required, before the apparatus was sealed. The alkali metal contained in a measured portion of glass capillary was sealed into tube B. The assembly inside the oven was heated to 300° under high vacuum for a number of hours to remove water from the salt and from the glass walls; at the same time the sodium was melted out of the capillary. The apparatus was cooled after bake out and the sodium distilled from one section of tube B to the next, and finally into C. After a measured quantity of ammonia had been distilled into bulb C, the apparatus was filled with helium to about 650 torr pressure. The helium was purified with activated charcoal at liquid nitrogen temperature. The device was then sealed from the vacuum system and placed in a low temperature thermostat. (The same device has been used for preparation of lithium solutions[3] for a study of phase separation in lithium–ammonia solutions.)

The thermostat permitted excellent temperature control and measurement and will accordingly be of interest to other investigators working with moderate-sized equipment at low temperatures. It consisted of a stirred bath of jet aircraft fuel JP-4 mounted inside a Revco SZC-657 ultra low temperature cabinet. A copper-lined plywood box was used for the bath. The oil was agitated by stirrers mounted externally on an insulated top made to fit the freezer. Jet fuel JP-4 remains fluid at the lowest temperatures attainable with the freezer; the viscosity increases from 0.82 cp. at 25° to 1.1 cp. at −75°, or from about that of water to about 40% more than that of water. The low viscosity made stirring effective at all temperatures. The electrical insulating properties are good and are maintained in spite of the inevitable condensation of small amounts of water in the bath liquid. Temperature control was obtained by setting the deep freeze at a value suitably below that desired in the bath and supplying intermittent heat to the bath with an electrical heater operated from a Mueller bridge in a much simplified version of the arrangement suggested by Fuoss, *et al.*[4] The circuit diagram is given in Fig. 2

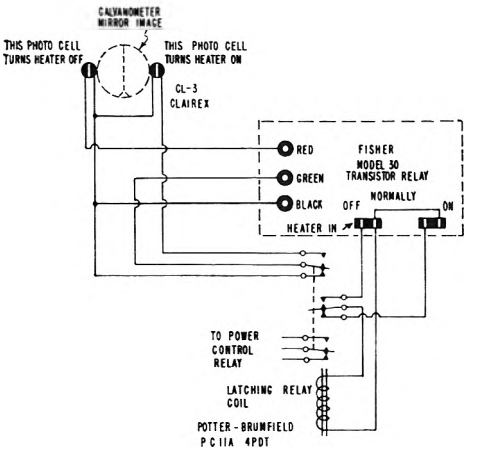

Figure 2. Wiring diagram for thermostat regulator. The photoconductive cells are mounted on an aluminum and plastic block (see Fuoss, ref. 4) which can be hung on the galvanometer scale to intercept the light spot but leave the spot free for visual observation of bridge balance; the block is moved to the desired position after Mueller bridge balance is obtained. When the contacts of the latching relay are in the position shown, the heater is on, and only the photocell on the left will operate the circuit. The Fisher relay must be switched to the "normally open" and "delay off" positions. The heater or heater control relay may be plugged into the "normally off" plug marked "heater in" or wired to additional contacts of the latching relay. A variable transformer used to control the heater input power is not shown here.

(3) P. D. Schettler, Jr., and A. Patterson, Jr., *J. Phys. Chem.*, **68**, 2865 (1964).

(4) J. J. Zwolenik, J. Lind, and R. M. Fuoss, *Rev. Sci. Instr.*, **30**, 575 (1959).

and the operation is explained in the legend. Temperature stability quite equivalent to that commonly possible near room temperature could be maintained, in the order of $\pm 0.01°$ or better, at any of the operating temperatures chosen. The platinum resistance thermometer and bridge were used for precise temperature measurement. As a word of caution, JP-4 is appreciably volatile at room temperature and is prone to build up electrostatic potential when agitated, so one must guard against the fire and explosion hazard associated with its use.

If the amounts of metal and ammonia used and the proportion of the apparatus were correct, following thorough mixing of the solution and attainment of temperature equilibrium, it was then possible to place a magnet at G to hold tube D in place, turn the apparatus upside down in the direction of the arrows, and allow the solution to run down and fill the main tube to H. Tube D was then lowered by the outside magnet, causing a sample of the less-dense phase to be displaced and run down the spiral side arm into tube I. Tip E was then sharply rapped against A with the magnet, breaking E. The pressure differential existing in the device caused tube D to fill half full of the denser phase. The apparatus was then rotated into its upright position in the direction opposite to the arrows, causing the concentrated phase to run into tube J and D to return to its original position. The remaining unseparated solution was discarded into C. Sealed tubes of each phase were then obtained by placing the apparatus in a flask of Dry Ice–alcohol and sealing off J at the constriction. The main tube of the device was then cut just above H, and tube D was removed and sealed at K. The solution was briefly exposed to possible entry of air at this point. While reaction with the air is not of any analytical consequence, loss of ammonia was very small, since tip E was extremely fine, the net motion of helium at the moment of opening was into tube D, and the vapor pressure of ammonia at $-78°$ is low. The sealed tubes were allowed to reach room temperature, washed in distilled water, dried, and kept for a period until they were weighed. They were then frozen in liquid nitrogen, broken open near the upper end, and the ammonia was allowed to evaporate into a stream of purified nitrogen. The metal was then oxidized in a stream of water vapor at reduced pressure; the pieces of glass were removed and carefully washed, dried, and weighed, and a titration conducted on the solution remaining with standard nitric acid. Titration was then made for iodide with standard silver nitrate solution. All titrations were conducted under an atmosphere of butane.

Results

The results are given in Table I and are plotted in Fig. 3. The temperatures used were -33.35, -56.50, and $-75.00°$. By extrapolating data at $-75°$ to zero sodium iodide concentration, values for the phase separation of sodium at this temperature have been obtained and are reported in ref. 3. At $-56°$ pairs of points with no sodium iodide present were included in the determinations, also reported in ref. 3. Data of Cubicciotti[2a] and Sienko[2b] are reproduced in Fig. 4, plotted in the same manner as Fig. 3, for comparison.

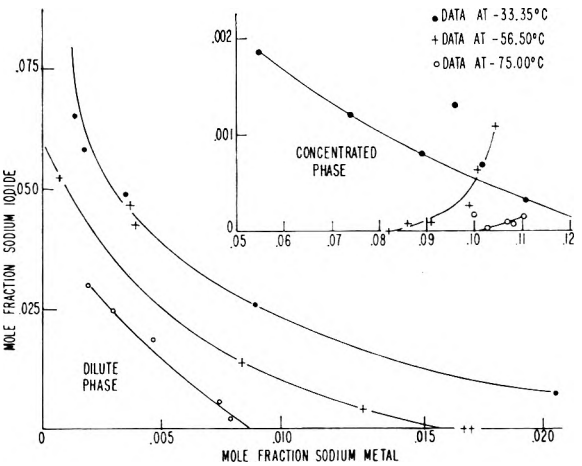

Figure 3. Plots of the data of Table I as mole fraction of sodium iodide *vs.* mole fraction of sodium metal for concentrated and dilute phases. Notice that the abscissa on the concentrated phase diagram does not start at zero mole fraction of sodium metal.

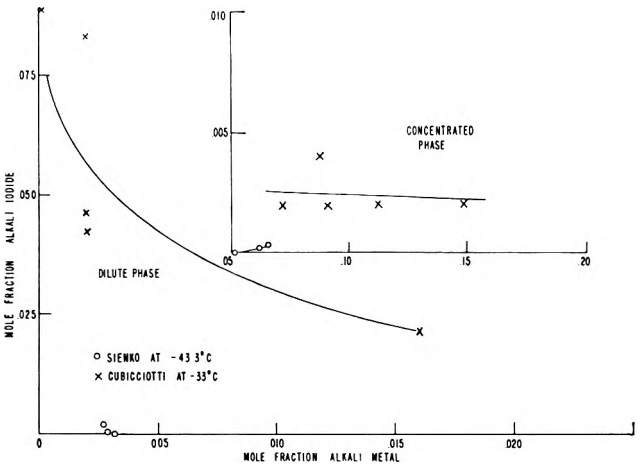

Figure 4. Plots of the data of Cubicciotti[2a] and Sienko[2b] as mole fraction of sodium iodide *vs.* sodium metal (or potassium iodide and potassium metal) for the concentrated and dilute phases. Notice that the abscissa on the concentrated phase diagram does not start at zero mole fraction of metal.

Table I: Phase Separation Data on Sodium–Sodium Iodide–Liquid Ammonia Solutions

Dilute phase		Concentrated phase	
N_2[a]	N_3	N_2'	N_3'
Temp. −75.00°			
0.007974	0.00255	0.09890	0.0001670
0.007406	0.006283	0.10265	0.0
0.003723	0.01906	0.10656	0.000118
0.002955	0.02500	0.10777	0.0000911
0.001975	0.03021	0.11072	0.0001665
Temp. −56.60°			
0.01705	0.0	0.07589	0.0
0.10670	0.0	0.07592	0.0
0.01349	0.000492	0.086421	0.0001437
0.008406	0.01243	0.09106	0.0001886
0.00395	0.04264	0.09937	0.0002633
0.00362	0.04702	0.10198	0.000652
0.0006123	0.05240	0.1045	0.0010806
Temp. −33.35°			
0.02061	0.007593	0.05493	0.00186
0.008996	0.02664	0.07411	0.00123
0.003552	0.04855	0.08946	0.000793
0.001707	0.05833	0.09618	0.001306
0.001497	0.06529	0.1014	0.000559
0.001183	0.08767	0.1161	0.000305

[a] N_2 = mole fraction sodium metal; N_3 = mole fraction sodium iodide. Unprimed quantities refer to dilute phase, primed to concentrated phase.

Discussion

The curves for the dilute phase are similar to each other, concave upward with negative slopes. They intercept the $N_3 = 0$ axis (zero sodium iodide) depending on whether the temperature is below or above the consolute temperature of the two-component diagram. At each temperature, as the sodium iodide concentration increases, the sodium concentration decreases. The concentrated-phase curves do not show such regularity. At −75° only a very small amount of silver nitrate was required to reach the iodide end point, the results are scattered, the experimental uncertainty in the iodide concentration is large, and no consistent trend of the results is apparent; the sodium concentration remains constant within 10%, although the concentration is comparatively large and tends toward larger values as the sodium iodide concentration in the dilute phase increases. At −56° the amount of sodium iodide in the concentrated phase shows a definite increase with increasing total sodium iodide and the sodium concentration increases as well. At −33° this trend is partly reversed, for the sodium iodide concentration decreases as the total added iodide concentration increases, but there is a relatively large increase in the sodium concentration.

An attempt at interpreting these data should start, ideally, with a calculation of the concentrations of all the species present in each phase and an analysis of the equality of the chemical potentials of each of these in each phase as the criterion for the possible existence of two phases in equilibrium with each other. The number of species present in each phase is considerable, including, according to a recent proposed model,[5] the following: Na^0, Na^+, Na_2^0, e^-, and $(Nae^-)^-$. All these species are in equilibrium with each other *via* three equilibrium reactions. Equilibrium constants for the interactions between these several species have been derived by Arnold over a range of temperature, although the precision and the limited temperature range of the experimental data used in calculating them restrict the number of significant figures in these constants and the temperature range over which they may be meaningfully applied. In principle, however, it is feasible to calculate the concentrations of all species in each phase, with due respect to the activities of the species. Practically, this can be done only for the dilute phase, and there with limited precision, for the concentrations are nearly ten times larger than those for which the calculation may be expected to be valid. The concentrated phase is far too concentrated to permit a meaningful calculation, although it is quite clear that in both phases the concentrations of the M^+ ion, M_2 dimer, and diamagnetic M' center are decidedly larger than those of the electron and the neutral atom. Sodium iodide is appreciably ionized in ammonia solution, though not completely so, and data on its degree of ionization at these concentrations are unavailable. Having all these data at hand, however, it still seems clear that there are at least a large, if not infinite, number of values of these equilibrium concentrations which might satisfy the requirements, whatever they may be, for the simultaneous existence of two liquid phases. The only experimentally available quantities are Na^0_{total} and I^- in each phase.

In the face of these several difficulties, some approximations can be attempted which may guide further study.

As a first approximation, Onsager[6] has suggested that a solubility product expression might correlate the data. While it is apparent from the discussion of the first paragraph that this will not hold at all temperatures studied, at −75° the expression $[Na^+][e^-] =$

(5) E. Arnold and A. Patterson, *J. Chem. Phys.*, accepted for publication; E. Arnold, Dissertation, Yale University, 1963. Arnold's terminology for the centers present is M, M^-, M_2, e, and M′, respectively.

(6) L. Onsager, private communication.

k, or the equivalent $(N_2 + N_3)(N_2)$ can be calculated, assuming complete ionization and lack of any associative reactions. Refer to Table II, in which are compared a number of products and quotients of ion concentrations; column A contains data calculated as just suggested. In such an approach the concentrated phase is regarded as analogous to the solid phase of a slightly soluble salt, and the ion product is written for the species in solution. As common ion is added, sodium "precipitates" into the concentrated phase. The concentration products so obtained vary from the mean by +22 to −24%. If the second and fifth points are omitted as excursions beyond experimental error (they cancel each other out in the calculation of the mean), then the variation is +2 to −0.6% from the mean. In the concentrated solution in equilibrium with the dilute phase, column B, the influence of N_3 is small even though the data are scattered, since N_3 is much smaller than N_2. As shown in B, there is a continuous trend from smaller to larger values of this product, of which note should be taken below in reference to column E.

The general dissatisfaction which one feels with this approach need hardly be remarked. Although it is true that activities and possible association reactions have been neglected, it is possibly more serious to neglect the suggestion that the value of $[Na^+][e^-]$ should be equal in the two phases, rather than equal to a constant, as has just been assumed. That is, if the activity coefficients do not change too rapidly with concentration, and barring complications from the many solution species present, the activities should be equal in the two phases and the ratio of the concentration products $[Na^+][e^-]$ in the two phases should equal a constant. Column C, representing the quotient of columns B/A, is a test of this possibility. The quotient varies more severely than does either column A or B if the five points in column A are included, or about the same as column A if the second and fifth points are excluded.

If one takes the theoretical calculations of Arnold, which have been performed for −33.5° as the lowest temperature owing to the scarcity of experimental data as noted above, extrapolates his graphs to the higher concentrations represented in the solutions here dealt with, and reads off values of $[Na^+]$ and $[e^-]$ corresponding to the concentrations of total sodium found in this paper (see Table I) at −75°, and calculates their products, one obtains the values shown as columns D_1 (dilute phase) and E (concentrated phase). The products found in column D_2 are obtained by adding to $[Na^+]$ the additional concentrations of Na^+ found in solution if the sodium iodide were wholly ionized in the solvent and multiplying by the same $[e^-]$ as in column D_1. The quotients of columns D_1 and D_2 divided into the theoretical ion products for the concentrated solutions (E) are given as columns F_1 and F_2. One may justify the use of data at −33.5° by noting that there are no inversions or changes of slope of the equilibrium constants as a function of decreasing temperature (see ref. 6); accordingly, although the concentrations are in error, their trend as a function of concentration is not markedly incorrect, and since they are used in ratios as normalizing functions only, no harm is done if the fact is kept in mind that the theoretical and experimental data are for different temperatures.

Column D_1 thus obtained varies widely; it must be kept in mind that in the solution under consideration, for which Na^0_{total} has been determined experimentally, this quantity was decreasing because Na^+ was being added in the form of sodium iodide. To compensate

Table II: A Variety of Ion Product and Quotient Calculations for Phase Separation

A. Dilute solution $(N_2 + N_3)(N_2)$[a]	B. Concentrated solution $(N_2 + N_3)(N_2)$[a]	C. (Ion prod.)$_{concd}$/(ion prod.)$_{dil}$ (B/A)[a]
8.38×10^{-5}	9.79×10^{-3}	1.17×10^{2}
10.1	10.53	1.04
8.47	11.37	1.34
8.27	11.62	1.40
6.33	12.27	1.93
Mean: 8.32×10^{-5}	Mean: 11.12×10^{-3}	Mean: 1.38×10^{2}
Dev.: +22, −24%	Dev.: +10, −12%	Dev.: +39, −24%

D_1, D_2.[b] Dilute solution $[Na^+][e^-]_{theor}$[c]		E. Concentrated solution $[Na^+][e^-]_{theor}$[c]	F_1, F_2. (Ion prod.)$_{concd}$/(ion prod.)$_{dil}$ (E/D_1, D_2)$_{theor}$[c]	
2.20	5.09×10^{-3}	7.56×10^{-2}	3.43	1.48×10^{1}
1.95	8.74	7.94	4.07	0.91
0.761	16.8	8.32	10.9	0.50
0.578	18.6	8.51	14.7	0.46
0.370	18.1	8.77	23.7	0.48
Mean: 1.17;	13.4×10^{-3}	Mean: 8.22×10^{-2}	Mean: 11.4;	0.77×10
Dev.: +88, −68%; +62, −24%		Dev.: +6.7, −8.0%	Dev.: +108, −70%; + 92, −40%	

G. (Ion prod.)$_{theor}$[c]/(ion prod.)$_{concd}$[d] (E/B)
7.72
7.54
7.32
7.32
7.12
Mean: 7.41
Dev.: +4.2, −3.5%

[a] These data are derived from Table I at −75°. [b] Column D_2 includes $[Na^+]$ from the added sodium iodide, assuming complete ionization. [c] Theoretical values are all for a temperature of −33.5°, and are taken from Arnold; see ref. 5. [d] The theoretical ion product is for calculations at −33.5° while the experimental data are for −75°.

for this, column D_2 has been calculated. The variation in the product is here somewhat less, but the trend is toward larger values of the product with increasing N_3. In the concentrated solution, column E, the behavior of which should correspond closely to that of column B, the trend is toward larger values of the product as the sodium iodide concentration in the dilute phase increases. Column F_2 is a numerical test of the way in which column C might have been expected to vary if our rather inadequate theoretical guidance were significant. The direction of the variation is reversed and the values of F_2 vary much more than do those in C. Were activity data available for the sodium iodide, this situation would be improved.

Finally, in column G are shown the quotients of the data in column E, theoretically derived and without complications of sodium iodide being present, divided by the data in column B, which are experimental and essentially (because of the very small amount of sodium iodide in the concentrated phase) under the same circumstances. These quotients are substantially constant, appreciably more so than any of the raw data found elsewhere in Table II. This is not surprising, since this is the situation in which the assumption of constancy of activities and noninterference in the complex equilibria by the added sodium and iodide may be expected to hold.

Similar calculations have been performed for the other temperatures, but the data are even less consistent, and, of course, there is no theoretical guidance to explain the inversion of the order of the values of N_3' at -56 and $-33°$.

Franklin and Kraus[7] have reported measurements of the degree of ionization of sodium iodide at $-33°$ derived from conductance studies. The range of concentrations covered does not extend as high as those involved in column D_1, nor are the data given for $-75°$; however, to demonstrate that if activity data were available considerable improvement would result in the character of calculations such as those in Table II, we have recalculated column D_2 with activities extrapolated from Kraus's data, ranging from degrees of dissociation of 0.36 to 0.15. Instead of values of D_2 between 5.09 and 18.1 $\times 10^{-3}$, mean 13.4 $\times 10^{-3}$ with deviations from the mean of $+62$ to -24%, we obtain values between 3.85 and 3.03 $\times 10^{-3}$, mean 3.41 $\times 10^{-3}$ with deviations of $+13$ and -11%.

Not only is the constancy of quotient columns E and B of interest, but it should be observed that the trend in each is toward larger values of the product $[Na^+]\cdot[e^-]$ as the concentration of sodium in the concentrated phase rises. Constancy of this product is not to be expected in either dilute or concentrated phases, owing to the interplay of the equilibria between other solute species also present. Indeed, it does not appear from Arnold's results that any other combination of concentration product functions will remain constant, for $[e^-]$ is increasing in this range of concentration more slowly than any other quantity. Accordingly, until one can compute or determine activities, any approach such as attempted in Table II is bound to fail. Further, in a system with as many degrees of freedom as here represented, it is not likely that each activity in one phase must be identical with that of the same specific solution species in the other phase.

Acknowledgment. This work was supported by the National Science Foundation.

(7) E. C. Franklin and C. A. Kraus, *J. Am. Chem. Soc.*, **27**, 191 (1905).

Boron Isotope Exchange between Boron Fluoride and Its Alkyl Halide Complexes. I. Relation between Equilibrium Constant of Isotopic Exchange Reaction, Stability, and Catalytic Activity of Boron Fluoride Complex

by Ryohie Nakane, Osamu Kurihara, and Akiko Natsubori

The Institute of Physical and Chemical Research, Bunkyo-ku, Tokyo, Japan *(Received December 30, 1963)*

Equilibrium constants of boron isotope exchange between boron fluoride gas on one side and boron fluoride–*t*-butyl chloride, –isopropyl chloride, and –methyl fluoride complexes on the other are found as 1.033, 1.021, and 1.026 at −112°. Toluene is found to be readily alkylated with *t*-butyl chloride as well as alkyl fluoride in the presence of boron fluoride. Moreover, it is suggested that if the equilibrium constant becomes large, the polarity of the complex will increase; hence, the stability and catalytic activity of the complex will become high. This leads to the following conclusion: boron fluoride–*t*-butyl chloride, –methyl fluoride, –methyl chloride, and –isopropyl chloride complexes are polar complexes, and the polarity of these complexes decreases in the order: $BF_3 \leftarrow ClC(CH_3)_3$ > $BF_3 \leftarrow FCH_3$ > $BF_3 \leftarrow ClCH(CH_3)_2$, $BF_3 \leftarrow ClCH_3$. The aromatic constituent reacts with boron fluoride–*t*-butyl chloride complex by a nucleophilic displacement reaction.

Introduction

Aromatic compounds are alkylated with alkyl halides in the presence of metal halides (Friedel–Crafts catalysts). Brown, *et al.*,[1] proved that in these reactions the aromatic constituent reacts with a polar alkyl halide–metal halide complex, $R\overset{\delta+}{X}\rightarrow\overset{\delta-}{M}X_3$ by a nucleophilic displacement reaction, although for tertiary alkyl halides which are easily ionized, they assumed the formation and reaction of a different carbonium ion complex, $R^+MX_4^-$.

The existence of metal halide–alkyl halide complexes has been proved by many studies. Olah, *et al.*,[2] found polar alkyl fluoride–boron fluoride complexes by measuring the specific conductivity at low temperatures. These complexes can alkylate readily aromatic compounds, but it has been believed[3] that aromatic compounds cannot be alkylated with alkyl chloride in the presence of boron fluoride, the cause of which has been explained as due to the greater stability of BF_4^- than BF_3Cl^-.

Recently, some of the authors proved by measuring the equilibrium constant of isotopic exchange and the absorption spectrum that boron fluoride can form σ-complexes only with polar monoolefins such as propylene,[4] 1-butene,[5] and *cis*-2-butene[5] at low temperatures, while the σ-complex formation with nonpolar monoolefins such as ethylene[4] and *trans*-2-butene[5] cannot be found except only as very unstable π-complexes.

Some of the authors found also that the equilibrium constant of isotopic exchange between boron fluoride gas and the boron fluoride–methyl fluoride complex is 1.020 at −95° and believed that the exchange distillation of boron fluoride–methyl fluoride complex at low temperatures is a most promising method for the separation of boron isotopes.[6]

(1) H. C. Brown, H. W. Persall, L. P. Eddy, W. J. Wallace, M. Grayson, and K. L. Nelson, *Ind. Eng. Chem.*, **45**, 1462 (1953).

(2) G. Olah, S. Kuhn, and J. Olah, *J. Chem. Soc.*, 2174 (1957); G. A. Olah and S. J. Kuhn, *J. Am. Chem. Soc.*, **80**, 6541 (1958).

(3) R. L. Burwell and S. Archer, *ibid.*, **64**, 1032 (1942); G. F. Hennion and R. A. Kurz, *ibid.*, **65**, 1001 (1943); G. A. Russell, *ibid.*, **81**, 4834 (1959).

(4) R. Nakane, T. Watanabe, and O. Kurihara, *Bull. Chem. Soc. Japan*, **35**, 1747 (1962); R. Nakane, T. Watanabe, O. Kurihara, and T. Oyama, *ibid.*, **36**, 1376 (1963).

(5) R. Nakane, T. Watanabe, and T. Oyama, *ibid.*, **37**, 381 (1964).

In the present work, measurements of the equilibrium constants of isotopic exchange between boron fluoride gas and several boron fluoride–alkyl halide complexes were made and the alkylation of toluene in the presence of boron fluoride was examined with *t*-butyl chloride. The obtained equilibrium constants and catalytic activities of these complexes are compared with those of many other boron fluoride complexes, and the relation between the equilibrium constants and the catalytic activities of boron fluoride complexes is discussed again in detail.

Experimental

Materials. Commercial tank boron fluoride was purified by low temperature distillation in a column (40 cm. in length and 1.5 cm. in internal diameter) packed with 1.5-mm. Dixon gauze rings of stainless steel. Isopropyl chloride and *t*-butyl chloride were commercial products; they were fractionated by repeated bulb-to-bulb distillation *in vacuo*. Methyl fluoride was prepared from methyl tosylates by reaction with potassium fluoride by the method of Edgell, *et al.*,[7] and purified by low temperature distillation in the column mentioned above. Toluene, which was the purest commercial product obtainable, was used directly.

Measurement of Isotope Effect. Experimental methods were exactly the same as those described in the previous papers.[4,8]

Determination of single-stage separation factor is made by the following procedure. Known amounts of purified boron fluoride and alkyl halide were introduced into a flask of approximately 300 ml. with a break-seal. The flask was closed and immersed in a low temperature bath at the melting point of carbon disulfide (−112°) or toluene (−95°). A two-phase system composed of liquid boron fluoride–alkyl halide complex and gaseous boron fluoride was then produced in the flask. From the known volume of the flask and the total amounts of introduced boron fluoride and alkyl halides, m moles of boron fluoride in the gas phase and M moles of boron fluoride in the liquid phase were calculated. Since a large excess of boron fluoride in liquid phase was used, the determination of single-stage separation factor was made only by measuring the B^{10}/B^{11} ratio in the gas phase before and after the equilibration.

The flask was vigorously shaken by a shaker for approximately 2 hr., after which boron fluoride gas in the flask was sampled and directly analyzed with a mass spectrometer, and the isotopic ratios of B^{10} to B^{11} at the peaks for mass 10 and mass 11 were measured. From the analyzed values corrected by the effect of m/M, the single-stage separation factor α was obtained. The error in α was ±0.001, since a precision of about ±0.0005 for the isotopic ratios of B^{10} to B^{11} was obtained from mass analyses repeated 40 times.

Alkylation of Toluene with Boron Fluoride–t-Butyl Chloride Complex. *t*-Butyl chloride (0.03 mole) was dissolved in 0.06 mole of toluene, then 0.03 mole of boron fluoride was absorbed completely in this solution at −95°. When the solution was allowed to warm up to room temperature, gas evolved vigorously. The gas was sampled and analyzed with the mass spectrometer.

Results

The melting points of boron fluoride–isopropyl chloride and –*t*-butyl chloride 1:1 addition complexes were −136 and −87°. The melting point of the boron fluoride–methyl fluoride complex was −110° as observed by Oláh, *et al.*[2] These complexes were colorless (by Oláh, *et al.*, the colors of boron fluoride–propyl fluoride and –*t*-butyl fluoride complexes are both yellow) and dissociated by reversible reaction into their respective components when the temperature was raised, while colorless boron fluoride–ethyl fluoride complex produced a brown-colored polymer when left for a long time at room temperature.[6]

The values of a single-stage separation factor at −112° for several mole ratios of isopropyl chloride to boron fluoride in the liquid phase are shown in Table I. When the mole ratios are equal to or larger than 1, the value of the factor is 1.021, a constant independent of the mole ratio. However, when the mole ratio is smaller than 1, the values become smaller and the plot

Table I: Single-Stage Separation Factor of Boron Fluoride–Isopropyl Chloride System

Mole ratio of isopropyl chloride to boron fluoride in the liquid phase	Temp., °C.	Vapor press., mm.	Single-stage separation factor, α
0.25	−112	260	1.013 ± 0.001
0.50	−112	225	1.016 ± 0.001
0.75	−112	190	1.019 ± 0.001
1.00	−112	160	1.021 ± 0.001
1.00	−112	160	1.021 ± 0.001
2.00	−112	90	1.022 ± 0.001
2.00	−112	90	1.021 ± 0.001
3.00	−112	60	1.021 ± 0.001
2.00	−95	310	1.016 ± 0.001
3.00	−95	250	1.017 ± 0.001
3.00	−95	250	1.016 ± 0.001

(6) R. Nakane, S. Isomura, and O. Kurihara, presented at the 3rd Stable Isotope Congress, Leipzig, Germany, Oct. 30, 1963.

(7) W. F. Edgell and L. Parts, *J. Am. Chem. Soc.*, **77**, 4899 (1955).

(8) R. Nakane and O. Kurihara, *Sci. Papers Inst. Phys. Chem. Res.* (Tokyo), **56**, 161 (1962).

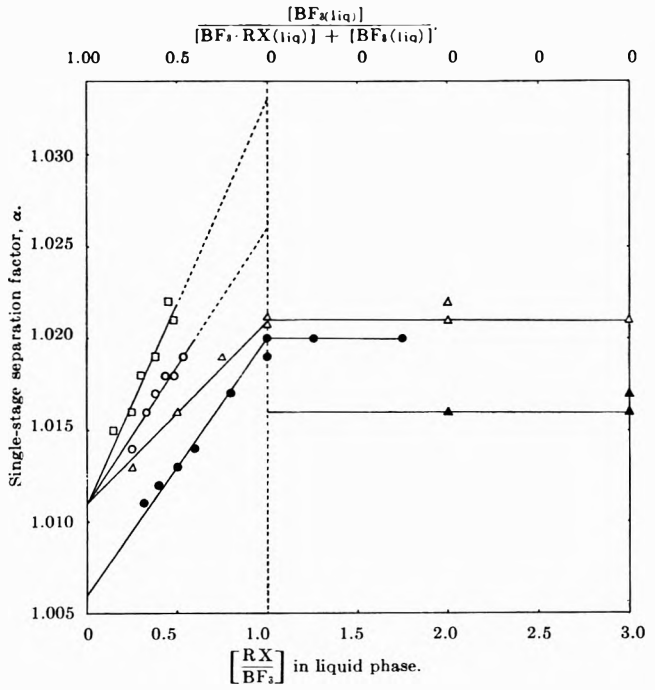

Figure 1. Single-stage separation factor *vs.* mole ratio of alkyl halide to boron fluoride in the liquid phase: ●, CH_3F at −95°; ○, CH_3F at −112°; ▲, *i*-C_3H_7Cl at −95°; △, *i*-C_3H_7Cl at −112°; □, *t*-C_4H_9Cl at −112°.

of the mole ratio *vs.* separation factor gives a straight line (Fig. 1).

This result can be explained as follows. By mass spectrometry, the gas was observed to be composed mostly of boron fluoride at −95 or −112°. Therefore, when in the liquid phase no free liquid boron fluoride exists, the isotopic exchange occurs only between gaseous boron fluoride and the liquid complex and the equilibrium constant of this isotopic exchange is given by

$$K_1 = \frac{[B^{10}F_3\cdot i\text{-}C_3H_7Cl_{(liq)}]}{[B^{11}F_3\cdot i\text{-}C_3H_7Cl_{(liq)}]} \Big/ \frac{[B^{10}F_{3(gas)}]}{[B^{11}F_{3(gas)}]} \quad (1)$$

However, if free liquid boron fluoride coexists with the complex, the isotopic exchange between gaseous boron fluoride and liquid boron fluoride occurs simultaneously and the equilibrium constant of this isotopic exchange is given by

$$K_2 = \frac{[B^{10}F_{3(liq)}]}{[B^{11}F_{3(liq)}]} \Big/ \frac{[B^{10}F_{3(gas)}]}{[B^{11}F_{3(gas)}]} \quad (2)$$

The equilibrium constant K_2 is known to be 1.011 at −112°.[4,8] In this system two isotopic exchanges must be involved and, hence, the obtained value of the single-stage separation factor α is given as a function of equilibrium constants K_1 and K_2 of both reactions as

$$\alpha = \frac{[B^{10}]_{liq}}{[B^{11}]_{liq}} \Big/ \frac{[B^{10}]_{gas}}{[B^{11}]_{gas}}$$

$$= \frac{[B^{10}F_3\cdot i\text{-}C_3H_7Cl_{(liq)}] + [B^{10}F_{3(liq)}]}{[B^{11}F_3\cdot i\text{-}C_3H_7Cl_{(liq)}] + [B^{11}F_{3(liq)}]} \Big/ \frac{[B^{10}F_{3(gas)}]}{[B^{11}F_{3(gas)}]}$$

$$= K_1 - (K_1 - K_2) \times \frac{[B^{11}F_{3(liq)}]}{[B^{11}F_3\cdot i\text{-}C_3H_7Cl_{(liq)}] + [B^{11}F_{3(liq)}]} \quad (3)$$

The concentrations of these isotopic molecules are given by

$$[B^{11}F_{3(liq)}] = a[BF_{3(liq)}] \quad (4)$$

$$[B^{11}F_3\cdot i\text{-}C_3H_7Cl_{(liq)}] = a'[BF_3\cdot i\text{-}C_3H_7Cl_{(liq)}] \quad (5)$$

in which a is nearly equal to a', for in a single-stage separation the change of isotopic abundance ratio is very small as given in Table I. Consequently

$$\alpha = K_1 - (K_1 - K_2)\frac{[BF_{3(liq)}]}{[BF_3\cdot i\text{-}C_3H_7Cl_{(liq)}] + [BF_{3(liq)}]}$$

$$= K_2 + (K_1 - K_2) \times \frac{[BF_3\cdot i\text{-}C_3H_7Cl_{(liq)}]}{[BF_3\cdot i\text{-}C_3H_7Cl_{(liq)}] + [BF_{3(liq)}]} \quad (6)$$

Since K_1 and K_2 are constants, the plot of α *vs.* $[BF_3\cdot i\text{-}C_3H_7Cl_{(liq)}]/([BF_{3(liq)}] + [BF_3\cdot i\text{-}C_3H_7Cl_{(liq)}])$ is a straight line and, when no free liquid boron fluoride exists, α is equal to K_1.

The obtained result shows the following facts. One mole of boron fluoride forms with one mole of isopropyl chloride the liquid 1:1 addition complex. When the mole ratio of isopropyl chloride to boron fluoride in the liquid phase is 1, the liquid phase is only of the complex. When it is larger than 1, the complex is dissolved into excess liquid isopropyl chloride. In these two cases, no free liquid boron fluoride exists and, thus, α obtained experimentally is equal to K_1, a constant; but when the mole ratio is smaller than 1, free liquid boron fluoride coexists with the complex in the liquid phase. In this case, the mole ratio of isopropyl chloride to boron fluoride in the liquid phase becomes equal to the mole fraction of complex in the liquid phase, $[BF_3\cdot i\text{-}C_3H_7Cl_{(liq)}]/([BF_3\cdot i\text{-}C_3H_7Cl_{(liq)}] + [BF_{3(liq)}])$, for one mole of isopropyl chloride forms with one mole of the boron fluoride complex. Therefore, a plot of α *vs.* mole ratio becomes a straight line.

Thus, it is evident that the equilibrium constant of isotopic exchange between gaseous boron fluoride and the liquid boron fluoride–isopropyl chloride complex is 1.021 at −112°. By a similar method, the equilibrium constant at −95° was found to be 1.016, which is given in Table I.

The values of single-stage separation factor at −95° for several mole ratios of methyl fluoride to boron fluoride are shown in Table II. When the mole ratio in the liquid phase is equal to or larger than 1, the values become constant, but when it is smaller than 1, the plot of α *vs.* mole ratio becomes a straight line as in the case of the boron fluoride–isopropyl chloride system. It was observed by mass spectrometry that even in the gas phase, methyl fluoride molecules coexisted with boron fluoride molecules. If both molecules can form a gaseous complex, the isotopic exchange between gaseous and liquid complexes should occur together with that between the gaseous boron fluoride and liquid complex and, thus, the value of the separation factor should depend also on the mole ratio in the gas phase, but such a positive relation between the value of α and the mole ratio in the gas phase could not be obtained.

Table II: Single-Stage Separation Factor of Boron Fluoride–Methyl Fluoride System

Mole ratio of methyl fluoride to boron fluoride		Temp.,	Vapor press.,	Single-stage separation
Liquid phase	Gas phase	°C.	mm.	factor, α
0.25	0.002	−112	205	1.014 ± 0.001
0.33	...	−112	180	1.016 ± 0.001
0.38	0.006	−112	160	1.017 ± 0.001
0.43	...	−112	140	1.018 ± 0.001
0.48	0.010	−112	125	1.018 ± 0.001
0.53	0.016	−112	105	1.019 ± 0.001
0.60	...	−112	...	...[a]
0.32	0.002	−95	680	1.011 ± 0.001
0.40	0.009	−95	530	1.012 ± 0.001
0.50	0.014	−95	420	1.013 ± 0.001
0.60	0.03	−95	330	1.014 ± 0.001
0.80	0.13	−95	200	1.017 ± 0.001
1.00	0.35	−95	140	1.020 ± 0.001
1.00	0.35	−95	140	1.019 ± 0.001
1.25	0.80	−95	110	1.020 ± 0.001
1.75	2.99	−95	110	1.020 ± 0.001

[a] Solid.

Therefore, in the boron fluoride–methyl fluoride system, too, the boron fluoride–methyl fluoride complex exists only in the liquid phase, and for the complex, the isotopic exchange between the gaseous boron fluoride and liquid complex alone occurs at low temperatures with the value of equilibrium constant 1.020 at −95°.

Boron fluoride–methyl fluoride and –*t*-butyl chloride complexes are both solid at −112°, but when the mole ratio of methyl fluoride or *t*-butyl chloride to boron fluoride in the liquid phase is smaller than 1, solid complexes are dissolved into liquid boron fluoride and the separation factors become measurable. The results are shown in Tables II and III. The plots of α *vs.* mole ratio are also straight lines. In the boron fluoride–*t*-butyl chloride system, the boron fluoride molecule alone is found by mass spectrometry to exist in the gas phase. Therefore, in these cases, two isotopic exchanges between gaseous boron fluoride and liquid complexes and between gaseous and liquid boron fluoride occur simultaneously. The values of the separation factor which are obtained at the mole ratio 1 by extrapolation of the straight lines, should become the equilibrium constants of these complex systems. Thus we obtain the equilibrium constant of the boron fluoride–methyl fluoride system as 1.026 and that of the boron fluoride–*t*-butyl chloride system as 1.033 both at −112°.

Table III: Single-Stage Separation Factor of Boron Fluoride–*t*-Butyl Chloride System

Mole ratio of *t*-butyl chloride to boron fluoride in liquid phase	Temp., °C.	Vapor press., mm.	Single-stage separation factor, α
0.15	−112	285	1.015 ± 0.001
0.25	−112	275	1.016 ± 0.001
0.30	−112	270	1.018 ± 0.001
0.38	−112	260	1.019 ± 0.001
0.45	−112	250	1.022 ± 0.001
0.48	−112	245	1.021 ± 0.001
0.50	−112	...	...[a]

[a] Solid.

Alkylation of Toluene by the Boron Fluoride–t-Butyl Chloride Complex. When boron fluoride gas was absorbed in a toluene solution of *t*-butyl chloride at low temperatures, the solution becomes almost colorless. When this solution was allowed to become warm, there was a vigorous gas evolution. Mass spectrometrical analysis of the evolved gas showed the production of hydrogen chloride and the disappearance of *t*-butyl chloride in this reaction, resembling the alkylation of alkyl benzene with alkyl fluorides except for the color change in the intermediate.[2]

The preceding paragraph shows for the first time that *t*-butyl chloride can readily alkylate toluene in the presence of boron fluoride, and the common assertion that boron fluoride cannot catalyze the alkylation of aromatic compounds with alkyl chloride is now denied, excepting the cases of methyl and propyl chlorides.

Discussion

The values of equilibrium constants of isotopic exchange between boron fluoride gas and many boron fluoride complexes at various temperatures are summarized in Table IV. The equilibrium constant is the largest for the system of strong complex that is stable even at room temperature; it is the smallest for the system of liquid boron fluoride or boron fluoride in nonpolar monoolefin solution in which an unstable π-complex is formed. The system of weak complexes that are stable only at low temperatures has an intermediate value. This suggests that the value of the equilibrium constant relates to the stability of the complex.

Table IV: Equilibrium Constant of Boron Isotope Exchange between Boron Fluoride Gas and Liquid Boron Fluoride Complexes

Liquid complex	Equilibrium constant, K 25°	−95°	−96.5°	−112°	Ref.
BF_3·CH_3OCH_3	1.028	(1.071)[a,b]		(1.082)[a,b]	*c*
BF_3·$C_2H_5OC_2H_5$	1.031	...[a]		...[a]	*d*
BF_3·$C_6H_5OCH_3$	1.032	...[a]		...[a]	*e*
BF_3·C_6H_5OH	1.027	...[a]		...[a]	*e*
BF_3·$(C_4H_9)_2S$	1.033	...[a]		...[a]	*e*
BF_3·$(C_2H_5)_3N$	1.023	...[a]		...[a]	*f*
BF_3·$(CH_2)_4O$	1.036	...[a]		...[a]	*f*
BF_3·H_2O	1.026	...[a]		...[a]	*d*
BF_3·*t*-C_4H_9Cl				1.033[a]	*g*
BF_3·SO_2			1.022	...[a]	*h*
BF_3·CH_3F		1.020		1.026[a]	*g*
BF_3·*i*-C_3H_7Cl		1.016		1.021	*g*
BF_3·CH_3Cl			1.016	1.021	*h*
BF_3·*cis*-2-C_4H_8		1.015		1.020	*i*
BF_3·C_3H_6		1.013		1.018	*j*
BF_3·1-C_4H_8		1.012		1.017	*i*
BF_3·$CHClF_2$			1.011	1.017	*h*
BF_3·C_2H_4				1.011	*j*
BF_3·*trans*-2-C_4H_8		1.006		1.011	*i*
BF_3		(1.006)[b]		1.011	*h, j*

[a] Solid. [b] Extrapolated from experimental equation. [c] See ref. 9. [d] S. V. Ribnikar, "Proceedings of the International Symposium on Isotope Separation," North Holland Publishing Co., Amsterdam, 1958, p. 204. [e] R. M. Healy and A. A. Palko, *J. Chem. Phys.*, **28**, 211 (1958). [f] S. V. Ribnikar and G. A. Bootsma, *Bull. Inst. Nucl. Sci., "Boris Kidrich"* (Belgrade), **9**, 91 (1959). [g] Present report. [h] See ref. 8. [i] See ref. 5. [j] See ref. 4.

Concerning the values of the equilibrium constants of systems of strong complexes, the two following points are noticeable. First, they all are approximately 1.03 at room temperature as shown in Table IV regardless of the sorts of donor molecules, and they may roughly be considered equal to each other when they are compared with the values of the constant of systems of complexes of other types. Second, Palko, *et al.*, worked on the isotopic exchange between boron fluoride gas on one side and boron fluoride–methyl ether,[9] –ethyl ether, and –tetrahydrofuran[10] complexes on the other, and found that only the isotopic shifts of two B–F antisymmetric stretching frequencies, which became lower by transformation of boron fluoride from planar to tetrahedral, had a very large effect upon the partition function ratio between isotopic complex molecules, and the contribution of the other vibrations such as B–O stretching to the ratio was much smaller.

It is well known[11] that in complex formation of boron fluoride with methyl ether, the boron and oxygen atoms are tetrahedrally bonded with a lone pair of electrons occupying the fourth orbital of the oxygen atom and the boron atom is situated at the center of the tetrahedral XY_3Z form, the symmetry of which is C_{3v}. It seems likely that in every molecule of all strong complexes boron valence bond angles are approximately tetrahedral, the B–F distance is presumably nearly equal to that of boron fluoride–methyl ether complex, and hence the B–F antisymmetric stretching frequencies of all these complexes are nearly equal to one another. For example, Palko, *et al.*, observed[10] that the B–F antisymmetric stretching frequencies of $B^{11}F_3$·$(CH_3)_2O$, $B^{11}F_3$·$(C_2H_5)_2O$, and $B^{11}F_3$·$(CH_2)_4O$ are nearly equal. Waddington, *et al.*,[12] reported also that those of BF_3·$POCl_3$, BF_3·$(C_2H_5)_2O$, and BF_3Cl^- (in PH_4BF_3Cl, $NOBF_3Cl$, and $(CH_3)_4NBF_3Cl$) except BF_3·C_5H_5N, are nearly equal. On the other hand, on other tetrahedral XY_3Z molecules (C_{3v}) such as methyl halides[13] or silyl halides,[14] it is known that X–Y antisymmetric stretching frequency does not change when the Z atom is replaced by another.

That the isotopic shift of antisymmetric stretching frequency is much larger than any of the isotopic shifts of other vibration frequencies is also found on tetrahedral XY_4 molecules (T_d), in which the Y atom is not hydrogen. When the center atom X in CF_4[15] or BF_4^-,[16]

(9) A. A. Palko, G. M. Begun, and L. Landau, *J. Chem. Phys.*, **37**, 552 (1962).

(10) G. M. Begun and A. A. Palko, *ibid.*, **38**, 2112 (1963).

(11) S. H. Bauer, G. R. Finlay, and A. W. Laubengayer, *J. Am. Chem. Soc.*, **65**, 889 (1943); **67**, 339 (1945).

(12) T. C. Waddington and F. Klanberg, *J. Chem. Soc.*, 2239 (1960).

(13) G. Herzberg, "Molecular Spectra and Molecular Structure. II. Infrared and Raman Spectra of Polyatomic Molecules," D. Van Nostrand, New York, N. Y., 1945, p. 135.

(14) C. Newman, J. K. O'Loane, S. R. Polo, and M. K. Wilson, *J. Chem. Phys.*, **25**, 855 (1956).

(15) J. Goubeau, W. Bues, and F. W. Kampmann, *Z. anorg. allgem. Chem.*, **283**, 123 (1956).

(16) J. Goubeau and W. Bues, *ibid.*, **268**, 221 (1952); N. N. Greenwood, *J. Chem. Soc.*, 3811 (1959).

for example, is replaced by its isotope, X–Y antisymmetric stretching frequency alone shows a large isotopic shift. Therefore, in all strong boron fluoride complexes it can be assumed that all values of the B–F antisymmetric stretching frequency are nearly equal and that the effect of isotopic shift upon the partition function ratio between isotopic complex molecules is far larger than that of other vibration frequencies. If so, the equilibrium constant will be nearly the same. The fact that all the observed values are approximately 1.03 at room temperature proves the assumption mentioned above being reasonable. Thus, for all the systems of a strong complex, the equilibrium constant will be approximately 1.08 at $-112°$, which agrees with the value 1.082 at $-112°$ calculated from the empirical formula given by Palko, *et al.*, for the boron fluoride–methyl ether system.

In an uncoordinated boron fluoride molecule, too, the isotope shift of the doubly degenerate B–F antisymmetric stretching frequency is the largest[17] and their effect upon the partition function ratio between isotopic boron fluoride molecules is much larger than that of the other frequencies. Therefore, it can be assumed, although roughly, that in boron fluoride complexes of all the types, B–Z stretch contributes only slightly to the partition function ratio and the isotopic shifts of B–F antisymmetric stretching frequencies alone have a very large effect on it. If so, the partition function ratio between isotopic complex molecules, $Q[B^{11}F_3 \cdot ZA]/Q[B^{10}F_3 \cdot ZA]$, becomes smaller and therefore the equilibrium constant

$$\frac{Q(B^{11}F_3)}{Q(B^{10}F_3)} \Big/ \frac{Q[B^{11}F_3 \cdot ZA]}{Q[B^{10}F_3 \cdot ZA]}$$

becomes larger as the B–F antisymmetric stretching frequency of the complex decreases. Thus, the observed result that the value of equilibrium constant of the system of weak complex is between the values of the constant of liquid boron fluoride and strong boron fluoride complex shows that the B–F antisymmetric stretching frequency of weak boron fluoride complex lies between the frequencies of uncoordinated boron fluoride and strong boron fluoride complex.

As the density of electrons localized on the vacant orbital of boron atoms increases, more boron fluoride molecules transform from planar into tetrahedral and the B–F antisymmetric stretching frequency becomes lower, although the density of localized electrons, which determines the strength of the B–Z bond, will be only indirectly related to the B–F stretch. Since the equilibrium constant depends mostly on the B–F antisymmetric stretching frequency as mentioned above, it follows that the density of localized electrons on the vacant orbital of boron atoms and hence the polarity of the complex becomes higher as the equilibrium constant becomes larger, causing the complex to become more stable.

Now, since the equilibrium constants obtained for boron fluoride–alkyl halide systems have intermediate values, all these boron fluoride–alkyl halide complexes will be weak polar complexes. Therefore, the boron fluoride–*t*-butyl chloride complex seems to be a polar complex, $\overset{\delta-}{B}F_3 \leftarrow \overset{\delta+}{Cl}C(CH_3)_3$, but not a carbonium ion complex, $BF_3Cl^- \cdot \overset{+}{C}(CH_3)_3$, although *t*-butyl chloride is easily ionized. The polarity of these complexes will decrease in the order: $\overset{\delta-}{B}F_3 \leftarrow \overset{\delta+}{Cl}C(CH_3)_3 > \overset{\delta-}{B}F_3 \leftarrow \overset{\delta+}{F}CH_3 > \overset{\delta-}{B}F_3 \leftarrow \overset{\delta+}{Cl}CH(CH_3)_2$, $\overset{\delta-}{B}F_3 \leftarrow \overset{\delta+}{Cl}CH_3$. If so, the boron fluoride–*t*-butyl chloride complex too should have catalytic activity similar to the boron fluoride–methyl fluoride complex. This presumption was proved to be correct, for *t*-butyl chloride can alkylate toluene readily in the presence of boron fluoride, although such a color change as observed by Oláh, *et al.*,[2] on alkylation with the boron fluoride–alkyl fluoride complex was not found. However, despite the alkylation of aromatic constituent with tertiary alkyl halide, it seems very likely that the alkylation does not proceed through the formation and reaction of the carbonium ion, for this complex is considered to be only a weak polar complex as mentioned above. Thus, the reaction is presumed to be that a stable intermediate colorless σ-complex is produced through an activated complex in a transition state and then it decomposes to alkyl benzene, hydrogen chloride, and boron fluoride by the process

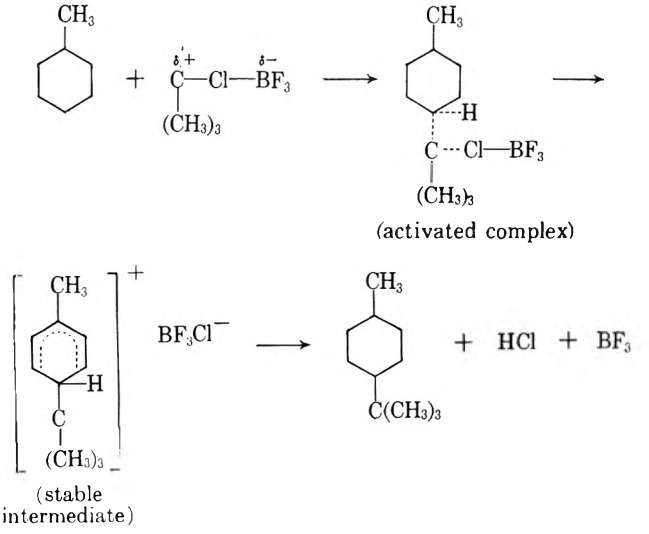

(17) J. Vancerryn, *J. Chem. Phys.*, **30**, 331 (1959).

On the other hand, the boron fluoride–isopropyl chloride complex, the equilibrium constant of which system is smaller than that of the boron fluoride–methyl fluoride system, cannot alkylate toluene despite being also polarized.

It is interesting to compare generally the equilibrium constants of boron fluoride complex systems with the catalytic activity of the boron fluoride complex. Boron fluoride–ether and –alcohol complexes, which are completely ionized and have large equilibrium constants, are very active catalysts. On the other hand, the boron fluoride–*t*-butyl chloride complex, which has a small value of equilibrium constant, is a less reactive catalyst but can alkylate toluene readily. However, the boron fluoride–alkyl halide complex, the equilibrium constant of which is smaller than 1.021 at −112°, cannot have even the catalytic activity for the alkylation. As shown in the previous works,[4,5] boron fluoride polar monoolefin σ-complex systems have such values of equilibrium constant as approximately 1.02 at −112°, yet none of the complexes can react with free olefin monomer molecules, and only when there are strong complexes, *e.g.*, $BF_3 \cdot H_2O$, whose systems have large values of equilibrium constant, does the polymerization of monoolefin proceed. Therefore, in order that boron fluoride complexes have any catalytic activity, the electrons from donor molecules must remain localized on vacant orbitals of boron atoms so that the value of the equilibrium constant becomes larger than approximately 1.03 at −112° and the catalytic activity becomes higher as the equilibrium constant increases.

Thermodynamics of the Liquid Potassium–Oxygen and Sodium–Oxygen Systems

by Amos J. Leffler and Norman M. Wiederhorn

Arthur D. Little, Inc., Cambridge, Massachusetts *(Received February 7, 1964)*

The oxygen pressure–melt composition for the potassium–oxygen system was observed at three different temperatures. From these data and the tabulated thermodynamic values for K_2O, the heats and free energies of formation of the melt compositions were calculated from $KO_{0.5}$ to $KO_{2.0}$, although experimentally it was not possible to reach compositions richer in oxygen than $KO_{1.75}$. A study was made of the oxygen pressure–melt composition for the liquid sodium–oxygen system between 780 and 980°. These results together with the thermodynamic data for Na_2O_2 were used to calculate the heats and free energies of formation of melt compositions between $NaO_{1.0}$ and $NaO_{0.5}$.

Introduction

The properties of the oxides of potassium have been partially investigated and thermodynamic values have been tabulated.[1] The most extensive experimental data are available for KO_2, including heats of formation,[2-4] specific heats from 20 to 373°K.,[5,6] and heats and free energies of decomposition[7,8] to K_2O_2 at 300–370° in the solid phase. An experimental heat of formation for K_2O[9] has been determined. The only available information on K_2O_2 is the heat and free energy of decomposition[7] in the 300–370° range. During a crystallographic study of KO_2[10] a phase transition was noted

(1) J. F. Coughlin, U. S. Bureau of Mines, Bulletin 542, U. S. Govt. Printing Office, Washington, D. C., 1953.

(2) P. W. Gilles and J. L. Margrave, *J. Phys. Chem.*, **60**, 1333 (1956).

(3) L. J. Kazarnovskaia and I. A. Kazarnovskii, *Zh. Fiz. Khim.*, **25**, 293 (1951).

(4) R. de Forcrand, *Compt. rend.*, **158**, 991 (1914).

between 60 and 120° which has not been noted in the tabulated thermodynamic data. In the present work a study was made of the dissociation pressures of potassium–oxygen melt compositions starting with KO_2 as a function of temperature and the results were used to calculate the heat and free energy of formation of these compositions in the liquid range.

The thermodynamic properties of the solid oxides of sodium have been well studied. In the case of sodium peroxide the enthalpy of formation[2] has been determined at 25° and the specific heat[11] measured up to the solid state transition at 596°. For sodium oxide the enthalpy of formation[12] and specific heat[13] up to the melting point are known. Due to the great reactivity of these oxides no satisfactory specific heat data have been obtained above their melting points. There has been one study[14] of the equilibrium between Na_2O and Na_2O_2 as a function of temperature and oxygen pressure. The reliability of these results is doubtful because of the nature of the crucibles used in the work, and the discrepancy of the results obtained by these investigators compared with other workers for the potassium and rubidium system. A study[15] of the phase diagram and effect of oxygen pressure in the Na_2O–Na_2O_2 system was reported, but it was noted that there was severe attack on all of the crucibles used in the work. It was, however, found that the melting point of Na_2O_2 is 675° and the eutectic containing 42% Na_2O_2 occurs at 575°. In the present work a study of the oxygen pressure–melt composition was made for melt compositions between $NaO_{1.0}$ and $NaO_{0.7}$ at pressures below 1 atm. The results were used to calculate thermodynamic values of the melt compositions and these are compared with tabulated values.

Experimental

The chief difficulty in obtaining satisfactory results in the liquid range has been in finding a satisfactory crucible. In the present investigation it has been shown that crucibles of single crystals of fused magnesium oxide (supplied by Semielements, Inc., Saxonburg, Pa.) were satisfactory to temperatures as high as 1000°. Pressure measurements were carried out both below and above atmospheric pressure. In the low pressure work a glass system was used while a metal system was used for measurements above 1 atm.

1. Low Pressure. The equipment used for the pressure measurements below 1 atm. consisted of a heated quartz reactor containing the crucible that was attached to a vacuum system equipped with a Toepler pump. Provision was made to introduce oxygen into the system and pressure was measured with a mercury manometer. In order to determine how much oxygen was evolved during an experiment, it was necessary to run a set of calibration experiments using only a known amount of gas at various starting pressures and heating the apparatus to various temperatures. Since only the tube in the furnace was heated, the final temperature of the entire system was an average which took into account both the heated and unheated volumes of the system. The final average temperature value is simply derived by the relation

$$\frac{P_i V_i}{T_i} = \frac{P_f V_f}{T_{av}} \qquad (1)$$

where P_i and P_f are the initial and final pressures, respectively; V_i and V_f are the initial and final volumes that differ because of the height of the mercury column; and T_i and T_{av} are the initial and final average temperatures, respectively.

It was found that the value of T_{av} was almost independent of initial oxygen pressure indicating that the heat leakage along the tube was not greatly influenced by pressure. Occasionally additional volumes were added during the work and this would affect the final average temperatures. However, it was not necessary to recalibrate the pressure if the heated volume remained constant. The heated volume could be derived from the relations

$$\frac{P_i V_i}{T_i} = \frac{P_f V_h}{T_h} + \frac{P_f(V_f - V_h)}{T_i} \qquad (2)$$

where V_h and T_h were the heated volume and furnace temperatures, respectively. No account was taken of the temperature gradient between the furnace and ambient since the value calculated for V_h was used only to recalculate T_{av} when the system volume was changed. This value of V_h was used for any size system, and the new final pressure was calculated from the equation above. Of course, new calibrations were necessary for new heating tubes.

(5) S. S. Todd, *J. Am. Chem. Soc.*, **75**, 1223 (1953).

(6) A. V. Vedeneev and S. M. Skuratov, *Zh. Fiz. Khim.*, **25**, 837 (1951).

(7) I. A. Kazarnovskii and S. I. Raikshtein, *ibid.*, **21**, 245 (1947).

(8) A. W. Petrocelli, Thesis, University of Rhode Island, 1960.

(9) E. Rengade, *Compt. rend.*, **145**, 236 (1907), **146**, 129 (1908).

(10) G. F. Carter, J. L. Margrave, and P. H. Templeton, *Acta Cryst.*, **5**, 851 (1952).

(11) M. S. Chandrasekhariah, R. J. Grimley, and J. L. Margrave, *J. Phys. Chem.*, **63**, 1505 (1959).

(12) L. Brewer, *Chem. Rev.*, **52**, 1 (1953).

(13) R. T. Grimley and J. L. Margrave, *J. Phys. Chem.*, **64**, 1763 (1960).

(14) M. Centeszwer and M. Blumenthal, *Bull. Intern. Acad. Polon., Classe Sci. Math.*, **1933A**, 499 (1933).

(15) E. G. Bunzel and E. J. Kohlmeyer, *Z. anorg. allgem. Chem.*, **254**, 1 (1947).

The equilibrium runs were made in the following manner. All transfers of KO_2 were made in a drybox. A sample of KO_2 was weighed out in the magnesium oxide crucible by difference. The sample was then brought back inside the drybox and loaded into the quartz reactor tube. The tube was quickly attached to the vacuum system, the system evacuated, the tube furnace heated to the desired temperature, and the tube with the crucible inserted. As the material heated up, there was an evolution of oxygen which could be followed on the manometer. At temperatures up to 500° the pressure reached a constant value after 15 min., but at 600° and above a slow increase was noted with time. All observations at 600° and above were made within a few minutes because of the slow change observed.

After reading the equilibrium pressure a portion of the evolved oxygen was pumped out into a known volume by the Toepler pump. This amount of gas removed was calculated by the gas law and the new pressure in the system observed. Since calibrations for the pressure–temperature relation for various temperatures and pressures were available, the remaining oxygen was calculated and this plus the amount removed found to be greater than the amount of oxygen in the tube at the start of the experiment, indicating that oxygen was evolved from the melt as the pressure was lowered. This removal procedure was then repeated to obtain the equilibrium at a still lower pressure. In many cases oxygen gas was added initially to keep down the decomposition of the KO_2. Thus the pressure above the melt at high O–K ratios could be determined.

When very low pressures of gas were measured, it was found that the bubbler manometer was not sufficiently accurate, and a Dubrovin gauge was added to the system. Such a gauge gives a ninefold multiplication of the pressure reading allowing readings to 0.1 mm.

The value of the oxygen pressure over the melt was that directly observed by the manometer. The initial amount of decomposition of KO_2 was calculated by measuring the total amount of oxygen in the system and subtracting that initially present as determined by pressure–volume relations, the difference being that evolved from the metal oxide. In the calculations, corrections were made for the impurities present in the starting material. As the series of withdrawals of oxygen from the system proceeded, the new concentrations of oxide could be determined by subtracting the oxygen removed from the system from the sum of the initial oxygen contained in the oxide and the gas phase. This yielded the oxygen in the oxide and in the gas phase, and since the latter value was known, the former could be determined by difference.

2. High Pressure. A static system, consisting of a heated Inconel vessel, was used. The vessel was heat treated in an oxygen atmosphere at about 1000° and checked for flaws by X-ray. Copper gaskets were found to be satisfactory for closure although it was necessary to substitute a new gasket after every second or third run. The heat for the reactor was supplied by a muffle furnace, which was controlled by the thermocouple in the reactor. Since the conditions of operation are fairly close to the temperature limit of the Inconel, a safety thermocouple was placed in the furnace to shut off the power if the temperature rose excessively due to control thermocouple or controller failure. Pressure was measured by means of a Dynisco 0–400 p.s.i. pressure transducer with a stated accuracy of 0.25%.

The procedure used to determine the oxygen evolved from the starting material in this apparatus was similar in principle to that in the low-pressure apparatus. A similar set of calibration runs was made. Since it was possible to work with much larger samples (in the order of 5 g.) of KO_2, a different crucible was used. This was made of sintered magnesium oxide made by the Norton Co. Although there was no reaction with the molten oxides, the crucible was somewhat porous over a period of hours. In order to avoid reaction of the oxide with the Inconel, a second crucible was placed underneath the sample holder. This arrangement worked satisfactorily to avoid contact of the oxide with the reactor walls.

The oxide sample was weighed out by the difference method as before. In loading the crucible into the reactor, the system was initially purged with dry oxygen for 10 min. The crucible plus oxide was then taken out of the weighing vessel and quickly placed in the Inconel reactor, which had been carefully dried. The reactor was then rapidly attached to the remainder of the system, the system pressurized to 100 p.s.i.g. of oxygen, and the pressure released. This process was repeated three more times in order to remove the nitrogen and other impurities. The system was next pressurized to 200 p.s.i.g. and allowed to stand for about 1 hr. to make certain that there were no leaks. Pressure was finally reduced to the desired starting value and heating commenced.

The heating rate was arranged to bring the reactor up to temperature in about 2 hr. During the course of the heating, a continuous record of the pressure was kept on a recorder. It was noted that there was always a sudden increase in pressure beyond that due to the expansion of the starting oxygen at about 190–

200°. This increase was taken to be due to the onset of decomposition of the oxide. After reaching the desired temperature, the reactor was allowed to stand for about 2 hr. to determine whether the pressure remained constant. It was noted that there was a slow pressure change in this period, varying from 1 to 2 p.s.i. For an equilibrium reading at lower pressure, a portion of the gas was bled out. The amount was measured by the pressure drop and also by passing the gas through a wet test meter; the two methods always agreed closely. The procedure was then repeated to obtain the new equilibrium pressure, but in this and following measurements, no pressure change was noted over a 2-hr. period.

3. Reproducibility and Accuracy of Measurements. In static measurements of this type it is most important to determine whether the system is at equilibrium. An attempt was made to approach a given pressure–melt composition point from both directions, but it was found that when an initial oxygen pressure was placed above the sample, the sample reached a lower O–K ratio then when all of the oxygen was evolved from the sample. A sample initially heated under vacuum was then pressurized with oxygen, and oxygen was absorbed, following which the oxygen was removed. This procedure was followed several times and the final O–K ratio had decreased to within about 0.03 unit of that obtained when starting with oxygen above the sample. It was also attempted to determine whether the O–K ratio of a sample initially heated under oxygen would change with cycling, but no change was found. Therefore, the values of O–K obtained in this manner were accepted as the most accurate values. The error due to nonattainment of equilibrium is estimated to be about ±0.03 unit based on this work.

An analysis of the method of calculation of oxygen liberated from the melt shows that all values for the amounts of oxygen involved in this work are based on the values obtained from the Toepler system. Since the pressures and temperatures of oxygen could be read to a much higher precision than the volume, the errors will be in the volume of the system. All amounts of oxygen calculated will be in error in the same direction with a constant per cent error. Since the amount of oxygen calculated to be evolved will be the difference between that observed in the system and that removed, it will also have the same per cent error. The error in the difference values would be random ones caused by such factors as incomplete removal of oxygen to the Toepler system or leakage and are difficult to estimate but are believed to be very small.

4. Analysis of Starting Materials. The potassium superoxide used in this work was obtained from Mine Safety Appliances Corp. and was analyzed for the amount of releasable oxygen present. The procedure used was that of Sayb and Kleinberg.[16] The analysis showed 34.7% superoxide oxygen by weight, corresponding to 95% KO_2 with the remainder being K_2O_2.

The sodium peroxide used in this work was Mallinckrodt Chemical Works "minimum" 90% pure and was analyzed by titration with HCl which showed that 98.3% of the calculated acid was used. This is the average of three determinations having values of 98.3, 98.3, and 98.25%. From this result and from the yellow color of the material, it was concluded that the difference between this and the theoretical value was due to the presence of NaO_2. The amount was calculated to give 94.2% Na_2O_2 and 5.77% NaO_2. Therefore, oxygen would be evolved at relatively low temperatures which was not due to the decomposition of sodium peroxide. At the completion of this, the remaining material would all be Na_2O_2 and would be 98.35% of the expected amount if the material were pure

Results and Discussion

The experimental results are shown in Fig. 1 and 2. The thermodynamic treatment of binary mixtures such as these are outlined in texts.[17] In the systems under consideration, we can measure the pressure of oxygen and calculate the melt composition. For the composition KO_x, from the reaction

$$K + \frac{x}{2} O_2 = KO_x \qquad (3)$$

partial molar free energy $\bar{F}_0$ of oxygen is defined

$$\bar{F}_0 = \frac{RT}{2} \ln f_0 + B(T) \qquad (4)$$

where f_0 is the fugacity of oxygen and $B(T)$ depends on the temperature and standard state. In the present work, the pressure of oxygen is used instead of fugacity since there will be little error in such a substitution. The standard state has been defined as that composition for each temperature having an oxygen pressure of 1 atm.

This then allows the simplification

$$\bar{F}_0 - \bar{F}_0^\circ = \frac{RT}{2} \ln P_0 \qquad (5)$$

(16) E. Sayb and J. Kleinberg, *Anal. Chem.*, 23, 115 (1951).

(17) See, for example, G. N. Lewis and M. Randall, "Thermodynamics," 2nd Ed., K. S. Pitzer and L. Brewer, Ed., McGraw Hill, New York, N.Y., 1961, Chapters 17, 19, and 20. See also O. Kubaschewski and E. L. Evans, "Metallurgical Thermochemistry," Pergamon Press, New York, N. Y., 1958.

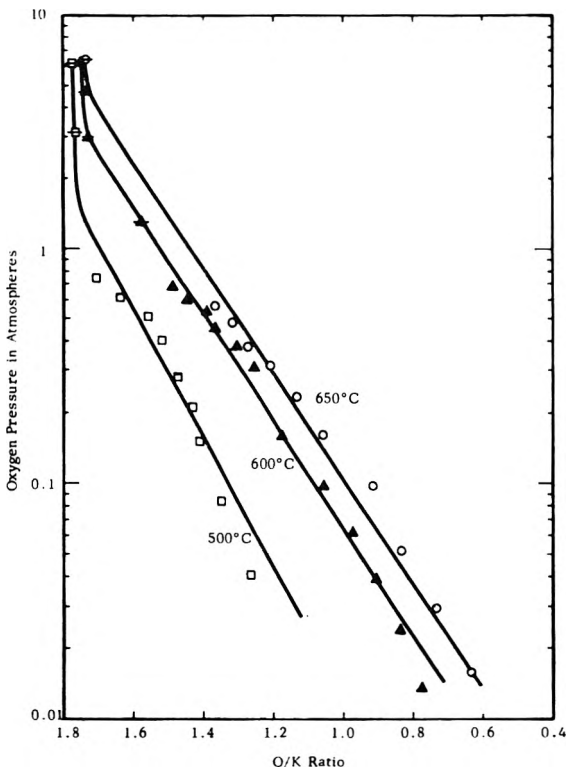

Figure 1. Plot of oxygen pressure *vs.* composition of potassium–oxygen melt.

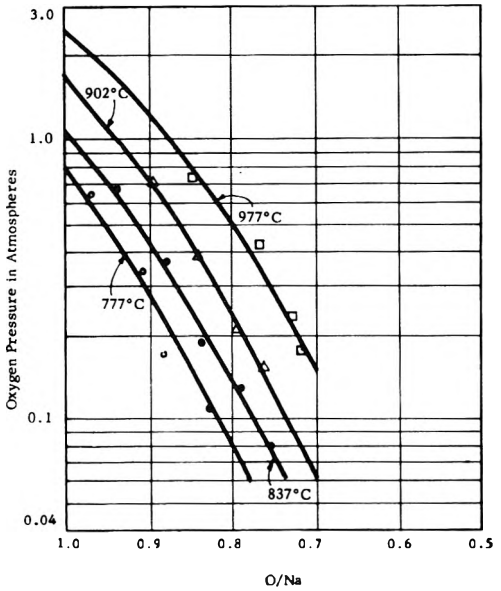

Figure 2. Pressure of oxygen over oxygen–sodium melt at various temperatures.

In order to obtain ΔF for reaction 3, it is necessary to integrate $\bar{F}_0$ using the relation

$$\Delta F = N_K \int_0^x \bar{F}_0 \, dx \qquad (6)$$

where $x = N_0/N_K$, and the definition is for a gram-atom of KO_x.

In the present work, the values of $\bar{F}_0$ could not be experimentally determined below a value for x of 0.63. In order to relate the values of ΔF for the compositions studied to standard free energies of formation, the values of $\bar{F}_0$ were extrapolated to an x of 0.5, which corresponds to the compound K_2O.[18]

The thermodynamic values for K_2O^2 were obtained from the experimental heat of formation at 298°K.[10] and estimated heat capacities. The values at any other composition can be related to the values for K_2O in the following manner. The free energy of formation of K_2O at any temperature can be defined as

$$\Delta F^\circ_{K_2O} = 0.666 \int_{0.0}^{0.5} \bar{F}_0 \, dx \qquad (7)$$

The value of $\Delta F^\circ_{K_2O}$ given in ref. 2 is in cal./mole and must be divided by three to refer to a gram-atom of K_2O. Using this value, the integral in (7) can be evaluated.

Now for any composition KO_x

$$\Delta F^\circ_{KO_x} = N_K \int_{0.0}^{x} \bar{F}_0 \, dx = \left[N_K \int_{0.0}^{0.5} \bar{F}_0 \, dx + \int_{0.5}^{x} \bar{F}_0 \, dx \right] \qquad (8)$$

Since the first integral on the right-hand side of eq. 8 is known and the second can be evaluated from plots of $\bar{F}_0$ *vs.* x at each temperature, it becomes possible to evaluate $\Delta F^\circ_{KO_x}$ for any composition where data is available.

In the case of the sodium–oxygen system, the extrapolation to the oxygen pressure over sodium peroxide was made to give a base for calculation of the thermodynamic values of the melt compositions. The calculation of the thermodynamic properties of the melt was made by a method analogous to that described for the potassium–oxygen system. The values of melts could then be calculated using the relation

$$\Delta F^\circ_{NaO_x} = N_{Na} \left[\int_{0.0}^{1.0} \bar{F}_0 \, dx + \int_{1.0}^{x} \bar{F}_0 \, dx \right] \qquad (9)$$

where $x = O/Na$.

The values of ΔH were calculated from the relation

$$\Delta H = \Delta F + T\Delta S \qquad (10)$$

(18) The extrapolation to an O–K ratio of 0.5 involves the crossing of the liquid–solid phase boundary. The value of ΔF° for K_2O should be corrected, but this has been neglected since the ΔH of fusion is small and the temperatures are close to the melting point of K_2O. For a discussion of this point see R. A. Swalin, "Thermodynamics of Solids," John Wiley and Sons, New York, N. Y., 1962, Chapter 11.

with ΔS being calculated from the definition

$$\Delta S = -\left(\frac{\partial \Delta F}{\partial T}\right)_{P,N} \qquad (11)$$

From the oxygen pressure–melt composition curves in the potassium system, it is evident that at all experimentally attainable pressures the maximum O–K ratio is about 1.75. At the present time there is not sufficient data to decide whether this ratio corresponds to a definite compound having the empirical formula K_4O_7. The calculated values of $\Delta F°$ and ΔH for the range of potassium–oxygen ratios of $KO_{0.5}$ to $KO_{1.75}$ and an extrapolation to $KO_{2.0}$ are given in Fig. 3 and 4. It is evident that there is a very considerable difference between the tabulated values from ref. 2 and experimental values in the present work. Since almost the entire range of interest is liquid, the abrupt changes in ΔF values in ref. 1 seem unlikely, and the smooth curve from the present work is more satisfactory. In addition, an examination of the values for KO_2 and $KO_{1.5}$ indicates that KO_2 is the more stable species at temperatures up to 600°, and this is experimentally incorrect. Since the heats of formation for both $KO_{2.0}$ and $KO_{1.5}$ were determined by the same worker,[4] and that for KO_2 has been verified by other workers,

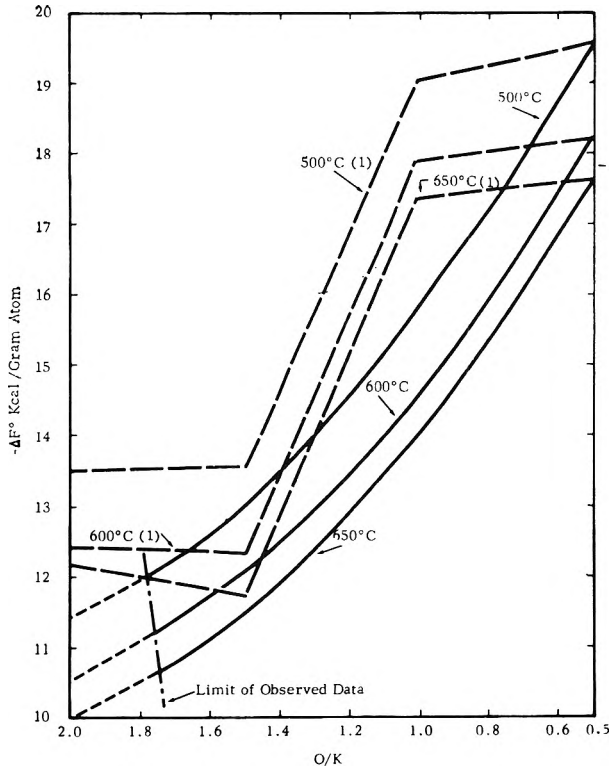

Figure 3. Plot of $\Delta F°$ in kcal./g.-atom for potassium–oxygen mixtures.

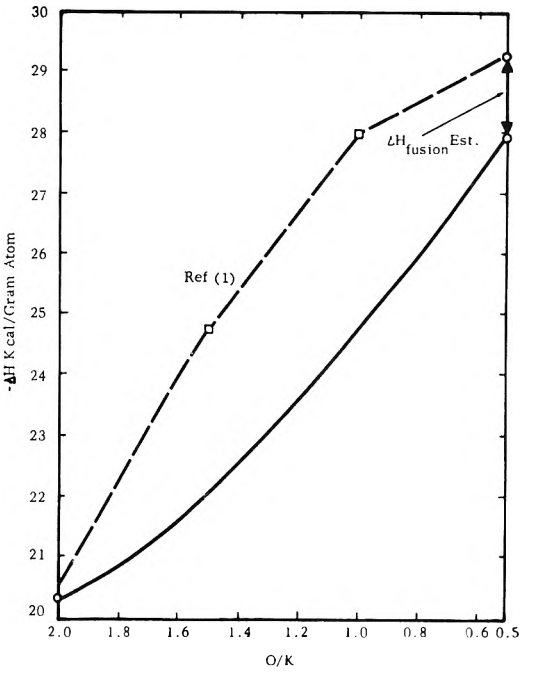

Figure 4. Plot of ΔH of formation per gram-atom of oxygen–potassium mixtures.

the extrapolation of the $\Delta F°$ values for $KO_{2.0}$ to the liquid state may be unreliable. In addition, as was pointed out earlier, there is a phase change of KO_2 which has not been included in the tabulated data.

An independent method of evaluating the reliability of the different $\Delta F°$ and ΔH values is to compare differences in $\Delta F°$ and ΔH for the various oxides as determined in this work and those calculated from the values tabulated in ref. 1. For the reaction

$$K_2O + 0.5O_2 = K_2O_2 \qquad (12)$$

the values of ΔF and ΔH are shown in Table I. The large discrepancies are believed to be due to the very high estimated values of ref. 1 for K_2O_2. As evidence of this it was observed that at 360°K the pressure of oxygen over solid K_2O_2 is 0.05 mm. which corresponds to a ΔF of reaction 12 of 6.05 kcal. This value is in

Table I: Values of ΔF and ΔH for Reaction 12 (cal./mole)

Temp., °C.	Bulletin 542		Present values	
	ΔF	ΔH	ΔF	ΔH
500	−17,700		−4700	
600	−16,850	−24,000	−3600	−15,000
650	−16,500		−3200	

good agreement with those reported in this work. It was also observed by Petrocelli[8] that at temperatures below 400° it is possible to reduce KO_2 to K_2O by prolonged pumping. If the tabulated values in Bulletin 542 are correct, the pressure of oxygen over K_2O_2 would be 1.4×10^{-15} atm. at 600°K. which is much too low to permit the reduction observed by Petrocelli. The values of ΔH of K_2O_2 in ref. 1 are only estimates and are probably high by about 10 kcal./mole. The values determined in the present work are less certain than free energy values since they depend so markedly on the slope of $\Delta F/T$ which is not known with high accuracy.

A similar comparison can be made for the reaction

$$K_2O_2 + O_2 = 2KO_2 \qquad (13)$$

In Table II are shown the results obtained from ref. 7 and 8 the present work in comparison with the values calculated from ref. 1.

Table II: Values of ΔF and ΔH for Reaction 13 (cal./mole)

Temp.,	Bulletin 542		Present values	
°C.	ΔF	ΔH	ΔF	ΔH
300			−8580	
327	−6300	−23,000		−18,000
343			−8140	
372			−7840	
500			−5840	
527	−5000			−22,600
600			−4800	
727	−3000			

The agreement between the tabulated and observed values is much better here than for eq. 12 indicating the differences in ΔF and ΔH of formation of KO_2 and K_2O_2 are in better agreement. However, the discrepancy between K_2O and K_2O_2 indicates that there is a large constant difference between the values for KO_2 and K_2O_2 in ref. 1 and what appear to be reasonable values based on ref. 8 and 9 and the present work.

It would seem that the differences in the ΔF and ΔH values from ref. 1 and the present work are due to a number of causes. These include the error in the values for $KO_{0.5}$, the uncertainty in the extrapolation of the $\bar{F}_0$ values to $KO_{0.5}$, and unaccounted for phase transitions of the oxides. Any revised determination of the ΔH and specific heat of K_2O would be the basis of a recalculation of the data and would remove one source of uncertainty from the results.

The values of $\Delta F°$ and ΔH for the sodium–oxygen

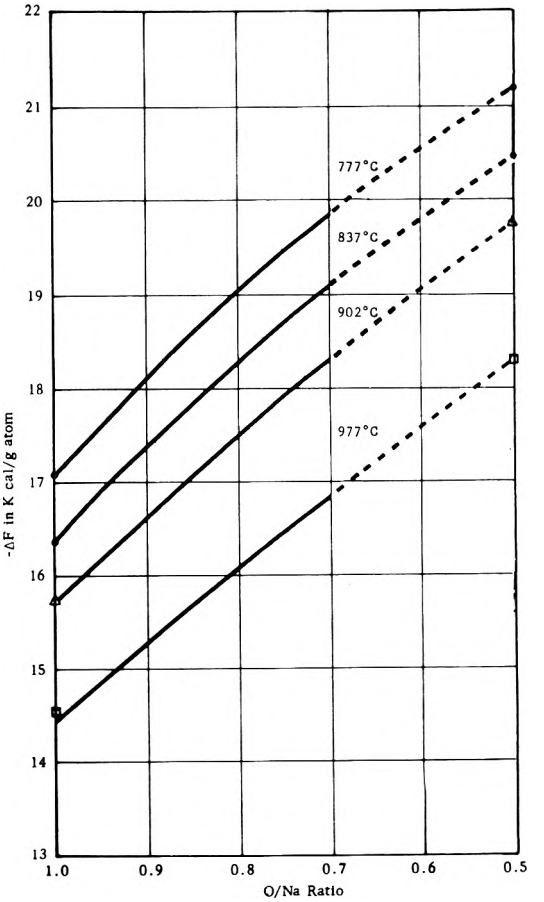

Figure 5. Plot of $\Delta F°$ for oxygen–sodium mixtures per gram-atom.

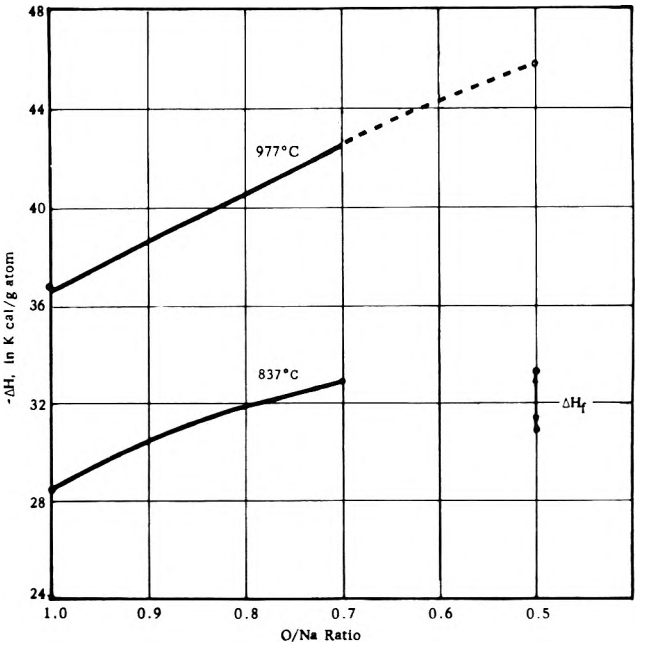

Figure 6. Plot of ΔH of formation per gram-atom of oxygen–sodium mixtures at 1100 and 1250°K.

system are given in Fig. 5 and 6. It was necessary to recalculate the tabulated thermodynamic values for Na_2O_2 given in ref. 1 in order to correct for a phase transition at 596° and the melting point at 675°. The values of ΔF were calculated as a function of melt composition at several different temperatures down to an O–Na ratio of 0.7 and extrapolated to the tabulated values as shown in Fig. 5. There is a break of ΔH for all oxide compositions at 914° owing to the heat of vaporization of sodium. Therefore, values of ΔH at 837 and 977° were calculated and are shown in Fig. 6.

The values for the melt compositions fall on a smooth curve between Na_2O_2 and Na_2O although a greater discrepancy was found with the values for ΔH due probably to the inaccuracies in ΔS. This is especially true above 914° where only one set of vapor pressure–melt composition observations was made.

Acknowledgment. This work was carried out under Contract AF 33(616)-8296. We wish to acknowledge the help of Messrs. Philip Sliney and Bruce Ostar in making the measurements and Drs. A. Buchler and J. Berkowitz for helpful discussions.

Radiation-Induced Reactions of Isopropylbenzene on Silica-Alumina

by Robert R. Hentz*

Socony Mobil Oil Company, Inc., Research Department, Paulsboro, New Jersey *(Received February 24, 1964)*

Experiments are reported on the reaction of isopropylbenzene on three γ-irradiated silica–aluminas that differed in impurity content and method of preparation. In each of these solids, radiation produces coloration; the solids are bleached by isopropylbenzene and benzene is formed. At high doses the yield of benzene reaches a limiting value that is different for each solid. This maximum benzene yield fails to correlate with iron content (the major impurity) but does correlate, perhaps fortuitously, with the inherent dealkylation activity of these three solids. The most active solid gave a limiting yield of 162×10^{17} benzene molecules/g. γ-Irradiation of a heterogeneous system comprised of isopropylbenzene and a high-purity silica–alumina also was studied over the entire range of isopropylbenzene electron fraction. G(benzene) = 1.2 from low surface coverage to beyond complete surface coverage. Gas yields for the irradiated heterogeneous system also are presented and interpreted in terms of a mechanism that involves hydrogen atoms generated from surface O–H bonds of the solid by absorbed radiation energy.

I. Introduction

This work is a continuation of a study of the radiation-induced dealkylation of isopropylbenzene on silica–alumina catalysts. In previous work[1,2] it was demonstrated that radiation absorbed in the heterogeneous system converts isopropylbenzene to benzene with a higher yield per unit energy input than is obtained by irradiation of pure liquid isopropylbenzene, even though the radiation is absorbed overwhelmingly by the solid. Further, the radiation-induced reaction on the solid surface was shown to be more specific than in pure liquid or gaseous isopropylbenzene; that is, the benzene yield is increased relative to the yields of all other products. However, the most striking observation was that

* Radiation Laboratory, University of Notre Dame, Notre Dame, Ind.

(1) R. R. Hentz, *J. Phys. Chem.*, **66**, 1625 (1962).

(2) R. R. Hentz, *ibid.*, **66**, 2714 (1962).

irradiation produced long-lived excitations[3] in the solid that made it possible to preirradiate the solid and then carry out the reaction. The present work was undertaken to provide some insight into the nature of these long-lived excitations and the mechanism of the reaction they promote, as well as to extend study of the radiation chemistry of the heterogeneous system.

II. Experimental

A. Chemicals. Eastman Kodak 1481 isopropylbenzene was used; purification procedures have been described.[1,2] Three different amorphous silica–aluminas were used. Properties of the solids are given in Table I; the methods of preparation follow.

Table I: Properties of Microporous Silica–Aluminas

	Solid A	Solid B	Solid C
Surface area, m.²/g.	400	388	372
Real density, g./ml.	2.30	2.28	2.23
Particle density, g./ml.	1.15	1.45	1.48
Pore volume, ml./g.	0.433	0.252	0.228
Alumina, wt. %	10	11.2	10.8
Impurities, wt. %			
Quantitative analysis			
Fe	0.030	0.005	0.030
Cr	<0.01	<0.01	
Cu	0.0086		0.0082
Qualitative emission spectroscopy[a]			
Fe	T	T	S
Cr	T	—	—
Cu	T	T	S
Mg	T	T	T
Pb	T	T	T
Sn	—	T	T
Ni	—	—	T
Ti	T	—	T
Mn	T	—	—
Ba	T	T	T
Na	T	T	T

[a] S is 0.01–0.1%, T is less than 0.01%, and — means sought but not detected.

Solid A. This is the solid used in previously reported work.[1,2] It is a conventional silica–alumina catalyst for which general methods of preparation have been described.[4]

Solid B. An alcoholic solution of aluminum chloride was mixed with tetraethyl orthosilicate, hydrolyzed with an alcoholic nitric acid solution, and then gelled with an alcoholic ammonium hydroxide solution to give a final pH ~8.6. The hydrogel was aged for 16 hr. at 50°, washed free of chloride, dried 20 hr. at 110°, and then calcined in air for 10 hr. at 540°.

Solid C. The method of preparation was identical with that for solid B except that an alcoholic solution of ferric nitrate was mixed with the aluminum chloride and silicate solutions in the initial step prior to acid hydrolysis.

B. Procedures. The general procedures and dosimetry have been described.[1,2] Solid A was used in the form of the original spherical beads (2–6 mm. in diameter). Solids B and C were crushed after preparation with a "Diamonite" mortar and pestle to particle sizes of less than 6 mm. in longest dimension.

In the absence of isopropylbenzene all three solids became very dark on irradiation at 36° with cobalt-60 to doses as low as 10^{20} e.v./g. (some coloration was observable at the lowest dose studied, 6×10^{18} e.v./g.). All were decolorized by addition of isopropylbenzene as previously described.[1,2] In the particular post-irradiation procedure used in this work, liquid nitrogen was used on the reaction cell for transfer of isopropylbenzene to the irradiated solid. A period of 1–3 hr. usually elapsed between the end of irradiation and introduction of isopropylbenzene. After warming to room temperature decolorization was usually complete in 0.5–4 hr., depending on experimental variables. The system was allowed to stand for 1–2 hr. after complete decolorization and then was allowed to stand overnight with liquid nitrogen placed on an adjoining trap. At the larger weights of isopropylbenzene used per gram of solid, some liquid transferred to the trap overnight. The previously described product recovery procedure[1,2] involving use of a boiling water bath on the reaction cell for 4 hr. with liquid nitrogen on the adjoining trap was then used.

Gas yields reported are for total gas volatile at −118°. Gas yields obtained in the reaction of isopropylbenzene on irradiated solid were too small for analysis. The gas product from one irradiation of isopropylbenzene adsorbed on solid B was analyzed mass spectrometrically. All liquid products were analyzed by gas–liquid chromatography on a Burrell Kromo-Tog K-7 with both a 2-m. silicone column at 250° and a 1.5-m. Apiezon-L column at 200–225°.

III. Results

A. Solid A. A complete study of the irradiation of isopropylbenzene adsorbed on solid A and preliminary

(3) The general expression "excitations" is used in the absence of definitive evidence for the mechanism of energy storage in the solid. It is considered probable that the long-lived excitations responsible for benzene formation are trapped electrons and/or concomitant positive holes.

(4) M. M. Marisic, U. S. Patent 2,384,946 (Sept. 18, 1945), to Socony-Vacuum Oil Co.

results on the reaction of isopropylbenzene on irradiated solid A have been reported.[1,2] Further results on the post-irradiation reaction are shown in Fig. 1.

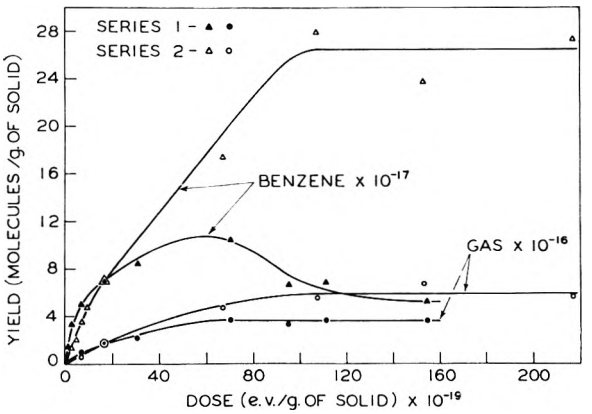

Figure 1. Reaction of isopropylbenzene on γ-irradiated silica-alumina A.

In series 1, 30–35 g. of solid was irradiated in each experiment and approximately 0.2 g. of isopropylbenzene was added to the irradiated solid; therefore, the per cent decomposition of isopropylbenzene increased with increasing dose and reached values in the neighborhood of 70%. With increasing dose, the number of long-lived excitations produced in the solid would be expected to increase and to approach a limiting value corresponding to saturation of the responsible defects; this would be manifested as an approach of product yields to a limiting value with increasing dose to the solid. Although the gas yield in series 1 exhibits such behavior, the benzene yield is seen to pass through a maximum and then to decrease considerably with further increase in dose. This would suggest that benzene is being destroyed or irreversibly chemisorbed by excitations which otherwise would react with isopropylbenzene. Although gas products apparently are not being removed by a similar process, gas yields may be low as a result of failure of isopropylbenzene to react with all the excitations.

In series 2, the number of molecules of isopropylbenzene added to the irradiated solid per electron volt of energy absorbed was kept approximately constant at 0.2; therefore, the per cent decomposition should be approximately constant at the lower doses and decrease towards zero at higher doses. Figure 1 shows that limiting values of both yields are reached in series 2 at large doses. Consequently, in post-irradiation experiments on all three solids the limiting yields of products were determined as the average value for points on the plateau attained at large doses under experimental conditions identical with those of series 2.

The gas product of the post-irradiation reaction on solid A was nearly 100% noncondensable at −196°.

B. Solid B. Yields for the reaction of isopropylbenzene on irradiated solid B are given in Table II. Some benzene was formed in blank experiments on the unirradiated solid but no gas was formed. The gas product of the post-irradiation reaction on solid B was 92–95% noncondensable at −196°.

Table II: Comparison of Yields[a] in Reaction of Isopropylbenzene on γ-Irradiated Silica-Aluminas

	Solid		
	A	B	C
Gas	0.59	1.17	0.68
Benzene	26.4	61.5	233
Zero-dose[b]	0.0	4.6	71
Corrected	26.4	56.9	162

[a] Yields are saturation values obtained by averaging yields on the plateau reached at large values of dose/g. of solid. Units are (molecules/g. of solid) × 10^{-17}. [b] Yields obtained in blank experiments on unirradiated solids.

Results for the irradiation of isopropylbenzene adsorbed on solid B are shown in Fig. 2 and 3. The *G* value is defined as the number of molecules formed/100 e.v. of energy absorbed by the whole system—solid plus isopropylbenzene. As in previously reported work on solid A,[1,2] for values of *F* less than 0.2, the ratio of dose absorbed by the system to weight of isopropylbenzene

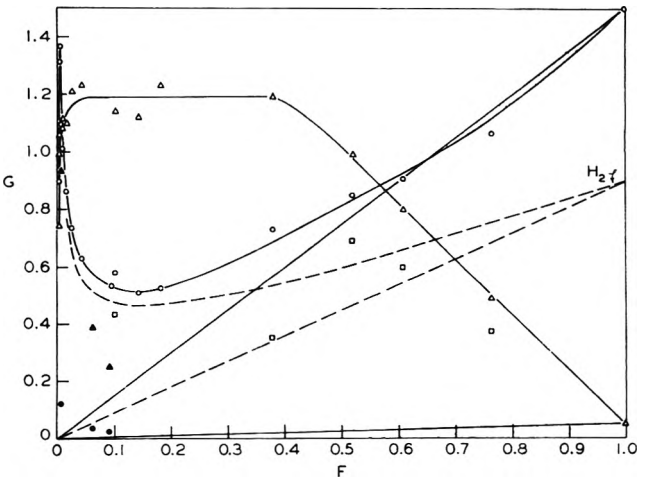

Figure 2. γ-Irradiation of isopropylbenzene and silica-alumina B. Irradiation of isopropylbenzene on silica-alumina: ○ gas × 5; △, C_6H_6; □, $C_{12}H_{18}$. Reaction of isopropylbenzene on irradiated silica-alumina: ●, gas × 5; ▲, C_6H_6.

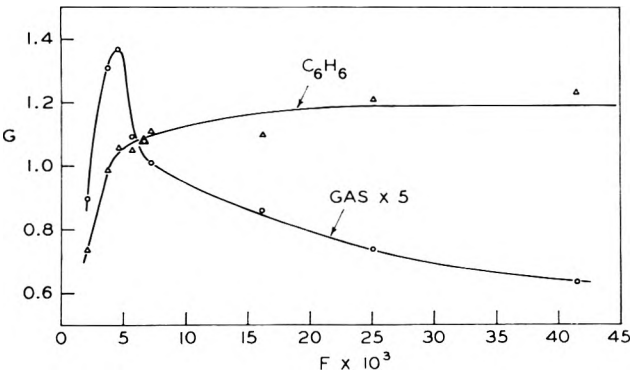

Figure 3. γ-Irradiation of isopropylbenzene on silica–alumina B at low F.

present was kept constant at about 2.7×10^{19} e.v./mg. At values of F greater than 0.2, experimental limitations necessitated that the ratio of dose to weight of isopropylbenzene decrease with increasing F. Because of the lower per cent decomposition, the curves in Fig. 2 may be slightly displaced upward for F greater than 0.2. Values of G(benzene) were calculated by subtraction of the blank yield from the yield of benzene obtained in an irradiation experiment. The maximum correction (at lowest F) amounted to 14%, but the correction was usually less than 10%.

Analysis of the gas product from irradiation of isopropylbenzene adsorbed on solid B at $F = 0.00665$ gave the following mole percentages: hydrogen, 96.6; methane, 0.7; ethane, 0.1; propene, 0.3; propane, 0.3; isobutane, 0.9; butenes, 0.1; *n*-butane, 0.8; and pentenes, 0.1%. The percentage of hydrogen is almost identical with that previously obtained in the gas product from irradiation of isopropylbenzene adsorbed on solid A at the same F.[1,2] In the latter case, the gas product was over 90% hydrogen at all values of F from zero to a point beyond complete surface coverage at which the effect of free liquid became appreciable, the liquid itself giving a gas product containing only 60% hydrogen. The curve in Fig. 2 for hydrogen yields was calculated from the analysis at $F = 0.00665$, the previously measured hydrogen yield for $F = 1$,[1,2] and by use of gas analyses obtained in the study of solid A at corresponding values of F.

At $F = 0.182$ free liquid first became evident on the walls of the reaction cell. If 50 Å.^{2} is taken as the cross section of an adsorbed isopropylbenzene molecule, formation of a monolayer would correspond to $F = 0.146$.

The straight lines in Fig. 2 represent the behavior expected if the absorbed radiation energy is initially partitioned between the two phases in proportion to their electron fractions and if adsorbed isopropylbenzene behaves exactly like the liquid without energy exchange or interaction with the solid.

C. Solid C. Results for the reaction of isopropylbenzene on irradiated solid C are given in Table III. An appreciable yield of benzene was obtained in the blank experiment on unirradiated solid. The gas product of the reaction on solid C was about 50% condensable at −196°, in distinct contrast to the gas product from reaction on the other two solids. The values in parentheses denote yields obtained on addition of a second portion of isopropylbenzene to the same solid; after the recovery procedure for the first portion and products, the solid at room temperature was pumped on the high-vacuum line for about 66 hr. prior to addition of the second portion.

Table III: Reaction of Isopropylbenzene on γ-Irradiated Solid C

Dose, (e.v./g.) × 10^{-19}	Yields, (molecules/g. of solid) × 10^{-17}		
	Benzene	Gas	$C_{12}H_{18}$[a]
0	71 (21)[b]	0.0	6.3 (7.4)
156	194	0.48	19.0
228	239 (33)	0.65 (0.17)	24.2 (30)
398	226	0.71	34.8

[a] Combined yield of diisopropylbenzenes (about 70% *meta* and 30% *para*). [b] Values in parentheses denote yields obtained on addition of a second portion of isopropylbenzene to the same solid.

IV. Discussion

A. Irradiation of Adsorbed Isopropylbenzene. In the work on irradiation of isopropylbenzene adsorbed on solid A,[1,2] the observed passage of G(benzene) through a sharp maximum at low surface coverage was attributed to saturation, at the value of F corresponding to the maximum, of those surface sites most effective in benzene formation so that additional isopropylbenzene occupies sites that compete for the transferred energy but are less efficient in benzene formation. The dependence of G(benzene) on F for solid B, as shown in Fig. 2 and 3, exhibits no such maximum. If the earlier interpretation is correct, this would suggest homogeneity of sites on the surface of solid B.

A decrease in G(benzene) might be expected to begin at a value of F corresponding to complete surface coverage, $F = 0.15$. Apparent constancy of G(benzene) to well beyond this value of F may be a result of experimental factors that would tend to obscure the onset of the decrease. As pointed out in section IIIB, the curve beyond $F = 0.2$ may be displaced upward

because of the decreasing over-all per cent decomposition necessitated by experimental limitations. In addition, excess isopropylbenzene may displace product from the surface, thus tending to maintain a lower product concentration on the surface.

Propylene which should be formed concomitantly with benzene is always a negligible product; apparently it is strongly chemisorbed on the solid. Reaction between adsorbed propylene and isopropylbenzene should occur with increasing probability as their concentrations increase on the surface, not only because of greater proximity but also because of a greater mobility of less strongly chemisorbed isopropylbenzene at higher surface coverages.[5] Evidence for such a reaction is seen in the diisopropylbenzene yield, Fig. 2, which approaches 75% of the benzene yield at large values of F.

Comparison of G values in Fig. 2 for reaction of isopropylbenzene on irradiated solid B with those obtained for irradiation of adsorbed isopropylbenzene—for identical values of all experimental parameters—is significant. The sharp decrease in post-irradiation G values reflects the approach to saturation of excitations in the solid, the two lowest G values corresponding to points on the plateau. At the larger doses per gram of solid corresponding to values of $F = 0.05$–0.1, a great deal of absorbed energy is not available for the post-irradiation reaction. It is also apparent that at $F = 0.09$ at least 80% of the benzene yield in irradiation of adsorbed isopropylbenzene cannot be formed in a catalytic reaction on radiation-produced sites during the recovery procedure.

Both the measured G(gas) and the calculated G (hydrogen) pass through a maximum at F near 0.0046 and then through a minimum at a value of F in the neighborhood of complete surface coverage. The behavior of G(hydrogen) in earlier work on solid A[1,2] looks very similar in retrospect although an insufficient number of points was obtained to define accurately the maximum and minimum. A reasonable explanation of this behavior is that energy absorbed in the solid produces hydrogen atoms by rupture of O–H bonds. At low surface coverage these atoms are largely recaptured by surface free valencies, but with increasing surface coverage, abstraction of hydrogen atoms from isopropylbenzene gives rise to increasing hydrogen yields. At a certain value of F additional isopropylbenzene molecules may act in such a manner as to prevent O–H ruptures giving rise to the observed maximum and subsequent decrease in G(hydrogen). Beyond complete surface coverage G(hydrogen) increases as a result of the contribution of direct radiation absorption in the unadsorbed excess liquid. This mechanism is supported by work in which hydrogen atoms were detected by electron spin resonance in silicas, aluminas, and silica–aluminas which had been γ-irradiated at $-196°$.[6,7] Emmett and co-workers[6] found G(H) = 0.09 in an irradiated silica–alumina that had been evacuated in pretreatment at 500°.

B. Reaction of Isopropylbenzene on Irradiated Solids. Comparison of plateau yields in Table II shows that solid B with its sixfold lower iron content gave larger yields of benzene than solid A both in blank and in post-irradiation experiments. Solid C which is essentially indistinguishable chemically from solid A gave still higher benzene yields than solid B in both the blank and post-irradiation experiments. If one benzene molecule were formed per iron atom, the corrected benzene yield on solid C would require 0.15 wt. % of iron as compared to the actual 0.030 wt. %. The discrepancy for solid B corresponds to a factor of ten. Thus, the phenomena appear to be associated not with impurity content but with properties inherent in the structure or composition of pure silica–alumina that are sensitive to variations in the preparation and pretreatment techniques.[8]

The appreciable benzene yields obtained on unirradiated solids B and C in blank experiments, as shown in Table II, indicate that reaction on certain inherent sites on the solid surface involves a free-energy decrease. Apparently, the dealkylation step on these sites is rapid, and the sites are poisoned by propylene at these low temperatures. Supporting evidence is shown in the zero-dose experiment of Table III. A 3.4-fold lower benzene yield was obtained on addition of a second portion of isopropylbenzene, but the diisopropylbenzene yield actually increased. Clearly, propylene formed on the first addition of isopropylbenzene blocked sites and was partially converted to diisopropylbenzenes by the second portion of isopropylbenzene. This phenomenon is shown again in the post-irradiation experiment in Table III at 228×10^{19} e.v./g.

The observation that unirradiated solids can produce benzene under the conditions used in these experiments suggests that a re-examination is warranted of the previously postulated[1,2] energy storage and transfer interpretation of the post-irradiation reaction. In section IIIA, evidence was presented for direct formation of benzene on contact of isopropylbenzene with irradiated solid A and subsequent destruction on excitations not

(5) J. A. Hockey and B. A. Pethica, *Trans. Faraday Soc.*, 58, 2017 (1962).

(6) P. H. Emmett, R. Livingston, H. Zeldes, and R. J. Kokes, *J. Phys. Chem.*, 66, 921 (1962).

(7) V. B. Kazansky, G. B. Pariisky, and V. V. Voevodsky, *Discussions Faraday Soc.*, 31, 203 (1961).

(8) M. W. Tamele, L. B. Eyland, L. D. Rampino, and W. G. Schlaffer, Proceedings of the 3rd World Petroleum Congress, The Hague, 1951, Section IV, p. 98.

deactivated by the added isopropylbenzene. Also, it was concluded in section IVA that at least 80% of the benzene yield in irradiation of isopropylbenzene adsorbed on solid B at $F = 0.09$ is not formed in a catalytic reaction on radiation-induced sites during the recovery procedure. The experiments at zero-dose and 228×10^{19} e.v./g. in Table III were undertaken to provide additional information on the post-irradiation mechanism. Addition of a second portion of isopropylbenzene to the irradiated solid resulted in a benzene yield not much larger than that obtained from the second isopropylbenzene addition in the blank experiment. Moreover, the slight increase could well be due to residual benzene not completely removed in the first recovery process. The recovery of additional gas (never formed in blank experiments) on addition of a second portion of isopropylbenzene lends credence to this interpretation.

Although the mechanism of the post-irradiation formation of benzene is not established by these experiments, the reaction is clearly not a catalytic dealkylaton on radiation-induced sites during the recovery procedure. Either the energy of an excitation is utilized to satisfy an energy requirement for dealkylation, or the excitation itself, acting like a strong catalytic site, induces dealkylation on contact with isopropylbenzene and is deactivated in the process.

A mechanism of the former type could involve transfer of an electron from isopropylbenzene to a trapped positive hole; the isopropylbenzene radical cation then may migrate to a trapped electron site, whereupon the combination energy causes dealkylation or the radical cation may rearrange and dissociate into propylene and a benzene radical cation that migrates to and is neutralized by a trapped electron. In either case the propylene remains strongly chemisorbed on the surface, probably on an acid site.

A plausible mechanism of the latter type follows. Isopropylbenzene is dealkylated by chemisorption on an acid site (H_s^+) of unirradiated silica–alumina, and the propylene is firmly bound to the site at low tempera-

$$H_s^+ + C_6H_5C_3H_7 = C_6H_6 + C_3H_6 \cdot H_s^+$$

ture (<100°). Irradiation of the solid in the absence of isopropylbenzene produces positive holes that become trapped at aluminum atoms, as illustrated below; the associated hydrogen atom becomes more acidic and

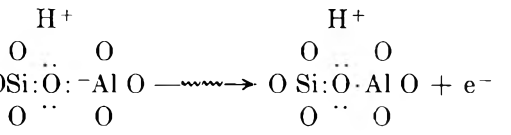

functions in the same manner as an inherent acid site. There is abundant evidence in the literature that aluminum atoms in a silica matrix function as positive hole traps and that various chemical and physical observations made on irradiated silica and quartz correlate with aluminum content.[9-13] Thus, the benzene yields attained on irradiation to large doses may be determined by the fraction of aluminum atoms which by virtue of some structural attribute[8] are able to trap positive holes. The corrected yields in Table II would correspond to the number of these trapping centers per gram of solid.

(9) M. C. M. O'Brien and M. H. L. Pryce, Bristol Conference on Defects in Crystalline Solids, Physical Society, London, 1955, p. 88.

(10) R. W. Ditchburn, E. W. J. Mitchell, E. G. S. Paige, J. F. Custers, H. B. Dyer, and C. D. Clark, *ibid.*, p. 92.

(11) E. Lell, *Phys. Chem. Glasses*, **3**, No. 3, 84 (1962).

(12) H. W. Kohn and E. H. Taylor, *Proc. Intern. Congr. Catalyse, 2e, Paris, 1960*, **2**, 1461 (1961).

(13) H. W. Kohn, *J. Catalysis*, **2**, 208 (1963).

Intermolecular Hydrogen Bond Involving a π-Base as the Proton Acceptor.

I. Detection by the Refractive Index Method

by Zen-ichi Yoshida, Eiji Osawa, and Ryohei Oda

Department of Synthetic Chemistry, Faculty of Engineering, Kyoto University, Kyoto, Japan
(Received March 14, 1964)

Complex formation between proton-donating molecules and aromatics and olefins in heptane, dioxane, and water as solvents was studied by the refractive index method. Of 108 pairs of proton donors and acceptors examined, 61 pairs showed complex formation. Hydrogen bond formation of this type seems to increase as the number of conjugated double bonds (and condensed rings) in the acceptor molecule increases. Even in water, a weak interaction was found to exist between alcoholic OH and sulfonated aromatic hydrocarbons. The results obtained lend some support to the current hypothesis on cellulose substantivity which assumes that the O–H···π-electron type bond between cellulosic OH and delocalized π-electron clouds of dye is partly responsible for the affinity of dyes for cellulosic materials.

Introduction

Recently, a new interpretation of the origin of substantive affinity of dyestuff on cellulosic substrates has been made,[1,2] which suggested that the interaction between cellulosic OH groups and delocalized π-electron clouds of dye molcules may be responsible for the affinity. Although such an association between proton donors and π-bases has long been known,[3] previous investigations of this type of hydrogen bonding have been done exclusively in nonaqueous media. Therefore, it appeared of interest to determine whether or not such a weak interaction can survive when exposed to competition with water for π-bases under dyeing conditions.

In this communication, the refractive index method developed by Giles and his school[4] was applied to detect the complex of the type X–H···π-base.

Experimental[5]

Materials. Sodium Naphthalene-1-sulfonate. Commercial reagent was recrystallized three times from water and dried for 2 hr. at 100° under reduced pressure. *Anal.* Calcd. for $C_{10}H_7SO_3Na$: Na, 9.99. Found: Na, 9.96.

Sodium Phenanthrene-3-sulfonate. Phenanthrene was sulfonated by the method of Fieser.[6] White leaflike crystals were obtained. *Anal.* Calcd. for $C_{14}H_9SO_3Na$: Na, 8.21. Found: Na, 8.07. *p*-Toluidine salt: m.p. 221–223° (lit.[6] m.p. 222°).

Disodium Pyrene-1,6-disulfonate. Pyrene was sulfonated according to the direction of Tietz and Bayer.[7] Yellow crystalline powder was obtained. *Anal.* Calcd. for $C_{16}H_8S_2O_6Na_2$: Na, 11.32. Found: Na, 11.32.

Sodium n-Butane-1-sulfonate. A mixture of 41 g. (0.3 mole) of *n*-butyl bromide and 300 ml. of saturated aqueous solution of sodium sulfite was refluxed for 10 hr. with stirring. After cooling, water was removed from the reaction mixture under reduced pressure and the residue was extracted with three 200-ml. portions of hot ethanol. From the combined extract ethanol was removed and the residue recrystallized twice from 75% ethanol to give long thin white plates.

(1) C. H. Bamford, *Discussions Faraday Soc.*, **16**, 229 (1954).

(2) W. L. Lead, *J. Soc. Dyers Colourists*, **73**, 464 (1957); **75**, 195 (1959).

(3) (a) G. C. Pimentel and A. L. McClellan, "The Hydrogen Bond," W. H. Freeman and Co., San Francisco, Calif., 1960, p. 202; (b) P. von R. Schleyer, D. S. Trifan, and R. Bacskai, *J. Am. Chem. Soc.*, **80**, 6691 (1958); (c) R. West, *ibid.*, **81**, 1614 (1959); (d) M. Oki and H. Iwamura, *Bull. Chem. Soc. Japan*, **34**, 1395 (1961).

(4) (a) C. H. Giles, *et al.*, *J. Chem. Soc.*, 3799 (1952); (b) F. M. Arshid, *et al.*, *ibid.*, 67 (1955); 72, 559, 1272 (1956); (c) D. S. E. Campbell, *et al.*, *J. Soc. Dyers Colourists*, **73**, 546 (1957); (d) I. C. L. Bruce, *et al.*, *J. Chem. Soc.*, 1310 (1958); 559 (1959).

(5) Melting points are corrected.

(6) L. F. Fieser, "Organic Syntheses," Coll. Vol. II, John Wiley and Sons, Inc., New York, N. Y., 1948, p. 482.

(7) E. Tietz and O. Bayer, *Ann.*, **540**, 201 (1939).

Anal. Calcd. for $C_4H_9SO_3Na$: Na, 14.36. Found: Na, 14.19.

Other commercially available reagents were purified immediately before use by the usual manner except for the following: Methanol, Eastman Kodak Spectrograde reagent, was used without further purification. Naphthalene was purified as the picrate (m.p. 80.7–80.9°; lit. m.p. 80.2°). Anthracene (crude anthracene) was converted to the maleic anhydride adduct, recrystallized from acetone, m.p. 262–263° (Found: C, 78.24; H, 4.39; O, 17.37), submitted to thermal decomposition in the presence of soda lime, sublimed, and then recrystallized from ethanol–benzene (m.p. 218.1–218.5°; lit. m.p. 218°). For glucose, sucrose, and cellobiose ($0.3H_2O$), the commercial reagents were dried and used directly (m.p.: 149.5–150.3°, 168–173° dec., and 225–230° dec., respectively; lit. m.p.: 147° dec., 160–186° dec., and 225° dec.).

Measurements of Refractive Indices. Various amounts of a solution of a proton donor and an equimolar solution of a proton acceptor were introduced into test tubes from the respective burets so as to keep the total concentrations constant, and the ratios of concentrations of each component variant. The test tubes were stoppered, shaken well, and left to stand overnight. The refractive indices of the solutions were measured with the Abbé refractometer[8] at constant temperature.

The mean n-values were squared and plotted against the molar concentrations of one of each pair of components. Straight lines were obtained when no complex was formed or its concentration was negligible. Complex formation was found by a sudden change in the slope, the mole ratio at the bending point showing the composition of the complex. Complicated complexes, in which the mole ratios of donor to acceptor were above 4:1 or below 1:4, were difficult to detect by the present method.

Results and Discussion

All combinations of proton donors and acceptors, shown in Table I, were examined in three solvents: n-heptane, dioxane, and water.

Of 108 pairs of donors and acceptors examined, 61 combinations showed at least one kind of complex formation. The data are summarized in Table II.

Changes in the slope of the n^2 *vs.* concentration plots were not as sharp and clear-cut as in the case of X–H···Y hydrogen bond pairs where X and Y = O, N, and S.[4] As sp^2 carbon is less electronegative than either the nitrogen or oxygen atom, both the equilibrium concentration and the polarization (contributing to molar refraction) of the complex may be smaller than those of the X–H···Y type hydrogen-bonding complexes.

Table I: Proton Donors and Acceptors

Solvent		Donors, D, and acceptors, A
n-Heptane	D[a]	Ethanol, acetic acid, and phenol
	A	Cyclohexene, benzene, cyclohexylbenzene, biphenyl, p-terphenyl,[b] decalin, tetralin, naphthalene, anthracene,[b] phenanthrene, pyrene, *trans*-stilbene, and fluorene
Water	D	D-Glucose, sucrose, cellobiose, pentaerythritol, and ethanol
	A	Sodium naphthalene-1-sulfonate, sodium phenanthrene-3-sulfonate, disodium pyrene-1,6-disulfonate, and sodium n-butane-1-sulfonate
Dioxane	D	Water, methanol, ethylene glycol, acetone, acetonitrile, ethyl acetoacetate, and diethyl malonate
	A	Decalin, tetralin, benzene, naphthalene, anthracene, pyrene, cyclohexylbenzene, biphenyl, and p-terphenyl

[a] Chloroform and piperidine, as examples of weak proton donors, were tested with naphthalene as an acceptor at a total concentration of 0.4 mole/l. at 27.4 and 27.6°, respectively, but complex formation was not observed in either case. [b] Benzene was used as a solvent because of the poor solubilities of anthracene and p-terphenyl in n-heptane.

n-Heptane Solution. Refractometry was carried out initially in an inert solvent, n-heptane, to distinguish the net effect from the solvation problem. A possible interaction between π-electron clouds of phenol and aromatics through dispersion force is not detected by this method, since the benzene–naphthalene system did not show any bending in the refractive index diagram. This kind of interaction appears to produce no observable change in the refractive index of the solution.

As is seen in Table III, as the conjugated system in the aromatic acceptors becomes larger in size, the complex formation tends to be detected more easily and the mole ratio (D/A) of the complex becomes larger. This means that the formation constant of the complex is increased by the use of large aromatics as proton acceptors. Indeed, the cyclohexene complex was not detected by the present method. Since the strengths of X–H···π-base interaction are not varied largely as far as nonsubstituted aromatics and ordinary proton donors are paired,[9] this tendency will be interpreted

(8) Accuracy of refractive index was ±0.0002. Scale calibration to the authentic samples was omitted.

(9) Z. Yoshida and E. Osawa, to be published.

Table II: Complexes Detected by Refractometry

Proton acceptor, A	Proton donor, D	Total concn., *M*	Temp., °C.	Complex mole ratio, A:D	Fig. no.
		n-Heptane solution[a]			
Benzene	Ethanol	0.2	28.2	1:1	
Cyclohexylbenzene	Ethanol	0.2	27.0	1:1	
Biphenyl	Ethanol	0.2	27.1	1:2	
p-Terphenyl[b]	Phenol	0.05	27.3	1:1, 1:3	
p-Terphenyl[b]	Acetic acid	0.05	27.9	1:1	
Naphthalene	Ethanol	0.3	28.0	1:1	
Naphthalene	Phenol	0.2	27.6	1:1	
Naphthalene	Acetic acid	0.3	27.0	1:1	
Anthracene	Ethanol	0.05	28.0	1:1, 1:2	
Anthracene	Phenol	0.05	27.0	1:2, 1:3	
Phenanthrene	Phenol	0.1	26.4	1:2	
Phenanthrene	Acetic acid	0.1	27.3	1:1	
Pyrene	Ethanol	0.1	27.6	1:1, 1:2	
Pyrene	Phenol	0.1	27.5	1:2	
Pyrene	Acetic acid	0.1	27.1	1:1	1
trans-Stilbene	Phenol	0.05	20.0	1:1, 1:3	
Fluorene	Ethanol	0.1	22.2	1:1	
Fluorene	Acetic acid	0.1	22.2	1:1	
		Aqueous solution[c]			
Na naphthalene-1-sulfonate	Pentaerythritol	0.2	23.4	1:2, 2:1	2
Na phenanthrene-3-sulfonate	Glucose	0.1	18.0	1:1	
	Sucrose	0.1	17.8	1:1	
	Cellobiose	0.05	18.1	1:1	
	Pentaerythritol	0.1	17.7	1:1	
Di-Na pyrene-1,6-disulfonate	Glucose	0.05	18.8	1:1	
	Sucrose	0.05	18.0	1:1	
	Pentaerythritol	0.05	17.3	1:1	
		Dioxane solution			
Decalin	Acetonitrile	0.1	21.0–22.0	1:1[d]	
Tetralin	Water	0.1	20.4	1:1	
Tetralin	Methanol	0.1	19.8	1:1	
Tetralin	Ethylene glycol	0.1	21.7	1:1	
Tetralin	Ethyl acetoacetate	0.1	20.9	1:1 (?)	
Benzene	Ethylene glycol	0.1	22.0	1:1	
Benzene	Acetonitrile	0.4	25.9	1:1	
Benzene	Ethyl acetoacetate	0.1	21.3	1:1 (?)	
Naphthalene	Water	0.1	18.8	1:1, 1:2, 1:3	
Naphthalene	Methanol	0.1	19.7	1:2	
Naphthalene	Ethylene glycol	0.1	22.5	1:2 (?)	
Naphthalene	Acetonitrile	0.1	18.9	1:2 (?)	
Naphthalene	Ethyl acetoacetate	0.1	18.9	1:2	
Naphthalene	Diethyl malonate	0.1	19.0	1:2	
Anthracene	Ethylene glycol	0.05	26.2	1:2	
Anthracene	Ethyl acetoacetate	0.05	27.2	1:1	
Anthracene	Diethyl malonate	0.05	27.2	1:1, 1:2 (?)	
Pyrene	Ethylene glycol	0.1	27.0	1:2	
Pyrene	Acetonitrile	0.1	27.0	1:1	
Pyrene	Diethyl malonate	0.1	27.0	2:3	
Cyclohexylbenzene	Ethylene glycol	0.1	22.0	1:1	
Biphenyl	Water	0.1	19.2	1:1	3
Biphenyl	Methanol	0.1	19.3	1:1	
Biphenyl	Ethylene glycol	0.1	22.4	1:1	
Biphenyl	Ethyl acetoacetate	0.1	19.1	1:2	
Biphenyl	Diethyl malonate	0.1	19.8	1:2 (?), 1:3 (?)	
p-Terphenyl	Water	0.05	25.1	1:1	
p-Terphenyl	Methanol	0.05	25.2	1:1 (?)	
p-Terphenyl	Ethylene glycol	0.05	26.0	1:1, 1:2 (?)	
p-Terphenyl	Ethyl acetoacetate	0.05	24.6	1:1 (?), 1:2 (?)	
p-Terphenyl	Diethyl malonate	0.05	24.6	1:1 (?)	

[a] Decalin showed no complex formation with any donor in *n*-heptane. [b] In benzene. [c] Sodium butane-1-sulfonate showed no complex formation with any donor. [d] Decalin showed complexing only with acetonitrile, in dioxane. Measurements were repeated at two different temperatures.

Table III: Complex Detecting Frequency (%) and the Number of Conjugated Double Bonds in Acceptor Molecules

No. of conjugated double bonds	Complex mole ratio (D/A), % 1:1	1:2	1:3	Sum
3	4.2	0	0	4.2
5	18.9	0	0	18.9
6	6.3	3.2	0	9.5
7	6.3	6.3	4.2	16.8
8	12.6	12.0	6.3	31.5
9	12.6	0	6.3	18.9

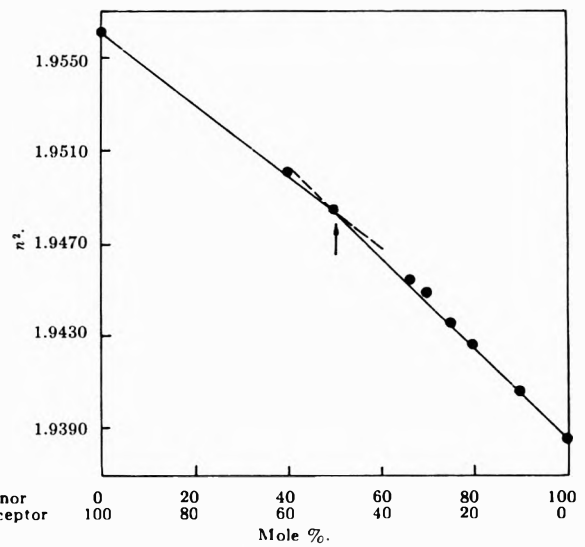

Figure 1. Pyrene–acetic acid in heptane; total concentration 0.1 mole/l. at 27.1°.

as follows. As Lead[2] has pointed out briefly, the fact that the interaction we now discuss is weak and the proton acceptors are extended π-electron clouds would suggest that the bonds formed are located indefinitely and have a higher degree of freedom than in the case of

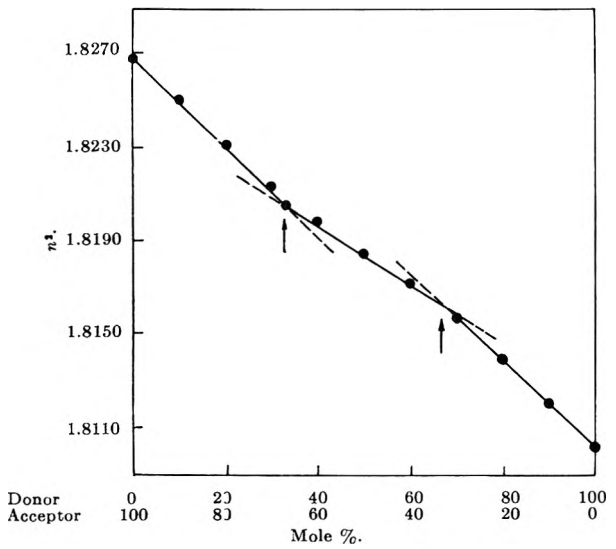

Figure 2. Sodium naphthalene-1-sulfonate–pentaerythritol in water; total concentration 0.2 mole/l. at 23.4°.

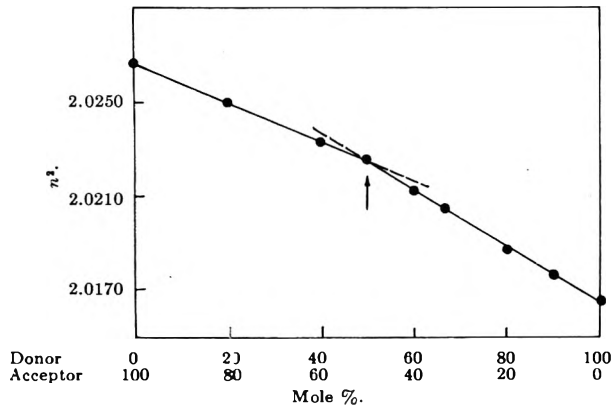

Figure 3. Biphenyl–water in dioxane; total concentration 0.1 mole/l. at 19.2°.

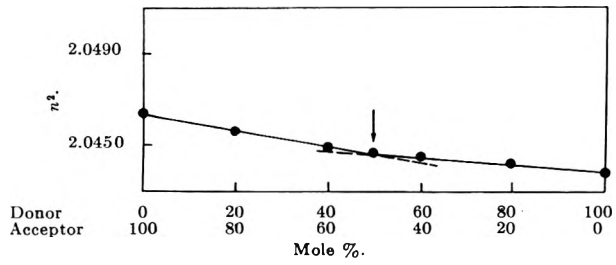

Figure 4. Decalin–acetonitrile in dioxane; total concentration 0.1 mole/l. at 21°.

the X–H···Y type hydrogen bonding. Therefore, the entropy of the system increases as the conjugation of π-base is extended, favoring complex formation. According to a more recent report by West,[10] $-\Delta S°$ of association of phenol with naphthalene and phenanthrene in CCl_4 solution (2.8 and 1.0 cal. deg.$^{-1}$ mole^{-1}) are smaller than that of benzene–phenol (4.0 cal. deg.$^{-1}$ mole^{-1}), which in turn is considerably smaller than that of alkyl ether–phenol (10–18 cal. deg.$^{-1}$ mole^{-1}), consistent with the above reasoning.

Aqueous Solution. As shown in Table II, even in water, several complexes were barely detected between alcohols and sulfonated aromatics, although the bending in the refractive index diagram is obscure. There is no possibility of electrostatic interaction between the sulfonate group and the alcoholic OH group because sodium *n*-butane-1-sulfonate produced no complexes with hydroxyl compounds (glucose, sucrose, cellobiose, and pentaerythritol).

Dioxane Solution. As the changes of slopes in the n^2 *vs.* concentration plots in water were all very obscure compared to those observed in heptane, refractometry was carried out in dioxane, whose proton-accepting power is less than that of water.[11] As shown in Table II, many instances were added for the existence of X–H···π-base interaction in hydrogen-bonding solvents. Complex formation in hydrogen-bonding solvents must be preceded by the desolvation of components, an energetically unfavored process. Indeed, it is suggested by Giles[12] on the basis of refractive index measurements and surface film experiments that ordinary hydrogen bonding to the solvated OH group of cellulose in water could not occur. Therefore, it is to be expected in the present experiments that the entropy effect referred to above might have played a subtle role in the free energy balance of the desolvation–complexing equilibrium.[13]

The present result, however, seems to provide some indirect support for the hypothesis[1,2] that this type of hydrogen bonding may contribute to substantive adsorption of dyes to highly solvated cellulosic materials in water.

In both heptane and dioxane solution, decalin naturally proved not to be a proton acceptor, since it has no π-electron, but the case of decalin–acetonitrile in dioxane was an exception. A 1:1 complex was detected on repeated measurements at two temperatures (Fig. 4). The nature of the intermolecular forces acting in this complex is yet unknown.

(10) R. West, International Symposium of Molecular Structure and Spectroscopy, Tokyo, Sept., 1962, D-117.

(11) M. Tsuboi, *Bull. Chem. Soc. Japan*, 25, 385 (1952).

(12) F. M. Arshid, C. H. Giles, and S. K. Jain, *J. Chem. Soc.*, 559 (1956).

(13) In this connection, further work is in progress in our laboratory on the thermodynamics of X–H···π-base type hydrogen bonding.

The Vapor Pressure of Palladium

by P. D. Zavitsanos

Missile and Space Division, General Electric Company, Philadelphia, Pennsylvania *(Received March 26, 1964)*

The vapor pressure and heat of vaporization of palladium were measured using a recording microbalance with the Knudsen technique. Over the temperature range of 1537–1841°K., the measured vapor pressure may be presented by: $\log P_{atm} = 5.99 - 18{,}898/T$. The mean heat of sublimation at 298°K. is 89.8 ± 0.9 kcal./mole and the normal boiling point was estimated to be 3150 ± 100°K.

The quantitative studies of the vaporization of palladium were rather unsatisfactory until Dreger and Margrave[1] measured the rate of sublimation in the temperature range 1220–1640°K. using the Langmuir technique. Using the same technique in the temperature range 1294–1488°K, Hampson and Walker[2] produced data that agreed quite well with Dreger and Margrave's work.

The only Knudsen effusion work on palladium was done by Haefling and Daane.[3] This work is in wide disagreement with the Langmuir results. The vapor pressure reported by these authors was one order of magnitude higher and the second-law heat of sublimation 10 kcal. lower.

Experimental

The apparatus used combines the Knudsen target technique with continuous microbalance recording. A detailed description of the technique will be given elsewhere.[4] The sample is heated by electron bombardment in a 2 × 2 cm. Knudsen cell while a well-defined fraction of the effusing vapor is condensed on a collector. The collector was made from molybdenum sheet rolled to a conical shape. The weight gain of the collector was followed by a Sartorius-Electrona microbalance and plotted by a recorder. A collimating slit of 0.325-cm. radius was placed 1.7 cm. above the cell orifice. The total rate of effusion, m, in g./cm.^{2} sec. is obtained from the observed condensation rate m' (g./sec.)

$$m = m'(C^2 + R'^2)/R'^2A$$

where R' is the radius of collimating slit, C is the distance of the collimating slit from the cell, and A = 0.0126 cm.^{2}, is the area of effusion hole. (The fraction of the effusing vapor that went through the slit and condensed on the target was about 0.0353.)

The vapor pressure was calculated from the Knudsen equation

$$\log P_{atm} = \log m + {}^1/_2 \log T - {}^1/_2 \log M - 1.647$$

where m is the rate of effusion in g. cm.$^{-2}$ sec.$^{-1}$ and M is the average molecular weight of the effusing vapor. In our calculations the monatomic species was considered as the only important species. The sample was obtained from Fisher Scientific Co. and was the "purified Pd black" type. The Knudsen cell was made out of tungsten because tungsten metal will not react with palladium.[3]

The rate of effusion was measured mainly by continuously recording the weight of the target during the vaporization process. Several runs, however were carried out where the rate was obtained by weighing the target before and after the run with the furnace cold. The temperature of the cell was kept constant with an emission regulator and was measured by focusing an optical pyrometer on a blackbody hole drilled on the side of the cell. The pyrometer was calibrated against an NBS lamp and all readings were adjusted for window corrections.

In the recording technique, the apparent weight of the target was influenced (reduced several micrograms)

(1) L. H. Dreger and J. L. Margrave, *J. Phys. Chem.*, **64**, 1323 (1960).

(2) R. F. Hampson and R. F. Walker, *J. Res. Natl. Bur. Std.*, **66A**, 177 (1962).

(3) J. F. Haefling and A. H. Daane, *Trans. AIME*, **212**, 115 (1958).

(4) P. D. Zavitsanos, *Rev. Sci. Instr.*, **35**, 1061 (1964).

by the momentum transfer of the vapor. This effect, however, should not affect the validity of these results since the momentum transfer exerts a constant force for constant temperature and this technique is only concerned with differences in target weight.

Results and Discussion

The results of the vaporization studies on palladium are summarized in Tables I and II.

Rates of effusion were measured (1) by continuously weighing the target, Table I, whereby the corresponding weight changes were only a few micrograms and (2) by weighing the target before and after the run (with the furnace cold), Table II, where large changes in weight (several hundred micrograms) are taking place. It is apparent that the results are essentially the same. A least-squares plot of the data, described by the equation

$$\log P_{atm} = 5.698 - \frac{18{,}425}{T}$$

is shown in Fig. 1 in comparison with the previous work at lower temperatures. Combination of the vapor pressures with the free energy functions from Stull and Sinke[5] produced an average third-law heat of vaporization at 298°K., $\Delta H°_{298} = 89.8 \pm 0.9$ kcal./mole.

Table I: Vapor Pressure Data on Palladium Metal—Continuous Weighing

T, °K.	Rate × 10^6, g. $min.^{-1}$	$-\log P$, atm.	$\Delta H°_{298}$
1832	17.5	4.22	88.93
1841	16.5	4.25	89.60
1587	0.23	6.124	91.38
1623	0.63	5.69	90.02
1624	0.50	5.792	90.83
1674	2.50	5.086	88.13
1721	3.60	4.92	89.24
1720	3.34	4.96	89.45
1702	2.25	5.13	89.95
1701	2.55	5.07	89.42
1649	1.60	5.28	88.33
1592	0.233	6.227	92.22
		$\Delta H°_{298}$ (av.) =	89.79 ± 0.90 kcal./mole

Table II: Vapor Pressure Data on Palladium Metal—"before and after" Weighing

T, °K.	Rate × 10^6, g. $min.^{-1}$	$-\log P$, atm.	$\Delta H°_{298}$
1792	5.35	4.74	91.35
1698	2.08	5.16	89.91
1649	0.861	5.55	90.36
1806	5.83	4.61	90.96
1537	0.242	6.12	88.38
1543	0.183	6.24	89.74
1570	0.456	5.84	88.21
		$\Delta H°_{298}$ (av.) =	89.84 ± 0.91 kcal./mole

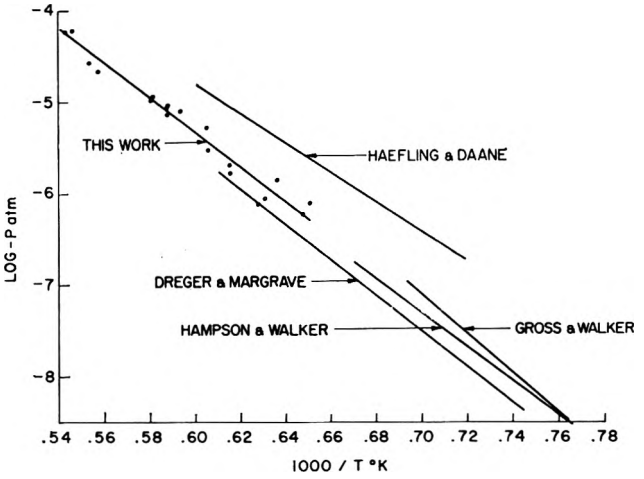

Figure 1. The vapor pressure of palladium.

The third-law method gives a $\Delta H°_{298} = 89.8 \pm 0.9$ kcal./mole. If one uses this value of $\Delta H°_{298}$ and the fef functions, the vapor pressure is represented by

$$\log P_{atm} = 5.99 - \frac{18{,}898}{T}$$

and a boiling point of 3150 ± 100°K. is calculated. The second-law value of $\Delta H°_{298}$ was 86.7 kcal./mole.

These results are in disagreement with the work of Haefling and Daane[3] and Walker, *et al.*,[6] but in good agreement with Dreger and Margrave,[1] where

$$\log P_{atm} = 6.195 - \frac{19{,}425}{T}$$

$$\Delta H°_{298} = 91 \pm 0.8 \text{ kcal./mole}$$

and Hampson and Walker,[2] where

$$\log P_{atm} = 5.869 - \frac{18{,}655}{T}$$

$$\Delta H°_{298} = 89.2 \pm 0.8 \text{ kcal./mole}$$

Additional confidence in these results is gained from

(5) D. R. Stull and G. C. Sinke, "Thermodynamic Properties of the Elements," Advances in Chemistry Series, No. 18, American Chemical Society, Washington, D. C., 1956.

(6) R. F. Walker, J. Efimenko, and N. Lofgren, "Proceedings of the Conference on Physical Chemistry in Aerodynamics and Space Flight," John Wiley and Sons, Inc., New York, N. Y., 1961.

the work of Alcock and Hooper.[7] Using the transpiration method, they reported the vapor pressure of palladium at two temperatures, 1673 and 1773°K., $\log P_{atm} = -5.34$ and -4.61, respectively.

From the observed agreement between these results and those obtained by the Langmuir and transpiration techniques, one can safely conclude: (a) The vaporization coefficient of Pd is close to unity. The calculated heats (89.79, 89.2, and 91.0) are in agreement within the experimental error of ±0.8–0.9 kcal. With this kind of uncertainty, it is rather difficult to say whether there is a small activation energy associated with the Langmuir results. (b) The high vapor pressure values obtained in the other Knudsen work could be due either to additional effusion through cracks or holes in the carbon cell, or to volatile impurities resulting perhaps from the reaction between Pd and carbon as suggested by Dreger and Margrave.[1]

Acknowledgments. The author wishes to acknowledge the assistance of Mr. G. R. Brownlee in obtaining the experimental data. This research was sponsored by the Ballistic Systems Division, USAF, Contract No. AF 04(694)-222.

(7) C. B. Alcock and G. W. Hooper, *Proc. Roy. Soc.* (London), **A254**, 559 (1960).

Steady-State Radiolysis of Gaseous Oxygen[1]

by Kenji Fueki and John L. Magee

Department of Chemistry and The Radiation Laboratory, University of Notre Dame, Notre Dame, Indiana
(Received March 30, 1964)

Gaseous oxygen under steady irradiation maintains a rather small amount of ozone, only a few parts per million, depending upon the pressure, rate of irradiation, etc. The hypothesis that the ozone concentration is limited by a negative ion–molecule chain decomposition (eq. 4 and 5 of the text) is considered in detail and found to be consistent with the known facts. At the higher gas densities where track effects must be considered the "sharp-boundary" method is employed.

1. Introduction

It has long been known[2] that although the initial G value for O_3 production in O_2 is relatively high, 8–12 under various conditions, the stationary concentration O_3 in irradiated O_2 is very low, only a few parts per million. It has been suggested that a chain reaction for the destruction of O_3 exists. The authors previously proposed[3] a negative ion–molecule chain for the destruction of ozone and subsequent consideration has tended to corroborate this view. This paper presents a treatment of the oxygen system under steady irradiation in a further attempt to establish the quantitative aspects of the problem.

There are potentially two types of complications in the explanation of the chemical action of high energy radiations. In the first place, a fairly complicated sequence of chemical reactions may be involved, and in the second place, track effects may require explicit consideration. The authors have presented a detailed study[3] of initial G values in the radiolysis of gaseous oxygen taking both complications into account. A digital computer was used to solve the ten coupled

(1) The Radiation Laboratory of the University of Notre Dame is operated under contract with the U. S. Atomic Energy Commission.

(2) J. F. Kircher, J. S. McNulty, J. L. McFarling, and A. Levy, *Radiation Res.*, **13**, 452 (1960).

(3) K. Fueki and J. L. Magee, *Discussions Faraday Soc.*, **36**, 19 (1963).

inhomogeneous partial differential equations required in the treatment. The difficulties involved in this study emphasize the desirability of a more simple method and the authors have turned to the "sharp-boundary" approximation[4-6] of the track for the description of the radiolysis of oxygen under steady irradiation. Estimates of initial G values by this simpler method indicate that it is adequate for the purpose at hand.

Study of the initial conditions for a track in oxygen gas[3] has shown that the negative ions have a much broader distribution than the positive ions. This situation results from the outward motion of the electrons before they are thermalized and captured in O_2 to form O_2^-. We have, therefore, considered explicitly a two-region model for our sharp-boundary tracks.

2. Reaction Mechanism

According to the previous study, in the pressure range (<30 atm. at 300°K.) in which clustering of ions is unimportant, the reaction mechanism for the radiolysis of oxygen is given by the following sequence of reactions.

$$O + 2O_2 \longrightarrow O_3 + O_2 \quad (1)$$

$$2O + O_2 \longrightarrow 2O_2 \quad (2)$$

$$O + O_3 \longrightarrow 2O_2 \quad (3)$$

$$O_2^- + O_3 \longrightarrow O_3^- + O_2 \quad (4)$$

$$O_3^- + O_3 \longrightarrow O_2^- + 2O_2 \quad (5)$$

$$O_2^+ + O_2^- \longrightarrow 2O + O_2 \quad (6)$$

$$O_2^+ + O_3^- \longrightarrow 3O + O_2 \quad (7)$$

The primary processes have been discussed[3] and are not indicated here. In later considerations of this reaction scheme, rate constants will be given the same number as the corresponding equations have here.

The positive ion–molecule reaction sequence

$$O_2^+ + O_3 \longrightarrow O_3^+ + O_2$$

$$O_3^+ + O_3 \longrightarrow O_2^+ + 2O_2$$

was excluded because the first step is endothermic by 0.6 e.v. (see Table I).

Excited atom chains are also excluded because quenching of the atoms is very efficient[7] and such chains could not have sufficient length to explain the experimental data.

The energetics of the reactions 4 and 5 above which constitute the proposed negative ion–molecule chain are not well known. All estimates, however, predict exothermicity for both steps. The heat of reaction 4 is just the negative of the difference between the electron affinity of ozone and oxygen as one can see by inspection. The large number of entries in Table I reflects the uncertainty in the electron affinity of O_2, which has been given many values between 0.15 and 1.47 e.v. The large electron affinity of O_3, 3 e.v., assures a negative heat of reaction in any case. The heat of the reaction

$$2O_3 \longrightarrow 3O_2$$

is fortuitously equal to −3 e.v. so that the heat of reaction 5 is numerically equal to the negative of the electron affinity of O_2. In Table I the symbols $EA(O_2)$ and $EA(O_3)$ refer to the electron affinities.

Table I: Energetics of the Ion–Molecule Reactions[a]

Ion-molecule reaction	ΔH, e.v.	Ref.
$O_2^+ + O_3 \rightarrow O_3^+ + O_2$	+0.6	*b, c*
$O_3^+ + O_3 \rightarrow O_2^+ + 2O_2$	−3.6	*b, c*
$O_2^- + O_3 \rightarrow O_3^- + O_2$	$EA(O)_2 - EA(O_3)$	
	−2.85	*d*
	−2.54	*e*
	$\geq$ −2.42	*f*
	−2.2	*g*
	−2.05	*h, i*
	$\geq$ −1.53	*j*
$O_3^- + O_2 \rightarrow O_2^- + 2O_2$	$-EA(O_2)$	
	−0.15	*d*
	−0.46	*e*
	$\leq$ −0.58	*f*
	−0.8	*g*
	−0.95	*h, i*
	$\leq$ −1.47	*j*

[a] The several values listed for the negative ion reactions indicate the uncertainties involved. [b] D. C. Frost and C. A. McDowell, *J. Am. Chem. Soc.*, **80**, 6183 (1958). [c] J. H. Herron and H. I. Schiff, *J. Chem. Phys.*, **24**, 1266 (1956). [d] R. S. Mulliken, *Phys. Rev.*, **115**, 1225 (1959). [e] A. V. Phelps and J. Pack, *Phys. Rev. Letters*, **6**, 111 (1961). [f] R. K. Curran, *J. Chem. Phys.*, **35**, 1849 (1961). [g] H. Eiber, "Ionization Phenomena in Gases," Vol. II, H. Maecker, Ed., North-Holland Publishing Co., Amsterdam, 1962. [h] H. O. Pritchard, *Chem. Rev.*, **52**, 529 (1953). [i] G. S. Hurst and T. E. Bortner, *Radiation Res. Suppl.*, **1**, 547 (1959). [j] W. Hauser and W. H. Hamill, private communication. These investigators have found that the O^- ion transfers a charge to form an O_2^- ion with a large cross section in what must be an exothermic process. This establishes the O_2^- affinity as *greater than* 1.47 ev.

3. Treatment of the Stationary State for the Homogeneous System

Under conditions of sufficiently low gas density there are no significant effects of inhomogeneity and the state

(4) J. L. Magee, *J. Am. Chem. Soc.*, **73**, 3270 (1951).
(5) J. L. Magee, *J. chim. phys.*, **52**, 528 (1955).
(6) A. H. Samuel, *J. Phys. Chem.*, **66**, 242 (1962).
(7) W. DeMore and O. F. Raper, *J. Chem. Phys.*, **37**, 2048 (1962).

of steady irradiation can be considered by standard kinetic techniques. All concentrations are spatially constant.

Let the concentrations be represented by C_1, C_2, C_3, C_4, and C_5 for O, O_2^+, O_2^-, O_3^-, and O_3, respectively.

The rate equations based on the proposed reaction mechanism are

$$\frac{dC_1}{dt} = G_1 I - k_1 C_1 - 2k_2 C_1^2 - k_3 C_1 C_5 + 2k_6 C_2 C_3 + 3k_7 C_2 C_4 \quad (3.1)$$

$$\frac{dC_2}{dt} = G_2 I - k_6 C_2 C_3 - k_7 C_2 C_4 \quad (3.2)$$

$$\frac{dC_3}{dt} = G_2 I - k_4 C_3 C_5 + k_5 C_4 C_5 - k_6 C_2 C_3 \quad (3.3)$$

$$\frac{dC_4}{dt} = k_4 C_3 C_5 - k_5 C_4 C_5 - k_7 C_2 C_4 \quad (3.4)$$

$$\frac{dC_5}{dt} = k_1 C_1 - k_3 C_1 C_5 - k_4 C_3 C_5 - k_5 C_4 C_5 \quad (3.5)$$

where I is the dose rate in hundreds of e.v./cm.^{3} and G_1 and G_2 are the initial G values for the formation of the oxygen atom and the oxygen ion, respectively.

The standard kinetic treatment of the stationary state requires that C_1, C_2, C_3, and C_4 are time independent. For simplicity we assume that $k_4 = k_5$ and $k_6 = k_7$. We are led to two simultaneous equations involving C_1 and C_5 to determine the condition in which the ozone concentration C_5 is also stationary.

$$C_1 = \frac{1}{4k_2}\left[-(k_1 + k_3 C_5) + \sqrt{(k_1 + k_3 C_5)^2 + 8k_2 \left\{G_1 + 2G_2 + \frac{G_2}{2 + \frac{\sqrt{G_2 I k_6}}{k_4 C_5}}\right\} I}\right] \quad (3.6)$$

$$C_5 = \frac{k_1 C_1}{k_3 C_1 + k_4 \sqrt{\frac{G_2 I}{k_6}}} \quad (3.7)$$

The condition of charge balance is used in this derivation.

Let us consider two special conditions.

(i) If $I \gg 4G_2 k_4^2 C_5^2/k_6$ and $I \gg (k_1 + k_3 C_5)^2/8k_2(G_1 + 2G_2)$

Equations 3.6 and 3.7 reduce to

$$C_1 \simeq \sqrt{\frac{(G_1 + 2G_2)I}{2k_2}} \quad (3.8)$$

and

$$C_5 \simeq \frac{k_1}{k_3 + k_4 \frac{2G_2 k_2}{(G_1 + 2G_2)k_6}} \quad (3.9)$$

respectively.

In this case, the stationary concentration of the oxygen atom is proportional to the square root of dose rate and that of ozone is independent of dose rate. (A steady condition with such a high intensity would be attained only in a pulse of relatively short duration.)

(ii) If $I \ll 4k_4^2 C_5^2/G_2 k_6$, $I \ll (G_2/k_6) \times [k_1 k_4/(G_1 + {}^5/_2 G_2)k_3]^2$

and

$$I \ll \frac{(k_1 + k_3 C_5)^2}{8k_2\{G_1 + 2G_2 + G_2/2 + \sqrt{G_2 I k_6/k_4 C_5}\}}$$

eq. 3.6 and 3.7 reduce to

$$C_1 \simeq \frac{(G_1 + {}^5/_2 G_2)I}{k_1} \quad (3.10)$$

and

$$C_5 \simeq \frac{(G_1 + {}^5/_2 G_2)}{k_4} \sqrt{\frac{k_6 I}{G_2}} \quad (3.11)$$

In this case, the stationary concentration of the oxygen atom is linearly proportional to dose rate and that of ozone is proportional to the square root of dose rate.

This result means that the oxygen atoms disappear by reaction with a major constituent, O_2, and the ozone is destroyed by ions whose concentration is limited by a recombination process. There are no experimental results available for systems to which this calculation applies. In the discussion we compare this calculation with the one presented in the next section which includes track effects.

4. Treatment of the Stationary State for the Inhomogeneous System

4.1. Fundamental Equations. In this section we propose a sharp-boundary model for the description of a track in which a reaction sequence occurs. In our previous paper[3] we found that at the initial stage of track expansion the spatial distribution of the negative ions is much broader than those of the positive ions and the neutral species. Therefore, we shall use a

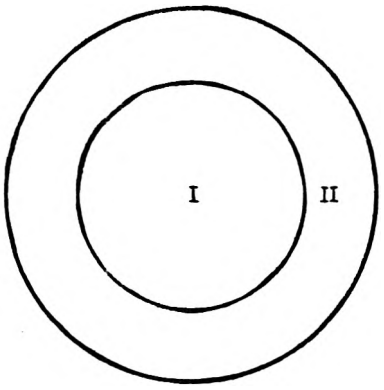

Figure 1.

sharp-boundary model[4-6] for the track with two different regions I and II as shown in Fig. 1. Region I contains the positive ions and the neutral species, and the region (I + II) contains the negative ions.

Let the number of O, O_2^+, O_2^-, O_3^-, and O_3 per unit track length (or per spur) be N_1, N_2, N_3, N_4, and N_5, respectively, and the background concentration of O, O_2^+, O_2^-, and O_3^- be Y_1, Y_2, Y_3, and Y_4. Then, N_3 can be divided into the number of O_2^- in the region I, N_3', and that in the region II, N_3''. In a similar way N_4 can be divided into the number of O_3^- in the region I, N_4', and that in the region II, N_4''. These relations are expressed as

$$N_3' = N_3\frac{V_-}{V_-},\quad N_3'' = N_3\left(1 - \frac{V_+}{V_-}\right)$$
$$N_4' = N_4\frac{V_-}{V_-},\quad N_4'' = N_4\left(1 - \frac{V_+}{V_-}\right) \qquad (4.1.1)$$

where V_+ and V_- are the volumes of the region I and the region (I + II), respectively.

The rate equations are described as

$$\frac{dN_1}{dt} = -k_1N_1 + 2k_6\frac{N_2N_3'}{V_+} + 3k_7\frac{N_2N_4'}{V_+} + Y_1\frac{dV_+}{dt} \qquad (4.1.2)$$

$$\frac{dN_2}{dt} = -k_6\frac{N_2N_3'}{V_+} - k_7\frac{N_2N_4'}{V_+} + Y_2\frac{dV_+}{dt} \qquad (4.1.3)$$

$$\frac{dN_3'}{dt} = -k_4C_5N_3' + k_5C_5N_4' - k_6\frac{N_2N_3'}{V_+} + Y_3\frac{dV_+}{dt} \qquad (4.1.4)$$

$$\frac{dN_4'}{dt} = k_4C_5N_3' - k_5C_5N_4' - k_7\frac{N_2N_4'}{V_+} + Y_4\frac{dV_+}{dt} \qquad (4.1.5)$$

$$\frac{dN_3''}{dt} = -k_4C_5N_3'' + k_5C_5N_4'' + Y_3\frac{d(V_- - V_+)}{dt} \qquad (4.1.6)$$

$$\frac{dN_4''}{dt} = k_4C_5N_3'' - k_5C_5N_4'' + Y_4\frac{d(V_- - V_+)}{dt} \qquad (4.1.7)$$

$$\frac{dN_5}{dt} = k_1N_1 - k_4C_5N_3 - k_5C_5N_4 \qquad (4.1.8)$$

where C_5 is the concentration of ozone.

We may neglect reactions 2 and 3, since these reactions are not important in the case of the low concentrations of O and O_3.

The conditions for the stationary state are given by

$$\left.\begin{aligned}
\int\left(\frac{dN_1}{dt}\right)dt &= -\bar{N}_1^\circ\\
\int\left(\frac{dN_2}{dt}\right)dt &= -\bar{N}_2^\circ\\
\int\left(\frac{dN_3}{dt}\right)dt &= -\bar{N}_3^\circ\\
\int\left(\frac{dN_4}{dt}\right)dt &= 0\\
\int\left(\frac{dN_5}{dt}\right)dt &= 0
\end{aligned}\right\} \qquad (4.1.9)$$

where $\bar{N}_1^\circ$, $\bar{N}_2^\circ$, and $\bar{N}_3^\circ$ are the number of O, O_2^+, and O_2^- formed per unit track length (or per spur) by irradiation, integration is carried out over a track lifetime (or a spur lifetime), t_m.[8]

Since the concentration of ozone in the stationary state is much higher than the concentrations of the intermediates, we may assume that C_5 is constant over a time period t_m.

The equation which gives the stationary concentration of ozone is (see Appendix I)

$$2k_5C_5\int N_4\,dt = \bar{N}_1^\circ + 2\bar{N}_2^\circ + \int\left\{(Y_1 + 2Y_2)\frac{dV_+}{dt} + Y_4\frac{dV_-}{dt}\right\}dt \qquad (4.1.10)$$

The background concentrations Y_1, Y_2, Y_3, and Y_4 are given by

$$\frac{dY_1}{dt} = -k_1Y_1 + 2k_6Y_2Y_3 + 3k_7Y_2Y_4 \qquad (4.1.11)$$

(8) Strictly speaking, the track lifetime for the negative ions should be different from those for the positive ions and the neutral species. However, in normal dose rates the track lifetime is long enough to allow the use of a common track lifetime for all the species.

$$\frac{dY_2}{dt} = -k_6Y_2Y_3 - k_7Y_2Y_4 \quad (4.1.12)$$

$$\frac{dY_3}{dt} = -k_4C_5Y_3 + k_5C_5Y_4 - k_6Y_2Y_3 \quad (4.1.13)$$

$$\frac{dY_4}{dt} = k_4C_5Y_3 - k_5C_5Y_4 - k_7Y_2Y_4 \quad (4.1.14)$$

The solutions of these equations are

$$Y_3 = \frac{1}{2(1 + k_6Y_2^\circ t)}\left[Y_2^\circ + (Y_3^\circ - Y_4^\circ)e^{-2k_4C_5t}\right] \quad (4.1.15)$$

$$Y_4 = \frac{1}{2(1 + k_6Y_2^\circ t)}\left[Y_2^\circ - (Y_3^\circ - Y_4^\circ)e^{-2k_4C_5t}\right] \quad (4.1.16)$$

$$Y_2 = Y_3 + Y_4 = \frac{Y_2^\circ}{1 + k_6Y_2^\circ t} \quad (4.1.17)$$

where Y_2°, Y_3°, and Y_4° are the initial values of Y_2, Y_3, and Y_4 for a time period, respectively. For simplicity we have assumed $k_4 = k_5$ and $k_6 = k_7$. Since Y_1 is much smaller than Y_2, Y_3, and Y_4, we may neglect Y_1 in the following treatment.[9]

4.2. Spherical Spur Model. The spur volume based on the sharp-boundary model is given by

$$V_+ = V_+^\circ\left(1 + \frac{D}{V_+^{\circ 2/3}}t\right)^{3/2}$$
$$V_- = V_-^\circ\left(1 + \frac{D}{V_-^{\circ 2/3}}t\right)^{3/2} \quad (4.2.1)$$

where V_+° and V_-° are the initial spur volumes and D is a diffusion coefficient, which is taken to be approximately the same for all the species.

From eq. 4.1.17 and 4.2.1, we get

$$\int Y_2\left(\frac{dV_+}{dt}\right)dt = \frac{3D^{3/2}t_m^{1/2}}{k_6} \times \left[1 - \frac{1}{(k_6Y_2^\circ t_m)^{1/2}}\tan^{-1}(k_6Y_2^\circ t_m)^{1/2}\right] \quad (4.2.2)$$

From eq. 4.1.16 and 4.2.1, we get

$$\int Y_4\left(\frac{dV_-}{dt}\right)dt \simeq \frac{3D^{3/2}t_m^{1/2}}{2k_6}\left[1 - \frac{1}{(k_6Y_2^\circ t_m)^{1/2}} \times \tan^{-1}(k_6Y_2^\circ t_m)^{1/2}\right] \quad (k_4C_5t_m \gg 1) \quad (4.2.3)$$

If $k_6Y_2^\circ t_m \ll 1$, eq. 4.2.2 and 4.2.3 reduce to

$$\int Y_2\left(\frac{dV_+}{dt}\right)dt \simeq Y_2^\circ V_m$$
$$V_m = (Dt_m)^{3/2} \quad (4.2.4)$$

$$\int Y_4\left(\frac{dV_-}{dt}\right)dt \simeq {}^1/_2Y_2^\circ V_m \quad (4.2.5)$$

respectively.

Now we use the following approximation (see Appendix II)

$$N_2 = \tilde{N}_2 + Y_2V_+ \quad (4.2.6)$$

where $\tilde{N}_2$ is the number of O_2^+ for the zero background case and is given by

$$\tilde{N}_2 = \frac{\tilde{N}_2^\circ}{1 + \frac{2k_6\tilde{N}_2^\circ}{DV_-^{\circ 1/3}}\left\{1 - \frac{1}{\left(1 + \frac{D}{V_-^{\circ 2/3}}t\right)^{1/2}}\right\}} \quad (4.2.7)$$

$\tilde{N}_4$ is given by

$$\tilde{N}_4 = \frac{\tilde{N}_2}{2}(1 - e^{-2k_4C_5t}) \quad (4.2.8)$$

Thus, if $k_6Y_2^\circ t_m << 1$ and $k_4C_5t_m >> 1$, we get (see Appendix III)

$$\int N_4\,dt = \int \tilde{N}_4dt + \int Y_4V_-\,dt \simeq \left\{\frac{\tilde{N}_2^\circ}{2(1 + \beta)} + {}^1/_5Y_2^\circ V_m\right\}t_m \quad (4.2.9)$$

where $\beta = 2k_6\tilde{N}_2^\circ/DV_-^{\circ 1/3}$.

Substitution of eq. 4.2.4, 4.2.5, and 4.2.9 in eq. 4.1.10 gives

$$C_5 = \frac{\tilde{N}_1^\circ + 2\tilde{N}_2^\circ + {}^5/_2Y_2^\circ V_m}{k_4\left(\frac{\tilde{N}_2^\circ}{1 + \beta} + {}^2/_5Y_2^\circ V_m\right)t_m} \quad (4.2.10)$$

Let ν be the number of spurs formed per unit time and unit volume. Then, we have the relations

$$\nu V_m t_m = 1$$
$$V_m = (Dt_m)^{3/2}$$
$$\nu = \frac{I}{\epsilon} \quad (4.2.11)$$

where I is the dose rate and ϵ is an average energy deposition per spur.

These relations allow eq. 4.2.10 to be written as (see Appendix IV)

(9) This situation results from the fact that the rate constant k_1 is large.

$$C_5 = \frac{(\bar{N}_1^\circ + 2\bar{N}_2^\circ) I + {}^5/_2 \left[\frac{\bar{N}_2^\circ}{(1+\beta)k_6}\right]^{1/2} D^{3/5}\epsilon^{1/10} I^{9/10}}{k_4 \left\{\frac{\bar{N}_2^\circ \epsilon^{2/5}}{(1+\beta)D^{2/5}} I^{3/5} + {}^2/_5 \left[\frac{\bar{N}_2^\circ \epsilon}{(1+\beta)k_6}\right]^{1/2} I^{1/2}\right\}} \quad (4.2.12)$$

5. Discussion

Using the equations presented in the previous section, the stationary concentration of ozone can be estimated. As an example, we consider the special case of oxygen at 10 atm. and 300°K. with a dose rate of 1 rad sec.$^{-1}$.

For this case the constants are chosen as

$$\epsilon = 60 \text{ e.v.}$$

$$V_+^\circ = \frac{4\pi}{3}(r_{0+})^3, \; r_{0+} = 10^{-5} \text{ cm.}$$

$$V_-^\circ = \frac{4\pi}{3}(r_{0-})^3, \; r_{0-} = 5 \times 10^{-5} \text{ cm.}$$

$$D = 10^{-2} \text{ cm.}^2 \text{ sec.}^{-1}$$

$$k_4 = 10^{-10}\text{–}10^{-11} \text{ cm.}^3 \text{ sec.}^{-1}$$

$$k_6 = 10^{-6} \text{ cm.}^3 \text{ sec.}^{-1}$$

$$\bar{N}_1^\circ = 4$$

$$\bar{N}_2^\circ = 2$$

The rate constant k_4 is not really known. We have assumed $k_4 \approx 10^{-10}$–10^{-11} cm.^{3} sec.$^{-1}$, since for most negative ion–molecule reactions the observed rate constants are in this range.[10]

The calculated stationary concentration of ozone from eq. 4.2.12 is 0.3–3 p.p.m., depending upon which value of k_4 is used, which is in agreement in order of magnitude with the experimental value obtained in the radiolysis of oxygen by Co^{60} γ-rays.[2]

The stationary concentration of ozone for a single-region sharp-boundary model, *i.e.*, V_-° is equal to V_+° ($r_{0+} = r_{0-} = 10^{-5}$ cm.), has also been estimated. The calculated stationary concentration of ozone is 0.5–5 p.p.m., which is slightly higher than the value obtained above. The slight increase in O_3 is a result of the decrease in concentration of ions because the smaller spur volume for the negative ions is more favorable to the neutralization reaction.

In order to estimate the influence of the track reactions we have calculated the stationary concentration of ozone under the same condition as described above, using eq. 3.11 derived for the homogeneous system. The calculated stationary concentration of ozone is 0.03–0.3 p.p.m., which is lower by one order of magnitude than the values obtained by the treatment including track effects. This result suggests that there is a considerable influence of inhomogeneity in concentration of intermediates on the stationary concentration of ozone.

Equation 4.2.12 shows that the stationary concentration of ozone is approximately proportional to the square root of dose rate. This result also agrees with experiments.[2]

The errors arising in this work because of the use of the sharp-boundary model are difficult to assess and would require a complete digital computer study to analyze. Kuppermann[11] has shown that a similar approximation which is sometimes used, called "prescribed diffusion," yields very accurate results for the one-radical case. The present calculation has in addition to the sharp-boundary model certain mathematical simplifications which seem to be necessary for solution with a reasonable amount of effort. It can be shown that these approximations introduce at most a small percentage error in the solution itself.

In conclusion it can be said that use of the sharp-boundary model in the form employed here for a complete reaction sequence gives a correct qualitative and roughly quantitative description of track effects. The calculation presented here of the stationary state concentration of ozone in irradiated oxygen is good support for the negative-ion chain decomposition mechanism.

Appendix I. Derivation of Eq. 4.1.10

Substitution of eq. 4.1.1 in eq. 4.1.2 and 4.1.3 gives

$$\frac{dN_1}{dt} = -k_1 N_1 + 2k_6 \frac{N_2 N_3}{V_-} + 3k_7 \frac{N_2 N_4}{V_-} + Y_1 \frac{dV_+}{dt} \quad (A1.1)$$

and

$$\frac{dN_2}{dt} = -k_6 \frac{N_2 N_3}{V_-} - k_7 \frac{N_2 N_4}{V_-} + Y_2 \frac{dV_+}{dt} \quad (A1.2)$$

respectively.

Addition of eq. 4.1.4 to eq. 4.1.6 gives

$$\frac{dN_3}{dt} = -k_4 C_5 N_3 + k_5 C_5 N_4 - k_6 \frac{N_2 N_3}{V_-} + Y_3 \frac{dV_-}{dt} \quad (A1.3)$$

(10) C. E. Melton, "Mass Spectrometry of Organic Ions," ed. by F. W. McLafferty, Academic Press, Inc., New York, N. Y., 1963, Chapter 4, p. 163.

(11) A. Kuppermann, "Actions Chimiqueset Biologiques des Radiations," Vol. V, ed. by M. Haissinsky, Academic Press, Inc., London, 1961, p. 87.

Addition of eq. 4.1.5 to eq. 4.1.7 gives

$$\frac{dN_4}{dt} = k_4C_5N_3 - k_5C_5N_4 - k_7\frac{N_2N_4}{V_-} + Y_4\frac{dV_-}{dt} \quad (A1.4)$$

Substitution of eq. 4.1.8 and A1.1–A1.4 in eq. 4.1.9, gives

$$\mathscr{S}\left(-k_1N_1 + 2k_6\frac{N_2N_3}{V_-} + 3k_7\frac{N_2N_4}{V_-} + Y_1\frac{dV_+}{dt}\right)\times dt = -\tilde{N}_1^\circ \quad (A1.5)$$

$$\mathscr{S}\left(-k_6\frac{N_2N_3}{V_-} - k_7\frac{N_2N_4}{V_-} + Y_2\frac{dV_+}{dt}\right)dt = -\tilde{N}_2^\circ \quad (A1.6)$$

$$\mathscr{S}\left(-k_4C_5N_3 + k_5C_5N_4 - k_6\frac{N_2N_3}{V_-} + Y_3\frac{dV_-}{dt}\right)\times dt = -\tilde{N}_3^\circ \quad (A1.7)$$

$$\mathscr{S}\left(k_4C_5N_3 - k_5C_5N_4 - k_7\frac{N_2N_4}{V_-} + Y_4\frac{dV_-}{dt}\right)\times dt = 0 \quad (A1.8)$$

$$\mathscr{S}(k_1N_1 - k_4C_5N_3 - k_5C_5N_4)dt = 0 \quad (A1.9)$$

From eq. A1.5 and A1.6, we get

$$\mathscr{S}\left\{-k_1N_1 + k_7\frac{N_2N_4}{V_-} + (Y_1 + Y_2)\frac{dV_+}{dt}\right\}dt = -(\tilde{N}_1^\circ + 2\tilde{N}_2^\circ) \quad (A1.10)$$

From eq. A1.9 and A1.10, we get

$$\mathscr{S}\left\{-k_4C_5N_3 - k_5C_5N_4 + k_7\frac{N_2N_4}{V_-} + (Y_1 + 2Y_2)\frac{dV_+}{dt}\right\}dt = -(\tilde{N}_1^\circ + 2\tilde{N}_2^\circ) \quad (A1.11)$$

From eq. A1.8 and A1.11, we get

$$\mathscr{S}\left\{-2k_5C_5N_4 + (Y_1 + 2Y_2)\frac{dV_+}{dt} + Y_4\frac{dV_-}{dt}\right\}dt = -(\tilde{N}_1^\circ + 2\tilde{N}_2^\circ) \quad (A1.12)$$

Since C_5 is assumed to be constant, eq. A1.12 reduces to eq. 4.1.10.

Appendix II. Equation 4.2.6

Use of eq. 4.2.6 for the second-order reaction term in the rate equation increases importance of the neutralization reaction by counting twice some reactions between ions in the spur and those in background. This means that the stationary concentration of ozone in the present calculation is estimated to be somewhat higher than the true value. We can show by an algebraic relation that the term $2\tilde{N}_2Y_2V_+$ which arises from the second-order reaction term mentioned above does not exceed the term $\tilde{N}_2^2 + Y_2^2V_+^2$ which must be taken into account. In the actual case of interest this approximation deviates less than 10% from the correct value as checked with a rigorous solution given by Samuel[6] for a one-radical track.

Appendix III. Equation 4.2.9

$$\mathscr{S}N_4dt = \frac{\tilde{N}_2^\circ}{2}(A + B) + \frac{D^{1/2}t_m^{1/2}}{k_6}\left[\tfrac{1}{3}t_m - \frac{1}{k_6Y_2^\circ}\left\{1 - \frac{1}{(k_6Y_2^\circ t_m)^{1/2}}\tan^{-1}(k_6Y_2^\circ t_m)^{1/2}\right\}\right] \quad (A3.1)$$

$$A = \frac{1}{\alpha(1+\beta)}\left[(1 + \alpha t_m) + \frac{2\beta}{1+\beta}(1 + \alpha t_m)^{1/2} - \frac{1+3\beta}{1+\beta} + 2\left(\frac{\beta}{1+\beta}\right)^2\ln\{(1+\beta)(1+\alpha t_m)^{1/2} - \beta\}\right] \quad (A3.2)$$

$$B = \frac{1}{1+\beta}\left[\frac{1}{2k_4C_5}(1 - e^{-2k_4C_5t_m}) + \frac{\beta}{1+\beta}\left(\frac{2}{k_4C_5\alpha}\right)^{1/2}e^{\frac{2k_4C_5}{\alpha}}\left\{\operatorname{erf}\left(\sqrt{\frac{2k_4C_5}{\alpha}(1+\alpha t_m)}\right) - \operatorname{erf}\left(\sqrt{\frac{2k_4C_5}{\alpha}}\right)\right\} + \frac{\beta^2}{\alpha(1+\beta)^2}e^{\frac{2k_4C_5}{\alpha}}\times\left\{E_i\left(-\frac{2K_4C_5}{\alpha}(1+\alpha t_m)\right) - E_i\left(-\frac{2k_4C_5}{\alpha}\right)\right\}\right] \quad (A3.3)$$

where $\alpha = D/V_-^{\circ 2/3}$ and $\beta = 2k_6\tilde{N}_2^\circ/DV_-^{\circ 1/3}$. If $k_6Y_2^\circ t_m << 1$ and $k_4C_5t_m >> 1$, eq. A3.1 reduces to eq. 4.2.9, since $\alpha t_m >> 1$ in normal dose rates.

Appendix IV. Equation 4.2.12

The boundary condition is defined as

$$N_{2m} = \tilde{N}_{2m} + Y_{2m}V_m = Y_2^\circ V_m \quad (A4.1)$$

where the subscript m designates the quantities at the time t_m.

Substituting eq. 4.1.7 and 4.2.7 in eq. A4.1, we get

$$Y_2^\circ = \frac{\tilde{N}_{2m}}{2V_m}\left\{1 + \left(1 + \frac{4V_m}{k_6t_m\tilde{N}_{2m}}\right)^{1/2}\right\} \quad (A4.2)$$

If $4V_m/k_6t_m\tilde{N}_{2m} >> 1$, using eq. 4.2.11 we get

$$Y_2^\circ \simeq \left[\frac{N_2^\circ I}{(1+\beta)k_6\epsilon}\right]^{1/2} \qquad \text{(A4.3)}$$

Substituting eq. 4.2.11 and A4.3 in eq. 4.2.10, we get eq. 4.1.12.

Surface Tension of Liquid Nitrate Systems

by G. Bertozzi and G. Sternheim

Chemistry Department, High Temperature Chemistry, Euratom, Ispra, Italy *(Received April 13, 1964)*

Surface tension measurements are reported for eight binary alkali nitrate systems and for five silver nitrate–alkali nitrate systems, in the temperature range from the melting point to about 400°. A linear dependence on temperature always holds. With regard to the alkali nitrate systems, it is found that the surface tension of the mixtures is well represented by the semiempirical expression: $j = x_1 j_1 + x_2 j_2 - 1900 x_1 x_2 [(d_1 - d_2)/(d_1 + d_2)]^2$, where j_1 and j_2 are the surface tensions of the two pure components and x_1 and x_2 are their mole fractions; d_1 and d_2 are the interionic distances of the pure salts. Mixtures of silver nitrate with the alkali nitrates as the second component exhibit surface tension isotherms which become more convex toward the abscissa as the radius of the alkali metal cation increases; the deviations from linearity of the surface specific enthalpy as a function of the composition are found to increase with the size of the alkali metal. This trend is interpreted as an increasing interaction of covalent character.

Introduction

Binary systems of molten nitrates were recently investigated by Kleppa and co-workers, who measured the heats of mixing of all the alkali nitrate binary systems[1,2] and of four silver nitrate–alkali nitrate systems.[3]

All the alkali nitrate mixtures are exothermic, and the thermal effect increases with the difference in size of the two alkali ions. Silver nitrate mixtures containing lithium or sodium nitrate were found to be endothermic, whereas those with potassium or rubidium nitrate were found to be exothermic.

We measured the surface tension of the same systems and tried to relate the results to the sizes of the ions in the mixture. Formerly, Boardman, Palmer, and Heymann[4] and Dahl and Duke[5] carried out measurements on the surface tension of sodium–potassium nitrate mixtures; silver–sodium and silver–potassium nitrate mixtures were investigated by Dahl and Duke[5] and by Bloom, Davis, and James.[6] All of these authors compared their experimental results with the values predicted by Guggenheim's equation for ideal mixtures.[7]

Experimental

The Wilhelmy slide method[8-10] was used; it consists of measuring the maximum pulling force necessary to detach a thin platinum plate from the liquid surface. For a straight edge, the force is proportional to the sur-

(1) O. J. Kleppa, *J. Phys. Chem.*, **64**, 1937 (1960).

(2) O. J. Kleppa and L. S. Hersh, *J. Chem. Phys.*, **34**, 351 (1961).

(3) O. J. Kleppa, R. B. Clarke, and L. S. Hersh, *ibid.*, **35**, 175 (1961).

(4) N. K. Boardman, A. R. Palmer, and E. Heymann, *Trans. Faraday Soc.*, **51**, 277 (1955).

(5) J. L. Dahl and F. R. Duke, U. S. Atomic Energy Commission Report ISC-923 (1958).

(6) H. Bloom, F. G. Davis, and D. W. James, *Trans. Faraday Soc.*, **56**, 1179 (1960).

(7) E. A. Guggenheim, "Mixtures," Oxford University Press, London, 1952.

face tension of the liquid. The force is measured as the maximum increase of the apparent weight of the plate, according to the formula, $\Delta W_{max} = 2aj$, where a is the length of the edge, W is the weight increase in dynes, and j is the surface tension in dynes/cm.

The platinum plate was 15 mm. in edge length and 0.1 mm. thick. A Mettler recording balance was used for weight measurements. The temperature was measured a few millimeters above the surface of the melt and was accurate to ±1°.

Merck and B.D.H. salts of analytical purity were carefully dried and used without further purification. Results were reproducible within 0.5% in the whole temperature range, from the melting point up to ~400°; measurements at higher temperature were not performed because of the thermal decomposition of silver and lithium salts.

Results

The surface tensions of the following binary systems were measured: (K–Li)NO_3, (K–Na)NO_3, (K–Rb)NO_3, (K–Cs)NO_3, (Li–Rb)NO_3, (Li–Cs)NO_3, (Na–Rb)NO_3, (Na–Cs)NO_3, (Li–Ag)NO_3, (Na–Ag)NO_3, (K–Ag)NO_3, (Rb–Ag)NO_3, and (Cs–Ag)NO_3. Besides the pure components, we selected the 25, 50, and 75% M mixtures of each system for the measurements. The surface tension of all the systems always shows a linear dependence on temperature, the temperature coefficient being of the order of 0.07 dyne/cm. deg. The surface tension equations for all of the mixtures are given in Table I.

The surface tension isotherms at 350° are plotted in Fig. 1–4.[11] The systems (K–Na)NO_3, (K–Rb)NO_3, (K–Cs)NO_3, and (Li–Ag)NO_3 exhibit nearly linear isotherms, whereas the isotherms of the other systems are more pronouncedly convex.

Discussion

It is well known that the surface tension of "ideal" systems is not a linear function of the composition. Guggenheim's treatment leads to the equation

$$\exp(-ja/kT) = x_1 \exp(-j_1 a/kT) + x_2 \exp(-j_2 a/kT)$$

This treatment, which was successfully applied to many systems, requires that the molecular surface areas of the components are equal; in our case this condition is not fulfilled for the major part of the systems; for instance, the surface area for lithium nitrate is 16.3 $\times 10^{-16}$ cm.^{2}/molecule, whereas for cesium nitrate it is 23.2 $\times 10^{-16}$ cm.^{2}/molecule. In addition to this, it was shown by Blander[12] that ionic mixtures with cationic radii different from each other in any case cannot be regarded as ideal. Guggenheim extended his treatment

Table I

KNO_3, mole %	$KNO_3 + LiNO_3$
100	$j = 139.8 - 0.081t$
75	$j = 133.6 - 0.070t$
50	$j = 129.6 - 0.062t$
25	$j = 127.9 - 0.056t$
0	$j = 129.9 - 0.055t$

KNO_3, mole %	$KNO_3 + NaNO_3$
75	$j = 138.5 - 0.076t$
50	$j = 139.7 - 0.076t$
25	$j = 139.8 - 0.072t$
0	$j = 137.6 - 0.060t$

KNO_3, mole %	$KNO_3 + RbNO_3$
75	$j = 138.5 - 0.083t$
50	$j = 136.9 - 0.083t$
25	$j = 135.0 - 0.082t$
0	$j = 134.3 - 0.083t$

KNO_3, mole %	$KNO_3 + CsNO_3$
75	$j = 133.7 - 0.079t$
50	$j = 129.4 - 0.077t$
25	$j = 125.1 - 0.074t$
0	$j = 122.1 - 0.074t$

$NaNO_3$, mole %	$NaNO_3 + RbNO_3$
75	$j = 135.4 - 0.068t$
50	$j = 133.7 - 0.073t$
25	$j = 132.5 - 0.076t$

$NaNO_3$, mole %	$NaNO_3 + CsNO_3$
75	$j = 130.5 - 0.068t$
50	$j = 127.3 - 0.074t$
25	$j = 123.4 - 0.072t$

$LiNO_3$, mole %	$LiNO_3 + RbNO$
75	$j = 125.0 - 0.059t$
50	$j = 129.6 - 0.074t$
25	$j = 130.0 - 0.075t$

$LiNO_3$, mole %	$LiNO_3 + CsNO_3$
75	$j = 124.3 - 0.070t$
50	$j = 124.3 - 0.076t$
25	$j = 122.9 - 0.075$

$AgNO_3$, mole %	$AgNO_3 + LiNO_3$
100	$j = 163.7 - 0.066t$
75	$j = 153.5 - 0.067t$
50	$j = 145.7 - 0.068t$
25	$j = 137.8 - 0.064t$

$AgNO_3$, mole %	$AgNO_3 + N_aNO_3$
90	$j = 159.2 - 0.066t$
75	$j = 153.0 - 0.065t$
50	$j = 146.7 - 0.066t$
25	$j = 141.6 - 0.065t$

$AgNO_3$, mole %	$AgNO_3 + KNO_3$
90	$j = 156.5 - 0.073t$
75	$j = 149.0 - 0.073t$
50	$j = 143.0 - 0.076t$
25	$j = 141.9 - 0.082t$

$AgNO_3$, mole %	$AgNO_3 + RbNO_3$
90	$j = 151.7 - 0.069t$
75	$j = 143.4 - 0.070t$
50	$j = 136.9 - 0.073t$
25	$j = 134.0 - 0.077t$

$AgNO_3$, mole %	$AgNO_3 + CsNO_3$
90	$j = 148.4 - 0.072t$
75	$j = 140.1 - 0.073t$
50	$j = 130.3 - 0.072t$
25	$j = 126.1 - 0.075t$

(8) L. Wilhelmy, *Ann. Physik*, **119**, 177 (1863).

(9) R. Ruissen, *Rec. trav. chim.*, **65**, 580 (1946).

(10) A. W. Adamson, "Physical Chemistry of Surfaces," Interscience Publishers, Inc. New York, N. Y., 1960.

(11) The surface tension of cesium nitrate at 350° was calculated by extrapolating below the melting point.

(12) M. Blander, *J. Chem. Phys.*, **34**, 697 (1961).

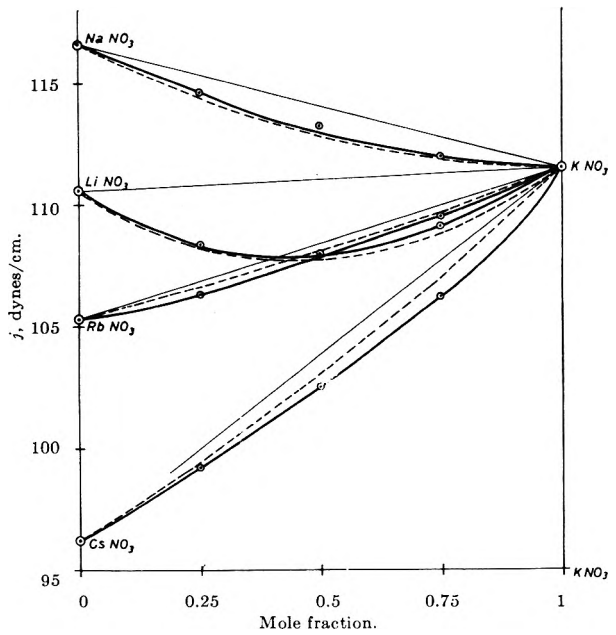

Figure 1. Surface tension isotherms at 350° for the systems $(K–Li)NO_3$, $(K–Na)NO_3$, $(K–Rb)NO_3$, and $(K–Cs)NO_3$: ⊙—⊙, experimental curve; - - - - -, eq. 2; ———, linearity.

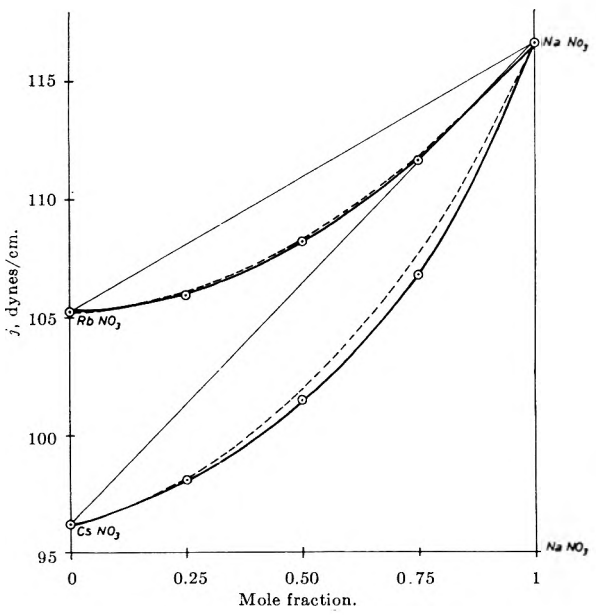

Figure 2. Surface tension isotherms at 350° for the systems $(Na–Rb)NO_3$ and $(Na–Cs)NO_3$: ⊙—⊙, experimental curve; - - - - -, eq. 2; ———, linearity.

to regular mixtures, and an improved derivation was later developed by Hoar and Melford[13] which is consistent with the Gibbs relation.

As in our case, deviations are often remarkable and cannot be accounted for by Guggenheim's or Hoar's

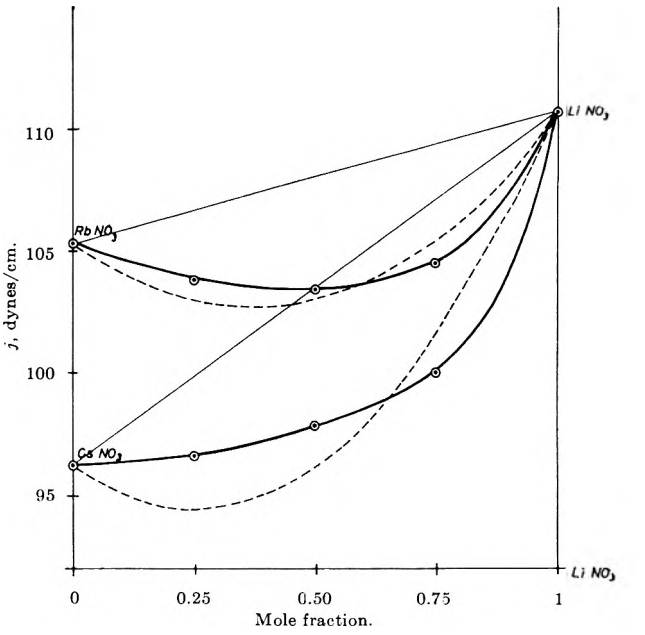

Figure 3. Surface tension isotherms at 350° for the systems $(Li–Rb)NO_3$ and $(Li–Cs)NO_3$: ⊙—⊙, experimental curve; - - - - -, eq. 2; ———, linearity.

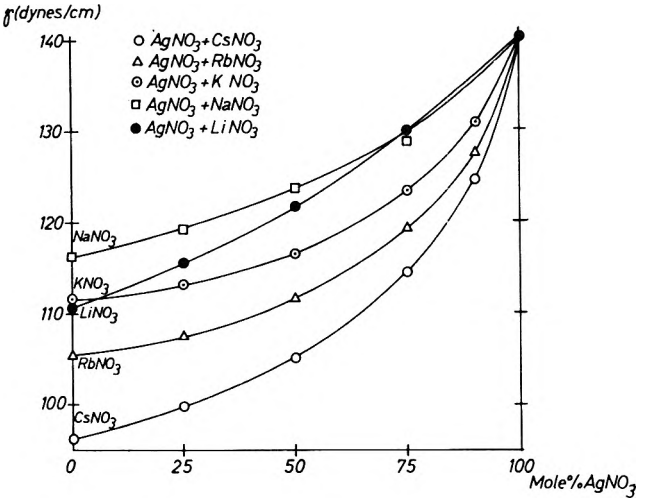

Figure 4. Surface tension isotherms at 350° for the systems $(Li–Ag)NO_3$, $(Na–Ag)NO_3$, $(K–Ag)NO_3$, $(Rb–Ag)NO_3$, and $(Cs–Ag)NO_3$.

equations for regular mixtures, even by allowing for large values of the interchange energy. We preferred to follow a suggestion by Blander[14] and tried to relate deviations from linearity to a semiempirical equation. Good agreement with the experimental results was found for the alkali nitrate systems.

(13) T. P. Hoar and D. A. Melford, *Trans. Faraday Soc.*, **53**, 315 (1957).

(14) M. Blander, private communication.

Alkali Nitrate Systems. In this case, deviations from linearity do not depend on the difference between the surface tension of the pure components but rather on the difference in size between the two alkali ions in the mixture.

In Fig. 5 we plotted the maximum values of the deviations of the surface tension isotherms from linearity for each system *vs.* the parameter $[(d_1 - d_2)/(d_1 + d_2)]^2$, where d_1 and d_2 are cation–anion center distances for salts 1 and 2, respectively, and were calculated as the sum of the radii of the cation and the anion (the Goldschmidt values were chosen).

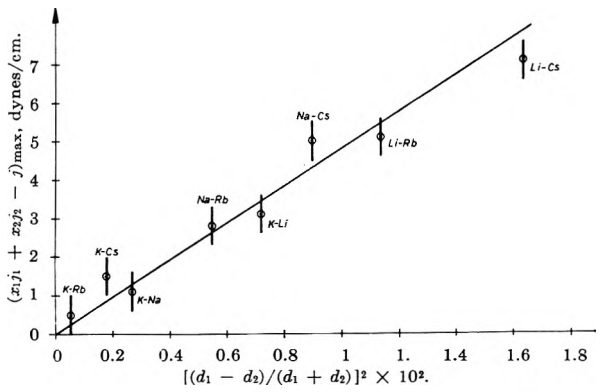

Figure 5. Maximum deviations of surface tension isotherms from linearity as a function of the parameter $[(d_1 - d_2)/(d_1 + d_2)]^2$.

A linear dependence holds

$$(x_1j_1 + x_2j_2 - j)_{max} = 475[(d_1 - d_2)/(d_1 + d_2)]^2$$

The choice of the parameter $[(d_1 - d_2)/(d_1 + d_2)]^2$ relies upon a calculation made by Forland[15] on the coulombic energy change on mixing in a linear array of ions, provided that the nearest and next nearest neighbors only are considered; the usefulness of this parameter was first tested by Kleppa and co-workers,[2] who found for the heats of mixing in liquid alkali nitrate systems the empirical expression

$$\Delta H = -x_1x_2U[(d_1 - d_2)/(d_1 + d_2)]^2 \quad \text{(cal./mole)}$$

Accordingly, we set up tentatively the semiempirical equation

$$\Delta j = x_1j_1 + x_2j_2 - j = Kx_1x_2[(d_1 - d_2)/(d_1 + d_2)]^2 \quad (1)$$

where x_1 and x_2 are the molar fractions of the components; the numerical value of K is 1900 for all the systems and was calculated by putting $Kx_1x_2 = 475$ when $x_1 = x_2 = 1/2$. Equation 1 can be rewritten as

$$j = x_1j_1 + x_2j_2 - Kx_1x_2[(d_1 - d_2)/(d_1 + d_2)]^2 \quad (2)$$

Thus we have an expression for the surface tension of the mixture as a functior of the composition, of the surface tension of the components, and of the size of the two alkali ions. The isotherms calculated from this equation are reported as dotted lines in Fig. 1–3. The agreement is satisfactory except for the systems (Li–Rb)NO_3 and (Li–Cs)NO_3; the behavior of these two systems can be interpreted by considering that here the lithium ion, which has a high polarizing power, is mixed with the largest ions which are easily polarizable, so that big changes in polarization energy arise which cannot be predicted by eq. 2.

Silver Nitrate–Alkali Nitrate Systems. In this case, the shape of the surface tension isotherms is not a function of the difference between the size of the cations in the mixture, so that the parameter $[(d_1 - d_2)/(d_1 + d_2)]^2$ is useless here. On the contrary, it is apparent from Fig. 4 that the surface tension isotherms are more convex, the larger the radius of the alkali ion, *i.e.*, increasingly in the order, Li < Na < K < Rb < Cs, independent of the value of the surface tension of the components. This behavior is apparent by comparing the isotherms of (Li–Ag)NO_3 with that of (K–Ag)NO_3: they have nearly the same limiting values but are greatly different with regard to the shape.

Similar trends were observed by Dahl and Duke[5] for lead chloride–alkali metal chloride systems and were interpreted by the authors on the basis of covalent character of the bonds in the melt increasing with decreasing the polarizing power of the alkali ions.

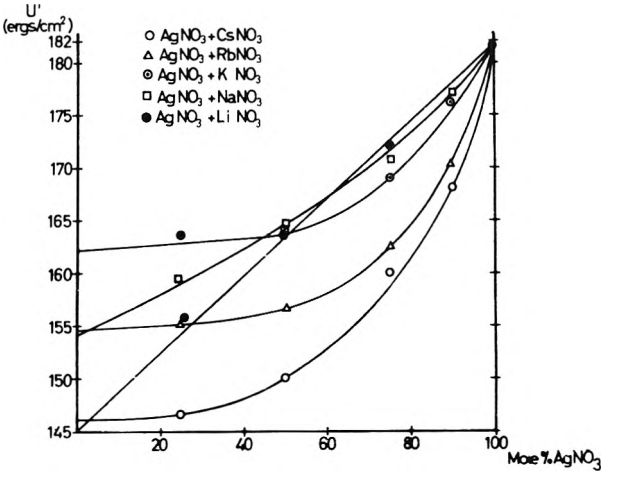

Figure 6. Surface specific enthalpy as a function of the composition.

(15) T. Forland *J. Phys. Chem.*, 59, 152 (1955).

Since the specific surface enthalpy, $U' = j - T(dj/dT)$, is more informative than the surface tension with regard to the structural nature of the interface,[10] and Bloom, Davis, and James[6] stated that this quantity could provide information on the nature of the bonds in melts, we plotted (Fig. 6) the surface specific enthalpy as a function of the composition. It shows a linear dependence on composition in the case of $(Li-Ag)NO_3$; there is a slight negative deviation from linearity for $(Na-Ag)NO_3$, whereas large negative deviations are present in the remaining systems increasing with the radius of the alkali ion.

This behavior can be interpreted as an increasing interaction of covalent character, in agreement with Thurmond's observations concerning liquid mixtures of silver bromide with lithium and rubidium bromides.[16] The author pointed out that in pure liquid silver bromide there is a resonance between covalent and ionic bonds; if a small cation such as Li^+ or Na^+ is added, its strong electric field will weaken this resonance, whereas large cations with a weak field will enhance the covalent bonding. This point of view was extended by Kleppa and co-workers[3] to the corresponding nitrate systems.

Acknowledgments. The authors are indebted to Mr. G. Soldani for having performed some surface tension measurements. They wish furthermore to acknowledge the interesting discussion which they had with Milton Blander from North American Aviation Science Center, during his visit.

(16) C. D. Thurmond, *J. Am. Chem. Soc.*, **75**, 3928 (1953).

The Stability of Wüstite by Electromotive Force Measurements on All-Solid Electrolytic Cells

by Giovanni B. Barbi

Euratom C.C.R. Ispra, High Temperature Chemistry Group Materials Department, Ispra, Italy
(Received April 13, 1964)

The field of stability of wüstite at temperatures below 1000° has been determined by means of e.m.f. measurements on all-solid galvanic cells, with a ceramic intermediate electrolyte. The electromotive force values experimentally found inside this field agree satisfactorily with those calculated assuming a random athermal mixing of neutral iron atoms and octahedral holes in the magnetic structure.

In a previous work,[1] the possibility was shown of determining the standard molar free energy of formation of the metallic oxides by means of e.m.f. measurements across all-solid galvanic cells of the types

$$\mathrm{Pt} \left| \mathrm{Me},\ \mathrm{MeO}_x \right| \begin{matrix} \text{intermediate} \\ \text{electrolyte} \end{matrix} \left| \begin{matrix} \mathrm{Me'O}_k,\ \mathrm{Me'O}_{y-}\ (T > T_0) \\ \hline \mathrm{Me'O}_k,\ \mathrm{Me'O}_z\ (T < T_0) \end{matrix} \right| \mathrm{Pt}$$

$$\mathrm{Pt} \left| \mathrm{Me},\ \mathrm{MeO}_x \right| \begin{matrix} \text{intermediate} \\ \text{electrolyte} \end{matrix} \left| \begin{matrix} \mathrm{Me'O}_{y+},\ \mathrm{Me'O}_z,\ (T > T_0) \\ \hline \mathrm{Me'O}_k,\ \mathrm{Me'O}_z\ (T < T_0) \end{matrix} \right| \mathrm{Pt}$$

provided that the intermediate electrolyte is a pure oxygen ion conductor and that the standard molar free

(1) G. Barbi, *J. Phys. Chem.*, **68**, 1025 (1964).

energy of formation of MeO_z, considered in the left-hand electrode as pure phase, is known.

At the right-hand side there are systems whose phases may vary in composition and structure with temperature; y_- and y_+ are the oxygen–metal ratios, α, of $Me'O_y$ phase in equilibrium with $Me'O_k$ and $Me'O_z$, respectively ($k < y_- < y_+ < z$).

It was also experimentally shown that, at the eutectoid temperatures T_0, such a change in the slope of the E *vs.* T curve takes place that it is possible to determine T_0.

If we consider a metal–oxygen phase diagram like that of Fig. 1 and we measure, at $T > T_0$, the e.m.f. across the cell

$$\text{Pt} \left| \begin{matrix} \text{MeO}_k, \text{MeO}_{y_-} \\ s \end{matrix} \right. \begin{matrix} \text{ZrO}_2 \\ (+\ \text{CaO}) \end{matrix} \left| \begin{matrix} \text{Me–O} \\ \text{(variable composition)} \end{matrix} \right| \text{Pt}$$

for an oxygen–metal ratio such as $k < \alpha < y_-$, the e.m.f. E is zero, while for $y_+ < \alpha < z$, E is independent of α. This happens because the oxygen chemical potential in a biphasic system is a function only of the temperature and is determined by the difference between the free energy changes of the two oxidation reactions, $MeO_k \rightarrow MeO_{y_-}$ and $MeO_{y_+} \rightarrow MeO_z$. In the field of stability of the monophase MeO_y, E is function of both α and T.

In this case, if the system may be considered as a solid homogeneous athermal mixture of two reference phases, the e.m.f. values are related to the activities of these two components of the mixture, activities expressed by the fundamental relations

$$R \ln a_1 = \frac{\partial \Delta S_m}{\partial n_1}$$

$$R \ln a_2 = \frac{\partial \Delta S_m}{\partial n_2}$$

where n_1 and n_2 are the molar fractions of the components and ΔS_m the entropy variation due to mixing. ΔS_m is given by the number of the distinguishable arrangements of the ions in the mixture, which number, in turn, depends on the spatial distribution of ions and vacancies in the lattice and on the kind of mixing.

Therefore, it appears evident that, in the case of athermal mixtures, the e.m.f. measurements may give a criterium for checking the reliability and the suitability of the choice of the two reference states, from the mixing of which the monophase is supposed to form. In other words, these electrochemical measurements may or may not confirm the correctness of a supposed mechanism of formation of the monophase.

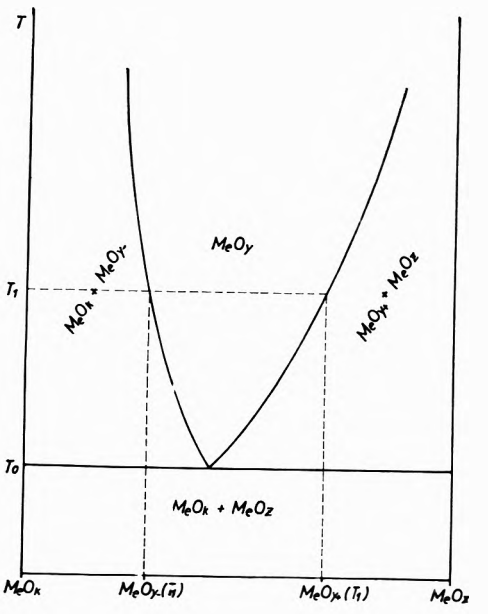

Figure 1.

These considerations were applied to the iron oxides in the interval Fe–Fe_3O_4 ($k = 0$, $z = 1.33$) in order to check the validity of this technique for the general problem of the metal–oxygen phase diagram determination. Furthermore, a check was made of the validity of Salmon's assumption which considers the reduction of magnetite to wüstite only as a random occupation of the vacant octahedral sites in the magnetite structure by neutral iron atoms.[2]

Apparatus and Materials

The cell with which the measurements were performed, the electrical device, as well as the preparations for the intermediate ceramic electrolyte and for the reference electrode biphasic system, have been described elsewhere.[1]

The preparation of the iron–oxygen systems were carried out by weighing very accurately iron and Fe_2O_3 powders (purities better than 99.996%) and then carefully mixing them together in the proper ratios. The starting materials were previously dried in a prepurified flowing argon atmosphere at 100° for several hours. After pressing the mixtures in the shape of pellets, as was previously described,[1] the latter were annealed at 930–950° for 15–20 hr. in a furnace, under pressure of less than 2×10^{-5} mm., then cooled and stored in a prepurified argon atmosphere.

(2) O. Salmon, *J. Phys. Chem.*, 65, 550 (1961).

The Field of Stability of Monophase Wüstite

The e.m.f. measurements carried out in the temperature interval 500–1050° on the galvanic cell

$$\text{Pt–Rh} \;\Big|\; \text{Fe, wüstite} \;\Big|\; \begin{matrix} ZrO_2 \\ (+\ CaO) \end{matrix} \;\Big|\; \begin{matrix} \text{Fe–O} \\ \text{(variable composition)} \end{matrix} \;\Big|\; \text{Pt–Rh}$$

are reported in Fig. 2.

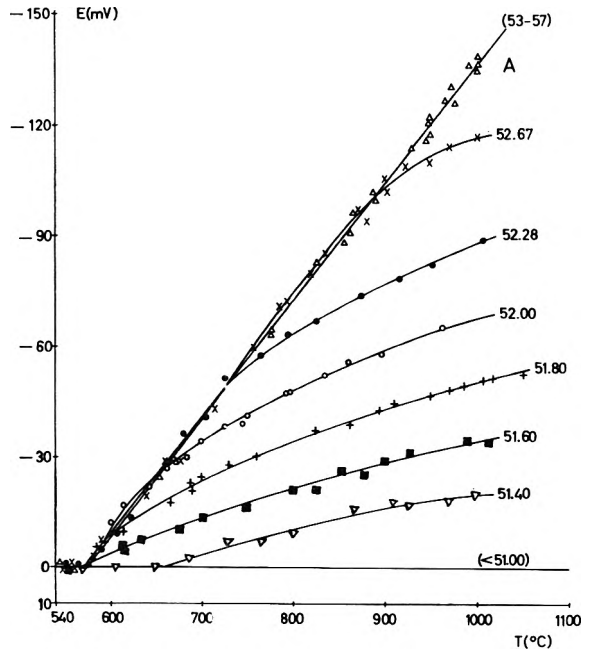

Figure 2. Plot of e.m.f. values *vs.* temperature for various oxygen contents in wüstite.

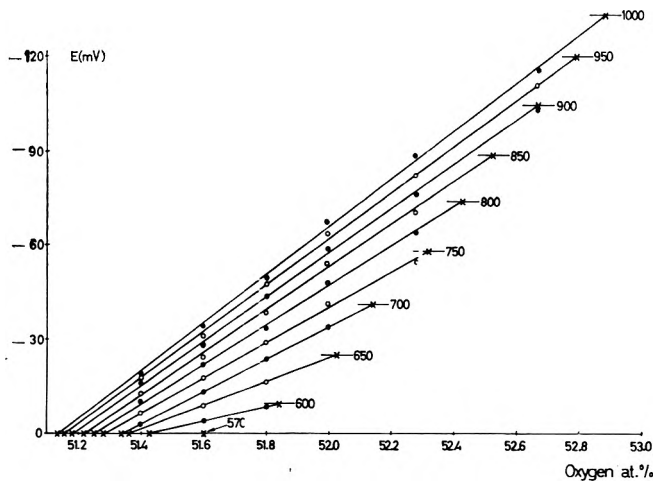

Figure 3. *E vs. C* isotherms.

For compositions below 51 atomic % of oxygen, all the e.m.f. values were found to be zero (±1 mv.). For oxygen contents between 53 and 57 atomic % of oxygen, all the *E vs. T* curves coincide with that marked "A."

Figure 3 shows the isothermal sections of Fig. 2 for temperature intervals of 50° as well as the potential levels corresponding to the curve "A." The intersections of the *E vs. C* curves with these levels are all points on the phase boundary of the monophase wüstite because, at a given temperature, they represent the composition at which magnetite appears (or disappears) as a pure phase.

With regard to the formation of iron as a pure phase, the same considerations apply to the intersections of the *E vs. C* curves with the abscissa.

The phase diagram so obtained is reported in Fig. 4. It is in close agreement with those obtained by other authors[3–5] but it diverges somewhat from that determined by Benard.[6]

Fe_3O_4 can be considered as an oxygen ions framework showing a cubic close-packed symmetry. The iron

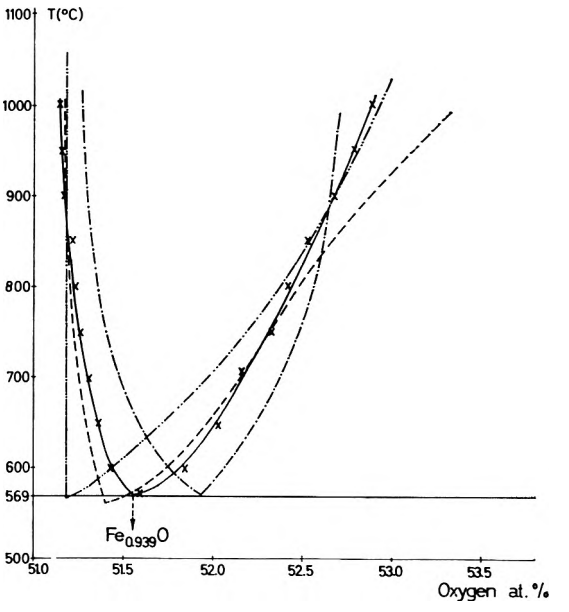

Figure 4. Phase diagram Fe–O in the region of wüstite between 500 and 1000°: —··—, L. B. Pfeil, *J. Iron Steel Inst.*, **123**, 237 (1931); –·–·–, E. R. Jette and F. Foote, *Trans. AIME*, **105**, 276 (1933); – – – –, L. S. Darken and R. W. Gurry, *J. Am. Chem. Soc.*, **67**, 1398 (1945); ———, this work.

(3) L. B. Pfeil, *J. Iron Steel Inst.*, **123**, 237 (1931).

(4) E. R. Jette and F. Foote, *Trans. AIME*, **105**, 276 (1933).

(5) L. S. Darken and R. W. Gurry, *J. Am. Chem. Soc.*, **67**, 1398 (1945).

(6) J. Benard, *Bull. soc. chim. France*, **16D**, 109 (1949).

ions are distributed in two kinds of positions corresponding to the inverse spinel structure. The available positions, octahedral and tetrahedral according to the distribution of the surrounding oxygen atoms, are, respectively, 32 and 16 (in the 32 oxygen double cell), but it should be noted that the probability of occupation of a tetrahedral site depends on the distribution of the iron ions and holes in its nearest neighbours.

In its field of stability, the monophase wüstite may be considered as a solid solution of FeO (although FeO does not exist, as such, it is possible to take it as a reference state) and of Fe_3O_4, assuming that the space charge distribution of the standard state of FeO is the same as that of Fe_3O_4.[7]

The standard states of Fe_3O_4 and FeO are chosen, respectively, as follows.

(1) Fe_3O_4: 0.25 trivalent iron ion in the octahedral positions, 0.25 bivalent iron ion in the octahedral positions, 0.25 trivalent iron ion in the tetrahedral positions (for each oxygen ion of the frame), thus giving an oxygen–metal ratio $\alpha = 1.33$. There is also 0.5 octahedral hole.

(2) FeO: 0.25 trivalent iron ion in the octahedral positions, 0.25 bivalent iron ion in the octahedral positions, 0.50 neutral iron atom in the octahedral positions, 0.25 trivalent positive hole in the tetrahedral positions, thus giving an oxygen–metal ratio $\alpha = 1.00$.

The formation of the intermediate phase FeO_y results from the random occupation of the octahedral holes in Fe_3O_4 by the neutral iron atoms; the contribution due to the mixing of trivalent ions and holes in tetrahedral position is neglected.[2]

The total process is considered athermal, and so the free energy change due to the mixing of the two reference states is only due to the variation of the configurational entropy.

Chemically speaking, it can be described by the over-all equation

$$6FeO + O_2 \rightleftharpoons 2Fe_3O_4$$

In our electrochemical chain, in equilibrium conditions, we may write

$$E = \mu_2 - \mu_1 = -\frac{RT}{4F} \ln \left[\frac{(a_{O_2})_y}{(a_{O_2})_{y_-}} \right]$$

where μ_1 and μ_2 are the chemical potentials of the oxygen in equilibrium with the systems FeO_{y_-} (left-hand electrode) and FeO_y (right-hand electrode), and a_{O_2} is the oxygen activity.

Since in isothermal conditions

$$\left[\frac{a_{O_2} a_{FeO}^6}{a_{Fe_3O_4}^2} \right]_{y_-} = \left[\frac{a_{O_2} a_{FeO}^6}{a_{Fe_3O_4}^2} \right]_y$$

we obtain

$$E = -\frac{RT}{4F} \ln \left[\frac{(a_{Fe_3O_4})_y}{(a_{Fe_3O_4})_{y_-}} \right]^2 \left[\frac{(a_{FeO})_{y_-}}{(a_{FeO})_y} \right]^6$$

From the above structural considerations it is easy to find

$$(a_{FeO})_y = \left[\frac{0.5n_1}{0.5n_1 + 2n_2} \right]^{0.5}$$

$$(a_{Fe_3O_4})_y = \left[\frac{2n_2}{0.5n_1 + 2n_2} \right]^2$$

where n_1 and n_2 are the mole fractions of FeO and Fe_3O_4, respectively. Identical relations may be rewritten for FeO_{y_-}. The n_1 and n_2 values for FeO_y and FeO_{y_-} are obtained by elementary lever-type calculations performed on the ground of the chemical composition and of the previously determined phase diagram (Fig. 4).

Thus, it is possible to calculate the theoretical values of E.

In the following table the calculated and the experimental values of E in mv. are compared for three temperatures.

Table I

C (atomic % oxygen)	700°		800°		900°	
	E_{calcd}	E_{found}	E_{calcd}	E_{found}	E_{calcd}	E_{found}
51.20	..	..	..	..	−1.5	−5
51.40	−4.5	−3.5	−10.5	−10.5	−17.5	−15
51.60	−16.5	−13	−24	−21.5	−32.5	−28
51.80	−28	−23.5	−34.5	−34	−46.5	−43.5
52.00	−38	−34	−47.5	−47.5	−58.5	−59
52.28	..	..	−62	−64	−76	−76.5
52.67	..	..	..	..	−95	−103

Remarks

Because of the negative coefficient of temperature of the electrical resistivity, it seems reasonable to predict a wide application of this technique to the phase diagram determination in metal–oxygen systems at high temperatures; in fact, at least at first sight, the decrease of the electrical impedance of the cell when the temperature increases should practically make the e.m.f. measurements easier and less delicate, quite the

(7) W. L. Roth, General Electric Research Laboratory Report 58-RL-2128.

contrary to what happens with other classical techniques.

Furthermore, since the slope of e.m.f. *vs.* T curves varies suddenly (and more by increasing temperatures) when a phase transition occurs, an eventual small and gradual variation with the temperature of the electron transport number of the intermediate electrolyte does not affect the applicability of the method.

Acidity of Hydrocarbons. XI. Activation Parameters for Exchange of Toluene-α-*d* with Lithium Cyclohexylamide in Cyclohexylamine[1]

by A. Streitwieser, Jr.,[2a] R. A. Caldwell,[2b] M. R. Granger, and P. M. Laughton[2c]

Department of Chemistry, University of California, Berkeley, California (*Received April 16, 1964*)

The dependence at two temperatures of the pseudo-first-order rate constants for exchange of toluene-α-*d* with cyclohexylamine on the concentration of the lithium cyclohexylamide catalyst leads to the thermodynamic parameters for the aggregation equilibrium of lithium cyclohexylamide and the activation parameters for the bimolecular exchange reaction. The equilibrium is unusual in that aggregation is accompanied by an *increase* in entropy; the exchange reaction itself has an unusually negative entropy of activation. These results are interpreted in terms of specific solvation effects.

In previous work[3] on the exchange reaction of toluene-α-*d* with lithium cyclohexylamide, we demonstrated that the kinetics was consistent with reactive monomeric lithium cyclohexylamide being in equilibrium with inert dimers, trimers, and higher aggregates. The present study is concerned with the temperature dependence of the reaction and the corresponding activation parameters. Because of the equilibria involving the active catalyst, isolated rate measurements at different temperatures do not suffice. These equilibria required a study of the kinetic order in catalyst over a wide range of concentration; the complete study of the effect of temperature on rate requires the temperature dependence of these equilibria and, consequently, a knowledge of the kinetic order of catalyst over a concentration range at more than one temperature.

Experimental

Preparation of toluene-α-*d* was reported previously.[3] The kinetics was followed using exchange procedure B[3] with some modifications. Butyllithium from Foote Mineral Co. was used to prepare the catalyst solutions. The infrared analyses for deuterium content were performed on a Perkin-Elmer 221 or 421 spectrophotometer with 10% solutions in carbon tetrachloride in 1-mm. cells or as the pure liquid sample, after isolation by gas–liquid chromatography, in a 0.1-mm. microcell. In later runs, and particularly the runs at low base concentration, the formal concentration of lithium cyclohexylamide was determined by reaction with excess dry bromobenzene, which was introduced at the

(1) Paper X: A. Streitwieser, Jr., and H. F. Koch, *J. Am. Chem. Soc.*, 86, 404 (1964). This work was supported by grants from the Petroleum Research Fund and by the United States Air Force Office of Scientific Research of the Air Research and Development Command.

(2) (a) Alfred P. Sloan Fellow, 1958–1962; (b) National Science Foundation Cooperative Graduate Fellow, 1962–1964; (c) ACS-PRF Faculty Awardee, 1962–1963; on leave from Carleton University, Ottawa, Canada.

(3) A. Streitwieser, Jr., D. E. Van Sickle, and W. C. Langworthy, *J. Am. Chem. Soc.*, 84, 244 (1962).

end of a run by typical vacuum line techniques, and by Volhard titration of the liberated bromide ion. The results are consistent with a 1:1 stoichiometry of lithium cyclohexylamide and reacted bromobenzene. Estimated accuracy of the titration is about 2%. In addition, in these runs, cyclohexylamine was dried by a final distillation on the vacuum line from lithium cyclohexylamide.

Several runs were carried out with a mixture of toluene-α-d and toluene-α-t. The tritium rates were followed by counting aliquots in a scintillation counter (Nuclear-Chicago Model 720) or with a radio-assay gas chromatography unit described previously.[1] The k_D/k_T isotope effects recorded in Table I will be discussed in a future paper.

Table I: Rates of Exchange of Toluene-α-d with Lithium Cyclohexylamide at 25.00 ± 0.01°

[Toluene-α-d], mole/l.	c,[a] mole/l.	$10^5 k_{expt}$,[b] sec.$^{-1}$	$10^5 k$,[c] sec.$^{-1}$	[LiNHC$_6$H$_{11}$],[d] mole/l.	$10^5 k_2$,[e] l. mole^{-1} sec.$^{-1}$
0.42[f]	0.0049	1.20	1.07[g]	0.0018	6.0
.48[f]	.0057	1.28	1.12[h]	.0020	5.5
.47	(.011)[i]	(0.52)	(0.46)		
.48	(.017)[i]	(1.45)	(1.28)		
.48	.017	2.19	1.92	.0033	5.9
.49	.021	2.3	2.1	.0035	5.8
.43[f]	.024	2.4	2.1[j]	.0037	5.7
.48	.038	2.5	2.2	.0043	5.0
.49[k]	.060	3.0	2.6	.0050	5.2
.33	.061	...	(3.2)[l]	.0050	6.4
.48	.075	3.6	3.2	.0053	6.0
.48[m]	.097	3.8	3.4	.0057	6.0
.47	.187	4.3	3.8	.0067	5.7
.50[n]	.027	8.3[o]	7.2[o]		
.43[f]	.0051	4.3[o]	3.8[o,p]		
.48[f]	.0032	3.3[o]	2.9[o,q]		
.53[f,r]	.33	15.8[o]	13.7[o,s]		

[a] Formal concentration of lithium cyclohexylamide. [b] Calculated from slope of log $(x - x_e)$ vs. time. [c] Corrected rate constant from eq. 8 of ref. 3. [d] Concentration of monomeric lithium cyclohexylamide from model 2. [e] Second-order rate constant from model 2. [f] These runs were carried out with a mixture of toluene-α-d and toluene-α-t, and both k_D and k_T were obtained. [g] $k_T = 0.38 \times 10^{-5}$ sec.$^{-1}$; $k_D/k_T = 2.8$. [h] $k_T = 0.38 \times 10^{-5}$ sec.$^{-1}$; $k_D/k_T = 2.9$. [i] Bromide titration method was not used and these results are considered to be in error. [j] $k_T = 0.80 \times 10^{-5}$ sec.$^{-1}$; $k_D/k_T = 2.6$. [k] Experiment by D. E. Van Sickle. [l] This experiment was run with toluene-α-t; k_D was obtained from $k_T = 1.16 \times 10^{-5}$ sec.$^{-1}$ and k_D/k_T was assumed to be 2.8. [m] Experiment by Dr. M. Feldman. [n] Experiment by Dr. H. F. Koch. [o] At 50°. [p] $k_T = 1.7 \times 10^{-5}$ sec.$^{-1}$; $k_D/k_T = 2.2$. [q] $k_T = 1.17 \times 10^{-5}$ sec.$^{-1}$; $k_D/k_T = 2.5$. [r] Experiment by G. R. Ziegler. [s] $k_T = 5.35 \times 10^{-5}$ sec.$^{-1}$; $k_D/k_T = 2.6$.

Results and Discussion

The previous results were interpreted analytically by a model (model 1) in which all equilibrium constants are equal for the equilibria

$$\mathrm{LiNHC_6H_{11}} + (\mathrm{LiNHC_6H_{11}})_n \underset{}{\overset{K_n}{\rightleftharpoons}} (\mathrm{LiNHC_6H_{11}})_{n+1} \quad (1)$$

An infinite series is required by the approach to zero slope at high concentration of a plot of log k vs. log c where k is the corrected pseudo-first-order rate constant[3] and c is the formal concentration of lithium cyclohexylamide. The value of K_n, however, is largely determined by the behavior of this plot at low values of c. In a study of the effect of ring substituents on the rate of exchange of toluene-α-d, we found that ring bromine is rapidly and completely removed as bromide ion with concomitant destruction of the catalyst.[1] This observation suggested the use of bromobenzene as a measure of the actual amount of lithium cyclohexylamide in our solutions rather than our customary procedure of titrating total base. The results showed that about 0.003 M base was present not as lithium cyclohexylamide and was presumably hydroxide resulting from residual traces of water. Better results were obtained more recently by distillation of cyclohexylamine from lithium cyclohexylamide rather than from molecular sieves. These results are summarized in Table I.

The results of recent runs at low base concentration at 50° are shown in Fig. 1. These results lead to $K_n = 60$ l. mole^{-1} rather than the value of 35 l. mole^{-1} adopted previously. For the activation parameters, a series of runs was made at 25° covering a 40-fold range of c from 0.005 to 0.2 M. Using the same model, the results are also fitted best by $K_n = 60$ l. mole^{-1}. Use of these values gives second-order rate constants,

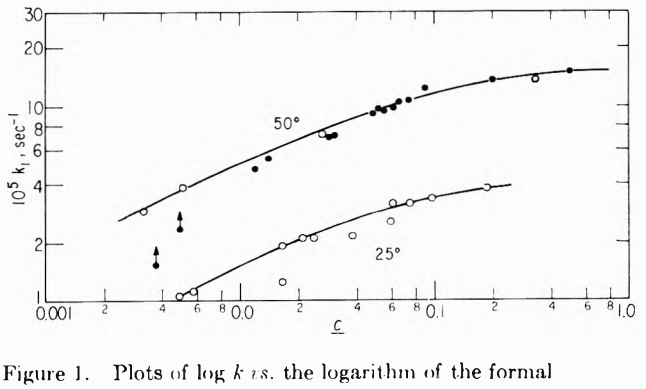

Figure 1. Plots of log k vs. the logarithm of the formal concentration of lithium cyclohexylamide at two temperatures. The solid lines are calculated from model 2. Open circles are reported in this paper, closed circles are data reported previously.

k_2, of 10.2 ± 0.8 × 10^{-3} (50°) and 3.0 ± 0.2 × 10^{-3} (25°) l. $mole^{-1}$ $sec.^{-1}$.

An alternative model for the equilibria (1) gives a somewhat better fit. In this model (model 2), each successive equilibrium constant, K_n', is proportional to $1/(n+1)$; that is, the probability of any aggregate adding an additional unit is constant, whereas the probability for dissociating one unit is proportional to the total number of monomer units in the aggregate. Both models clearly embody rather drastic simplifying approximations; an argument can be made that model 2 is in better accord with chemical intuition. This model also has an analytical solution[3]

$$c = [\mathrm{LiNHC_6H_{11}}] \exp K_n'[\mathrm{LiNHC_6H_{11}}]$$

For K_n' = 500 l. $mole^{-1}$, the corresponding second-order rate constants k_2', are 19.1 ± 1.0 × 10^{-3} (50°) and 5.7 ± 0.3 × 10^{-3} (25°) l. $mole^{-1}$ $sec.^{-1}$. The two curves in Fig. 1 are derived from this model. The second-order rate constants have comparable orders of magnitude from both models but are sensitive to the value chosen for the equilibrium constant. Consequently, for most purposes, such rate constants do not have more meaning than relative rates taken at equal catalyst concentrations.

It is important that in both models, the equilibrium constants are essentially independent of temperature over the range studied. This result also follows simply from the near constancy of $[k(50°)/k(25°)]_c$ over the range of c studied. For equilibrium 1, $\Delta H° \cong 0$ and $\Delta S° = 8$, $\Delta S°' = 2$ e.u. for models 1 and 2, respectively. It is noteworthy not only that the enthalpy change is nil but also that the entropy change is positive for the aggregation of two units into one in this equilibrium. We normally expect aggregation to occur because additional bonding forces within the aggregate overbalance the decrease of entropy associated with the loss of three modes of translational freedom. We suggest that the lithium cation in lithium cyclohexylamide ion pair binds at least one solvent molecule and that such solvation is diminished in the aggregates; that is, within the aggregate, the lithium cyclohexylamide units "solvate" each other. Hence, each time a monomeric lithium cyclohexylamide combines with an aggregate to form a higher aggregate, some solvent is freed leading to an increase in entropy. Furthermore, the bonding forces within the aggregate must balance the solvation bonds to the monomeric ion pair such that the net enthalpy change is small. In this view, the driving force for aggregation comes from the solvation required by the small lithium cation.

The activation parameters for the exchange reaction are determined from the second-order rate constants. In both models, the ratio of $k_2(50°)/k_2(25°)$ is essentially the same and leads to ΔH^* = 8.8 kcal./mole, a rather small value. The corresponding entropy of activation, ΔS^* = −39 e.u. (model 2; standard state: 1 M), is also unusually low, much more negative than the ∼−20 e.u. expected for loss of three translational degrees of freedom typical for bimolecular reactions. We interpret these findings in terms of the solvation requirements of ion pair reactions in comparatively nonpolar solvents. We already know from conductivity studies[4] that the Li–N bond in lithium cyclohexylamide is almost completely ionic. We postulate that the high concentration of negative charge on the nitrogen demands close proximity of the lithium cation. In turn, this "solvation" of lithium cation by cyclohexylamide anion limits the amount of further solvation of the cation by solvent. In the transition state, the negative charge is extensively dispersed, and the anion is no longer as effective in "solvating" lithium cation. We further postulate that this solvation role is now assumed by additional solvent molecules; hence, the potential energy requirements of the transition state are largely met by increased solvation energy of the cation but at the expense of consequent extensive solvent organization and associated entropy changes.

(4) A. Streitwieser, Jr., W. M. Padgett, II, and I. Schwager, *J. Phys. Chem.*, **68**, 2922 (1964).

Acidity of Hydrocarbons. XII. Aggregation of Lithium Cyclohexylamide in Cyclohexylamine by Isopiestic Measurement[1a]

by A. Streitwieser, Jr., and W. M. Padgett, II[1b]

Department of Chemistry, University of California, Berkeley, California *(Received April 16, 1964)*

Isopiestic molecular weight measurements of lithium cyclohexylamide in cyclohexylamine show a degree of aggregation in semiquantitative agreement with theories derived previously from kinetic measurements. A modified technique for such isopiestic measurements is described.

From previous studies of the kinetics of hydrogen–deuterium exchange of toluene-α-d by lithium cyclohexylamide in cyclohexylamine, it was proposed that monomeric lithium cyclohexylamide is in mobile equilibrium with dimers, trimers, etc.[2] The kinetic results were interpreted with the aid of two simple models for the component equilibria and equilibrium constants were derived. These treatments lead to predicted values of the average degree of agglomeration of lithium cyclohexylamide which are capable, in principle, of independent confirmation.

For the determination of mean molecular weights with exclusion of air or moisture at a given temperature (the kinetics was run at 25 and 50°), the method of isopiestic measurement or isothermal distillation appeared to be most accurate and convenient. The original procedure of Signer[3] has borne several modifications,[4] but the general method has been to follow the course of equilibration volumetrically by draining the equilibration chambers periodically into graduated receivers.

In the experiments described here, the distillation is followed instead by spectrophotometric means. The apparatus designed for this purpose consists of a glass vessel in the shape of an H which carries ground-glass stoppers at the top of each arm, and which can be connected to a vacuum line through a stopcock on the crosspiece. The bottom of one arm is a spectrometer cell; both arms contain small glass-enclosed magnetic stirrers. The glass stoppers allow entry of the reagents *via* hypodermic syringe or pipet and provide a means of cleaning between runs. In the general procedure, a known volume, of known formal concentration, of the solution to be tested was placed in the "sample" arm, and a known volume, of known concentration, of a solution of a suitable chromophore was placed in the arm containing the spectrometer cell ("reference" arm). After degassing and evacuating, the entire apparatus was immersed completely in a 50° thermostat and the solutions were stirred intermittently. Periodically, the absorption of the chromophore solution was measured and progress to equilibrium was determined. These experimental data are sufficient to give the mean molecular weight of the test substrate.

For the present experiments, no single compound was found which served as a suitable chromophore in the concentration region of interest to us; hence, a mixture was used of a major solute, hexaethylbenzene, serving as a nonvolatile and nonabsorbing substrate, plus a minor solute, 1,2,5,6-dibenzanthracene, whose absorption at 395 mμ could be measured readily.

The procedure was tested with triphenylmethane in benzene (Table I). We could determine an experimental molecular weight, but for our purposes we preferred to determine the rate of approach to the theoretical equilibrium. In eq. 1, which is convenient for this purpose, C and V are the starting concentra-

(1) (a) This research was supported in part by a grant from the United States Air Force Office of Scientific Research. (b) National Science Foundation Summer Fellow, 1960.

(2) (a) A. Streitwieser, Jr., D. E. Van Sickle, and W. C. Langworthy, *J. Am. Chem. Soc.*, **84**, 244 (1962); (b) A. Streitwieser, Jr., R. A. Caldwell, M. R. Granger, and P. M. Laughton, *J. Phys. Chem.*, **68**, 2916 (1964).

(3) R. Signer, *Ann.*, **478**, 246 (1930).

(4) E. P. Clark, *Anal. Chem.*, **13**, 820 (1941); L. M. White and R. T. Morris, *ibid.*, **24**, 1063 (1952); C. E. Childs, *ibid.*, **26**, 1963 (1954).

tions and volumes, respectively. A_0 and A_∞ are the optical densities at the start and at equilibrium, and the primes refer to the substrate under test. The equation is a straightforward derivation assuming that A is proportional to the reference concentration and that the concentrations of substrate and reference are equal at equilibrium. This run shows that close approach to equilibrium can be accomplished but requires several days.

$$A_\infty = A_0\left[\frac{C'V' + CV}{C(V + V')}\right] \qquad (1)$$

Table I: Test of Isothermal Distillation with Triphenylmethane at 50°

Run 82: 3.0 ml. of 0.073 *M* C_6Et_6 and 8.0 ml. of 0.053 *M* Ph_3CH (in benzene)

Time, hr.	A^a
0	0.481
43.5	.449
114.5	.405
158.5	.391
217.5	.386
230	[b]
Calcd. at equil.[c]	.385

Run II-4: 3.0 ml. of 0.038 *M* C_6Et_6 and 3.0 ml. of 0.025 *M* Ph_3CH (in cyclohexylamine)

Time, hr.	A^a
0	0.393
19.8	.388
53.5	.382
137	.365
159.8	.360
183.5	.358
Calcd. at equil.[b]	.326

[a] Absorbance of 1,2,5,6-dibenzanthracene at 395 mμ contained in the C_6Et_6 side. [b] Cell leaked. [c] Equation 1.

This technique should be useful for comparatively volatile solvents but is inconveniently long with less volatile solvents; unfortunately, cyclohexylamine, the solvent of our present interest, falls in the latter class. Run II-4 in Table I, triphenylmethane in cyclohexylamine, shows only partial approach to equilibrium at 50° even after 183 hr. At 200 hr., leakage into the cell from the thermostat ended the run. Such leaks occurred frequently in the runs with lithium cyclohexylamide; hence, in these runs, a small crystal of 4,5-methylenephenanthrene was included in the test solution. The intense red color of the corresponding carbanion[5] served as a suitable indicator; the development of even minute leaks caused immediate extinction of the color. Although these limitations restricted the quantitative nature of the results obtained, repeated runs did show that agglomeration of lithium cyclohexylamide is important. Because of such leaks, we present in this paper only a selected set of those runs which were successful over prolonged periods.[6]

Two such experiments, runs 83 and 125, are summarized in Fig. 1 and 2. In these runs, the formal concentration of lithium cyclohexylamide was close to the concentration of the reference solution. The pronounced distillation of solvent into the reference side shows that the lithium cyclohexylamide is actually more dilute than indicated by the formal concentra-

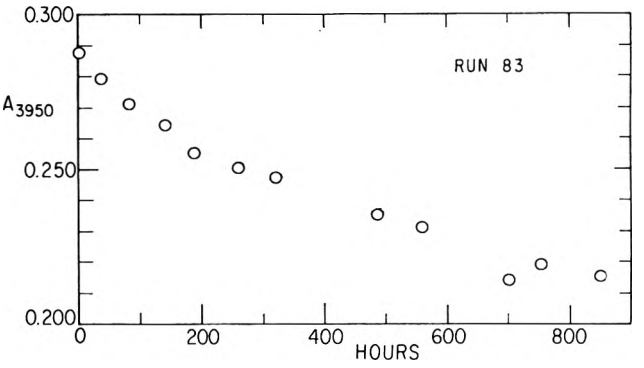

Figure 1. Run 83: 8.0 ml. of 0.072 *F* $LiNHC_6H_{11}$ *vs.* 3.0 ml. of 0.070 *M* C_6Et_6.

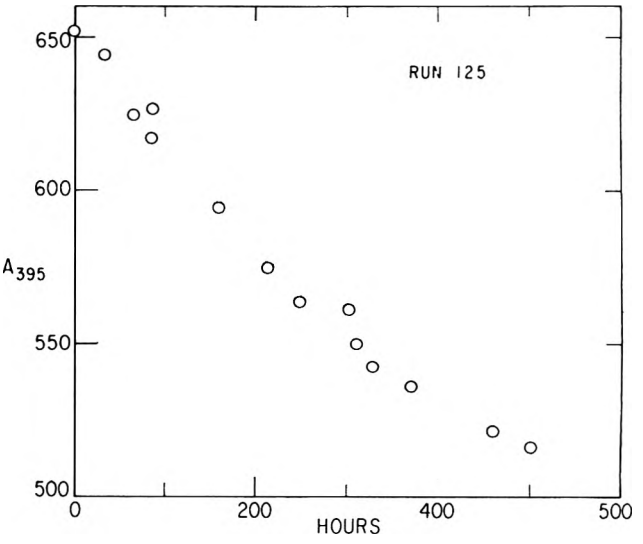

Figure 2. Run 125: 4.0 ml. of 0.056 *F* $LiNHC_6H_{11}$ *vs.* 3.0 ml. of 0.056 *M* C_6Et_6.

(5) A. Streitwieser, Jr., and J. I. Brauman, *J. Am. Chem. Soc.*, **85**, 2633 (1963).

(6) For further details, see W. M. Padgett, II, Dissertation, University of California, 1962.

tion; that is, aggregation does occur. The average degree of aggregation, α, may be derived by eq. 2.

$$\alpha = \frac{C'}{C}\,\frac{V'}{\left(\frac{A_\infty}{A_0}\right)(V' + V) - V} \qquad (2)$$

Runs 83 and 125 have not reached equilibrium; from the last A values observed we derive $\alpha = >1.6$ from both runs.

For the two models of the aggregation equilibria and the equilibrium constants obtained from the kinetic measurements,[2b] we may derive the corresponding theoretical values of α as a function of the formal concentration of lithium cyclohexylamide. The results are shown in Fig. 3. The final concentrations of lithium cyclohexylamide in runs 83 and 125 (0.08 and 0.07, respectively) are close to the concentration region where the α-curves for the two models overlap; both theories predict $\alpha = 2.6$–2.9 in this concentration range.

The approach to equilibrium was from the same side in both of the above runs. Several other experiments showed the same qualitative trends, but leaks frequently developed after only a few days, especially at the glass stoppers. Consequently, a modified apparatus was developed which had only a single entry tube and which could be sealed off completely to leave only the two arms in an inverted U.

Run II-19 (Fig. 4) was accomplished with this apparatus. After equilibrium was allowed to progress from one side for 400 hr., distillation of additional solvent was forced (dotted line in Fig. 4). The results show that thereafter equilibrium was approached from the other side and that the equilibrium position is bracketed by this procedure. The A values at 400 and 500 hr. yield $\alpha = 1.9$–2.9. The corresponding lithium cyclohexylamide concentrations are 0.07 and 0.09, respectively, for which the theoretical models gave $\alpha = 2.6$–3.0.

Because of the concentration region chosen, the present experiments do not distinguish between the two theoretical models. Run II-19, the most complete and successful of the runs made, appears to lead to an equilibrium α similar to the theoretical models, but probably somewhat lower. These results clearly demonstrate the qualitative correctness of the aggregation picture of lithium cyclohexylamide in cyclohexylamine but point up the simplifying approximations made in rendering an infinite array of equilibrium constants mathematically tractable.

Experimental

Hexaethylbenzene (Eastman), m.p. 127–129°, was dried under vacuum and stored over dried silica gel.

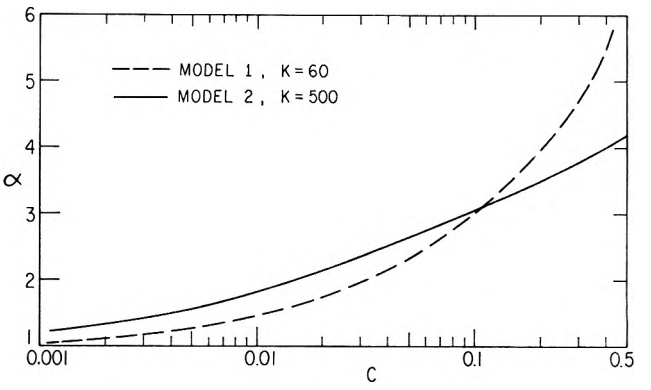

Figure 3. The form of α as a function of the formal concentration of lithium cyclohexylamide from the theoretical models 1 and 2.

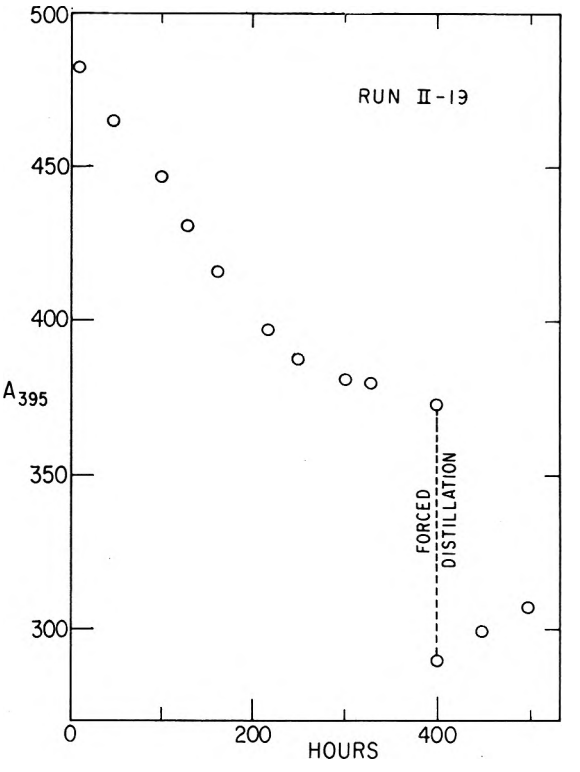

Figure 4. Run II-19: 5.0 ml. of 0.060 F $LiNHC_6H_{11}$ *vs.* 10 ml. of 0.050 M C_6Et_6 in the sealed apparatus.

1,2,5,6-Dibenzanthracene (Rutgerswerke-Aktiengesellschaft) was recrystallized from acetic acid and chromatographed as a benzene solution on Woelm alumina. The white flakes produced had m.p. 266.0–266.2° (Kofler hot stage) and were stored over silica gel. The reference solutions were prepared by dissolving weighed amounts in benzene. Benzene was removed on a vacuum line, and a known amount of cyclohexylamine was distilled from molecular sieves onto the

evacuated solid residues. When solution was complete, an aliquot was transferred with a syringe or volumetric pipet to the spectrometer cell side of the previously degassed apparatus. Lithium cyclohexylamide was prepared as described previously[2a] from cyclohexylamine and butyllithium in a cylindrical flask from which a capillary tube carrying a stopcock emerged from the bottom and terminated in a syringe needle. Using argon pressure, the solution was forced through the needle and a serum cap into the other chamber of the isopiestic apparatus, which contained graduation markings for determination of volume. During these transfers, any exposures of contents to the atmosphere were avoided by use of an argon purge. When the apparatus was properly stoppered, both solutions were thoroughly degassed, then frozen, and the apparatus was evacuated. In the modified apparatus, the single opening was sealed off at this point.

After thawing, the entire apparatus was placed in an underwater magnetic stirring system that provided intermittent stirring, and immersed completely in the thermostat. Periodically, the apparatus was placed in a Beckman DU spectrophotometer, and the absorption at 395 mμ was measured under standardized conditions. Dibenzanthracene in cyclohexylamine has bands at 374, 384.3, and 394.8 mμ. Beer's law is obeyed and the molar absorptivity of the last band is 1190. In principle, equilibrium is reached when the absorbance no longer changes. In practice, impractically long times are required, and we were forced to be satisfied with an approach to equilibrium. Three of the several runs made are summarized in Fig. 1, 2, and 4.

Acidity of Hydrocarbons. XIII. Some Conductivity Studies of Lithium Cyclohexylamide, Fluorenyllithium, and Lithium Perchlorate in Cyclohexylamine[1a]

by A. Streitwieser, Jr., W. M. Padgett, II,[1b] and I. Schwager

Department of Chemistry, University of California, Berkeley 4, California *(Received April 16, 1964)*

An apparatus is described for determining conductivities in an inert atmosphere. Measurements with lithium perchlorate, lithium fluorenyl, and lithium cyclohexylamide in cyclohexylamine at 49.5° give ion-pair dissociation constants in the range 10^{-10} to 10^{-12} mole/l. These results indicate that the bonds to lithium in each of these salts are about equally ionic; the results confirm the conclusions reached in previous studies of kinetics of exchange with lithium cyclohexylamide in cyclohexylamine that free ions are not significantly involved in the concentration region used.

As part of our general study of acid–base exchange reactions and equilibria between hydrocarbons and lithium cyclohexylamide in cyclohexylamine,[2] we have carried out a limited study of the ionogenic[3] properties of this system. We report conductivity measurements of lithium cyclohexylamide and of an ionic organometallic compound, fluorenyllithium. For comparison, we have studied also a typical salt, lithium perchlorate. An apparatus was developed for preparing the solutions and carrying out the conductivity measurements

in an inert atmosphere. The results are not as accurate as conventional conductivity measurements in aqueous solutions but do have features of interest.

Experimental

The conductivity apparatus is diagramed in Fig. 1. Its use with lithium cyclohexylamide solutions is described by the following procedure.[4] The reaction vessel, R, is similar in dimensions to those used in our other exchange studies in this series. The lithium cyclohexylamide was prepared from ethyllithium or butyllithium and cyclohexylamine in the usual way

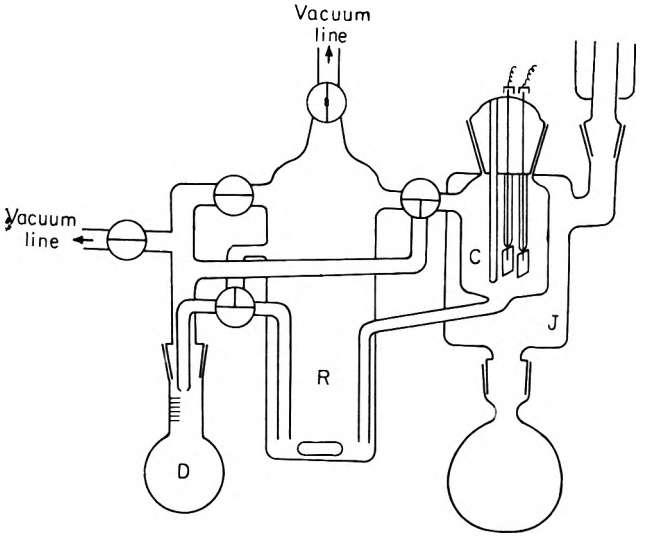

Figure 1. Conductivity apparatus for use in an inert atmosphere.

with the normal precautions of degassing, freezing, and thawing of solutions. By proper manipulation of stopcocks and the use of vacuum and argon pressure, the solution was drawn up into the conductivity cell, C. This cell contains in its glass stopper a thermocouple well and two electrodes of shiny platinum foil, 3 mils thick, attached to platinum leads which extend from glass support rods. The cells used were calibrated with 0.01 demal KCl solutions. The entire conductivity cell is contained within a vapor jacket. Refluxing cyclopentane (b.p. 49.5°) was used in this study so that the temperature would correspond to that at which many chemical studies were made in this system. After temperature equilibrium was reached, resistance of the cell was measured using a commercial bridge, Model 250-DA, Electromeasurements, Inc., Portland, Ore. The bridge was checked using standard resistors. After this measurement, the solution was allowed to flow back into R and was cooled to room temperature. A known amount of solution was transferred to flask D and the solvent was distilled from D to R. The residue of lithium cyclohexylamide in D was removed and titrated. The diluted solution in R was drawn up into C for measurement. Several such successive dilutions are possible in a given run.

The fluorenyllithium runs were handled in a similar manner. A weighed amount of recrystallized fluorene was treated with excess lithium cyclohexylamide in cyclohexylamine in R. Fluorene is converted completely to lithium salt with lithium cyclohexylamide.[5] In the subsequent conductivity measurements, the generally small contribution of the excess lithium cyclohexylamide to the conductivity was subtracted. The lithium perchlorate run used a weighed amount of the dried salt in cyclohexylamide with the technique of successive dilutions described above.

The results obtained are summarized in Table I in which are tabulated the formal concentrations of salt, the specific conductivity, L_s, and the equivalent conductance, Λ_e.

The viscosity of cyclohexylamine was determined to be 1.16 c.p.s. at 49.0° by comparison with water with a flow viscometer.

Results and Discussion

In aqueous solvents and in other solvents of high dielectric constant, conductivity properties of ions are usually considered in terms of ion-atmosphere effects. In solvents of low polarity or dielectric constant (smenogenic solvents),[3] the formation of ion pairs is important. The actual concentration of free ions may be so small that ion-atmosphere effects are negligible.[6]

Much early literature exists on conductivity studies in amines. Some examples are silver nitrate and lithium iodide in benzylamine,[7] lithium, sodium, and potassium iodides in dimethylamine,[8] and tetraalkylammonium iodides in aniline.[9] Plots of the equivalent con-

(1) (a) Taken in part from the dissertations of W. M. P., 1962, and I. S., 1964, University of California. This research was supported in part by grants from the Petroleum Research Fund administered by the American Chemical Society, and from the United States Air Force Office of Scientific Research. (b) National Science Foundation Summer Fellow, 1960.

(2) For paper XII, see A. Streitwieser, Jr., and W. M. Padgett, II, *J. Phys. Chem.*, 68, 2919 (1964).

(3) R. M. Fuoss, *J. Chem. Educ.*, 32, 527 (1955).

(4) For more complete details, see W. M. Padgett, II, Dissertation, University of California, 1962.

(5) A. Streitwieser, Jr., and J. I. Brauman, *J. Am. Chem. Soc.*, 85, 2633 (1963).

(6) C. A. Kraus, *J. Chem. Educ.*, 35, 324 (1958).

(7) P. Walden, *Z. physik. Chem.*, A148, 45 (1930).

(8) E. Swift, Jr., *J. Am. Chem. Soc.*, 60, 2611 (1938).

(9) P. Walden in Ostwald and Drucker's "Handbuch der allgemeinen Chemie," Band IV, Teil II, Leipzig, 1924; J. N. Pierce, *J. Phys. Chem.*, 19, 14 (1915).

Table I: Conductivity Studies in Cyclohexylamine at 49.5°

Run	Concn., $\times 10^3$ moles/l.	$10^3 \times L_s$,[a] mhos/cm.	$10^3 \times \Lambda_c$, mho cm.^{2}/equiv.
		Lithium perchlorate[b]	
	45.4	61.3	13.5
	22.7	11.8	5.2
	11.4	3.13	2.7
	5.68	1.18	2.1
	2.84	0.597	2.1
	1.42	0.311	2.2
	0.71	0.288	4.1
	0.36	0.163	4.5
	0.18	0.203	11.3
		Lithium fluorenyl[c]	
A[b]	40	800	200
B[b]	10	24.4	24
	5	8.2	16
	2.4	2.4	10
C[b]	1	1.5	15
	0.5	1.0	20
D[d]	66	2000	300
	30	390	130
	14	45	32
		Lithium cyclohexylamide	
A[d]	225	10.6	0.47
B[d]	125	7.0	0.56
	60	4.4	0.72
C[d]	80	5.2	0.64
D[d]	38	4.6	1.22
	21	2.8	1.34
	9	1.71	1.90
	3.5	1.04	2.97
E[d]	...	<0.6	
F[d]	103	6.9	0.67
	55	5.0	0.90
	26	3.0	1.13
G[d]	...	0.024[e]	...
	...	0.029[f]	...
H[b]	118	13.0	1.10
I[b]	58	8.1	1.41
	22	5.7	2.6
	7.5	2.7	3.5

[a] At 1000 c.p.s. [b] Run by I. Schwager. [c] L_s corrected for contribution by lithium cyclohexylamide also present. [d] Run by W. M. Padgett. [e] Determined with a 9.1-megohm resistor and 5-$\mu\mu$f. capacitor in parallel with cell. [f] Determined with a 5.00-megohm resistor and 5-$\mu\mu$f. capacitor in parallel with the cell.

ductance against the logarithm of the salt concentration show a characteristic pattern for most such salts. Starting with dilute solutions, Λ_c decreases in an almost linear fashion from 10^{-6} to 10^{-3} M, passes through a minimum at about 10^{-2} M, then rises to a maximum at about 1 M and falls again at higher concentration. The concentrations at which the minimum and maximum Λ_c occur are almost independent of the nature of the amine, although the magnitude of Λ_c at these points reflect clearly the polarity and viscosity of the solvent. This behavior of Λ_c with increasing concentration is generally interpreted to reflect the following phenomena.[10] At low concentrations, ion-pair formation is important and the free ions responsible for conduction appear to obey the Ostwald dilution law. At higher concentrations, ion triplets become important, causing the minimum in Λ_c and the subsequent increase in Λ_c with increasing concentration. Two effects combine to hold Λ_c to a maximum value—the onset of ion quadruplets and higher aggregates and the increase in viscosity of the solution, which, in lowering the ion mobilities, overcomes the effect of increase in ion-triplet concentration.

Plots of Λ_c *vs.* log c for lithium perchlorate and fluorenyllithium in Fig. 2 show clearly that both salts follow

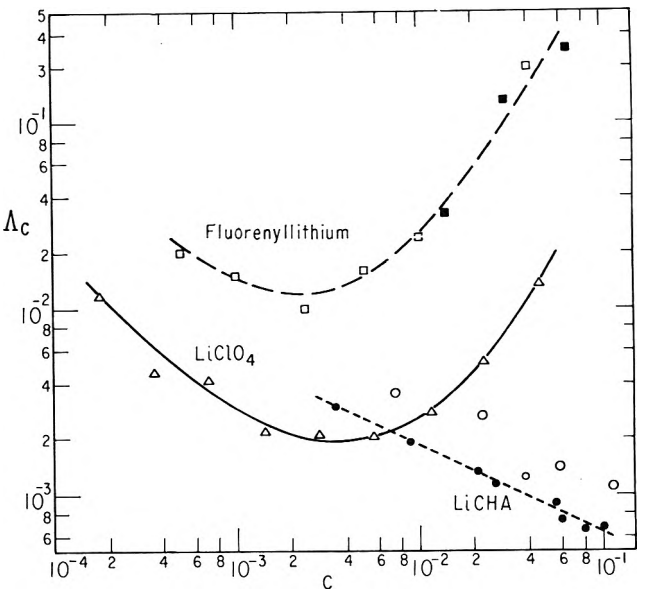

Figure 2. Equivalent conductivities of lithium salts in cyclohexylamine at 49.5° as functions of concentration. Open points were determined by I. S., closed points by W. M. P.

the expected pattern. The magnitude of Λ_c at the minima, 10^{-2} to 10^{-3}, may be compared with those for lithium chloride in benzylamine, 0.2,[11] lithium bromide in benzylamine, <0.01,[7] and sodium iodide in dimethylamine, 0.05.[8]

The ion-pair dissociation constant may be obtained from the experimental data in the following way. The

(10) C. A. Kraus, *J. Phys. Chem.*, 58, 673 (1954).

(11) F. L. Shinn, *ibid.*, 11, 537 (1907); F. F. Fitzgerald, *ibid.*, 16, 621 (1912).

equivalent conductance at infinite dilution, Λ_0, for each ion may be estimated from results in other solvents and the solvent viscosity, η, by the Walden product rule

$$\Lambda_0\eta = \text{constant} \qquad (1)$$

From such data summarized by Kraus,[6] we derive for cyclohexylamine that for Li^+, $\Lambda_0^+ \cong 25$, for ClO_4^-, $\Lambda_0^- \cong 35$. Actually, the equivalent conductances of a variety of anions are approximately the same in solvents of low polarity so that the value used for ClO_4^- may also be assumed for fluorenyl anion and for cyclohexylamide anion. When the conductivity is low, Kraus and Bray's[12] derivation for K_d takes the form

$$K_d = c(\Lambda_c/\Lambda_0)^2$$

This equation, of course, can only be applied when the conductivity results from free ions and not from ion triplets; that is, only data to the left of the minima in Fig. 2 can be used. In this way, our results yield $K_d \cong 2\text{–}6 \times 10^{-12}$ mole/l. for $LiClO_4$ and $\sim 60 \times 10^{-12}$ mole/l. for lithium fluorenyl. Both values are extremely low and point up the smenogenic character of cyclohexylamine. The significantly higher value for lithium fluorenyl undoubtedly reflects the larger size and more highly distributed charge of the fluorenyl anion. This result also shows that there can be no significant degree of covalent C–Li bonding in lithium fluorenyl; that is, the C–Li bond in this compound must be as ionic as the O–Li bond in $LiClO_4$.

The discrepancy between the two sets of values determined for lithium cyclohexylamide in independent investigations (Fig. 2) probably arises from an unaccounted change in cell parameters. The two studies do show the same type of concentration dependence of the conductance and are in satisfactory agreement considering the very low conductance levels and highly reactive nature of the solutions. Actually, the precise values of Λ_c are not important because lithium cyclohexylamide represents a more complex case; this compound is known to be aggregated in cyclohexylamine[2] and each aggregate should have its own dissociation constant. We might expect higher aggregates to have higher dissociation constants, but the resulting larger ions would also have lower mobility and carry less current. In Table I and in Fig. 2, the Λ_c values are calculated in terms of the formal concentration of lithium cyclohexylamide, c. We may consider two extremes—that the current-carrying ions come only from dissociation of monomer and that the current is carried equally by ions from each aggregate species present. In both cases, the lithium cyclohexylamide points in Fig. 2 are displaced upward and to the left, the displacement being more marked for the first case. Nevertheless, for both extreme cases, the points tend to group in the concentration region 10^{-3} to 10^{-2} mole/l. and the Λ_c values tend to be $\sim 10^{-2}$; hence, in this region, $K_d \cong 10^{-10}$. Clearly, lithium cyclohexylamide dissociates into ions to about the same extent as lithium perchlorate and lithium fluorenyl. The Li–N bond is as ionic as the bonds to lithium in the other salts. We conclude that monomeric lithium cyclohexylamide is best described as an ion pair, and its aggregates are ion multiplets. Nevertheless, the actual degree of dissociation to free ions is very small and it seems clear that in our exchange reactions between hydrocarbons and lithium cyclohexylamide, no significant amount of reaction involves such free ions.

(12) C. A. Kraus and W. C. Bray, *J. Am. Chem. Soc.*, **35**, 1315 (1913).

Polarizabilities from δ-Function Potentials[1a,b]

by E. R. Lippincott and J. M. Stutman

Department of Chemistry, University of Maryland, College Park, Maryland *(Received April 17, 1964)*

Molecular polarizabilities have been calculated from a semi-empirical δ-function model by using a variational method and δ-function electronic wave functions. The model enables one to obtain simple expressions for the parallel and perpendicular components and the mean polarizabilities for diatomic systems. Through use of a δ-function potential network for polyatomic systems the model has been extended to give polarizability components for polyatomic molecules which can be summed to give the mean values. Polarizability contributions from bond region electrons are distinguished from those due to nonbond region electrons. For polar molecules improved results are obtained by introducing a polarity correction. A comparison of observed and computed mean polarizabilities indicates that the results are quite reasonable with the average deviation being 10% for the 55 molecules studied. The approach used has the advantage that calculations can be made on large molecular systems without undue computational difficulties. Bond polarizabilities are not necessarily transferable from one molecular system to another owing to the strong dependence of the bond parallel component on bond length and the effect of configuration on the summation rules.

Introduction

The electrical polarizability is one of the fundamental physical properties of a molecular system being the microscopic analog of the index of refraction, a macroscopic bulk measurable. These are linked by the well-known Lorentz–Lorenz equation

$$^4/_3\pi N\alpha = \left(\frac{n^2-1}{n^2+2}\right)\left(\frac{M}{d}\right) \qquad (1)$$

where α is the mean molecular polarizability; n, the index of refraction; N, Avogadro's number; d, the density; and M, the molecular weight.[2]

Many calculations in recent years have been made in the attempt to obtain atomic and molecular polarizabilities from quantum mechanical models. In 1930 Hasse[3a] obtained polarizability values for the helium atom and lithium ion He used a variational method in testing several types of ground-state wave functions together with several types of perturbed state wave functions in terms of the perturbing potential. Buckingham's[3b] approach is based on Kirkwood's[3c] variation method and heavier atoms are considered, leading to complex determinantal self-consistent field wave functions. Bell and Long[4] compare polarizability values obtained from six different unperturbed wave functions chosen for H_2^+ and H_2 molecules and conclude that the polarizability is not very sensitive to the wave function chosen for the unperturbed molecule. The calculated values agree with experiment, 15% deviation being the maximum for any wave function chosen and about 3% being the minimum.

Abbott and Bolton[5] studied N_2 and used the polariz-

(1) (a) Taken in part from the thesis submitted by J. M. S. in partial fulfillment of the requirements for the degree of Doctor of Philosophy, University of Maryland; (b) this work was supported in part by a grant to the University of Maryland for a Materials Science Program by the Advanced Research Projects Agency, Department of Defense.

(2) The polarizability is strictly a tensor

$$\alpha = \begin{pmatrix} \alpha_{xx} & \alpha_{xy} & \alpha_{xz} \\ \alpha_{yx} & \alpha_{yy} & \alpha_{yz} \\ \alpha_{zx} & \alpha_{zy} & \alpha_{zz} \end{pmatrix}$$

and the value of α_{ij} gives the magnitude of the dipole induced in the i direction by a unit electrical field in the j direction. However, the mean molecular polarizability obtained experimentally is the average of the three diagonal components.

(3) (a) H. R. Hasse, *Proc. Cambridge Phil. Soc.*, **26**, 542 (1930); (b) R. A. Buckingham, *Proc. Roy. Soc.* (London), **A160**, 94 (1937); (c) J. G. Kirkwood, *Physik. Z.*, **33**, 57 (1932).

(4) R. P. Bell and D. A. Long, *Proc. Roy. Soc.* (London), **A203**, 364 (1950).

(5) J. A. Abbott and H. C. Bolton, *J. Chem. Phys.*, **20**, 762 (1952); *Proc. Roy. Soc.* (London), **A216**, 477 (1953).

ability as a criterion for determining the molecular wave function of a system by a self-consistent field method and imply that the polarizability is more sensitive to the wave function chosen than other measurable physical properties. This is just what one would expect from a conceptual frame of reference, *i.e.*, that the polarizability is a measure of the ease with which the electron probability distribution may be distorted and thus would be a sensitive indicator of the correctness of the wave function used.

Kolker and Karplus[6] have recently presented the first attempt at the calculation of the polarizability tensor $\bar{\alpha}$ with *ab initio* wave functions for a series of first row diatomic molecules. Their results again indicated that the polarizability could be a useful criterion for testing the accuracy of wave functions. Essentially no work has been done on more complicated systems.

The δ-function model of chemical binding is useful in predicting vibrational energies of both diatomic and polyatomic systems and also in generating an internuclear potential function. Lippincott and Dayhoff[7] using this semi-empirical method predict ω_e, $\omega_e X_e$, D_e, and r_e for both diatomic systems and bonds of polyatomic molecules. In view of the studies of Abbott and Bolton and more recently of Kolker and Karplus that the polarizability is an effective criterion of how well the wave function approximates the real situation and since the δ-function model performs reasonably well in the prediction of the other molecular constants, we present this investigation as an attempt to test the acceptability of the δ-function wave functions with respect to calculations of electric polarizabilities.

The δ-Function Model

It will be necessary to review briefly those aspects of the δ-function model of chemical binding which have application to the calculations of polarizabilities for molecular systems.[7,8]

The potential energy for the n-electron problem is taken to be the sum of single δ-function potentials each having the following form for a diatomic system

$$V = -\left[A_1 g\delta\left(x - \frac{a}{2}\right) + A_2 g\delta\left(x + \frac{a}{2}\right)\right] \quad (2)$$

where x is the coordinate of motion along the internuclear axis, a is the δ-function spacing, A_1 and A_2 are the δ-function strengths or reduced electronegativities (REN) for nucleus 1 and 2, respectively, g is the unit δ-function strength (the values for the hydrogen atom), and $\delta(x)$ is a δ-function whose properties are

$$\delta(x) = 0 \text{ when } x \neq 0 \quad (3)$$

$$\delta(x) = \infty \text{ when } x = 0 \quad (4)$$

$$\int_{-\infty}^{+\infty} \delta(x)\, dx = 1 \quad (5)$$

for any argument x of δ.

Thus for the case in question the potential is zero everywhere except at the δ-function positions, *i.e.*, $x = a/2$ and $x = -a/2$.

The REN or A values are, in principle, obtainable from separated atom energies and the equation

$$A = \sqrt{-2E_i} \quad (6)$$

which is obtained from the solution of the atomic problem using the δ-function model.[9] For molecules involving other than hydrogen atoms, other approaches for determining the REN values were needed. Empirical rules were developed and in Table I the REN values of the elements are listed.

The solution to the Schroedinger equation for the molecular problem has the form

$$\psi_i = N\left[e^{-c|x_i + a/2|} \pm e^{-c|x_i - a/2|}\right] \quad (7)$$

where

$$N = [(2/c)(1 \pm e^{-ca} \pm ace^{-ca})]^{-1/2} \quad (8)$$

$$c = (-2E_i)^{1/2} \quad (9)$$

and E_i is the separated atom energy for the ith particle. In the above equations, the positive sign corresponds to a bound state and the negative to a repulsive state. See Fig. 1 for an illustration of the probability density function for both states of the H_2^+ molecule.

Frost's[8] δ-function branching condition can be used to obtain an expression for c as a function of the internuclear distance.

$$\frac{\psi'\Big|_{\frac{a}{2}+\epsilon}^{\frac{a}{2}-\epsilon}}{\psi} = -2Ag \quad (10)$$

(6) H. J. Kolker and M. Karplus, *J. Chem. Phys.*, **39**, 2011 (1963).

(7) E. R. Lippincott and M. O. Dayhoff, *Spectrochim. Acta*, **16**, 807 (1960).

(8) A. A. Frost, *J. Chem. Phys.*, **22**, 1613 (1954); *ibid*, **25**, 1150 (1956); *ibid.*, **23**, 985 (1955).

(9) One of the better empirical equations for the reduced electronegativity is

$$A = [X/(2.6n - 1.7p - 0.8D + 3.0F)]^{1/2}$$

where X is the electronegativity of the atom taken from Pauling; n is the principal quantum number; p is 1 for atoms with p electrons in valence shell, 0 for atoms with no p electrons in valence shell; D is the total number of completed p and d shells in atom; F is the total number of completed f shells in atom.

and

$$\begin{vmatrix} -\frac{a}{2}+\epsilon & \\ & \psi' \\ -\frac{a}{2}-\epsilon & \end{vmatrix} = -2Ag \qquad (11)$$

$$\psi$$

These two conditions give solutions for the homonuclear case of the form

$$c_i = Ag[1 \pm e^{-ac_i}] \qquad (12)$$

By combining eq. 12 with 6 we have

$$\lim_{a\to\infty} c_i = Ag = \sqrt{-2E_{i(a=\infty)}} \qquad (13)$$

Lippincott and Dayhoff[7] by-pass the problem of obtaining the c_i for each individual electron by generating a "super" one-electron situation from the

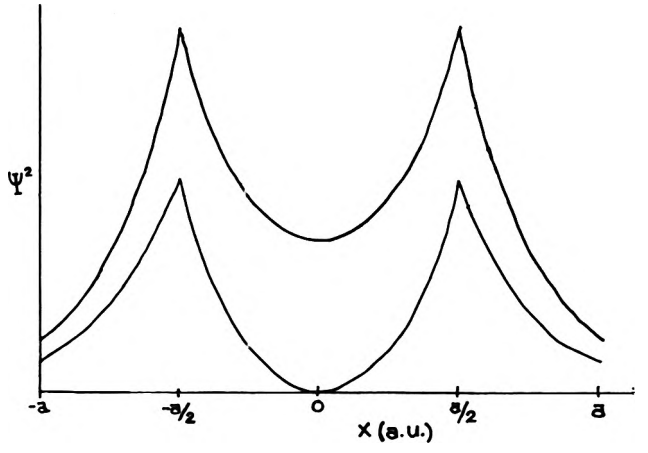

Figure 1. δ-Function electron probability density as a function of position for H_2^+ (unnormalized).

corresponding n-electron situation. A resultant c is obtained (written c_R) and is assumed to account for an electron pair. For the homonuclear situation

$$c_R = A\sqrt{nN} \qquad (14)$$

where A is the one-electron δ-function strength for the atom, n is the principal quantum number, and N is two times the column number in the periodic table. Heteronuclear diatomics are readily treated by forming a geometric mean molecular δ-function strength $c_{R_{12}}$

$$c_{R_{12}} = \sqrt{c_{R_1}c_{R_2}} = (\sqrt{n_1n_2N_1N_2A_1A_2})^{1/2} \qquad (15)$$

and then solving the wave equation as if the molecule were homonuclear.

The model can be extended to polyatomic molecules by forming linear combinations of atomic δ-function wave functions and by making use of the branching condition.[8] For example, if we consider a triatomic molecule as in Fig. 2, and allow the molecular wave

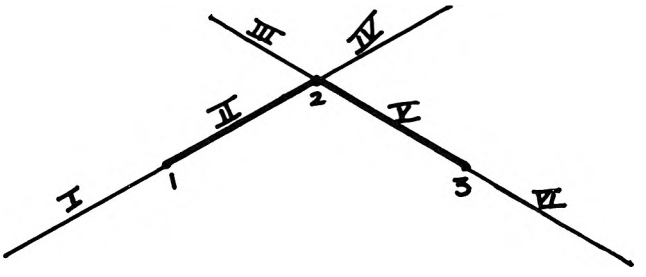

Figure 2. δ-Function network potential system for a bent triatomic molecule.

function to have $2n$ branches at each atom involved in n bonds, the molecular wave function is

$$\psi = a_1\psi_1 + a_2\psi_2 + a_3\psi_3 \qquad (16)$$

providing that the atomic wave function is defined along the given branch. Thus

$$\Psi_I = \Psi_{II} = \Psi_{IV} = a_1\psi_1 + a_2\psi_2 \qquad (17)$$

and

$$\Psi_{III} = \Psi_V = \Psi_{VI} = a_2\psi_2 + a_3\psi_3 \qquad (18)$$

Now using

$$\psi_i = e^{-c_i|x_b|} \qquad (19)$$

where b refers to the bond coordinate, we have for the regions indicated in Fig. 2

$$\psi_I = a_1e^{c_1x} + a_2e^{c_2(x - R_1)} \qquad (20)$$

$$\psi_{II} = a_1e^{-c_1x} + a_2e^{c_2(x - R_1)} \qquad (21)$$

$$\psi_{IV} = a_1e^{-c_1x} + a_2e^{-c_2(x - R_1)} \qquad (22)$$

$$\psi_{III} = a_2e^{c_2y} + a_3e^{c_3(y - R_2)} \qquad (23)$$

$$\psi_V = a_2e^{-c_2y} + a_3e^{c_3(y - R_2)} \qquad (24)$$

$$\psi_{VI} = a_2e^{-c_2y} + a_3e^{-c_3(y - R_2)} \qquad (25)$$

At branching points 1, 2, and 3, there are two, four, and two branches respectively. The δ-function condition gives

$$\left(\frac{\psi'_{II(x\uparrow)} + \psi'_{I(x\downarrow)}}{\psi_I}\right)_{x=0} = \frac{-2a_1c_1}{a_1 + a_2e^{-c_2R_1}} = -2A_1g \qquad (26)$$

$$\left(\frac{\psi'_{\mathrm{II}(x\downarrow)} + \psi'_{\mathrm{IV}(x\uparrow)} + \psi'_{\mathrm{III}(y\downarrow)} + \psi'_{\mathrm{V}(y\uparrow)}}{\psi_{\mathrm{II}}}\right)_{\substack{x = R_1 \text{ or} \\ y = 0}} = \frac{-4a_2c_2}{a_1e^{-c_1R_1} + a_2} = -4A_2g \quad (27)$$

$$\left(\frac{\psi'_{\mathrm{II}(x\downarrow)} + \psi'_{\mathrm{IV}(x\uparrow)} + \psi'_{\mathrm{III}(x\downarrow)} + \psi'_{\mathrm{V}(x\uparrow)}}{\psi_{\mathrm{III}}}\right)_{\substack{x = R_1 \text{ or} \\ y = 0}} = \frac{-4a_2c_2}{a_2 + a_3e^{-c_3R_2}} = -4A_2g \quad (28)$$

$$\left(\frac{\psi'_{\mathrm{V}(y\downarrow)} + \psi'_{\mathrm{VI}(y\uparrow)}}{\psi_{\mathrm{V}}}\right)_{y = R_2} = \frac{-2a_3c_3}{a_2e^{-c_2R_2} + a_3} = -2A_3g \quad (29)$$

where $(x\uparrow)$ implies the derivative is taken from the nucleus to $x > 0$, *i.e.*, $\mathrm{d}|x|/\mathrm{d}x = 1$; similarly $(x\downarrow)$ implies $\mathrm{d}|x|/\mathrm{d}x = -1$. Because of the presence of four branches at atom 2, eq. 26, 27, 28, and 29 give two three-by-three determinantal solutions

$$\begin{vmatrix} \left(1 - \frac{c_1}{A_1g}\right)p_{21} & 1 & 0 \\ 1 & \left(1 - \frac{c_2}{A_2g}\right)p_{11} & 0 \\ 0 & 0 & \left(1 - \frac{c_3}{A_3g}\right)p_{22} \end{vmatrix} = 0 \quad (30)$$

and

$$\begin{vmatrix} \left(1 - \frac{c_1}{A_1g}\right)p_{21} & 1 & 0 \\ 0 & \left(1 - \frac{c_2}{A_2g}\right)p_{32} & 1 \\ 0 & 1 & \left(1 - \frac{c_3}{A_3g}\right)p_{22} \end{vmatrix} = 0 \quad (31)$$

where $p_{ij} = e^{c_iR_j}$. Secular eq. 30 and 31 when expanded into element-cofactor form give the following two-by-two determinants

$$\begin{vmatrix} \left(1 - \frac{c_1}{A_1g}\right)p_{21} & 1 \\ 1 & \left(1 - \frac{c_2}{A_2g}\right)p_{11} \end{vmatrix} = 0 \quad (32)$$

and

$$\begin{vmatrix} \left(1 - \frac{c_2}{A_2g}\right)p_{32} & 1 \\ 1 & \left(1 - \frac{c_3}{A_3g}\right)p_{22} \end{vmatrix} = 0 \quad (33)$$

respectively.

These solutions are identical with those which would be obtained if the triatomic molecule were considered to consist of two diatomic molecules. This circumstance is a by-product of allowing the atomic δ-function wave function to exist only along the internuclear axis involved and allowing the axis to extend infinitely in both directions, by prohibiting interaction of neighboring bonds.

When eq. 30 and 31 are considered in detail we find that the two representations are generated because of the two forms which the wave function can take at nucleus 2. Of course, the values of these two forms must be identical at this nucleus. Of greater significance, however, is the fact that the secular determinant can take on a different form for each form that the common ψ can assume and thus the method is general for any molecular system with localized bonds. For example, one of these determinants for methane is given in eq. 34.

$$I = \begin{vmatrix} \left(1 - \frac{c_1}{A_1g}\right)p_{21} & 1 & 0 & 0 & 0 \\ 1 & \left(1 - \frac{c_2}{A_2g}\right)p_{11} & 0 & 0 & 0 \\ 1 & 0 & \left(1 - \frac{c_3}{A_3g}\right)p_{12} & 0 & 0 \\ 1 & 0 & 0 & \left(1 - \frac{c_4}{A_4g}\right)p_{13} & 0 \\ 1 & 0 & 0 & 0 & \left(1 - \frac{c_5}{A_5g}\right)p_{14} \end{vmatrix} = 0 \quad (34)$$

Note that the determinant given in eq. 34 reduces to

$$\begin{vmatrix} \left(1 - \frac{c}{A_{1g}}\right)p_{21} & 1 \\ 1 & \left(1 - \frac{c}{A_{2g}}\right)p_{11} \end{vmatrix} = 0 \quad (35)$$

where $p_{ij} = e^{c_i R_j}$ where R_j is the internuclear distance between atom 1 (the carbon atom) and atom $(j + l)$. The other three determinants are the same as I except for the changing p_{ij} and the position of the 1 in the first row.

$$\text{First row (I)} = \left(1 - \frac{c_1}{A_{1g}}\right)p_{21} \quad 1 \quad 0 \quad 0 \quad 0$$

$$\text{First row (II)} = \left(1 - \frac{c_1}{A_{1g}}\right)p_{32} \quad 0 \quad 1 \quad 0 \quad 0$$

$$\text{First row (III)} = \left(1 - \frac{c_1}{A_{1g}}\right)p_{43} \quad 0 \quad 0 \quad 1 \quad 0$$

$$\text{First row (IV)} = \left(1 - \frac{c_1}{A_{1g}}\right)p_{54} \quad 0 \quad 0 \quad 0 \quad 1$$

Lippincott and Dayhoff[7] further consider heteronuclear bonds in polyatomic molecules as pseudohomonuclear and treat them by the same method as were similar bonds in diatomics. Thus the determinantal eq. 32 and 33 are changed so that

$$\left(1 - \frac{c_1}{A_{1g}}\right)\left(1 - \frac{c_2}{A_{2g}}\right) = \left(1 - \frac{c_{12}}{A_{12g}}\right)^2 \quad (36)$$

where A_{12} is the geometrical mean of A_1 and A_2. This approximation does not contribute significantly to the polarizability calculations since the term involving the δ-function strengths is very small.

The δ-Function Model Applied to Molecular Polarizabilities

Since

$$\alpha_m = {}^1/_3(\alpha_1 + \alpha_2 + \alpha_3) \quad (37)$$

where α_1, α_2, and α_3 refer to the three principal polarizability components, one must have a method of generating component polarizabilities in order to compute molecular (average) polarizabilities. It is necessary to build the molecular values from a consideration of the bond and atomic polarizabilities and to determine some summation rules. In this section we will discuss the calculation of parallel bond components from the molecular δ-function model, the generation of bond perpendicular components from atomic δ-function polarizabilities, corrections to the parallel component due to nonbond-region electrons, polarity corrections to both the parallel and perpendicular components, and the method by which these bond components are summed to give the average molecular polarizability.

General Approach. Hirschfelder, Curtiss, and Bird[10a] discuss a variational treatment first introduced by Hylleraas[10b] and Hasse.[3a] We use this method here with the perturbing potential H_1 taken as

$$H_1 = -\sqrt{Ag}\mathcal{E}_x\left[-\sum_{i=1}^{n} x_i + \sum_{\alpha=1}^{v} Z_\alpha X_\alpha\right] \quad (38)$$

If there are n equivalence classes of electrons, the equivalence being based on identical radial wave functions, x_i is the coordinate of any one of the electrons which falls in the ith equivalence class. In eq. 38 A is the reduced electronegativity (REN) (in atomic units) of the nucleus (if it is an *atom* which is perturbed) or the root mean square of the reduced electronegativities of the two nuclei involved in a bond (if it is a *bond* which is perturbed), g is the unit δ-function strength, $\mathcal{E}_x$ is the electric field component in the x direction, i is the electron equivalence class index, and α is the nuclear index. One must use Ag in this equation rather than e because of the fact that in the model used the equivalent of Ag is e^2. Thus an equation for α_{xx} is generated

$$a_{xx} = \frac{4nA}{a_0}\left[\overline{(x_1 - \bar{x})^2} - (n-1)\overline{(x_1 - \bar{x}_1)(x_2 - \bar{x}_2)}\right]^2 \quad (39)$$

where x_1 is the coordinate of any electron in the first equivalence class and $\bar{x}$ is the average coordinate of any one of these electrons. It is to be noted that $\overline{(x_1 - \bar{x}_1)(x_2 - \bar{x}_2)} = 0$ since the δ-function wave functions allow no interaction between coordinates. The model with the mean δ-function strengths predicts $\bar{x} = 0$ so that eq. 39 becomes

$$a_{xx} = \frac{4nA}{a_0}\left[\overline{x_1^2}\right]^2 \quad (40)$$

or equivalently

$$\alpha_{xx} = \frac{4A}{a_0}\sum\left[\overline{x_i^2}\right]^2 \quad (41)$$

where n is the number of equivalence classes. For instance, if there are four electrons in the bond region, two forming a π-bond, and two forming a σ-bond, there are two equivalence classes of electrons and $n = 2$. The implied assumption is that there will be as

(10) (a) J. O. Hirschfelder, C. F. Curtiss, and R. B. Bird, "Molecular Theory of Gases and Liquids," John Wiley and Sons, Inc., New York, N. Y., 1954; (b) E. Hylleraas, *Z. Physik*, 65, 209 (1930).

much a contribution to the bond component of the polarizability from a σ-bond as there is from a π-bond. This, of course, is only an approximation to the real situation. In the case where no reasonable single structural form can be written for the molecule, n is taken to be the bond order, *e.g.*, in SO_2, n for the S–O bond is $^3/_2$.

For atoms in their ground state, $n = 1$, *i.e.*, all electrons in the valence shell of an atom are considered to have nearly the same charge distribution so that they would all belong to the same equivalence class; the atomic polarizability problem reduces to a one-class-electron problem.

Thus the procedure is to generate values for $\overline{x^2}$ for the system using the δ-function wave functions and the empirical δ-function strength (reduced electronegativities) obtained by Lippincott and Dayhoff.[7] Once this expectation value is obtained, it is used in eq. 40 to obtain the desired polarizability component.

Atomic Polarizabilities. To obtain x^2 values for atoms, we assume the atom is isotropic and that $\overline{x^2} = \overline{y^2} = \overline{z^2} = \overline{r^2}/3$; we calculate $\overline{r^2}$ using the δ-function located at the nucleus. Thus in polar coordinates[11]

$$\psi = Ne^{-Ar} \tag{42}$$

Normalization gives

$$N = A^{3/2}\Pi^{-1/2} \tag{43}$$

Further, the expectation value of r^2 is

$$\overline{r^2} = \int_0^{\pi}\int_0^{2\pi}\int_0^{\infty} \Psi r^2 \Psi r^2 \sin\theta \, d\theta d\phi dr = 3/A^2 \tag{44}$$

thus

$$\overline{x^2} = 1/A^2 \tag{45}$$

Solution of the Hamiltonian for negative E gives

$$-^1/_2 \frac{\partial^2\Psi}{\partial r^2} = -\frac{A^2}{2}\Psi = E\Psi \tag{46}$$

Thus $A = \sqrt{-2E}$ is the same δ-function strength of the atom obtained either from the first ionization potential or from the REN values given in Table I. Finally, the polarizability along the x-axis of an atom is

$$\alpha_{xx} = \frac{4}{a_0{}^3A^3} \tag{47}$$

Table II is a compilation in periodic chart form of atomic polarizabilities calculated from eq. 47. Many experimental values have been calculated from homonuclear molecules on the basis that there are no bond components, *e.g.*, the average polarizability of the chlorine molecule α_{Cl_2} is given in Batsanov's[12a] text as

Table I: Reduced Electronegativities[a,b]

	IA	IIA	IIIA	IVA	VA	VIA	VIIA	VIII
1	H 1.00							He
2	Li 0.439	Be 0.538	B 0.758	C 0.846	N 0.927	O 1.00	F 1.065	Ne
3	Na 0.358	Mg 0.414	Al 0.533	Si 0.583	P 0.630	S 0.688	Cl 0.753	Ar
4	K 0.302	Ca 0.327	Ga 0.472	Ge 0.536	As 0.564	Se 0.617	Br 0.633	Kr
5	Rb 0.286	Sr 0.319	In 0.422	Sn 0.483	Sb 0.496	Te 0.538	I 0.584	Xe
6	Cs 0.255	Ba 0.289	Tl 0.326	Pb 0.352	Bi 0.365	Po 0.399	At 0.421	Rn
7	Fr	Ra						

[a] In a.u. [b] The REN values tabulated here are the A values of ref. 6 in the text.

twice the average polarizability of the chlorine atom α_{Cl}. As Denbigh[12b] points out, perfect additivity could only occur if all the atoms in the molecule were entirely without effect on each other, so that no bonds were formed. Thus, it is inaccurate to assume that atomic polarizabilities sum up to equal the molecular polarizability, and it is likewise inaccurate to assume the molecular polarizability could be broken down into only atomic components.

A diatomic molecule has an axis of symmetry so that

$$\alpha_M = ^1/_3(\alpha_{||} + 2\alpha_{\perp}) \tag{48}$$

where $\alpha_{||}$ is the polarizability along the bond and $\alpha_{\perp}$ is the polarizability perpendicular to the bond. Denbigh[12b,13] calculates these components knowing two of the three experimental quantities, the Kerr constant, the refractive index, and the depolarization ratio. One finds that the perpendicular components which he obtains are qualitatively equal to the sum of the respective atomic polarizabilities calculated from eq. 47.

Whenever possible therefore, we have taken the perpendicular components of Denbigh to obtain experimental values with which to compare our atomic polarizabilities (see Table III). The rationale behind

(11) The wave function corresponding to a one-dimensional model in Cartesian coordinates, $\psi = Ne^{-c(|x|+|y|+|z|)}$, would not give the spherical distribution which is expected.

(12) (a) S. S. Batsonov, "Refractometry and Chemical Structure," translated by P. P. Sutton, Consultants Bureau, New York, N. Y., 1961; (b) K. G. Denbigh, *Trans. Faraday Soc.*, **36**, 936 (1940).

(13) B. C. Vickery and K. G. Denbigh, *ibid.*, **44**, 61 (1948).

Table II: Atomic Polarizabilities[a] Calculated from the δ-Function Model

	I		II		III		IV		V		VI		VII	VIII
1	H	5.92												He
2	Li	69.93	Be	38.02	B	13.58	C	9.78	N	7.43	O	5.92	F	4.90	Ne
3	Na	128.84	Mg	83.70	Al	39.18	Si	29.88	P	23.67	S	18.20	Cl	13.88	Ar
4	K	215.93	Ca	154.76	Ga	56.35	Ge	38.48	As	33.02	Se	25.24	Br	19.41	Kr
5	Rb	252.39	Sr	182.42	In	78.67	Sn	52.56	Sb	48.64	Te	38.02	I	29.72	Xe
6	Cs	357.17	Ba	245.84	Tl	171.18	Pb	136.09	Bi	121.75	Po	93.34	At	79.28	Rn
7	Fr		Ra												

[a] $\times 10^{25}$ cm.^{3}.

this approach is that, although there is a change in the shape of the individual electron distribution, the change in the electron density perpendicular to the bond is, in general, small, except in the cases where highly polar bonds are formed.

Polarizabilities of Diatomic Molecules

The x-axis for a diatomic molecule is taken to be the internuclear axis with the zero point at the center of the electronic charge distribution. Thus for a homonuclear diatomic molecule, $\bar{x} = 0$. We have separated the parallel component of a diatomic molecule into two parts: (1) the contribution made by the electrons in the bond region ($\alpha_{\parallel b}$), and (2) the contribution made by the electrons not in the bond region ($\alpha_{\parallel n}$). The former is obtained from the molecular δ-function wave function with the number of equivalence classes being taken as the bond order. For the latter contribution, the molecular electronic configuration is assumed to be the most stable configuration from the Linnett[14] tetrahedral orbital model.

Bond-Region Parallel Component. To obtain $\alpha_{\parallel b}$ we recall the δ-function bonding wave function for a homonuclear one-electron diatomic

$$\Psi = N\left[e^{-c|x + a/2|} + e^{-c|x - a/2|}\right] \qquad (49)$$

where A is the δ-function separation, and c is the one-electron a-dependent δ-function strength, $c = Ag(1 + e^{-ca})$. The normalization condition yields the expression for N

$$N = \left[\frac{2}{c}(1 + e^{-ca} + ace^{-ca})\right]^{-1/2}$$

Since $\bar{x} = 0$ for the homonuclear diatomic, the expression for the polarizability becomes, as in the case of atoms

$$\alpha_{zz} = \frac{4nA}{a_0}[\overline{x^2}]^2 \qquad (50)$$

or

$$\alpha_{zz} = \frac{4A}{a_0}\sum[\overline{x_i^2}]^2 \qquad (51)$$

where A is the δ-function strength of one of the atoms. Consider the three regions

$$\text{I} \quad -\infty \leq x \leq -\frac{a}{2}$$

$$\text{II} \quad -\frac{a}{2} \leq x \leq \frac{a}{2}$$

$$\text{III} \quad \frac{a}{2} \leq x \leq \infty$$

Then

$$\overline{x^2} = \langle x^2\rangle_{\text{I}} + \langle x^2\rangle_{\text{II}} + \langle x^2\rangle_{\text{III}} \qquad (52)$$

where

$$\langle x^2\rangle_{\text{I}} = \int_{-\infty}^{-\frac{a}{2}} \Psi_{\text{I}}^2 x^2\,dx = N^2\left[\frac{a^2}{8c} + \frac{a}{4c^2} + \frac{1}{4c^3}\right] \times (1 + e^{-ac})^2 \qquad (53)$$

$$\langle x^2\rangle_{\text{II}} = \int_{-\frac{a}{2}}^{\frac{a}{2}} \Psi_{\text{II}}^2 x^2\,dx = N^2\left[\frac{a^2}{4c}(1 - e^{-2ca}) - \frac{1}{2c^2}([ac + 1]e^{-2ca} + [ac - 1]) + \frac{a^3e^{-ca}}{6}\right] \qquad (54)$$

and

$$\langle x^2\rangle_{\text{III}} = \int_{+\frac{a}{2}}^{\infty} \Psi_{\text{III}}^2 x^2\,dx = N^2\left[\frac{a^2}{8c} + \frac{a}{4c^2} + \frac{1}{4c^3}\right] \times (e^{-ca} + 1)^2 \qquad (55)$$

For $\overline{x^2}$ we have on simplification

$$\overline{x^2} = \frac{a^2}{4} + \frac{1}{2c^2} - \frac{a^3ce^{-ac}}{6(1 + [ac + 1]e^{-ac})} \qquad (56)$$

(14) J. W. Linnett, *J. Am. Chem. Soc.*, **83**, 2643 (1961).

If the δ-function spacing, a, is allowed to equal R, the internuclear separation, eq. 56 becomes

$$\overline{x^2} = \frac{R^2}{4} + \frac{1}{2c^2} - \frac{R^3 c e^{-cR}}{6(1 + [Rc + 1]e^{-cR})} \quad (57)$$

It should be noted that the $R^2/4$ term gives the major contribution to $\overline{x^2}$. The last term is generally very small compared to the other terms and can therefore usually be neglected.

One of the significant features of eq. 57 is that it demonstrates an explicit dependence of $\overline{x^2}$ on R^2. The REN value corresponding to A in eq. 47 and 50 is also a function of the equilibrium bond length, R_e, with A being proportional to R_e^{-1}.[15] Substitution[7] of $1.1/R_e$ into eq. 57 indicates that $\alpha_\parallel$ is roughly proportional to R_e^3. Similar considerations apply to $\alpha_\perp$ with the result that α_{mean} is proportional to R_e^3. This result is in agreement with the work of Clark[16a] and Goss,[16b] who found a linear empirical relationship between the mean polarizability and R_e^3. Equation 57 is quite useful in that it is applicable to general molecular systems and approximates to an unusually simple form for $\alpha_\parallel$ as a function of equilibrium internuclear distance, R_e.

For diatomics with two electrons in the bond region c can no longer be taken as $c = Ag(1 + e^{-ca})$. The two-electron problem, however, can be approximated by an equivalent one-electron pair problem by defining a resultant c value

$$c^2 = c_1^2 + c_2^2 \quad (58)$$

and if the molecule is homonuclear

$$c = c_1\sqrt{2} \quad (59)$$

The resultant c values are taken the same as those in the Lippincott–Dayhoff[7] investigation of bond energies.

For the general electron pair problem in which polyelectronic atoms are involved, one can obtain resultant c's from the expression

$$c = (nN)^{1/2}A \quad (60)$$

where n is the principal quantum number of the valence shell, N is two times the column number in the periodic table, and A is the individual electron δ-function strength; c in reality is a slowly changing function of R, but it is taken nevertheless to be a constant for the purposes of calculating the α_b component of the polarizability. Thus if the diatomic molecule is homonuclear, the second term in eq. 57 is $1/2c^2$. For the heteronuclear case, a mean reduced δ-function strength is obtained

$$c_{mn} = \sqrt{c_m c_n} \quad (61)$$

such that the second term in eq. 57 is $1/2c_m c_n$. It is to be noted that this approximation was good enough to permit Lippincott and Dayhoff[7] to predict ω_e's, $\omega_e x_e$'s, r_e's, and D_e's of heteronuclear species which involved relatively small errors, considering the simplicity of the model. In the case of $\overline{x^2}$, one finds that in general $1/2c^2$ is negligible with respect to $R^2/4$, and that the approximation does not alter significantly the major contribution to the parallel component.

The third term in eq. 57 is two to three orders of magnitude smaller than the second term and has a negligible effect on $\overline{x^2}$. This term has been dropped from our calculations, whereas the second term has been retained for the sake of precision.

Substitution of the value obtained for $\overline{x^2}$ from eq. 57 into eq. 50 gives the value of the polarizability component along the bond axis direction. In most cases bond components are within a reasonable range of the "observed" values. However, in cases involving polar molecules, a correction was found to be necessary.

Example 1. Sample calculation of $\alpha_{\parallel b}$ parallel component of the polarizability of the oxygen molecule.

$$R_e = 1.207 \times 10^{-8} \text{ cm.}$$

$$A = 1.00 \text{ a.u.}$$

$$c_R = (2 \times 10)^{1/2} \times 1.89 \times 10^8 = 9.25 \times 10^8 \text{ cm.}^{-1}$$

$$\overline{x^2} = \frac{R^2}{4} + \frac{1}{2c_R^2} = 0.3703 \times 10^{-16} \text{ cm.}^2$$

$$\alpha_{\parallel} = \frac{4nA}{a_0}[\overline{x^2}]^2 = 20.73 \times 10^{-25} \text{ cm.}^3$$

In Table IV is found a representative sample of bond (parallel) components of the polarizability of diatomic molecules, together with the derived values obtained from Denbigh's[12b,13] comprehensive work.

Nonbond-Region Parallel Component

We note particularly from Table V for those bonds which contain electrons not in the bond region from the Linnett[14] picture (with the exception of H_2) the calculated values are smaller than the derived values. This implies that there is an additional contribution to the parallel component due to the presence of these electrons. For instance, in the example of O_2, Fig. 3 shows the most stable Linnett[14] electronic configuration. The "dots" represent electrons with spins

(15) AR was found to be nearly constant at 1.1. This generates an equivalent expression for α_{zz}: $\alpha_{zz} = 4.4/R[\overline{x^2}]^2$.

(16) (a) C. H. D. Clark, *Proc. Leeds Phil. Lit. Soc. Sci. Sect.*, **3**, 208 (1936); (b) F. R. Goss, *ibid.*, **3**, 23 (1936).

Table III: Comparison of Calculated Atomic Polarizabilities with Experimental Values Obtained from Denbigh's[a] Perpendicular Components[b]

	$\alpha_{at(calcd)}$	$\alpha_{at(derived)}$
H	5.92	4.45
N	7.43	7.15
O	5.92	5.95
C	9.78	10.35
Cl	13.88	18.1
Br	19.41	28.7

[a] See ref. 11 in text. [b] $\times 10^{25}$ cm.^{3}.

Table IV: Calculated and Derived Parallel Polarizability Components[a] of Diatomic Molecules

	$\alpha_{\parallel(calcd)}$	$\alpha_{\parallel(exptl)}$[b]
H_2	3.26	6.8
O_2	22.13	24.3
N_2	21.62	24.3
Cl_2	58.17	66.0
CO	22.22	26.0
HCl	11.76	31.3
HBr	16.13	42.3
HI	25.65	65.8

[a] $\times 10^{25}$ cm.^{3}. [b] See ref. 11 in text.

Table V: Contributions to the Bond Parallel Polarizability Component[a] of Selected Diatomic Molecules[b]

	$\alpha_{\parallel b}$	$\alpha_{\parallel n}$	$\alpha_{\parallel(calcd)}$	$\alpha_{\parallel(exptl)}$[c]
H_2	3.26	0.0	3.26	6.8
O_2	22.13	7.89	30.02	24.3
N_2	20.22	5.95	26.17	24.3
Cl_2	58.17	23.79	81.96	66.0
CO	22.22	6.86	29.08	26.0
HCl	11.76	11.89	23.65	31.3
HBr	16.13	16.64	32.77	42.3
HI	25.65	25.47	51.12	65.8

[a] $\times 10^{25}$ cm.^{3}. [b] $\alpha_{\parallel b}$ and $\alpha_{\parallel n}$ are the bond-region and nonbond-region contributions, respectively. [c] See ref. 11 in text.

of $+1/2$ and the "crosses," electrons with spins of $-1/2$. Originally we had considered the parallel component of the polarizability to be produced entirely by two pairs of electrons in the bond region. However, there certainly must be a residual polarizability of the two oxygen atoms along the internuclear axis, and this additional component is expected to be independent of bond length. Therefore we assume the additional term can be obtained from the atomic polarizability,

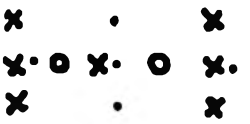

Figure 3. Oxygen electronic configuration using Linnett's model.

weighted such that electrons involved in bond formation are not included in this term since they were included in $\alpha_{\parallel b}$. Thus, to the parallel component, $\alpha_{\parallel b}$, already calculated, $4/3$ of an oxygen atomic polarizability should be added to give the complete parallel component.

$$\alpha_{\parallel} = \alpha_{\parallel b} + \alpha_{\parallel n} = \alpha_{\parallel b} + 4/3\alpha_{(0)} \qquad (62)$$

where

$$\alpha_{\parallel n} = \Sigma f_j \alpha_j \qquad (63)$$

f_j is the fraction of the electrons of the jth atom which are not in the bond region, and α_j is the atomic polarizability of the jth atom. In the case of Cl_2, $12/7$ of a chlorine atomic polarizability would then be included with its bond parallel component to produce the total molecular parallel component. Thus, if an atom is not sharing all of its valence electrons when bonding, one must account for an additional parallel component due to the nonbond-region valence electrons and this is done by adding to the bond parallel component the fractional part of the atomic polarizability which remains. An alternative method for including the nonbond parallel component would be to use in eq. 57 individual electron pair c's rather than resultant c's as defined in eq. 60.

In Table V are listed values of the total parallel bond components for several species, together with parallel components without the nonbonded valence electron correction, and the derived parallel component values of Denbigh.[12b]

Perpendicular Component. As remarked previously, the perpendicular component of a diatomic molecule cannot be obtained rigorously by this one-dimensional model. However, we may approximate the situation: assume that the electronic shape of an atom viewed from a point on a line perpendicular to the internuclear axis and passing through the nucleus approximates that of the nonbonded atom (Fig. 4). Then the perpendicular component of a diatomic molecule AB may be written as

$$\alpha_{\perp} = \alpha_A + \alpha_B \qquad (64)$$

where α_A and α_B are atomic polarizabilities calculated from the atomic δ-function strengths of atoms A and B, respectively. It will be recalled that using this rule

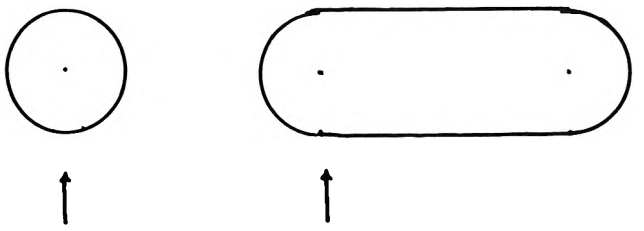

Figure 4. Assumed relationship between bond perpendicular and atomic polarizabilities.

Table III was constructed to compare atomic polarizabilities calculated from the atomic δ-function model with those obtained from perpendicular components derived by Denbigh.[12b]

Sample Calculation. For the O_2 molecule, $A = 1.0$ a.u.

$$\alpha_\perp = 2\alpha_{(0)} = \frac{8a_0^3}{A^3(\text{a.u.})} = 11.84 \times 10^{-25} \text{ cm.}^3$$

Average Polarizability of a Diatomic Molecule. In the preceding sections the methods of calculating the parallel and perpendicular polarizability components of a diatomic molecule from the δ-function model are given. In order to obtain the average molecular polarizability, one needs merely to substitute these calculated values into

$$\alpha_M = {}^1/_3(\alpha_\parallel + 2\alpha_\perp) \qquad (65)$$

The calculated and experimental values of the average polarizabilities of several diatomic molecules are listed in Table VI together with the corresponding parallel and perpendicular components.

Consider the polar diatomic system AB, where atom A is less electronegative than atom B (see Fig. 5). A reasonable assumption is that the average magnitude of the bond perpendicular component is a function of the charge separation. Thus, instead of weighting atomic contributions equally as was done in eq. 64, the atomic contributions should be weighted according to the square of their respective electronegativities, *i.e.*

$$\alpha_\perp = \frac{1}{X_A^2 + X_B^2}(X_A^2\alpha_A + X_B^2\alpha_B) \qquad (66)$$

This gives a greater contribution to the bond perpendicular component for the atom which possesses in its vicinity the larger charge distribution.

The parallel bond component also must be corrected to allow for a charge density not in the bond region by virtue of the polarity induced by the electronegativity difference of the atoms. Pauling[17] defines the degree of polarity, ρ, as

$$\rho = 1 - \exp\left[-\frac{(X_A - X_B)^2}{4}\right] \qquad (67)$$

The charge density in the bond region, then should be related to the per cent covalent character, σ

$$\sigma = \exp\left[-\frac{(X_A - X_B)^2}{4}\right] \qquad (68)$$

The correction which we make to the parallel component is to multiply the bond parallel component (as obtained from the molecular δ-function model) by σ, the degree of covalency, *i.e.*

$$\alpha_{\parallel_t} = \sigma\alpha_{\parallel_b} \qquad (69)$$

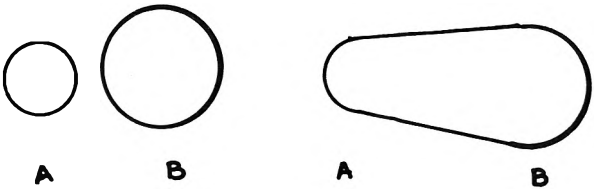

Figure 5. Polarizability ellipsoid for a polar bond.

Table VI: Average Polarizabilities[a] of Selected Diatomic Molecules (No Corrections)

	$\alpha_{M(calcd)}$	$\alpha_{M(obsd)}$	Ref.
H_2	8.98	7.9	*b*
O_2	17.90	16.0	*b*
N_2	19.10	17.6	*b*
Cl_2	45.83	46.10	*b*
Br_2	67.55	64.3	*b*
CO	20.17	19.5	*c*
NO	18.29	16.95	*d*
HF	9.97	8.0	*c*
HCl	20.11	26.3	*c*
HBr	28.43	36.1	*c*
HI	40.80	54.4	*c*
Li_2	135.89	(100)[e]	*f*
Na_2	230.44	(181)	*f*
K_2	411.54	(344)	*f*
Rb_2	449.19	(421)	*f*
Cs_2	632.51	(522)	*f*

[a] $\times 10^{25}$ cm.^{3}. [b] K. G. Denbigh, *Trans. Faraday Soc.*, **36**, 936 (1940). [c] J. O. Hirschfelder, C. F. Curtiss, and R. B. Bird, "Molecular Theory of Gases and Liquids," John Wiley and Sons, Inc., New York, N. Y., 1954. [d] E. A. Moelwyn-Hughes, "Physical Chemistry," Pergamon Press, New York, N. Y., 1957. [e] Parentheses indicate that the value derived from experimental data is uncertain. [f] S. S. Batsonov, "Refractometry and Chemical Structure," translated by P. P. Sutton, Consultants Bureau, New York, N. Y., 1961.

(17) L. Pauling, "The Nature of the Chemical Bond," 3rd Ed., Cornell University Press, New York, N. Y., 1960.

$$\alpha_{\parallel} = \alpha_{\parallel_p} + \alpha_{\parallel_n} \quad (70)$$

it is to be noted that $\alpha_{\parallel_p}$ is the parallel bond component before adding the nonbond-region electron contribution.

The average diatomic molecular polarizability is then obtained from eq. 65. Table VII compares values of $\alpha_{\parallel}$, $\alpha_{\perp}$, and α_M calculated from eq. 70, 66, and 65, respectively, with experimentally determined values. With respect to the polarity correction for multiply bonded systems, it seems unreasonable to assume that all the electrons in the bond region should be influenced to the same extent. Thus, the polarity correction when applied to multiply bonded systems probably gives too large a correction.

Table VII: Component and Average Polarizabilities[a] of Selected Diatomic Molecules (with Corrections)[b]

	Calculated			Observed[c]		
	$\alpha_{\parallel_p} + \alpha_{\parallel_n}$	$\alpha_{\perp}$	α_M	$\alpha_{\parallel}$	$\alpha_{\perp}$	α_M
CO	24.19	14.45	17.70	26.0	16.2	19.5
NO	26.93	13.12	17.72	...	...	16.95
HF	6.68	10.41	9.17	...	...	8.0
HCl	23.18	20.93	21.68	31.3	23.9	26.3
HBr	32.61	26.33	28.43	42.3	33.2	36.1
HI	51.12	35.14	40.49	65.8	48.9	54.4

[a] $\times 10^{25}$ cm.^{3}. [b] $\alpha_{\parallel_p}$ is the contribution from the bond region electrons multiplied by the per cent covalency; $\alpha_{\parallel_n}$ is the contribution from the nonbond-region electrons. [c] See ref. 11 in text.

Further, it will appear throughout this investigation that values for molecules of the heavier halogens are in error to a larger extent than those of most other elements. It is possible that this occurs because the values of the corresponding reduced electronegativities of these elements are in error to a limited extent.

Polyatomic Molecules

The construction of the δ-function atomic-orbital molecular wave function so that each has $2n$ branches per atom involved in n bonds results in a separate secular determinant for each bond in the molecule. Thus the model implies that each bond can be treated as if it were a separate coordinate and that the molecular wave function for an n-bond polyatomic may be divided up into n-bond wave functions which are identical to diatomic wave functions. Therefore, the method to obtain bond parallel components of the polarizability of polyatomics is the same as that of diatomics with the exception that the bond parallel components of polyatomics do not necessarily correspond to any symmetry axis of the molecule.

Thus, to obtain the molecular α_{xx}, α_{yy}, and α_{z^2} components, consider a molecule to be made up of n bonds. Let the angle between the ith bond and the z-axis be θ_i and the angle between the projection of the ith bond on the xy plane and the x axis to be ϕ_i where the x, y, and z coordinates are referred to some arbitrary molecular axis. Then α_{xx}, α_{yy}, and α_{zz} for the molecule are

$$\alpha_{xx} = \sum_i [(\alpha_{\parallel_i} \sin^2\theta_i + \alpha_{\perp} \cos^2\theta_i) \cos^2\phi_i + \alpha_{\perp_i} \sin^2\phi_i] \quad (71)$$

$$\alpha_{yy} = \sum_i [(\alpha_{\parallel_i} \sin^2\theta_i + \alpha_{\perp} \cos^2\theta_i) \sin^2\phi_i + \alpha_{\perp_i} \cos^2\phi_i] \quad (72)$$

$$\alpha_{zz} = \sum_i [\alpha_{\parallel_i} \cos^2\theta_i + \alpha_{\perp_i} \sin^2\theta_i] \quad (73)$$

where $\alpha_{\parallel_i}$ and $\alpha_{\perp_i}$ are the bond parallel and perpendicular components of the ith bond, and the internuclear axis is considered the major axis. The average molecular polarizability is

$$\alpha_M = {}^1/_3(\alpha_{xx} + \alpha_{yy} + \alpha_{zz}) \quad (74)$$

or, after incorporating (71), (72), and (73) into (74)

$$\alpha_M = {}^1/_3\left[\sum_i \alpha_{\parallel_i} + \sum_i 2\alpha_{\perp_i}\right] \quad (75)$$

which indicates that the average molecular polarizability, α_M, is independent of bond angles and can be obtained easily if the individual bond parallel and perpendicular components for the particular molecule are known.

Clearly, $\sum_i \alpha_{\parallel_i}$ can be obtained at once knowing the internuclear distance and the mean resultant δ-function strength for each bond. The nonbond-region electron polarizability $\alpha_{\parallel_n}$, is added to the parallel component sum as in the diatomic situation. One must be careful, however, to allow a given set of nonbond-region electrons to contribute to the parallel component of only one bond. The problem of obtaining the average polarizabilities reduces to finding the sum of the perpendicular components, $\sum_i 2\alpha_{\perp_i}$. A reasonable treatment of this problem is to use the atomic polarizabilities obtained from the atomic δ-function model and the following approach.

Consider, for convenience, a triatomic system with the atoms in a nonbonded triangular arrangement (Fig. 6). Each atom in this system has three degrees of "polarizability" freedom. Further, the average polarizability for this system will be

$$\alpha_M = {}^1/_3(3\alpha_A + 3\alpha_B + 3\alpha_C) = \alpha_A + \alpha_B + \alpha_C \quad (76)$$

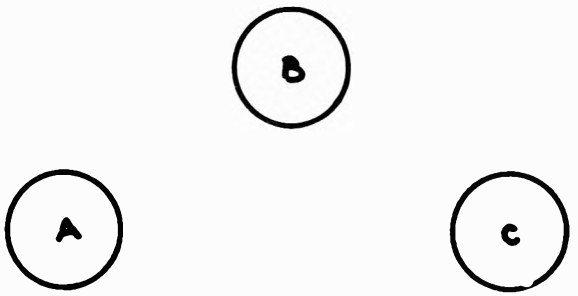

Figure 6. Nonbonded triatomic system.

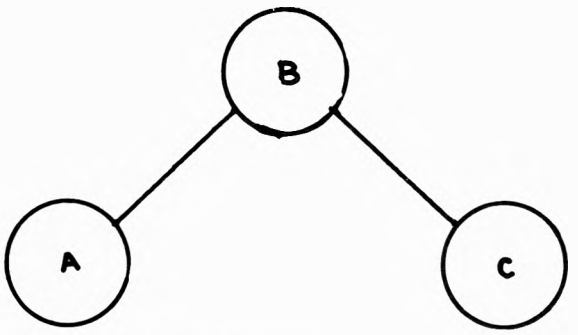

Figure 7. Bonded triatomic system.

Consider, now, the same system but with bonds between A and B and between B and C (Fig. 7). It is seen that one degree of atomic "polarizability" freedom is taken up per bond per atom, *i.e.*, α_{AB} in Fig. 7 replaces one α_A and one α_B in Fig. 6; thus

$$\alpha_M = {}^1/_3(\alpha_{AB} + \alpha_{BC} + \alpha_B + 2\alpha_A + 2\alpha_C) \quad (77)$$

or

$$\alpha_M = {}^1/_3\left(\alpha_{AB} + \alpha_{BC} + \sum_i 2\alpha_{\perp,i}\right) \quad (78)$$

where the first attempt at $\sum_i 2\alpha_{\perp,i}$ is written as

$$\sum_i 2\alpha_{\perp,i} = \sum_j (3 - n_j)\alpha_j \quad (79)$$

where n_j is the number of bonds in which the jth atom is involved.

For methane this term would be

$$\Sigma 2\alpha_{\perp,i} = 8\alpha_H - \alpha_C$$

Equation 79 thus appears to weight very heavily exterior atoms of a molecule, giving a negative contribution to central atoms. This is probably not the case.

An alternative approach is to weight the atomic contributions over the total remaining atomic degrees of freedom, *e.g.*, for the molecule ABC

$$\sum_i 2\alpha_{\perp,i} = 3\left[\frac{\alpha_A + \alpha_B + \alpha_C}{3}\right] \quad (80)$$

and for methane

$$\sum_i 2\alpha_{\perp} = 7\left[\frac{\alpha_C + 4\alpha_H}{5}\right]$$

Thus a general equation for $\Sigma 2\alpha_{\perp,i}$ is obtained which weights both internal and external atoms the same

$$\sum_i 2\alpha_{\perp,i} = \frac{3N - 2n_b}{N} \sum_j \alpha_j \quad (81)$$

where N is the number of atoms in the molecule, n_b is the number of bonds, and α_j is the atomic polarizability of the jth atom calculated from the atomic δ-function model.

Table VIII shows $\sum_i 2\alpha_{\perp,i}$ for a series of molecular systems calculated from eq. 81, together with $\alpha_{\parallel,i}$, α_M (calcd.), and the corresponding experimentally determined α_M. The agreement for nonpolar molecules is quite satisfactory. However, it is to be noted that in general the deviation of the calculated values from experimental values is greater for polar molecules. Thus a polarity correction is probably necessary if this molecular polarizability treatment is to be useful for a wide range of molecular systems.

Polarity Corrections. The sum $\Sigma\ 2\alpha_{\perp,i}$ of the perpendicular components in the previous section was calculated in such a way as to weight all atomic polarizabilities equally. However, where bond electron density asymmetry is believed to exist, the perpendicular component should contain a greater contribution from the atom which would tend to have the larger portion of electron density in its vicinity. This is easily done by weighting the atomic contributions to the total perpendicular component according to the square of the electronegativity of the element. Thus eq. 81 must be replaced by

$$\sum_i 2\alpha_{\perp,i} = (3N - 2n_b)\frac{\Sigma X_j^2\alpha_j}{\Sigma X_j^2} \quad (82)$$

where X_j is the electronegativity of the jth atom. The form of the functional dependence on electronegativity which we have chosen is partially justified by the fact that the accepted definition of polarity relates to the square of the electronegativities.[17] A polarity correction is similarly made to the individual bond parallel components before incorporating the nonbonded valence electron correction and before summing up to obtain $\alpha_{\perp}$. Just as in the diatomic situation, use is made of Pauling's definition of the per cent ionic character[17]

$$\rho = 1 - \exp\left[-\frac{(X_A - X_B)^2}{4}\right] \qquad (83)$$

Table VIII: Polarizabilities (No Polarity Corrections)[a]

Molecule	$\Sigma 2\alpha_\perp$	$\Sigma\alpha_{\parallel b_i}$	$\Sigma f_j\alpha_j$	$\alpha_{M(calcd)}$	$\alpha_{M(obsd)}$	Ref.
			Carbon compounds			
C(graphite)	0	34.19	0	11.39	11.06	*b*
C_2H_2	62.80	39.41	0	34.07	33.30	*c*
C_2H_4	72.07	54.36	0	42.14	42.60	*c*
C_2H_6	68.85	67.94	0	45.60	44.70	*c*
C_6H_6	141.30	187.59	0	109.63	103.20	*c*
HCN	46.26	29.88	2.97	26.37	25.90	*c*
C_3H_8	90.67	104.05	0	64.90	62.9	*c*
n-C_6H_{14}	155.71	218.67	0	124.79	115.68	*d*
CH_3OH	52.51	47.84	3.95	34.77	32.3	*c*
Dioxane	98.32	177.97	7.89	94.73	84.08	*d*
CH_3Cl	57.98	61.47	11.90	43.79	45.60	*c*
CH_2Cl_2	69.13	89.77	23.79	60.90	64.80	*c*
$CHCl_3$	80.27	119.65	35.68	78.53	82.30	*c*
			Polyatomic hydrides			
CH_4	46.84	28.05	0	24.96	26.0	*c*
NH_3	37.79	16.41	2.97	19.06	21.45	*d*
OH_2	29.60	8.99	3.94	14.18	14.44	*d*
SiH_4	74.99	77.74	0	50.91	43.39	*b*
GeH_4	87.03	83.89	0	56.97	49.66	*b*
SH_2	50.08	27.08	14.62	30.59	36.40	*d*
SeH_2	61.80	40.39	16.83	39.67	45.73	*b*
			Molecules with polar bonds			
BF_3	49.49	38.01	12.60	33.37	23.82	*b*
CF_4	41.13	56.97	16.80	38.24	28.57	*b*
SiF_4	69.27	86.24	16.80	57.44	33.01	*b*
GeF_4	81.31	112.91	16.80	70.34	36.46	*b*
PF_5	64.22	111.49	21.00	65.57	36.46	*b*
SF_6	61.20	146.57	25.20	77.66	44.78	*b*
SeF_6	70.25	181.73	25.20	92.39	52.47	*b*
TeF_6	86.68	238.84	25.20	116.91	58.73	*b*
$HgCl_2$	294.74	134.33	23.79	150.95	90.67	*b*
BCl_3	96.63	102.08	35.68	78.13	80.05	*b*
CCl_4	91.41	149.90	47.58	96.30	102.56	*b*
$SiCl_4$	119.55	208.58	47.58	125.24	111.76	*b*
$TiCl_4$	194.63	243.90	47.58	162.03	141.00	*b*
$GeCl_4$	131.60	228.57	47.58	135.92	121.23	*b*
$SnCl_4$	151.31	323.49	47.58	174.13	137.08	*b*
$SbCl_5$	157.39	453.29	59.48	223.38	156.78	*b*
$HgBr_2$	316.86	152.67	33.27	167.60	115.96	*b*
BBr_3	125.69	123.08	49.91	99.56	114.13	*b*
$SiBr_4$	150.53	255.37	66.55	157.48	156.14	*b*
$SnBr_4$	182.28	375.01	66.55	207.94	189.07	*b*
HgI_2	358.10	192.29	50.95	200.44	164.74	*b*
SnI_4	240.02	492.83	101.90	278.25	277.81	*b*

[a] $\times 10^{25}$ cm.^{3}. [b] S. S. Batsonov, "Refractometry and Chemical Structure," translated by P. P. Sutton, Consultants Bureau, New York, N. Y., 1961. [c] J. O. Hirschfelder, C. F. Curtiss, and R. B. Bird, "Molecular Theory of Gases and Liquids," John Wiley and Sons, Inc., New York, N. Y., 1954. [d] E. A. Moelwyn-Hughes, "Physical Chemistry," Pergamon Press, New York, N. Y., 1961.

and the per cent covalent character

$$\sigma = \exp\left[-\frac{(X_A - X_B)^2}{4}\right] \qquad (84)$$

and the parallel component of the polarizability must be multiplied by this factor (σ) in order to compensate for the lower effective expectation value of x^2, *i.e.*, the electron will be found in a region of x^2-space nearer to the atom with the higher electronegativity. Thus the corrected parallel component is

$$\sum \alpha_{\parallel(\text{corrected})} = \sum_i \sigma_i\alpha_{\parallel_i} + \sum_j f_j\alpha_j \qquad (85)$$

where σ_i is the per cent covalency and $\alpha_{\parallel_i}$ is the bond parallel component of the polarizability of the ith bond. α_j is the atomic polarizability of the jth atom and f_j is the fraction of the electrons of the jth neutral atom which are not involved in bonding according to the Linnett[14] picture. The resulting expression for the average molecular polarizability is

$$\alpha_M = {}^1/_3\left[\sum_i \sigma_i\alpha_{\parallel} + \sum_j f_j\alpha_j + (3N - 2n_b)\frac{\sum_j X_j^2\alpha_j}{\sum_j X_j^2}\right] \qquad (86)$$

where i is the summation index for bonds and j is the summation index for atoms. In calculating α_M for certain molecular systems there is one further point to consider: the term in eq. 86, $(3N - 2n_b)$, which is supposed to give the number of remaining atomic degrees of polarizability freedom. Clearly this number is 7 for methane, 5 for water, etc.; but when linear or planar molecules are considered, the number of degrees of freedom increases. HCN, for example, has two bonds and three atoms and would be predicted to have five atomic "degrees of freedom" remaining. Fig. 8 shows, however, that since the molecule is linear, the carbon atom does not lose a second degree of freedom since the second bond is contained within the same degree of freedom as the first. Similarly, BF_3 is a

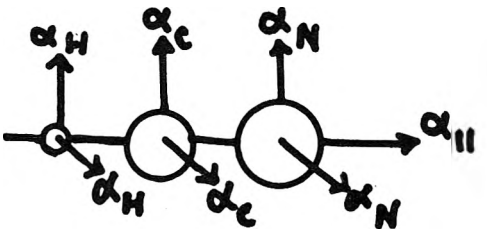

Figure 8. Residual atomic polarizability degrees of freedom for HCN.

Table IX: Polarizabilities[a] (with Polarity Corrections)

Molecule	$\Sigma 2\alpha_{\perp_i}$	$\Sigma\sigma_i\alpha_{\parallel b_i}$	$\Sigma f_j\alpha_j$	n_{df}	$\alpha_{M(calcd)}$	$\alpha_{M(obsd)}$	Ref.
Carbon compounds							
C(graphite)	0	34.19	0	0	11.39	11.06	*b*
C_2H_2	62.20	39.41	0	8	33.87	33.30	*c*
C_2H_4	71.40	54.36	0	10	41.92	42.60	*c*
C_2H_6	68.29	67.94	0	10	45.41	44.70	*c*
C_6H_6	139.94	187.59	0	18	109.18	103.20	*c*
HCN	45.80	28.47	2.97	6	25.75	25.90	*c*
C_3H_8	89.88	103.76	0	13	64.55	62.90	*c*
C_6H_{14}	154.34	218.23	0	36	124.19	115.68	*d*
CH_3OH	51.60	42.45	3.95	8	32.67	32.30	*c*
Dioxane	95.92	161.60	7.89	14	88.47	84.08	*d*
CH_3Cl	60.31	55.12	11.90	7	42.44	45.60	*c*
CH_2Cl_2	72.47	77.53	23.79	7	57.93	64.80	*c*
$CHCl_3$	83.26	101.59	35.68	7	73.51	82.30	*c*
Polyatomic hydrides							
CH_4	46.51	28.05	0	7	24.85	26.00	*c*
NH_3	38.30	15.75	2.97	6	19.01	21.45	*d*
OH_2	29.60	7.37	3.94	5	13.64	14.44	*d*
B_2H_6	57.46	61.79	0	8	39.75	51.12	*b*
SiH_4	59.39	63.74	0	7	41.04	43.39	*b*
GeH_4	65.83	71.31	0	7	45.71	49.66	*b*
SH_2	49.01	27.08	14.62	5	30.24	36.40	*d*
SeH_2	58.46	39.99	16.83	5	38.43	45.73	*b*
Molecules with polar bonds							
BF_3	39.08	14.06	12.60	7	21.91	23.82	*b*
CF_4	37.41	32.47	16.80	7	28.89	28.57	*b*
SiF_4	42.93	25.87	16.80	7	28.53	33.01	*b*
GeF_4	45.90	33.87	16.80	7	32.21	36.46	*b*
PF_5	47.24	44.60	21.00	8	37.61	36.46	*b*
SF_6	51.59	83.55	25.20	9	53.45	44.78	*b*
SeF_6	54.71	96.31	25.20	9	58.74	52.47	*b*
TeF_6	57.51	95.54	25.20	9	59.42	58.73	*b*
$HgCl_2$	180.05	99.40	23.79	6	101.08	90.67	*b*
BCl_3	96.88	79.62	35.68	7	70.73	80.05	*b*
CCl_4	92.91	125.92	47.58	7	88.80	102.56	*b*
$SiCl_4$	106.41	146.01	47.58	7	100.00	111.72	*b*
$TiCl_4$	125.83	139.02	47.58	7	104.14	141.00	*b*
$GeCl_4$	111.38	160.00	47.58	7	106.32	121.23	*b*
$SnCl_4$	119.52	226.44	47.58	7	131.18	137.08	*b*
$SbCl_5$	135.86	335.44	59.48	8	176.92	156.78	*b*
$HgBr_2$	219.41	125.19	33.27	6	125.96	115.96	*b*
BBr_3	129.94	104.62	49.91	7	94.82	114.13	*b*
$SiBr_4$	142.73	199.19	66.55	7	136.16	156.14	*b*
$SnBr_4$	157.60	292.51	66.55	7	172.22	189.07	*b*
HgI_2	285.92	174.98	50.95	6	170.61	164.74	*b*
SnI_4	225.69	433.69	101.90	7	253.76	277.81	*b*

[a] $\times 10^{25}$ cm.^{3}. [b] S. S. Batsonov, "Refractometry and Chemical Structure," translated by P. P. Sutton, Consultants Bureau, New York, N. Y., 1961. [c] J. O. Hirschfelder, C. F. Curtiss, and R. B. Bird, "Molecular Theory of Gases and Liquids," John Wiley and Sons, Inc., New York, N. Y., 1954. [d] E. A. Moelwyn-Hughes, "Physical Chemistry," Pergamon Press, New York, N. Y., 1961.

trigonal planar molecule (four atoms, three bonds implies six remaining degrees of freedom), and since the third B–F bond is contained within the plane of the two degrees of freedom already lost, the molecule has then seven remaining "degrees of freedom." Thus we have the final expression for the average polarizability

$$\alpha_M = {}^1/_3\left[\sum_i \sigma_i\alpha_{\parallel b_i} + \sum_j f_j\alpha_j + n_{df}\frac{\sum_j \alpha_j X_j^2}{\sum_j X_j^2}\right] \quad (87)$$

where n_{df} is the number of residual atomic degrees of freedom. In Table IX are found $\sum_j \sigma_i\alpha_{\parallel b_i}$, $\sum_j f_j\alpha_j$, n_{df}, $\frac{\sum \alpha_j X_j^2}{\sum X_j^2}$, and α_M for a random assortment of molecular systems.

Sample Calculation: CF_4

$R = 1.317 \times 10^{-8}$ cm., $A_C = 0.846$ a.u., $A_F = 1.065$ a.u., $X_C = 2.5$, $X_F = 4.0$

$$\sigma = 0.570$$

$$c_{CF} = 4.37 \text{ a.u.}$$

$$\alpha_C = 9.78 \times 10^{-25} \text{ cm.}^3$$

$$\alpha_F = 4.90 \times 10^{-25} \text{ cm.}^3$$

$$\overline{x_{CF}^2} = \frac{R^2}{4} + \frac{a_0^2}{2c^2} = 0.4409 \times 10^{-16} \text{ cm.}^2$$

$$\alpha_{CF} = \frac{4A_{CF}}{a_0}\left[(\overline{x_{CF}^2})\right]^2\sigma_i + {}^6/_7\alpha_F = 12.15 \times 10^{-25} \text{ cm.}^3$$

$$\sum_i \alpha_{\parallel_i} = 48.60 \times 10^{-25} \text{ cm.}^3$$

$$\sum_i 2\alpha_{\perp_i} = 6\frac{\sum X_j^2\alpha_j}{\sum X_j^2} = 37.41 \times 10^{-25} \text{ cm.}^3$$

$$\alpha_M = 28.67 \times 10^{-25} \text{ cm.}^3$$

Summary of Steps to Obtain Molecular Polarizabilities. (1) For the atomic reduced electronegativities (Table I), calculate atomic polarizabilities, α_j's, the resultant c_j's, the mean c_i's, and the mean A_i's; (2) from the bond distances and the mean resultant c_i's calculate $\overline{x_i^2}$; (3) from the electronegativities, calculate X_j^2 for atoms and σ_i's for bonds; (4) then using $\overline{x_i^2}$, mean A_i's, σ_i's, α_j's calculate $\alpha_{\parallel b_i}$'s, and $\sum_i \alpha_{\parallel i}$; (5) finally, with X_j^2, α_j calculate $\sum_i 2\alpha_{\perp_i}$ and α_M.

The results for the mean polarizabilities of polyatomic molecules as given in Table VIII indicate that the model is quite satisfactory in giving rather reliable predictions for nonpolar molecules, particularly carbon compounds where the average per cent deviation is 5.19 for 14 molecules. The results for polyatomic hydrides are not quite so good (11.6%). The importance of the polarity correction is indicated by the fact that for the 23 molecules studied in the polar bond category the average per cent deviation is reduced from 32.2 to 11.0% through the introduction of

the polarity corrections (Table IX). The over-all average deviation for the 55 molecules involved is slightly under 10%.

The proposed model may be useful in estimating mean polarizabilities somewhere within the range of the above errors. However, the limitations and assumptions of the method should be considered. In particular, little work has been done in applying the method to systems which are essentially ionic in nature.

Discussion

In the past it has been customary to discuss bond polarizabilities from the viewpoint of additivity. The historical development of this concept may be reviewed in several texts. It is now convenient to consider two subconcepts of additivity, namely, summability and transferability. By summability, we mean simply that for a given molecule the sum of the individual bond polarizabilities equals the molecular polarizability. By transferability, we mean that the component or average polarizability of a given bond type in one molecular species is equal to the component or average polarizability of the same bond type in another molecular species.

Since the bond perpendicular component is a linear combination of atomic polarizabilities and is independent of the internuclear distance R, whereas the parallel component is proportional to R^4, the δ-function model indicates that the perpendicular components will be transferable only to the extent that the two molecules have similar configurations, and that the parallel components will be transferable only if the internuclear distances of the bonds in the two different molecules are nearly identical. Hence, no claim is made here as to the transferability of either the average, the parallel, or the perpendicular component of the bond polarizability for any bond.

That there are restrictions on the transferability of either the parallel component of the polarizability or the average polarizability had been recognized by Vickery and Denbigh[13] in their calculation of bond refractions for a series of paraffins. The least squares analysis used in their calculations to find average C–H and C–C polarizabilities was weighted in favor of the larger paraffins so that the polarizability of methane using the average C–H polarizability is slightly low. Viewed from the frame of reference of the δ-function model, this low value for methane is easily explained: The average C–H bond in a long-chain hydrocarbon is shorter than that in methane; thus, the value for methane should be low if the average polarizability for the C–H bond were taken as a mean from paraffins in the neighborhood of 5–12 carbons. This dependence on bond length is probably not the only factor in the nontransferability of the average bond polarizabilities. Vickery and Denbigh[13] make a special point concerning chain branching and calculate constants which are a function of the number and extent of the branches.

In Table X will be found calculated bond components of the polarizability together with their derived counterparts from Denbigh.[12a] It is to be noted that the derived components given by this author were obtained by averaging over several similar molecular systems, whereas the calculated components refer to the individual molecular system denoted.

Table X: Bond Polarizabilites and Components[a,b]

	$\alpha\|$(calcd)	$\alpha_i\|$(exptl)	$\alpha\perp$(calcd)	$\alpha\perp$(exptl)	α_M(calcd)	α_M(exptl)
C–C	23.00	18.8	0.73	0.2	8.15	6.40
C–Cl	31.48	36.7	17.56	20.8	22.20	26.1
S–O	33.35	29.0	12.52	14.7	19.46	19.47
N–H	6.24	5.8	6.39	8.4	6.34	7.5
C–H	7.01	7.9	5.81	5.8	6.21	6.5
O_2	30.02	24.3	11.84	11.9	17.90	16.0
C≡O	29.08	26.0	15.71	16.2	20.17	19.5
C=O	20.54	19.9	10.82	7.5	14.06	11.6
C O	24.25	22.5	5.86	4.8	11.99	10.7
C=C	28.24	28.6	11.50	10.6	17.08	16.6
N≡N	27.57	24.3	14.87	14.3	19.10	17.6
C≡N	25.84	31.0	17.32	14.0	20.16	19.7
C≡C	26.67	35.4	18.84	12.7	21.45	20.3

[a] $\times 10^{25}$ cm.^{3}. [b] Experimental values obtained from ref. 11 in text.

Since this δ-function model gives explicit equations showing the R dependence of the parallel component of the polarizability and the R-independent form of the perpendicular, applications of these relationships to other problems should be possible. For example, Raman intensities are proportional to $(\partial\alpha/\partial q)^2$, the square of the polarizability derivative for a given mode of vibration. Thus it should be possible to obtain some results concerning Raman intensities from the proposed model.

A Geometric Effect at the Solution–Surface Interface and Its Relationship to Ion Solvation[1a,b]

by Bobby L. McConnell, Kenneth C. Williams, John L. Daniel, Jimmy H. Stanton, Bobby N. Irby, Donald L. Dugger, and Russell W. Maatman[1c]

Department of Chemistry, The University of Mississippi, University, Mississippi *(Received April 18, 1964)*

The consequences of diminished concentration of the larger species in solution near a solution–phase boundary are discussed. The diminished concentration, a "geometric effect," while general and not dependent upon the absence of other reactions, is experimentally observable only in systems in which the interface:volume ratio is hundreds of square meters per milliliter. This condition is sometimes met in colloidal systems. A method for treating quantitatively the geometric effect in solution–gel systems is presented. Use of the method is illustrated by considering ion–gel–water systems; estimates of the radii of 42 solvated ions are given. All radii calculated are in the range found by other methods, suggesting that the geometric interpretation of the experimental results is correct.

Introduction

Schachman and Lauffer[2] suggested that some hydration of tobacco mosaic virus in serum albumin or sucrose solutions is only apparent; Schumaker and Cox[3] made the same observation concerning proteins in salt solution. The effect is geometric (Fig. 1) and its explanation is due to Kauzmann, whom Schachman and Lauffer cite. The center of the smaller species in a two-component solution has access to the volume between the planes AA′ and BB′ (perpendicular to the plane of the diagram and parallel to the surface plane SS′), while the center of the larger species does not have access to this volume. Consequently, the concentration of the larger species increases in the bulk when the solution contacts the surface. This is a geometric effect existing wherever a solution of molecules of unequal size contacts an interface. Even where there is a surface reaction (such as hydration of the surface) there is a new surface and the geometric effect exists.[2]

The purpose of the present work is to give a quantitative treatment of the geometric effect more general than the one given in our earlier work.[4] Use of the procedure developed is illustrated by applying it to gel–ion–solvent systems. This illustrative application yields values of radii of ion solvates which are roughly the same as those obtained from more reliable methods. The geometric method is not an absolute method, however, since its use depends upon assigning a radius to one ion. The rough agreement between this method and others suggests that the geometric interpretation of bulk enrichment of solute is correct.

Schachman and Lauffer[2] showed that it is sufficient to assume that from the center of a species contacting the surface to the surface its concentration is zero, while everywhere else its concentration is the bulk value. To show the magnitude of the geometric effect, let V_A and V_B be the volumes available to the smaller and larger species, respectively (Fig. 1); let c_i be the concentration of the larger species in a boundless system,

(1) (a) Taken in part from theses presented by B. L. McConnell and J. H. Stanton to the graduate faculty of the University of Mississippi in partial fulfillment of the requirements for the Ph.D. degree, and K. C. Williams, D. L. Dugger, and J. L. Daniel for the M.S. degree; (b) this work was supported by a Petroleum Research Fund grant and AEC Contract No. AT-(40-1)-2759; B. N. I. was a participant in the National Science Foundation Research Participation Program for High School Teachers; (c) correspondence should be sent to this author at Dordt College, Sioux Center, Iowa.

(2) H. K. Schachman and M. A. Lauffer, *J. Am. Chem. Soc.*, **71**, 536 (1949).

(3) V. N. Schumaker and D. J. Cox, *ibid.*, **83**, 2445 (1961).

(4) (a) R. W. Dalton, J. L. McClanahan, and R. W. Maatman, *J. Colloid Sci.*, **17**, 207 (1962); (b) J. Stanton and R. W. Maatman, *ibid.*, **18**, 132 (1963); (c) R. W. Maatman, J. Netterville, H. Hubbert, and B. Irby, *J. Miss. Acad. Sci.*, **8**, 201 (1962); (d) J. Stanton and R. W. Maatman, *J. Colloid Sci.*, **18**, 878 (1963).

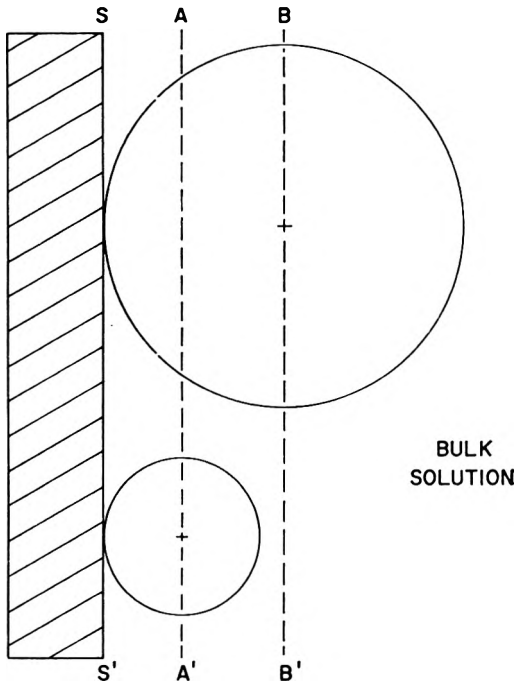

Figure 1. Two-component solution contacting plane surface.

i.e., before the solution contacts SS′, and let c_f be the concentration after contact. Then

$$\frac{c_i}{c_f} = \frac{V_B}{V_A} \quad (1)$$

Two cases are considered.

Case 1. Flat Surface. If r_B and r_A are the radii of the species and S is the interfacial area

$$V_A - V_B = S(r_B - r_A) \quad (2)$$

Combining eq. 1 and 2

$$\frac{c_i}{c_f} = 1 - \frac{S}{V_A}(r_B - r_A) \quad (3)$$

This effect is usually very small: if close-packed 200 mesh spheres (whose surfaces are essentially flat when considering molecular dimensions) were just covered with a two-component solution of molecules differing in radius by 10 Å., c_i/c_f would deviate from unity by only *ca.* 0.01%. However, in many colloidal systems S/V_A is hundreds of square meters per milliliter; eq. 3 (strictly applicable only to plane surfaces) indicates that c_i/c_f in such cases differs from unity by as much as 10%.

Case 2. Cylindrical Pores. It is difficult to study the geometric effect when it is complicated by considerable surface–solution reaction and/or a high Donnan potential. Ahrland, Grenthe, and Noren[5] and others have, however, reported that at low pH the silanol (–SiOH) groups of silica gel do not ionize and that the surface does not adsorb acid. To facilitate the following general derivation, reference is made to the low pH ion–silica gel–water systems which we studied and which serve as the illustrative example.

The simplifying assumption that gel pores are cylindrical was made. (This assumption is usually made in calculating pore size distributions, even though low angle X-ray evidence indicates the pores are spherical.[6]) The hydrated surface, according to Iler,[7] consists of parallel rows of –SiOH groups. About 10% of the water which entered the pore volume of our gels formed most of the surface hydroxyl groups. If the solute has access to most of the "trough" between surface hydroxyl groups, about 2.5 Å. wide, these groups (*i.e.*, surface water) will appear to act as solvent. Since only part of the solute molecule or ion need be in the "trough" to meet this condition, surface water may act as solvent for fairly large solutes. Some of the smaller ions (Cs^+ and NO_3^-) penetrate as much of the pore volume as water does,[4a] and others penetrate almost as well.[4c] Apparently, for at least the smaller ions, it is correct to consider that the surface water acts as solvent.

The volume available to the larger species is, where the pore size distribution is approximated by a series of pores of length l_j, the total pore length per unit weight of gel of radius r_j

$$V_B = V_A - P_A W + W\sum_j l_j\pi(r_j - r_B)^2 \quad (4)$$

with $r_j > r_B$, and where V_A is the volume of solution mixed with weight W of gel whose pore volume per unit weight (the volume species A penetrates) is P_A. For the weight W of gel, the summation term is the volume inside the pores available to species B and $V_A - P_A W$ is the volume outside the pores. The pore volume per unit weight available to species A in the jth pore is

$$P_{Aj} = l_j\pi(r_j - r_A)^2 \quad (5)$$

with $r_j > r_A$. Determination of the pore volume distribution as a function of pore radius frequently depends upon the use of the Kelvin equation; to lend validity to its use in the micropore region, the area under the distribution curve is in this work normalized to P_A, where A refers to the solvent. Then P_{Aj} is the area of the jth element of the area under the pore volume distribution curve.

(5) S. Ahrland, I. Grenthe, and B. Noren, *Acta Chem. Scand.*, **14**, 1059 (1960).

(6) A. S. Serikov, *Zh. Tekh. Fiz.*, **25**, 112 (1955).

(7) R. K. Iler, "The Colloid Chemistry of Silica and Silicates," Cornell University Press, Ithaca, N. Y., 1955, p. 243.

Combining eq. 1, 4, and 5

$$\frac{c_i}{c_f} = 1 - (W/V_A)\left[P_A - \sum_j \frac{P_{Aj}(r_j - r_B)^2}{(r_j - r_A)^2}\right] \quad (6)$$

where only the pores in which $r_B > r_j$ are considered. For convenience of calculation, eq. 6 is rearranged to

$$\frac{c_i}{c_f} = 1 - (W/V_A)(P_A - Q_1 r_B^2 + Q_2 r_B - Q_3) \quad (7)$$

where $Q_1 = \sum_j Q_j$, $Q_2 = \sum_j 2r_j Q_j$, $Q_3 = \sum_j r_j^2 Q_j$, and $Q_j = P_{Aj}/(r_j - r_A)^2$.

Experimental

Materials. The procedure of water-washing and acid-washing Code 40 Davison silica gel, 6–12 mesh, has been described.[4a,b] The pore volume, by absorption of either water, 0.5 *M* NaCl, or 5.0 *M* LiCl, is 0.40 ± 0.01 ml. The B.E.T. surface areas, determined by the sorptometer method referred to below, are 594 and 498 m.²/g. for the water-washed and acid-washed gels, respectively; these values are lower than those determined using a titration method.[4a,b]

Compounds and their sources were: nitrates of Nd^{3+}, Pr^{3+}, Y^{3+}, and Sm^{3+}, Fairmount; Cs^+ salts, Fairmount; $Ce(NO_3)_3 \cdot 6H_2O$, C.P., and some $La(NO_3)_3 \cdot 6H_2O$, purified, Fisher; some $La(NO_3)_3 \cdot 6H_2O$, A. D. Mackay; $Fe(ClO_4)_3$ (containing a small amount of $HClO_4$), K and K Laboratories; $Gd(NO_3)_3$, Lindsay Chemical. The tetraalkylammonium halides were Eastman White Label and used as received.

Anal. Calcd. for $(CH_3)_4NCl$: Cl, 32.35. Found: Cl, 32.22. Calcd. for $(C_2H_5)_4NCl$: Cl, 21.40. Found: Cl, 21.40. Calcd. for $(CH_3)_4NBr$: Br, 51.87. Found: Br, 51.32. Calcd. for $(n\text{-}C_4H_9)_4NBr$: Br, 24.79. Found: Br, 24.67. The other chemicals were reagent grade.

Pore Volume Distribution. The distribution of pore volume with pore radius was determined by the method of Cranston and Inkley[8] from the nitrogen adsorption isotherm at liquid nitrogen temperature. The isotherms were determined with a sorptometer, which uses the gas chromatography principle, built in this laboratory[9] and similar to the one described by Nelson and Eggertsen.[10] Isotherms were obtained for water-washed and acid-washed gels which were predried in a helium stream at 275° for 2 hr. Pore volume distributions calculated from the isotherms are given in Fig. 2.

Equilibration Procedure. The absolute amounts of gel and solution (kept in contact in bottles at room temperature for at least 48 hr.) varied, but W/V_A was 0.60 g./ml. With Al^{3+}, Cu^{2+}, Cr^{3+}, Ni^{2+}, and Fe^{3+} the solutions were made 1.5 *M* in the acid of the salt anion to repress complicating ion exchange with the surface. Reaction with the surface was slight enough (as measured by pH change) with the other ions to make acid addition unnecessary. To determine c_i/c_f, aliquots of both stock and equilibrium solutions were analyzed.

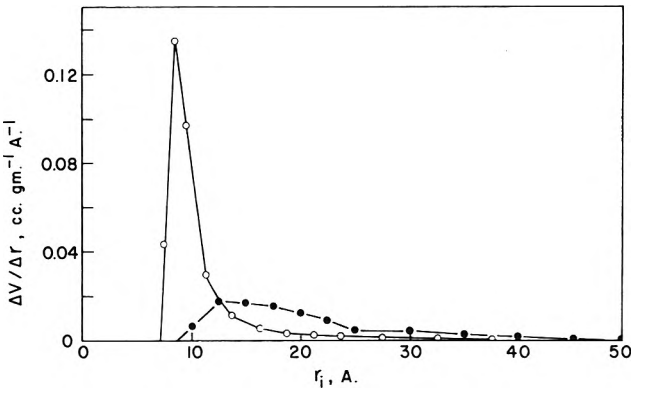

Figure 2. Pore volume distribution (per gram): ●, acid-washed; ○, water-washed.

Analytical. $Cr(NO_3)_3$ solutions were determined spectrophotometrically. The alkali metal nitrate solutions (centrifuged prior to analysis) were analyzed by drying at 110° to constant weight. Halide and acid solutions were determined by silver nitrate and base titration, respectively. All other cations were determined by EDTA titration.

Results and Discussion

Calculation of Q Coefficients. The *Q* coefficients of eq. 7, calculated for each solid from the pore volume distributions of Fig. 2 for both r_A = 1.7 and 2.0 Å., are given in Table I; the coefficients for the larger pore Code 70 Davison silica gel, used in work reported elsewhere,[11] are included. For water, the value of r_A = 1.7 Å. is a lower limit, since for Cs^+, which sees the same volume as water,[4a] the crystal radius is 1.69 Å. The arbitrary choice of r_A = 2.0 Å. is based on the estimate that Cs^+ is slightly hydrated. (In the earlier work 0.9 Å. was chosen for r_A). Other workers usually assume the radius of the water molecule in the liquid to be about 1.4 Å.; an average cluster is probably the water species of interest in a study of the geometric

(8) R. W. Cranston and F. A. Inkley, *Advan. Catalysis*, **9**, 143 (1957).

(9) H. L. Lutrick, K. C. Williams, and R. W. Maatman, *J. Chem. Educ.*, **41**, 93 (1964).

(10) F. M. Nelsen and F. T. Eggertsen, *Anal. Chem.*, **30**, 1387 (1958).

(11) K. C. Williams and R. W. Maatman, *J. Miss. Acad. Sci.*, **9**, 44 (1963).

effect at the interface. The arbitrary choice of the value of the radius of one ion, and therefore of r_A for water, is probably correct (for a given definition of solvation) within several tenths of an Ångstrom. Therefore, all radii obtained by this method can be in error by about the same amount, although relative values are more reliable. The relationship between c_i/c_f and r_B is shown in Fig. 3.

Table I: Q Coefficients of Eq. 7[a]

Gel	r_A, Å	Q_1, g.$^{-1}$ Å.$^{-1}$ ($\times 10^{-13}$)	Q_2, g.$^{-1}$ ($\times 10^{-14}$)	Q_3, Å.$^{-1}$-g.$^{-1}$ ($\times 10^{-15}$)
Code 40, w.w.[b]	1.70	6.56	12.2	5.88
Code 40, w.w.[b]	2.00	7.14	13.2	6.36
Code 40, a.w.[c]	1.70	1.91	5.81	4.95
Code 40, a.w.[c]	2.00	2.00	6.08	5.15
Code 70[d]	1.70	0.323	3.89	12.2
Code 70[d]	2.00	0.327	3.94	12.3

[a] Q coefficients are to be summations over only those pore size intervals for which r_i is greater than both r_A and r_B: here this means that all intervals of each of the three gels are used. [b] Water-washed; r_i is midpoint of 1-Å. interval; $P_A = 0.40$ ml./g.; $W/V = 0.60$ g./ml.; $S = 594$ m.^{2}/g. [c] Acid-washed; r_i is midpoint of 2-Å. interval; $P_A = 0.40$ ml./g.; $W/V = 0.60$ g./ml.; $S = 498$ m.^{2}/g. [d] r_i is midpoint of 2-Å. interval; $P_A = 1.15$ ml./g.; $W/V = 0.40$ g./ml.; $S = 352$ ml.^{2}/g.

Adsorption Correction. Solute adsorption (not the exchange referred to earlier) complicated the measurement of c_i/c_f for the tetraalkylammonium halides. (Impurity in the water-washed gel may be responsible for adsorption.) The total amount of solute per gram of solid, y, is

$$y = y_d + y_a = \frac{c_i V_A - c_f(V - WP_A)}{W} \quad (8)$$

where y_d and y_a are the amounts of dissolved and adsorbed salt in the pore volume, respectively. The linearity of y *vs.* c_f at high concentrations (Fig. 4) indicates y_a is constant in this region, the horizontal portion of the adsorption isotherm. Therefore, y_d is the ordinate of the curve (not shown) which is parallel to the linear segment of the observed curve and which passes through the origin. Thus

$$y_d = \frac{c_i' V_A - c_f(V - WP_A)}{W} \quad (9)$$

where c_i' is the initial concentration in the hypothetical nonadsorption case; using eq. 9, c_i' is calculated. When there is adsorption, c_i'/c_f is used in connection with the geometric effect where the term c_i/c_f is called for.

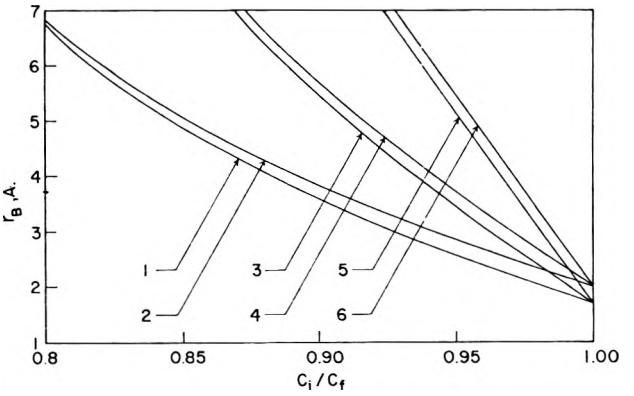

Figure 3. Plot of r_B *vs.* c_i/c_f. Curve, gel, r_A: 1, Code 40 w.w., 1.70 Å.; 2, Code 40 w.w., 2.00 Å.; 3, Code 40 a.w., 1.70 Å.; 4, Code 40 a.w., 2.00 Å.; 5, Code 70, 1.70 Å.; 6, Code 70, 2.00 Å.

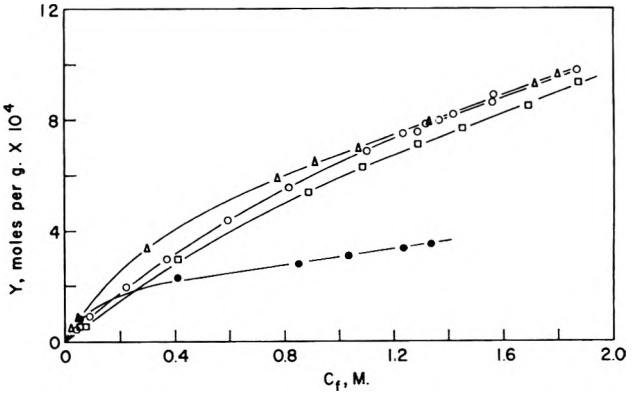

Figure 4. Amount of tetraalkylammonium halide in pores/g. of w.w. gel *vs.* c_f; △, $(C_2H_5)_4NCl$; ○, $(CH_3)_4NCl$; □, $(CH_3)_4NBr$; ●, $(n\text{-}C_4H_9)_4NBr$; temp., 22°. See footnote *b*, Table I, and Table II for further details.

Solvate Sizes. The values of c_i/c_f at rounded off concentrations for the new systems studied are given in Table II. Comparisons in the earlier work were made by extrapolation to infinite dilution to avoid the concentration effect; the extrapolated value of c_i/c_f is given in the last column.

Solvate radii, which are r_B values, for 42 ions (from the present and earlier work) are given for the three gels in Table III. The value of 2.0 Å. for r_A is chosen; r_B is slightly different (Fig. 3) if the value of 1.7 Å. is chosen. Although c_i/c_f is measured for an electrolyte, the r_B value usually can be assigned to one of the ions. Thus, since $c_i/c_f = 1$ for $CsNO_3$, the value for any other nitrate (always less than unity) can be used to determine cation size; similarly, with other cesium salts anion size can be determined. With three of the four tetraalkylammonium halides, however,

Table II: Values of c_i/c_f at Various Concentrations

Solute	No. of expts.	c_i/c_f 0.5 M	0.1 M	0.01 M	0.000 M[b]
HNO_3[a]	4	0.923	0.918	...	0.916
$LiNO_3$[a]	9	0.915	0.885	...	0.877
KNO_3[a]	10	0.941	0.921	...	0.917
$Mg(NO_3)_2$[c,d]	5	...	0.881	0.881	0.881
$Al(NO_3)_3$[a]	9	0.893	0.887	...	0.886
$AlCl_3$[a,e]	10	0.910	0.896	...	0.892
$Al(NO_3)_3$[c,d]	4	0.876	0.858	...	0.854
$Cr(NO_3)_3$[a]	9	...	0.909	0.887	0.885
$Fe(ClO_4)_3$[a]	10	0.940	0.881	...	0.866
$Ni(NO_3)_2$[a]	29	0.904	0.882	...	0.876
$Cu(NO_3)_2$[a]	8	...	0.920	0.920	0.920
$Y(NO_3)_3$[a]	5	...	0.894	0.894	0.894
$La(NO_3)_3$[a]	10	0.903	0.893	...	0.890
$Ce(NO_3)_3$[a]	5	...	0.896	0.896	0.896
$Pr(NO_3)_3$[a]	5	...	0.898	0.898	0.898
$Nd(NO_3)_3$[a]	5	...	0.905	0.905	0.905
$Sm(NO_3)_3$[a]	5	...	0.892	0.892	0.892
$Gd(NO_3)_3$[a]	5	...	0.901	0.901	0.901
$CsCl$[a]	8	0.982	0.981	...	0.981
$CsBr$[a]	8	0.970	0.961	...	0.959
CsI[a]	8	0.960	0.950	...	0.948
$(CH_3)_4NCl$[c,f]	15	...	...	...	0.983
$(CH_3)_4NBr$[c,f]	9	...	...	...	0.987
$(C_2H_5)_4NCl$[c,f]	9	...	...	...	0.981
$(n\text{-}C_4H_9)_4NBr$[c,f]	6	...	...	...	0.851

[a] Acid-washed gel. [b] By extrapolation; average error <0.01. [c] Water-washed gel. [d] Recent results which supersede earlier reported values. [e] Results based on anion analysis. [f] Results based on anion analysis. Curves in Fig. 4 imply that c_i/c_f is the same at all concentrations and consequently only the extrapolated value is given.

Table III: Summary of r_B Values[a]

Ion	r_B, Å. Code 70	Code 40, w.w.	Code 40, a.w.
H^+	...	4.0	5.0
Li^+	5.1	4.1	6.7
Na^+	4.8	4.0	...
K^+	3.4	3.3	5.0
Rb^+	...	2.6	...
Cs^+	...	(2.0)[b]	...
Be^{+2}	...	5.4	...
Mg^{+2}	5.4	4.3	...
Ca^{+2}	...	4.2	...
Sr^{+2}	5.8	4.1	...
Ba^{+2}	...	4.4	...
Al^{+3}	7.0	5.0	6.3(6.1)[c]
In^{+3}	...	5.3	...
Cr^{+3}	5.7	5.3	6.4
Mn^{+2}	...	4.1	...
Fe^{+3}	...	...	7.3
Co^{+2}	5.6	4.8	...
Ni^{+2}	...	4.6	6.8
Cu^{+2}	...	4.3	4.9
Y^{+3}	...	...	5.9
Ag^+	...	3.8	...
La^{+3}	...	...	5.9
Ce^{+3}	...	...	5.8
Pr^{+3}	...	...	5.8
Nd^{+3}	...	...	5.5
Sm^{+3}	...	...	6.0
Gd^{+3}	...	...	5.6
Th^{+4}	...	...	6.6
UO_2^{+2}	...	4.1	6.3
NO_3^-	...	$\leq$2.0[d]	...
Cl^-	...	...	2.7
Br^-	...	...	3.4
I^-	...	...	3.8
$(CH_3)_4N^+$	...	$\leq$2.2[e]	...
$(C_2H_5)_4N^+$	...	$\leq$2.3[f]	...
$(n\text{-}C_4H_9)N^+$	...	5.0	...
$Co(NH_3)_6^{+3}$	...	4.9	...
$Co(en)_3^{+3}$[g]	...	3.5	...
$Co(pn)_3^{+3}$[g]	...	2.7	...
$Co(hen)_3^{+3}$[g]	...	2.7	...
$Co(eten)_3^{+3}$[g]	...	2.4	...
NH_4^+	...	3.4	...

[a] See footnotes to Table I for description of gels. Values of r_B not derived from Table II are derived from ref. 1c and 8. Average error <0.4 Å., except for Be^{+2} and In^{+3}, where error is ±0.8 Å. [b] Choice of $r_A = r_B = 2.0$ Å. in Cs^+ system is the basis of all other values. [c] Value in parentheses based upon Cl^- analyses in $AlCl_3$ experiments (see Table II). [d] r_B for NO_3^- is <2.0 Å. if Cs^+ is limiting factor in $CsNO_3$ experiments. [e] Value obtained from both Cl^- and Br^- experiments; r_B value given may be halide size. [f] Value obtained from Cl^- experiments. [g] en = ethylenediamine; pn = 1,2-propylenediamine; hen = N-hydroxyethylethylenediamine; eten = N-ethylethylenediamine.

only an upper limit on cation size can be given. With $Fe(ClO_4)_3$ it is probable that the cation is larger.

To preserve electroneutrality, the concentration of the smaller ion of the cation–anion pair cannot, even in the surface region, be greater than that of the larger ion. Yet the center of the smaller ion tends to approach the surface more closely, causing the activity coefficient of nearby large ions to diminish. Because cation–anion radii differences are usually smaller than the diameter of the smaller ion, it is assumed that the activity coefficient effect is not large. Therefore, c_i/c_f is assumed under the conditions used to depend upon the radius of the larger ion and to be independent of the radius of the smaller ion.

The cylindrical-pore assumption apparently does not lead to serious error. Thus, if in the water-washed Code 40 gel the surface area of 594 m.^{2} g. were the surface of a uniform pore of a pore volume of 0.40 ml./g., the radius of this pore would be 13.5 Å. For a typical hydrated ion of r_B = 4.3 Å. (corresponding to Mg^{+2}) eq. 6 gives (since W/V_A = 0.600 g./ml. for experiments with this gel) c_i/c_f = 0.914, assuming r_A

to be 2.0 Å. If, on the other hand, the pores are assumed to be uniform spheres, such that their area is 594 m.²/g. with a pore volume of 0.40 ml./g., the sphere radius would be 20.2 Å. The centers of 4.3-Å. hydrated ion spheres have access to 66.5% of the volume accessible to 2.0-Å. water spheres in a spherical pore of a radius of 20.2 Å. Therefore, 33.5% of the 0.40 ml./g. water pore volume, or 0.134 ml./g., is not accessible to the hydrated ion. When W/V_A = 0.600 g./ml., 1.667 ml. of solution contact 1 g. of gel, while the solute is concentrated in 1.667 − 0.134 ml., or 1.533 ml. Thus for the idealized spherical case, c_i/c_f = 1.533/1.667 = 0.920, almost identical with the 0.914 value of the idealized cylindrical case.

The average error in extrapolated c_i/c_f (footnote *b*, Table II), due principally to error in metal ion analysis, is 1%. If, for example (see Fig. 3), c_i/c_f is measured to be 0.94 instead of 0.95, the corresponding error in r_B on curves 2, 4, and 6 is therefore 3, 9, and 13%, respectively.

In general, for the r_B values given it is concluded that (1) the values for different ions on a given gel have a logical relationship to one another, *i.e.*, the ions generally thought to hydrate more are indeed those with the larger r_B values, (2) the values for a given ion on different gels are in poor agreement, and (3) the values are within the range found using other methods.

Conclusions. The ion results are presented here primarily to illustrate the geometric effect, an effect which should be general and which may have been observed by some who did not recognize it for what it is. For example, Redfern and Patrick[12] were unable to explain partial exclusion of aqueous alkali and alkaline earth halides and dextrose from part of the pore volume of silica gel. Konyushka[13] ascribed partial exclusion of several nonelectrolytes in aqueous solution entirely to preferential adsorption of water by the gel. Glasstone[14] also neglected the geometric effect in suggesting that "negative adsorption," *i.e.*, exclusion of aqueous KCl at low concentration by blood charcoal, could be treated by the Gibbs equation. Others who ascribed solute exclusion from the surface entirely to solvent adsorption are Krestinskaya and Khakinov,[15] who observed a negative adsorption of Ag_2SO_4 on silica gel, and Kohn,[16] who determined the volume of hydrated particles in suspension and the amount of adsorbed water by observing the bulk enrichment of an ionic indicator.

The ion species whose "size" is measured by the use of the geometric effect is the kinetic entity which collides with the uncharged gel surface and is thereby stripped of some of its water of solvation. The correction for the amount of water stripped away should be less than the correction applied in the use of Debye–Hückel theory to calculate ion solvate radii,[17] since the latter correction is for the collision between charged ions.

For unhydrated nonspherical ions the value of r_B should lie between the minimum and maximum values of the crystal radius. For example, r_B for $Co(eten)_3^{3+}$, probably unhydrated, is 2.4 Å. using the gel which gives the lowest values; from a model the minimum and maximum values of the unhydrated ion are calculated to be *ca.* 2 and 6 Å.

(12) S. Redfern and W. A. Patrick, *J. Phys. Chem.*, 42, 497 (1938).

(13) (a) I. M. Konyushka, *Uch. Zap. Belorussk. Gos. Univ.*, 140 (1953); (b) *ibid.*, 282 (1956); (c) *Vestsi Akad. Navuk Belarus. SSR, Ser. Fiz-Tekh Navuk*, 111 (1956).

(14) S. Glasstone, "Textbook of Physical Chemistry," 2nd Ed., D. Van Nostrand Co., New York, N. Y., 1946, p. 1216.

(15) V. N. Krestinskaya and Z. V. Khakinov, *J. Gen. Chem. USSR*, 14, 129 (1944).

(16) R. Kohn, *Chem. Zvesti*, 15, 81 (1961).

(17) R. A. Robinson and R. H. Stokes, "Electrolyte Solutions," 2nd Ed., Butterworths Scientific Publications, London, 1959, pp. 245–250.

Electrical Conductivity of Liquid Ammonia during γ-Ray Irradiation[1]

by Rolland W. Ahrens,[2] Bulusu Suryanarayana, and John E. Willard

Department of Chemistry, University of Wisconsin, Madison 6, Wisconsin *(Received April 27, 1964)*

A reversible increase in the electrical conductivity of liquid ammonia has been observed upon exposure to γ-irradiation at a dose rate of about 10^{18} e.v. g.$^{-1}$ min.$^{-1}$ ($\sim 10^6$ r. hr.$^{-1}$). This implies escape of radiation-produced electrons from the parent positive ions to form separated ion pairs. If the equivalent conductance is assumed to have the value reported for sodium in liquid ammonia, and the recombination rate constant is assumed to be the same as that for the reaction of solvated electrons in water with hydronium ion, the steady-state ion-pair concentration was about 4×10^{12} ml.$^{-1}$ and G(ion pairs) for the different types of measurements made fell in the range 0.5 to 3. Any reasonable choice of the variable parameters seems to require substantial electron escape. Technical problems in the determination of the conductivity of liquid ammonia during irradiation are discussed.

Introduction

Roberts and Allen[3] have sought evidence for the existence of a steady-state concentration of electrons in liquid ammonia while exposed to ionizing radiation, by comparing the electrical resistance before and during irradiation. At the X-ray dose rate of 1.8×10^5 r./hr. which they used, there was no evidence for a change in the specific resistance of the ammonia as a result of irradiation, nor did they observe any change when the cell was exposed to a beam of 2-Mev. electrons, which, however, did not penetrate to the vicinity of the electrodes.

Using Co^{60} γ-rays at a dose rate of about 10^6 r./hr., we have explored further the possibility of detecting radiation-produced ions in liquid ammonia by measurement of the conductivity change in the liquid when the radiation is suddenly removed. The study has included an investigation of the rate of release of conducting impurities from the glass walls of the conductivity cell by the radiation and of the change in resistance of the liquid caused by the heat generated by the radiation.

Experimental[2]

Ammonia was purified on a vacuum line by passing through moist KOH pellets to remove CO_2 and through dry KOH to remove H_2O, followed by several distillations from dissolved potassium metal in successive traps.[4] Finally, it was distilled into a conductivity cell which consisted of a Pyrex annulus containing a pair of concentric cylindrical bright platinum electrodes 7.6×10^{-3} cm thick, 2 cm. high, with a separation of 3.75 mm. The calculated cell constants (separation of electrodes/average surface area of electrodes) for the two cells with which most of the measurements were taken were 0.022 and 0.024 cm.$^{-1}$. The center hole of the annulus was designed to allow the 2-cm. high 1-cm. diameter 250-c. Co^{60} source to be lowered through a guide tube in the center. The source, contained in an aluminum capsule on the end of a stainless steel rod, was housed in a manner similar to that described earlier.[5]

The conductivity cell was sealed from the vacuum line while the ammonia was frozen in a side arm. For irradiation it was placed in a mechanically stirred chloroform–Dry Ice bath which maintained a temperature of −70° in a 4-l. dewar flask. Platinum wires welded to the electrodes led through tungsten–Pyrex

(1) This work was supported in part by the U. S. Atomic Energy Commission under Contract AT(11-1)-32 and by the W. F. Vilas Trust of the University of Wisconsin.

(2) Further details of part of this work are given in the Ph.D. Thesis of R. W. Ahrens, University of Wisconsin, 1959, available from University Microfilms, Ann Arbor, Mich.

(3) R. Roberts and A. O. Allen, *J. Am. Chem. Soc.*, **75**, 1256 (1953).

(4) J. Cueilleron and M. Charret, *Compt. rend.*, **239**, 168 (1954).

(5) (a) R. F. Firestone and J. E. Willard, *Rev. Sci. Instr.*, **24**, 904 (1953); (b) R. J. Neddenriep, Ph.D. Thesis, University of Wisconsin, 1959; (c) R. J. Harrahan, *Intern. J. Appl. Radiation Isotopes*, **13**, 254 (1962).

seals to mercury pools in side arms in which copper wires leading to the conductivity bridge were immersed. The Leeds and Northrup conductivity bridge was of the type discussed in detail by Jones and Josephs[6] and by Dike.[7] A Hewlett-Packard Model 200c oscillator was used to apply to the bridge a root mean square potential of 0.70 v. at 1000 c.p.s. Bridge imbalance was amplified by an audiofrequency amplifier. The bridge was isolated from changes in the electrostatic potential of the oscillator and amplifier by shielded transformers. The output was filtered by a 1000-c.p.s. wave filter and observed on an oscilloscope, visually or by photographing traces triggered first with the Co^{60} source in position and then at the instant it had been removed from the cell.

The heating effect of the Co^{60} source was compared with that of an electrically heated replica of the source assembly with the aid of a small calorimeter designed to approximate the conditions involved during radiation of the conductivity cell. It was concluded from these measurements that the source-simulator operating at 1 w. produced a heating effect in the irradiation assembly somewhat greater than the effect of the Co^{60} source. All observations of changes in conductivity of liquid ammonia in the conductivity cell caused by exposure to the Co^{60} source were compared to changes produced by identical exposure to the source simulator operating at 1 w. The temperature coefficient of the specific resistance of liquid ammonia is about 1.8%/°C. as found both in the present work and previous work.[4,8] Determinations of the resistance over the temperature range −70 to −50° gave straight-line plots for log R *vs.* $1/T$ with a value of 1487 cal. mole^{-1} for E in the expression $R = ke^{-E/RT}$.

Results

When the conductivity cell had been allowed to achieve thermal equilibrium with the thermostating bath, the resistance readings were constant to within about 0.002% (0.001°) or better per min. Figures 1 and 2 show examples of the changes in resistance which occurred when the source simulator, operated at 1 w. (Fig. 1), and the Co^{60} source (Fig. 2) were brought into successively closer positions to the cell and then rapidly removed. In both figures time A indicates the time at which the source was lowered out of its storage turret to a position 21.5 cm. above the center of the conductivity cell. At time B it was lowered to within 11.5 cm. of the standard irradiation position, at time C to within 1.5 cm., and at time D it was finally positioned at the center of the conductivity cell annulus. Resistance readings were taken at 30-sec. intervals during the period of successive insertions and

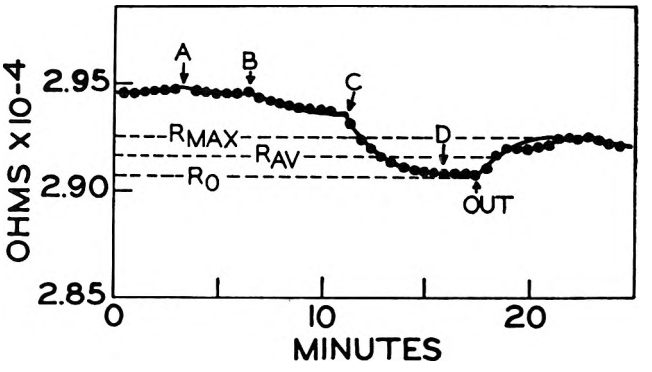

Figure 1. Resistance of conductivity cell of liquid NH_3 at −70° as a function of position of source simulator heated at 1 w. Distance from irradiation position: A, 21.5 cm.; B, 11.5 cm.; C, 1.5 cm.; D, irradiation position.

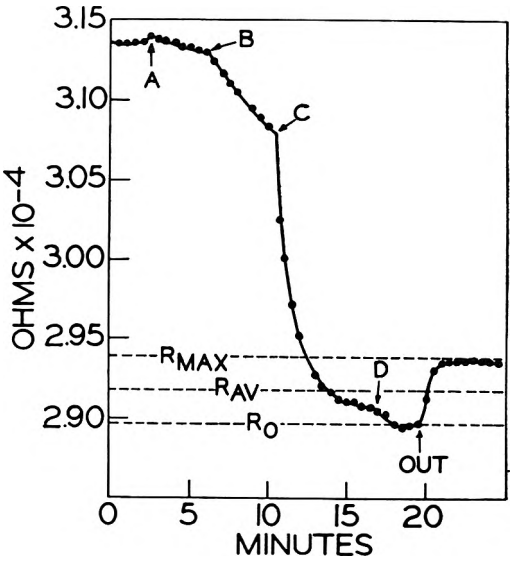

Figure 2. Resistance of conductivity cell of liquid NH_3 at −70° as a function of position of Co^{60} source. Distance from irradiation position: A, 21.5 cm.; B, 11.5 cm.; C, 1.5 cm.; D, irradiation position.

also following rapid removal of the simulator or source. Both Fig. 1 and Fig. 2 show a nearly constant resistance before insertion, which decreases progressively more rapidly with increased proximity of the inserted element to the irradiation position. The decrease as the simulator was inserted is attributed to an increase in temperature of the liquid ammonia (about 0.7° total) while that produced by the Co^{60} source must result from a combination of the effects of increase in temperature, production of conducting im-

(6) G. Jones and R. C. Josephs, *J. Am. Chem. Soc.*, **50**, 1049 (1928).
(7) P. H. Dike, *Rev. Sci. Instr.*, **2**, 379 (1931).
(8) K. Fredenhagen, *Z. anorg. allgem. Chem.*, **136**, 1 (1930).

purities at the walls or electrodes of the cell by the radiation, and the steady-state concentration of ions maintained in the ammonia by the ionizing radiation during exposure. The production of impurities at the walls or electrodes would be expected to produce an irreversible lowering of the resistance, and this was regularly observed in successive determinations with the same cell filling. Similar aging effects with radiation have been reported in studies on aqueous systems.[9] The results shown in Fig. 2 are typical of those obtained when a cell had been "aged" by irradiation and had been thoroughly rinsed with liquid ammonia prior to filling. New cells gave much larger resistance changes. Although ideally the temperature effect would be completely reversible, the viscous chloroform–Dry Ice medium did not provide sufficient long-term temperature constancy to show this. The conductivity due to the steady-state concentration of ions should be reversible with insertion and removal of the source. As a means of distinguishing the radiation-induced steady-state conductivity from the other effects reflected in the curves in Fig. 2, we have used the plots of Fig. 3 where $(R - R_0)/R_{av}$ is plotted against time. As shown in Fig. 1 and 2, R_0 is the resistance at the instant prior to rapid removal of the source from the cell, R is the resistance at time t thereafter, and R_{av} is $(R_{max} - R_0)/2$. Curves A, B, and C give the results obtained on removal of the Co^{60} source in three different experiments on the same cell filling. Curves D and F were obtained on removal of the simulator while operating at 1 w. and curves E and G while operating at 0.75 w. Experimental errors tend to be magnified somewhat in plots of this type since $(R - R_0)$ is a small difference between two large numbers. The unusual sharp maximum in curve A 3 min. after removal of the source is assumed to be due to a temperature fluctuation. Such a fluctuation appears also to have occurred during the measurement of the simulator curve D. The downward trends following the maxima are the result of slow warming of the bath.

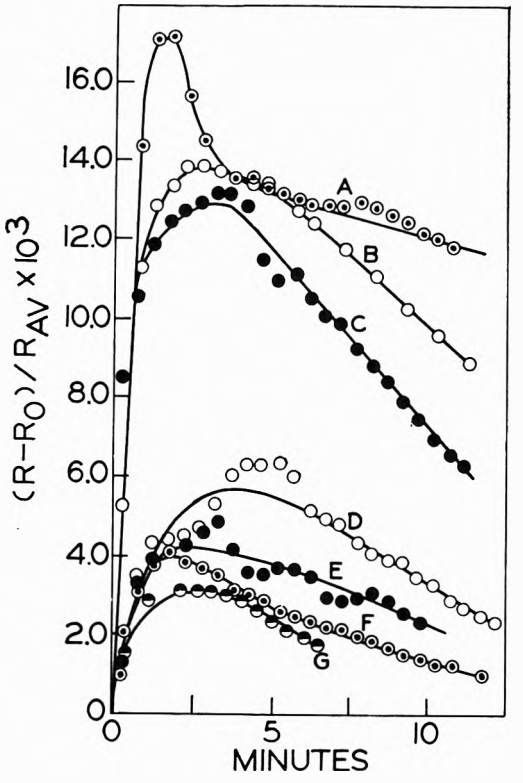

Figure 3. Fractional change in resistance as a function of time after removal of Co^{60} source from liquid NH_3 conductivity cell (curves A, B, C) and after removal of source simulator from liquid NH_3 conductivity cell (curves D and F simulator at 1 w.; curves E and G simulator at 0.75 w.).

The differences in the maximum value of $(R - R_0)/R_{av}$ achieved in the Co^{60} experiments, as compared to the simulator experiments, are far greater than the errors of measurement and seem to indicate clearly a contribution to the conductivity by a steady-state concentration of ions maintained by the presence of the radiation. During these measurements the cell resistance was in the range 2.7–3.4 $\times$ 10^4 ohms, indicating a concentration of conducting species in the absence of radiation of about 2.5 $\times$ 10^{-6} equiv./l. Similar sets of determinations using ammonia which gave cell resistances in the range of 1–4 $\times$ 10^3 ohms yielded $(R_{max} - R_0)/R_{av}$ values of only about 5 $\times$ 10^{-3}, the curves coinciding closely with the simulator curves of Fig. 3. The concentrations of conducting species present as impurities in the latter two sets of experiments were three to eight times the concentration in the experiments of Fig. 2. If it is assumed that the steady-state concentration of radiolytically produced ions was independent of the concentration of conducting species present as impurities, then the steady-state concentration of radiolytically produced ions should have been the same in all three samples. Therefore, the *fraction* of the cell current carried by the steady-state concentration of ions would have been less by factors of three to eight in the latter experiments. Under these conditions the change in conductivity due to the radiolytically produced ions could no longer be distinguished from the change in conductivity produced by temperature increase due to the heating effect of the source on the conductivity cell.

As a basis for a more quantitative evaluation of the data, it was assumed that curve D of Fig. 2 represents

(9) T. Rigg, G. Stein, and J. Weiss, *Proc. Roy. Soc.* (London), **A211**, 375 (1952).

an upper limit of the heating effect due to the Co^{60} source. Plots were made of the difference $\Delta R/R_{av}$ between curve D and each of the curves A, B, and C. These showed an initial rapid rise to a maximum followed by a relatively small downward slope which was extrapolated back to the time of removal of the Co^{60} source to give $(\Delta R/R_{av})_0$. It was assumed that this value indicated the fractional change in resistance due to recombination of radiolytically produced ions. From the equations

$$C = 1000(k/\Lambda)(1/R) \quad (1)$$

$$dC = -1000(k/\Lambda)(dR/R^2) \quad (2)$$

where C is the concentration of conducting species, k is the cell constant, and R is the cell resistance, it is possible to obtain an approximate relation involving $(\Delta R/R_{av})_0$ and ΔC, the concentration change.[2]

$$C = -1000(k/\Lambda)(1/R_{av})(\Delta R/R_{av})_0 \quad (3)$$

The equivalent conductance of sodium ions and ammoniated electrons at infinite dilution is about 1020 ohm^{-1} $cm.^2$.[10] If this value is assumed, the average of the three determinations of ΔC is 3.8×10^{12} ion pairs $ml.^{-1}$. The dose rate received by the liquid ammonia sample with the source in its lowest position was about 10^{18} e.v. $ml.^{-1}$ $min.^{-1}$.

From the steady-state concentration and dose rate, it may be estimated that the average lifetime of radiation-produced ion pairs during irradiation lies in the range of 0.01 to 0.2 sec., if G(ion pairs) is in the plausible range between 3 and 0.1. Consequently, when the Co^{60} source was removed in experiments of the type of Fig. 2, the concentration of radiation-produced ion pairs must have decreased to a level indistinguishable from the thermal effect in a time of the order of 1 sec. or less. In measurements of the type of Fig. 2, it required about 5 sec. to balance the bridge for each reading when the conductivity of the cell was not changing rapidly. Accurate measurements were difficult to obtain when the conductivity was changing rapidly. Measurements were made at intervals of 30 sec. These features of the measurement obscured the rapidity of the change in conductivity following removal of the source and, in all probability, account for the variation in position of the initial points on curves A, B, and C of Fig. 3. They do not affect the estimate of the magnitude of the conductivity change resulting from the recombination of the steady-state radiation-produced ion pairs.

In order to minimize these problems and to measure the change in conductivity at a time interval after removal of the source from the conductivity cell sufficiently short so that thermal effects would be negligible, a second measurement procedure was employed. After the conductivity had stabilized with the source in the irradiation position, the bridge was balanced and the source was removed rapidly. Electrical contacts were provided to trigger a sweep of the monitoring oscilloscope just as the upward motion started and again when the source was completely removed from the cell, less than 1 sec. later. Each oscilloscope trace showed the extent of imbalance of the bridge at the time it was taken. The two traces were recorded on a photographic plate exposed to the oscilloscope face during the period of removal of the source. The deflections were calibrated in terms of resistance change in the cell arm of the bridge by substituting a series of known resistances for the cell. Prior to removal of the source or simulator from the cell, the bridge was balanced to give a horizontal trace on the oscilloscope. Slight temperature drifts always resulted in a low intensity sine wave signal when a trace was subsequently triggered by the upward movement of the source. Figure 4 shows this signal and the much larger signal given by the cell immediately after source removal, for a cell containing liquid ammonia giving a resistance of about 15,000 ohms. The difference in imbalance of the bridge indicated by the traces of Fig. 4 indicates a change in resistance of 0.1%. When a source simulator operating at 1 w. was removed from the cell, the two traces triggered by the upward movement were essentially superimposed. This was also true when an unheated source simulator loaded with inactive cobalt and operated with the cell in the same lead housing used for the active source was tested.

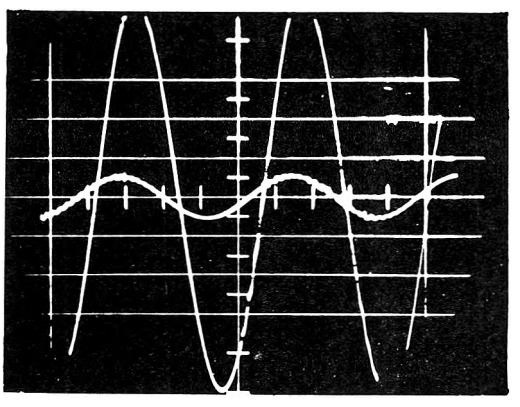

Figure 4. Oscilloscope traces showing imbalance of conductivity bridge at start of removal of Co^{60} source from liquid NH_3 conductivity cell (small amplitude trace) and immediately after removal (large amplitude trace).

(10) C. A. Kraus, *J. Chem. Educ.*, **30**, 83 (1953).

Similar experiments with different cell fillings of liquid ammonia with resistances in the 5000- to 10,000-ohm range showed curves similar to Fig. 4 but with lower percentage bridge imbalance on removal of the source, as expected. The value for the estimated radiation-produced steady-state concentration of ion pairs derived from the data of Fig. 4 for the time at which the second oscilloscope trace was triggered is 0.95×10^{12} ml.$^{-1}$. The fact that the change in conductivity due to recombination of ion pairs as indicated by the data of Fig. 4, and similar experiments, is substantially less than that indicated by Fig. 3 is interpreted to mean that ion recombination was only partially complete in the few hundredths of a second estimated to have been required to raise the source to the point where the second oscilloscope sweep was triggered. Thus the data of Fig. 4 illustrate the rapid change of conductivity upon removal of the source, in times short compared to those required for thermal effects, but do not show its full magnitude. The experiments using this technique were all made with rapid removal of the source in order to minimize effects due to temperature change.

Discussion

The data of Fig. 3 and 4 indicate that a steady-state concentration of charge carriers was maintained in the conductivity cells by exposure to γ-irradiation and that these carriers disappeared rapidly when the irradiation was stopped. It appears that most of these carriers must be ion pairs formed from the liquid ammonia by the high energy electrons ejected from it and from the electrodes.[11]

Assuming the steady-state ion-pair concentration during irradiation of 3.8×10^{12} ml.$^{-1}$, estimated from the result of Fig. 3, and assuming a recombination rate constant (k) equal to that for $e_{aq}^- + He_3O_{aq}^+$ (2.4×10^{10} M^{-1} sec.$^{-1}$),[12] the rate of production of ion pairs may be calculated from the relation: rate of production = rate of removal = kc^2, where c is the steady-state concentration of radiation-produced ion pairs which recombine when the irradiation is discontinued. This estimate yields a value of three electrons entering the steady state of conducting species per 100 e.v. absorbed.

This value of 3 for $G(e^-)$ is very close to gas phase values. It is in rather close correspondence to the value for liquid water (2.3–2.8)[12] and is much higher than the values observed for liquid hexane (0.2 and 0.09),[13,14] as might be expected from the known ability of liquid ammonia to stabilize electrons from alkali metal solutes. Because of the assumptions involved, it must, of course, be regarded as only an order of magnitude estimate.

The assumption that the equivalent conductance is the same as that in dilute solutions of sodium in liquid ammonia is probably good, since the conductivity of NH_3^+ or NH_4^+ ions is probably not far different from that of Na^+, and in the case of all three ions the major portion of the current would be expected to be carried by the solvated electrons. If the equivalent conductance of the radiolytically produced cations is higher than that of Na^+ because of proton transfer or other reasons, the value deduced for the steady-state concentration would be reduced by a proportionate amount, and $G(e^-)$ would be reduced in proportion to the square of this concentration.

The assumption that the rate constant for combination of the solvated electrons with the positive ions is equal to that determined in aqueous solutions for the reaction $e_{aq}^- + H_3O_{aq}^+$ may be inaccurate for several reasons, including the lower dielectric constant and longer dipole relaxation time in ammonia, and differences in energies of solvation. If the rate constant were much higher than 2.4×10^{10} M^{-1} sec.$^{-1}$, as in the case of $H_3O_{aq}^+ + OH_{aq}^- \rightarrow 2H_2O$, for which[15] k is 1.4×10^{11} M^{-1} sec.$^{-1}$, it would require a $G(e^-)$ much higher than 3, which seems improbable.

Allen and Hummel[14] were able to determine the average mobility of the radiation-produced ions in hexane and from this and the measured conductivity to compute the steady-state concentration of ions. This is not feasible in the liquid ammonia system, where the concentration of stable "impurity" ions initially present and produced by the radiation is much in excess of the additional transitory steady-state concentration of ions maintained during irradiation. Allen and Hummel[14] were also able to determine the recombination rate of the radiation-produced ions in hexane from a plot of the reciprocal cell current *vs.* time after interruption of radiation which gave a straight line measurable over a period of 40 sec. or more. The pos-

(11) Estimates indicate that the total number of primary electrons which the γ-rays ejected in the 160-mg. cm.$^{-2}$ platinum electrodes and which escaped from the electrodes into the liquid ammonia between them was about 10^{10}/sec. An applied potential of 0.7 v., at a resistance of 3×10^4 ohms, would produce a current flow of 2×10^{-5} amp. or 10^{14} electrons/sec. The fractional decrease in resistance with exposure to the radiation $(\Delta R/R_{av})_0$ was 0.008. This indicates an increase in electron flow of about 8×10^{11}/sec. This is greater, by a factor of some 80-fold, than the number of electrons ejected from the platinum into the liquid ammonia between the electrodes.

(12) S. Gordon, E. J. Hart, M. S. Matheson, J. Rabani, and J. K. Thomas, *J. Am. Chem. Soc.*, **85**, 1375 (1963).

(13) G. R. Freeman, *J. Chem. Phys.*, **38**, 1022 (1963).

(14) A. O. Allen and A. Hummel, *Discussions Faraday Soc.*, **36**, 95 (1963).

(15) M. Eigen and L. deMayer, *Z. Elektrochem.*, **59**, 986 (1955).

sibility of analogous measurements in liquid ammonia is restricted because the conductivity due to the transient ions produced by the radiation must be differentiated from that due to pure NH_3 and to the ionic impurities. To do this demands much higher transient ion concentrations than needed in hexane, and these produce much higher recombination rates. Allen and Hummel state that the ion-pair concentrations in their experiments were 10^9 ml.$^{-1}$ or less, while the liquid ammonia experiments reported here required of the order of 10^{12} ion pairs ml.$^{-1}$ at the steady state. At this 1000-fold higher concentration of transitory ions, the initial half-time of recombination was clearly much less than 1 sec. and very likely similar to the time required for removal of the source.

A specific conductivity as low at 10^{-11} ohm^{-1} cm.$^{-1}$ has been reported for highly purified liquid ammonia[16] but 1 week of washing the conductivity cell was required to achieve 10^{-9}.[16] The lowest achieved in this work was 4.5×10^{-7}. In view of the irreversible increase in conductivity with γ- irradiation, achievement of the highest purities would probably not be profitable in investigations of the present type. It is possible that the major impurity introduced by irradiation is water formed by the reaction of ammonia with absorbed O_2 on the electrodes and walls or with oxygen bound in the silicates in the walls. Conducting impurities are relatively unimportant in carefully purified hydrocarbon solvents. Allen and Hummel[14] used hexane having a specific conductivity of 10^{-15} to 10^{-17} ohm^{-1} cm.$^{-1}$.

(16) V. F. Hnizda and C. A. Kraus, *J. Am. Chem. Soc.*, **71**, 1565 (1949).

Application of Crystallization Theory to the Behavior of Greases

by J. Panzer

Esso Research and Engineering Company, Linden, New Jersey *(Received April 29, 1964)*

Theoretical equations derived in the literature for nucleation and growth rates in crystallization have been modified and combined to obtain the effects of isolated reaction variables on the rate of particle size change. Under the conditions used to make greases, the equations show that the average grease thickener particle size is reduced as the average temperature of reaction is reduced, as the thickener concentration is reduced, and as the oil viscosity is decreased. The predicted results agree well with numerous experimental observations reported in the literature. The effects of oil composition and surfactants on interfacial free energy and the effect of changes in the latter on particle size depend on the surface energy of the grease thickener and the manner in which adsorption on the solid surface takes place. The relationship between particle size, as a function of reaction variables, on grease properties, such as flow behavior and oil separation, will also be discussed.

There are many illustrations in the grease literature of the effect of thickener particle size and shape on grease properties.[1] Although some recent work suggests that aggregates are more important than the primary particles,[2] it seems quite clear that the size and shape of the primary particles will influence strongly the nature of the aggregates. It is also well

(1) G. V. Vinogradov and V. V. Sinitsyn, *J. Inst. Petrol.*, **47**, 357 (1961).

known that variation in the reaction conditions during grease preparation will affect the particle shape and size distribution and hence affect the properties of the grease. It was of interest to determine how well the theories of crystallization explain and predict the effects of reaction conditions on the formation of grease thickeners. In order to achieve this objective, some of the mathematical relationships described by currently accepted crystallization theory were manipulated so that the effect of several reaction variables on particle size could be defined. The predictions resulting from these equations were then compared with experimental observations made on many greases and some colloidal dispersions reported in the literature.

Derivation of Crystallization Equations

The formation of grease thickeners by the reaction of two or more components or by precipitation from a hot solution is a crystallization process involving two steps as in all crystallization processes—nucleation and growth. Nucleation involves some type of combination of molecules until a critical-sized embryo is formed, after which growth takes place by deposition of molecules from the supersaturated solution onto the nuclei. Usually, after the initial nuclei are formed, further nucleation and growth proceed simultaneously until the supersaturation of the system is relieved.

The theories of nucleation and growth show that the rates of both these steps are proportional to the diffusion rate of the crystallizing molecules and the degree of their supersaturation and are inversely proportional to the surface free energy of the nuclei.[3] For any system, it is possible to show for different reaction conditions related to the above variables that either nucleation rate or growth rate is predominant and, hence, determines how the particle size will change.

The Becker–Döring equation for the rate of homogeneous nucleation may be expressed as[3]

$$R_N \propto \frac{E^{1/2}S^2}{T^2} e^{-E^3/T^3(\ln S)^2} \qquad (1)$$

where E is the interfacial free energy between the embryo of the nucleus and supersaturated solution, S is the supersaturation ratio (ratio of concentration in supersaturated system to that at saturation), and T is the temperature. All other terms in the original equation are considered as constant and characteristic of any particular system under study. Diffusion rate has been considered in the above equation and is expressed as a function of temperature. The rate equation for heterogeneous nucleation is similar to eq. 1 and has an additional term which considers the interfacial energy between the heterogeneous nuclei and the crystallizing material. Since this term is characteristic of the particular system, it has been disregarded in this qualitative treatment.

In attempting to express R_N as a function of individual variables it is necessary to make some assumptions about the relationships of S, T, and E to each other. Because all the factors in the Becker–Döring equation which are characteristic of specific crystallizing systems are not known quantitatively, the assumed relationships between S, T, and E are rather primitive.

It is known that in most systems containing a given quantity of solute and solvent, a reduction in temperature will increase the supersaturation for a finite time. Thermodynamics suggests that the relationship between S and T may not be linear, but for the sake of simplifying this qualitative treatment, it has been speculated that a linear relationship exists which may be expressed as $S \propto 1/T$. Thermodynamics also shows that interfacial free energy is linearly related to temperature and in a system in which all other variables are constant, it can be assumed that $E \propto T$. As mentioned above the diffusion rate has been incorporated into eq. 1 as a function of temperature, using the Nernst diffusion law. Substituting these simple relationships into eq. 1 the following was obtained

$$R_{N(T)} \propto T^{-3.5} e^{-1/(\ln T)^2} \qquad (2)$$

Holding T and E constant for any system, R_N may be expressed as a function of supersaturation

$$R_{N(S)} \propto S^2 e^{-1/(\ln S)^2} \qquad (3)$$

Finally by considering T and S constants, R_N as a function of E was obtained

$$R_{N(E)} \propto E^{1/2} e^{-E^3} \qquad (4)$$

A relation for growth rate has been derived by Tausch[3] and may be expressed

$$R_G \propto \frac{TD(S-1)\ln S}{E\left(1 + \frac{K}{Y_0} + K' \ln Y_0\right)} \qquad (5)$$

D = diffusion rate; $Y_0 \propto E/T \ln S$; K and K' are constants characteristic of any system.

Unless the values for K and K' are known, it is

(2) R. Vold, *VLGI Spokesman*, 15 (10), 9 (1952); A. S. Michaels and J. C. Bolger, *Ind. Eng. Chem. Fundamentals*, 1, 24 (1962).

(3) F. W. Tausch, Jr., Ph.D. Thesis, Massachusetts Institute of Technology, 1961; review of literature, containing many references to original papers on theory.

difficult to use eq. 5 to determine the relative effects of temperature, supersaturation, and interfacial energy on growth rate. Numerical analysis of eq. 5 indicated that changes in the denominator caused by changes in the variables are directionally the same as those in the numerator and showed that the denominator changes at a much lower rate than the numerator. Thus, by disregarding the denominator in eq. 5 similar relationships were obtained, and the equation can be used to determine relative changes in R_G. R_G was now expressed as

$$R_G \propto \frac{TD(S-1)\ln S}{E} \tag{6}$$

R_G as a function of temperature only may be obtained by considering again the relationships between T, S, and E. $D \propto T$ by the Nernst diffusion law. Therefore

$$R_{G(T)} \propto (T-1)\ln T \tag{7}$$

R_G as a function of S, only with T, D, and E constant, is

$$R_{G(S)} \propto (S-1)\ln S \tag{8}$$

Finally, R_G as a function of E may be obtained by holding T, D, and S constant.

$$R_{G(E)} \propto \frac{1}{E} \tag{9}$$

In attempting to combine the over-all effect of the variables in both nucleation and growth steps on the rate of particle size increase, R_p, it has been assumed that R_p is proportional to the growth rate and inversely proportional to the nucleation rate as in expression 10. The nucleation and growth terms are

$$R_p \propto R_G + \frac{1}{R_N} \tag{10}$$

used additively in the particle size equation since the two crystallization steps are sequential. For the purposes of this qualitative discussion it does not matter whether we express R_p as in eq. 10 or as

$$R_p \propto \frac{R_G}{R_N}$$

since both equations give similarly shaped curves.

The effects of the variables on R_p may be expressed by the equations

$$R_p \propto (T-1)\ln T + T^{3.5}e^{1/(\ln T)^2} \tag{11}$$

$$R_p \propto (S-1)\ln S + S^{-2}e^{1/(\ln S)^2} \tag{12}$$

$$R_p \propto \frac{1}{E} + E^{-1/2}e^{E^2} \tag{13}$$

Comparison of Theory and Literature Observations

In the following discussions each variable is treated individually so that comparisons with observations reported in the literature may be made.

A. Effect of Temperature. A graphical representation of eq. 2 and 7 is shown in Fig. 1. Before interpreting the curves in Fig. 1, one should keep in mind that the curves in this and in other figures to follow merely represent the *relative* effect of a particular variable on crystallization. The actual shapes of the curves for a specific system would depend on the constants characteristic of the system. The important

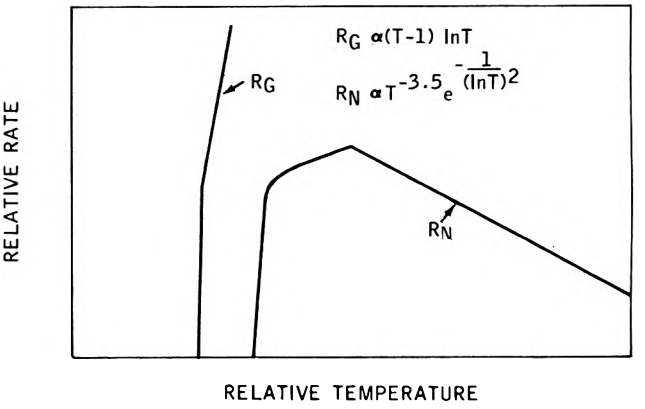

Figure 1. Effect of temperature on nucleation and growth rates.

point is that the general habit of the curves, indicating directionally the changes in growth and nucleation rates, would be the same for all systems.

In Fig. 1, as the temperature is increased up to some critical temperature characteristic of the system, the nucleation rate and growth rate both increase rapidly. Above the critical temperature the growth rate continues to rise but the nucleation rate decreases.

This effect is shown more clearly in Fig. 2 where the rate of particle size increase, R_p, is plotted as a function of temperature (eq. 11). Figure 2 shows that the rate of particle size increase falls to a minimum level at some critical temperature and then rises with increasing temperature. This observation suggests that each grease system has some characteristic critical temperature at which particle growth rate may be carefully controlled to obtain a desired particle size. Consistent with this suggestion is the finding that some soap-thickened greases have transition temperatures at which optimum fiber formation occurs.[4]

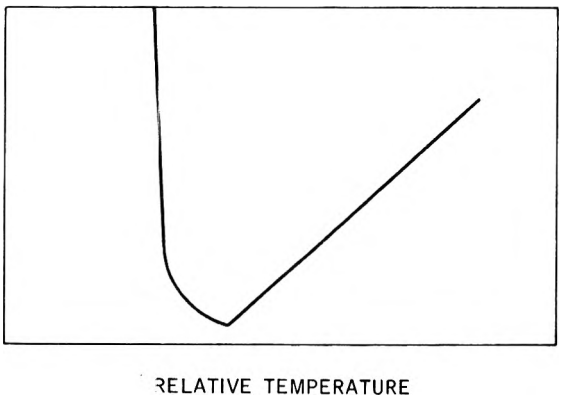

Figure 2. Effect of temperature on rate of particle size increase.

For a given grease manufacturing procedure it is difficult to say what effect temperature has on particle size unless one knows the critical temperature for the system. However, in order to obtain grease thickener particles of suitable size at a reasonable rate, the average temperature used in most greases would probably be above the critical point. The theory predicts that the lower this average temperature (or the greater the cooling rate), the lower the average particle size. This prediction is supported by an equation derived by Packter, showing the effect of temperature on particle size, insofar as it affects solubility and supersaturation.[5] A summary of the data reported in the literature for several different greases shows agreement with the predictions in every case (see Table I).

Particle size observations in most instances were made by electron microscopy after eluting the oil from the grease with a suitable solvent. In some of the older reports the observations depended on light microscopy. Viscosity measurements on the greases were made with the ASTM penetrometer which measures the penetration of a weighted cone into a cup of grease. It is believed that this measurement provides an indication of yield stress and viscosity at low shear rates. In several reports describing fluid suspensions, viscosity measurements were made with conventional viscometers. Shear breakdown is the extent to which a grease softens, as measured by the penetrometer, after it is sheared in a fixed, arbitrary manner. Oil separation measurements were determined by the amount of oil which passed through a filter or screen after a grease had been subjected to the forces of gravity or additional pressure.

Table I: Effect of Cooling Rate on Grease Properties

	Effect of increase in rate on			
Grease type	Particle size of thickener	Grease viscosity	Oil separation	Ref.
Sodium	Decrease	Increase	Decrease	*a*
Lithium	Decrease		Decrease	*b*
Lithium	Decrease	Increase		*c*
Lithium	Decrease; shorter fibers	Increase		*d*
Lithium	Decrease		Decrease	*e*
Arylurea	Decrease	Increase	Decrease	*f*

[a] I. E. Puddington, *NLGI Spokesman*, **9** (9), 1 (1945); W. Gallay and I. E. Puddington, *Can. J. Res.*, **B22**, 90 (1944). [b] V. V. Sinitsyn, *et al.*, *Kolloidn. Zh.*, **22**, 469 (1960). [c] B. W. Hotten and D. H. Birdsall, *J. Colloid Sci.*, **7**, 284 (1952). [d] A. A. Trapeznikov, *et al.*, *Izv. Akad. Nauk SSSR, Ser. Fiz.*, **23**, 777 (1959). [e] A. A. Trapeznikov and G. G. Shchegolev, *Kolloidn. Zh.*, **24**, 104 (1962). [f] J. J. Chessick and J. B. Christian, *NLGI Spokesman*, **26**, 172 (1962).

The significance of the temperature effect is that as the particle size decreases, the grease viscosity (or consistency) increases, and the oil separation decreases. A more complete summary of the observed effects of particle size decrease on grease properties, regardless of how reaction variables affect particle size, is shown in Table II. The few deviations in Table II from the general effects suggest that for any grease system there may be an optimum particle size on either side of which changes in particle size may have opposite effects on grease properties.

B. Effect of Thickener Concentration. The concentration of the thickener in solution determines the degree of supersaturation, one of the variables in the crystallization equations. An increase in concentration would also increase the diffusion rate, but offsetting this is an increase in viscosity produced by the higher concentration. Because of these effects and because both nucleation and growth rates are related to diffusion rate in the same way, for all practical purposes we can ignore the effect of the concentration on diffusion rate in comparing the two crystallization steps and consider only supersaturation at any given temperature.

Therefore, the effect of the concentration on the nucleation and growth rates may be expressed by eq. 3 and 8. These equations are shown graphically in Fig. 3. Although both rates increase as supersaturation increases, the growth rate increases faster initially, but more slowly after some level of supersaturation.

The over-all effect of concentration (or supersaturation) on particle size is defined by eq. 12. The curve representing this function is shown by Fig. 4 and indi-

(4) J. B. Matthews, *J. Inst. Petrol.*, **39**, 265 (1953); R. M. Suggitt, *NLGI Spokesman*, **24**, 367 (1960).

(5) A. Packter, *J. Phys. Chem.*, **62**, 1025 (1958).

Table II: Effect of Decrease in Particle Size on Grease Properties

Grease type	Effect on: Viscosity	Shear breakdown	Oil separation	Ref.
Lithium	Increase			*a*
Lithium		Decrease		*b*
Lithium (decrease L/D)[c]		Increase	Decrease	*d*
Lithium			Decrease	*e*
Aluminum			Increase	*f*
Calcium acetate	Increase	Increase	Decrease	*g*
Calcium carbonate	Increase			*h*
Calcium carbonate	Increase			*i*
Starch	Increase			*j*
Glass spheres	Increase	Increase		*k*
(Several greases compared)[l]			Decrease	*m*
Sodium	Increase		Decrease	*n*
Arylurea	Increase		Decrease	*o*

[a] See ref. *c*, Table I. [b] T. A. Renshaw, *Ind. Eng. Chem.*, **47**, 834 (1955). [c] The change in particle size for this system involved the length to diameter ratio (L/D). [d] A. C. Borg and R. H. Leet, *Sci. Lubrication* (London), **9** (6), 24 (1957); *Lubrication Eng.*, **13**, 156 (1957); *ibid.*, **15**, 450 (1959). [e] See ref. *b*, Table I. [f] A. Rochow, "Physical Methods of Organic Chemistry," Vol. I, Part 3, A. Weissberger, Ed., John Wiley and Sons, Inc., New York, N. Y., 1954. [g] J. Panzer, *Lubrication Eng.*, **15**, 453 (1959). [h] H. W. Siesholtz and L. H. Cohan, *Ind. Eng. Chem.*, **41**, 390 (1949). [i] A. C. Zettlemoyer and G. W. Lower, *J. Colloid Sci.*, **10**, 29 (1955). [j] H. R. Kruyt and F. G. van Selms, *Rec. trav. chim.*, **62**, 407 (1943). [k] P. S. Williams, *Discussions Faraday Soc.*, **11**, 47 (1951). [l] This study did not consider differences in thickener type. [m] B. W. Hotten and D. H. Birdsall, *Ind. Eng. Chem.*, **47**, 447 (1955). [n] I. E. Puddington, footnote *a*, Table I. [o] See ref. *f*, Table I.

cates that as S increases from unity, R_p falls rapidly to a minimum and then increases. Von Weimarn's rule that an increase in S would reduce the particle size is predicted from the left portion of the curve.

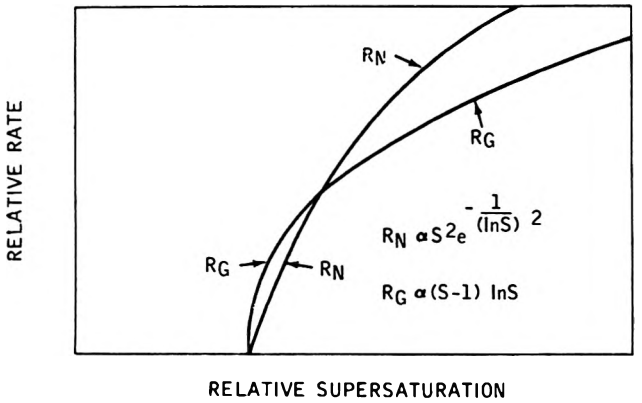

Figure 3. Effect of supersaturation on nucleation and growth rates.

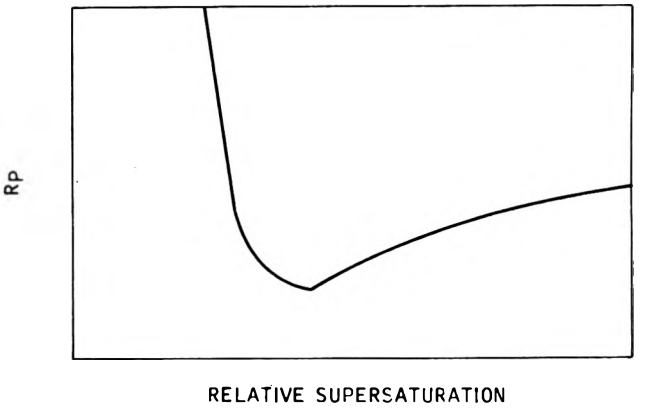

Figure 4. Effect of supersaturation on rate of particle size increase.

To achieve crystallization at the high rate that is generally practiced in grease manufacture, the value of S would probably be high enough so that a further increase in S would result in larger particles. Thus, one would predict that the greater the concentration, the larger the ultimate particle size. Packter's equation shows a similar prediction for systems with a given solubility.[5] Two literature reports on sodium greases are in agreement with this prediction (see Table III).

Table III: Effect of Increase in Thickener Concentration on Grease Properties

Grease type	Effect on particle size of thickener	Ref.
Sodium	Increase L/D	*a*
Sodium	Increase L/D	*b*

[a] See ref. *a*, Table I. [b] B. B. Farrington and D. H. Birdsall *NLGI Spokesman*, **11** (1), 4 (1947).

C. Effect of Oil Viscosity. The viscosity of the base oil in a grease affects the diffusion rate, but this variable is related in the same way to both nucleation and growth rate (directly proportional). Therefore, the theoretical equations do not indicate which rate will predominate unless one knows the magnitude of the constant terms in the equations (characteristic of the particular system). One may speculate that, because nucleation is the first step in crystallization, its rate would determine the particle size. An increase in viscosity would decrease the diffusion rate which in turn would decrease the nucleation rate. Although the growth rate also would be decreased, the fact that the material in solution would not be used up too

rapidly in nucleation means that particle growth could proceed to some extent. If the reaction time were long enough, one would expect an increase in particle size as the viscosity increases.

This prediction is borne out in most cases, as shown in Table IV. The grease system showing the reverse behavior illustrates the difficulty in making a prediction when diffusion affects both rates in the same way.

Table IV: Effect of Increase in Oil Viscosity on Grease Properties

	Effect on			
Grease type	Particle size of thickener	Grease viscosity	Oil separation	Ref.
Sodium	Decreases L/D		Decrease	*a*
Sodium	Increases L/D			*b*
Lithium	Increase		Decrease	*c*
Lithium			Decrease	*d*
Lithium (thermally dispersed)	Increases L/D	Decrease		*e*
Lithium		Increase	Decrease	*f*
Lithium–calcium			Decrease	*g*
Barium			Decrease	*h*
Calcium			Decrease	*i*
Aluminum		Decrease		*e*
Silica		Increase		*e*
Bentone 34		Increase		*e*

[a] See ref. *a*, Table I. [b] A. Bondi, *et al.*, *World Petrol. Congr., Proc. 3rd, The Hague*, **VII**, 373 (1951). [c] V. V. Sinitsyn, *et al.*, *Zh. Prikl. Khim.*, **31**, 1202 (1958). [d] V. V. Sinitsyn, *et al.*, *Kolloidn. Zh.*, **22**, 469 (1960). [e] B. W. Hotten and A. L. McClennan, *NLGI Spokesman*, **24**, 268 (1960). [f] G. S. Bright and J. H. Greene, *ibid.*, **26**, 294 (1962). [g] J. L. Zakin and G. W. Murray, Jr., *ibid.*, **25**, 354 (1962). [h] T. D. Smith, F. Arnott, and L. W. McClennan, *ibid.*, **14** (4), 10 (1950). [i] B. B. Farrington and R. L. Humphreys, *Ind. Eng. Chem.*, **31**, 230 (1930).

The effects of oil viscosity on grease properties are also worth noting in Table IV. The effect of oil viscosity on grease viscosity varies. If there were no particle size change and the base oil viscosity increased, we would expect an increase in grease viscosity. This is borne out with silica and bentonite greases. Therefore, the decrease in grease viscosity (as oil viscosity increases) observed with the other greases indicates that particle size has a substantial effect. Probably an increase in particle size causes a decrease in grease viscosity more than offsetting the increase contributed by the oil itself.

Wherever oil separation was studied, it was found to decrease as oil viscosity increased. It is difficult to say, from the data available, the extent to which particle size affects oil separation, but the decrease in mobility of the particles caused by a viscosity increase would easily account for a decrease in oil separation.

D. Effect of Oil Composition and Surfactants. Variation in oil composition and the use of surface-active additives can affect particle size by changing the interfacial free energy, E, between the particles and the supersaturated solution. Therefore, the relationships expressed in eq. 4 and 9 should apply to these variables. The curves for these two equations are shown in Fig. 5.

The relative effect of any change in the energy on nucleation and growth rate depends on the value of E at which the observations are initiated. For example, if E is below some critical value (represented by $E = 0.5$, Fig. 5), a further reduction in E would produce an increase in growth rate and a decrease in nucleation rate and larger particles would be expected to form. If E is initially at some point higher than this critical level, a reduction in E would produce a larger increase in nucleation rate, so that smaller particles form. The net effect of nucleation and

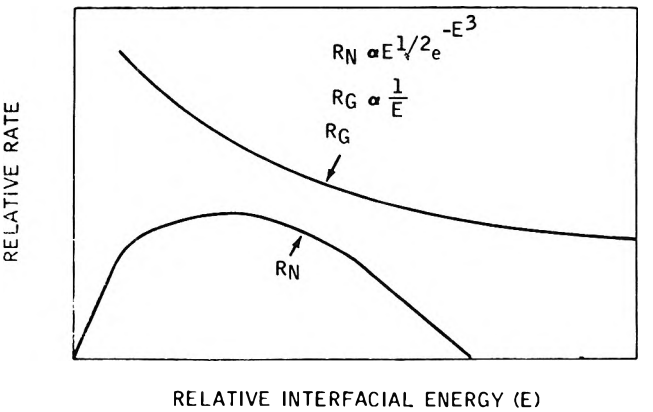

Figure 5. Effect of interfacial free energy on nucleation and growth rates.

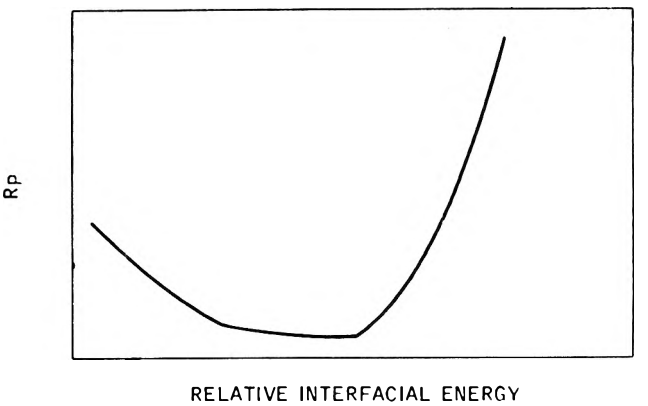

Figure 6. Effect of interfacial free energy on rate of particle size increase.

growth on the rate of particle size increase is expressed by eq. 13 and is plotted in Fig. 6.

Further complicating the picture is how a change in composition actually affects E. One would expect that the more polar the oil (or with the use of surfactants), the greater the reduction of E. However, the polar materials may adsorb on the crystal surface and limit further growth by sterically hindering deposition of new molecules, thus reducing the average particle size. If the adsorption occurs preferentially on one crystal face, the particle shape may be altered. Also depending on which part of the crystal the polar material adsorbs, it may decrease or increase E.

Because of all these possibilities, it is difficult to predict how a change in oil composition will affect particle size. Still the theory may be useful in one respect. After carrying out a few experiments on a given system and observing the actual effects of changes in oil composition, some estimates can be made regarding the mechanism of the action of polar materials in the oil. An understanding of the mechanism may suggest how to control grease properties by the selection of oils or surfactants.

The summary of literature studies in Table V shows different effects of base oil viscosity index, VI, on particle size (the higher the VI, the less polar the oil) further illustrating the difficulty in making predictions. However, there is no doubt, from the work done on greases and on other systems, that oil composition does affect particle size. It is interesting to note that in all cases where oil separation was studied, an increase in VI increased separation. Unfortunately, it is not yet known to what extent the interactions between the particles and oil alone (irrespective of particle size) are responsible for this effect.

Table V: Effect of Oil Composition on Grease Properties

Grease type	Effect on: Oil variation	Effect on: Particle size of thickener	Effect on: Oil separation	Ref.
Sodium	Increase VI	Decrease		*a*
Lithium	Increase VI		Increase	*b*
Lithium	Increase VI	Increase		*c*
Lithium–calcium	Increase VI		Increase	*d*
Carbon black suspension	Increase VI		Increase	*e*
(Unidentified)	Increase VI		Increase	*f*
	Unspecified effects			
Sodium				*g*
Lithium				*h, i*
Carbon black	Affects oil separation			*j*
Lithium–calcium	Affects oil separation			*k*

[a] See ref. a, footnote *a*, Table I. [b] See ref. *b*, Table I. [c] See ref. *c*, Table I. [d] S. J. M. Auld, H. M. Davies, and E. G. Ellis, *World Petrol. Congr., Proc., 3rd, The Hague*, **VII**, 355 (1951). [e] M. van der Waarden, *J. Colloid Sci.*, **5**, 317 (1950). [f] S. F. Calhoun, *NLGI Spokesman*, **22**, 70 (1958). [g] See ref. *b*, Table IV. [h] See ref. *c*, Table IV. [i] V. V. Sinitsyn, *et al.*, *Khim. i Tekhnol. Topliv. i Masel.*, **3** (11), 51 (1958). [j] F. H. Garner, *et al.*, *J. Inst. Petrol.*, **38**, 974 (1952). [k] See ref. *g*, Table IV.

Conclusion

Relationships have been derived from crystallization theory to show the effect of several reaction conditions on the particle size of grease thickeners. Agreement with experimental data reported in the literature is excellent. Therefore, the theoretical treatment can be useful in indicating directionally what changes should be made in a grease to achieve a desirable particle size distribution or shape. It would be of interest to determine the relative effects of the several reaction variables on particle size for a single system. Qualitative evaluation of the equations suggests that the factors affecting interfacial free energy would far outweigh variation in temperature or supersaturation.

Before the theory can be used to make quantitative predictions, more must be learned about the factors which are characteristic of each system. Also, quantitative determinations of how surfactants affect the interfacial free energy need to be made. Finally, in order to apply particle size information to the quantitative predictions of grease properties it is necessary to establish first the physical interactions among the grease components themselves.

Single Electrode Potentials

by Irwin Oppenheim

Department of Chemistry, Massachusetts Institute of Technology, Cambridge, Massachusetts
(Received April 30, 1964)

A nonthermodynamic technique for measuring absolute values of single electrode potentials is proposed. The technique involves the measurement of the quadrupole radiation emitted by an electrode which is made to execute harmonic motion by mechanical or ultrasonic means. Thus, the concept of a single electrode potential becomes operationally meaningful.

Introduction

There has been for many years a controversy concerning the operational significance of single electrode potentials. Indeed, single electrode potentials cannot be determined by thermodynamic type measurements. Thus, in a sense, the measurement of a single electrode potential does not yield thermodynamically useful information. Since charge cannot be transported independently of mass (*i.e.*, it is always associated with electrons, ions, etc.), the work done in transporting a charge across a phase boundary consists of two parts: electrical work against the electric field and nonelectrical work against the electromotive force due to the difference in composition of the two phases. Therefore, the evaluation of the difference of electrostatic potential between two phases, differing in composition, cannot be determined by a charge-transfer experiment. This is in distinction to the measurement of the electrostatic potential at any point in a homogeneous system by determining the electrostatic work done in transporting a unit test charge from infinity to the point in question. It is, of course, a simple matter to determine the difference in electrostatic potential between the electrodes of a galvanic cell, and the single electrode potentials which are often listed in the literature are actually potentials of the given electrode relative to the normal hydrogen electrode as a standard.

We take the point of view that the electrostatic potential at any point in space in any medium is determined by the charge distribution over all space. Thus, if there exists an experimental technique which measures the charge distribution, the electrostatic potential is determined and becomes operationally significant. In this paper, we propose an experimental method for measuring the relevant charge distribution which determines a single electrode potential. The experiment is described and the analysis of the experiment is sketched. The analysis is not carried through in complete detail because of complicated geometric effects. However, it is carried through far enough to demonstrate that single electrode potentials can be measured at least in principle. We note that it is, of course, sufficient to measure the absolute potential of only one electrode since the potentials of all other electrodes can be determined by usual techniques using that electrode as a standard.

Model of a Single Electrode

We consider, for definiteness, a half-cell which consists of a metallic electrode M partially immersed in an electrolyte solution MX which contains the metallic ion M^+. We denote the metallic electrode as phase (1) and the electrolyte solution as phase (2). The phase boundary is impermeable to some charge carriers. The constant electrostatic potential in the interior of the metal is ϕ^1 and the constant electrostatic potential in the interior of the electrolyte is ϕ^2. The experiment that we shall propose is capable of measuring ϕ^1 and/or $\phi^1 - \phi^2$.

We assume that the charge distribution which gives rise to the electrostatic potential difference $\phi^1 - \phi^2$ is a double layer at the surface of the electrode immersed in the electrolyte. The electrostatic potential ϕ^1 can be determined by a measurement of the double layer at the surface of the electrode which projects above the surface of the electrolyte solution.

Thus, by a measurement of the strengths of the double layers ϕ^1 and/or $\phi^1 - \phi^2$ can be determined. Either ϕ^1 or $\phi^1 - \phi^2$ may be considered to be the single

electrode potential depending upon which convention one wishes to use.

Description of Proposed Experiment

We propose to measure the strengths of the double layers described above by observation of the quadrupole radiation emitted when the double layers are accelerated. The half-cell is made to execute simple harmonic motion perpendicular to one of the faces of the electrode. The oscillation is produced either mechanically or by using ultrasonic techniques. The oscillating double layers emit quadrupole radiation which is characterized by its angular dependence. The intensity of the radiation can be measured at least in principle by properly tuned receivers. The frequency of the radiation is the same as the frequency of the oscillation. The quantities which must be measured in order to determine the strength of the double layers are the intensity and frequency of the radiation, the amplitude of the oscillation, and the pertinent geometric factors. A complete analysis of the experiment would also require the description of the hydrodynamic effects set up by the oscillation of the double layer. These effects can be predicted, at least in principle, for given experimental conditions and for a given model of the double layer.

Analysis of the Experiment

An accelerating point charge e gives rise to an electric field vector $\vec{E}$ of the form

$$\frac{4\pi\epsilon}{e}\vec{E}(\vec{r}_0,t) = \frac{1}{\left(r - \frac{\vec{u}\cdot\vec{r}}{c}\right)^3}\left(\vec{r} - r\frac{\vec{u}}{c}\right)\left(1 - \frac{u^2}{c^2}\right) + \frac{1}{c^2\left(r - \frac{\vec{u}\cdot\vec{r}}{c}\right)^3}\left[\vec{r}\times\left[\left(\vec{r} - \frac{r\vec{u}}{c}\right)\times\vec{u}\right]\right] \quad (1)$$

where ϵ is the dielectric constant of the medium, $\vec{r}\,(t')$ is the time dependent distance between the point of observation $\vec{r}_0$ and the accelerating charge $\vec{r}_s$, $\vec{u}(t')$ is the time dependent velocity of the charge, $\dot{\vec{u}}(t')$ is the acceleration of the charge, $t' = t - r/c$ is the retarded time, t is the time of observation, and c is the velocity of light. If $u/c << 1$, we can neglect relativistic effects and eq. 1 simplifies to

$$\frac{4\pi\epsilon}{e}\vec{E} = \frac{\vec{r}}{r^3} + \frac{1}{c^2r^3}(\vec{r}\times[\vec{r}\times\dot{\vec{u}}]) \quad (2)$$

If the charge executes simple harmonic motion along the z-axis centered at the origin with amplitude A and angular frequency ω, then

$$\vec{r}(t') = \vec{r}_0 - \hat{z}A\sin\omega t'$$
$$\vec{u}(t') = -\frac{d\vec{r}}{dt'} = \hat{z}A\omega\cos\omega t' = \hat{z}u(t') \quad (3)$$
$$\dot{\vec{u}}(t') = \frac{d^2\vec{r}}{dt'^2} = \hat{z}A\omega^2\sin\omega t' = \hat{z}\dot{u}(t')$$

where $\hat{z}$ is a unit vector along the z-axis. Substitution of eq. 3 into eq. 2 yields

$$\frac{4\pi\epsilon}{e}\vec{E}(\vec{r}_0,t) = \frac{(x,y,z)}{r^3} + \frac{\dot{u}(t')(xz,yz,-(x^2+y^2))}{c^2r^3} \quad (4)$$

where the symbol (a, b, c) stands for a vector with x-component equal to a, y-component equal to b, and z-component equal to c.

The electric field vector $\vec{E}_D(\vec{r}_0,t)$ at $\vec{r}_0$ at time t due to a dipole with dipole moment $m\hat{z}$ which executes simple harmonic motion along the z-axis centered at the origin with amplitude A and angular frequency ω is easily obtained from eq. 4 in the form

$$4\pi\epsilon\vec{E}_D = -m\frac{\partial\vec{E}}{\partial z}$$
$$= -m\left\{\frac{(0,0,1)}{r^3} - 3z\frac{(x,y,z)}{r^5} + \frac{\dot{u}(x,y,o)}{c^2r^3} - \frac{3\dot{u}z(xz,yz,-(x^2+y^2))}{c^2r^5} + \frac{\partial\dot{u}}{\partial z}\frac{(xz,yz,-(x^2+y^2))}{c^2r^3}\right\} \quad (5)$$

where

$$\frac{\partial\dot{u}}{\partial z} = -A\frac{\omega^3}{c}\frac{z}{r}\cos\omega(t - r/c) \quad (6)$$

We next consider a dipole layer with dipole moment per unit area $\tau\hat{z}$ which executes simple harmonic motion in the z-direction centered at the origin with amplitude A and angular frequency ω. The z-axis passes through the center of the dipole layer. The vector position of the point of observation $\vec{r}_0$ is given by (x_0, y_0, z_0). The vector position of a point in the dipole layer $\vec{r}_s$ is given by $(x_s, y_s, z_s(t))$ where $z_s(t) = A\sin\omega(t - r/c)$. The vector distance $\vec{r} = \vec{r}_0 - \vec{r}_s$ is given by $(x_0 - x_s, y_0 - y_s, z_0 - z_s(t))$. The electric field vector at $\vec{r}_0$ at time t due to the oscillating dipole layer $\vec{E}_{DL}(\vec{r}_0,t)$ is given by

$$\vec{E}_{DL}(\vec{r}_0,t) = \frac{\tau}{m}\int_a\vec{E}_D\,dx_s dy_s \quad (7)$$

where $\vec{E}_D$ is given by eq. 5, and the integral is over the area of the dipole layer. In order to simplify the cal-

culation, since we are not interested in an exact analysis at this time, we assume that the linear dimensions of the dipole layer are small compared to r. Under these conditions eq. 7 becomes

$$\vec{E}_{DL}(\vec{r}_0,t) = \frac{\tau a}{m}\vec{E}_D(\vec{r}_0,t) \tag{8}$$

where a is the area of the dipole layer. Further, we are interested only in that part of $\vec{E}_D$ which falls off as $1/r$ since this is the part that contributes to the radiation field. We denote the radiation field by $\vec{E}_{DL}^{rad}$ and find from eq. 5, 6, and 8 that

$$4\pi\epsilon\vec{E}_{DL}^{rad}(\vec{r}_0,t) = \tau a A\frac{\omega^3}{c^3}\cos[\omega(t - r/c)] \times \frac{(xz^2, yz^2, -z(x^2+y^2))}{r^4} \tag{9}$$

The polar components of E_{DL}^{rad} are given by

$$\begin{aligned} E_{DL}^{rad}{}_r &= 0 \\ E_{DL}^{rad}{}_\phi &= 0 \\ E_{DL}^{rad}{}_\theta &= \frac{\tau a A}{8\pi\epsilon}\frac{\omega^3}{c^3}\cos\omega(t - r/c)\frac{\sin 2\theta}{r} \end{aligned} \tag{10}$$

which are characteristic of quadrupole radiation. The amount of energy radiated per unit time per unit solid angle $I(\theta,t)$ is given by

$$I(\theta,t) = \epsilon c(E_{DL}^{rad})^2 r^2 \tag{11}$$

which is in order of magnitude

$$I(\theta,t) \sim \frac{a^2A^2}{64\pi^2}\epsilon\left(\frac{\tau}{\epsilon}\right)^2\frac{\omega^6}{c^5}\sin^2 2\theta \tag{12}$$

where we have used eq. 10.

The crucial fact is that the potential difference across a dipole layer is related to the dipole moment per unit area by an expression of the form

$$\Delta\phi = \tau/\epsilon \tag{13}$$

where the dielectric constant appearing in eq. 13 and in fact in all of the equations of this section is that for the bulk medium. In the analysis of an actual experiment, an additional factor depending on the geometry involved would appear in eq. 13; the value of $\Delta\phi$ is independent of geometry for electrodes of macroscopic dimensions. For our purposes, we can use eq. 13 as it stands. Substitution of eq. 13 into eq. 12 yields the final result

$$I(\theta,t) \sim \frac{a^2A^2}{64\tau^2}\frac{\omega^6}{c^5}\epsilon(\Delta\phi)^2\sin^2 2\theta \tag{14}$$

Thus a measurement of I determines $\Delta\phi$ if a, A, ω, and ϵ are known. Equation 14 is in m.k.s. units so that the units of I are coulomb volts/sec., the unit of length is the meter, the unit of ϵ is farads/m., the units of $\Delta\phi$ is volts, and the unit of time is the second.

In order to arrive at an estimate of the intensity of radiation to be expected, we shall carry through a calculation using typical experimental parameters. We choose $a = 10^{-3}$ m.^{2}, $A = 10^{-3}$ m., $\epsilon = 10^7/4\pi c^2$, the dielectric constant of free space, and we assume that $\Delta\phi$ will be of the order of 1 v. for a typical electrode. Substitution of these quantities into eq. 14 results in

$$\begin{aligned} I(\theta,t) &\sim 5.75 \times 10^{-69}\omega^6\sin^2 2\theta \text{ coulomb v./sec./steradian} \\ &= 3.6 \times 10^{-50}\omega^6\sin^2 2\theta \text{ e.v./sec./steradian} \\ &= 5.75 \times 10^{-62}\omega^6\sin^2 2\theta \text{ ergs/sec./steradian} \\ &= 5.5 \times 10^{-35}\omega^5\sin^2 2\theta \text{ photons/sec./steradian} \end{aligned} \tag{15}$$

The maximum frequency of oscillation which can be obtained using ultrasonic techniques is approximately 10^8/sec. Thus the intensity of radiation $I(\theta,t)$ becomes

$$\begin{aligned} I(\theta) &\sim 5.75 \times 10^{-14}\sin^2 2\theta \text{ ergs/sec./steradian} \\ &= 5.5 \times 10^5\sin^2 2\theta \text{ photons/sec./steradian} \end{aligned} \tag{16}$$

at a frequency of 10^8/sec. or a wave length of 20 m. This radiation is to be detected by a receiver which can be designed to cover a large solid angle.

Our aim has not been to suggest that the experimental method described here is practicable with present techniques but to emphasize that a single electrode potential is measurable in principle.

Acknowledgment. The author is grateful for the support given this work by a grant from the National Science Foundation.

Catalysis over Supported Metals. II. The Effect of the Support on the Catalytic Activity of Nickel for Ethane Hydrogenolysis

by W. F. Taylor, D. J. C. Yates, and J. H. Sinfelt

Esso Research and Engineering Co., Process Research Division, Linden, New Jersey *(Received April 30, 1964)*

The kinetics of hydrogenolysis of ethane to methane were studied over a series of nickel catalysts in which the nickel was supported on three different oxides: silica, alumina, and silica–alumina. The rate measurements were made in a differential flow reactor at temperatures in the range of 175 to 275°. The nickel surface areas of the catalysts were determined by hydrogen chemisorption. This made it possible to determine the specific catalytic activity of the nickel in terms of rate of hydrogenolysis per unit area of nickel surface. Effects of the support over and above those due simply to differences in the degree of dispersion of the nickel could therefore be determined. The specific catalytic activity of the nickel varied over 50-fold for the various supports. The activity was highest for the silica support and lowest for the silica–alumina. The results of these studies suggest a specific interaction between the nickel and support.

I. Introduction

In supported metal catalysts, the effect of the support on the properties of the catalyst has commonly been assumed to be physical in nature. For example, it is clear that the support disperses the metal and leads to higher metal surface areas (although the cause of this high dispersion is not clear). The dispersion retards crystal growth by sintering and hence stabilizes the high surface area of the metal.[1] These are important advantages for supported metal systems and account for their wide use as catalysts in actual practice.

If we adopt the view that the metal and support do not interact chemically, the catalytic properties of a metal should be essentially independent of the support, apart from effects arising from differences in dispersion of the metal. However, evidence for specific metal–support interactions in supported systems has recently emerged from infrared studies of molecules adsorbed on supported metals[2–4] and from studies on the electronic properties of supported metals.[5] Effects of the support on the catalytic activities of metals have also been reported.[5–7] These observations indicate that supported metal catalysts are more complex than has commonly been thought. In this connection, however, it should be realized that the phenomenon of bifunctional catalysis, in which the metal and support have separate catalytic properties of their own, has been recognized for some time in the reactions of hydrocarbons over metal–acidic oxide catalysts.[8–10] This phenomenon is not necessarily related to a metal–support interaction, since the role of the support in such systems may be simply one of catalyzing the further reaction of an intermediate which forms on the metal sites and migrates to acidic sites on the support. That is, the metal and acidic sites can act independently; such an effect has been shown by several investigators.[11–13]

(1) G. C. Bond, "Catalysis by Metals," Academic Press, Inc., New York, N. Y., 1962, pp. 38–42.

(2) R. P. Eischens and W. A. Pliskin, *Advan. Catalysis*, **10**, 2 (1958).

(3) C. E. O'Neill and D. J. C. Yates, *J. Phys. Chem.*, **65**, 901 (1961).

(4) C. E. O'Neill and D. J. C. Yates, *Spectrochim. Acta*, **17**, 953 (1961).

(5) G. M. Schwab, J. Block, W. Muller, and D. Schultze, *Naturwiss.*, **44**, 582 (1957).

(6) E. B. Maxted and S. Akhtar, *J. Chem. Soc.*, 1995 (1960).

(7) E. B. Maxted and J. S. Elkins, *ibid.*, 5086 (1961).

(8) F. G. Ciapetta and J. B. Hunter, *Ind. Eng. Chem.*, **45**, 147 (1953); **45**, 155 (1953).

(9) F. G. Ciapetta, *ibid.*, **45**, 159 (1953); **45**, 162 (1953).

(10) G. A. Mills, H. Heinemann, T. H. Milliken, and A. G. Oblad, *ibid.*, **45**, 134 (1953).

(11) P. B. Weisz and E. W. Swegler, *Science*, **126**, 31 (1957).

While there is evidence for specific metal–support interactions in supported metal catalysts, there are no accurate data available to demonstrate an effect of the support on the specific catalytic activity of a metal, *i.e.*, the activity per unit surface area of the metal. This is due primarily to the fact that data on the surface area of the supported metal itself are seldom available. Information of this kind is absolutely essential in defining the effect of the support, and in the absence of such information any effect on catalytic activity could be entirely confused by possible differences in dispersion of the metal.

In the present investigation, the effect of the support on the specific catalytic activity of nickel for ethane hydrogenolysis has been determined, using alumina, silica, and silica–alumina as supports. The surface areas of the supported nickel were determined by hydrogen chemisorption, and the data on the kinetics of ethane hydrogenolysis were obtained in a differential flow reactor. This approach makes it possible to obtain a clear definition of the effect of the support on the intrinsic catalytic activity of the metal. The particular supports chosen are very representative of the supports commonly used in nickel catalysts. Consequently, the results of this investigation have a definite bearing on the functioning of real catalyst systems.

II. Experimental

Apparatus and Procedure. The apparatus used for the hydrogen chemisorption work was a conventional glass vacuum system with an 80 l./sec. oil diffusion pump. By use of a trap cooled in liquid nitrogen, ultimate dynamic vacua of about 10^{-7} torr were obtained. The sample cells were made of Pyrex glass and had two stopcocks to permit hydrogen to flow through the bed of material.

Samples of each of the three catalyst preparations, weighing about 2 g., were put in a vacuum apparatus. After evacuation at 100° for a short time, hydrogen was passed through the bed of the sample at a flow rate of 500 cm.^{3}/min. The temperature of the sample was then increased, in the flowing hydrogen, to 370°. This temperature was maintained overnight, and then the sample was evacuated for 1 hr. at the same temperature. After cooling to 18°, a hydrogen isotherm was measured. Nickel surface areas were calculated from the isotherms, assuming that the amount adsorbed at 10 cm. represented a monolayer. In the measurement of an isotherm, four or five points up to a pressure of about 30 cm. were usually obtained, as discussed in a previous paper.[14] The nickel surface areas were calculated on the basis that each nickel atom in the surface adsorbs one hydrogen atom and that each hydrogen atom occupies 6.5 Å.^{2}.[15] Nickel surface areas of the catalysts are given in Table I. It is of interest to note that the support affects quite markedly the degree of metal dispersion, despite the similarity of preparation and reduction techniques.

Table I: Summary of Nickel Surface Areas and Kinetic Parameters for Ethane Hydrogenolysis

	Ni on SiO_2	Ni on Al_2O_3	Ni on SiO_2–Al_2O_3
Nickel surface area, m.^{2}/g. of catalyst	13.3	15.6	6.83
Rate of ethane hydrogenolysis at 191° (p_E = 0.030 atm., p_H = 0.20 atm.), mole/hr./g. of catalyst	20.6×10^{-4}	12.9×10^{-4}	0.20×10^{-4}[a]
Specific catalytic activity, moles of ethane converted/hr./m.^{2} of Ni at 191°[b]	15.5×10^{-5}	8.25×10^{-5}	0.293×10^{-5}
Apparent activation energy, kcal./mole	40.6	41.5	39.2

[a] Value extrapolated from an Arrhenius plot of data in the range 272 to 233°. [b] p_H = 0.20 atm., p_E = 0.030 atm.

Measurements of the extent of reduction of the catalysts using a vacuum microbalance indicated that reduction of the nickel took place at temperatures as low as 250°, and that the reduction was extensive at this temperature. Consequently, the 370° reduction temperature employed in the present studies should have resulted in essentially complete reduction of the different nickel catalysts.

The ethane hydrogenolysis data were obtained in a flow reactor system at atmospheric pressure, by use of a vertically mounted stainless steel reactor tube 1.0 cm. in diameter and 8.0 cm. in length. Details of the reactor assembly, flow rate measurements, and the gas chromatographic analysis of the reaction products have been reported previously.[16] The ethane and hydrogen were mixed with helium and passed downflow through a bed containing 0.20 g. of catalyst diluted uniformly with 0.50 g. of ground Vycor glass. By appropriate adjustment of the helium flow rate, it was possible to vary the partial pressures of ethane and hydrogen individually. The total gas flow was main-

(12) S. G. Hindin, S. W. Weller, and G. A. Mills, *J. Phys. Chem.*, **62**, 244 (1958).

(13) J. H. Sinfelt, H. Hurwitz, and J. C. Rohrer, *ibid.*, **64**, 892 (1960).

(14) D. J. C. Yates, W. F. Taylor, and J. H. Sinfelt, *J. Am. Chem. Soc.*, **86**, 2996 (1964).

(15) D. F. Klemperer and F. S. Stone, *Proc. Roy. Soc.* (London), **A243**, 375 (1958).

(16) J. H. Sinfelt, *J. Phys. Chem.*, **68**, 344 (1964).

tained at 1 l./min. throughout. In a typical run, the reactant gases were passed over the catalyst for 3 min. prior to sampling products for analysis. The ethane was then cut out and the hydrogen flow continued for 10 min. prior to another reaction period. As an insurance against possible complications due to changing catalyst activity, most of the reaction periods were bracketed by periods at a standard set of conditions, so that the kinetic data could be expressed as rates relative to the rate at the standard conditions. Prior to any reaction rate measurements, the catalysts were reduced overnight in flowing hydrogen at 370° in the reactor.

Materials. The nickel catalysts used in the present work contained 10 wt. % nickel impregnated on three different supports: silica, alumina, and silica–alumina. The silica used was Cabosil HS 5 (340 m.²/g. surface area), obtained from the Cabot Corp., Boston, Mass. This is a very finely powdered nonporous form of silica (150–200 Å. particle size) prepared by burning silicon tetrachloride in air; small amounts of chlorine impurities are present in the resulting silica. The alumina was prepared by heating β-alumina trihydrate, obtained from Davison Chemical Co., for 4 hr. at 600°. The surface area of the alumina was 295 m.²/g., and the pore volume 0.30 cc./g. The principal impurities in the alumina were silicon, iron, sodium, calcium, and magnesium. The total amount of all these impurities, as estimated from emission spectral analysis, was less than 0.1 wt. %. The silica–alumina used in the present work was Type DA-1 cracking catalyst (nominally 13% Al_2O_3, 87% SiO_2), also obtained from the Davison Chemical Co. The surface area was 450 m.²/g. and the pore volume 0.40 cc./g. Principal impurities in the silica–alumina are alkali and alkaline earth metals, principally sodium, and iron. The total amount of such impurities is estimated to be less than 0.1 wt. %.

In the process of impregnating the various supports with nickel, the support was first wetted with deionized water prior to adding $Ni(NO_3)_2 \cdot 6H_2O$ dissolved in deionized water. In the case of the alumina and silica–alumina, 100 g. of the support was wetted with 50 cc. of deionized water. In the case of Cabosil, it was necessary to add much more deionized water, 800 cc. to 100 g. of Cabosil, to obtain satisfactory wetting of the support. In all cases the impregnation with nickel was accomplished by adding 55 g. of $Ni(NO_3)_2 \cdot 6H_2O$ dissolved in 30 cc. of deionized water to the wet support. The material was then dried overnight at 105°, after which it was pressed at about 10,000 p.s.i. into wafers which were subsequently crushed and screened to a size between 45 and 60 mesh. In the case of the Ni on Al_2O_3 catalyst, it was not necessary to press the material into wafers prior to crushing and screening. Visual inspection of the catalysts indicated uniform impregnation by the nickel in all three preparations.

The ethane used in this work was obtained from the Matheson Co. A chromatographic analysis showed no detectable impurities. It is estimated that an impurity, *e.g.*, methane, would have been detected by the chromatographic analysis if it were present at a concentration above 0.01 wt. %. High purity hydrogen was obtained from the Linde Co., Linden, N. J. It was further purified in a "Deoxo" unit containing palladium catalyst to remove trace amounts of oxygen. The water formed was then removed by a trap cooled in Dry Ice or by a molecular sieve dryer, the latter having been employed for the hydrogen used in the kinetic measurements.

III. Results

The hydrogenolysis of ethane to methane was studied at low conversion levels (0.02 to 8%). Rates were calculated from the relation

$$r = (F/W)x$$

where F represents the feed rate of ethane to the reactor in moles/hr., W represents the weight in grams of the catalyst, and x represents the fraction of ethane converted to methane. The reaction rate r is thus expressed as moles of ethane converted to methane/hr./g. of catalyst.

In a run to measure reaction rates, the catalyst was first prereduced with hydrogen with the identical schedule of temperatures used in the hydrogen chemisorption equipment. This was done to ensure that the nickel surface area of the freshly reduced catalyst would correspond exactly to that measured by the hydrogen chemisorption technique. Then the temperature was lowered in flowing hydrogen, and at a standard set of hydrogen and ethane partial pressures (p_H = 0.20 atm., p_E = 0.030 atm.) the activity of the freshly reduced catalyst was measured. Then rates were measured at a series of temperatures in a rising temperature sequence. The data for the three catalysts are shown in the Arrhenius plots in Fig. 1. From the slopes of these plots, the apparent activation energies of the ethane hydrogenolysis reaction were determined and are given in Table I. The maximum difference between apparent activation energies is less than 6%, which is within the experimental accuracy.

After determining the effect of temperature on rates, the temperature was lowered to an intermediate value, and a series of measurements using the "bracketing

technique" was made to determine the effects of the partial pressures of hydrogen and ethane on the rates. For each set of conditions the rate r relative to the rate r_0 at the standard conditions (p_E = 0.030 atm., p_H = 0.20 atm.) was expressed as a ratio r/r_0. These data are presented in Table II.

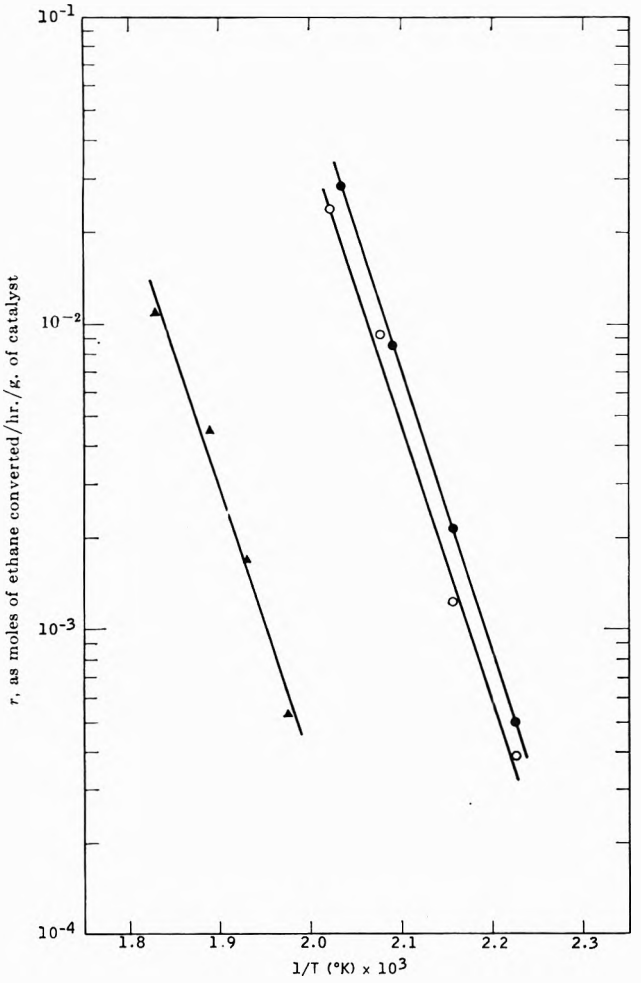

Figure 1. Effect of temperature on the rate of ethane hydrogenolysis over supported nickel catalysts at p_E = 0.030 atm. and p_H = 0.20 atm.: ●, Ni on SiO_2; ○, Ni on Al_2O_3; ▲, Ni on SiO_2–Al_2O_3.

For all three catalysts the data in Table II show that the rate of ethane hydrogenolysis increases with increasing ethane partial pressure, but decreases markedly with increasing hydrogen partial pressure. The dependence of the rate on the partial pressures of ethane and hydrogen can be expressed in the form of a simple power law, $r = kp_E^n p_H^m$.[17] Approximate values of the exponents n and m as derived from the experimental data are summarized here.

Catalyst	n	m
Ni on SiO_2 (177–191°)	1.0	−2.4
Ni on Al_2O_3 (177°)	0.9	−2.0
Ni on SiO_2–Al_2O_3 (246°)	0.9	−1.7

The general features of the kinetics of ethane hydrogenolysis over the catalysts employed in this study are in accord with the earlier studies of Taylor and coworkers,[17] in which the kinetics were investigated over nickel catalysts of unknown nickel area.

In order to compare the activity of nickel supported on the three different materials, the specific activity per unit area of nickel at 191° was calculated. This was done by dividing the measured rates over the freshly reduced Ni on SiO_2 and Ni on Al_2O_3 at 191° by their respective nickel areas. The specific activity of the Ni on SiO_2–Al_2O_3 catalyst at 191° had to be calculated by extrapolation of data obtained in the temperature range 233 to 272°, as the rate was too low to measure at 191°. The values are given in Table I.

IV. Discussion

The results of this investigation have shown clearly that the support can have a very large effect on the

Table II: Relative Rates of C_2H_6 Hydrogenolysis as a Function of C_2H_6 and H_2 Partial Pressures

Catalyst	p_H, atm.	p_E, atm.	r/r_0[a]
Ni on SiO_2 (177–191°)	0.10	0.030	4.03
	0.20	0.030	1.00
	0.40	0.030	0.14
	0.20	0.010	0.37
	0.20	0.030	1.00
	0.20	0.100	3.91
Ni on Al_2O_3 (177°)	0.05	0.030	9.88
	0.10	0.030	3.03
	0.20	0.030	1.00
	0.30	0.030	0.28
	0.20	0.010	0.35
	0.20	0.030	1.00
	0.20	0.100	2.72
Ni on SiO_2–Al_2O_3 (246°)	0.10	0.030	2.66
	0.20	0.030	1.00
	0.40	0.030	0.27
	0.20	0.010	0.33
	0.20	0.030	1.00
	0.20	0.100	2.40

[a] Rate relative to the rate at the standard conditions (p_H = 0.20 atm., p_E = 0.030 atm.) for the particular catalyst and temperature in question; the r/r_0 values cannot be used by themselves to compare the activities of the catalysts.

(17) A. Cimino, M. Boudart, and H. S. Taylor, *J. Phys. Chem.*, **58**, 796 (1954).

specific catalytic activity of a metal. In considering an explanation for these results, one might inquire about differences in the accessibility of the nickel on the various supports. To some degree this has been accounted for in the hydrogen chemisorption measurements, which at least indicate the accessibility of the nickel surface to hydrogen. The possibility that the accessibility might be very different for a molecule such as ethane seems unlikely, since the work of Schuit and van Reijen[18] indicated that for impregnated type nickel catalysts, similar to those of the present work, the accessibility to molecules like carbon monoxide and ethylene is similar to that of hydrogen. Furthermore, calculations by the method of Weisz and Prater[19] indicate effectiveness factors at the conditions of this work to be close to unity for the Ni on Al_2O_3 and Ni on SiO_2–Al_2O_3 catalysts, taking their average pore radii to be 20 and 18 Å., as derived from the data on pore volumes and surface areas. This indicates that pore diffusion is not a limitation for these catalysts, and it is also not likely to be a limitation in the case of the Ni on SiO_2 catalyst, since the pores created in the pressing of the 150–200 Å. Cabosil particles into pellets prior to crushing and screening are probably larger than those of Al_2O_3 and SiO_2–Al_2O_3.

It has been proposed by Reinen and Selwood[20] in their studies of the magnetic properties of supported nickel that the effect of the support is probably one of altering either the particle size or particle size distribution of the metal crystallites. While the effect on particle size distribution may well be a factor in the magnetic studies, it is difficult to see how it could be of controlling importance in the present studies, for the following reason. If we assume that the nickel crystallites are spheres or cubes, the average particle diameter d would be inversely proportional to the surface/volume ratio S of the nickel ($d = 6/S$), or, for a constant amount of nickel in the catalyst, to the surface area of the nickel per unit weight of catalyst. As the support was varied from silica to silica-alumina, the surface area of the nickel decreased about twofold, from 13.3 to 6.83 m.^{2}/g., corresponding to an approximate twofold increase in average particle size. However, the rate of ethane hydrogenolysis per unit weight of catalyst was over 100-fold higher for the silica-supported catalyst; *i.e.*, the effect of the support on the catalytic activity was far greater than the effect on the average particle size of the nickel crystallites. When the rates are expressed as rates per unit of nickel surface area, so that the effects of average particle size or nickel surface area are accounted for, there is still more than a 50-fold difference in the activities of the Ni on SiO_2 and Ni on SiO_2–Al_2O_3 catalysts. A similar effect can be seen if the Ni on SiO_2 and Ni on Al_2O_3 catalysts are compared. Despite the higher nickel area using alumina as the support (15.6 *vs.* 13.3 m.^{2}/g.), the reaction rate per unit weight of catalyst is 1.7 times as high for the silica supported nickel, as compared with the alumina supported nickel. On the basis of rate per unit area of nickel, the rate is about 1.87 times greater for the nickel on silica. Thus, it seems reasonable that some specific chemical or electronic interaction between metal and support is responsible for the effects observed in the present work.

It is interesting that the differences in the catalytic activities of the nickel over the various supports are not accompanied by significant differences in the apparent activation energy. While the data in Table I indicate small differences in apparent activation energy, there is no consistent trend in the activation energy with decreasing catalytic activity as the support is changed from silica to alumina to silica-alumina, and in any case the differences are probably within the range of experimental error. Taking the apparent activation energies to be the same over all three catalysts, the differences in catalytic activity would then have to be due to a variation in the pre-exponential factor k_0 in the Arrhenius expression $k = k_0 \exp(-E/RT)$. This is similar to the situation in ethylene hydrogenation over metal films, where the apparent activation energy is reported to be constant over a series of metals,[21] despite large variations in catalyst activity. The fact that the apparent activation energy for ethane hydrogenolysis is constant over the various supported nickel catalysts in the present work, however, does not necessarily mean that the true activation energy is constant. For instance, if the surface is only sparsely covered by the reactive intermediate, the apparent activation energy E is related to the true activation energy E_t by the expression $E = E_t - q$, where q is the heat of adsorption. It is possible that q and E_t both vary by about the same amount, thus causing E to be essentially independent of the variation in the support for the nickel.

(18) G. C. A. Schuit and L. L. van Reijen, *Advan. Catalysis*, **10**, 242 (1958).

(19) P. B. Weisz and C. D. Prater, *ibid.*, **6**, 143 (1954).

(20) D. Reinen and P. W. Selwood, *J. Catalysis*, **2**, 109 (1963).

(21) O. Beeck, *Discussions Faraday Soc.*, **8**, 118 (1950).

On the Radiolysis of Alkali Halides in Aqueous Solutions Saturated with Nitrous Oxide

by M. Anbar, D. Meyerstein, and P. Neta

The Weizmann Institute of Science and the Soreq Research Establishment, Rehovoth, Israel
(Received May 7, 1964)

The radiolytic oxidation of iodide ions in N_2O-saturated solutions has been investigated over the range of 10^{-4} to 1.0 *M* KI. $G(I_2)$ was found to increase with iodide concentration up to 3.65 at 1 *M* KI. This result implies the formation of oxidizing species other than OH radicals in radiolyzed solutions. Fluoride, chloride, and bromide ions were also shown to react with these species.

The radiolytic oxidation of halide ions in aqueous solutions is one of the very simplest oxidation–reduction reactions, as it does not involve any bond cleavage in the oxidized species. It seems reasonable that a quantitative study of this oxidation process may throw light on the identity and kinetic behavior of the primary oxidizing species formed in water under radiolysis. The reaction of the products of halide oxidation with the reducing species formed in radiolyzed solutions as well as their solvolysis limits, however, the ambiguity of quantitative interpretation. Even in the case of oxidation of iodide ions in neutral solution, where solvolysis may be neglected, a steady-state concentration of iodine is obtained at very low doses of radiation.[1,2] The application of pulse techniques makes it possible to follow the appearance of oxidized species like Cl_2^- or I_2^- before these undergo subsequent reactions.[3] Using conventional radiolytic techniques, conditions had to be found under which no steady-state conditions were attained. In recent photochemical studies[4] of solutions of potassium iodide saturated with nitrous oxide, it has been shown that under these conditions aquated electrons oxidize iodide instead of reducing iodine. It has been decided, therefore, to investigate the radiolysis of alkali halides in neutral solutions saturated with nitrous oxide. The results obtained indicate the formation of primary oxidizing species other than OH radicals.

Experimental

Materials. Triple-distilled water was used throughout the experiments. Distilled water was redistilled over alkaline potassium permanganate and subsequently with dilute phosphoric acid in an all-glass still. All the salts were of Baker Analyzed or Fluka Puriss grade and were used without further treatment. The nitrous oxide was obtained from the Matheson Co., East Rutherford, N. J.

Preparation of the Samples and Their Irradiation. The pH of the solutions was determined using a Metrohm Kompensator Type E 148 C, with an accuracy of ±0.05 pH unit. Samples (2 ml.) saturated with nitrous oxide in uniform test tubes were irradiated for 1 and 2 min. with γ-rays from a Co^{60} source (Gammacell 200, Atomic Energy of Canada, Ltd.) at a dose of 7800 r./min. (determined by the Fricke dosimeter, 0.1 *N* H_2SO_4, taking $G(Fe^{+3}) = 15.5$).

Analysis. The amount of iodine formed was determined by adding 2 ml. of 0.2 *N* KI and measuring the optical density at 352 mμ, using a Hilger Uvispek spectrophotometer. The I_2 concentrations were calculated from the extinction coefficient of I_3^- (ϵ 26,400).[5] The presence of up to 0.25 *M* of other halides in the measured solutions was shown not to affect the results

(1) E. R. Johnson, *J. Chem. Phys.*, **21**, 1417 (1953); H. A. Schwarz, J. P. Losee, Jr., and A. O. Allen, *J. Am. Chem. Soc.*, **76**, 4693 (1954).

(2) A. O. Allen, "The Radiation Chemistry of Water and Aqueous Solutions," D. Van Nostrand Co., Inc., Princeton, N. J., 1961, pp. 108, 109.

(3) M. Anbar and J. K. Thomas, *J. Phys. Chem.*, in press.

(4) J. Jortner, M. Ottolenghi, and G. Stein, *ibid.* **66**, 2037 (1962); **68**, 247 (1964); F. S. Dainton and S. A. Sills, *Bull. soc. chim. Belges*, **71**, 801 (1962).

(5) D. Meyerstein and A. Treinin, *Trans. Faraday Soc.*, **59**, 1114 (1963).

by more than 1%.[5] The G values obtained were calculated from the mean of at least four experiments and had a standard deviation $< \pm 0.10$.

In order to calculate the dose absorbed in the more concentrated solutions (>0.1 M), the formula

$$D_c = D_F \times \frac{\epsilon_s}{\epsilon_F}$$

was used, where D_c is the corrected dose, D_F the dose as measured by the Fricke dosimeter, and ϵ_s and ϵ_F the electron densities of the irradiated solutions and of the dosimeter, respectively, as calculated from the densities of the solutions.[6] No correction was made for the photoelectric effect[7] nor for the absorption of low energy scattered radiation inside the Co^{60} source by materials of high atomic number.[7,8] The $G(I_2)$ obtained in a 0.5 M CsCl solution as compared with a 0.5 M NaCl solution (Table II) verified the adequacy of the applied approximation in the range of concentrations under study.

Results and Discussion

The results for pure potassium iodide solutions are given in Table I. It can be seen that $G(I_2)$ changes from 1.17 at 10^{-4} M I^- up to 3.65 at 1 M I^-. The mechanism suggested for the formation of iodine under the experimental conditions is

$$OH + I^- \longrightarrow OH^- + I \quad (1)$$

$$I + I^- \longrightarrow I_2^-;\ I_2^- + I_2^- \longrightarrow I_3^- + I^- \quad (2)$$

$$N_2O + e_{aq}^- + H^+ \longrightarrow N_2OH \quad (3)$$

$$N_2OH + I^- \longrightarrow N_2 + OH^- + I \quad (4)$$

alternatively

$$N_2OH \longrightarrow N_2 + OH$$

$$I_2^- + H_2O_2 \longrightarrow 2I^- + HO_2 + H^+ \quad (5)$$

$$I_3^- + H_2O_2 \longrightarrow 3I^- + 2H^+ + O_2 \quad (6)$$

$$I_2 + HO_2 \longrightarrow I_2^- + H^+ + O_2 \quad (7)$$

$$I_2^- + HO_2 \longrightarrow 2I^- + H^+ + O_2$$

$$H + I_2 \longrightarrow H^+ + I_2^- \quad (8)$$

Reaction 6 is an equilibrium reaction, but in the case of neutral solutions it is shifted totally to the right.[2] (It has been shown that changing the pH from 5.5 to 9.0 has no effect on the formation of iodine in pure iodide solutions.) The interaction of aquated electrons with nitrous oxide was shown to yield N_2OH (reaction 2),[9] an intermediate which has a lifetime long enough to permit chemical reaction. The expected $G(I_2)$ according to this scheme is $G(I_2) = \frac{1}{2}(G_e + G_{OH} - G_H) - G_{H_2O_2}$ taking $G_e = 2.8$, $G_{OH} = 2.8$,[10-13] $G_{H_2O_2} = 0.8$, and $G_H = 0.6$. $G(I_2) = 1.70$ is expected, which is the value obtained for the 1×10^{-3} M solutions.

Table I: The Formation of Iodine in Potassium Iodide Solutions Saturated with Nitrous Oxide[a]

[KI], M	$G(I_2)$[b]	$G(I_2)_{cor}$[c]
1×10^{-4}	1.17	..
2×10^{-4}	1.25	..
5×10^{-4}	1.41	..
1×10^{-3}	1.60	..
2×10^{-3}	1.78	..
5×10^{-3}	1.83	..
1×10^{-2}	2.16	..
2×10^{-2}	2.20	..
5×10^{-2}	2.30	..
1×10^{-1}	2.86	2.83
2×10^{-1}	3.28	3.21
5×10^{-1}	3.66	3.52
1.0	3.94	3.65

[a] All solutions at pH 6. [b] The observed value for $G(I_2)$. [c] Value obtained after correcting for mass effect.

Increasing the concentration of the iodide above 1×10^{-3} M, the yield of iodine is still growing. This effect is not a mass absorption effect, above the correction included, as is evident by comparing the results in the presence of cesium chloride with those of sodium chloride (Table II). Under similar irradiation conditions it has been shown by Anderson[14] that the photoelectric effect does not have an appreciable specific contribution up to 4 M iodide, which is four times our maximum concentration. Further, it can be seen from Table I that the per cent increase in $G(I_2)$ when increasing iodide concentration is 37, 35, 35, and 28%, respectively, when (I^-) is increased from 10^{-4} to 10^{-3}, 10^{-2}, 10^{-1}, and 1.0 M, respectively. If some kind of "direct" action would be involved, the increase in $G(I_2)$ going from 0.1 to 1.0 M I^- would be much larger than that when changing iodine concentration from

(6) "Handbook of Chemistry and Physics," 44th Ed., Chemical Rubber Publishing Co., Cleveland, Ohio, 1963, pp. 2056–2062.

(7) E. Hayon, *J. Phys. Chem.*, **65**, 1502 (1961).

(8) W. Bernstein and R. H. Schuler, *Nucleonics*, **13**, No. 11, 110 (1955).

(9) M. Anbar, R. A. Munoz, and P. Rona, *J. Phys. Chem.*, **67**, 2708 (1963).

(10) In the cases where $G_{OH} = 2.2$ has been reported,[11-13] G_H was not taken into consideration and it is obvious that the H atoms formed cancel an equivalent yield of OH radicals.

(11) See ref. 2, p. 47.

(12) M. S. Matheson, *Ann. Rev. Phys. Chem.*, **13**, 77 (1962).

(13) F. S. Dainton and W. S. Watt, *Nature*, **195**, 1294 (1962).

(14) R. Anderson and B. Knight, Abstracts of the 2nd International Congress of Radiation Research, 1962, p. 71.

0.01 to 0.1. It may be concluded that the increase in $G(I_2)$ with iodide concentration has to be explained in terms of "indirect action."

Table II: The Effect of Added Halide Ions on $G(I_2)$[a]

Additive	Concn., M: 0	10^{-2}	3×10^{-2}	10^{-1}	5×10^{-1}	5×10^{-1}[b]
None	1.60					
KF				1.68[c]	1.76[d]	1.74
NaCl		1.75	1.82	1.87	2.08	2.04
CsCl					2.15	2.06
NaBr		2.06	2.29	2.55	2.89	2.84

[a] In 10^{-3} N potassium iodide solutions at pH 6. [b] Corrected for mass effect. [c] pH 6.8. [d] pH 7.5.

The increase in $G(I_2)$ at high iodide concentration may be interpreted, at first sight, by scavenging of the precursor of the molecular hydrogen peroxide, possibly OH radical,[15] by the iodide, leading to the formation of iodine instead of its reduction. Assuming that *all* primary OH radicals are scavenged by iodide ions, this effect may lead to an upper limit of $G(I_2) = {}^1/_2(G_e + G_{OH} - G_H) + G_{H_2O_2} = 3.30$.

$G(I_2) = 3.65$ obtained for the 1.0 M potassium iodide solution cannot be explained by this mechanism alone since it significantly exceeds $G(I_2)$ calculated for this mechanism. Iodide was shown to scavenge the formation of molecular hydrogen peroxide to the same extent as bromide.[16a] Taking the value of $G_{H_2O_2} = 0.4$ obtained in the presence of 1 M bromide,[16b] $G(I_2)$ is not expected to exceed 2.50 up to 1 M iodide. It must be concluded, therefore, that a substantial fraction of iodine is formed by a mechanism which does not involve OH radicals.

In order to get a better understanding of the observed increase in $G(I_2)$, the effect of added fluoride, chloride, and bromide on the formation of iodine has been examined. All the X atoms or X_2^- radicals formed[3] are expected to oxidize I^- to I_2. The results are summarized in Table II. The results with added sodium bromide show a similar behavior to those of concentrated iodide solutions, though the yields of I_2 are lower, probably due to the lower reactivity of bromide in the oxidation processes. The increase in $G(I_2)$ in the case of added sodium chloride is much smaller, but this effect is of special interest owing to the fact that chloride ions are not oxidized by OH radicals in neutral solutions.[3,17a,b] Fluoride ions have also shown a small, but significant, effect on $G(I_2)$.

A mechanism which might account for the increase in $G(I_2)$ at high iodide concentration was suggested by Anderson, who attributed the increase in $G(H_2)$ in iodide solutions to the interaction of I^- with subexcitation electrons.[14,18] This mechanism is however inconsistent with the results of Kuppermann on the possible excitation energies of these electrons.[19]

Another process which may contribute to the increased yield of iodine is the $I^- + H_2O^+ \rightarrow I + H_2O$ reaction which will partially inhibit the $e_{aq}^- + H_2O^+ \rightarrow H_2O$ combination process, resulting in an over-all increase in G_{-H_2O}. It should be noted that inhibition of the recombination of H and OH radicals does not affect $G(I_2)$.

The interaction of halides at high concentrations with H_2O^+ has been suggested as a mechanism for the formation of Cl_2^- in neutral solution.[3] The effect of chloride ions on $G(I_2)$ presented in Table II may be due to this reaction. H_2O^+ has also been postulated in other radiolytic processes.[20]

An alternative mechanism by which $G(I_2)$ may be increased at high iodide concentrations is the oxidation of iodide by excited water molecules.

$$X^- + H_2O^* \longrightarrow X + e_{aq}^-$$

Excited water molecules were suggested to be formed in radiolyzed solutions.[21-24] It was suggested that these species are the precursors of the so-called residual hydrogen.[25-28] It has been suggested that excited water molecules oxidize halide ions[24,28] and thus G_{-H_2O} may be increased again.

Fluoride ions, which obviously do not react with OH radicals, were shown not to compete for H_2O^+ with chloride ions.[3] On the other hand, these ions have been shown to be oxidized in radiolyzed solutions[24] and this process was attributed to their reaction

(15) M. Burton and K. C. Kurien, *J. Phys. Chem.*, **63**, 899 (1959).

(16) (a) See ref. 2, p. 64; (b) M. Anbar, S. Guttmann, and G. Stein, *J. Chem. Phys.*, **34**, 703 (1961).

(17) (a) See ref. 2, p. 63; (b) A. O. Allen, C. J. Hochanadel, J. A. Ghormley, and T. W. Davis, *J. Phys. Chem.*, **56**, 575 (1952).

(18) H. C. Sutton in "Radiation Effects in Physics, Chemistry and Biology," M. Ebert and A. Howard, Ed., North Holland Publishing Co., Amsterdam, 1963, p. 56.

(19) See ref. 18, p. 67.

(20) J. J. Weiss, *Radiation Res. Suppl.*, **4**, 141 (1964).

(21) F. S. Dainton and D. B. Peterson, *Proc. Roy. Soc.* (London), **A265**, 443 (1962).

(22) F. S. Dainton and W. S. Watt, *ibid.*, **A275**, 447 (1963).

(23) D. N. Sitharamaro and J. F. Duncan, *J. Phys. Chem.*, **67**, 2126 (1963).

(24) M. Anbar and D. Meyerstein, Israel AEC Reports, IA-851 (1963).

(25) J. T. Allan and G. Scholes, *Nature*, **187**, 218 (1960).

(26) S. Nehari and J. Rabani, *J. Phys. Chem.*, **67**, 1609 (1963).

(27) E. Hayon, *Nature*, **196**, 533 (1962).

(28) M. Anbar and D. Meyerstein, *J. Phys. Chem.*, **68**, 1713 (1964).

with H_2O^*. The oxidation of Tl^+ to Tl^{+2} by H_2O^* may account for the increased apparent yield of OH observed by Hayon.[7] The formation of e_{aq}^- by the reaction of iodide with H_2O^* may also explain the increased yield of "molecular hydrogen" in concentrated iodide solutions.[14,18]

The existence of oxidizing species other than OH radicals in neutral irradiated solution has been reported recently by different investigators[29,30] and their identity has not been finally established. These species manifest themselves only in rather concentrated solutions, in analogy to the experiments described in the present study. It is suggested here that either H_2O^+ or H_2O^* or most probably both are liable for these findings. Both species are undoubtedly primary products of the act of radiation on water.[31] The only question is whether these will not dissociate or undergo deactivation before having a chance to interact with solutes. Our postulation is that water molecules which are both in the inner and outer hydration shells of a given ion and which undergo a radiolytic ionization or excitation are liable to interact with their central ion rather than dissociate to $H^+ + OH$ or $H + OH$, respectively, or alternatively undergo neutralization or de-excitation. The rate of interaction of H_2O^+ or H_2O^* formed in the hydration shell of a given solute with their central atom or molecule may be of the order of electronic transition within a molecule, *i.e.*, $<10^{-14}$ sec. This is the order of lifetime postulated for H_2O^+ and H_2O^+.[31]

(29) A. O. Allen, *Radiation Res. Suppl.*, **4**, 54 (1964).
(30) C. R. Maxwell, *Radiation Res.*, **22**, 213 (1964).
(31) M. S. Matheson, *Radiation Res. Suppl.*, **4**, 1 (1964).

The Negative Adsorption of Anions (Anion Exclusion) in Systems with Interacting Double Layers

by F. A. M. de Haan

Laboratory of Soils and Fertilizers, State Agricultural University, Wageningen, The Netherlands
(Received May 13, 1964)

Starting with the standard double layer theory, expressions are derived for the negative adsorption of anions in mixed ionic systems with interacting double layers. The effect of interaction is calculated and expressed as the fraction of the original negative adsorption in corresponding systems without interaction. As a general conclusion it is found that the decrease of negative adsorption does not exceed 5% as long as the reduced thickness of the water layer around the colloidal particles is ≥ 1.5. The calculations are experimentally verified, showing a good agreement between theoretical expectations and experimental results.

Introduction

The predominantly negative charge on most soil colloids leads to a decrease of the anion concentration in the close vicinity of the colloidal particles as compared with the concentration in the equilibrium solution. This deficit of anions has been termed negative adsorption or anion exclusion. An expression for the negative adsorption, based on theoretical model calculations, was derived by Schofield[1] and Klaarenbeek,[2] and later extended by Bolt and Warkentin.[3] These

calculations, however, were worked out only for systems containing single salts. The extension to systems of mixed ionic composition (thus containing mono- and divalent cations and anions) was given by de Haan and Bolt.[4] The last mentioned derivations were limited to systems with a relatively high liquid content for which the thickness of the electric double layer may be assumed not to exceed the thickness of the water layer around the particles.

It is the purpose of this paper to present expressions which are equally valid for systems with interacting double layers between opposing particles. The theoretical considerations are verified experimentally.

Theoretical

In Fig. 1 the cation and anion concentrations in the vicinity of a charged clay surface are represented schematically for a system in equilibrium with a single salt solution of a concentration C_0 in moles/l. Although both anion and cation concentration reach a

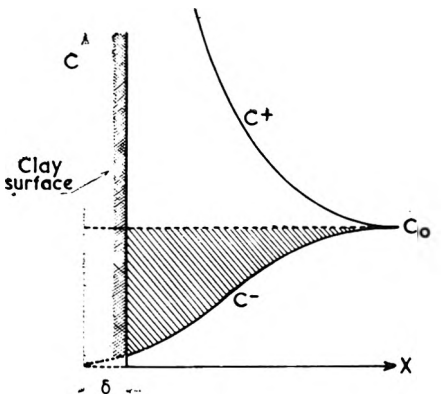

Figure 1. The ionic distribution at a planar, charged surface.

finite value at the clay surface, the concentration curves may be extended for mathematical convenience over a distance δ beyond the location of the charged surface to the point where C^- and C^+ reach the values zero and infinity, respectively. At this point the total counter charge reaches infinity. It also represents the point where, for the given ion distribution, an infinitely highly charged surface should be located.

The negative adsorption of anions, in mequiv./cm.^{2} of surface area, Γ_-, is represented by the cross-hatched area in Fig. 1. Introducing the distance coordinates x (measured from the charged surface) and $X = x + \delta$, and following the standard double layer theory, the negative adsorption for systems in which the thickness of the liquid layer grossly exceeds the thickness of the double layer is found as

$$\Gamma_z^- = N_0^- \int_0^\infty \left(1 - \frac{1}{u^{z^-}}\right) dx$$

$$= N_0^- \left\{\int_0^\infty \left(1 - \frac{1}{u^{z^-}}\right) dX - \int_0^\delta \left(1 - \frac{1}{u^{z^-}}\right) dX\right\} \quad (1)$$

in which z^- is the valence of the anion expressed as a positive number, N_0^- is the equilibrium concentration of the anion in mequiv./ml., and $1/u^{z^-} = \exp(z^- e \cdot \psi/kT)$, the Boltzmann factor for the anion of valence z^-, where e is electronic charge, ψ is the electric potential, k is the Boltzmann constant, and T is the absolute temperature.

As is indicated in Fig. 1, the second integral of eq. 1 may be approximated by $z^- C_0 \delta$ ($= N_0^- \delta$). It can be shown that the exact value of this integral may be evaluated, proving that the error due to the approximation introduced in using $z^- C_0 \delta$ amounts to less than 3% if the surface charge density $\geq 10^{-7}$ mequiv./cm.^{2} and $C_0 \leq 10^{-1}$ M. It was shown by Schofield that the distance δ is a function of the surface charge density of the clay and may be approximated quite well by the relation

$$\delta \simeq \frac{4}{z^+ \beta \Gamma} \quad (2)$$

in which Γ represents the surface charge density, expressed in mequiv./cm.^{2} of surface; values of Γ may be estimated for different clays from the cation-exchange capacity and the specific surface area; z^+ represents the valency of the dominant cation in the system and β a constant of double layer theory, equal to $8\pi F^2/1000\epsilon RT$, in which F is the Faraday, ϵ the dielectric constant, and R the gas constant; at 25° β equals 1.06×10^{15} cm./mmole. For Na and Ca montmorillonite the value of δ equals roughly 4 and 2 Å., respectively.

In evaluating the first integral of eq. 1 Bolt and Warkentin used the expression obtained by the first integration of the Poisson–Boltzmann equation of the electric double layer, *viz.*

$$\frac{d\frac{e\phi}{kT}}{dX} = \frac{d \ln u}{dX} = \pm\sqrt{\beta}\sqrt{\Sigma C - \Sigma C_0} \quad (3)$$

in which ΣC and ΣC_0 indicate the total ionic concentra-

(1) R. K. Schofield, *Nature*, **160**, 408 (1947).
(2) F. W. Klaarenbeek, Ph.D. Thesis, Utrecht, 1946.
(3) G. H. Bolt and B. P. Warkentin, *Kolloid-Z.*, **156**, 1 41 (1958).
(4) F. A. M. de Haan and G. H. Bolt, *Soil Sci. Soc. Am. Proc.*, **27**, 6. 636 (1963).

tion in moles/l in the double layer and in the equilibrium solution, respectively.

Combining eq. 1 and 3 one finds

$$\frac{\Gamma_{z^-}}{N_0^-} = \int_{X=0}^{X=\infty} \frac{\left(1 - \frac{1}{u^{z^-}}\right) \mathrm{d} \ln u}{\sqrt{\beta}\sqrt{\Sigma C - \Sigma C_0}} - \delta \qquad (4)$$

Equation 4 represents the general expression for the negative adsorption of anions in systems without interacting double layers.

If this condition does not prevail, as may be the case in highly concentrated suspensions of a colloid with a large specific surface area, the anion concentration must be integrated over a distance from the plate to the point midway between two opposing clay plates. The electric potential at the "end" of the double layer is not zero in this case, but has a definite value, ψ_c. The corresponding value of u is indicated by u_c. It should be pointed out that in a suspension one may not expect all clay plates to be in parallel position with respect to each other. As long as the suspension is not flocculated, the repulsion between adjacent particles must lead to an arrangement which should be very close to parallel for adjacent plates. In flocculated systems (and specifically so at low suspension concentration) parallel arrangement may be absent in which case one could expect sizable deviations from the calculations based on such an arrangement. Derivations are given for a system containing monovalent cations and mono- and divalent anions, and for a system containing mono- and divalent cations and monovalent anions.

Given below are derivations of the expressions for the negative adsorption of anions in a system with interacting double layers containing monovalent cations and mono- and divalent anions (+1, −1, − 2).

This system may be described in the following manner. If N_0 represents the total salt concentration in the equilibrium solution in mequiv./ml. and f^{-2} stands for the equivalent concentration fraction of the divalent anion, then the concentrations of the different ions in mequiv./ml. are equal to N_0 for the monovalent cation, $f^{-2}N_0$ for the divalent anion, and $(1 - f^{-2})N_0$ for the monovalent anion. Thus, in this case

$$\Sigma C - \Sigma C_0 = N_0\{u + (1 - f^{-2})u^{-1} + {}^1/_2 f^{-2}u^{-2} - u_c - (1 - f^{-2})u_c^{-1} - {}^1/_2 f^{-2}u_c^{-2}\} \qquad (5)$$

Substitution of (5) in (4), using the integration limits for the interaction case and replacing d ln u by $1/u$ du, gives, for the monovalent anion

$$\frac{\Gamma_-}{(1 - f^{-2})N_0} = \pm\frac{1}{\sqrt{\beta N_0}} \int_\infty^{u_c} \frac{\left(1 - \frac{1}{u}\right) \mathrm{d}u}{\sqrt{(u - u_c)\left\{u^2 - u\left(\frac{1 - f^{-2}}{u_c} + \frac{f^{-2}}{2u_c^2}\right) - \frac{f^{-2}}{2u_c}\right\}}} - \delta \qquad (6)$$

Designating the expression under the root sign in eq. 6 by I

$$\frac{\Gamma_-}{(1 - f^{-2})N_0} = \pm\frac{1}{\sqrt{\beta N_0}}\left\{\int_\infty^{u_c} \frac{\mathrm{d}u}{\sqrt{I}} - \int_\infty^{u_c} \frac{\mathrm{d}u}{u\sqrt{I}}\right\} - \delta \qquad (7)$$

In the same manner the expression for the divalent anion is found as

$$\frac{\Gamma_{-2}}{f^{-2}N_0} = \pm\frac{1}{\sqrt{\beta N_0}} \int_\infty^{u_c} \frac{\left(1 - \frac{1}{u^2}\right) \mathrm{d}u}{\sqrt{I}} - \delta = \pm\frac{1}{\sqrt{\beta N_0}}\left\{\int_\infty^{u_c} \frac{\mathrm{d}u}{\sqrt{I}} - \int_\infty^{u_c} \frac{\mathrm{d}u}{u^2\sqrt{I}}\right\} - \delta \qquad (8)$$

It is noted that the left-hand side of these equations represents the equivalent distance over which no anions appear to be present, *i.e.*, the amount of anions excluded per cm.^{2} of colloid surface expressed as the number of cm.^{3} of solution per cm.^{2} surface, which appears to be free of anions. This distance may be termed the equivalent distance of exclusion (d^-, d^{-2}, or d^{-3} for mono-, di-, and trivalent anions, respectively). Solution of the integrals of eq. 7 and 8 requires the roots, α, of $I = 0$, which are

$$\alpha_1 = u_c$$

$$\alpha_2 = \frac{1}{2}\left(\frac{1 - f^{-2}}{u_c} + \frac{f^{-2}}{2u_c^2}\right) + \frac{1}{2}\sqrt{\frac{(1 - f^{-2})^2}{u_c^2} + \frac{2f^{-2}(1 - f^{-2})}{2u_c^3} + \frac{(f^{-2})^2}{4u_c^4} + \frac{2f^{-2}}{u_c}}$$

$$\alpha_3 = \frac{1}{2}\left(\frac{1 - f^{-2}}{u_c} + \frac{f^{-2}}{2u_c^2}\right) - \frac{1}{2}\sqrt{\frac{(1 - f^{-2})^2}{u_c^2} + \frac{2f^{-2}(1 - f^{-2})}{2u_c^3} + \frac{(f^{-2})^2}{4u_c^4} + \frac{2f^{-2}}{u_c}}$$

Substituting the solutions of the integrals appearing in (7) one finds

$$\frac{\Gamma_-}{(1 - f^{-2})N_0} = \frac{Q_t'}{\sqrt{\beta N_0}} - \delta \qquad (9)$$

Table I: The Influence of Double Layer Interaction on the Negative Adsorption of Anions in a (+1, −1, −2) System[a]

	$\frac{1}{u_c}$	$D\sqrt{\beta N_0}$	Fraction of original negative adsorption left (Q_i/Q_a) Monovalent	Divalent	Trivalent
			$Q_a' = 2.000$	$Q_a'' = 2.667$	$Q_a''' = 3.067$
	0.1	0.997 (0.994)	0.473 (0.472)	0.373 (0.371)	0.334 (0.324)
	0.2	1.419 (1.405)	0.638 (0.632)	0.526 (0.524)	0.467 (0.457)
	0.3	1.762	0.748		
$f^{-2} = 0.0$	0.4	2.076 (1.987)	0.825 (0.795)	0.729 (0.700)	0.671 (0.635)
	0.5	2.362 (2.221)	0.872 (0.833)	0.806 (0.755)	0.745 (0.696)
	0.6	2.716	0.929		
	0.7	3.090	0.959		
	0.8	3.570 (2.810)	0.972 (0.843)	0.961 (0.801)	0.940 (0.769)
	0.9	4.340	1.000		
			$Q_a' = 1.912$	$Q_a'' = 2.526$	
$f^{-2} = 0.6$	0.5	2.326	0.901	0.833	

[a] Q_a values refer to systems without interacting double layers. The numbers within brackets are the values calculated when neglecting the anions.

with

$$Q_i' = \frac{2}{\sqrt{u_c - \alpha_3}}\left(1 - \frac{1}{\alpha_2}\right)F(\pi/2,k) + \frac{2(u_c - \alpha_2)}{\alpha_2 u_c\sqrt{u_c - \alpha_3}}\Pi(\pi/2,\zeta,k) \qquad (10)$$

in which $k = \sqrt{(\alpha_2 - \alpha_3)/(u_c - \alpha_3)}$, $\zeta = -\alpha_2/u_c$, and $F(\pi/2,k)$ and $\Pi(\pi/2,\zeta,k)$ are complete elliptic integrals of the first and third kind, respectively. As may be seen from eq. 9 and 10, Q_i represents the variation of the distance of exclusion due to the ionic composition of the system and the degree of interaction.

The third kind elliptic integral has never been tabulated and its value must be calculated from the series expansion

$$\Pi(\pi/2,\zeta,k) = \frac{\pi}{2}\left[1 - {}^1/_2\zeta\left(1 - {}^1/_2\frac{k^2}{\zeta}\right) + {}^3/_8\zeta^2\left(1 - {}^1/_2\frac{k^2}{\zeta} + {}^3/_8\frac{k^4}{\zeta^2}\right) - {}^5/_{16}\zeta^3\left(1 - {}^1/_2\frac{k^2}{\zeta} + {}^3/_8\frac{k^4}{\zeta^2} - {}^5/_{16}\frac{k^6}{\zeta^3}\right) + {}^{35}/_{128}\zeta^4\left(1 - {}^1/_2\frac{k^2}{\zeta} + {}^3/_8\frac{k^4}{\zeta^2} - {}^5/_{16}\frac{k^6}{\zeta^3} + {}^{35}/_{128}\frac{k^8}{\zeta^4}\right) - \cdots\cdots\right]$$

By using a recurrence procedure, the second integral of eq. 8 may be converted into the ones appearing in eq. 7, yielding

$$\frac{\Gamma_{-2}}{f^{-2}N_0} = \frac{Q_i''}{\sqrt{\beta N_0}} - \delta \qquad (11)$$

in which

$$Q_i'' = \frac{2}{\sqrt{u_c - \alpha_3}}\left[\left\{1 + \frac{1 - f^{-2}}{\alpha_2 f^{-2}} - \frac{u_c}{f^{-2}}\right\}F(\pi/2,k) + \frac{u_c - \alpha_3}{f^{-2}}E(\pi/2,k) - \frac{1 - f^{-2}}{f^{-2}}\frac{u_c - \alpha_2}{\alpha_2 u_c}\Pi(\pi/2,\zeta,k)\right] \qquad (12)$$

where $E(\pi/2,k)$ is a complete elliptic integral of the second kind. Thus using eq. 9 and 11 the negative adsorption of the anions may be calculated for different f^{-2} values at each stage of interaction (different u_c values). The results corresponding to $f^{-2} = 0.6$ and $u_c = 2$ are given in Table I and represented by the crosses 1 and 2 in Fig. 2.

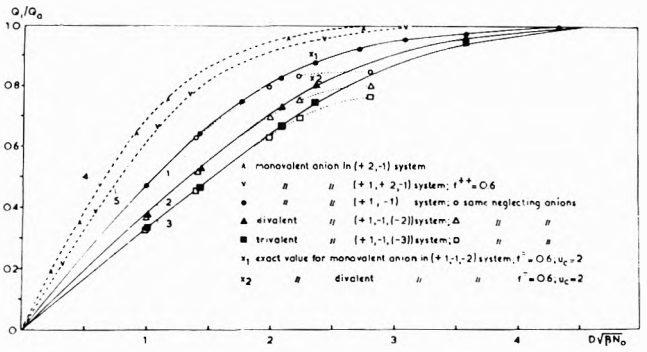

Figure 2. Depression of the negative adsorption of anions in systems with interacting double layers, Q_i/Q_a, as a function of $D\sqrt{\beta N_0}$.

Although the negative adsorption of anions may be calculated according to the above, it seems unlikely that the rather involved application of series expansion

of the Π-function is warranted from a practical point of view. It may easily be shown that the influence of a varying anionic composition at a constant electrolyte level on the equivalent distance of exclusion of the anions is relatively small. This is understandable since the value of this distance is determined by the potential distribution in the double layer, which in turn is determined to a large extent by the cationic (*i.e.* counterionic) composition. This is so since the total charge of the coions is usually insignificant in comparison to the charge of the counterions. This condition applies specifically to systems with interacting double layers, the coions being efficiently repelled from the entire double layer system (at least if $u_c >> 1$).

It thus follows that the calculation of the distance of exclusion of the mono- and divalent anions in the above mixed system could be approximated very closely by the result obtained when assuming that $f^{-2} \simeq 0$. Applying this condition, the roots of I are found as $\alpha_1 = u_c$, $\alpha_2 = 1/u_c$, and $\alpha_3 = 0$. By using these roots, the integrals of eq. 7 and 8 are readily solved in terms of complete elliptic integrals of the first and second kind only, and one finds

$$Q_i'\ (f^{-2} = 0) \simeq Q_i' = \frac{2(1 - u_c)}{\sqrt{u_c}} F\left(\pi/2, \frac{1}{u_c}\right) + 2\sqrt{u_c}\, E\left(\pi/2, \frac{1}{u_c}\right) \quad (13)$$

$$Q_i''\ (f^{-2} = 0) \simeq Q_i'' = \left\{\frac{8}{3\sqrt{u_c}} - \frac{4\sqrt{u_c}}{3}\left(u_c + \frac{1}{u_c}\right)\right\} F\left(\pi/2, \frac{1}{u_c}\right) + \frac{4\sqrt{u_c}}{3}\left(u_c + \frac{1}{u_c}\right) E\left(\pi/2, \frac{1}{u_c}\right) \quad (14)$$

Finally, the above treatment may be extended to the case of the trivalent anion (again assumed to have negligible influence on the potential distribution of the double layer), yielding

$$Q_i'''\ (f^{-3} = f^{-2} = 0) \simeq Q_i''' = \left[\left\{1 + {}^4/_{15}\left(u_c + \frac{1}{u_c}\right)\right\}\frac{2}{\sqrt{u_c}} + \left\{{}^3/_5 - {}^8/_{15}\left(u_c + \frac{1}{u_c}\right)^2\right\} 2\sqrt{u_c}\right] F\left(\pi/2, \frac{1}{u_c}\right) - \left\{{}^3/_5 - {}^8/_{15}\left(u_c + \frac{1}{u_c}\right)^2\right\} 2\sqrt{u_c}\, E\left(\pi/2, \frac{1}{u_c}\right) \quad (15)$$

The results of the above approximations, together with the exact results obtained for $f^{-2} = 0.6$ and $u_c = 2$, are given in Table I and represented by the solid lines 1, 2, and 3 in Fig. 2. In Table I the distance of exclusion is given as a fraction of its value at $u_c = 1$ (*i.e.*, in the absence of interaction), as a function of $1/u_c$. As u_c is directly related to the half-distance between the plates, D, and the equilibrium concentration, N_0, according to

$$D\sqrt{\beta N_0} = \frac{2}{\sqrt{u_c}} F(\pi/2, k) \quad (cf.\ \text{eq. } 7)$$

the value of $D\sqrt{\beta N_0}$ (the interaction parameter which may be determined experimentally) is also indicated. In Fig. 2 a plot of Q_i/Q_a against $D\sqrt{\beta N_0}$ is given, Q_a representing the corresponding Q values in the absence of interaction (*cf.* de Haan and Bolt[4]).

Carrying the above approximation to the extreme, one may also venture to estimate the depression of the negative adsorption from the values found for systems in which the anionic concentrations are *all* negligible in comparison with the cationic concentrations (*i.e.*, neglecting also the influence of the monovalent anions). Obviously this approximation will be valid only at fairly high values of u_c. The equations are much less involved in this case and yield

$$Q_i'\ (N_0^{z^-} = 0) = \left(1 - \frac{1}{2u_c}\right)\frac{\pi}{\sqrt{u_c}} \quad (16)$$

$$Q_i''\ (N_0^{z^-} = 0) = \left(1 - \frac{3}{8u_c^2}\right)\frac{\pi}{\sqrt{u_c}} \quad (17)$$

$$Q_i'''\ (N_0^{z^-} = 0) = \left(1 - \frac{5}{16u_c^3}\right)\frac{\pi}{\sqrt{u_c}} \quad (18)$$

For comparison, the values $Q_i\ (N_0^{z^-} = 0)/Q_a$ are shown in Table II (numbers within brackets) together with the corresponding value of $D\sqrt{\beta N_0}$ $(= \pi/\sqrt{u_c})$ and plotted as the open symbols in Fig. 2. It is seen that the neglect of anions does not make any difference up to values of $D\sqrt{\beta N_0}$ of 2 (high interaction). Beyond 2, however, a considerable deviation starts to appear, indicating that the approximation introduced leads to a fairly large error in the final result in this region.

Below is given the derivation of the expression for a system with interacting double layers containing mono- and divalent cations and monovalent anions. In view of the above results the system containing two types of cations warrants further investigation. Deriving the exact expression for a system of the composition (+2, +1, −1, $u_c \neq 1$) one finds

Table II: The Influence of Interaction on the Negative Adsorption in a (+1, +2, −1) System[a]

$\frac{1}{u_c}$	$D\sqrt{\beta N_0}$ at f^{+2} = 1.0	0.8	0.6	0.4	0.2	0.0	Q_i/Q_a at f^{+2} = 1.0	0.8	0.6	0.4	0.2	0.0
							Q_a = 1.035	1.102	1.171	1.296	1.465	2.000
0.1	0.222		0.265			0.997	0.199		0.217			0.473
0.2	0.447		0.554			1.419	0.357		0.385			0.638
0.4	0.905		1.054			2.076	0.650		0.663			0.825
0.5	1.152	1.233	1.326	1.500	1.721	2.362	0.759	0.766	0.775	0.820	0.850	0.872
0.8	2.140		2.421			3.570	0.956		0.970			0.972
0.9	2.775		3.097			4.340	0.989		0.998			1.000

[a] Q_a values refer to systems without interaction.

$$\frac{\Gamma_-}{N_0} = \pm \frac{1}{\sqrt{\beta N_0}} \cdot \int_\infty^{u_c} \frac{\left(1 - \frac{1}{u}\right) du}{\sqrt{(u - u_c)u \left\{\frac{f^{+2}}{2} u^2 + \left(1 - f^{+2} + \frac{f^{+2}}{2} u_c\right) u - \frac{1}{u_c}\right\}}} - \delta \quad (19)$$

in which f^{+2} stands for the equivalent concentration fraction of the divalent cation. Designating the form under the root sign by J

$$\frac{\Gamma_-}{N_0} = \pm \frac{1}{\sqrt{\beta N_0}} \sqrt{\frac{2}{f^{+2}}} \left\{\int_\infty^{u_c} \frac{du}{\sqrt{J}} - \int_\infty^{u_c} \frac{du}{u\sqrt{J}}\right\} - \delta \quad (20)$$

The roots of J are

$$\alpha_1 = u_c$$

$$\alpha_2 = \left(1 - {}^1/_2 u_c - \frac{1}{f^{+2}}\right) + \sqrt{{}^1/_4 u_c^2 - \left(1 - \frac{1}{f^{+2}}\right) u_c + 1 - \frac{2}{f^{+2}} + \frac{1}{(f^{+2})^2} + \frac{2}{f^{+2} u_c}}$$

$$\alpha_3 = 0$$

$$\alpha_4 = \left(1 - {}^1/_2 u_c - \frac{1}{f^{+2}}\right) - \sqrt{{}^1/_4 u_c^2 - \left(1 - \frac{1}{f^{+2}}\right) u_c + 1 - \frac{2}{f^{+2}} + \frac{1}{(f^{+2})^2} + \frac{2}{f^{+2} u_c}}$$

The general solution of Q_i' is then given by

$$Q_i' = \sqrt{\frac{2}{f^{+2}}} \left[\frac{2}{\sqrt{\alpha_1(\alpha_2 - \alpha_4)}} \left\{\left(1 - \frac{1}{\alpha_2}\right) F(\varphi,k) + \frac{\alpha_1 - \alpha_2}{\alpha_1 \alpha_2} \left(\frac{1}{1 - k^2} E(\varphi,k) - \frac{k^2 \sin \varphi \cos \varphi}{(1 - k^2)\sqrt{1 - k^2 \sin^2 \varphi}}\right)\right\}\right] \quad (21)$$

with $F(\varphi,k)$ and $E(\varphi,k)$ incomplete elliptic integrals of the first and second kind, respectively.

$$k^2 = \frac{\alpha_2(\alpha_1 - \alpha_4)}{\alpha_1(\alpha_2 - \alpha_4)}$$

The value of φ is found by filling in the integration limits into

$$u = \frac{\alpha_2(\alpha_1 - \alpha_4) \sin^2 \varphi - \alpha_1(\alpha_2 - \alpha_4)}{(\alpha_1 - \alpha_4) \sin^2 \varphi - (\alpha_2 - \alpha_4)}$$

D is now found as the first integral of eq. 20 multiplied by $\sqrt{2/f^{+2}}$; thus

$$D\sqrt{\beta N_0} = \sqrt{\frac{2}{f^{+2}}} \frac{2}{\sqrt{\alpha_1(\alpha_2 - \alpha_4)}} F(\varphi,k) \quad (22)$$

Calculations of Q_i' were executed for a range of u_c values at the conditions $f^{+2} = 1$ and $f^{+2} = 0.6$, respectively, and for a range of f^{+2} values at $u_c = 2$. Q_i' values were again compared with the corresponding Q_a values (no interaction). Results are given in Table II and plotted as the broken lines 4 and 5 in Fig. 2.

Combining all results obtained, the reduced value of the negative adsorption due to interaction (*i.e.*, Q_i/Q_a) was plotted in Fig. 3 against the reduced thickness of the water layer (*i.e.*, D/D^z, in which $D^z = Q_a/\sqrt{\beta N_0}$). Presented in this manner, the effect of interaction appears to be described satisfactorily for most practical purposes by means of the central line of the "band" in which all points are situated. As a further refinement it may be noted that in the case that the ratio of cationic valence to anionic valence, p, is greater than 1 (*e.g.*, Cl^- repulsion in predominantly Ca systems) the interaction effect is somewhat enlarged (points situated below central line) whereas for p smaller than 1 (*e.g.*, SO_4^{-2} repulsion in predominantly Na systems) the interaction effect is depressed. As is shown in Fig. 3 the reduction of the negative

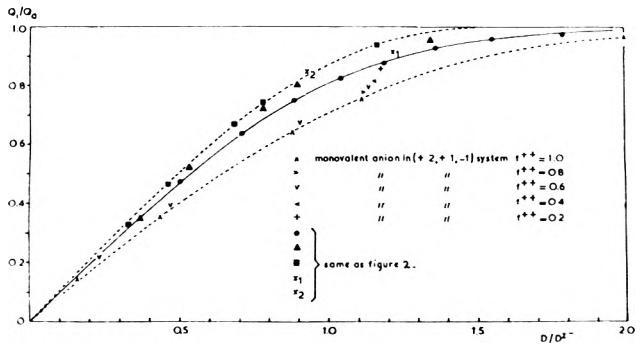

Figure 3. Depression of the negative adsorption of anions in systems with interacting double layers, Q_i/Q_a, as a function of the reduced thickness of the water layer, D/D^{z-}.

adsorption is less than about 5% as long as $D/D^{z-} \geq 1.5$.

Experimental

The experimentally accessible measure of the negative adsorption of anions is given by the volume of exclusion, V_{ex}, in ml./g. of colloid, which in fact equals the product of the equivalent distance of exclusion and the specific surface area of the planar sides of the colloidal particles. V_{ex} thus represents the volume in which no anions appear to be present. According to the foregoing theoretical considerations, the value of V_{ex} is expected to decrease at increasing interaction.

V_{ex} is found experimentally as the difference between the actual solution volume of the system, V_{tot}, and the apparent volume, V_{app}, in which the anion appears to be dissolved at the equilibrium concentration n_0^-, both expressed in milliliters per total system. This can be represented by the formula

$$V_{ex} = (V_{tot} - V_{app})/W \qquad (23)$$

in which W stands for the amount of solids in the system in grams. V_{tot} is simply found from weighing data, assuming a solution density of 1.0. V_{app} is found by means of isotopic dilution according to

$$V_{app} = \frac{V_a A_a^*}{A_e^*} \qquad (24)$$

in which V_a represents the added amount of labeling solution containing a radioisotope of the anion of interest, and A_a^* and A_e^* are the activities, in counts min.$^{-1}$ ml.$^{-1}$, of the labeling solution and the equilibrium solution, respectively.

The colloidal material used in the experiment was the fraction $<2\ \mu$ of Osage montmorillonite with a homoionic Na composition of the adsorption complex. The specific surface area, as measured according to negative anion adsorption data, turned out to be 700 m.^{2}/g.

As small values for $D\sqrt{\beta N_0}$ are required to obtain a detectable decrease of negative adsorption, several problems arise with respect to the experimental procedure. To attain small values of D one must operate with highly concentrated suspensions. Moreover the salt concentration must be maintained as low as possible. These factors are acting ino pposite directions as regards the fluidity of the suspension. Since the equilibrium solution is obtained by employment of dialysis bags, a minimum level of fluidity is necessary to attain equilibrium between the suspension and the solution in the bags in a reasonable time period. Cl^{36} not being available at high specific activity, the low Cl level requires additions of minute amounts of Cl^- in the labeling solution, resulting in an extended counting time for the activity determination.

Prior to the execution of the experiment, part of the Na montmorillonite stock suspension was brought into a pressure membrane apparatus. By applying pressure, the suspension was concentrated, and, in the meantime, the chloride concentration of the filtrate was measured. During this concentration procedure, a mat of clay was formed at the bottom of the apparatus, causing a salt-sieving effect. The clay mat was broken with a spatula at regular time intervals, and the pressure filtration was continued until a steep decrease in the salt concentration of the effluent was found (*cf.* Bolt[5]). In this way a clay paste of about 12% montmorillonite was prepared. The paste was diluted with distilled water and shaken for a long time until a very thick, but more or less "fluid," homogeneous suspension was obtained. Parts of this suspension were brought into polyethylene bottles, together with a known amount of a dilute Cl^{36}-labeling solution. Precalculated amounts of distilled water were added to acquire a range of suspension concentrations. Finally two dialysis bags, containing distilled water, were added and the systems were agitated during 12 days. After equilibration, five samples were made of each dialyzate for the activity determination, thus allowing the calculation of V_{ex}. Values of N_0 were determined from the specific electric conductivity of the dialyzates. As per system two dialysis bags were employed, values for V_{ex} and N_0 could be determined in duplicate for each system. For further details on the experimental procedure of anion adsorption determinations the reader is referred to de Haan.[6] The

(5) G. H. Bolt, *Kolloid-Z.*, **175**, 33, 144 (1961).

(6) F. A. M. de Haan, "Adsorption of Inorganic Anions by Clays and Soils," Verslagen Landbouwkundige Onderzoekingen, Wageningen, in press.

Table III: Comparison between the Theoretically Expected and the Measured Decrease of the Negative Adsorption of Cl^- in Systems with Interacting Double Layers (Na–Cl montmorillonite, Osage)[a]

No.	Clay content, %	D, Å.	N_0, mequiv./ml.	$\frac{1}{\sqrt{\beta N_0}}$, Å.	$D\sqrt{\beta N_0}$	Theoretically expected decrease according to Fig. 2, %	d^-, Å.	V_{ex}, theoretical, assuming specific surface area of 700 m.²/g., ml./g. of clay	V_{ex}, measured, ml./g. of clay	Measured decrease of V_{ex}, %
1	6.631	201.2	1.04×10^{-3}	95.2	2.11	17	186.4	13.05	10.79	17.3
2	6.020	223.0	1.07×10^{-3}	93.9	2.38	12	183.8	12.87	11.36	11.7
3	5.512	244.9	1.03×10^{-3}	95.7	2.56	10	187.4	13.12	11.86	9.6
4	5.003	271.3	1.05×10^{-3}	94.8	2.86	6	185.6	12.99	12.17	6.3
5	2.218	629.8	0.95×10^{-3}	100.3	4	0	196.6	13.76	13.68	0.0

[a] The data presented are the mean values of duplicate measurements.

experimental results are given in Table III. The data of this table were compiled in the following way. From the clay content in each system (which was determined in triplicate) the value of D (thickness of water layer around the particles) was calculated, assuming the measured value of 700 m.²/g. for the specific surface area of the clay involved.[7] The D value and the salt concentration of the equilibrium solution resulted in values for $D\sqrt{\beta N_0}$. Accordingly, the theoretically expected decrease of the negative adsorption for each system was then found from Fig. 2.

The theoretical value for the distance of exclusion in the noninteraction case is found as

$$d^- = \frac{Q_a'}{\sqrt{\beta N_0}} - \delta$$

in which Q_a' equals 2.000 because of pure Na–Cl system and δ equals 4 Å. if this distance of exclusion is multiplied by the specific surface area, one arrives at the volume of exclusion per gram of clay, which should be expected in each system if no interaction prevails. This value was compared with the measured exclusion volume, resulting in the experimentally determined decrease of the negative adsorption.

A comparison between the theoretically predicted and measured values shows an excellent agreement. In contrast with the experimental complications described above it is mentioned here that the presence of a relatively large amount of clay in each system results in a large difference between the actual volume and the apparent volume, thus allowing an accurate determination of V_{ex}.

Finally, it should be pointed out that the experiment could be performed even better for SO_4^{-2}, S^{35} being available at high specific activity. Moreover, due to its bivalency, the sulfate ion is more sensitive to interaction of double layers, the distance of exclusion being larger than for chloride under comparable conditions (*cf.* also Fig. 2).

Acknowledgment. The author is greatly indebted to Professor Dr. G. H. Bolt for many helpful suggestions and discussions in connection with this paper.

(7) This value was found from repeated measurements in extended series at low clay concentrations (*cf.* ref. 4).

Fluorine Bomb Calorimetry. IX. The Enthalpy of Formation of Magnesium Difluoride[1,2]

by Edgars Rudzitis, Harold M. Feder, and Ward N. Hubbard

Chemical Engineering Division, Argonne National Laboratory, Argonne, Illinois *(Received May 14, 1964)*

The energy of formation of magnesium difluoride was measured by direct combination of the elements in a bomb calorimeter. The standard enthalpy and Gibbs energy of formation at 298.15°K. were determined to be -268.7 ± 0.3 and -256.0 ± 0.3 kcal. mole^{-1}, respectively. The value for the enthalpy of formation is in agreement with more uncertain values derived indirectly from reaction calorimetry and high temperature equilibria.

Introduction

This research is part of a program to obtain thermochemical data by fluorine bomb calorimetry. The determination of the enthalpy of formation of MgF_2 by direct combination of its elements in a calorimeter was made to supplement previous determinations by various indirect methods and to reduce the existing uncertainty. A method[2,3] which had been successful for burning cadmium and zinc in fluorine was tried first. It was observed that the violence of the magnesium–fluorine reaction caused sputtering of the burning, liquefied metal and excessive melting of the magnesium fluoride support dishes. The ensuing submergence of part of the sample in the melt resulted in low combustion yields. These difficulties, which were reflected in excessive scatter of the data, led to two modifications of the experimental technique. The interior nickel surfaces of the bomb were protected from the sputtering metal by a liner of purified, pressed magnesium fluoride, and the sample, in the form of a triangular sheet, was suspended in the bomb by a magnesium wire. In this arrangement the sample ignites while suspended and reaches a sufficiently high temperature so that substantially complete combustion is obtained.

Experimental

Materials. (*a*) *Magnesium.* A magnesium ingot (Dow Chemical Co., 99.999 grade) was rolled into 0.6-mm. sheet and 0.1-mm. foil. Chemical and spectrochemical analysis showed the following significant impurities (in p.p.m.): H, 20; C, 64; N, 78; O, 400; Fe, 200; Na, 200. By difference, the sample contained 99.91 wt. % magnesium. If the impurities are assumed to be present as the chemical species, C, Mg_3N_2, MgO, Fe, and Na, the calculated content of elemental magnesium in the sample is also 99.91 mole %. The hydrogen was assumed to be in solution.

(*b*) *Fluorine.* The fluorine used was purified by distillation.[4] Its impurity content was approximately 0.01%.

(*c*) *Magnesium Fluoride.* Optical grade magnesium fluoride (A. D. Mackay) was found to contain approximately 0.2% magnesium oxide. Under the combustion conditions, an incomplete reaction between the oxide and fluorine occurred. To make the appropriate thermal correction required an analysis for oxygen in the combustion gases[2,3]; this determination introduced an appreciable uncertainty. Three methods for decreasing the oxide content of the magnesium fluoride were tried: (a) treatment with fluorine gas at 700°; (b) autoclaving with anhydrous hydrogen fluoride at 250° at 100–200 atm. pressure; (c) similar to (b) but with the addition of chlorine trifluoride. The oxide content of MgF_2 was decreased by treatment (c) to such an extent that no fluorine–oxide reaction was detected by gas analysis.

(1) This work was performed under the auspices of the U. S. Atomic Energy Commission.

(2) For the previous paper in this series see E. Rudzitis, H. M. Feder, and W. N. Hubbard, *J. Phys. Chem.*, **68**, 617 (1964).

(3) E. Rudzitis, H. M. Feder, and W. N. Hubbard, *ibid.*, **67**, 2388 (1963).

(4) L. Stein, E. Rudzitis, and J. L. Settle, "Purification of Fluorine by Distillation," ANL-6364 (1961).

Apparatus and Experimental Procedure

The calorimetric system (ANL-R1-Ni-4) and the calibration procedure has been previously described.[3,5] A calibration series of six benzoic acid experiments, immediately preceding the Mg combustion series, yielded a value of ε_{calor} of 3433.46 cal. deg.$^{-1}$ with a standard deviation of 0.79. The arrangement in the bomb is shown in Fig. 1. The magnesium fluoride

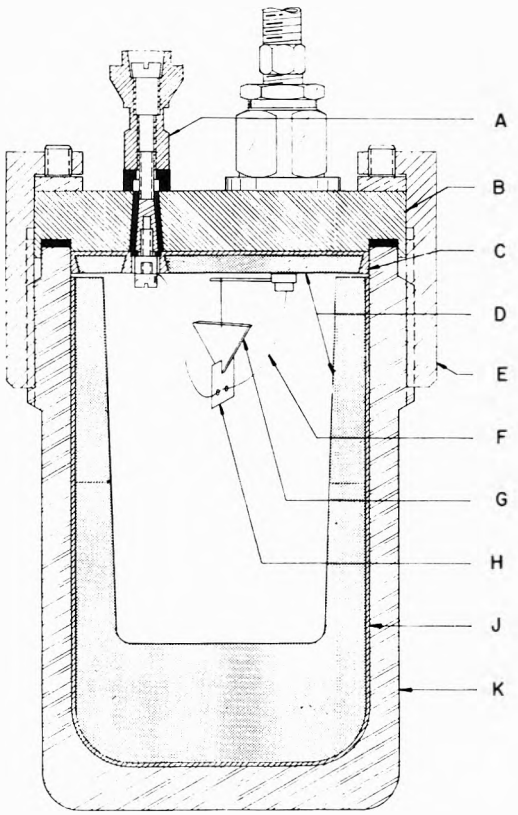

Figure 1. Combustion bomb and sample arrangement: A, insulated electrode terminal; B, bomb head; C, dish; D, liner; E, sealing nut; F, ignition wire; G, sample; H, foil; J, cup; K, bomb body.

liner (D) was contained in a nickel cup (J) and dish (C). The cup, which closely fitted the internal dimensions of the bomb (K), was filled approximately 2 cm. deep with fluoride powder, a tapered nickel block was placed in the center, and the space between the block and the cup was filled by tamping in additional powder. The dish was filled with powder which was compacted by means of a hydraulic press. The vertical surfaces of the dish were undercut to retain the powder compact in the inverted position. The compacted powders were sintered at 900°. After removal of the block the magnesium fluoride liner withstood handling without crumbling.

The calorimetric samples were prepared as follows: a triangle (G), cut from the sheet, was slit in one corner and a piece of foil (H) was inserted; the ignition wire (F) was threaded through two holes in this foil. The sample was suspended from a nickel rod by a looped magnesium wire. The ignition and suspension "wires" were actually 0.2-mm. wide strips cut from the foil.

The calorimetric samples were preconditioned by exposure to fluorine at 13 atm. for 18 hr., and their weight changes were noted. The purpose of the preconditioning was to minimize reaction between the sample and fluorine in the bomb prior to ignition.

The calorimetric combustions were initiated by passing an electrical current through the fuse wire; the electrical energy input was measured with a calibrated current-integrating device. The initial fluorine presssure was 13 atm. After each combustion the bomb was opened and those parts of the liner surface which had been affected by the combustion were removed for analysis, while the rest of the liner was left intact for re-use. The amount of unburned magnesium in the portion removed was determined by the hydrogen evolution method.[3] Trial determinations with milligram amounts of magnesium were accurate to within 5%. The reaction product of the combustions, MgF_2, was identified by its X-ray diffraction pattern.

Results

Six of a series of seven combustion experiments were acceptable; the results are summarized in Table I. Energy quantities are expressed in terms of the defined calorie equal to (exactly) 4.184 absolute joules. The entries in the table are: (1) the mass of magnesium burned and percentage of introduced samples; (2) the observed increase in the calorimeter temperature, corrected for the heat exchanged between the calorimeter and its surroundings; (3) the energy equivalent of the calorimeter multiplied by the negative of the corrected temperature increase; (4) the energy equivalent of the initial and final contents of the bomb, each multiplied by its appropriate portion of the corrected temperature increase; (5) the net correction of the bomb gas to the standard state; (6) the electrical energy input for the ignition; (7) the impurity correction; and (8) the energy change per gram of magnesium for the reaction

$$Mg(c) + F_2(g) \longrightarrow MgF_2(c) \qquad (1)$$

with the reactants and product in their respective standard states at 25°.

(5) E. Greenberg, J. L. Settle, H. M. Feder, and W. N. Hubbard, *J. Phys. Chem.*, **65**, 1168 (1961).

Table I: Results of Magnesium Combustion Experiments[a]

		Expt. no. 1	2	3	5	6	7
1.	Mass, g.	0.48057	0.28573	0.45998	0.39759	0.45712	0.42426
	(%)	(98.40)	(99.85)	(99.08)	(99.97)	(99.99)	(99.78)
2.	Δt_c,[b] deg.	1.49861	0.89444	1.44093	1.24608	1.43164	1.33113
3.	ε(calor.)$(-\Delta t_c)$, cal.	−5145.4	−3071.0	−4947.4	−4278.4	−4915.5	−4570.4
4.	ΔE(cont.),[c] cal.	−146.7	−85.0	−134.8	−111.5	−125.9	−114.3
5.	ΔE(gas), cal.	−0.9	−0.5	−0.8	−0.7	−0.8	−0.8
6.	ΔE(ignition), cal.	———	———	———	−0.1	———	———
7.	ΔE(impurities), cal.	6.0	3.6	5.8	5.0	5.7	5.3
8.	$\Delta Ec/M$, cal. g.$^{-1}$	−11,001	−11,034	−11,038	−11,030	−11,019	−11,031
		Mean $\Delta E_c°/M$ = −11,027					
		Std. dev. of mean, ±6 cal. g.$^{-1}$ or 0.05%.					

[a] The symbols are explained in ref. 6. [b] $\Delta t_c = t^f - t^i + \Delta t_{cor.}$ [c] $\Delta E(\text{cont.}) = [\varepsilon^f(\text{cont.}) - \varepsilon^i(\text{cont.})](25 - t^i) + \varepsilon^f(\text{cont.})(-\Delta t_c)$.

For the calculation of item 1 the mass of sample introduced was corrected for its known impurity content, for unburned magnesium, and for the increase in weight owing to preconditioning. The latter corrections were based on the assumption that MgF_2 was the product formed during preconditioning. The weight increases were 0.24, 0.24, 0.35, 0.30, 0.42, and 0.19 mg. for the six experiments as listed. For the calculation of item 4 on, the following values were used: C_p: Mg,[6] 5.71; Ni,[6] 6.21; MgF_2,[7] 14.72; and NiF_2,[8] 15.37; C_v: F_2,[9] 5.50 cal. mole^{-1} deg.$^{-1}$. The contents of the bomb consisted of 195.8 g. of Ni, 0.56 g. of NiF_2, and 323.26, 310.88, 304.47, 287.48, 280.83, and 272.00 g. of MgF_2 for the six experiments as listed. For the calculation of item 5 on the standard state, correction was applied in the usual manner.[10] The internal volume of the empty bomb was 0.354 l. For calculation of item 7 the following $\Delta H_f°_{298}$ values were used: MgF_2,[11] −268.7; MgO,[12] −143.7; Mg_3N_2,[12] −110.2; FeF_3,[13] −235; NaF,[13] −136.3; HF, −64.8[14]; and CF_4,[14] −220.4 kcal. mole^{-1}. The heat of solution of hydrogen in magnesium was assumed to be −9 kcal. g.-atom^{-1}. The total impurity correction amounted to 12 cal./g. of sample. An uncertainty of ±2 cal. was assigned to this value. Item 8 was calculated by summation of items 3 through 7 and division by item 1.

The following standard thermal data in kcal. mole.$^{-1}$ were derived for the formation of MgF_2(c) at 25° according to eq. 1: $\Delta E_f° = -268.1$, $\Delta H_f° = -268.7$, and $\Delta G_f° = -256.0$. An uncertainty of 0.3 kcal. mole^{-1} has been assigned to the derived data. It is equal to twice the combined standard deviation arising from the scatter of the $\Delta E_c°/M$ values and of the analytical and calibration data. The atomic weight of magnesium[15] was taken as 24.312 g. (g.-atom)$^{-1}$. The entropies, $S°_{298}$, were taken as: Mg, 7.81[16]; F_2, 48.5[16]; and MgF_2, 13.68[16] cal. deg.$^{-1}$ mole^{-1}.

Discussion

The value of $\Delta H_f°_{298}$ (MgF_2) obtained by the present study has been compared in Table II with values derived from a high temperature equilibrium study,[17] from a metathetical reaction in a calorimeter,[18] and from two studies[19,20] by solution calorimetry. The values of $\Delta H_f°_{298}$ (MgF_2) reported in the table have been derived or recalculated from the original sources

(6) F. Rossini, D. D. Wagman, W. H. Evans, S. Levine, and I. Jaffe, "Selected Values of Chemical Thermodynamic Properties," National Bureau of Standards, Circular 500, Washington, D. C., 1952.

(7) S. S. Todd, *J. Am. Chem. Soc.*, 71, 4115 (1949).

(8) E. Catalano and J. W. Stout, *J. Chem. Phys.*, 23, 1284 (1955).

(9) W. H. Evans, T. R. Munson, and D. D. Wagman, *J. Res. Natl. Bur. Std.*, 55, 147 (1955).

(10) W. N. Hubbard, "Experimental Thermochemistry," Vol. II, H. A. Skinner, Ed., Interscience Publishers, Ltd., London, 1961, Chapter 6.

(11) This work.

(12) "JANAF Thermochemical Data," Dow Chemical Co., Midland, Mich., 1962.

(13) "Preliminary Report of the Thermodynamic Properties of Selected Light-Elements and Some Related Compounds," NBS Report 7192, 1961.

(14) G. T. Armstrong, Chemical Propulsion Information Agency Publ. No. 44 (U), Vol. I, 1964, p. 59.

(15) A. E. Cameron and E. Wichers, *J. Am. Chem. Soc.*, 84, 4175 (1962).

(16) K. K. Kelley and E. G. King, U. S. Bureau of Mines Bulletin 592, U. S. Government Printing Office, Washington, D. C., 1961.

(17) L. Domange, *Ann. Chim.*, [11] 7, 225 (1937).

(18) P. Gross, C. Hayman, and D. L. Levi, *Trans. Faraday Soc.*, 50, 477 (1954).

(19) H. von Wartenberg, *Z. anorg. allgem. Chem.*, 249, 100 (1942).

(20) D. R. Torgeson and Th. G. Sahama, *J. Am. Chem. Soc.*, 70, 2156 (1948).

Table II: Derived Heats of Formation of Magnesium Fluoride

Reaction	Ref.	Temp., °C.	$\Delta H_f°_{298}$, kcal. mole^{-1}	$\Delta H_f°_{298}$, kcal. mole^{-1}
$MgO(c) + 2HF(g) = MgF_2(c) + H_2O(g)$	17	900, 1000, 1100	−51.46, −51.73, −52.22	−267.3 ± 1.1
$Mg(c) + 2HF(soln.) = MgF_2(ppt.) + H_2(g)$	19	20	−109.6 ± 0.7	−262.5 ± 1
$Mg(OH)_2(c) + 2HF(soln.) = MgF_2(ppt.) + 2H_2O(soln.)$	20	73.7	− 30.3 ± 0.0	−268.1 ± 0.5
$Mg(c) + PbF_2(c) = MgF_2(c) + Pb(c)$	18	32.4	−109.5 ± 0.3	−269.1 ± 0.6
$Mg(c) + F_2(g) = MgF_2(c)$	This work	25.0		−268.7 ± 0.3

with the use of more recent auxiliary data. The quoted uncertainties have also been adjusted so that they are comparable with those of the present work. A slight trend in the results of the third law calculations indicates the possibility of a systematic error in the equilibrium measurements.[17] Gross, *et al.*,[17] derived a value of −268.0 kcal. mole^{-1} for $\Delta H_f°_{298}$ (MgF_2) by the use of the Circular 500[7] value, −158.5 kcal. mole^{-1}, for $\Delta H_f°_{298}$ (PbF_2). They expressed some doubt about the validity of their result, and cited some possible error sources. The recalculated value given in Table II incorporates the value of $\Delta H_f°_{298}$ (PbF_2), −159.6 kcal. mole^{-1}.[12] The derivation of the value of $\Delta H_f°_{298}$ (MgF_2) from Torgeson and Sahama's measurements[20] incorporates the following $\Delta H_f°_{298}$ values (kcal. mole^{-1}): $Mg(OH)_2$, −221.0[7]; $H_2O_{(liq)}$, −683[7]; and HF (20.1% soln.), −76.4.[21] The apparent molal heat capacity of 20.1% HF was taken as 6.05 cal. deg.$^{-1}$.[22] Except for von Wartenberg's calorimetric study,[19] the results agree satisfactorily with this work.

Acknowledgments. The authors wish to acknowledge the technical assistance of Rosemary Terry. The magnesium sheet and foil was prepared by F. J. Karasek. Much of the equipment was fabricated under the direction of B. Stanis. The assistance of M. Barsky, A. Venters, and T. Rush for performing special analysis is acknowledged. Thanks are due to Professor T. F. Young for valuable discussions.

(21) This value was obtained by the application of a correction of −0.84 kcal. mole^{-1} to the Circular 500 value, as suggested by W. H. Evans in ref. 14.

(22) T. G. Ryss, "The Chemistry of Fluorine and Its Inorganic Compounds," State Publishing House of Scientific Technical and Chemical Literature, Moscow, 1956 (AEC-tr-3927), Chapter IV.

Fluorescence and Phosphorescence of Hexafluoroacetone Vapor

by Peter G. Bowers[1] and Gerald B. Porter

Department of Chemistry, University of British Columbia, Vancouver, Canada *(Received May 16, 1964)*

The emission spectrum of hexafluoroacetone consists of both fluorescence and phosphorescence, of which the latter is quenched by trace quantities of either biacetyl or oxygen. From a quantitative study of the emission of biacetyl, direct and sensitized by hexafluoroacetone, and of the emission of hexafluoroacetone, the following quantum yields have been obtained at −78°: phosphorescence, 0.51, and fluorescence, 0.05.

While there is good evidence from studies of the photodissociation of hexafluoroacetone (HFA) that the excited triplet state is involved,[2a,b] no phosphorescence was reported by Okabe and Steacie,[3] who originally measured the emission spectrum of this molecule. This contrasts with both acetone and trifluoroacetone,[4a,b] where, except at elevated temperatures, most of the emission is phosphorescence.

Besides the fact that the lifetime for phosphorescence is several orders of magnitude greater than that for fluorescence, the two kinds of emission may be readily distinguished by observing the effect of oxygen. In these simple ketones, where the upper state to which the molecule is excited is $^1(n\pi^*)$, it is well known that oxygen has little effect on the fluorescent emission from this state, but efficiently quenches phosphorescence from the triplet state $^3(n\pi^*)$.

It was felt that phosphorescence from HFA might best be recognized at a very low temperature, where competing thermal dissociation of triplet state molecules would be completely inhibited. This paper reports the result of such a study.

Experimental

Hexafluoroacetone gas, supplied by Allied Chemical, was outgassed for 2 hr. in a LeRoy–Ward still[5] at −125° and collected at −110°. It was outgassed for a further 2 hr. at −196° just prior to use. A sample prepared from HFA hydrate (Merck of Canada) gave similar spectra. Eastman Kodak biacetyl was fractionally distilled on the vacuum line and a middle fraction collected. Samples for use were thoroughly outgassed. Oxygen was prepared by heating A.R. grade potassium permanganate.

The T-shaped fluorescence cell for work at 25°, 4 cm. long and 2 cm. in diameter, was of Pyrex with three quartz windows attached with an epoxy resin. This cell was blackened on the outside and used without thermostating. The low temperature cell was similarly constructed; it was housed in a light metal casing insulated with paraffin wax (1 cm.) and polyfoam plastic (2 cm.). During a run, the cell walls were completely surrounded by pulverized Dry Ice, which was frequently stirred to ensure good thermal contact. Evacuated guard tubes were attached to the cell windows to prevent condensation. HFA was dosed into this cell at room temperature, and 20 min. was allowed for cooling after adding Dry Ice.

Light from an Osram HBO 200 medium pressure mercury lamp passed through a Bausch and Lomb grating monochromator and a Corning 9863 filter, and thence, as an approximately parallel beam, along the axis of the cell. The window on the T-arm of the cell faced the entrance slit of a Hilger *f*/4.4, D285 spectrometer with glass optics. Fluorescent light, after passing through the spectrometer, was measured with an RCA 7265 photomultiplier. Emission spectra could be recorded between 7000 and 3800 Å. by means of an automatic scan. Radiation transmitted by the cell was recorded using an RCA 935 photocell.

Corrections were applied for variation in response of

(1) Holder of a University of British Columbia Fellowship, 1962–1963, and a National Research Council Bursary, 1963–1964.

(2) (a) P. B. Ayscough and E. W. R. Steacie, *Proc. Roy. Soc.* (London), **A234**, 476 (1956); (b) G. Giacometti, H. Okabe, and E. W. R. Steacie, *ibid.*, **A250**, 287 (1959).

(3) H. Okabe and E. W. R. Steacie, *Can. J. Chem.*, **36**, 137 (1958).

(4) (a) R. E. Hunt and W. A. Noyes, Jr., *J. Am. Chem. Soc.*, **70**, 467 (1948); (b) P. Ausloos and E. Murad, *J. Phys. Chem.*, **65**, 1519 (1961).

(5) D. J. LeRoy, *Can. J. Res.*, **B28**, 492 (1950).

both photocell and photomultiplier with wave length. Allowance was also made for change in the dispersion of the D285 spectrometer over the wave lengths recorded. The manufacturers' specifications were used in considering these corrections.

Results

(*a*) *Hexafluoroacetone.* A typical emission trace as recorded is reproduced in Fig. 1. The band at 25° extends from below 3800 Å. to at least 7000 Å. with a broad maximum between 4500 and 4900 Å. Addition of a few mm. of oxygen decreases the intensity considerably and shifts the maximum to shorter wave lengths. No further changes occur on introducing more oxygen; it is probable that much less oxygen than was actually used completes the quenching. The form of the spectrum was essentially constant with ketone pressure between 30 and 150 mm.

It would thus appear that even at 25° a considerable part of the emission is phosphorescence. The unquenched fluorescence band is almost identical with that previously reported,[3] but in that work there was apparently some impurity present which almost completely quenched the phosphorescence.[6]

In Fig. 2, where the corrections have been made for instrumental sensitivity, the two contributions to the total emission are shown separately. The effect of oxygen is even more marked at −78°. The phosphorescence has a maximum between 4900 and 5000 Å. at both temperatures, and at 25° there is a smaller peak near 4600 Å. The fluorescence extends to 6000 Å., with a maximum intensity close to 4300 Å. at each temperature.

Table I shows the relative magnitudes of the integrated intensities, I, found by measuring the area under appropriate corrected curves such as those in Fig. 2.

Table I: Integrated Emission Intensities from HFA Vapor, and the Effect of Biacetyl and Oxygen; 3130-Å. Radiation Was Used for Excitation, Except in Run 4B (4358 Å.)

Run	System	T, °C.	$I(a)/I(b)$
1a	HFA (110 mm.)	25	3.77
b	HFA + O_2 (1.9 mm.)		
2a	HFA (30 mm.)	−78	10.95
b	HFA + O_2 (0.9 mm.)		
3a	HFA (30 mm.)	−78	15.38
b	HFA (30 mm.)	25	
4a	HFA (33 mm.); biacetyl (14.7 mm.)	25	0.24
b	HFA (33 mm.); biacetyl (14.7 mm.)		
5a	HFA (33 mm.)	25	0.50
b	HFA + biacetyl (2 mm.)		

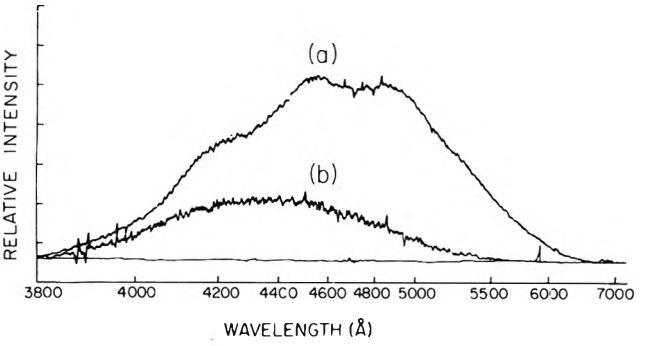

Figure 1. (a) Emission trace from 110 mm. of HFA at 25°. (b) The effect on mixing 1.9 mm. of O_2 with ketone; 3130 Å. was used for excitation.

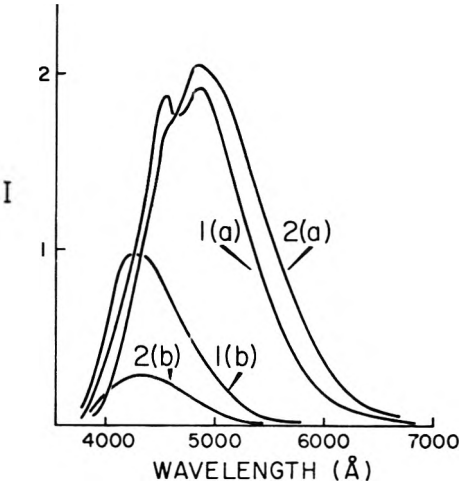

Figure 2. (a) Phosphorescence and (b) fluorescence from 1, 110 mm. of HFA at 25°, and 2, 30 mm. of HFA at −78°. Relative intensities at the different temperatures are not comparable.

(*b*) *Hexafluoroacetone–Biacetyl Mixtures.* It was found that irradiation of HFA at 25° with 3130 Å. radiation in the presence of a small concentration of biacetyl sensitized the strong characteristic green emission of biacetyl. In a mixture of 70 mm. of HFA with 1.3 mm. of biacetyl, the emission between 7000 and 4500 Å. due to biacetyl was followed by a much weaker "tail" extending to 3800 Å. which corresponds closely to the fluorescence band of HFA. Neither fluorescence nor phosphorescence from biacetyl extend below 4400 Å.[7]

(6) The emission observed here is not that of hexafluorobiacetyl, present either as a trace impurity or as a product of the reaction. The emission spectrum of hexafluorobiacetyl has its principal maxima at 5400 and 5800 Å.

(7) H. Okabe and W. A. Noyes, Jr., *J. Am. Chem. Soc.*, **79**, 801 (1957).

In run 4 (Table I), the concentrations of each component were such that the mixture absorbed radiation to the same extent at both 3130 Å. (due to HFA) and 4358 Å. (due to biacetyl). Hence, the direct and sensitized biacetyl emission intensities (4800–7000 Å.) could be compared.

A comparison was also made (run 5) of the intensity of the total HFA emission with that of the biacetyl emission sensitized by the same sample.

Discussion

We rewrite the sequence of primary events proposed by Giacometti, Okabe, and Steacie,[2b] and include a phosphorescence step

$$A + h\nu \longrightarrow {}^1A^* \quad (1)$$

$${}^1A^* \longrightarrow \text{dissociation} \quad (2)$$

$$A + {}^1A^* \longrightarrow {}^1A^0 + A \quad (3)$$

$${}^1A^0 \longrightarrow {}^3A^0 \quad (4)$$

$${}^1A^0 \longrightarrow A + h\nu_f \quad (5)$$

$${}^1A^0 \longrightarrow A^* \quad (6)$$

$${}^3A^0 \longrightarrow A + h\nu_p \quad (7)$$

$${}^3A^0 \longrightarrow \text{dissociation} \quad (8)$$

$${}^3A^0 \longrightarrow A^* \quad (9)$$

$^1A^0$ and $^3A^0$ represent excited singlet and triplet state molecules, respectively, with no vibrational energy in excess of that required for thermal equilibration. The superscript * denotes vibrationally excited species.

It will be convenient to associate quantum yields, ϕ, with some of these processes. Thus, ϕ_2 is the quantum yield for dissociation from $^1A^*$, ϕ_4 is the yield of formation of triplet molecules, and so on. In this nomenclature, even if reaction 8, say, were perfectly efficient in the sense that all triplet molecules decomposed, ϕ_8 need not necessarily be unity.

According to this scheme, the ratio of phosphorescence to fluorescence is

$$\phi_7/\phi_5 = k_4k_7/(k_7 + k_8 + k_9)k_5$$

independent of concentration. At the two temperatures studied, this ratio (Table I) is

$$(\phi_7/\phi_5)_{25^\circ} = 2.77; \quad (\phi_7/\phi_5)_{-78^\circ} = 9.95$$

and, after allowing for a small change in absorption coefficient with temperature

$$(\phi_7 + \phi_5)_{-78^\circ}/(\phi_7 + \phi_5)_{25^\circ} = 16.7$$

These figures show that the phosphorescence yield increases with decreasing temperature to a much greater extent than that of fluorescence

$$(\phi_7)_{-78^\circ}/(\phi_7)_{25^\circ} = 20.7; \quad (\phi_5)_{-78^\circ}/(\phi_5)_{25^\circ} = 5.75$$

This effect would be at least partly due to the fact that triplet dissociation, which competes with phosphorescence at 25°, is completely inhibited at the lower temperature.[8]

There are two paths by which transfer of electronic energy from HFA to biacetyl could occur, which result in sensitized emission from biacetyl

$${}^3A^0 + B \longrightarrow {}^3B^0 + A \quad (10)$$

$${}^3B^0 \longrightarrow B + h\nu_p \quad (11)$$

and

$${}^1A^0 + B \longrightarrow {}^1B^0 + A \quad (12)$$

$${}^1B^0 \longrightarrow {}^3B^0 \quad (13)$$

$${}^3B^0 \longrightarrow B + h\nu_p \quad (11)$$

Complementary studies of the dissociation of HFA under these conditions[8] suggest that reaction 12 is much the less efficient, but that even a few tenths of a mm. of biacetyl completely deactivates all triplet HFA molecules. The fact that the fluorescence band of HFA can still be observed in the presence of biacetyl supports this view. For purposes of the approximate calculations to follow, reaction 12 will be neglected. This is analogous to the acetone–biacetyl system.[9]

Since biacetyl emission excited by 4358 Å. radiation at 25° is 98% phosphorescence,[7] we obtain

$$\frac{\phi_{11}(\text{sensitized at } 3130 \text{ Å.})}{\phi_{11}(4358 \text{ Å.})} = 0.45$$

where the value of 0.24 in Table I has been adjusted for the relative intensities of 4358 and 3130 Å. exciting lines.

We can now use the fact that triplet biacetyl is formed with almost unit quantum efficiency at 4358 Å.[10,11] Then, by assuming that the same fraction of these triplet biacetyl molecules emit after direct and sensitized excitation (*i.e.*, at 4358 and 3130 Å.), and that all triplet HFA is quenched by reaction 10, we obtain

(8) P. G. Bowers and G. B. Porter, to be published.

(9) J. Heicklen and W. A. Noyes, Jr., *J. Am. Chem. Soc.*, 81, 3858 (1959).

(10) G. B. Porter, *J. Chem. Phys.*, 32, 1587 (1960).

(11) H. L. J. Bäckström and K. Sandros, *Acta Chem. Scand.*, 14, 48 (1960).

$$\phi_{10} \simeq \phi_4 = 0.45$$

That is, at 33 mm., about half of all HFA molecules excited eventually reach the triplet state at 25°. We have found the triplet dissociation yield, ϕ_8, to be 0.22 when HFA is irradiated alone under these conditions.

Finally, taking ϕ_{11}(4358 Å., 25°) to be 0.15[12] allows an estimate to be made of ϕ_7 at 25°, using the data of runs 4 and 5 in Table I

$$\phi_{7(25°)} = \left[\frac{\phi_{11}(\text{sensitized})}{\phi_{11}(4358\ \text{Å.})}\right] \phi_{11}(4358\ \text{Å.}) \times \left[\frac{(\phi_7 + \phi_5)}{\phi_{11}(\text{sense})}\right]\left[\frac{\phi_7}{\phi_7 + \phi_5}\right]$$

$$= 0.025$$

Hence, $\phi_{7(-78°)} = 0.51$. Corresponding values for the fluorescence quantum yields are 0.009 (25°) and 0.051 (−78°).

There is, of course, a considerable accumulated error in these last figures, possibly up to 30%. Nevertheless, the results do indicate that phosphorescence is a major event in the primary processes at the low temperature.

Radiationless conversion, reaction 9, evidently competes with phosphorescence much less effectively as the temperature is decreased. With $\phi_4 = 0.45$ and $\phi_7 + \phi_8 = 0.25$ at 25°, the ratio k_9/k_7 is about 10. At −78°, with $\phi_7 \simeq 0.5$, this same ratio cannot be much greater than unity. If, as is likely, k_7 is temperature independent, then k_9 would have an apparent activation energy of at least 0.6 kcal./mole. This fact, together with any corresponding changes in k_4 and k_6 with temperature, may be another reason for the greater degree of enhancement of phosphorescence as compared to fluorescence as the temperature is decreased. The data here do not allow any further deductions to be made about this aspect of the primary processes.

It would be of interest to measure relative emission efficiencies as a function of pressure at −78°. The greatly increased intensity should allow observations to be made at much lower concentrations, where effects of multistage collisional deactivation might become evident.[13]

Acknowledgment. This research was made possible through a grant from the National Research Council of Canada.

(12) G. M. Almy and P. R. Gillette, *J. Chem. Phys.*, 11, 188 (1943).
(13) D. J. Wilson, B. Noble, and B. Lee, *ibid.*, **34**, 1392 (1961).

Pure Quadrupole Resonance of Halogens in Some $R_2[MX_6]$ Type Complexes

by Daiyu Nakamura and Masaji Kubo

Department of Chemistry, Nagoya University, Chikusa, Nagoya, Japan *(Received May 18, 1964)*

The pure quadrupole resonance of halogens in some hexahaloplatinates(IV) was observed at various temperatures. The hexachloroplatinates(IV) and hexabromoplatinates(IV) show a single resonance line in agreement with the $K_2[PtCl_6]$ structure of these complexes. Ammonium hexaiodoplatinate(IV) shows a single resonance line at room and Dry Ice temperatures, but two lines at liquid nitrogen temperature, indicating that the symmetry of the crystal is lower than cubic symmetry. Rubidium hexaiodotellurate(IV) shows three transition points at about −40, −16, and 55°, above which the crystal has cubic symmetry. The resonance frequency of halogens in $K_2[PtCl_6]$ type crystals increases progressively while the absolute value of the temperature coefficients of resonance frequencies decreases with increasing size of cations and decreasing temperature. Ammonium hexachloroplatinate(IV) and hexabromoplatinate(IV) are exceptions to this rule, a rotational transition being found to exist at 0–1° for the latter compound.

Introduction

We have observed the pure quadrupole resonance of halogens in various hexahalo complexes of the general type $R_2[MX_6]$ having different central metal atoms M.[1-6] The main object of the study was the quantitative estimation of the covalent character of metal–ligand bonds in these complexes from the quadrupole resonance frequencies at liquid nitrogen temperature. Owing to the high accuracy obtainable in radiowave spectroscopy, it is possible to determine the possible effect of temperature and neighboring cations on the electronic structure of complex anions. From the observed temperature dependence of the resonance frequencies, one can discover phase transitions in crystals which are less readily accessible by more laborious methods such as X-ray crystallography and heat capacity measurements. We have therefore prepared a number of hexahaloplatinates(IV) differing in the kind of cations and rubidium hexaiodotellurate(IV) and determined the pure quadrupole resonance frequencies at temperatures between room and liquid nitrogen temperatures.

Experimental

Apparatus. A Dean type self-quenching superregenerative spectrometer already described was used for the observation of quadrupole signals of chlorine isotopes.[1] For detecting the resonance frequencies of bromine and iodine, a self-quenching super-regenerative spectrometer equipped with Lecher lines was employed.[1] Resonance frequencies were determined at room, Dry Ice, and liquid nitrogen temperatures. Whenever the existence of transition points was suspected from data at these temperatures, measurements were also made between −70 and 70° at temperature intervals of several degrees or less.

Materials. All the complexes studied were synthesized in accordance to methods described in the literature. Ammonium hexachloroplatinate(IV) was prepared by adding ammonium chloride to a solution of hexachloroplatinic(IV) acid in hydrochloric acid.[7] The resulting yellow powder crystals were washed several times with dilute hydrochloric acid. Hexabromoplatinic(IV) acid enneahydrate was obtained by the dissolution of platinum black in an aqueous solution of bromine and hydrobromic acid followed by the

(1) D. Nakamura, Y. Kurita, K. Ito, and M. Kubo, *J. Am. Chem. Soc.*, **82**, 5783 (1960).

(2) K. Ito, D. Nakamura, Y. Kurita, K. Ito, and M. Kubo, *ibid.*, **83**, 4526 (1961).

(3) D. Nakamura, K. Ito, and M. Kubo, *ibid.*, **84**, 163 (1962).

(4) D. Nakamura, K. Ito, and M. Kubo, *Inorg. Chem.*, **1**, 592 (1962).

(5) D. Nakamura, K. Ito, and M. Kubo, *ibid.*, **2**, 61 (1963).

(6) K. Ito, D. Nakamura, K. Ito, and M. Kubo, *ibid.*, **2**, 690 (1963).

(7) G. Brauer, "Handbuch der präparativen anorganischen Chemie," Ferdinand Enke Verlag, Stuttgart, 1954, p. 1174.

removal of excess bromine and hydrogen bromide.[8] In order to prepare sodium hexabromoplatinate(IV) hexahydrate, sodium bromide was added to a solution of hexabromoplatinic(IV) acid in dilute hydrobromic acid.[8] Orange-yellow crystals were separated and washed several times with dilute hydrobromic acid. Ammonium hexaiodoplatinate(IV) was prepared by adding hexachloroplatinic(IV) acid to a concentrated solution of excess ammonium iodide.[9] Black powder crystals formed were washed twice with cold water. Complexes differing from the foregoing ones in the kind of cations were synthesized in a similar manner. Rubidium hexaiodotellurate(IV) was formed when rubidium iodide was added to a solution of tellurium dioxide in hydriodic acid.[3] The resulting black crystals were washed with hydriodic acid solution and dried. Since no data for this compound were available in the literature, chemical analysis was performed for the identification of the complex. *Anal.* Calcd. for Rb_2TeI_6: Te, 12.0; I, 71.8. Found: Te, 12.1; I, 71.1.

Results

The resonance frequencies of ^{35}Cl, ^{79}Br, and ^{127}I observed at room, Dry Ice, and liquid nitrogen temperatures are listed in Table I. Those of less abundant isotopes are omitted, because they give correct isotope frequency ratios, $\nu(^{35}Cl)/\nu(^{37}Cl) = 1.269$ and $\nu(^{79}Br)/\nu(^{81}Br) = 1.197$.

Discussion

Number of Resonance Lines and the Crystal Structure. All hexachloroplatinates(IV) and hexabromoplatinates(IV) studied show a single resonance line. This is in agreement with the results of X-ray crystal analysis on ammonium, rubidium, and cesium hexachloroplatinates(IV) and hexabromoplatinates(IV), which are reported[10] to form $K_2[PtCl_6]$ type face-centered cubic crystals at room temperature, except for rubidium hexabromoplatinate(IV). We have found by the analysis of Norelco X-ray diffraction patterns that this compound also forms $K_2[PtCl_6]$ type crystals with a lattice constant $a = 10.405$ Å. Hexabromoplatinic(IV) acid enneahydrate gives rise to a single resonance line at room temperature. At lower temperatures, the line escaped detection presumably owing to line broadening. Sodium hexabromoplatinate(IV) hexahydrate shows a single resonance line at all temperatures studied. This is rather surprising in view of the fact that sodium hexachloroplatinate(IV) hexahydrate, which forms triclinic pinacoidal crystals and is isomorphous with sodium hexabromoplatinate(IV) hexahydrate,[11] gives rise to three ^{35}Cl resonance lines at

Table I: Pure Quadrupole Resonance Frequencies of Halogens in Some $R_2[MX_6]$ Complexes

Compound		Temp., °C.	Frequency, Mc./sec.	Multiplet component
$(NH_4)_2PtCl_6$		26.0	26.065 ± 0.002	
		−75	26.160 ± 0.002	
		Liquid N_2	26.282 ± 0.001	
Rb_2PtCl_6		25.0	26.29 ± 0.03	
		−77	26.37 ± 0.03	
		Liquid N_2	26.44 ± 0.03	
Cs_2PtCl_6		25.1	26.60 ± 0.05	
		−74	26.66 ± 0.05	
		Liquid N_2	26.70 ± 0.05	
$H_2PtBr_6 \cdot 9H_2O$		19.8	201.52 ± 0.08	
$Na_2PtBr_6 \cdot 6H_2O$		19.3	206.40 ± 0.08	
		−77	206.82 ± 0.08	
		Liquid N_2	207.44 ± 0.08	
$(NH_4)_2PtBr_6$		21.8	202.524 ± 0.015	
		−75	203.175 ± 0.025	
		Liquid N_2	203.983 ± 0.010	
Rb_2PtBr_6		21.8	204.37 ± 0.07	
		−74	204.98 ± 0.07	
		Liquid N_2	205.63 ± 0.03	
Cs_2PtBr_6		23.1	207.19 ± 0.07	
		−77	207.78 ± 0.07	
		Liquid N_2	208.32 ± 0.07	
$(NH_4)_2PtI_6$	ν_1	22.0	199.84 ± 0.07	
	ν_1	−77	203.54 ± 0.07	
	ν_1	Liquid N_2	205.69 ± 0.07	
	ν_1	Liquid N_2	205.48 ± 0.07	
Rb_2PtI_6	ν_1	22.0	203.40 ± 0.07	
	ν_1	−78	204.32 ± 0.07	
	ν_1	Liquid N_2	205.33 ± 0.05	
	ν_2	Liquid N_2	410.66 ± 0.03	
Rb_2TeI_6	ν_1	18.5	150.934 ± 0.015	I
	ν_1	18.5	148.789 ± 0.030	II
	ν_1	−78	152.508 ± 0.025	III
	ν_1	−78	152.298 ± 0.025	III
	ν_1	−78	150.27 ± 0.05	IV
	ν_1	Liquid N_2	153.903 ± 0.015	III
	ν_1	Liquid N_2	153.240 ± 0.015	III
	ν_1	Liquid N_2	151.995 ± 0.020	IV
	ν_2	20.0	301.50 ± 0.03	I
	ν_2	20.0	297.57 ± 0.05	II
	ν_2	−75	304.42 ± 0.03	III
	ν_2	−75	304.15 ± 0.03	III
	ν_2	−75	300.50 ± 0.05	IV
	ν_2	Liquid N_2	306.619 ± 0.025	III
	ν_2	Liquid N_2	305.636 ± 0.025	III
	ν_2	Liquid N_2	303.688 ± 0.030	IV

(8) E. Bülmann and A. C. Andersen, *Ber.*, **36**, 1565 (1903).

(9) R. L. Datta, *J. Am. Chem. Soc.*, **35**, 1186 (1913).

(10) G. Engel, *Z. Krist.*, **90**, 341 (1935); ASTM Cards 10-422 (1960) and 9-400 (1959), American Society for Testing Materials.

(11) P. Groth, "Chemische Kristallographie," Vol. 1, Verlag von Wilhelm Engelmann, Leipzig, 1906, p. 543.

room temperature.[12] It is not altogether inconceivable that only a very weak line of sodium hexabromoplatinate(IV) hexahydrate was observable while other lines of the multiplet were undetectable owing to their weak intensity.

The quadrupole coupling constants eQq and asymmetry parameter η of hexaiodo complexes were calculated as shown in Table II. Ammonium hexaiodoplatinate(IV) shows a single ν_1 resonance line at room and Dry Ice temperatures, whereas two ν_1 lines were observed at liquid nitrogen temperature. We have found by X-ray powder patterns that the crystal structure of this compound at room temperature is the same as that of potassium hexachloroplatinate(IV) and that a = 11.15$_5$ Å. Therefore, it is concluded that between Dry Ice and liquid nitrogen temperatures a transition point exists, below which the symmetry of the crystal is lower than cubic symmetry. The determination of the corresponding ν_2 lines was unsuccessful owing to the low sensitivity of available spectrometers in the high-frequency region. On the other hand, rubidium hexaiodoplatinate(IV) yields a single line at all temperatures studied. X-Ray powder analysis carried out at room temperature indicated the $K_2[PtCl_6]$ type structure of the crystal with a = 11.21$_1$ Å. At liquid nitrogen temperature, the ν_1 resonance signal was strong and ν_2 could also be observed. The frequency ratio, ν_1/ν_2, almost exactly equal to 0.5, leads to the asymmetry parameter η equal to zero within 0.008. These facts along with the normal temperature dependence of the resonance frequency indicate that the crystal structure of the $K_2[PtCl_6]$ type persists down to liquid nitrogen temperature.

Rubidium hexaiodotellurate(IV) shows two ν_1 lines at room temperature and three ν_1 lines at Dry Ice and liquid nitrogen temperatures. The same is true with ν_2 resonance. Accordingly, two kinds of crystallographically nonequivalent iodine atoms exist in crystals at room temperature and three kinds of such iodine atoms exist in crystals at Dry Ice and liquid nitrogen temperatures. On the basis of the temperature dependence of resonance frequencies, we could locate three transitions taking place at about −40, −16, and 55° (see Fig. 1 and 2). With increasing temperature from −70°, the intensity of the two high-frequency components of ν_1 and ν_2 triplets begins to decrease at −40° and the lines disappear at −36°. Two new lines of slightly lower frequencies appear at −40°. These lines coalesce at −16° to yield a single line. On lowering the temperature, the reverse process can be followed except that the gradual transition takes

Table II: Quadrupole Coupling Constants and Asymmetry Parameters of ^{127}I in Hexaiodo Complexes

Compound	Temp., °C.	eQq, Mc./sec.	η	Multiplet component
$(NH_4)_2PtI_6$	22.0	1332.3	0	
	−77	1356.9	0	
	Liquid N_2	1371.3	0	assumed
		1369.9	0	
Rb_2PtI_6	22.0	1356.0	0	
	−78	1362.1	0	
	Liquid N_2	1368.9 ± 0.1	0.000 ± 0.008	
Rb_2TeI_6	20.0	1005.15 ± 0.07	0.029 ± 0.002	I
		991.90 ± 0.10	0.000 ± 0.005	II
	−78	1015.16 ± 0.08	0.038 ± 0.003	III
		1014.15 ± 0.08	0.032 ± 0.003	
		1001.8 ± 0.2	0.00 ± 0.01	IV
	Liquid N_2	1022.69 ± 0.06	0.055 ± 0.002	III
		1019.23 ± 0.06	0.046 ± 0.002	
		1012.46 ± 0.08	0.028 ± 0.003	IV

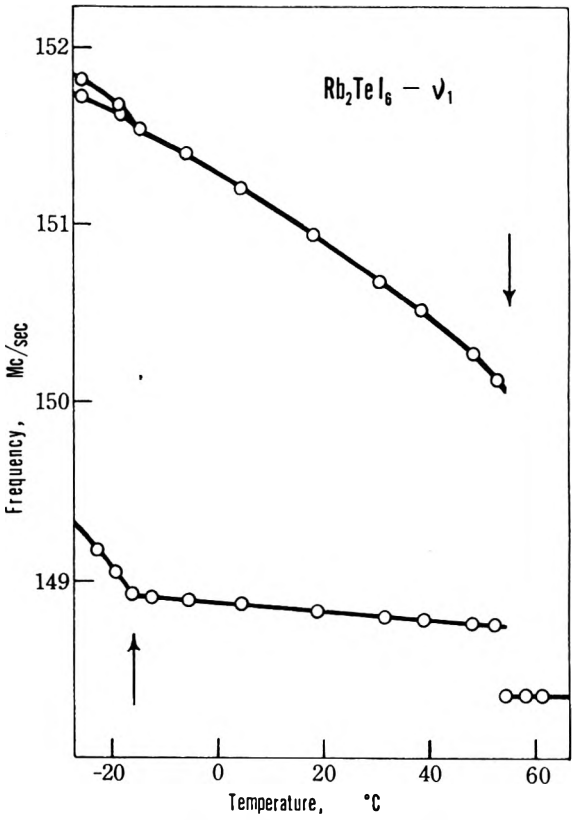

Figure 1. Temperature dependence of the ν_1 triplet lines of iodine in rubidium hexaiodotellurate(IV).

(12) K. Ito, K. Ito, D. Nakamura, and M. Kubo, *Bull. Chem. Soc. Japan*, **35**, 518 (1962)

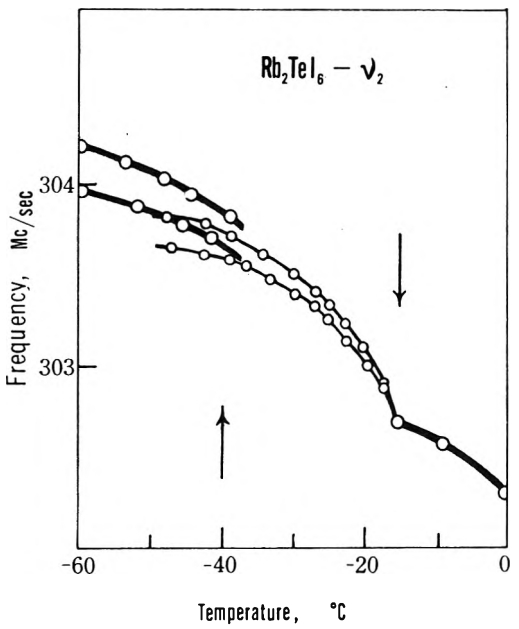

Figure 2. Temperature dependence of two high-frequency components of the ν_2 triplet of iodine in rubidium hexaiodotellurate(IV).

place at about −47°. On the other hand, the low-frequency component of each triplet shows a sudden increase in its intensity at −16° with increasing temperature. The slope of the resonance frequency plotted against temperature also changes at this temperature. It was rather surprising to find that this line shows no discontinuity in its frequency and intensity at about −40°. It is evident that iodine atoms responsible for this line are indifferent to the phase transition at this temperature. Presumably, the transition is related to the torsional oscillation or rotation of hexaiodotellurate(IV) ions about Te–I axes involving the iodine atoms in question, as pointed out by Morfee, *et al.*,[13] for hexachlorostannate(IV) ions in potassium hexachlorostannate(IV). With increasing temperature from −16°, the doublet structure of each of the ν_1 and ν_2 resonances gives way to a single line at 55°, about which the frequency ratio, $\nu_1/\nu_2 = (148.34 \pm 0.05)/(296.63 \pm 0.01) \approx 0.5$, yields a vanishing asymmetry parameter. This suggests that rubidium hexaiodotellurate(IV) crystallizes in the $K_2[PtCl_6]$ type structure at temperatures above 55°. In order to confirm this point, X-ray powder patterns were taken at 60–70° by means of a Norelco X-ray diffractometer using the Cu Kα line filtered through a nickel foil. The patterns could be interpreted (see Table III) as resulting from a $K_2[PtCl_6]$ structure having a lattice constant, a = 11.62 Å., which is close to that of cesium hexaiodotellurate(IV),[3] a = 11.64 Å.

On the other hand, the X-ray powder patterns taken at room temperature indicated clearly that the symmetry of the crystals is lower than cubic symmetry. Thus, it is established that the transition at 55° corresponds to the transformation of a less symmetric low-temperature modification into a cubic structure at higher temperatures. The quadrupole coupling constant eQq and the asymmetry parameter η were evaluated at various temperatures below 55° by use of Livingston and Zeldes' Table.[14] The correspondence was made between ν_1 and ν_2 lines by taking into account the theoretical requirement that $2\nu_1 \geq \nu_2$ and the similarity of the temperature dependence of the resonance frequencies, as shown in the last column of Table I. A pair of lines, ν_1 = 148.78 and ν_2 = 297.57 Mc./sec. at 20°, gives eQq = 991.9 Mc./sec. and η = 0. The former is almost independent of temperature and is close to the quadrupole coupling constant eQq = 989.0 Mc./sec. of the high temperature crystalline phase at 55.5°. The latter is also unchanged (η = 0.000) between −16 and 55°. This indicates that the iodine atoms in question have their surroundings that are insensitive to the change in crystal structure and lattice vibrations. In other words, the fourfold axial symmetry of electron distribution about a Te–I axis is retained even in the less symmetric structure below 55°.

Lattice Constants and Quadrupole Resonance Frequencies. The quadrupole resonance frequencies of

Table III: Comparison between Calculated and Observed $\sin^2\theta$ Values for Rubidium Hexaiodotellurate(IV) at 60–70°; a = 11.62 ± 0.01 Å.

hkl	$\sin^2\theta_{obsd}$	$\sin^2\theta_{calcd}$	Intensity
111	0.0133	0.0132	Medium
200	0.0177	0.0176	Medium
311	0.0483	0.0483	Weak
222	0.0528	0.0527	Very strong
400	0.0705	0.0703	Very strong
331	0.0833	0.0835	Weak
420	0.0879	0.0879	Weak
333, 511	0.1187	0.1186	Very weak
440	0.1406	0.1406	Strong
531	0.1539	0.1538	Very weak
442, 600	0.1583	0.1582	Weak
622	0.1933	0.1933	Medium
444	0.2109	0.2109	Weak

(13) R. G. S. Morfee, L. A. K. Staveley, S. T. Walters, and D. L. Wigley, *J. Phys. Chem. Solids*, 13, 132 (1960).

(14) R. Livingston and H. Zeldes, "Table of Eigenvalues for Pure Quadrupole Spectra, Spin $^5/_2$," ONRL report 1913, Oak Ridge National Laboratory, Oak Ridge, Tenn., 1955.

chlorine and bromine in potassium, ammonium, rubidium, and cesium hexachloroplatinates(IV) and hexabromoplatinates(IV), all of which show the same type of crystal structures, increase progressively with increasing lattice constant of these crystals as shown in Table IV. (Sodium salts are omitted from the discussion, because they crystallize with water of crystallization.) Since X-ray crystal analysis has shown that the Pt–Cl bond distance (2.32–2.36 Å.) in various hexachloroplatinates(IV)[15] is almost independent of the kind of cations, it is presumed that the frequency increase results primarily from the increasing size of cations. Therefore, the field gradient $q_z^{(1)}$ at a halogen atom X due to eight cations R^+ nearest to the complex anion in question was calculated for a point charge model, where the z-axis was taken along the M–X direction. The field gradient is negative and is, roughly speaking, proportional to the square of the M–X distance and inversely proportional to the fifth power of the R–R distance. On the other hand, the field gradient $q_{c.i.}$ originating from charges within the complex ion except for the X nucleus is positive, because the halogen atom has partial vacancy in the p_z orbital whereas both p_x and p_y orbitals are filled. Accordingly, the quadrupole frequency

$$\nu = {}^1/_2|eQq| = {}^1/_2|eQ|(q_{i.c.} + q_z^{(1)})$$

increases with increasing lattice constant in qualitative agreement with the results of the present investigation. Numerical calculations were carried out for potassium hexachloroplatinate(IV) (a_0 = 9.755 Å., l(Pt–Cl) = 2.330 Å.) and cesium hexachloroplatinate(IV) (a_0 = 10.215 Å., l(Pt–Cl) = 2.340 Å.) by including $q_z^{(2)}$ due to 12 second neighbors (anions) and q_z^3 due to 24 third neighbors (cations). One has

$$q_{\text{calcd}}(K_2[PtCl_6]) = (-7.801 + 1.866 + 0.539) \times 10^{22}e$$
$$= -5.40 \times 10^{22}e$$
$$q_{\text{calcd}}(Cs_2[PtCl_6]) = (-6.680 + 1.478 + 0.435) \times 10^{22}e$$
$$= -4.77 \times 10^{22}e$$

in e.g.s. e.s.u., where e denotes the absolute value of the electronic charge. The difference $\Delta q_{\text{calcd}} = q(\text{Cs}) - q(\text{K})$ between these two calculated values is $0.63 \times 10^{22}e$. In order to check the convergence of the series expansion, further numerical calculations were performed by including all other ions within a sphere of 19 Å. (for the potassium salt) or 20 Å. (for the cesium salt) radius having the chlorine ion in question (rather than the center of the complex ion) as its center. The sphere comprises 236 cations and 115 complex anions in addition to the central anion. One has

$$q_{\text{calcd}}(K_2[PtCl_6]) = -6.05 \times 10^{22}e$$
$$q_{\text{calcd}}(Cs_2[PtCl_6]) = -5.30 \times 10^{22}e$$

leading to $\Delta q_{\text{calcd}} = 0.75 \times 10^{22}e$. This value is presumed to be correct at least with regard to its sign and the order of magnitude, although the numerical agreement with the foregoing value, $0.63 \times 10^{22}e$, is rather poor. It leads to the quadrupole frequency difference $\Delta\nu$ between the two complexes given by

$$h\Delta\nu = {}^1/_2|eQ|\Delta q_{\text{calcd}}$$

where h is the Planck constant and Q, the nuclear quadrupole moment of ^{35}Cl, is equal to -0.07894×10^{-24} cm.^{2}. The calculated frequency difference, 0.010 Mc., is one or two orders of magnitude smaller than the observed difference, 0.79 Mc., at room temperature. Owing to the highly symmetric structure of these crystals, the direct electrostatic effect of charges of other ions on the field gradient at the halogen nucleus under observation is rather insignificant. The field gradient comes largely from the charge distribution within the complex anion, the electronic structure of which is affected by surrounding ions. Conceivable causes are the polarization of the complex ion by the electrostatic field from neighboring ions, etc., as well as the suppression of bending vibrations of M–X bonds, which increases the frequency of quadrupole resonance.[16]

Table IV: Pure Quadrupole Resonance Frequencies, ν, of ^{35}Cl and ^{79}Br and Lattice Constants a of $K_2[PtCl_6]$ Type Crystals at Room Temperature[a]

Compound	ν, Mc./sec.	$\Delta\nu/\nu_0$, %	a, Å.	$\Delta a/a_0$, %
$K_2[PtCl_6]$	25.81	0	9.755	0
$(NH_4)_2[PtCl_6]$	26.07	1.0	9.858	1.1
$Rb_2[PtCl_6]$	26.29	1.9	9.901	1.5
$Cs_2[PtCl_6]$	26.60	3.1	10.215	4.7
$K_2[PtBr_6]$	200.2	0	10.293	0
$(NH_4)_2[PtBr_6]$	202.5	1.1	10.367	0.7
$Rb_2[PtBr_6]$	204.4	2.1	10.405[b]	1.1
$Cs_2[PtBr_6]$	207.2	3.4	10.643	3.4

[a] $\Delta\nu = \nu - \nu_0$ and $\Delta a = a - a_0$, where subscripts 0 refer to $K_2[PtCl_6]$ and $K_2[PtBr_6]$ taken as references. [b] Determined by an analysis of Norelco X-ray diffraction patterns.

(15) L. E. Sutton, "Tables of Interatomic Distances and Configuration in Molecules and Ions," The Chemical Society, London, 1958, p. M101.

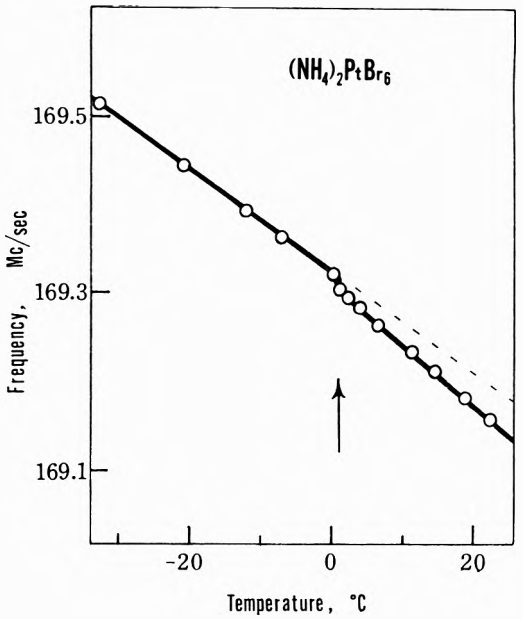

Figure 3. Temperature dependence of the quadrupole resonance frequency of ^{81}Br in ammonium hexabromoplatinate(IV).

Temperature Coefficient of Resonance Frequencies. The average temperature coefficients, $\Delta\nu/\Delta T$, of the resonance frequencies were calculated between liquid nitrogen and Dry Ice temperatures and between Dry Ice and room temperatures, as shown in Table V. In general, the absolute value of the (negative) temperature coefficient $\Delta\nu/\Delta T$ decreases with increasing size of cations and decreasing temperature, except for ammonium hexachloro- and hexabromoplatinates(IV), which show some deviations.

The exceptional behavior of the ammonium complexes must be looked for in the structure of ammonium ions. If ammonium ions rotate in crystals, they simulate spherical symmetry inherent to alkali metal ions. If the rotation does not take place, the symmetry is lowered to T_d. Therefore, the electrostatic effect of ammonium ions on halogens in $[PtX_6]^{2-}$ ions must be different from that of rotating ammonium ions. Since the fixation of ammonium ions in crystals gives rise to a discontinuous change in the field gradients about halogen atoms, one may expect some discontinuity in the temperature dependence of quadrupole resonance frequencies. As shown in Fig. 3, ammonium hexabromoplatinate(IV) shows a discontinuity of $d\nu/dT$ at 0–1°. No such discontinuity was observed for ammonium hexachloroplatinate(IV) between room and Dry Ice temperatures, the relation between the resonance frequency and temperature being strictly linear. However, the value at liquid nitrogen temperature deviates from this linear relation to the high-frequency side, whereas the curves of pure quadrupole resonance frequencies plotted against temperature are normally concave to the abscissa. This suggests the existence of a rotational transition, as observed for ammonium hexabromoplatinate(IV), at some temperature between Dry Ice and liquid nitrogen temperatures.

Table V: Temperature Coefficients $\Delta\nu/\Delta T$ of Quadrupole Resonance Frequencies of ^{35}Cl and ^{79}Br in $K_2[PtX_6]$ Type Crystals

Compound	$\lvert\Delta\nu/\Delta T\rvert$, kc./deg. Liquid N_2–Dry Ice	$\lvert\Delta\nu/\Delta T\rvert$, kc./deg. Dry Ice–room temp.
$K_2[PtCl_6]$	0.92	0.98
$(NH_4)_2[PtCl_6]$	1.01	0.94
$Rb_2[PtCl_6]$	0.59	0.78
$Cs_2[PtCl_6]$	0.33	0.61
$(NH_4)_2[PtBr_6]$	6.7	6.7
$Rb_2[PtBr_6]$	5.3	6.4
$Cs_2[PtBr_6]$	4.5	5.9

(16) H. Bayer, *Z. Physik*, 130, 227 (1951).

Radiolysis of Cyclohexene. II. Effects of Additives[1]

by B. R. Wakeford and G. R. Freeman

Department of Chemistry, University of Alberta, Edmonton, Alberta *(Received May 18, 1964)*

The addition of benzene and 1,3-cyclohexadiene inhibited the formation of all of the major products of the cyclohexene radiolytic system, the latter additive having the more marked effects. The addition of 1,4-cyclohexadiene enhanced the cyclohexane yield slightly, but inhibited the formation of the remaining "cyclohexene" products. Of the three additives, 1,3-cyclohexadiene gave a relatively much greater yield of polymer and had the highest rate of disappearance. Benzene apparently gave "sponge type" protection to cyclohexene. Activation transfer from cyclohexene to 1,3-cyclohexadiene was clearly demonstrated by the formation of dicyclohexadienyl in good yield ($G \approx 6$) at low diene concentrations (about 2 mole %). This diene probably also acted as a radical scavenger. The effects of 1,4-cyclohexadiene appeared to be best explained by a combination of activation transfer and free radical reactions.

Introduction

In the first paper of this series, the radiolysis of pure cyclohexene was discussed.[2] This paper is concerned with the effects, on the liquid cyclohexene radiolytic system, of the addition of each of benzene (B), 1,3-cyclohexadiene (1,3-D), and 1,4-cyclohexadiene (1,4-D).

Experimental

The techniques described previously[2] apply also to this work.

The samples were irradiated at 22 ± 2° at a dose rate of 8×10^{18} e.v./g. hr. The dose given most of the samples was 1.5×10^{20} e.v./g.

1,3-D (Columbia Organic Chemicals and Aldrich Chemical Co.) and 1,4-D (Aldrich Chemical Co.) were purified by vacuum distillation and vapor phase chromatography (v.p.c.). Research grade benzene (Phillips Petroleum) was used as supplied.

A dimer of 1,3 D (tricyclo[4,4,$2^{7,10}$,0]dodeca-2,8-diene) was prepared by heating 1,3-D at 200° for 20 hr. *in vacuo*[3a,b] with about 0.05 mole % of added 2,2-diphenyl-1-picrylhydrazyl to inhibit free radical processes. The product was purified by v.p.c. The mass and n.m.r. spectra of this material were consistent with the expected structure.[4]

Results

It is convenient to compare the effects of different additives on the cyclohexene product yields in terms of the extent to which the formation of each product is inhibited or sensitized. The basis for this comparison is taken as the "expected yield" of a product P, $G_{ex}(P)$, which is defined by

$$G_{ex}(P) = G_c^0(P)\epsilon_c + G_a^0(P)\epsilon_a$$

where $G_c^0(P)$ and $G_a^0(P)$ are the yields of the product P from pure cyclohexene and pure additive, respectively, and ϵ_c and ϵ_a are their respective electron fractions in the solution. The dashed lines in the figures indicate G_{ex}.

Hydrogen. The yields of hydrogen ($G(H_2)$) from the pure compounds at a dose of 1.4×10^{20} e.v./g. were: cyclohexene, 1.28; benzene, 0.038; 1,3-cyclohexadiene, 0.24; and 1,4-cyclohexadiene, 1.19. The yield of hydrogen from cyclohexene is independent of dose (the region 2.5×10^{18} to 2.2×10^{20} e.v./g. was studied), so the yield from each of the other compounds listed can also be assumed to be independent of dose in this region.

(1) The authors are grateful to the National Research Council of Canada for partial support of this work. B. R. W. is indebted to Consolidated Mining and Smelting Co. for the award of a Cominco Fellowship in 1960.

(2) B. R. Wakeford and G. R. Freeman, *J. Phys. Chem.*, **68**, 2635 (1964).

(3) (a) K. Alder and G. Stein, *Ann. Chem.*, **496**, 197 (1932); (b) B. A. Kazanskii and P. F. Svirskaya, *J. Gen. Chem. USSR*, **29**, 2550 (1960).

(4) B. R. Wakeford, Ph.D. Thesis, University of Alberta, 1964.

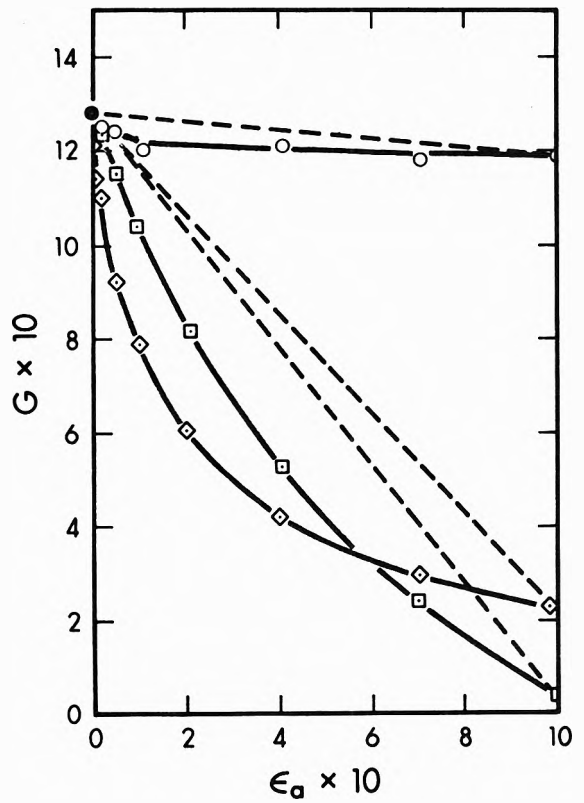

Figure 1. Hydrogen yields: ●, pure cyclohexene; ○, 1,4-D solutions; □, B solutions; ◇, 1,3-D solutions.

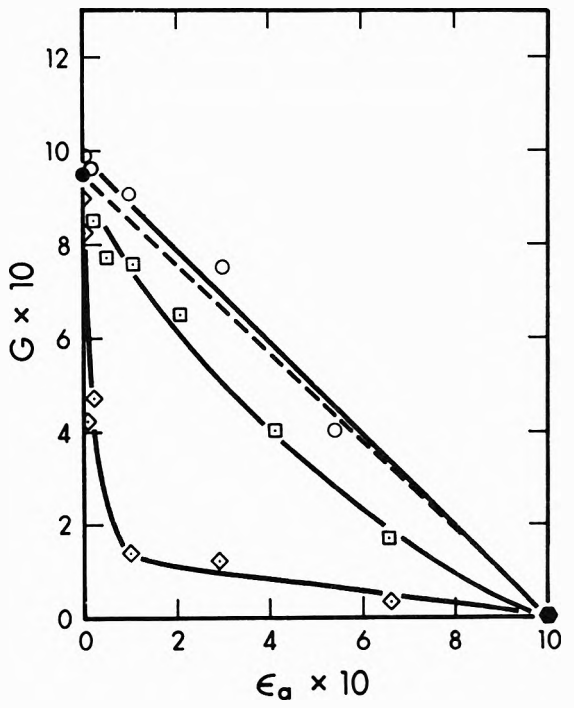

Figure 2. Cyclohexane yields: ●, pure cyclohexene; ○, 1,4-D solutions; □, B solutions; ◇, 1,3-D solutions.

The hydrogen yields from the binary solutions of 1,3-D, 1,4-D, and B in cyclohexene are given in Fig. 1. All of the additives appeared to give some inhibition of the hydrogen yield, the greatest effect being observed for 1,3-D.

Cyclohexane. B inhibited the formation of cyclohexane to about the same degree as it had inhibited hydrogen formation (Fig. 1 and 2). 1,4-D caused a slight sensitization of cyclohexane formation. With added 1,3-D, the yield of cyclohexane fell sharply to $G < 0.2$ as $\epsilon_{1,3\text{-D}}$ was increased to 0.1. The residual yield of cyclohexane was inhibited only slightly or not at all by 1,3-D (Fig. 2).

"Cyclohexene Type" Dimers.[2] Each of the three additives inhibited all of the "cyclohexene type" dimers, namely, 2,2′-dicyclohexenyl (Fig. 3), 3-cyclohexylcyclohexene (Fig. 4), dicyclohexyl (Fig. 5), and the unidentified dimer, designated D-1 (Fig. 6). The most effective inhibitor was 1,3-D in each case.

"New" Dimers. The yields of new dimers formed in the solutions of B in cyclohexene were negligible ($G < 0.1$).

A dimer of 1,3-D (dicyclohexadiene) was formed in good yield even at small concentrations of 1,3-D

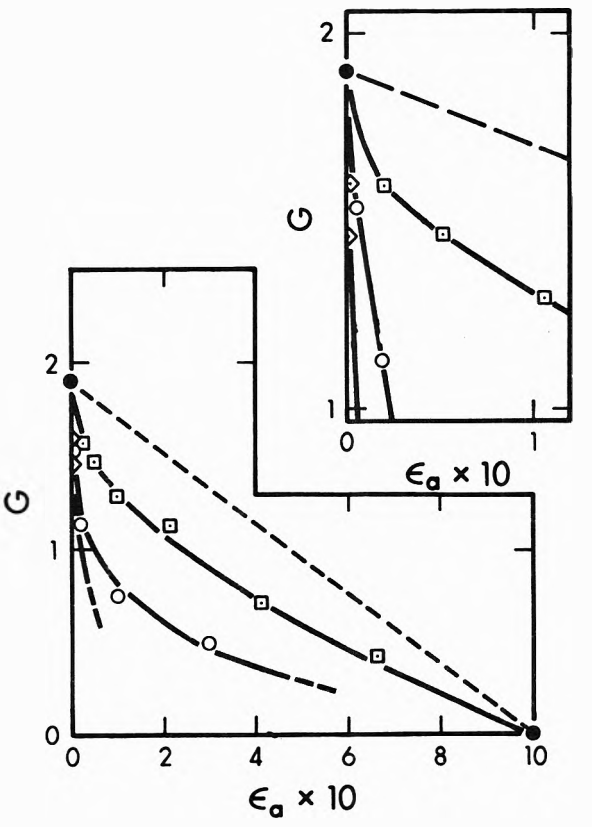

Figure 3. 2,2′-Dicyclohexenyl yields: ●, pure cyclohexene; ○, 1,4-D solutions; □, B solutions; ◇, 1,3-D solutions.

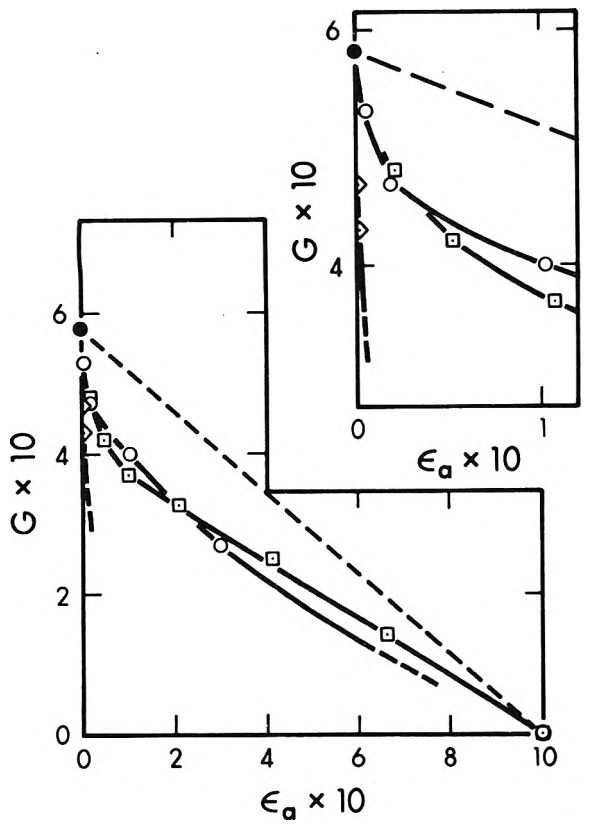

Figure 4. 3-Cyclohexylcyclohexene yields: ●, pure cyclohexene; ○, 1,4-D solutions; □, B solutions; ◇, 1,3-D solutions.

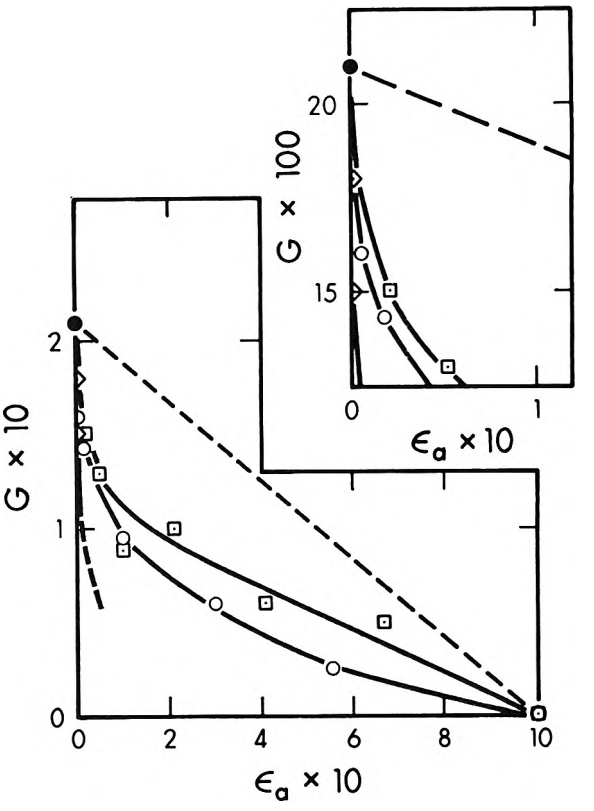

Figure 5. Dicyclohexyl yields: ●, pure cyclohexene; ○, 1,4-D solutions; □, B solutions; ◇, 1,3-D solutions.

(Fig. 7A). This product was separated from all of the "cyclohexene type" dimers on two v.p.c. columns and had the same retention time as the authentic dicyclohexadiene (*i.e.*, tricyclo[4.4.$2^{7,10}$.0]dodeca-2,8-diene) on both columns. Irradiation of a 6×10^{-4} mole fraction solution of 1,3-D in *cyclohexane* also gave rise to dicyclohexadiene. The mass spectra of the dicyclohexadiene formed in the irradiated cyclohexane solution and of the authentic dicyclohexadiene were similar, but the discrepancies indicated that some different isomeric forms of the dimer were probably present in the two samples.[4] The yield of dicyclohexadiene from the cyclohexene solutions increased rapidly with increasing 1,3-D concentration up to G = 6.3 at $\epsilon_{1,3\text{-D}} \approx 0.05$. As the 1,3-D concentration was further increased, the yield of dicyclohexadiene decreased.

Figure 7B gives the yields of dimeric products (excluding dicyclohexadiene) from the 1,3-D solutions. The initial decrease with increasing $\epsilon_{1,3\text{-D}}$ is due to the rapid decrease of the "cyclohexene type" dimers. The yield begins to increase at about $\epsilon_{1,3\text{-D}} \approx 0.2$, presumably due to dimeric products involving 1,3-D.

When 1,4-D was added to cyclohexene, no dicyclohexadiene formation was observed. However, two dimeric products, designated D-2 and D-3, were formed (Fig. 8B). These products were tentatively identified as cyclohexenylcyclohexadiene and dicyclohexadienyl, respectively, on the basis of their retention times on two v.p.c. columns.[4] The yields of these products increased rapidly as $\epsilon_{1,4\text{-D}}$ was increased to ~0.05, but became relatively independent of $\epsilon_{1,4\text{-D}}$ at higher concentrations of the diene.

Polymer. The yields of polymer (excluding dimers) from the three types of solution are given in Fig. 9. The 1,3-D solutions produced polymer in relatively much higher yields than did the 1,4-D or B solutions.

C_6-Hydrocarbon Products. No new C_6-hydrocarbon products were detected when B was added to cyclohexene. 1,3-D was formed in the solutions of 1,4-D in cyclohexene (Fig. 8A), the yield increasing rapidly with increasing $\epsilon_{1,4\text{-D}}$ at low concentrations. No 1,4-D formation could be detected in the 1,3-D solutions.

The yield of B from the 1,3-D solutions (Fig. 7A) increased more rapidly at low than at high 1,3-D concentrations. B was apparently formed in the 1,4-D solutions, but meaningful measurements were not obtained due to analytical difficulty.

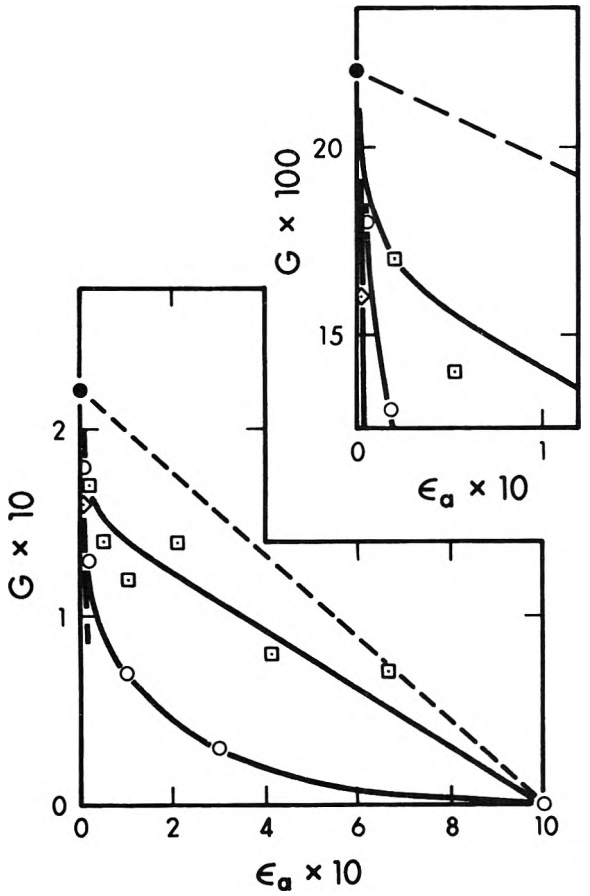

Figure 6. Unidentified dimer (D-1) yields: ●, pure cyclohexene; O, 1,4-D solutions; □, B solutions; ◇, 1,3-D solutions.

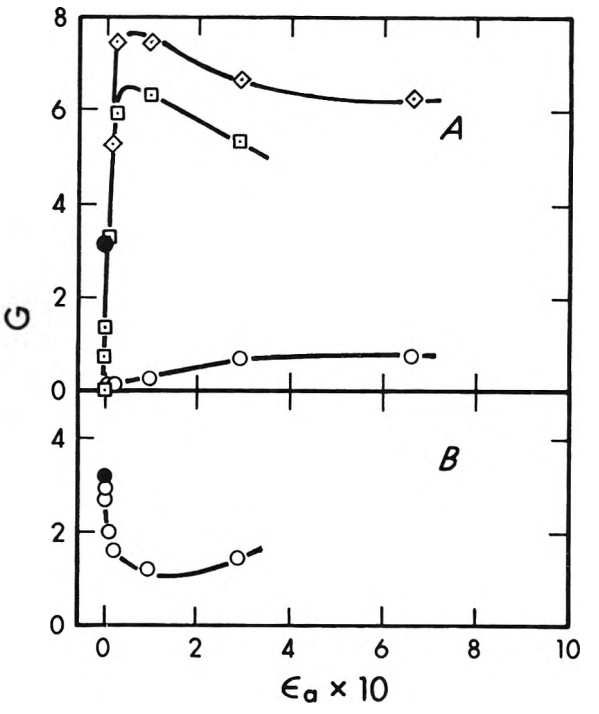

Figure 7. Yields of products from 1,3-D solutions. A: ●, total dimer yield from pure cyclohexene; ◇, total C_{12} products; □, dicyclohexadiene; O, benzene. B: ●, total dimer yield from pure cyclohexene; O, dimer yield, excluding dicyclohexadiene.

Additive Consumption. The rates of 1,3-D and 1,4-D disappearance could be measured in the dilute solutions (Fig. 10). 1,3-D had a high rate of disappearance that increased rapidly with increasing concentration. 1,4-D reacted much less extensively than did 1,3-D. The rate of B consumption was so small that it could not be measured with the analytical technique used.

Discussion

Benzene Addition. The yields of all of the major cyclohexene products were reduced to a similar extent by the addition of B. This general inhibition is consistent with "sponge type" protection.[5]

1,3-Cyclohexadiene Addition. 1,3-D was a more effective inhibitor than either B or 1,4-D for all of the cyclohexene type products. This may be due to a higher probability of activation transfer from excited or ionized cyclohexene molecules to the additive when the additive is 1,3-D. Values for the appearance potentials of singly ionized molecular species of the compounds used in this work[6] are given in Table I. Only

Table I: Appearance Potentials

Ion	Appearance potential, e.v. This work[a]	Appearance potential, e.v. Other	Ionization potential, e.v. (spectroscopic)
(Cyclohexene)$^+$	9.2 ± 0.2	9.24 ± 0.07[b,c]	9.2 ± 0.05[d]
(Cyclohexene-d_{10})$^+$	9.2 ± 0.2		
(Benzene)$^+$	9.9 ± 0.3	9.52[e,c]	9.24[f]
(1,3-Cyclohexadiene)$^+$	8.7 ± 0.3		
(1,4-Cyclohexadiene)$^+$	9.2 ± 0.2		

[a] Xenon was used as the internal standard. [b] J. D. Morrison and A. J. L. Nicholson, *J. Chem. Phys.*, **20**, 1021 (1952). [c] Values, obtained by electron impact, have been reported in the range 9.2–9.7 e.v. for (cyclohexene)$^+$ and 9.2–9.9 e.v. for (benzene)$^+$. See F. H. Field and J. L. Franklin, "Electron Impact Phenomena," Academic Press, New York, N. Y., 1957. [d] W. C. Price and W. T. Tutte, *Proc. Roy. Soc.* (London), **A174**, 207 (1940). [e] J. D. Morrison, *J. Chem. Phys.*, **19**, 1305 (1951). [f] W. C. Price, *Chem. Rev.*, **41**, 257 (1947).

(1,3-D)$^+$ had an appearance potential lower than that of (cyclohexene)$^+$. The appearance potentials

(5) M. Burton and S. Lipsky, *J. Phys. Chem.*, **61**, 1461 (1957).

(6) The radiolysis of cyclohexene-d_{10} will be reported in a later communication.

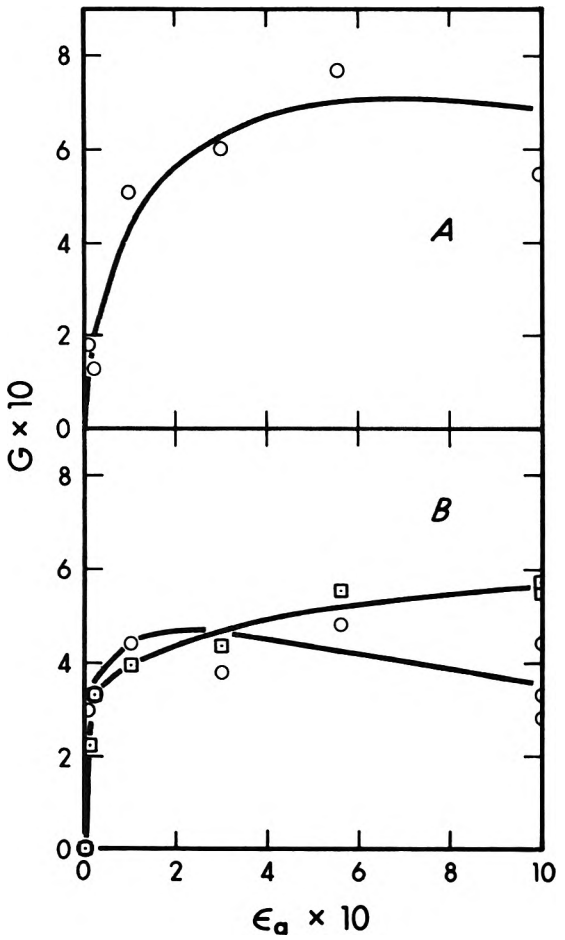

Figure 8. Yields of products from 1,4-D solutions. A: O, 1,3-cyclohexadiene; B: O, D-2 (cyclohexenylcyclohexadiene?); □, D-3 (dicyclohexadienyl?).

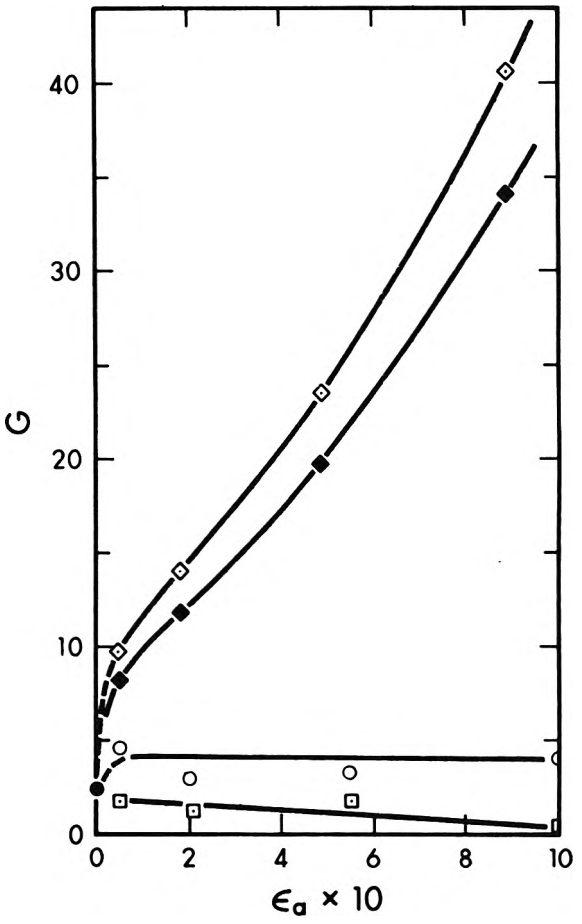

Figure 9. Polymer yields (C_6 units): ●, pure cyclohexene; O, 1,4-D solutions; □, B solutions; ◇, 1,3-D solutions; ◆, 1,3-D solutions, with oxygen correction. Analysis of the residue of the 89% 1,3-cyclohexadiene, 11% cyclohexene solution gave a composition of $(C_6H_8O)_n$ with an average value of $n = 8.7$. If the oxygen addition took place before the polymer was weighed,[2] and it is assumed that oxygen addition took place in all of the 1,3-D solutions to the same extent, then the values for G(polymer) will be those given by ◆.

were measured using a Metropolitan–Vickers MS2 mass spectrometer. The results were calculated by the method described by Lossing, *et al.*[7]

The high yield of dicyclohexadiene formed at low 1,3-D concentrations clearly indicates that some form of activation transfer from the cyclohexene system to the added 1,3-D was occurring. Discussion of the nature of such a process would be very speculative at this stage.

Although the yields of the cyclohexene type dimers could not be measured for $\epsilon_{1,3\text{-D}} > 0.002$, due to analytical difficulty, it is clear that their yield was decreasing more rapidly than was the hydrogen yield with increasing 1,3-D concentration. A possible explanation is that the decreases in the dimer yields were not due to activation transfer alone, but also to radical scavenging. Although hydrocarbon radicals do not add to cyclohexene at an appreciable rate under the present conditions.[2] 1,3-D is a much better radical scavenger than is cyclohexene. Methyl radicals add about 700 times more readily to 1,3-D than to cyclohexene.[8]

Of the C_6 ring olefins studied in this work, only 1,3-D can readily undergo long chain polymerization. In the cases of both cyclohexene and 1,4-D, formation of a trimer by successive addition of C_6 ring units is sterically hindered and formation of a tetramer is extremely difficult without some ring cleavage. The observed high yield of polymer in the 1,3-D solutions may presumably be initiated either by a free radical or an ion.

(7) F. P. Lossing, A. W. Tickner, and W. A. Bryce, *J. Chem. Phys.*, 19, 1254 (1951).

(8) J. Gresser, A. Rajbenbach, and M. Szwarc, *J. Am. Chem. Soc.*, 83, 3005 (1961).

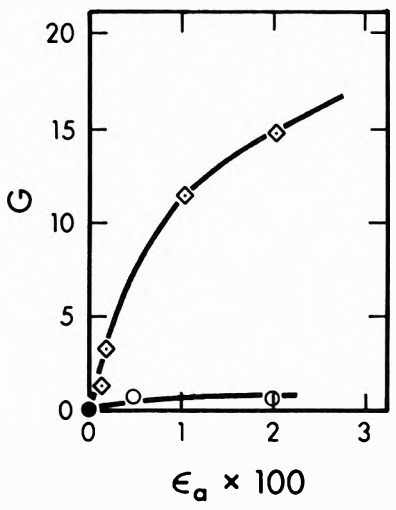

Figure 10. Additive disappearance from cyclohexene solutions: O, 1,4-D solutions; ◇, 1,3-D solutions.

1,4-Cyclohexadiene Addition. It has been suggested[2] that, under the conditions of the present experiments, essentially all of the dicyclohexyl, 3-cyclohexylcyclohexene, and 2,2′-dicyclohexenyl and part of the cyclohexane arise from radical combination and disproportionation reactions. Addition of 1,4-D inhibits the formation of the above-mentioned "dimers" but slightly enhances the formation of cyclohexane. Activation transfer from cyclohexene to 1,4-D cannot alone explain these results.

Cyclohexyl and 2-cyclohexenyl radicals can react with 1,4-D by reaction 1 to yield the resonance stabilized

$$R + c\text{-}C_6H_8 \longrightarrow RH + c\text{-}C_6H_7 \qquad (1)$$

cyclohexadienyl radical. The reaction will be exothermic in both cases.[9] However, reaction 1 will be 15–20 kcal./mole more exothermic when R is a cyclohexyl than when it is a 2-cyclohexenyl radical.[10] Thus the inhibition of the cyclohexene-type dimers cannot be due to reaction 1 alone, since in such a case the formation of dicyclohexyl should be much more effectively inhibited than is the formation of 2,2′-dicyclohexenyl, and the cyclohexane yield would be markedly enhanced.

The rate of addition of hydrocarbon radicals to the isolated double bonds in 1,4-D is probably very similar to that of addition to cyclohexene, and therefore negligible under the present conditions.[2]

It appears, therefore, that both activation transfer and the radical reaction 1 are occurring simultaneously. Both mechanisms can be expected to give rise to cyclohexadienyl radicals, since this radical species has been observed in irradiated 1,4-D[11] and is also the radical product of reaction 1.

The similarity in the dependence of the yields of 1,3-D, D-2, and D-3 on $\epsilon_{1,4\text{-D}}$ suggests that the formation of the three products might involve a common precursor, presumably the cyclohexadienyl radical. This is support for the tentative identification of D-2 and D-3 as cyclohexenylcyclohexadiene and dicyclohexadienyl, respectively.

(9) A. Rajbenbach and M. Szwarc, *Proc. Chem. Soc.*, 347 (1958).
(10) R. Klein and M. D. Scheer, *J. Phys. Chem.*, **67**, 1876 (1963).
(11) R. W. Fessenden and R. H. Schuler, *J. Chem. Phys.*, **39**, 2147 (1963).

Electrostriction in Polar Solvents. II[1,2]

by James F. Skinner and Raymond M. Fuoss

Contribution No. 1759 from the Sterling Chemistry Laboratory, Yale University, New Haven, Connecticut
(Received May 25, 1964)

Viscosities and densities in acetonitrile of solutions (maximum concentration 3 g./100 ml.) of a variety of compounds satisfy the equations $\eta = \eta_0(1 + Ac^{1/2} + Bc)$ and $\rho = \rho_0 + g(1 - v_s\rho_0)$ where η is viscosity of the solution, η_0 is that of the solvent, ρ and ρ_0 are the corresponding densities, c is molar concentration, g is weight concentration, and v_s is the volume in solution of the solute. For ideal hydrodynamic spheres, $400B = Mv_s$, where M is molecular weight of solute. This relationship is closely approximated by tetraphenyllead, -tin, -silane, and -methane. Triphenylamine, -phosphine, -arsine, and -stilbine contribute less to viscosity than one would expect from their volumes. By comparing mono-, di-, and trinitrobenzenes and -toluenes, it is shown that the total scalar dipole field (rather than the net molecular moment) determines the effect on viscosity; for example, *p*- and *m*-dinitrobenzene have practically equal B-values. Results with the three nitroanilines and *p*-phenylenediamine suggest that hydrogen bonding to acetonitrile occurs with these compounds. Smaller diffusion constants are found for compounds which show large B-values, confirming the hypothesis that local dipole fields tighten solvent structure around polar molecules.

In the aprotic solvent, acetonitrile, viscosity B-coefficients and the corresponding density coefficients were found to be additive for solutions of 1–1 electrolytes.[3] For large ions, such as those of tetrabutylammonium tetraphenylboride, the B-coefficient could be calculated from the density–concentration coefficient on the assumptions (1) that the latter coefficient measures the volume of the solute in the solution and (2) that the B-coefficient (times concentration) has the Einstein value of five-halves the volume fraction. For smaller ions, the observed B-coefficient was found larger than the Einstein value calculated from the density coefficient, while for neutral molecules, especially those containing no permanent dipoles, the viscosity coefficient was smaller than that predicted. The hypothesis was made that, in the former case, electrostriction in the solvent near the ion enhanced the viscosity, while, in the latter case, the electroneutral molecules could more easily slip through holes in the solvent. The primary purpose of this paper is to present measurements on solutions of dipolar solutes; some neutral and electrolytic solutes will also be considered for comparison. It will be shown that polarity in a molecule increases its contribution to solution viscosity, presumably due to local dipole–dipole attraction between solvent and solute. The effect is proportional to the *summed* polarity. For example, B for *o*-dinitrobenzene is 0.243 and for *p*-dinitrobenzene (which has zero net moment) is 0.266. This and similar results show that the effect on viscosity is due to short-range forces around the individual dipoles in the molecule, rather than to its long-range average field.

Experimental

Methods and apparatus have already been described.[3] All measurements were made in acetonitrile[3] at 25.00°, except those on the tetraphenyl series (D, E, F, G), which were made in carefully dried and fractionated benzene (f.p. 5.51°).

Some of the solutes were used as received, and some were further purified. Their description follows; a code for identification is given in Table I. For later

(1) This paper is based on part of a thesis presented by James F. Skinner to the Graduate School of Yale University in partial fulfillment of the requirements for the degree of Doctor of Philosophy.

(2) Grateful acknowledgment is made to the donors of the Petroleum Research Fund, administered by the American Chemical Society, for partial support of this work.

(3) D. F.-T. Tuan and R. M. Fuoss, *J. Phys. Chem.*, 67, 1343 (1963)

use, the specific volumes (±0.005 ml./g.) of the pure solutes at 25° are given in the last column of the table. **Triphenylsulfonium tetraphenylboride** was precipitated by mixing a 5% aqueous solution of triphenylsulfonium chloride (Aldrich) with an equivalent solution of sodium tetraphenylboride. It was thoroughly washed with water and dried at room temperature. It decomposes at 110°. No solvent satisfactory for recrystallization was found. **Diphenyliodonium iodate** was prepared[4] from iodosobenzene and iodoxybenzene, and **diphenyliodonium tetraphenylboride** was prepared from a solution of the iodate by precipitation with sodium tetraphenylboride, also in aqueous solution. The salt was purified by dissolving 1 g. in 3 ml. of ethanol, followed by 30 ml. of hot acetone. After filtering the hot solution, 200 ml. of distilled water was added. Fine colorless needles were obtained, which were dried at 70° and 1 mm., m.p., 140°. Matheson ***n*-hexadecyltrimethylammonium bromide** was used as received.

Table I: Catalog of Compounds

		Specific volume
A	$Ph_3S{\cdot}BPh_4$	0.856
B	$Ph_2I{\cdot}BPh_4$	0.807
C	$n\text{-}C_{16}H_{37}NMe_3{\cdot}BPh_4$	0.890
D	Ph_4Pb	0.605
E	Ph_4Sn	0.670
F	Ph_4Si	0.835
G	Ph_4C	0.850
H	Ph_3Sb	0.675
I	Ph_3As	0.770
J	Ph_3P	0.855
K	Ph_3CH	0.895
L	Ph_3N	0.860
M	Mesitylene	1.165
N	2,4-Dinitrotoluene	0.665
O	*o*-Dinitrobenzene	0.640
P	*m*-Dinitrobenzene	0.635
Q	*p*-Dinitrobenzene	0.615
R	1,3,5-Trinitrobenzene	0.595
S	Phthalonitrile	0.750
T	1,2-Dimethyl-3-nitrobenzene	0.880
U	1,3-Dimethyl-2-nitrobenzene	0.910
V	1,4-Dimethylnitrobenzene	0.890
W	*p*-Phenylenediamine	0.880
X	*o*-Nitroaniline	0.690
Y	*m*-Nitroaniline	0.700
Z	*p*-Nitroaniline	0.700

Triphenylstibine (K and K Laboratories) was recrystallized from petroleum ether (3.5 g. in 15 ml.), m.p. 53.6°. **Triphenylarsine** (K and K) was also recrystallized from petroleum ether (2.0 g. in 10 ml.), m.p. 60.1°. **Triphenylphosphine** (Aldrich) was recrystallized from diethyl ether (5.9 g. in 15 ml.), m.p. 80.1°. **Triphenylamine** (Matheson) was recrystallized from ethyl acetate (2.8 g. in 12 ml.), m.p. 126.2°. **Triphenylmethane** (Matheson) was recrystallized from 95% ethanol (3.5 g. in 10 ml.), m.p. 93.8°.

Tetraphenyllead (K and K) was recrystallized from benzene (3.0 g. in 30 ml.), m.p. 231°. **Tetraphenyltin** (Matheson) and **tetraphenylsilane** (K and K) were recrystallized from pyridine; m.p. 231 and 239°, respectively. **Tetraphenylmethane** (K and K) was recrystallized from benzene (3.5 g. in 140 ml.), m.p. 284°.

1,3,5-Trinitrobenzene (Eastman) was recrystallized from acetone by chilling a 50% solution to −80°. **Phthalonitrile** was recrystallized from ethanol (4 g. in 30 ml.), m.p. 137°. ***o*-Dinitrobenzene** (K and K) was recrystallized from 95% ethanol (5 g. in 50 ml.), m.p. 118°. ***o*-Nitroaniline** was recrystallized from water (2.5 g. in 350 ml.) and dried at 5 μ at room temperature, m.p. 73.8°. ***m*-Nitroaniline** was recrystallized from water (4.3 g. in 150 ml.) and also dried at 5 μ at room temperature, m.p. 114°. **Mesitylene, 1,2-dimethyl-3-nitrobenzene, 1,3-dimethyl-2-nitrobenzene, 1,4-dimethylnitrobenzene, 2,4-dinitrotoluene, *p*-phenylenediamine, *m*-dinitrobenzene**, and ***p*-dinitrobenzene** were used as received from Eastman.

Results and Discussion

Up to concentrations of several weight per cent, specific volumes of many two-component systems can be reproduced to a precision of about 0.02% by the linear equation

$$v = (1 - w)v_0 + v_s w \qquad (1)$$

where v_0 is the specific volume of the solvent, w is the weight fraction of solute, and v_s is the specific volume of the solute *in the solution*. Excluding aqueous and other hydrogen-bonded solutions, v_s is always positive and usually is only a little larger than the specific volume of the pure solute. Translating into densities, (1) becomes

$$\rho = \rho_0 + g(1 - v_s\rho_0) \qquad (2)$$

$$= \rho_0 + (Mc/1000)(1 - v_s\rho_0) \qquad (3)$$

where g is weight concentration (g. of solute/ml. of solution), M is molecular weight of solute, and c is molar concentration (moles/l. of solution). The molar volume V in solution is Mv_s ml. mole. For

(4) H. J. Lucas and E. R. Kennedy, *Org. Syn.*, **22**, 52 (1942).

determining v_s from density data, it is convenient to define a function $F(\rho,g)$, where

$$F(\rho,g) = (\rho_0 - \rho + g)/\rho_0 = v_s g \qquad (4)$$

Then a plot of F against g determines v_s as the slope of the line through the origin and the experimental points. Since all our data gave linear plots, the large body of data may be compactly summarized by giving the values of v_s; these are collected in Table II. They reproduce our observed densities within 0.02% up to $g = 0.02$–0.03.

Table II: Constants for Density and Viscosity Equations

Key	v_s	B	$10^3B/M$	R_v	R_η	Q
A	0.776	1.80	3.09	4.08	5.64	1.60
B	0.697	1.67	2.78	3.74	5.41	1.63
C	0.904	1.24	3.41	5.03	5.41	1.50
D	0.581	0.85	1.65	4.97	5.09	1.14
E	0.714	0.80	1.86	4.97	4.99	1.05
F	0.875	0.75	2.33	4.89	4.92	1.02
G	0.864	0.72	2.23	4.80	4.87	1.03
H	0.696	0.40	1.14	4.60	3.99	0.65
I	0.778	0.38	1.23	4.55	3.91	0.63
J	0.874	0.35	1.32	4.49	3.81	0.60
K	0.900	0.37	1.53	4.45	4.01	0.68
L	0.862	0.33	1.36	4.39	3.75	0.63
M	1.171	0.031	0.26	3.83	0.79	0.088
N	0.698	0.279	1.53	3.60	3.53	0.88
O	0.672	0.243	1.44	3.55	3.39	0.86
P	0.655	0.261	1.55	3.53	3.46	0.95
Q	0.629	0.266	1.58	3.49	3.49	1.01
R	0.573	0.37	1.74	3.66	3.89	1.21
S	0.870	0.201	1.57	3.53	3.18	0.72
T	0.862	0.163	1.08	3.72	2.96	0.50
U	0.877	0.148	0.98	3.75	2.87	0.45
V	0.877	0.158	1.05	3.76	2.91	0.48
W	0.814	0.224	2.07	3.27	3.29	1.02
X	0.725	0.232	1.70	3.41	3.33	0.94
Y	0.733	0.245	1.77	3.42	3.39	0.97
Z	0.721	0.294	2.13	3.40	3.62	1.18

Similarly, at low concentrations, solution viscosities are reproduced by the Jones–Dole equation[5]

$$\eta/\eta_0 = 1 + Ac^{1/2} + Bc \qquad (5)$$

where A can be theoretically computed[6] from single ion conductances or be empirically determined by graphical methods. (For nonelectrolytes, A is zero, of course.) For a system which may be represented by spheres in a hydrodynamic continuum, Einstein[7] showed that the viscosity increment depends on the volume of the solute, so that

$$Bc = 1000Bg/M = 5\phi/2 \qquad (6)$$

where ϕ is the volume fraction of solute.[8] For such an ideal system

$$400B/M = v_s \qquad (7)$$

and viscosities are predictable from densities, and *vice versa*. For large solute particles, such as tetraphenylmethane or the ions of tetrabutylammonium tetraphenylboride,[3] the observed coefficients do in fact satisfy (7); smaller ions, however, give higher viscosities than one would expect from their volumes, while neutral, and especially nonpolar, molecules give lower viscosities. For analysis of the viscosity data, it is convenient to define a viscosity function $G(\eta,g)$ by the equation

$$G(\eta,g) = 0.4(\eta/\eta_0 - 1 - Ac^{1/2}) = 0.4Bc \qquad (8)$$

$$= Qv_s g \qquad (9)$$

where Q is unity for an ideal system. For a real system

$$Q = 400B/Mv_s \qquad (10)$$

where B and v_s are the observed values. Over our working range of concentrations ($g \leq 0.03$ g./ml.), G was a linear function of g or c. The viscosity data are summarized by the B and Q values given in Table II. (For the electrolytes A, B, and C, the coefficient A is zero within our experimental error; the Bc term is very much larger than the square root term and effectively swamps it.)

We consider first the electrolytes. For triphenylsulfonium tetraphenylboride, $B = 1.80$. Subtracting Tuan's value[3] of 0.68 for the anion, the viscosity coefficient B^+ for the cation is 1.12. This is very much larger than the values found for quaternary ions ($B^+ = 0.33$ for Me_4N^+, 0.68 for Bu_4N^+); the positive charge in the Ph_3S^+ ion is not sterically shielded as is the charge in the quaternary ammonium ions, and interaction with the polar acetonitrile molecules is correspondingly greater. The effect of the bare charge is emphasized if we compare the value 1.12 with the neutral model compound triphenylmethane for which $B = 0.37$. The volumes of Ph_3CH and Ph_3S^+ must be very nearly the same; the ion–dipole interaction

(5) G. Jones and M. Dole, *J. Am. Chem. Soc.*, **51**, 2950 (1929).

(6) H. Falkenhagen and M. Dole, *Physik. Z.*, **30**, 611 (1929).

(7) A. Einstein, *Ann. Physik.*, **19**, 289 (1906); **34**, 591 (1911).

(8) As the coefficient of concentration expressed in moles/l., B has awkward dimensions. Physically more significant is $10^3B/M$, the coefficient of weight concentration g, and still more useful intuitively is $10^3B/Mv_s$, the coefficient of volume fraction (ml. of solute/ml. of solution). For similar reasons, eq. 2 is preferred to eq. 3 for density. For both viscosity and density, it is the *volume* of solute which is physically significant, not the number of moles.

in the latter produces twice the viscosity increment due to the Einstein volume effect. Diphenyliodonium tetraphenylboride is similar: $B = 1.67$, whence $B^+ = 0.99$. For diphenylmethane and diphenyl ether, Tuan[3] finds 0.21, so here the unshielded charge on the iodine produces four times the viscosity increment in addition to that due to the volume of the ion. Perhaps part of the large B for this ion may be due to its approximately cylindrical shape, but the model compounds must have similar geometry. The effect of shape may, however, be shown in the case of *n*-hexadecyltrimethylammonium bromide, for which $B = 1.24$. Using $B^- = 0.25$ from Tuan's result with tetrabutylammonium bromide, B^+ here is 0.99, which is considerably larger than 0.68 for Bu_4N^+ which has about (16 *vs.* 19) the same number of carbon atoms, but symmetrically arranged. The charge is also less shielded in the hexadecyltrimethylammonium ion. From these results and those of Tuan, it is clear that the viscosity coefficient B measures at least three properties of an ion in a given solvent: its volume, its shape, and the intensity of its field. Studies of selected series of electrolytes promise to show a number of interesting correlations between B / M and structure.

The neutral series tetraphenyllead, -tin, -silane, and -methane, especially the last three, behave practically like ideal hydrodynamic spheres in benzene. The radii, calculated from v_s are 5.09, 4.99, 4.92, and 4.87 Å., respectively; their volumes are therefore about an order of magnitude greater than the volume of a benzene molecule, and that this solvent appears like a continuum to the tetraphenyl molecules is not at all surprising. That the B values decrease from 0.852 for lead to 0.716 for carbon as the central atom is merely the numerical consequence of the fact that B is the coefficient of concentration in moles l. The Q-values, which eliminate the trivial effects of molecular weight, are 1.14, 1.05, 1.02, and 1.03.

The triphenyl compounds (H–L inclusive) present a different picture; they all increase viscosity by considerably less than one would expect from their volumes. Their Q-values average to 0.64, which is nearer to the values for the diphenyl series ($Q = 0.50$ for diphenyl ether and diphenylmethane) than to those for the tetraphenyl series just discussed. One similarity, which may be only incidental, between the di- and tri- series should be mentioned: the Q-values for the compounds with one proton are higher than for the other members of the series: $Q(Ph_2NH) = 0.71$ and $Q(Ph_3CH) = 0.68$. The triphenyl series, while less effective than Stokes spheres in producing viscosity, are more effective than the one trialkyl compound measured (tri-*n*-butylamine, for which $Q = 0.26$ in acetonitrile). The volume effect is, however, present in the neutral series Ph_2CH_2, Ph_3CH, Ph_4C, for which $Q = 0.49$, 0.68, and 1.03, in that the sequence of coefficients at least increases regularly with increasing size.

In Table II are also given values of the radii of the spheres equivalent to the solutes, as calculated from v_s ($\mathring{R}_v$ in the table) and from the viscosity, assuming the validity of eq. 7 ($\mathring{R}_\eta$ in the table). For the three electrolytes, *cationic* radii R^+ are tabulated; these were obtained from our coefficients using Tuan's values[3] for the BPh_4^- and bromide ions. When $Q = 1$, $R_v = R_\eta$. As before, we assume that only R has physical significance. All the latter are in good agreement with expected values. But paralleling the Q-values, the viscosity radius is too large for the electrolytes, and too small for most of the other compounds.

Finally, we consider the substituted benzenes. With no polar group, the viscosity coefficient B / M is much smaller than the Einstein value, as shown by mesitylene. From v_s, we obtain $\mathring{R}_v = 3.83$ as the radius of the equivalent sphere calculated from the density, which is quite reasonable. But from viscosity, if we assume $Bc = 5\phi/2$, R_η calculates to 0.79 which is obviously absurd. The value of Q is only 0.088, as compared with unity for ideal spheres. Just as soon, however, as a polar group such as the nitro group is attached to the ring, a significant increase in the viscosity coefficient appears. The three mononitro compounds (T, U, V) have Q near 0.5; permuting methyl groups around the polar group has very little influence on the coefficients. With two nitro groups, Q practically doubles. Again, insertion of a methyl group has little effect; in fact, Q for 2,4-dinitrotoluene is a little smaller than for *m*-dinitrobenzene. This might mean that the methyl group adjacent to the 2-nitro group sterically blocks attraction of solvent dipoles. The same steric argument might be applied also to the *ortho*, *meta*, *para* sequence, where there is a small but systematic increase of Q as the two nitro groups get farther apart. The same sequence is observed with the nitroanilines, compounds X, Y, and Z. That dipole strength is more significant than the nature of the dipole is shown by the similarity between phthalonitrile and the dinitro series; the moments of the nitrile and the nitro groups are nearly the same. With three nitro groups, Q increases still more. These results are summarized in Fig. 1 where Q is plotted against the scalar sum of the moments in the molecule (NO_2, 4.0; NH_2, 1.5; CH_3, 0.3). The point marked "PA" is for picric acid.[3] For no moment, there is a small volume effect (*cf.* points for mesitylene and xylene[3]), and then Q increases about linearly with the summed moments. The viscosity-creating potential of a mole-

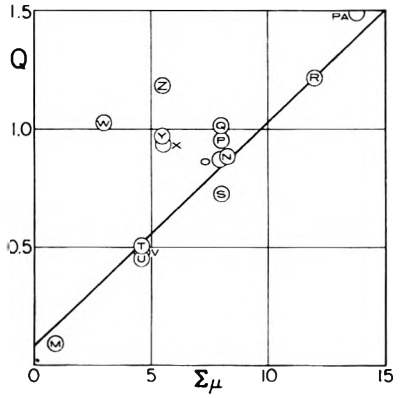

Figure 1. Dependence of viscosity effect on total polarity.

cule is clearly the result of short-range forces; Fig. 1 proves this point. The most direct proof, however, is the large values of Q for *p*-dinitrobenzene and 1,3,5-trinitrobenzene. Both of these molecules have zero net moments (just like xylene and mesitylene), but still they give large viscosity increments. We conclude that the viscosity increase is due to local dipole–dipole interaction between individual polar groups and solvent molecules, independent of the net moment of the whole molecule.

It will be noted that the three nitroanilines lie above the line in Fig. 1, as does the point W for *p*-phenylenediamine. This means that these compounds increase viscosity even more than corresponds to their total polarity. Hydrogen bonding between the amino group and acetonitrile, which would increase the volume of the kinetic entity, would account for this increase. We plan to investigate the nitrophenols which should show a similar effect if hydrogen bonds are involved.

For comparison with the earlier results,[3] the coefficient B is plotted against the molar volume Mv_s in Fig. 2. Points for ideal systems would lie on the solid line representing eq. 7. The three electrolytes, despite their large volume, lie considerably above the line, showing much stronger interaction than tetrabutylammonium tetraphenylboride (which is almost ideal). The tetraphenyl series gives a cluster of points nearly on the line, showing that the viscosity effect of these compounds is almost a pure volume effect; in other words, for these compounds the solvent behaves like a continuum. The triphenyl series, however, gives a cluster below the line, showing that these compounds can slip through acetonitrile more readily than spheres equivalent in volume to those deduced from the density measurements. The nitro compounds on this plot form a confused cluster near the origin; as already shown in Fig. 1, they are best understood on the basis of total polarity.

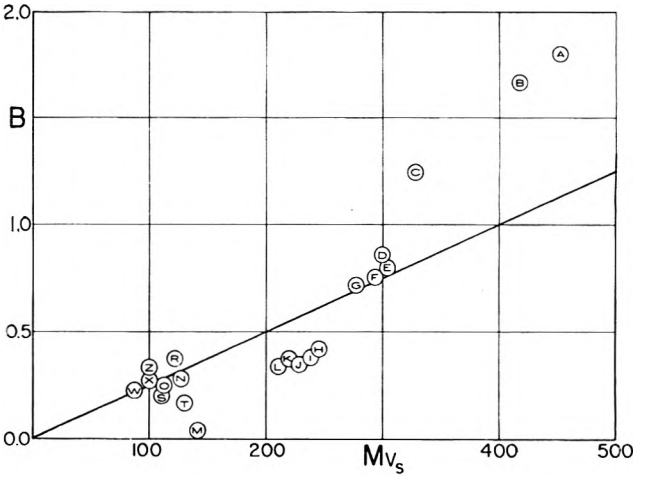

Figure 2. Comparison of viscosity and density parameters; key in Table I.

The observed correlation between the summed scalar moments of a molecule and its capability to increase viscosity in a polar solvent supports the hypothesis that short-range dipole–dipole forces constrict the solvent around the solute molecule. We would then expect an analogous correlation between summed moments and diffusion coefficients for molecules of the same shape and size. In Table III are summarized

Table III: Diffusion Constants in Acetonitrile at 25°

c	10^5D
Mesitylene	
0.0594	2.772
0.1362	2.658
p-Nitroaniline	
0.0252	2.459
0.0549	2.422
1,3,5-Trinitrobenzene	
0.0249	2.194
0.0551	2.154
0.0850	2.108

the results for diffusion of mesitylene, *p*-nitroaniline, and 1,3,5-trinitrobenzene in acetonitrile at 25° (concentration c in moles l.). The measurements were made by the Gouy interference method[9]; we are grateful to Professor P. A. Lyons for the use of his apparatus and to Mr. H. E. Meissner for making the measurements. The data, extrapolated linearly to

(9) L. J. Gosting, E. M. Hansen, G. Kegeles, and M. S. Morris, *Rev. Sci. Instr.*, **20**, 209 (1949).

zero concentration, give the following values for the limiting diffusion coefficients: mesitylene, 2.85×10^{-5}; *p*-nitroaniline, 2.49×10^{-5}; and 1,3,5-trinitrobenzene, 2.22×10^{-5}. As expected, the polar molecules diffuse more slowly than the nonpolar mesitylene. The differences in 10^5D are 0.36 and 0.63, respectively, for *p*-nitroaniline and trinitrobenzene compared to mesitylene. Thus both viscosity coefficients and diffusion constants show the effects of local molecular interaction.

Conductance of Copper *m*-Benzenedisulfonate Hexahydrate in N-Methylpropionamide from 20 to 40°[1]

by Thomas B. Hoover

National Bureau of Standards, Washington, D. C. *(Received May 25, 1964)*

The conductance of copper *m*-benzenedisulfonate hexahydrate in N-methylpropionamide was measured at 5° intervals from 20 to 40°, and in the concentration range of 3×10^{-4} to 1×10^{-2} *M*. Viscosity, conductance, and solubility observations indicate that water of crystallization does not remain associated with the electrolyte in solution. The Fuoss–Onsager conductance equation represents the data satisfactorily, although there is a barely significant, temperature-dependent contribution from higher order terms in concentration. The ion-size parameter, $\mathring{a}$, increases from 3.0 to 4.5 with increasing temperature, while the mean hydrodynamic (Stokes) radius is 4.9 Å. The limiting equivalent conductance is 25% larger than that of potassium chloride in the same solvent.

Introduction

Despite the remarkably high dielectric constant of N-methylpropionamide (NMP), previous conductance measurements[2] indicated that potassium chloride was appreciably associated in this solvent. That conclusion was based primarily on the unrealistically small values of the ion-size parameter, $\mathring{a}_J$, needed to fit the conductance data to the Fuoss–Onsager equation for strong electrolytes. Both the ion-pair association of potassium chloride and the large effect of salts on the viscosity of solutions in NMP were indicative of pronounced ion–solvent interactions. Such effects were expected to be enhanced by more highly charged ions; hence, the present conductance study of the 2–2 electrolyte, copper *m*-benzenedisulfonate (CuBDS), was undertaken. This salt is not only readily soluble in NMP but previous conductance measurements[3] have shown that it is fully dissociated in aqueous solution, in contrast to most 2–2 salts.

Dawson and co-workers[4] have measured conductances of a number of multivalent electrolytes in the related solvent, N-methylacetamide. Apart from some anomalies that were attributed to traces of acetate ion in the solvent, the salts all behaved as typical strong electrolytes.

(1) Presented, in part, before the Division of Physical Chemistry at the 145th National Meeting of the American Chemical Society, New York, N. Y., September 9–13, 1963.

(2) T. B. Hoover, *J. Phys. Chem.*, **68**, 876 (1964).

(3) G. Atkinson, M. Yokoi, and C. J. Hallada, *J. Am. Chem. Soc.*, **83**, 1570 (1961).

(4) L. R. Dawson, J. W. Vaughn, G. R. Lester, M. E. Pruitt, and P. G. Sears, *J. Phys. Chem.*, **67**, 278 (1963).

Experimental

The conductance bridge, cells, and techniques have been described.[2] The solvent used in the present study had a specific conductance in the range 0.8 to 1.3 $\times$ 10^{-7} ohm^{-1} cm.$^{-1}$ at 25°. Analysis of the solvent by gas chromatography showed no more than 0.05% by volume of water and less than 0.01% propionic acid.

The CuBDS, in the hexahydrate form, was very kindly supplied by Dr. Gordon Atkinson and was used without further purification. An attempt was made to prepare an anhydrous stock solution. A portion of the hydrate, when dried to constant weight at 130° and cooled over P_2O_5, showed a weight loss of 22.79%. A quantity of the dried salt, sufficient to give a 2.829% solution, was quickly transferred to NMP. The copper content of this stock solution was determined by electrodeposition to be 0.5720%. Thus, the copper content of the original salt, as received, was 15.61%. The theoretical copper content of $CuBDS \cdot 6H_2O$ is 15.58%. Because of the difficulty of making accurate dilutions of the stock solution and of weighing the dried material, nearly all the solutions used for conductance were prepared from the "as-received" sample, and concentrations were calculated on the basis of the analytical, rather than the theoretical, composition. The density of the hexahydrate, needed for making vacuum corrections to the weighings, was found to be 1.74 by pycnometric displacement of hexane at room temperature.

Densities of solutions were measured in a modified Sprengel pycnometer having a capacity of 20 ml. At all temperatures the densities were represented by the equation

$$\rho = \rho_0(1 + 0.21m) \qquad (1)$$

where ρ_0 is the density of the solvent[2] and m is the concentration in g.-atoms of copper/kg. of total solvent including water introduced with the solute. Molarities (c) were calculated from m by the equation

$$c\ m = \rho_0(1 + 0.21m)\ (1 + 0.300m) \qquad (2)$$

Thus, all concentrations were calculated for anhydrous salt in slightly wet solvent, although the solute was usually introduced as the hexahydrate.

Viscosities were measured in two Cannon–Fenske, size 50, viscometers, which were calibrated with NBS Oil H, Lot 12. The same solution was run in each viscometer and the measurements were repeated at least once. Solutions were transferred to the auxiliary bulb by pressure of dried air and were allowed to drain in a closed system to minimize contamination from atmospheric moisture. Each viscometer was timed by its own stopwatch both during calibration and measurement. All flow times were longer than 15 min.

Since preliminary results indicated an effect of water on viscosity, 12 solutions were prepared according to an incomplete block design covering electrolyte concentrations of 0 to 0.020 M and water concentrations, including that added with the electrolyte, of 0 to 1.0 wt. %. The solutions were measured in a randomized order, each at three or more temperatures, also chosen in a randomized order. The variate used in the statistical analysis of the results was

$$Y = (\eta/\eta_0) - 1 - S_\eta c^{1/2} \qquad (3)$$

where η is the viscosity of the solution and η_0 is that of the solvent at the same temperature; S_η is the Falkenhagen coefficient, estimated from Λ_0[5] and shown in Table I. The analysis revealed no significant temperature or cross-product terms. Within experimental error, the data were represented by the equation

$$Y = 4.2c + 0.020w \qquad (4)$$

where w is the weight per cent of water, including that of hydration. The standard deviation from eq. 4 was 0.5%. The standard deviation of the relative differences between the two viscometers was 0.2%. The viscosity of the solvent, shown in Table I, was about 1% lower at all temperatures than the previously reported values.[2] The difference is tentatively ascribed to greater purity of the recently prepared solvent.

Table I: Viscosity Parameters for Solutions of CuBDS in NMP

t, °C.	η_0, poise	S_η
20	0.0602	0.0265
25	.0522	.0272
30	.0456	.0277
35	.0400	.0280
40	.0352	.0285

Results and Discussion

Values of the equivalent conductance, Λ, are presented in Table II. No correction has been made for hydrolysis or solvolysis. In aqueous solution, hydrolysis was small but not negligible.[3] The function Λ_η' is defined by the equation

$$\Lambda_\eta' = (Y + 1)\Lambda + Sc^{1/2} - Ec \log c \qquad (5)$$

where $(Y + 1)$ is a viscosity correction based on eq. 4, S and E are theoretical constants of the Fuoss–Onsager equation, and c is the concentration, expressed in gram-

(5) R. M. Fuoss and F. Accascina, "Electrolytic Conductance," Interscience Publishers, Inc., New York, N. Y., 1959, p. 234.

Table II: Equivalent Conductance of $CuBDS \cdot 6H_2O$ in NMP

-20°		-30°		-35°		-40°	
10^4c	Λ	10^4c	Λ	10^4c	Λ	10^4c	Λ
3.60	10.554	3.57	13.912	3.56	15.779	3.54	17.818
9.16	10.225	13.62	13.181	9.04	15.291	13.51	16.903
9.16	10.230	19.01	12.960	9.04	15.318	18.84	16.593
19.17	9.843	23.96	12.744	13.57	14.973	18.84	16.593
30.32	9.299	45.59	12.044	18.92	14.710	23.76	16.318
61.85	8.870	45.59	12.021	23.86	14.465	38.65	15.624
61.85	8.872	48.88	11.982	38.81	13.862	45.20	15.373
91.58	8.471	61.32	11.649	45.40	13.637	48.46	15.300
-25°		65.45	11.592	48.67	13.575	60.79	14.875
10^4c	Λ	65.45	11.577	61.06	13.204	64.89	14.788
3.59	12.159	90.80	11.116	65.17	13.129	90.02	14.194
9.12	11.783	106.08	10.825	105.62	12.264	105.17	13.804
9.12	11.788						
19.09	11.338						
39.15	10.700						
61.59	10.203						
91.19	9.741						

atoms of copper per liter. The theory predicts that Λ_η' should be a linear function of c but plots of Λ_η' *vs.* c showed slight curvature. Accordingly, the data were fitted by the method of least squares to an equation of the form

$$\Lambda_\eta' = \Lambda_0 + Ac + Bc^{3/2} \qquad (6)$$

All points were given equal weight. Table III presents the values of S and E used in eq. 5[6] and the values found for Λ_0, A, and B, together with their standard deviations. Figure 1, in which the broken curves correspond to the regression equation (6), portrays the extent of curvature and the experimental scatter at three temperatures.

Table III: Conductance Parameters and Constants for Eq. 6

	20°	25°	30°	35°	40°
S	29.223	34.452	40.434	47.190	54.612
E	12.457	16.456	21.572	28.790	37.142
Λ_0	11.126	12.835	14.676	16.698	18.872
Std. dev. of Λ_0	0.008	0.012	0.018	0.015	0.025
A	61	85	136	176	224
Std. dev. of A	7	12	12	12	18
B	171	133	−140	−249	−362
Std. dev. of B	76	122	110	116	166
$\eta_0\Lambda_0$	0.6696	0.6701	0.6685	0.6673	0.6643

Effect of Water. If Cu^{+2} is solvated by water in preference to NMP, differences in viscosity and conductance would be expected depending on whether or not the solution contained sufficient water to satisfy the coordination number of the ion. As a test, solutions

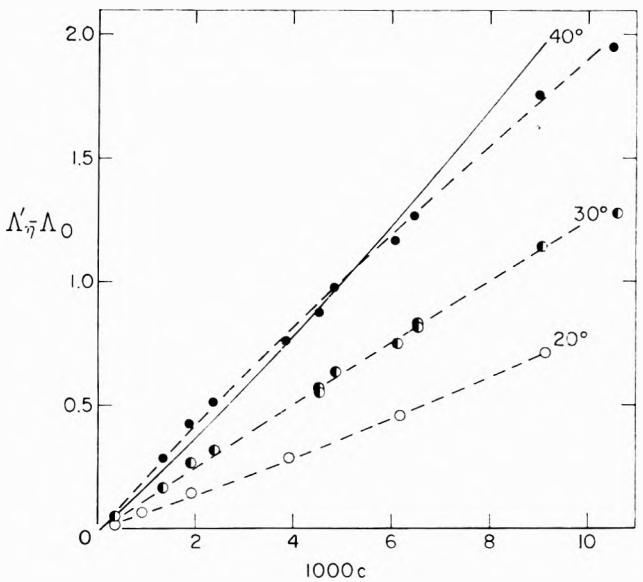

Figure 1. Conductance of $CuBDS \cdot 6H_2O$ in NMP at 20, 30, and 40°. The solid curve was calculated according to eq. 9 with $\mathring{a} = 4.0$.

were prepared, containing 0.02, 0.007, and 0.005 mole/l. of the oven-dried CuBDS, the analysis of which corresponded to 0.8 mole of water/atom of copper. Thus, these solutions certainly held less than 4 moles of water/copper ion. The viscosity measurements failed

(6) S. J. Bass, W. I. Nathan, R. M. Meighan, and R. H. Cole, *J. Phys. Chem.*, 68, 509 (1964), give values for the dielectric constant of NMP 7% lower than those of ref. 2. Pending a resolution of the discrepancy, the higher set of values is adopted here. While this paper was in press, Prof. Cole informed the author that his latest results agree with those of ref. 2 within 0.5%, the estimated error of the latter.

to establish any specific interaction between water and electrolyte concentrations, but the equivalent conductances of these solutions were uniformly 2% higher than for those of the corresponding concentrations of hydrated salt. Since solvation by water rather than NMP should result in smaller ions with greater mobility, the latter result may be indicative of partial hydrolysis of the salt during drying. These conductance results are not included in Table II.

Water was added to a solution 0.006128 *M* in CuBDS to give a concentration of 0.76% water (11 times that introduced with the salt). The equivalent conductance of the resulting solution was 3% lower than that for the same concentration of $CuBDS \cdot 6H_2O$ in dry solvent. Application of a viscosity correction according to eq. 4 removed about two-thirds of the discrepancy. When allowance was made for the effect of the water on the dielectric constant[2] and viscosity of the solvent in computing the parameters S and E, this measurement was brought into good agreement with the data for solutions containing no added water beyond the water of crystallization. This represented the extreme example of alteration of the solvent properties, and in all other cases the parameters listed in Table III were used without regard for the negligible effects due to differences in water content. Although the data and analysis given here apply to solutions of $CuBDS \cdot 6H_2O$, it appears that the results for anhydrous solutions would not differ appreciably.

The foregoing viscosity and conductance measurements are consistent with the view that the hydrate water does not remain intimately associated with the copper ion in NMP solution. This conclusion was reached by Dawson, *et al.*,[4] with regard to hydrated salts in N-methylacetamide and is supported by qualitative observations of solubility. The sulfates of copper, potassium, and lithium are very insoluble in NMP. The addition of five volumes of NMP to a concentrated aqueous solution of $CuSO_4$ produced an immediate, blue flocculent precipitate in a colorless liquid. The addition of a solution of H_2SO_4 in NMP to solutions of KNO_3 or LiCl in the same solvent produced immediate precipitation but a similar addition to solutions of CuBDS, $Cu(NO_3)_2$, or $CuCl_2$ (all added as hydrates) had no apparent effect and the mixtures remained blue and clear indefinitely at room temperature. When these solutions were heated nearly to the boiling point, or better, were refluxed with a little toluene, the specimens of copper nitrate, and sometimes of CuBDS, were decolorized with the formation of a fine, pale precipitate. At room temperature $CuSO_4$ apparently precipitates from NMP only if the copper ion is hydrated. The addition of an NMP solution of H_2SO_4 to a small volume of *aqueous* solution of $Cu(NO_3)_2$ or of CuBDS formed an initially clear mixture. In 5 to 30 min., however, a flocculent or finely crystalline blue precipitate slowly formed. On the other hand, when the copper ion was first dissolved in NMP, there was no apparent reaction with H_2SO_4. Thus, copper evidently loses its water of hydration in NMP solution.

Conductance Results and the Ion-Size Parameter. The limiting equivalent conductance, Λ_0, shown in Table III is appreciably larger than that found for KCl in the same solvent,[2] in contrast to the results for aqueous solutions. The Walden product, presented in the same table, shows a slight change with temperature, which is practically identical in magnitude and direction with that of KCl. The hydrodynamic radii, R_H, corresponding to values of the Walden product are shown in Table IV. Zwanzig[7] has calculated a correction of the Stokes hydrodynamic radius due to the dielectric friction on an ion moving through a medium of dipoles that are much smaller than the ion. The recently measured dielectric relaxation times for NMP[8] are inconsistent with Zwanzig's equation. Evidently the relaxation process in hydrogen-bonded NMP is more complicated than a simple rotational orientation of the dipoles.

Table IV: Ion-Size Parameters for CuBDS in NMP

t, °C.	R_H, Å.	$\mathring{a}_J$	$\mathring{a}_1$	$\mathring{a}_2$
20	4.90	2.3–3.1	2.9–3.3	3.5
25	4.90	2.6–3.6	3.0–3.6	
30	4.91	3.9–4.7	3.7–4.3	
35	4.92	4.2–4.9	4.0–4.4	
40	4.94	4.4–5.2	4.1–4.6	(4.0)

The three-parameter Fuoss–Onsager conductance equation[9] may be written

$$\Lambda_\eta' = \Lambda_0 + Gc + (0)c^{3/2} \qquad (7)$$

where terms in $c^{3/2}$ or higher powers of c were shown to be negligible for $\kappa a < 0.2$. The coefficient G is made up of several terms that depend only on the ion-size parameter, $\mathring{a}$, and a term containing an empirical ion-pair association constant, K, multiplied by the square of the mean ionic activity coefficient, $f_\pm$. In the recently completed two-parameter version,[10] K

(7) R. W. Zwanig, *J. Chem. Phys.*, **38**, 1606 (1963).

(8) R. H. Cole, private communication. Values given for the relaxation times of NMP and NMA in Table III of ref. 6 should be multiplied by 10.

(9) See ref. 5, p. 239.

(10) R. M. Fuoss and L. Onsager, *J. Phys. Chem.*, **68**, 1 (1964).

is developed automatically and G is a function only of $\mathring{a}$ and $f_\pm$, while $c^{3/2}$ terms are still neglected.

The empirical need for higher order terms in c in representing the data of the present study is shown by the regression analysis according to eq. 6. The coefficients, B, shown in Table III, are more than twice as large as their standard deviations at the extreme temperatures and show a monotonic variation with temperature. Except for the point at 25°, the values form a remarkably smooth plot with respect to temperature. This does not prove, of course, that $c^{3/2}$ is necessarily the proper representation of the higher order contribution to conductance. Atkinson and co-workers[3] found evidence for the same effect in aqueous solutions. Although barely significant for CuBDS, the $c^{3/2}$ contribution was appreciable for the unsymmetric and 3–3 electrolytes.

The data may be fitted to the theoretical equations in three ways, giving different empirical evaluations of the parameter $\mathring{a}$. In choosing among these estimates we shall adopt as a criterion that $\mathring{a}$ should be independent of temperature if it has the physical significance given it in the theory. For the first trial, we use the three-parameter theoretical eq. 7 and assume complete ionization, thus reducing it to two parameters, Λ_0 and $\mathring{a}$. Further, we neglect the higher order term in the empirical eq. 6. Then A of eq. 6 may be equated to G of eq. 7. With the omission of the ion-pair association constant, the G coefficient corresponds to the conventional J term for strong electrolytes[11] and the resulting ion-size parameters have been labeled $\mathring{a}_J$ in Table IV. These values show an appreciable variation with temperature. The range of values at each temperature in Table IV corresponds to twice the standard deviation of A.

A second estimate is obtained by applying the new two-parameter equation in the following form,[12] again neglecting the $c^{3/2}$ term in the empirical eq. 6.

$$\Lambda' = \Lambda_0 + (D_1\Lambda_0 + D_2)c + (0)c^{3/2} \qquad (8)$$

$$D_1 = \sigma_1'[N' + 1/(2 - 2T_1) + 1.1515 \log (3\sigma_1') - 3f_\pm^2 K] \qquad (8a)$$

$$D_2 = 2\sigma_2'\{F + 0.3905 - f_\pm^2[0.8669 + 1/6b^2 + 0.5758 \log (3\sigma_1') + 3K/2]\} \qquad (8b)$$

The functions N', T_1, K, and F of b have been defined and tabulated[13]; $b = z^2e^2/aDkT$ is a function only of a for a given solvent and temperature; $\sigma'_1 = \kappa^2a^2b^2/12c$ and $\sigma'_2 = \kappa ab\beta/8c^{1/2}$. The activity coefficient, $f_\pm$, was evaluated for $c = 0.005$, about the middle of the experimental range. As in the previous trial, the coefficient of c in eq. 8 was calculated for a series of values of a and compared with the experimental A. The resulting values for the ion-size parameter, labeled $\mathring{a}_1$ in Table IV, show somewhat less variation with temperature than the former series.

For the third approach, the nonlinearity of the experimental results was ascribed to the variation of $f_\pm^2$ and the two-parameter equation was rearranged to the form

$$\Lambda' = \Lambda_0 + Hc - Lf_\pm^2c \qquad (9)$$

with

$$H = \sigma_1'[N' + 1/(2 - 2T_1) + 1.1515 \log (3\sigma_1')]\Lambda_0 + 2\sigma_2'(F + 0.3905) \qquad (9a)$$

and

$$L = 3\sigma_1'K\Lambda_0 + 2\sigma_2'[0.8669 + 0.5758 \log (3\sigma_1') + 1/6b^2] - 3\sigma_2'K \qquad (9b)$$

At 20°, this form fits the data quite as well as eq. 6. The ion-size parameter was evaluated by computing $(\Lambda_\eta' - \Lambda_0)/c$ and $f_\pm^2$ for each experimental point. Then, for an assumed value of L, H was calculated and found to approach a constant value at the higher concentrations. Repetition with a few values of L established an experimental function $(H - L)$ *vs.* H, which was essentially linear. Then, for a series of assumed values of a, H and L were calculated by eq. 9a and 9b. The resulting theoretical function $(H - L)$ *vs.* H was also linear, but of opposite slope, intersecting the experimental line at a point corresponding to $\mathring{a} = 3.5$ Å. The method of evaluating $\mathring{a}$ did not provide an estimate of the precision.

At the higher temperatures, a difficulty immediately became apparent. Theoretically, L of eq. 9 is positive for reasonable values of $\mathring{a}$ in this system, but experimentally, since $f_\pm^2$ is an inverse function of c, L has the opposite sign of the B coefficient in eq. 6 and, therefore, changes sign with increasing temperature. At 40°, eq. 9 predicts the wrong curvature, concave up. In Fig. 1, the solid curve represents the theoretical function for $a = 4.0$ Å., which was picked as the best compromise.

In summary, no one value for the ion-size parameter was found that could fit the data at all temperatures. Estimates obtained from the new two-parameter equation vary less than those from the three-parameter

(11) See ref. 5 p. 197.

(12) At the time of writing, the final installment of the theory had not been published, but all the theoretical contributions to conductance had been computed and only a simple algebraic substitution and collection of terms was required to obtain eq. 8.

(13) R. M. Fuoss and L. Onsager, *J. Phys. Chem.*, 67, 621, 628 (1963).

equation, ranging from about 3 Å. at 20° to 4.5 Å. at 40°. The variation is comparable to that found for potassium chloride in the same solvent. At all temperatures the conductance size parameters are smaller than the hydrodynamic radii. As was found for potassium chloride, the a parameter for CuBDS was smaller in NMP than in aqueous solution. Atkinson, Yokoi, and Hallada[3] found $\mathring{a}_J$ = 5.02 Å. at 25° in water. When their data were treated according to the second procedure, above, a value of 4.6 Å. was found for $\mathring{a}_1$. If Cu^{+2} is solvated by NMP in the organic solvent, then one would expect the effective ionic size to be considerably greater than in water. The smaller values actually found may be in compensation for a greater extent of ion-pair formation than is predicted by the theory. Such an effect would be anticipated if the effective dielectric constant near an ion is reduced from that of the bulk solvent.

The conductances of solutions of CuBDS in NMP, like those of potassium chloride, yield estimates of the ion size that are temperature dependent and much smaller than expected. These results may be the consequence of short-range ion–solvent interactions, which do not seem to be appreciably greater for divalent than for univalent ions.

Acknowledgments. The author is indebted to Mr. R. A. Paulson and Mr. E. L. Weise for the copper determination and gas chromatography, respectively, and to Mr. J. M. Cameron for the statistical analysis of the conductance data.

The Adsorption of Gelatin to a Silver Bromide Sol

by H. G. Curme and C. C. Natale

Research Laboratories, Eastman Kodak Company, Rochester, New York 14650 *(Received June 28, 1963)*

Adsorption of lime-processed, acid-processed, and acetylated gelatins to a silver bromide sol stabilized with excess bromide was studied. The specific area of the sol was determined by measuring the adsorption of a cyanine dye. Adsorption of dye in the presence of gelatin was the same as in its absence, but less gelatin was adsorbed in the presence of the dye than in its absence. Gelatin coverages of the order of 5–8 $\times$ 10^{-4} mg./cm.^{2} at surface saturation were observed, with no indication of multilayer adsorption, and limiting adsorption was proportional to the 0.23 power of weight-average molecular weight. These figures support a loop and bridge model for the adsorbed layer. Adsorbed molecules were found to occupy more or less space on the surface as pH and ionic strength were varied, and these variations appeared to be largely determined by electrostatic interactions. Adsorption at pH values well removed in either direction from the isoelectric point was less than at the isoelectric point. Comparison with light-scattering dimensions in solution indicated that adsorbed molecules are compacted compared with their configuration in solution, or are elongated in a direction normal to the surface, or show both effects. Gelatins of different chemical constitution showed similar adsorption behavior when compared under conditions of similar net charge and molecular weight.

Introduction

The adsorption of a series of gelatin fractions to a silver bromide precipitate has been studied by Pouradier and Roman.[1] These authors measured the amount of gelatin left on silver bromide grains after the grains were washed with water at 50°. Coverages at apparent surface saturation amounted to layers which would be 25–40 Å. thick if the gelatin were densely packed, as in the dry state. Saturation adsorption was found to increase slightly with molecular weight and to increase somewhat with increasing pAg. Pouradier and Roman postulated that gelatin molecules are adsorbed by a few of their polar groups and that the remainder of the molecules extend toward the solution. This model of adsorption at a few segments, with solvated loops and bridges in the polymer chain extending toward the solution, is similar to one proposed by Jenckel and Rumbach[2] for the adsorption of certain nonionic polymers out of organic solvents. The loop and bridge model seems to apply to the adsorption of other nonionic polymers from organic solvents,[3–5] and theoretical treatments of this type of adsorption have been presented by Simha, Frisch, and Eirich[6] and by Silberberg.[7]

Several papers dealing with the adsorption of charged synthetic polymers or proteins indicate that the relative net charges of the adsorbent and the adsorbate play an important role in adsorption, but are by no means the only determining factors. Certain synthetic polymers of fixed charge density show adsorption to oppositely charged mercury surfaces and no adsorption to mercury of the same charge.[8] The adsorption of gelatin[9] and of some synthetics carrying carboxyl groups,[10,11] to near-neutral or negatively charged

(1) J. Pouradier and J. Roman, *Sci. Ind. Phot.*, **23**, 4 (1952).

(2) E. Jenckel and B. Rumbach, *Z. Elektrochem.*, **55**, 612 (1951).

(3) G. Kraus and J. Dugone, *Ind. Eng. Chem.*, **47**, 1809 (1955).

(4) J. Koral, R. Ullman, and F. R. Eirich, *J. Phys. Chem.*, **62**, 541 (1958).

(5) B. J. Fontana and J. R. Thomas, *ibid.*, **65**, 480 (1961).

(6) (a) R. Simha, H. L. Frisch, and F. R. Eirich, *ibid.*, **57**, 584 (1953); (b) H. L. Frisch and R. Simha, *ibid.*, **58**, 507 (1954); (c) H. L. Frisch, *ibid.*, **59**, 633 (1955); (d) H. L. Frisch and R. Simha, *J. Chem. Phys.*, **27**, 702 (1957).

(7) A. Silberberg, *J. Phys. Chem.*, **66**, 1872, 1884.

(8) (a) I. R. Miller and D. C. Grahame, *J. Am. Chem. Soc.*, **79**, 3006 (1957); (b) I. R. Miller, *Trans. Faraday Soc.*, **57**, 301 (1961); (c) I. R. Miller and D. C. Grahame, *J. Colloid Sci.*, **16**, 23 (1961).

(9) A. M. Kragh and W. B. Langston, *ibid.*, **17**, 101 (1962).

Table I: Adsorption and Solution Properties of Various Gelatins

Gelatin	% loss during clarification[a]	$\bar{M}_w$	pH	μ,[b] mole/l.	$[\eta]$,[c] dl./g.	a_s,[d] mg./cm.^{2}	ν	K, ml./mg.	Charge, equiv./g.
A			4.7	0.0185	0.616	8.0×10^{-4}	1.0	29	$+0.50 \times 10^{-4}$
A			4.7	0.0635	0.667	6.9	1.4	23	+0.50
A			3.6	0.0635	0.860	5.3	2.5	45	+6.15
A			6.9	0.0635	0.892	6.1	1.7	35	−3.43
B	3	[580,000]	4.7	0.0185	0.61				+0.50
C	3.5	[320,000]	4.7	0.0185	0.520	6.8	1.1	51	+0.50
D(30)	0	80,000	4.7	0.0185	0.295	5.3	1.2	33	
D(40)	5	[146,000]	4.7	0.0185	0.379	6.1	1.2	29	
D(50)	0	263,000	4.7	0.0185	0.478	6.8	1.5	37	
D(60)	0	450,000	4.7	0.0185	0.593	7.8	1.2	28	
C-acetyl	2	[150,000]	4.7	0.0185	0.577	4.3	1.9	51	−3.92
C-acetyl			4.7	0.0635	0.502	4.8	1.8	43	−4.21
C-acetyl			3.6	0.0635	0.365	6.7	1.4	32	+1.5
E(7)	0	117,000	8.6	0.0185	0.346	6.4	1.7	30	0
E(7)			8.6	0.0635	0.359	6.0	1.9	42	0

[a] For methods of clarification see text. [b] Ionic strength $= \Sigma\, c_i Z_i^2/2$. [c] Intrinsic viscosity. [d] Limiting adsorption.

surfaces, has been shown to decrease as the negative charge on the polymer increased. Adsorption of certain proteins to negatively charged kaolinite[12] has been found to be greater in pH regions near to, or somewhat on the acid side of, their isoelectric points than in pH regions either more acid or more basic. This behavior has been interpreted in terms of variations with pH of both the degree of ionization of the proteins and the number of ionized sites on the surface.

In the present work the influence of some of the ionizing groups (carboxyl and ϵ-amino) on adsorption has been studied. This has been done by changing both the degree of ionization (through pH changes) of the groups, and by actual chemical alterations. Since such changes are necessarily accompanied by changes in the size of the molecule in solution,[13] adsorption studies were accompanied by viscosity and light-scattering measurements.

Experimental

Characterization of the Gelatins. Gelatins A, B, and C were the first extractions of limed calfskins. D(30), D(40), D 50), and D(60) were fractions of such a gelatin prepared by precipitation from aqueous solution by propanol. Gelatin C-acetyl was a sample of gelatin C which was treated with 10% by weight of acetic anhydride. Titration data, using the criteria of Kenchington and Ward,[14] showed that about 80% of the amino groups of the parent gelatin were acetylated. Gelatin E(7) was a fraction of an acid-processed pigskin gelatin prepared by precipitation by propanol.

Viscosities of gelatin solutions were obtained in Cannon–Fenske–Ostwald viscometers having flow times for water of about 200 sec. Solutions were filtered through Corning medium sintered glass filters (maximum pore size 15 μ) before viscosity measurements were made. This procedure removed less than 1% of the gelatin from solution. The adsorption from unfiltered solutions was found to be identical with that from solutions treated in this way in a number of tests, and adsorption measurements were routinely made using unfiltered gelatin solutions. Intrinsic viscosities, $[\eta]$, listed in Table I, were obtained by measuring $(\eta_{rel} - 1)/c$ at concentrations of 0.2, 0.4, and 0.8 g./100 ml. and extrapolating the values to zero concentration. Gelatin weights were corrected for moisture content by heating samples at 105° for 15 hr.

Difficulty with extraneous suspended material is frequently encountered in making light-scattering measurements on commercial gelatins.[15,16] Treatments which have small effects on viscosity may produce substantial reductions in weight-average molecular weights as calculated from light scattering. For this reason, more drastic means were taken to clarify

(10) A. S. Michaels and O. Morelos, *Ind. Eng. Chem.*, **47**, 1801 (1955).

(11) W. Schmidt and F. R. Eirich, *J. Phys. Chem.*, **66**, 1907 (1962).

(12) A. D. McLaren, *ibid.*, **58**, 129 (1954).

(13) G. Stainsby, *Nature*, **169**, 662 (1952).

(14) A. W. Kenchington and A. G. Ward, *Biochem. J.*, **58**, 202 (1954).

(15) G. Stainsby, *Nature*, **177**, 745 (1956).

(16) B. E. Tabor, *ibid.*, **194**, 372 (1962).

samples for light scattering than those for adsorption or viscosity. Gelatin B was centrifuged for 2 hr. at 60,000*g*. Gelatins C and C–acetyl were filtered through fine porcelain filters. Gelatins D and E were clarified by filtration through Pyrex ultrafine filters (maximum pore size 1.4 μ). Several of the gelatins showed no loss of material during these more rigorous treatments. In other cases, the treatments removed a few per cent of the protein originally present in the samples. The loss of gelatin experienced during light-scattering clarification in such cases is shown in Table I. Weight-average molecular weights of samples which showed such losses are shown in brackets, and it must be remembered that these bracketed figures may not truly represent the molecular weights of the materials actually used in adsorption studies. Molecular weights used in the discussion are, except for C–acetyl, those of samples which showed no loss on clarification. Scattering measurements were made by Dr. G. L. Beyer,[17] of these laboratories, who measured scattering of the 436-mμ mercury line with an instrument similar to the Phoenix instrument. Refractive increments of the scattering solutions were measured with a differential refractometer.

Some idea as to the polydispersity of these samples was desired in connection with calculations of the dimensions of the molecules. The number-average molecular weight of gelatin B was measured by Dr. J. E. Koller,[18] of these laboratories, in a glass and Plexiglas osmometer of the Fuoss–Mead type. Measurements were made at 40° in an acetate buffer of pH 4.7 and ionic strength (μ) of 0.5. Half-sum and static elevation methods gave the same results, and equilibrium pressures were obtained in less than 4 hr. When an ultrafine very dense[19] membrane was used and static readings were extrapolated to zero time, a value of 108,000 for $\bar{M}_n$ (number-average molecular weight) was found, with essentially no diffusion of protein through the membrane. On the other hand, when a medium membrane was used, a value of 142,000 was obtained for the nondiffusible protein, with about 6% of the protein diffusing through. These results show that gelatin B is surprisingly polydisperse, displaying a $\bar{M}_w/\bar{M}_n$ ratio of 5.4. Pouradier and Accary-Venet[20] have recently reported weight- and number-average molecular weights of single-extract gelatins derived from limed ossein. The ratio of the two averages for the fourth extract is 4.7, whereas the first three extracts, all of which are of substantially lower molecular weight, show lower ratios. Comparison of Beyer's light-scattering data[17] with osmotic-pressure data of Pouradier and Venet[21] also indicates that lower-molecular-weight gelatins, both whole and fractions, show less polydispersity. Koller[18] found that a fraction of a lime-processed calfskin gelatin of $\bar{M}_w$ of 51,000 showed $\bar{M}_w/\bar{M}_n$ of 1.36.

Treatment of the gelatins in mixed bed ion-exchange resins[22] gave the following isoelectric points: all lime-processed gelatins, 4.8; C–acetyl, 3.9; E(7), 8.6. Values of net charge on the gelatin samples under each set of conditions studied were determined by titration and are listed in Table I.

Silver Bromide Sol. Silver bromide sol, 0.02 *M*, in silver bromide and potassium nitrate and stabilized with 10^{-3} *M* potassium bromide was prepared by the method of Sheppard, O'Brien, and Beyer.[23] The age of the sol, used for adsorption experiments, was 3–20 days. Samples older than this were discarded. The sol was stored at room temperature and all operations with it were carried out under a red safelight.

Measurements of the specific surface were made by measuring the adsorption of the sensitizing dye, 1,1′-diethyl-2,2′-cyanine nitrate, to the sol. Mixtures of the dye (30 ml.) and the sol (10 ml.), with or without gelatin, were tumbled or shaken at 40° for periods up to 24 hr. The bromide concentration was held at 10^{-3} *M* in all experiments, but details of pH and ionic strength were varied with conditions of gelatin adsorption.

Dye and gelatin adsorption experiments were carried out by mixing buffer and sol to give the concentrations shown in Table II. After equilibration with the dye, the sol was centrifuged for 30 min. at 10,000*g* in a thermostated Servall SS-1 centrifuge, and a sample of the supernatant solution was analyzed spectrophotometrically. Dye adsorption was found to be independent of concentration over the range of 1–3.5 $\times$ 10^{-5} mole/l. free dye concentration, both in the presence and the absence of gelatin. Dye adsorption was independent of the time of shaking dye and sol together. Several careful correlations of dye adsorption with electron microscope counts of 1000–2000 particles of the sol yielded an area of 63 Å.^{2} per dye molecule, and this figure was used for subsequent calculations of the specific surface of the sol under other conditions. The sol particles were assumed to be spherical for the

(17) G. L. Beyer, unpublished work.

(18) J. E. Koller, private communication.

(19) Schleicher and Schuell Co., Keene, N. H.

(20) J. Pouradier and A. M. Accary-Venet, *J. chim. phys.*, **58**, 778 (1961).

(21) J. Pouradier and A. M. Venet, *ibid.*, **47**, 391 (1950).

(22) J. W. Janus, A. W. Kenchington, and A. G. Ward, *Research* (London), **4**, 247 (1951).

(23) S. E. Sheppard, A. S. O'Brien, and G. L. Beyer, *J. Colloid Sci.*, **1**, 213 (1946).

Table II: Concentrations of Salts Used in Adsorption Experiments[a]

pH	μ	NaOAc	HOAc	KBr	KNO_3	KH_2PO_4	K_2HPO_4
3.6	0.0635	0.050	0.50	10^{-3}	0.0125	...	...
4.7	0.0635	0.050	0.050	10^{-3}	0.0125	...	...
4.7	0.0185	0.0050	0.00475	10^{-3}	0.0125	...	...
6.9	0.0635	...	...	10^{-3}	0.0125	0.0125	0.0125
8.6	0.0185	...	...	10^{-3}	0.0125	2.7×10^{-5}	0.00166
8.6	0.0635	...	...	10^{-3}	0.0125	2.7×10^{-4}	0.0166

[a] All concentrations expressed as moles/l.

purposes of calculation, although they showed some surface irregularities and coagulation ripening. West, Carroll, and Whitcomb[24] have assigned an area of 79 Å.^{2} to this molecule adsorbed to flat, photographic emulsion grains. The agreement is considered sufficiently good for the purposes of this work. The specific area of the sol was about 10^5 cm.^{2}/g., depending on its age and prehistory. The specific area of the sol was measured in conjunction with each measurement of gelatin adsorption.

Gelatin Adsorption. In measurements of gelatin adsorption, 25 ml. of sol was mixed with 15 ml. of gelatin solution and buffer, and the mixtures were shaken or tumbled at 40°. Samples were then centrifuged for 1 hr. in the thermostated centrifuge. Gelatin remaining in supernatant solution was analyzed by the centrifuge modification of the biuret color test, as described by Robinson and Hogden.[25] With this method, 1 mg. of gelatin in a volume of 15 ml. (5-cm. path length) gives an optical density of 0.060 ± 0.003. Measurements of adsorption by difference became inaccurate at high gelatin concentrations, and the gelatin on the grains was therefore measured directly. Sol–gelatin mixtures containing 0.047 g. of silver bromide were centrifuged, leaving the supernatant solution quantitatively free of silver. The tubes were then carefully drained. The residual silver bromide was dissolved in 8 ml. of 12% KCNS; the biuret reagents were added, and the spectrophotometric determination was completed. A slow increase of turbidity (probably silver sulfide) was noticed after 10–15 min. in these solutions and its effect minimized by working only with very fresh samples and by using known solutions containing silver bromide.

Results

Surface Area of the Sol. Slow changes in the specific area of the silver bromide sol made it necessary to measure this area carefully in conjunction with each measurement of gelatin adsorption. Addition of dye to the sol stopped these changes, since the same dye-adsorption results were obtained after 24 hr. as after 1 hr. when dye was mixed with sol alone, or in the presence of buffer, or in the presence of buffer and gelatin. When the sol was stored at room temperature, its specific area, as measured by dye adsorption, decreased about 20% over the 2-week storage period. Neither buffers nor gelatin interfered with dye adsorption when all reagents were added to the sol at the same time. However, dye adsorption was about 10% lower than this initial adsorption if the sol was shaken with buffer at 40° 15 hr. before dye was added. When the sol, the buffer, and the gelatin were shaken 15 hr. before the dye was added, 30–35% less dye was adsorbed than when the dye was present initially, and 20–25% less than when the sol and the gelatin were shaken only 2 hr. before the dye was added. Electron micrographs of the sol before and after equilibration with buffer and with gelatin were taken and counts involving 1000–2000 grains were made. Areas calculated from the micrographs showed slow decreases with time which were proportional to the decrease in capacity of the sol to adsorb dye. In all cases areas calculated from the micrographs agreed within 5% with areas calculated by dye adsorption. It appears, therefore, that the slow decrease in capacity of the sol to adsorb dye when it is in the presence of gelatin is due to a slow growth of the silver bromide grains in the presence of gelatin. A final confirmation of this point is presented below. Studies of the changes in specific surface of silver bromide sols of this type, and of silver bromide flocs, have been made by Kolthoff and Bowers.[26,27]

The changes in capacity of the sol for dye adsorption in the presence of gelatin progressed at about the same rate at all conditions of pH and ionic strength studied,

(24) W. West, B. H. Carroll, and D. H. Whitcomb, *J. Phys. Chem.*, **56**, 1054 (1952).

(25) H. W. Robinson and C. G. Hogden, *J. Biol. Chem.*, **135**, 707 (1940).

(26) I. M. Kolthoff and R. C. Bowers, *J. Am. Chem. Soc.*, **76**, 1503 (1954).

(27) I. M. Kolthoff and R. C. Bowers, *ibid.*, **76**, 1510 (1954).

and at concentrations of free gelatin ranging from 0.05 to 5.0 mg./ml. However, to remove all uncertainties in the surface area of the sol, *every* measurement of gelatin adsorption was followed by a measurement of dye adsorption to the same grains to which gelatin had been adsorbed.

Gelatin Adsorption. Time dependence of gelatin adsorption paralleled the changes in capacity of the sol to adsorb dye in the presence of gelatin: 20–25% less gelatin was found on the grains after 15 hr. of shaking with the sol than after 2 hr. (This was not due to changes in the gelatin in solution during the equilibration time, since gelatin solutions held at 40° for 15 hr. and then added to the sol showed the same adsorption as solutions added to the sol directly, without the holding time.) This slow decrease in gelatin adsorption is further evidence that the grains are slowly growing in the presence of gelatin. Adsorption of gelatin A per unit area, with area calculations based on subsequent dye adsorption to the same grains, is shown in Fig. 1. (A number of measurements

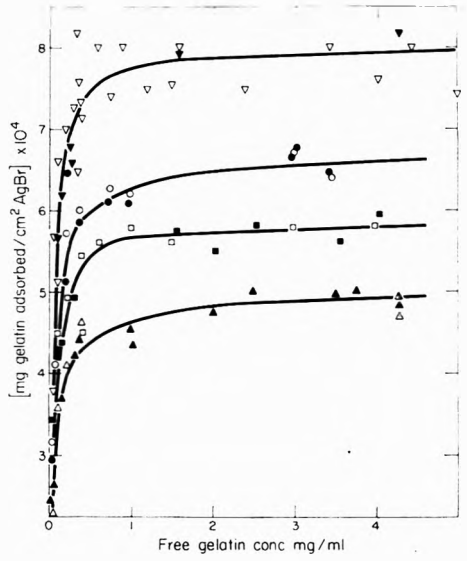

Figure 1. Adsorption of gelatin A as a function of pH and ionic strength: ▼, pH 4.7, μ = 0.0185, 2 hr.: ▽, pH 4.7, μ = 0.0185, 15 hr.: ●, pH 4.7, μ = 0.0635, 2 hr.: ○, pH 4.7, μ = 0.0635, 6 hr.: ■, pH 6.9, μ = 0.0635, 2 hr.: □, pH 6.9, μ = 0.0635, 15 hr.: ▲, pH 3.6, μ = 0.0635, 2 hr.: △, pH 3.6, μ = 0.0635, 4 hr.: ◭, pH 3.6, μ = 0.0635, 8 hr.

made at low concentrations have been omitted to prevent crowding the figures.) These data, as well as data not shown taken at intermediate times, indicate clearly that adsorption per unit area is substantially time-independent over the range 2–15 hr. (pH 4.7 and 6.9) and over the range 2–8 hr. (pH 3.6); adsorption at times longer than 8 hr. was not investigated at pH 3.6. Similar evidence, not shown, was obtained for gelatin B at pH 4.7. Although other workers have often conducted experiments on adsorption of polymers longer than 2 hr., the actual time necessary to reach saturation values seems to depend on the nature of both the adsorbent and the adsorbate. Koral, Ullman, and Eirich,[4] for example, have found that adsorption of polyvinyl acetate to iron and tin powders was complete within 1 hr., whereas adsorption to alumina was not complete after 7 hr. The iron and tin powders are described as smooth and nonporous, but the alumina surface was "very irregular."

Gelatins C, D, and E were lower in viscosity than A and B, and adsorption equilibrium might, if anything, be expected to be established faster than that of A and B. As a result, 2 hr. was chosen as the time of equilibration of these gelatins with sol. Decrease of surface area of the sol during this period was, in all cases, about 10%. Adsorptions of gelatins C-acetyl and D are shown in Fig. 2 and 3.

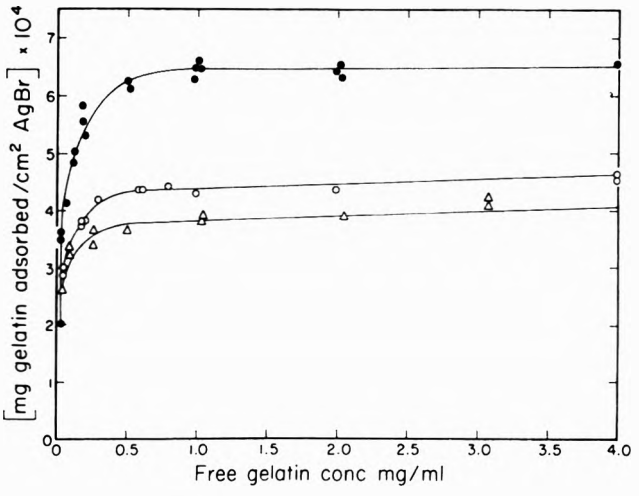

Figure 2. Adsorption of gelatin C-acetyl as a function of pH and ionic strength: ●, pH 3.6, μ = 0.0635; ○, pH 4.7, μ = 0.0635; △, pH 4.7, μ = 0.0185.

A summary of adsorption results is presented in Table I. Isotherms are described in terms of a_s, limiting adsorption in mg./cm.² area, and in terms of the parameters ν and K in the Frisch–Simha–Eirich[5] (FSE) equation

$$\frac{\theta}{\nu(1-\theta)^{\nu}} = Kc$$

In this expression $\theta = a/a_s$, where a is the amount of adsorbed gelatin at concentration c, expressed in

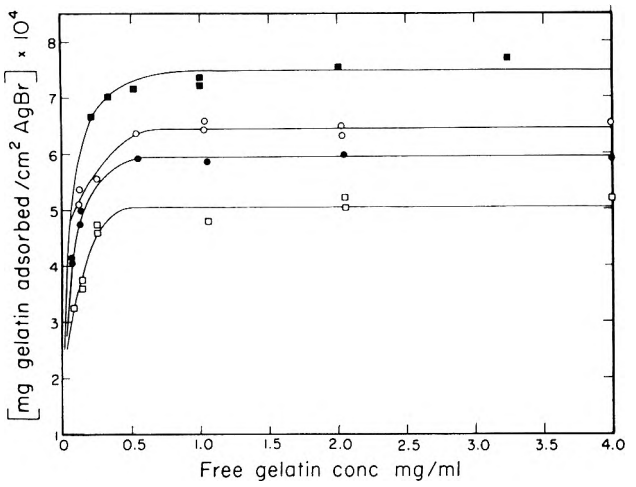

Figure 3. Adsorption of fractions of gelatin D at pH 4.7 and μ = 0.0185: ■, D(60) (M_w = 450,000); ○, D(50) ($\bar{M}_w$ = 263,000); ●, D(40) (M_w = 146,000); □, D(30) ($\bar{M}_w$ = 80,000).

mg./ml. At least ten experimental points were used in determining each isotherm. Free gelatin concentrations ranged from 0.03 mg./ml. (or less) to 5.0 mg./ml. in each case, corresponding to values of θ of 0.5 or less to almost 1. Values for a_s were determined by plotting $1/a$ against $1/c$ and extrapolating to $1/c$ = 0. Most of these curves showed more adsorption at lower concentrations than would be predicted from the slopes at 1/c = 0. These deviations from the Langmuir form were described in terms of the FSE parameters by making log–log plots of $1 - a/a_s$ *vs.* $c(a_s/a)$. Values of ν and K calculated from the slope and intercepts of these plots are listed in the table. Values of ν and K cannot be interpreted in terms of the mechanism of adsorption as they were in the FSE treatment, since the conditions of this work are not those (low surface coverage, nonionic polymers) for which the equation was derived. They are nevertheless convenient in describing the experimental data. The average deviation of experimental values of a from the curves described by these parameters was about 5%.

In a set of experiments designed to test the reversibility of the system, gelatin was adsorbed to the grains and the system then diluted several-fold. No desorption whatsoever was noted, even at coverages near surface saturation.

In another type of experiment, sol and dye were shaken for 3 hr. at pH 4.7, μ (ionic strength) = 0.0185 mole/l. Gelatin was then added, and 2 to 15 hr. later gelatin adsorption was measured. An amount of gelatin was found on the grains amounting to 40% of that found in the absence of the dye. Either the dye and the gelatin are both adsorbed to the silver bromide surface at different sites, or a layer of gelatin is adsorbed on top of the dye.

Dimensions of Gelatin Molecules in Solution. It is of interest to compare the actual coverage of the molecules with that which they would show if they occupied the same space on the surface as they do in solution. In a subsequent section such calculations are outlined based on radii of gyration in solution derived from the Flory–Fox relationship

$$[\eta] = \frac{\Phi 6^{3/2}\langle(\bar{s}^2)^{3/2}\rangle_n}{\bar{M}_n} \qquad (1)$$

In this expression $[\eta]$ is the intrinsic viscosity, $\bar{M}_n$ is the number-average molecular weight, $\langle(\bar{s}^2)^{3/2}\rangle_n$ is the number-average of the three-halves power of the square of the radius of gyration, and Φ is a universal constant, the best value of which is about 2.5×10^{21} when $[\eta]$ is expressed in dl./g.,[28,29] s in cm., and M in molecular weight units. In order for this relation to hold, the distribution of segments of gelatin molecules about their center of gravity must be approximately gaussian. Gelatin is a completely denatured derivative of collagen, with little or no helical structure remaining in the polypeptide chains. Although Courts and Stainsby[30] have shown that some gelatin molecules may consist of several polypeptide chains, Beyer,[31] Gouinlock, Flory, and Scheraga,[32] and others have shown that gelatin is quite similar to a randomly coiled chain in its viscosity behavior. This indicates that the Flory–Fox equation is, indeed, applicable.

As an experimental check on the applicability of the equation, a careful Zimm grid analysis was made of the light scattering of one of the higher-molecular-weight gelatins, gelatin B, which showed little or no evidence of suspended impurities after clarification. This gave a value of $\langle\bar{s}^2\rangle_z^{1/2}$ of 555 Å. in 0.1 ionic strength KCl, pH 4.7. This was compared with the Flory–Fox value through the relation

$$\langle\bar{s}^2\rangle_z^{1/2} = \left(\frac{[\eta]M_w}{2.5 \times 10^{21} \times 6^{3/2}}\right)^{1/3}\left(\frac{\bar{M}_w}{\bar{M}_n}\right)^{13/24} \qquad (2)$$

which may be derived from eq. 1, following the ap-

(28) S. Newman, W. R. Krigbaum, C. Laugier, and P. J. Flory, *J. Polymer Sci.*, **14**, 451 (1954).

(29) P. J. Flory, "Principles of Polymer Chemistry," Cornell University Press, Ithaca, N. Y., 1953, p. 617.

(30) A. Courts and G. Stainsby, "Recent Advances in Gelatin and Glue Research," G. Stainsby, Ed., Pergamon Press, New York, N. Y., and London, 1958, p. 100.

(31) G. L. Beyer, paper presented at 126th National Meeting of the American Chemical Society, New York, N. Y., Sept., 1954.

(32) E. V. Gouinlock, Jr., P. J. Flory, and H. A. Scheraga, *J. Polymer Sci.*, **16**, 383 (1955).

proach of Newman, Krigbaum, Laugier, and Flory. The value of $\langle \overline{s^2} \rangle_z^{1/2}$ calculated from the known values of $\bar{M}_w$, $\bar{M}_n$, and $[\eta]$ (0.61, also after clarification and under the same conditions) was 531 Å.

Discussion

Configuration of Adsorbed Layers. Coverages shown in Table I and in the figures are close to those reported by Pouradier and Roman[1] and are evidence for the loop and bridge model of adsorption. Adsorption of peptide chains that are close-packed on the surface would be expected to be no greater than coverage of close-packed peptide chains on liquid surfaces, which has been estimated from surface pressure measurements on several proteins[33] to be of the order of 1.2×10^{-4} mg./cm.^{2}. Spreading experiments suggest that coverages of gelatin on water[1] or mercury surfaces[34] are actually less than this. Although coverages on silver halides are many times these values, the isotherms show no indication of multilayer adsorption.

The molecular weight data also support the loop and bridge model. Fractions D(30)–D(60) show the relationship $a_s = K\bar{M}_w^n$, where n is 0.23. Adsorption at the end or at a single site on the chain would lead to first-power dependence on molecular weight, whereas adsorption of flat monolayers would lead to little or no dependence on molecular weight.

Effects of Electrostatic Interactions on Gelatin Adsorption. Although changes in saturation adsorption with pH and ionic strength may be due to a number of factors, inspection of Table I shows that these changes closely parallel changes in electrostatic interactions between segments of adsorbed molecules. Gelatin A, for example, shows more adsorption near the isoelectric point, where it has a small net charge, than it does with either a higher positive charge (at pH 3.6), or with a higher negative charge (at pH 6.9). Gelatin C–acetyl also shows more adsorption with a small net charge (at pH 3.6) than it does with a higher one (at pH 4.7), despite the fact that the effect on adsorption of changing the pH from 4.7 to 3.6 is exactly opposite for the two gelatins. These results suggest that a high net charge on the molecule causes it to occupy more space on the surface. Expansion and contraction of polyelectrolytes in solution with changes in pH and ionic strength are, of course, well known, and are shown in this case by the changes of intrinsic viscosity with conditions shown in Table I.

Electrostatic repulsion may also cut down the approach to surface saturation as concentration is increased, resulting in adsorption isotherms with "plateaus," which rise slowly over a wide concentration range. The isotherms in Fig. 1 and 2 seem to show slight effects of this sort, which appear in Table I as somewhat higher values of ν necessary to fit the data away from the isoelectric point than at the isoelectric point.

The effect of added salt is to decrease electrostatic interactions. Away from the isoelectric point, as with gelatin C–acetyl at pH 4.7, the net charge causes an over-all repulsion between molecular segments. When the salt concentration is increased, this repulsion is decreased and more gelatin is adsorbed. However, near the isoelectric point, as with gelatin A at pH 4.7 or gelatin E(7) at pH 8.6, the net electrostatic effect is an attraction between the nearly equal numbers of positive and negative segments. Addition of salt causes a decrease in the attraction and a decrease in the amount of gelatin adsorbed.

The fact that a_s is higher for the untreated gelatin when its net charge is near zero than when it is quite positive is particularly interesting in view of the excess of potential-determining bromide ions in the system, which cause the surface potential of the silver bromide to be negative. If there is any tendency for limiting adsorption to be enhanced by the increased interaction between the negative surface and the gelatin molecules with their net positive charge, it is outweighed by the repulsion between like charges on segments of the adsorbing molecules.

Comparison of Configuration of Gelatin on the Surface with That in Solution. The intrinsic viscosity data of Table I show that conditions of salt and pH which lead to expansion of a gelatin in solution usually lead to lower a_s values on the surface. The parallel is not, however, perfect, as may be seen by comparing data for gelatin A at pH 3.6 and 6.9. Although viscosity is higher at pH 6.9, adsorption is also higher at this pH; the net charge is lower. The most probable interpretation of the data is that charge plays a more important role in determining a_s than the interactions responsible for solution viscosity. (The changes of viscosity with pH at this ionic strength roughly parallel those found by Stainsby.[13] Dissimilarities between the viscosity–charge relationship of a gelatin on the two sides of its isoelectric point under other conditions have been noted by Boedtker and Doty.[35])

The extensive changes in the configuration of the molecules brought about by their adsorption are illustrated by a simple calculation. For these purposes, to each molecule in solution may be assigned an area equal to πs^2. The weight of such an array, packed

(33) H. B. Bull, *Advan. Protein Chem.*, **3**, 95 (1947).

(34) R. L. Keenan, *J. Phys. Chem.*, **33**, 371 (1929).

(35) H. Boedtker and P. Doty, *ibid.*, **58**, 968 (1954).

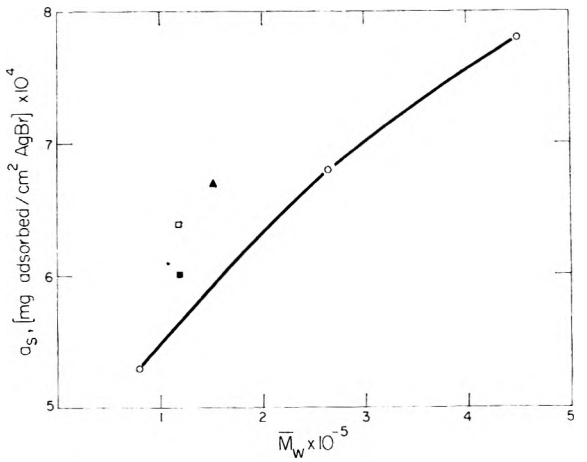

Figure 4. Limiting adsorption of near-isoelectric gelatins as a function of weight-average molecular weight: O, lime-processed fractions, μ = 0.0185; □, acid-processed fraction, μ = 0.0185; ■, acid-processed fraction, μ = 0.0635; ▲, acetylated, μ = 0.0635.

together on a unit area of imaginary surface in the solution, would be $\bar{M}_n/N\pi\langle s^2\rangle_n$, where N is Avogadro's number. Since M for gelatin varies approximately linearly with s^2, the coverage of such an array would be roughly independent of molecular weight. Substitution of light-scattering values of $\bar{M}_w$ and Flory–Fox values of $\langle(\bar{s}^2)^{3/2}\rangle_n$, derived from viscosity data, along with approximate heterogeneity corrections, gives coverages of the order of 6×10^{-5} mg./cm.^{2}, 10 to 15 times below the observed values. This indicates that the molecules in the adsorbed phase are extended in a direction normal to the surface, have higher segment densities than those of the coils in solution, or show both effects. In this connection, Janus and Darlow[36] have concluded from comparison of water flow times in clean and gelatin-coated capillaries that the adsorbed, hydrated gelatin layer on glass is actually "several hundred Ångström units" thick.

Groups Involved in Adsorption. An attempt has been made to evaluate the contributions of carboxyl and amino side-chain groups in gelatin to the over-all adsorption. To do this, a_s values for gelatins bearing different numbers of these side-chain groups were measured and have been plotted as a function of their molecular weight under conditions of nearly the same net charge and, if possible, the same ionic strength. This plot is seen in Fig. 4. The lime-processed and acid-processed gelatins are those which showed no loss of material on clarification for light scattering, and the adsorption values of these gelatins near their isoelectric points at μ = 0.0185 are plotted. Adsorption of the acid-processed sample is seen to fall about 10% above the curve for the lime-processed samples.

The acetylated gelatin showed a 2% loss on clarification but is plotted nevertheless, since no other sample of this type was available. Since the molecular-weight dependence of adsorption is not strong, it is doubtful whether a_s would have been measurably lower if the clarified sample used for light scattering had been used for adsorption measurements, rather than the unclarified. This gelatin at μ = 0.0635 shows about 10% more adsorption than would be expected on the basis of the adsorption of the acid-processed gelatin at the same ionic strength. Although the reasons for this may be quite complex, one explanation is that, near its isoelectric point, the acetylated gelatin is simply a more compact molecule. This may be seen in Table I: near their isoelectric points and at μ = 0.0635, the acid-processed and acetylated gelatins have nearly the same viscosities, but the acetylated gelatin shows a molecular weight about 30% higher.

These isoelectric gelatins differed considerably in the number and state of ionization of their side groups. Lime-processed gelatin differs from acid-processed samples in that almost all of the amide groups attached to dicarboxylic acid residues in the original collagen are hydrolyzed to free carboxyl in the lime-processed samples, whereas about 30% of these carboxyl groups in the acid-processed samples are present as amide.[14] The net result is that isoelectric acid-processed gelatin has amidized carboxyls in place of the free carboxyls shown by isoelectric lime-processed gelatins, and the weakly basic groups (α-amino, imidazole) in the acid-processed gelatins are not ionized. In the acetylated sample, on the other hand, almost 80% of the amino groups were acetylated, and the molecule near its isoelectric point had about half as many ionized carboxyls as the others. It is clear that these differences in chemical constitution are not paralleled by any substantial differences in saturation adsorption.

Acknowledgment. The authors wish to thank Drs. E. J. Perry, G. L. Beyer, and J. W. Gates, Jr., of these laboratories, for helpful discussions and advice.

(36) J. W. Janus and R. L. R. Darlow, *Nature*, **194**, 1075 (1962).

Thermal Conductivity of Liquids

by Sheng Hsien Lin, Henry Eyring, and Walter J. Davis

Department of Chemistry, University of Utah, Salt Lake City, Utah (*Received June 1, 1964*)

The significant structure theory of liquids is applied to calculate the thermal conductivities of liquids. Pressure and temperature effects on thermal conductivities are discussed. For the three substances, nitrogen, argon, and methane, the discrepancy between the calculated and experimental results is less than 4%.

I. Introduction

Application of the method of significant structure theory to both thermodynamical and transport properties of liquids has been made with good results.[1-3] The purpose of this paper is to examine the thermal conductivity of liquids based on the "significant structure" model, *i.e.*

$$K_l = (V_s/V)K_s + (1 - V_s/V)K_g \qquad (1)$$

where K_l is the contribution to the liquid thermal conductivity, K_s is the contribution by the "solid-like" or lattice vibrational degrees of freedom, and K_g is the contribution by the "gas-like" or fluidized degrees of freedom. For the calculation of K_s, we use the phonon theory first developed by Peierls[4,5] and then modified by Klemens[6] and Callaway.[7] Since the contribution of K_g to the liquid thermal conductivity is small, generally less than 5% except in the critical region, we use the ideal gas formulas for the calculation of K_g. Three substances—argon, nitrogen, and methane—are chosen for calculating the liquid thermal conductivity. Pressure and temperature effects on the thermal conductivity are also discussed.

II. Thermal Conductivity of Solids

When a temperature gradient is applied to a solid, the equilibrium state will be disturbed, and the average distribution of phonons should be determined from the Boltzmann equation

$$-\vec{C}_s \cdot \text{grad } T \, dN/dT = \partial N/\partial t \qquad (2)$$

where N is the number of phonons per unit volume and C_s the group velocity of solids. The left-hand side of eq. 2 represents the rate of change of N due to the transport of phonons, and this is balanced by the rate of change due to scattering processes indicated on the right-hand side. Since the exact solution of eq. 2 is impossible,[4] an approximation is made by putting[6]

$$N = N^0 + n \qquad (3)$$

Where N^0 is the equilibrium distribution, $N^0 = (e^{\hbar\omega/kT} - 1)^{-1}$. It is apparent that if the temperature gradient is small, then $n << N^0$, so $dn/dT << dN^0/dT$ thus

$$\vec{C}_s \cdot \vec{\nabla} T \, dN^0/dT = \partial N/\partial t \qquad (4)$$

In terms of phonons, the heat current is just the energy flux due to the transport of phonons each of which carries energy $\hbar\omega$, so if we let $f(\vec{k})d\vec{k}$ represent the number of normal modes in the wave-number interval $\vec{k}$ and $\vec{k} + d\vec{k}$, we obtain for the heat flux in the direction of $\vec{\nabla} T$

$$Q = \sum_j \iiint N_j(\vec{k})\hbar\omega \frac{\vec{k} \cdot \text{grad } T}{|\vec{k}||\vec{\nabla} T|} C_{sj}(\vec{k}) f(\vec{k}) d\vec{k} \qquad (5)$$

where the summation is over different polarizations. Since $N_j^0(\vec{k}) = N_j^0(-\vec{k})$, $N_j(\vec{k})$ in eq. 5 can be replaced by $n_j(\vec{k})$, *i.e.*, only the deviation n_j contributes to the heat flux, because the integration in eq. 5 over

(1) G. Blomgren, *Ann. N. Y. Acad. Sci.*, **79**, 781 (1959).

(2) C. M. Carlson, "Theory of Fused Salts and Molten Metals," Doctoral Dissertation, University of Utah, 1960.

(3) E. J. Fuller, "Significant Liquid Structures," Doctoral Dissertation, University of Utah, 1960.

(4) R. Peierls, *Ann. Phys.*, **3**, 1055 (1929).

(5) R. Peierls, "Quantum Theory of Solids," Oxford University Press, London, 1955.

(6) P. G. Klemens, *Proc. Roy. Soc.* (London), **A208**, 108 (1951).

(7) J. Callaway, *Phys. Rev.*, **113**, 1046 (1959).

the equilibrium distribution N_j^0 vanishes. This is generally the case for the transport phenomena in nonequilibrium statistical mechanics.

Next we assume that the discontinuous processes tend to obliterate exponentially any deviations from equilibrium, *i.e.*

$$\partial N/\partial t = -(N - N^0)/\tau = -n/\tau \qquad (6)$$

where τ is an over-all relaxation time and is assumed to be dependent on ω and T. For an isotropic solid, we may use spherical coordinates in k-space with the axis of symmetry in the direction of temperature gradient. If we let θ be the angle between k and grad T, eq. 4 becomes, after substitution of eq. 6 into eq. 4

$$n = \tau C_s \cos\theta \, dT/dZ \times dN^0/dT = \tau C_s \cos\theta \frac{dT}{dZ} \frac{e^{\hbar\omega/kT}(\hbar\omega/kT^2)}{(e^{\hbar\omega/kT} - 1)^2} = (\tau C_s/\hbar\omega) C_{ph} \cos\theta \, dT/dZ \qquad (7)$$

where C_{ph} is the specific heat of phonons. Combining eq. 7 and 5 and integrating the angular parts of eq. 5, we obtain

$$Q = 4\pi/3 \, dT/dZ \sum_j \int \tau_j(k) C_{s_j}(k)^2 C_{ph_j}(k) f(k) \, dk \qquad (8)$$

or

$$K_s = 4\pi/3 \sum_j \int \tau_j(k) C_{s_j}(k)^2 C_{ph_j}(k) f(k) \, dk \qquad (8a)^1$$

Because of lack of knowledge of crystal vibrational spectra, it is impossible to integrate eq. 8a exactly. If Debye's model is used, then we have

$$4\pi f(k) \, dk = \frac{4\pi}{C_s^3} \nu^2 d\nu = \frac{4\pi\omega^2 d\omega}{C_s^3 (2\pi)^3} \qquad (9)$$

where ν is the frequency. If no distinction is made between longitudinal and transverse phonons,[7] eq. 8a becomes

$$K_s = \frac{k}{2\pi^2 C_s} \int_0^{\omega_{max}} \tau(\omega) \frac{\hbar^2\omega^2}{k^2T^2} \frac{e^{\hbar\omega/kt}\omega^2}{(e^{\hbar\omega/kT} - 1)^2} d\omega \qquad (10)$$

where τ is the over-all relaxation time, and ω_{max} the Debye cut-off frequency. Equation 10 has been used to explain the thermal conductivity of solids at low temperature successfully.[7-10]

From the specific heat theory of solids, we know that in the high temperature region the Einstein model is a good approximation. With this approximation, we have

$$4\pi f(k) \, dk = N/V_s \delta(\omega - \omega_e) \, d\omega \qquad (11)$$

where ω_e is the Einstein characteristic frequency, N is Avogadro's number, and $\delta(\omega - \omega_e)$ Dirac's δ-function. Substituting eq. 11 into eq. 8,[1] we obtain

$$K_s = \sum_j N/3V_s \tau_j C_{s_j}^2 C_{ph_j} = \sum_j l_j C_{s_j} C_{v_j}/3 \qquad (12)$$

where $l_j = \tau_j C_{s_j}$, the relaxation path length, and $C_{v_j} = (NC_{ph_j})/V_s$, the heat capacity of solids per unit volume for the jth polarization. Equation 12 has been used by Kittel[11] to explain the thermal conductivity of glasses at low temperatures. If no distinction is made between polarizations, eq. 12 can be written as

$$K_s = \frac{\tau C_s^2}{V_s} \times R \times \frac{(\hbar\omega_e/kT)^2 e^{\hbar\omega_e/kT}}{(e^{\hbar\omega_e/kT} - 1)^2} \qquad (13)$$

where $R = Nk$, the gas law constant, and C_s is the sound velocity of solids.

As with Klemens,[6] we assume that each scattering process can be represented by a relaxation time, *i.e.*, $1/\tau = \sum_l 1/\tau_l$, and existence of the following processes is assumed: (1) normal three-phonon processes where the relaxation time[9] is taken to be proportional to $(\omega^2 T)^{-1}$; (2) the Umklapp process with a relaxation time proportional to $(e^{-a/T}\omega^2 T)^{-1}$ where a is a constant characteristic of the vibrational spectrum of the material; (3) lattice imperfection scattering[6,11] whose relaxation time is independent of temperature and proportional to ω^{-4}. The other processes such as size effect, etc., are neglected because we are interested only in high temperature regions. Thus we can write

$$\tau^{-1} = A\omega^4 + BT\omega^2 \qquad (14)$$

where $A\omega^4$ represents the scattering by lattice imperfections, and the term $BT\omega^2$ includes the normal and Umklapp processes. Combining eq. 14 and 13 we obtain

$$K_s = \frac{C_s^2 R}{V_s(A\omega_e^4 + BT\omega_e^2)} \frac{(\hbar\omega_e/kT)^2 e^{\hbar\omega_e/kT}}{(e^{\hbar\omega_e/kT} - 1)^2} \qquad (15)$$

III. Thermal Conductivity of Gases

Various formulas for the thermal conductivity of gases K_g are derived from kinetic theory.[12] The general results are usually expressed as

$$K_g = \epsilon \eta_g C_{v_g} \qquad (16)$$

where ϵ is a pure number, η_g the viscosity, and C_{v_g} the specific heat at constant volume. As we already mentioned, the contribution of gas thermal conductivity to the liquid thermal conductivity is generally small. For our present purpose, therefore, we may use the

(8) B. A. Agrawal and G. S. Verma, *Phys. Rev.*, **126**, 25 (1962).
(9) J. Callaway and H. C. von Baeyer, *ibid.*, **120**, 1149 (1960).
(10) P. Carruthers, *Rev. Mod. Phys.*, **33**, 92 (1961).
(11) C. Kittel, *Phys. Rev.*, **75**, 972 (1949).
(12) L. B. Loeb, "Kinetic Theory of Gases," McGraw-Hill Book Co., Inc., New York, N. Y., 1927, Chapter 6.

ideal gas equations for ϵ, η_g, and C_{v_g}, namely, $\epsilon = (9\gamma - 5)/4$, where γ is the ratio of specific heat at constant pressure to that at constant volume, and $\eta_g = m\bar{c}/(3\sqrt{2}\pi\sigma^2)$, where m is the mass of a molecule, σ the molecular diameter, and $\bar{c}$ the average velocity, $\bar{c} = (8kT/\pi m)^{1/2}$. For the temperature and pressure ranges of concern, K_g is less than or around 5×10^{-5} cal./cm. deg. for all three substances. For the rigorous treatment of K_g, one should refer to the literature.[13,14]

IV. Thermal Conductivity of Liquids

Substituting eq. 15 and 16 into eq. 1, we obtain the equation for the liquid thermal conductivity as

$$K_l = \frac{RC_s^2}{V(A' + B'T)} \frac{(\hbar\omega_e/kT)^2 e^{\hbar\omega_e/kT}}{(e^{\hbar\omega_e/kT} - 1)^2} + \frac{V - V_s}{V} \epsilon\eta_g C_{v_g} \tag{17}$$

where $A' = A\omega_e^4$ and $B' = B\omega_e^2$. The first term on the right-hand side of eq. 17 represents the contribution to thermal conduction due to the vibration of molecules sitting near equilibrium position and the second term, the contribution due to the random motion of molecules. For $\hbar\omega_e/kT < 1$, we may put $x^2e^x/(e^x - 1)^2 = 1$; this is generally the case for the liquid thermal conductivity. Furthermore, if the pressure is not very large, C_s is constant, and it is convenient to absorb C_s and R into constants A' and B'.

The temperature range considered in this paper is from the normal melting point to the critical temperature for the three substances. For argon, we use $P = 12$ atm., $T = 106.1$°K., $K_e = 2.44 \times 10^{-4}$ cal./deg. cm., and $P = 12$ atm., $T = 93.6$°K., $K_l = 2.81 \times 10^{-4}$ cal./deg. cm.[15] with $C_s = 1310$ m./sec.[16] to calculate the parameters A and B. They are 2.50×10^{-40} and 5.52×10^{-16} for A and B, respectively, using $\omega_e = 7.85 \times 10^{12}$.[17] The corresponding values obtained for nitrogen and methane are $A = 1.82 \times 10^{-40}$, $B = 5.64 \times 10^{-16}$, and $A = 1.60 \times 10^{-40}$, $B = 1.77 \times 10^{-16}$, respectively. Below the critical temperatures, the liquid thermal conductivity is nearly a linear function of temperature at constant pressure as shown in Fig. 1 and 2.

To consider the pressure effects on the liquid thermal conductivity, we use $C_s = (\gamma_s/\rho_s\beta_T)^{1/2}$ to estimate the dependence of C_s on the pressure, where γ_s is the ratio of specific heats of solids, ρ_s, the density of solids, and β_T, the isothermal compressibility coefficient of solids. C_s does not vary very much with pressure, so we have to consider the pressure dependence of C_s only at very high pressures. Because of being limited by the availability of data for β_T, only two values of K_l under the pressure of $800K_g/\text{cm.}^2$ have been calculated for argon. The data used for the calculation are $P = 0$, $\beta_T = 6.2 \times 10^{-5}$ cm.$^2/K_g$, and $P = 800K_g/\text{cm.}^2$, $\beta_T = 4.36 \times 10^{-5}$ cm.$^2/K_g$.[16] $V = 28.89$ cm.^{3}/mole at $T = 119.6$ °K.; $V = 27.54$ cm.^{3}/mole[18] at $T = 102.2$ °K. The results obtained by using eq. 17 are $K_l = 3.30 \times 10^{-4}$ cal./deg. cm. at $P = 800K_g/\text{cm.}^2$, $T = 119.6$°K., and $K_l = 3.91 \times 10^{-4}$ cal./deg. cm. at $P = 800K_g/\text{cm.}^2$, $T = 102.2$°K., in comparison with the extrapolated experimental values of Rice.[19] $K_l = 3.40 \times$

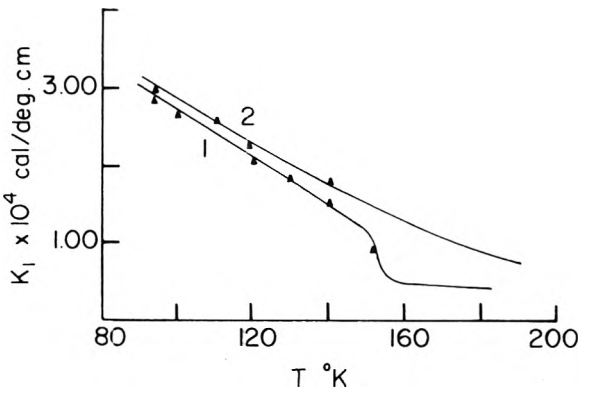

Figure 1. Temperature dependence of K_l of argon: ———, experimental values; ▲, calculated values; curve 1, $P = 48$ atm., curve 2, $P = 120$ atm.

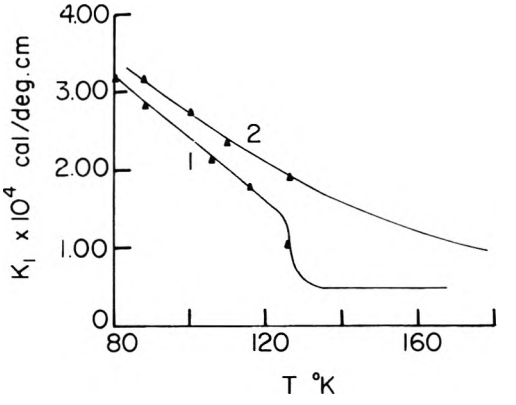

Figure 2. Temperature dependence of K_l of nitrogen: ———, experimental values; ▲, calculated values; curve 1, $P = 33.5$ atm.; curve 2, $P = 134$ atm.

(13) J. O. Hirschfelder, C. F. Curtiss, and R. B. Bird, "Molecular Theory of Gases and Liquids," John Wiley and Sons, Inc., New York, N. Y., 1954.

(14) S. Chapman and T. G. Cowling, "The Mathematical Theory of Non-uniform Gases," Cambridge University Press, London, 1953.

(15) H. Ziebland and J. Burton, *Brit. J. Appl. Phys.*, **9**, 52 (1958).

(16) J. W. Stewart, *J. Phys. Chem. Solids*, **1**, 146 (1956).

(17) E. J. Fuller, T. Ree, and H. Eyring, *Proc. Natl. Acad. Sci. U. S.*, **45**, 1594 (1959).

(18) P. W. Bridgman, *Proc. Am. Acad. Arts Sci.*, **70**, 1 (1935).

(19) L. D. Ikenberry and S. A. Rice, *J. Chem. Phys.*, **39**, 1961 (1963).

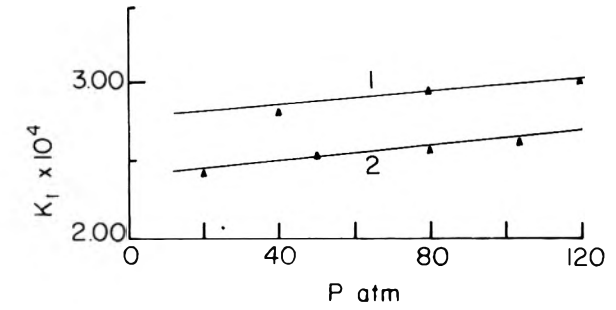

Figure 3. Pressure effect on K_1 of argon: ———, experimental results; ▲, calculated values; curve 1, T = 93.3°K.; curve 2, T = 106.1°K.

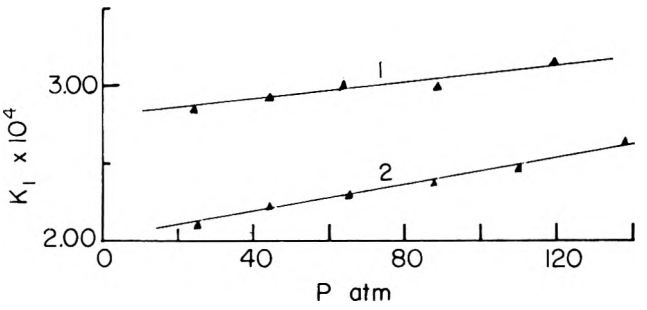

Figure 4. Pressure effect on K_1 of nitrogen: ———, experimental results; ▲, calculated values; curve 1, T = 87.7°K.; curve 2, T = 105.6°K.

10^{-4} cal./deg. cm., $K_1 = 3.80 \times 10^{-4}$ cal./deg. cm., respectively. The liquid thermal conductivity *vs.* pressure for pressures below 140 atm. are shown in Fig. 3 and 4. It can be seen that for small ranges of pressure, K_1 is linear with respect to pressure.

Some of the calculated results of K_1 for the three substances are tabulated in Table I, in comparison with the experimental values. The discrepancy, as can be seen from the table, is less than 4%. In concluding this paper, it is interesting to notice that K_s's calculated from eq. 15 by using the values of A and B obtained from liquids are in good agreement with the experimental values of K_s; for example, at P = 180 atm., T = 83.6°K., K_s (calcd.) = 4.29×10^{-4} cal./deg. cm., K_s (exptl.) = 4.27×10^{-4} cal./deg. cm.,[15] and at T = 77°K., K_s (calcd.) = 4.22×10^{-4} cal./deg. cm., K_s (exptl.) = 4.20×10^{-4} cal./deg. cm. If this is the case, we may assert that the structure of the solid part of liquids is not much different from that of solids at high temperatures, but in view of the limited amount of data of K_s at high temperatures ($T > \theta_0$, Debye's characteristic temperature) which are available, it seems that further justification is necessary.

Table I: Results of Calculation[a]

Temp., °K.	Pressure, atm.	K_1 (calcd.) × 10^4, cal./deg. cm.	K_1 (exptl.) × 10^4, cal./deg. cm.
		Argon[b]	
93.3	48	2.87	2.90
93.3	72	2.89	2.93
93.3	120	2.96	3.04
100	48	2.68	2.70
130	48	1.84	1.793
120	48	2.10	2.11
125.7	19.3	1.89	1.88
125.7	72	2.01	1.99
140	48	1.54	1.48
150.7[d]	48[d]	0.914	
102.2	774	3.91	3.80[c]
119.6	774	3.30	3.40[c]
		Nitrogen[b]	
87.7	134	3.18	3.14
87.7	67	2.93	2.97
87.7	33.5	2.88	2.90
98.3	67.0	2.53	2.60
105.8	33.5	2.20	2.17
105.8	50.3	2.24	2.25
105.8	100.5	2.50	2.46
116.1	33.5	1.83	1.75
126.1[d]	33.5[d]	1.04	
80	33.5	3.22	3.26
		Methane[c]	
99.0	1.6	4.97	4.946
99.0	50.5	5.01	5.06
125.6	50.1	4.05	4.096
150.3	25.9	3.26	3.176
150.3	49.7	3.30	3.284

[a] V_s = 22.5 ml./mole for argon, 26.14 ml./mole for nitrogen, and 30.90 ml./mole for methane. [b] Experimental data of K_1 are from H. Ziebland and J. Burton, *Brit. J. Appl. Phys.*, **9**, 52, (1958). [c] Experimental data of K_1 are from L. D. Ikenberry and S. A. Rice, *J. Chem. Phys.*, **39**, 1961 (1963). [d] The critical point. The data used to calculate A and B are P = 8.4 atm., T = 88.2°K., $K_1 = 2.79 \times 10^{-4}$, and P = 27.6 atm., T = 80.9°K., $K_1 = 3.18 \times 10^{-4}$ for nitrogen, and P = 25.3 atm., T = 99°K., $K_1 = 4.999 \times 10^{-4}$, and P = 24 atm., T = 125.6°K., $K_1 = 4.016 \times 10^{-4}$ for methane.

Acknowledgment. Acknowledgment is made to the Army Ordnance under Contract DA-ARO(D)-31-124-G298 for financial support of this research.

Lattice Parameter and Density in Germanium–Silicon Alloys[1]

by J. P. Dismukes, L. Ekstrom, and R. J. Paff

RCA Laboratories, Radio Corporation of America, Princeton, New Jersey *(Received June 1, 1964)*

The lattice parameter and density of chemically analyzed samples of homogeneous Ge–Si alloy have been measured throughout the entire alloy system. The temperature dependence of the lattice parameter was measured from 25 to 800°. Compositional dependences of the lattice parameter and density are accurate to about ±0.3 atomic % in alloy composition. Lack of chemical analysis or sample inhomogeneity may explain the large discrepancies between previous investigations of these properties. The excess volume of mixing is given by $\Delta V_m^{xs} = -0.24 c_{Ge} c_{Si}$ cm.^{3} mole^{-1}. Deviations from Vegard's law are negative as predicted by models based on first-order elasticity theory, but smaller in absolute magnitude. This discrepancy is about the size of the positive deviations calculated from second-order elasticity theory.

Introduction

Composition in the Ge–Si alloy system can be accurately determined from measurements either of density or of lattice parameter provided the dependences of lattice parameter and density on composition are known. However, the large discrepancy between the results of previous investigations of these properties[2–5] corresponds to an uncertainty in composition for a definite value of lattice parameter or density of ±4 atomic % Ge throughout most of the system. This discrepancy can be attributed to the fact that no previous investigator has both evaluated sample homogeneity and determined composition by chemical analysis. Therefore the variation of lattice parameter and density at room temperature has been reinvestigated throughout the Ge–Si alloy system, using chemically homogeneous specimens. The temperature dependence of lattice parameter has also been measured in the range 25–800° for several alloy compositions.

Experimental Procedure

Homogeneous Ge–Si alloy ingots were prepared from high purity Ge and Si by zone leveling using the procedure described by Dismukes and Ekstrom.[6] Typical mass spectrographic analyses of impurities in these materials are shown in Table II. The procedure for this study consisted of first measuring the density and then measuring either the lattice parameter or the chemical composition of the material.[7]

Table I: Previous Investigations of Lattice Parameter and Density in the Ge–Si Alloy System

Authors	Method of preparation	Lattice parameter	Density[a]	Method of analysis
Stöhr and Klemm[b]	Sintering	D	ND	None[c]
Johnson and Christian[d]	Slow cooling from the melt	D	D	Polarographic
Wang and Alexander[e]	Zone leveling	D	D	None[f]
Busch and Vogt[g]	Zone leveling	D	D	None[h]
Sandulova, *et al.*[i]	Vapor transport	D	ND	None[j]

[a] D = determined; ND = not determined. [b] See ref. 2a. [c] Composition assumed to be that of the mixed components before sintering. [d] See ref. 2b. [e] See ref. 3. [f] Composition assumed to be that of the mixed components before some leveling. [g] See ref. 4. [h] Composition determined from the results of Johnson and Christian. [i] See ref. 5. [j] Composition assumed to be that of the mixed components before vapor transport.

(1) This research has been supported by the U. S. Navy Bureau of Ships under Contract No. NObs-88595.

(2) (a) H. Stöhr and W. Klemm, *Z. anorg. allgem. Chem.*, **241**, 313 (1939); (b) E. R. Johnson and S. M. Christian, *Phys. Rev.*, **95**, 560 (1954).

(3) C. C. Wang and B. H. Alexander, Final Technical Report on Investigation of Germanium–Silicon Alloys, Bureau of Ships Contract No. NObsr-63180, Feb. 17, 1955.

(4) G. Busch and O. Vogt, *Helv. Phys. Acta*, **33**, 437 (1960).

(5) A. V. Sandulova, P. S. Bogoiavlenski, and M. I. Droniuk, *Dokl. Akad. Nauk SSSR*, **143**, 610 (1962).

(6) J. P. Dismukes and L. Ekstrom, to be published.

(7) K. L. Cheng and B. L. Goydish, *Anal. Chem.*, **35**, 1273 (1963).

Table II: Mass Spectrographic Analyses for Impurities in Ge, Si, and Ge–Si Alloy

	Typical impurity contents, atomic p.p.m.						
Materials	Fe	Cu	Al	Mg	O	C	H
Ge–Si	1	0.2	5	1	300	30	100
Ge	6	ND[a]	0.4	0.4	10	100	30
Si	1	0.2	1	1	300	100	10

[a] ND = not detected.

Densities were measured by the method of hydrostatic weighing,[8] employing Archimedes' principle. The samples in the form of slices weighed 0.7–1.5 g., and the weight loss in water was 0.1–0.3 g. The samples were suspended from a 0.003-in. diameter tungsten wire and were weighed to a precision of 0.02 mg. using a semimicrobalance. Water, to which a small amount of wetting agent had been added to reduce the surface tension, was used as the immersion liquid. The measurements were corrected for water temperature and for the air displaced by the sample, but not for effects due to the wetting agent, dissolved air, or atmospheric pressure. The absolute accuracy of these density measurements is shown to be within $\pm 0.1\%$ by comparison in Table III of measurements made on Si and Ge corrected to 25° with the values of Smakula and Sils.[8]

Samples for lattice parameter measurements were ground to pass through a 325-mesh screen. The sieved powder was mixed with Duco cement and was then rolled into a fiber approximately 0.1 mm. in diameter. The fiber was mounted in a 114.6-mm. diameter camera using the asymmetric method of mounting the film. Powder patterns were obtained using Ni-filtered Cu radiation, with an exposure time of about 24 hr. and at room temperature of 25 ± 1°. The back reflection lines, both $K\alpha_1$ and $K\alpha_2$, were measured to within ±0.05 mm. The lattice parameter for each reflection was calculated, and the final value was obtained by extrapolation using the Nelson–Riley function. The absolute accuracy of the lattice parameter measurements is shown to be within ±0.0005 Å. by comparison in Table III of measurements made on Si and Ge with the values of Smakula and Kalnajs.[9] The variation of lattice parameter with temperature in the range 25–800° was determined by scanning the (531) and (620) diffraction peaks with a diffractometer. Values of the lattice parameter at each temperature were obtained by averaging the lattice parameter values for the two peaks. Good agreement between the diffractometer

Table III: Experimental Values of Density, Lattice Parameter, and Chemical Composition for Ge–Si Alloy Samples

d, g. cm.$^{-3}$	a, Å.	C, at. % Ge
2.6382	...	7.5
2.6319	...	8.0
2.6357	...	8.0
2.6330	5.4492	...
3.0047	...	18.9
3.0098	...	20.0
3.0710	...	21.4
3.0830	...	21.7
3.0120	5.4726	...
3.0822	5.4772	...
3.0884	...	22.6
3.1118	...	23.5
3.2723	...	28.2
3.2844	5.4898	...
3.3634	...	30.5
3.3585	...	31.6
3.4735	5.5032	...
3.4762	...	35.4
3.5181	...	35.5
3.5715	...	36.6
3.6312	5.5151	...
3.6313	...	38.8
3.6340	...	39.8
3.6874	...	40.3
3.6766	...	41.4
3.7750	5.5250	...
3.7827	...	44.5
3.7883	...	44.6
3.9915	5.5404	...
3.8944	...	48.0
3.9940	...	49.9
4.0037	...	50.6
4.0749	5.5475	...
4.0673	...	53.8
4.0897	...	54.8
4.1652	...	57.0
4.1923	5.5567	...
4.5289	5.5841	...
4.5170	...	68.0
4.4969	...	68.9
4.6817	5.5966	...
4.6652	...	71.9
4.6735	...	72.3
4.8246	...	79.4
4.8513	...	79.4
4.8410	5.6112	...
5.0752	5.6325	...
5.0754	...	87.3
5.0728	...	87.9
5.0970	...	88.8
5.0410	...	89.4
5.1090	...	90.8
5.1697	5.6419	...
5.1669	...	94.8
5.3256	5.6575	Ge[a]
5.32674	5.65754	Ge[b]
2.3277	5.4310	Si[a]
2.32902	5.43072	Si[b]

[a] Present work. [b] See ref. 9 and 10.

(8) A. Smakula and V. Sils, *Phys. Rev.*, **99**, 1744 (1955).

(9) A. Smakula and J. Kalnajs, *ibid.*, **99**, 1737 (1955).

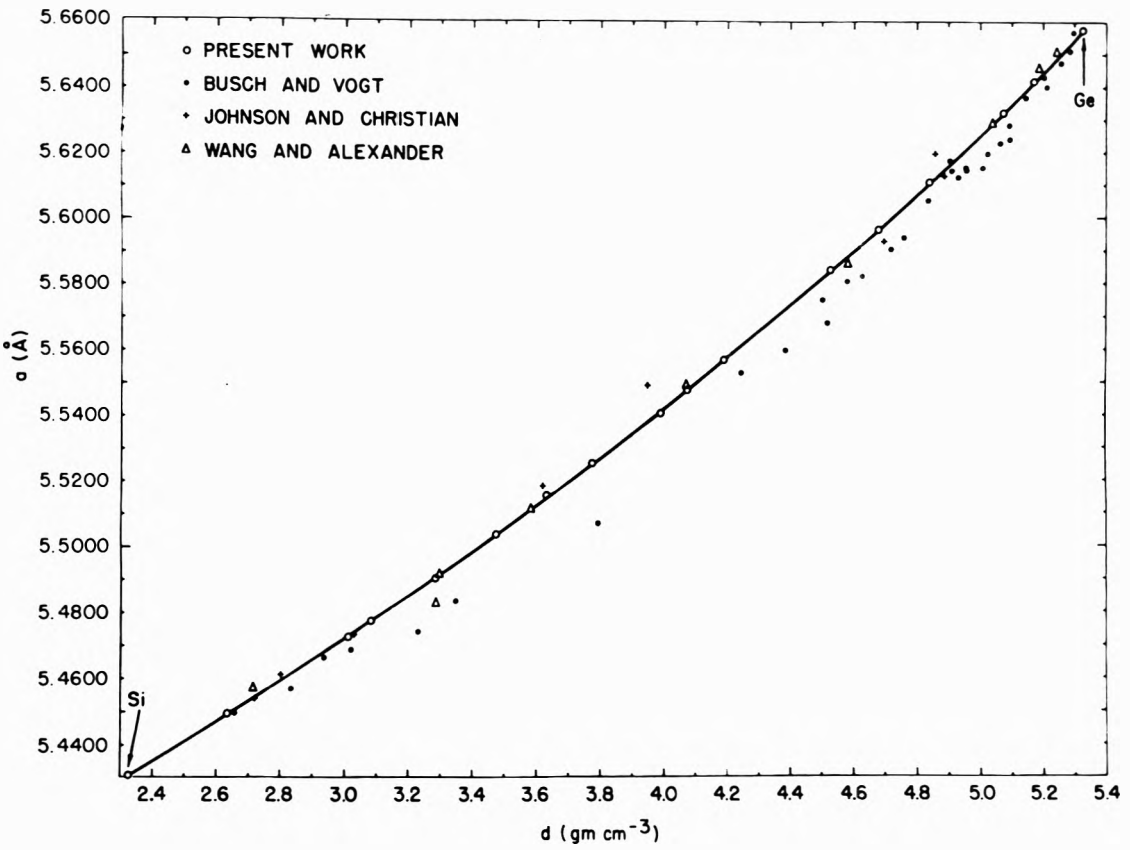

Figure 1. Variation of lattice parameter with density in the Ge–Si alloy system.

method and the Debye–Scherrer method was obtained at room temperature.

Chemical composition was determined by analyzing the material for its Ge content by the method of Cheng and Goydish[7] using samples containing 150–300 mg. of Ge.

Results

Data on measurements of density and lattice parameter at 25° for different alloy compositions are listed in Table III. The variation of lattice parameter with density is shown in Fig. 1, and this is compared with published data. The curve is drawn through the data from the present study.

The scatter in the data of Johnson and Christian[2b] and of Busch and Vogt,[4] and the large systematic error in the latter data, may be due to sample inhomogeneity. The preparative procedure employed by Johnson and Christian, slow cooling from the melt, could lead to this condition, since the growth rate was not controlled and the melt composition changed during growth. The growth rates employed by Busch and Vogt[4] appear to have been too large for preparing homogeneous material by zone leveling in the middle of the system,[6] where the discrepancy is greatest. There is good agreement between our results and the data of Wang and Alexander,[3] who have shown that their material was homogeneous.

The curve for the variation of density with chemical composition, shown in Fig. 2, was drawn through the points determined by chemical analysis. Uncertainty in the recovery factor for Ge, ±0.3%, is probably the largest source of error in the analysis.[7] This effect contributes to the relatively large scatter at the Ge-rich end of the system. We also calculated from the curve in Fig. 1 the average atomic weight, $\bar{A}$, using the relation

$$\bar{A} = da^3N/8 \qquad (1)$$

where N is Avogadro's number,[10] and from this the

(10) The value of N on the universal C^{12} scale, 6.02311×10^{23} (mole)$^{-1}$, was obtained from the value of Cohen and DuMond[11] on the O^{16} scale using the conversion factor of Cameron and Wichers.[12] Spectroscopically determined atomic weights on the C^{12} scale were 72.628 and 28.086 for Ge and Si, respectively.[12]

(11) E. R. Cohen and J. W. M. DuMond, *Phys. Rev. Letters*, 1, 291 (1958).

(12) A. E. Cameron and E. Wichers, *J. Am. Chem. Soc.*, 84, 4175 (1962).

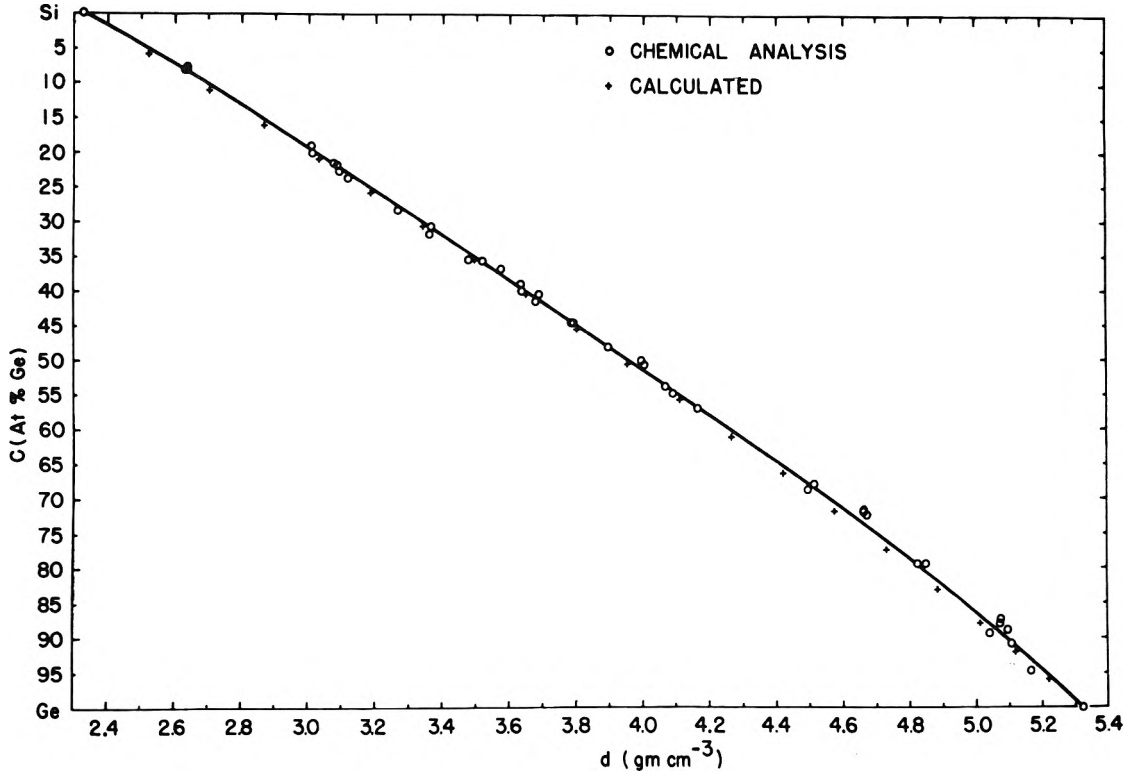

Figure 2. Variation of density with chemical composition in the Ge–Si alloy system.

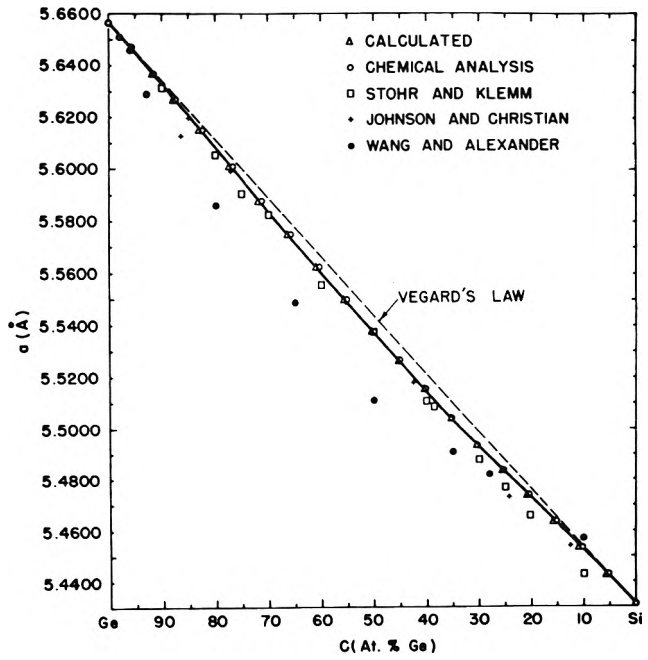

Figure 3. Variation of lattice parameter with composition in the Ge–Si alloy system.

alloy composition. Points for density *vs.* composition determined in this manner are also shown in Fig. 2.

The variation of lattice parameter with composition is shown in Fig. 3. The chemical composition was determined by (a) combining Fig. 1 and 2, and (b) using eq. 1. The results of Johnson and Christian[2b] (Fig. 3) show some scatter, which could be due to sample inhomogeneity as discussed above, or to error in the polarographic analytical method as was pointed out by Cheng and Goydish.[7] The results of Stöhr and Klemm[2a] are in better agreement with our data, but they show a large deviation at low Ge concentration. The values of Wang and Alexander[3] show a large disagreement when plotted against the given compositions. This suggests that their specimens, though chemically homogeneous, differed in composition from the intended values by an average of about 7 atomic % Ge. The lattice parameter data of Busch and Vogt[4] were not compared with the results of the present work, because of both the lack of chemical analysis and of the large deviation observed in Fig. 1.

In Table IV are listed values of density and lattice parameter at 25° for composition intervals of 5 atomic % Ge. These values are derived from Fig. 1–3, and their absolute accuracy is probably within ± 0.3 atomic % Ge. Values of density were taken as the mean of those from the curve in Fig. 2 and of those calculated from eq. 1. The departure in lattice

Table IV: Accurate Values of Density and Lattice Parameter for Ge–Si Alloy Derived from Fig. 1–3

C, at. % Ge	d, g. cm.$^{-3}$	a, Å.	$a - a_V$, Å.
0	2.3277	5.4310	...
5	2.5100	5.4419	−0.0004
10	2.6825	5.4522	−0.0014
15	2.8490	5.4624	−0.0026
20	3.0075	5.4722	−0.0041
25	3.1660	5.4825	−0.0051
30	3.3265	5.4928	−0.0062
35	3.4840	5.5038	−0.0065
40	3.6405	5.5149	−0.0067
45	3.7950	5.5261	−0.0068
50	3.9470	5.5373	−0.0069
55	4.0990	5.5492	−0.0063
60	4.2465	5.5609	−0.0060
65	4.3905	5.5727	−0.0055
70	4.5335	5.5842	−0.0053
75	4.6730	5.5960	−0.0048
80	4.8115	5.6085	−0.0027
85	4.9445	5.6206	−0.0019
90	5.0740	5.6325	−0.0023
95	5.1990	5.6448	−0.0013
100	5.3256	5.6575	...

parameter from Vegard's law, Δ, given by

$$\Delta = a_{Ge-Si} - \{a_{Si} + (a_{Ge} - a_{Si})c_{Ge}\} \quad (2)$$

where c_{Ge} = atomic fraction Ge is also listed in Table IV. This quantity is negative throughout the system and reaches a broad minimum in the middle of the system.

The excess volume of mixing, ΔV_m^{xs}, calculated using the expression

$$\Delta V_m^{xs} = \frac{N}{8}[a_{Ge-Si}^3 - \{a_{Si}^3 + (a_{Ge}^3 - a_{Si}^3)c_{Ge}\}] \quad (3)$$

is also small and negative throughout the alloy system. From the plot of $\Delta V_m^{xs}/(c_{Ge}c_{Si})$ against c_{Ge} given in Fig. 4, it is seen that ΔV_m^{xs} can be expressed by the empirical relation

$$\Delta V_m^{xs} = -0.24 c_{Ge}c_{Si} \text{ cm.}^3 \text{ mole}^{-1} \quad (4)$$

where c_{Si} is the atomic fraction of Si.

The temperature dependence of the lattice parameter of Ge, Si, and three Ge–Si alloys is shown in Fig. 5 together with the average values of the linear expansion coefficient, $\bar{\alpha}$, between 25 and 800°. For Ge and the Ge–Si alloys, α is independent of temperature, but the data for Si indicate an increase in α of about 50% from 25 to 800°. A larger increase in α with temperature has been reported by Dutta.[13]

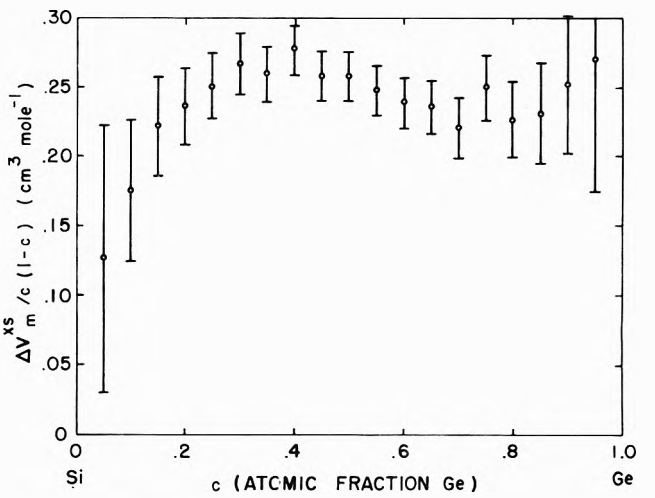

Figure 4. Variation of reduced volume of mixing, $\Delta V_m^{xs}/c_{Ge}c_{Si}$, with c_{Ge} at 25°.

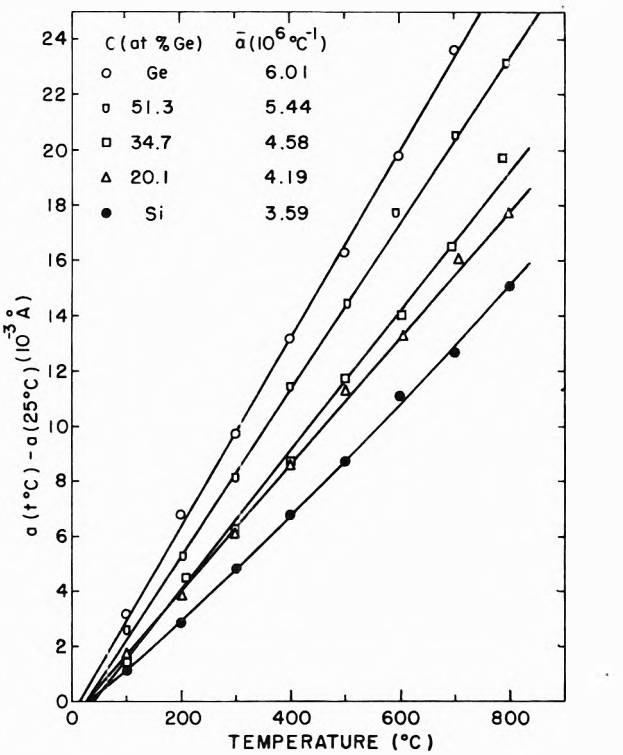

Figure 5. Variation of lattice parameter with temperature for Ge, Si, and some Ge–Si alloys.

For the alloys containing 20.1 and 34.7 atomic % Ge, the deviation from Vegard's law and the excess volume of mixing are constant with temperature within the experimental uncertainty of about ±15% of these quantities. In the 51.7 atomic % Ge alloy, these deviations decrease about 25% between 25 and 800°.

(13) B. N. Dutta, *Phys. Status Solidi*, 2, 984 (1962).

Discussion

Volume of Mixing. The observation that ΔV_m^{xs} can be expressed by eq. 4 suggests that the Ge–Si alloy system might show a simple type of thermodynamic behavior.[14] Since ΔV_m^{xs} is not zero, the system is not an ideal solution, in agreement with Thurmond's[15] conclusion from the nature of the phase diagram. The next simplest type of behavior is regular solution theory in which $\Delta S_m^{xs} = 0$. The quasichemical approach to regular solution theory[16] leads to the expression

$$\Delta H_m^{xs} = \Omega c_{Ge} c_{Si} \qquad (5)$$

where Ω is related to the bond energies H_{Ge-Ge}, H_{Si-Si}, and H_{Ge-Si} by

$$\Omega = 4[H_{Ge-Si} - {}^1/_2\{H_{Ge-Ge} + H_{Si-Si}\}] \qquad (6)$$

From quasichemical theory one would expect that Ω and ΔV_m^{xs} have the same sign. Rastogi and Nigam[17a] have calculated a value of +20 kcal. mole^{-1} for Ω from a quasichemical regular solution treatment of the Ge–Si alloy phase diagram. We have repeated their calculation considering a larger section of the phase diagram, and obtain the value +2.4 kcal. mole^{-1}. This is in good agreement with the value +2.2 kcal. mole^{-1} obtained by Romanenko and Ivanov-Omskii.[17b] Thus while the value of Ω is quite uncertain, the sign is probably correct. Since Ω and ΔV_m^{xs} are not of the same sign, a more refined model will be required to explain the thermodynamic properties of the Ge–Si alloy system.

Deviations from Vegard's Law. The Ge–Si alloy system is an attractive one for comparing experimental deviations from Vegard's law with theoretical calculations, since there is only one crystal structure in the system, no relative valency effect, and only small differences in size and electronegativity between the constituents. A summary of the theoretical work on this topic was recently given by Gschneidner and Vineyard.[18] The deviations from Vegard's law predicted by theories which require data only on the elastic properties of the pure components are shown in Fig. 6. Pines[19] used an elastic sphere model to derive the equation

$$\Delta = c_A c_B (a_B - a_A)\left[\frac{{}^4/_3\mu_A(\chi_A - \chi_B)}{1 + {}^4/_3\mu_A(c_B\chi_A + c_A\chi_B)}\right] \qquad (7)$$

where A refers to the solvent, B to the solute, μ is the shear modulus, and χ is the compressibility. Fournet[20] considered the effects of nearest neighbor interactions to obtain the equation

$$\Delta = c_A c_B (a_B - a_A)\left[\frac{(\chi_A/\chi_B) - 1}{c_A + c_B(\chi_A/\chi_B)}\right] \qquad (8)$$

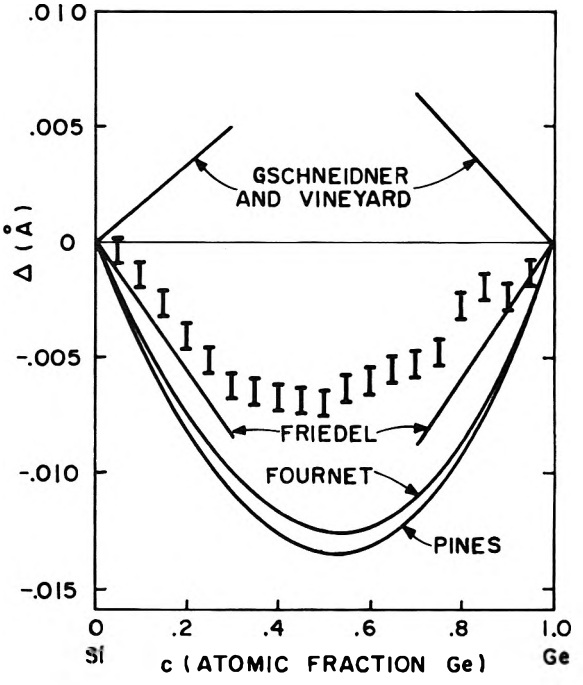

Figure 6. Deviations from Vegard's law in the Ge–Si alloy system predicted by several theories.

Both eq. 7 and 8 predict negative deviations when the element with the larger atom is softer. Thus they give the correct sign of the deviation for the Ge–Si alloy system, but the predicted magnitude is about twice the experimental value.

Friedel[21] treated the elastic sphere model so as to obtain the equation

$$\Delta = c_B(a_B - a_A)\{(\chi_A/\chi_B) - 1\}/\left[\frac{(1 + \sigma_A)\chi_A}{2(1 - 2\sigma_A)\chi_B} + 1\right] \qquad (9)$$

where σ_A is Poisson's ratio. This equation is valid only for dilute solutions, but within this limit it is in better agreement with experiment than those of Pines[19] and Fournet.[20]

(14) J. H. Hildebrand and R. L. Scott, "The Solubility of Nonelectrolytes," 3rd Ed., Reinhold, New York, N. Y., 1950, p. 141.

(15) C. D. Thurmond, *J. Phys. Chem.*, **57**, 827 (1953)

(16) R. A. Swalin, "Thermodynamics of Solids," John Wiley and Sons, Inc., New York, N. Y., 1962, Chapter 9.

(17) (a) R. P. Rastogi and R. K. Nigam, *Proc. Natl. Inst. Sci. India*, **26**, 184 (1960); V. N. Romanenko and V. I. Ivanov-Omskii, *Dokl. Akad. Nauk SSSR*, **129**, 553 (1959).

(18) K. A. Gschneidner, Jr., and G. H. Vineyard, *J. Appl. Phys.*, **33**, 3444 (1962).

(19) B. J. Pines, *J. Phys.* (USSR), **3**, 309 (1940).

(20) G. Fournet, *J. phys. radium*, **14**, 374 (1953).

(21) J. Friedel, *Phil. Mag.*, **46**, 514 (1955).

Gschneidner and Vineyard[18] applied second-order elasticity theory to obtain the equation

$$\Delta = 2\left(\frac{d\mu}{dp} - \frac{\mu}{B}\right)\frac{(a_A - a_B)^2}{a_A} c_B \qquad (10)$$

where p is pressure and B is the bulk modulus. This equation is also valid only for dilute solutions. They suggest the approximation

$$\left(\frac{d\mu}{dp} - \frac{\mu}{B}\right) \cong 6\alpha V\mu/c_V \qquad (11)$$

where V is the molar volume and c_V is the molar heat capacity. This equation predicts only positive deviations from Vegard's law. However, the magnitude of its effect is comparable to the amount by which the first-order theories overestimate the negative deviations. This suggests that a theory combining both first- and second-order elasticity effects would be a considerable improvement over current theories for predicting deviations from Vegard's law.

Acknowledgments. The authors wish to thank B. Goydish for performing the chemical analyses, H. H. Whitaker for performing the mass spectrographic analyses, and J. G. White for measurements of the temperature dependence of the lattice parameter of Ge and Si.

Kinetic Study on the Reaction of Sodium Chlorite with Potassium Iodide

by Antonio Indelli

Chemistry Department, University of Ferrara, Ferrara, Italy *(Received June 1, 1964)*

The rate of the reaction of sodium chlorite with potassium iodide was measured by the polarized platinum electrode method at 25° and at different concentrations of the reactants. The orders with respect to the hydrogen, iodide, and chlorite ions were substantially one in all cases. The reaction shows a negative salt effect in the presence of $NaNO_3$ and $Ba(NO_3)_2$, a stronger retardation in the presence of $Th(NO_3)_4$, and a remarkable acceleration in the presence of $UO_2(NO_3)_2$ and a trace of $FeSO_4$. From the rates at different temperatures, ranging from 15 to 50°, an activation energy of 14.4 kcal. can be calculated.

The oxidation of the iodides by the oxyacids of the halogens has been investigated by several authors since 1890[1]; recently, the effects of different salts on the reaction between iodate and iodide has been studied in this department,[2] and earlier a similar research had been carried on the reaction between bromate and iodide.[3] No data seem to exist on the analogous reaction between chlorite and iodide, despite the fact that the chlorites are now widely used as bleaching agents in the textile industry.[4] A better knowledge of the oxidizing characteristics of the chlorites seems therefore desirable, and a comparison with the other oxy acids of the halogens could also be interesting.

Experimental

Materials. Sodium chlorite was prepared from a technical B.D.H. product, containing about 80%

(1) G. Magnanini, *Gazz. chim. ital.*, **20**, 390 (1890); (b) S. Dushman, *J. Phys. Chem.*, **8**, 453 (1904); (c) A. A. Noyes, *Z. physik. Chem.*, **19**, 599 (1896); E. Abel and F. Stadler, *ibid.*, **122**, 49 (1926); (d) K. Weber and R. Valič, *Ber.*, **72B**, 1488 (1939); (e) E. Abel, *Helv. Chim. Acta*, **33**, 785 (1950); (f) K. J. Morgan, M. G. Peard, and C. F. Cullis, *J. Chem. Soc.*, 1865 (1951).

(2) A. Indelli, *J. Phys. Chem.*, **65**, 240 (1961).

(3) A. Indelli, G. Nolan, Jr., and E. S. Amis, *J. Am. Chem. Soc.*, **82**, 3233 (1960).

(4) G. P. Vincent, E. G. Fenrich, J. F. Synan, and E. R. Woodward, *J. Chem. Educ.*, **22**, 283 (1945).

$NaClO_2$. It was dissolved in hot water, filtered through a sintered glass, and crystallized by cooling. Approximately the first 20% was discarded, and a second crop of crystals of $NaClO_2 \cdot 2H_2O$, amounting to about 50% of the original quantity, was filtered, washed with a small amount of ice water, and dehydrated and dried for 2 weeks in a vacuum desiccator containing solid KOH.[5] It was analyzed by adding an excess of potassium iodide and of perchloric acid, and, almost immediately, by neutralizing with sodium hydrogen carbonate; finally, the mixture was titrated with sodium thiosulfate, using starch as an indicator. The salt was found to be 98.9% pure in $NaClO_2$. The other chemicals were Carlo Erba RP products and were used without further purification.

Procedure. The rate of the reaction was measured by a method that was similar to that used to investigate the reaction between iodate and iodide.[2] The usual care was taken to add the thiosulfate only when a certain amount of iodine was present, so that an excess of reductant was present only at the end of each time interval. From six to twelve points were taken during each run, and the reaction was followed for about 5 to 12% of its course. The reaction rate, under these conditions, did not vary with the time, and the plots of amount of added thiosulfate against time were substantially linear, as Fig. 1 shows. The initial reaction rate was therefore measured with an accuracy of about 5%, as judged from the results of duplicate runs. Each experimental result reported in the tables or in the figures is the average of at least two experiments.

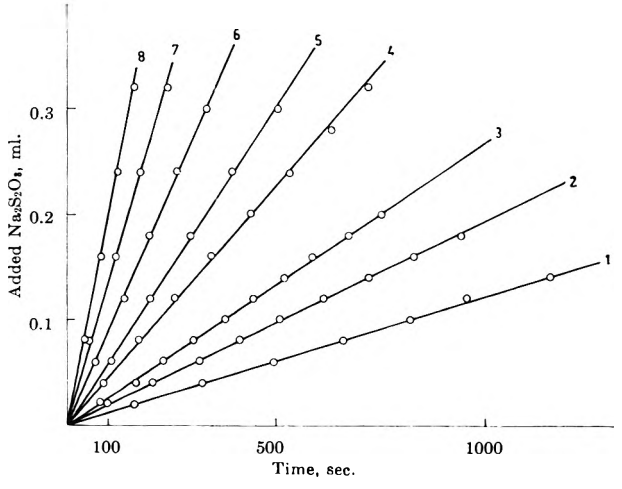

Figure 1. Typical rate plots, ml. of 0.1 M $Na_2S_2O_3$ against time, for the reaction between chlorite and iodide at different temperatures. Total volume = 400 ml.; $10^4[KI] = 5.0$; $10^4[NaClO_2] = 1.66$; $10^4[HClO_4] = 5.0$; 10^6 EDTA = 7.5 moles $l.^{-1}$. Temperatures: 1, 15°; 2, 20°; 3, 25°; 4, 30°; 5, 35°; 6, 40°; 7, 45°; 8, 50°.

Some runs were made to check the influence of the reaction of the chlorite with the thiosulfate. In these runs the additions were made immediately after the appearance of the iodine, so that a certain excess of thiosulfate was always present, except during the brief instant necessary to reveal the presence of the free iodine. The concentration of thiosulfate at the moment of each addition was known and could be varied; this method had already been used to obtain approximate data on the persulfate–thiosulfate reaction.[6] The rate of the reaction of the chlorite with the thiosulfate could be determined in this way with reasonable accuracy.

Results

Reaction Orders. The logarithms of the reaction rates, calculated as $-d[ClO_2^-]/dt$ mole $l.^{-1}$ $sec.^{-1}$, are plotted in Fig. 2 against the logarithms of the concentrations of the reactants. The slopes of the three straight lines, corresponding to the orders with respect to the chlorite, the iodide, and the hydrogen ions, are 1.15, 0.91, and 0.97, respectively. The deviations from 1.0 are not large and probably are partly due to the experimental uncertainty. In fact, at the lowest iodide concentrations and at the highest chlorite con-

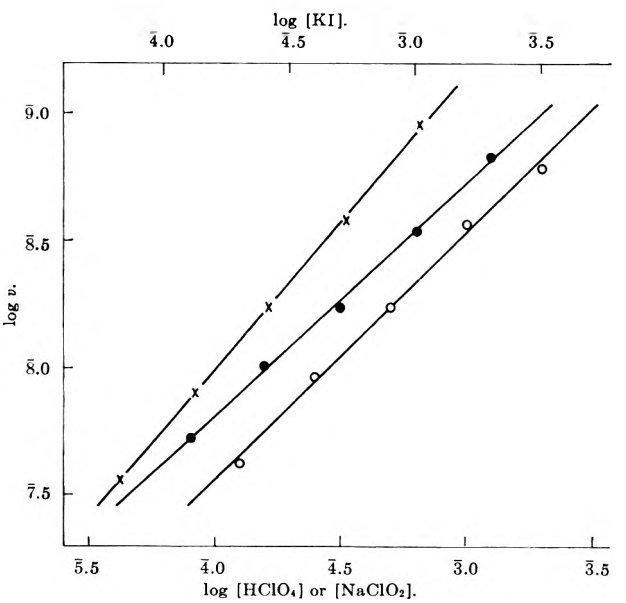

Figure 2. Logarithms of the rate plotted against the logarithms of the concentrations of the reactants. Upper scale, log [KI]; lower scale, log $[HClO_4]$ and log$[NaClO_2]$; open circles, $HClO_4$; filled circles, KI; crosses, $NaClO_2$.

(5) G. R. Levi, *Atti R. accad. Lincei*, [5] **31**, 214 (1922); *Gazz. chim. ital.*, **52**, 418 (1922).

(6) A. Indelli and E. S. Amis, *J. Am. Chem. Soc.*, **82**, 332 (1960).

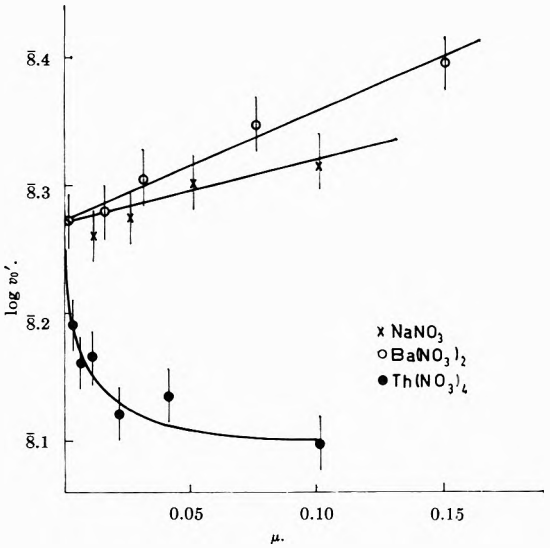

Figure 3. Log v_0' (eq. 2) against the ionic strength, μ.

centrations it is difficult to eliminate the influence of the reaction between the chlorite and the thiosulfate. It can be safely concluded, therefore, that the main activated complex contains one ClO_2^-, one I^-, and one H^+ ion, although probably there are also other reaction paths of smaller importance.

Activation Energy. Table I reports the average rates measured at different temperatures, v, and the rates, v_{int}, calculated by means of the equation

$$\log v_{int} = 2.813 - \frac{3.15}{T} \times 10^3$$

The concentrations of the reactants are those indicated under Fig. 1. From four to eight runs were made at each temperature.

Table I: Reaction Rates, v, $-d[ClO_2^-]/dt$ (mole $l.^{-1}$ $sec.^{-1}$) at Different Temperatures, and Corresponding Interpolated Values, v_{int}[a]

Temp., °C.	15	20	25	30	35	40	45	50
$10^9 v$, mole $l.^{-1}$ $sec.^{-1}$	7.5	12.1	17.3	26.0	39	55	81	120
$10^9 v_{int}$	7.6	11.7	17.7	26.4	39	57	82	116

[a] $10^4[KI] = 5.0$; $10^4[NaClO_2] = 1.66$; $10^4[HClO_4] = 5.0$; $10^6[EDTA] = 7.5$ moles $l.^{-1}$.

From the temperature dependence of the reaction rate, an activation energy of 14.4 kcal. can be calculated.

Salt Effects. Table II reports the results obtained in the presence of different salts. The negative salt effect expected for a reaction between two anions and a cation is observed in the presence of sodium and barium nitrates. The rates obey the equation

$$\log v = \log v_0 - 2A \frac{\mu^{1/2}}{1 + \mu^{1/2}} + B\mu \qquad (1)$$

where μ is the ionic strength, A is the Debye constant (for water at 25°, $A = 0.5085$[7]), and B is an empirical coefficient, which for $NaNO_3$ is 0.5 and for $Ba(NO_3)_2$ 0.8. $Th(NO_3)_4$ gives a much stronger retardation, which cannot be fitted by eq. 1. This is shown in Fig. 3, where $\log v_0'$, defined as

$$\log v_0' \equiv \log v + 2A \frac{\mu^{1/2}}{1 + \mu^{1/2}} \qquad (2)$$

is plotted against μ.[8] The points for $NaNO_3$ and for $Ba(NO_3)_2$ are fitted by straight lines, whereas those for $Th(NO_3)_4$ are on a curve, whose initial slope is very large and negative. The vertical lines represent the $\pm 5\%$ experimental error.

Table II: Reaction Rates, v, in the Presence of Different Salts at 25°[a]

$NaNO_3$	0	100	250	500	1000	
$10^9 v$	17.3	14.3	13.6	13.0	11.8	
$Ba(NO_3)_2$	50	100	250	500		
$10^9 v$	14.6	14.2	13.4	12.9		
$Th(NO_3)_4$	2	5	10	20	40	100
$10^9 v$	13.7	12.2	11.7	9.8	9.2	7.1
$UO_2(NO_3)_2$	200					
$10^9 v$	39					
$FeSO_4$	0.005[b]					
$10^9 v$	47[b]					

[a] $10^4[KI] = 5.0$; $10^4[NaClO_2] = 1.66$; $10^4[HClO_4] = 5.0$; $10^6[EDTA] = 7.5$ moles $l.^{-1}$. Added salt concentrations = 10^{-4} mole $l.^{-1}$. [b] No EDTA present.

The uranyl and iron salts have a catalytic action, which clearly has nothing to do with the salt effects. Their action is rather irregular, and the reproducibility is poor.

The Reaction between Chlorite and Thiosulfate. The product of the reaction of $S_2O_3^{-2}$ with ClO_2^- is $S_4O_6^{-2}$.[9] Persulfate[10] and iodate[11] also oxidize thiosulfate to

(7) E. A. Guggenheim and R. H. Stokes, *Trans. Faraday Soc.*, **54**, 1646 (1958).

(8) E. A. Guggenheim and J. E. Prue, "Physicochemical Calculations," North Holland Publishing Co., Amsterdam, 1956, p. 466.

(9) G. R. Levi and C. Castellani-Bisi, *Gazz. chim. ital.*, **87**, 336 (1957).

(10) C. V. King and O. F. Steinbach, *J. Am. Chem. Soc.*, **52**, 4779 (1930).

(11) R. Rieder, *J. Phys. Chem.*, **34**, 2111 (1930).

tetrathionate. Recently $Na_2S_2O_4$ has been obtained in good yield by reaction of $NaClO_2$ with HCl and $Na_2S_2O_3$.[12] Therefore, when both iodide and thiosulfate are oxidized by the chlorite in the same time, the two concurrent reactions can be assumed to be

$$ClO_2^- + 4H^+ + 4I^- \longrightarrow Cl^- + 2I_2 + 2H_2O \quad (3)$$

followed by

$$2I_2 + 4S_2O_3^{-2} \longrightarrow 4I^- + 2S_4O_6^{-2} \text{ very fast} \quad (3')$$

and

$$ClO_2^- + 4H^+ + 4S_2O_3^{-2} \longrightarrow Cl^- + 2H_2O + 2S_4O_6^{-2} \quad (4)$$

The rate of reaction 3 has been called v and can be considered constant, under our conditions, during each run. If we assume that reaction 4 is first order with respect to the thiosulfate, its rate can be expressed as $k_1[S_2O_3^{-2}]$.[13] The total rate of disappearance of the thiosulfate will be given by

$$-d[S_2O_3^{-2}]/dt = 4v' = 4v + 4k_1[S_2O_3^{-2}] \quad (5)$$

where v is the sum of the rates of the two concurrent reactions. It can be shown[6] that

$$\frac{v}{v'} = \frac{v}{k_1[S_2O_3^{-2}]_0} \ln\left(1 + \frac{k_1[S_2O_3^{-2}]_0}{v}\right) \quad (6)$$

where $[S_2O_3^{-2}]_0$ is the concentration of the thiosulfate at the moment when the addition is made. k_1 can be calculated by successive approximations, and Table III reports a selection of values of k_1, together with the experimental v', for different $[S_2O_3^{-2}]_0$. In all cases k_1 was found substantially constant, although $[S_2O_3^{-2}]_0$ changes by a factor of six, and this justifies the assumption that the reaction is first order with respect to the thiosulfate. The first-order rate constant k_1 varies with the concentrations of perchloric acid, sodium chlorite, and potassium iodide, and Fig. 4 reports plots of log k_1 against log $[HClO_4]$, log $[NaClO_2]$, or log [KI]. The orders with respect to ClO_2^- and H^+ are a little less than 0.8 and 0.6, respectively. No definite order can be given with respect to the iodide, which, however, has a clear inhibiting action.

Discussion

The reactions between the halide and the XO_3^- ions, where X is a halogen, have the common feature that the order with respect to the hydrogen ion is two,[1,2] or perhaps even larger.[14] This has been interpreted as due to the intervention of a XO_2^+ ion as an intermediate.[15] The fact that in this reaction the order with respect to H^+ is substantially one suggests that neutral $HClO_2$ acts as an intermediate. The following series

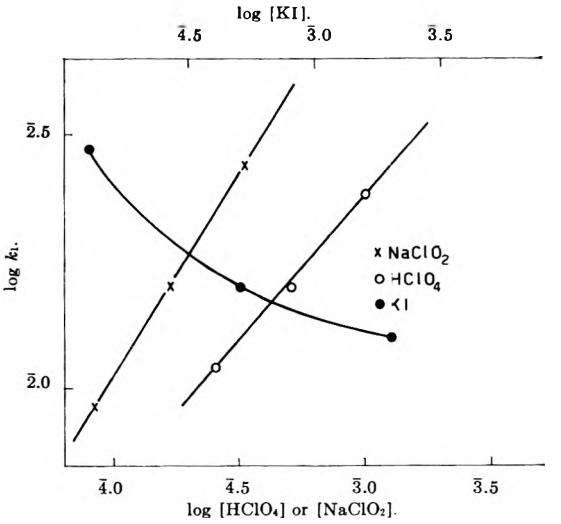

Figure 4. Log k_1 against log $[HClO_4]$, log $[NaClO_2]$, and log [KI] for the reaction between $Na_2S_2O_3$ and $NaClO_2$. Upper scale, log [KI]; lower scale, log $[HClO_4]$ and log $[NaClO_2]$.

Table III: Reaction Rates, v', of Chlorite in the Presence of Different Initial Concentrations of Thiosulfate, and First-Order Rate Constants, k_1, of Reaction 4[a]

$10^6[S_2O_3^{-2}]_0$, mole l.$^{-1}$	5	10	15	20	25	30
10^8v, mole l.$^{-1}$ sec.$^{-1}$	9.9	14.7	19.9	25	28.5	30
10^2k_1, sec.$^{-1}$	5.6	5.0	5.0	5.1	4.9	4.3

[a] Temperature: 25°; reactant concentrations: same as in Table II; 10^8v = 17.3 mole l.$^{-1}$ sec.$^{-1}$.

of reactions is consistent with the experimental orders.

$$ClO_2^- + H^+ \rightleftharpoons HClO_2 \text{ rapid equilibrium} \quad (7)$$

$$HClO_2 + I^- \longrightarrow HClO + IO^- \text{ rate determining} \quad (8)$$

$$H^+ + HClO + 2I^- \longrightarrow Cl^- + H_2O + I_2 \text{ fast} \quad (9)$$

$$2H^+ + IO^- + I^- \longrightarrow H_2O + I_2 \text{ fast} \quad (10)$$

Minor reaction paths probably involve a rapid reaction of the iodide ion with some active intermediate formed by decomposition of the chlorite ion and of the chlorous acid. This is indicated both by the deviations from 1.0 of the different reaction orders and by the fact that sodium chlorite reacts with iodides even at pH 8.[16]

(12) A. Indelli and V. Bartocci, unpublished results.

(13) The subscript 1 or 2 indicates that k_1 or k_2 is, respectively, a first-order or a second-order constant.

(14) O. E. Myers and J. W. Kennedy, *J. Am. Chem. Soc.*, 72, 897 (1950).

(15) K. J. Morgan, M. G. Peard, and C. F. Cullis, *J. Chem. Soc.*, 1865 (1951).

Equilibrium 7 has been investigated by different authors, and, although there is no complete agreement, there is no doubt that pK for the chlorous acid is of the order of two.[17] Under the conditions of the present experiments, therefore, $HClO_2$ is largely dissociated. To make a rough evaluation of the activation parameters of reaction 8, we have neglected the minor reaction paths and have assumed that the orders with respect to $HClO_2$ and I^- are exactly one; also, we have taken for pK of $HClO_2$ at 20° the value of 1.97 given by Davidson[17b] at zero ionic strength, and for ΔH of dissociation the value of 3.5 kcal.[17a] We have corrected the dissociation constants at the ionic strength of the reaction mixture by means of a Güntelberg formula[18] and we have calculated the concentrations of $HClO_2$ at each temperature. From the rates reported in Table I we have calculated the bimolecular rate constants k_2[13] of reaction 8, defined as

$$k_2 = \frac{v}{[HClO_2][I^-]} \qquad (11)$$

For the rate constant, k_2, at 25°, the activation energy, E_A, the frequency factor, A, the activation enthalpy, ΔH^*, the activation entropy, ΔS^*, the following values are found: $k_2 = 5.60$ l. mole^{-1} sec.$^{-1}$; $E_A = 17.8$ kcal.; $A = 10^{13.8}$ l. mole^{-1} sec.$^{-1}$; $\Delta H^* = 17.2$ kcal.; $\Delta S^* = +2.6$ e.u. The values for the frequency factor and for the activation entropy are reasonable for a reaction between a neutral molecule and an ion.[19]

The negative salt effects exerted by $NaNO_3$ and $Ba(NO_3)_2$ are in agreement with the series of reactions 7 to 10. In fact, the rate constant of the rate-determining step 8 will not be appreciably influenced, but the concentration of $HClO_2$ will be decreased because of the influence of the ionic strength on equilibrium 7. This situation is similar to that of the ammonium cyanate–urea conversion,[20] and any nonchain mechanism which involves an activated complex containing a ClO_2^-, a H^+, and an I^- ion will give a rate which obeys the equation

$$v = v_0 f_1^3 / f_1 \qquad (12)$$

Introducing for f_1 the expression

$$\log f_1 = -A \frac{\mu^{1/2}}{1 + \mu^{1/2}} + b\mu \qquad (13)$$

eq. 1 is obtained. B in eq. 1 is given by

$$B = b_{ClO_2^-} + b_{H^+} + b_{I^-} - b_* \qquad (14)$$

The effects of $Th(NO_3)_4$, $UO_2(NO_3)_2$, and $FeSO_4$, clearly, are not consistent with this picture. For $Th(NO_3)_4$ there is probably the formation of ion pairs, or complexes, with the chlorite, of decreased reactivity. Additional informations, from independent sources, on this ionic association would be required for a more thorough discussion, but Fig. 3 suggests that at a thorium ion concentration of 0.01 mole l.$^{-1}$, most of the chlorite is in the form of ion pairs. There is in fact a definite leveling of the curve after the initial fall.

A possible mechanism of the catalytic action of the ferrous sulfate consists in its oxidation to ferric ion, which is reduced by the iodide ion. A similar mechanism had been proposed for the catalysis of the persulfate–iodide reaction, although later work has shown that a mechanism based on the formation of intermediate ion pairs is more likely.[21] For uranyl nitrate an intermediate oxidation–reduction of the uranium is very unlikely,[22] so that in this case, too, an ion-pair mechanism is suggested. Uranyl nitrate is also a catalyst in the persulfate–thiosulfate reaction and in the bromate–iodide reaction.[3,6]

(16) V. P. Tolstikov, *Sb. Statei po Obshch. Khim., Akad. Nauk SSSR*, **2**, 1249 (1953); *Chem. Abstr.*, **49**, 2921e (1955).

(17) (a) J. Bjerrum, G. Schwarzenbach, and L. G. Sillén, "Stability Constants," Part II, The Chemical Society, London, 1958, p. 27; (b) G. F. Davidson, *J. Chem. Soc.*, 1649 (1954); (c) K. Tachiki, *J. Chem. Soc. Japan*, **65**, 346 (1944); *Chem. Abstr.*, **41**, 3347g (1947); (d) M. W. Lister, *Can. J. Chem.*, **30**, 879 (1952).

(18) E. A. Guggenheim and T. D. Schindler, *J. Phys. Chem.*, **38**, 543 (1934).

(19) (a) E. A. Moelwyn-Hughes, "The Kinetics of Reactions in Solution," 2nd Ed., Clarendon Press, Oxford, 1956, p. 71; (b) S. Glasstone, K. J. Laidler, and H. Eyring, "The Theory of Rate Processes," McGraw-Hill Book Co., New York, N. Y., 1941, p. 433; (c) A. Indelli, *Ric. Sci.*, **28**, 1676 (1958).

(20) (a) A. A. Frost and R. G. Pearson, "Kinetics and Mechanism," John Wiley and Sons, Inc., New York, N. Y., 1953, p. 260; (b) I. Weil and J. C. Morris, *J. Am. Chem. Soc.*, **71**, 1664 (1949).

(21) D. A. House, *Chem. Rev.*, **62**, 185 (1962).

(22) A. Indelli, *Ann. Chim.* (Rome), **53**, 620 (1963).

Shock Waves in Chemical Kinetics: The Rate of Dissociation of Fluorine[1a]

by Charles D. Johnson and Doyle Britton

School of Chemistry, University of Minnesota, Minneapolis 14, Minnesota *(Received June 6, 1964)*

The rate of dissociation of molecular fluorine has been determined in the presence of argon in the temperature range 1300–1600°K. by observing spectrophotometrically the disappearance of molecular fluorine behind shock waves in a shock tube. Dissociation rate constants for the reaction, $M + F_2 \rightarrow M + F + F$, were determined in 5, 10, and 20% F_2 in Ar mixtures. In the 5% mixtures the results may be summarized by log k_D (mole^{-1} l. sec.$^{-1}$) = 9.85 − 6520/T, which corresponds to an apparent activation energy of 30 ± 4 kcal./mole. The measurements were made behind incident shock waves; for reasons not clearly understood, the results of observations behind reflected shock waves were inconsistent with these and much more highly scattered. The recombination rate constant calculated from the above values is only about one-tenth as large as the corresponding constants for I_2, Br_2, Cl_2, and H_2, all of which are roughly equal. Fluorine may be somewhat more effective than argon as a third body.

Introduction

The rates of dissociation of most of the halogens have been measured at high temperatures behind shock waves in the last few years. Iodine,[2] bromine,[3-8] chlorine,[7,9,10] and hydrogen[11-15] have been studied in some detail, but for fluorine there is no information beyond a determination of the dissociation energy from shock velocity measurements in F_2–Ar mixtures.[16] We report here a shock tube measurement of the rate of dissociation of molecular fluorine in the presence of a large excess of argon. With one exception,[8] all of the studies mentioned above were made in incident shock waves. As the extinction coefficient for F_2 is much lower than that for the other halogens, it was originally felt that it would be impossible to study fluorine dissociation behind incident shock waves in our apparatus. However, as will be described, the results behind the reflected shock waves in F_2–Ar mixtures were inexplicably erratic, and another set of experiments, which appear more acceptable, were run behind incident shock waves.

The rate constants mentioned above are indicated more explicitly by

$$X_2 + M \underset{k_R}{\overset{k_D}{\rightleftharpoons}} X + X + M$$

$$\frac{d(X_2)}{dt} = -k_D(M)(X_2) + k_R(M)(X)^2$$

All concentrations are in moles/liter and all times in the rate expressions in seconds.

Experimental

Apparatus. The experimental setup was essentially that customarily used in this laboratory.[5,8] The shock tube had a 10-cm. i.d., a 240-cm. drive section, and a 480-cm. downstream section. The final 240

(1) Presented at the U. S. Army Research Office, Durham, Symposium on Chemical Reactions in Shock Tubes, Durham, N. C., April, 1964.

(2) (a) D. Britton, N. Davidson, and G. Schott, *Discussions Faraday Soc.*, **17**, 58 (1954); (b) D. Britton, N. Davidson, W. Gehman, and G. Schott, *J. Chem. Phys.*, **25**, 804 (1956).

(3) D. Britton and N. Davidson, *ibid.*, **25**, 810 (1956).

(4) H. B. Palmer and D. F. Hornig, *ibid.*, **26**, 98 (1957).

(5) D. Britton, *J. Phys. Chem.*, **64**, 742 (1960).

(6) G. Burns and D. F. Hornig, *Can. J. Chem.*, **38**, 1702 (1960).

(7) H. Hiraoka and R. Hardwick, *J. Chem. Phys.*, **36**, 1715 (1962).

(8) C. D. Johnson and D. Britton, *ibid.*, **38**, 1455 (1963).

(9) T. A. Jacobs and R. R. Giedt, *ibid.*, **39**, 749 (1963).

(10) D. Britton and M. van Thiel, *Intern. Congr. Pure Appl. Chem., 18th, Montreal*, 6 (1961).

(11) W. C. Gardiner, Jr., and G. B. Kistiakowsky, *J. Chem. Phys.*, **35**, 1765 (1961).

(12) J. P. Rink, *ibid.*, **36**, 262 (1962).

(13) J. P. Rink, *ibid.*, **36**, 1398 (1962).

(14) R. W. Patch, *ibid.*, **36**, 1919 (1962).

(15) E. A. Sutton, *ibid.*, **36**, 2923 (1962).

(16) K. L. Wray and D. F. Hornig, *ibid.*, **24**, 1271 (1956).

cm. of the downstream section, hitherto Pyrex pipe, was replaced by a section of 10-cm. i.d. aluminum tubing with 2.5-cm. thick walls in which ports for windows were machined. Circular blocks of quartz or sapphire, 19 mm. in diameter, were cemented[17] onto blanks 25 mm. in diameter and the larger blank seated against a shoulder in a port machined so that the 19-mm. disk fit snugly and joined as smoothly as possible on the inside of the tube. A vacuum seal was made with a Teflon O-ring against the back of the window. A flat 19-mm. window in a round 10-cm. diameter tube leads to an irregularity of 0.46 mm. Experiments with artificial irregularities in shock waves in Br_2–Ar mixtures in a glass tube led us to the opinion that this irregularity was tolerable and would not lead to any observable effects, but that this was about the maximum acceptable size for an abrupt disturbance at the walls. Larger steps at the walls led to anomalous oscilloscope traces.

There were two triggering stations 50 cm. apart and an observation station 10 cm. after the second triggering station. To minimize any possible effects of shock wave attenuation, it would have been desirable to have the observation station between the velocity measurement stations, so that the rate measurements might be made at a point where the true velocity of the shock wave was closer to the observed (average) velocity. In earlier work,[5] however, observations made 10 cm. after the first window had been indistinguishable from observations made 10 cm. after the second window, so that we think any possible attenuation effects may be ignored. For reflected shock waves an insert brought a smooth surface for the reflection to 1.0 cm. past the observation station.

A vacuum line in which the gas mixtures were prepared was attached to the shock tube. The modifications to the previously described system[5] were the addition of a Pyrex spiral manometer[18] and a fluorine handling system. The spiral manometer was used as a null indicator to avoid hysteresis problems; it had a sensitivity of about 0.3 mm. The fluorine inlet system consisted of the fluorine tank, a Matheson 15F-670 reducing valve, and a trap to remove hydrogen fluoride; the exhaust system was a sodium chloride trap, a soda lime trap, and a vacuum pump. All of these items were contained in a hood and were connected to a nitrogen flushing system and also to the regular vacuum line.

Gas mixtures were made as described previously,[5] but the filling of the tube was done in a different way to minimize the contact time of the fluorine mixture with the windows, diaphragms, etc., in the shock tube itself. A bulb of known volume was filled with enough mixture at a known high pressure to fill the bulb and the shock tube, whose volume was also known, at the desired lower pressure. The bulb was filled accurately, with no need for haste, in the all-glass system; the previously exhausted shock tube was filled by opening it to the bulb and allowing the pressure to equilibrate, which took about 0.5 min. This meant that shocks could be, and usually were, run within 0.5 min. of filling the aluminum tube with the mixture. However, there was no observable loss of fluorine, nor change in the shock behavior, whether the delay period was 0.5 or 5 min. (See further comments in the section on Extinction Coefficients.)

It was feared that the cellulose acetate diaphragms used in previous work in the shock tube would be rapidly attacked by the fluorine. In order to protect against this, a layer of 1-mil aluminum foil was placed in front of the 3 to 10-mil cellulose acetate diaphragm. This aluminum foil tended to wrinkle and leak, and caused considerable extra work thereby. In desperation, some shocks were tried without the aluminum foil, and it was found that in the time of the experiment no measurable decrease in the fluorine concentration nor any noticeable weakening of the cellulose acetate diaphragm took place. Therefore, in the later experiments the aluminum foil was omitted. In the hottest shocks there was trouble with the fragments of the burst diaphragm charring in the hot fluorine mixture after the shock. This did not affect the measurements in any way, but it made cleaning the tube quite difficult. To avoid this, Mylar was used in place of cellulose acetate in the strongest shocks even though it does not break as reproducibility as the cellulose acetate. The drive gas was helium rather than hydrogen, which had been used in all the earlier work.

The triggering system used previously,[5] which depended on a change in optical density at the shock front, was not possible here since only one ultraviolet light source was available, and fluorine does not absorb in the visible range. Therefore, a schlieren arrangement with visible light was used. When the schlieren system was carefully adjusted, shocks in which the initial pressure of argon was 0.1 atm. and in which the density doubled at the shock front could be consistently detected.

(17) The most successful cementing arrangement was to grease the windows lightly with Kel-F grease from the Kellog Mfg. Co. and press them together. This produced a transparent and completely adequate mount. Later samples of Kel-F grease from another manufacturer were not of the same quality and contained too large a fraction of volatile components to be suitable. Canada Balsam was reluctantly used as a substitute. It did not appear to be attacked by the fluorine in the experimental conditions used.

(18) J. D. Ray, *Rev. Sci. Instr.*, 32, 600 (1961); we wish to thank Professor Ray for his gift of this manometer.

For the observation of the disappearance of F_2 a PEK-109 mercury arc lamp was used as light source.[19] This was mounted about 200 cm. from the windows and focused (through a quartz lens of 50-cm. focal length) at the center of the shock tube. This gave a beam that was small enough to be passed through the bottom half of one 19-mm. window, reflected from the back silvered lower half of the opposite window, reflected from the silvered top half of the first window, and passed out the top half of the opposite window without losing much of the beam and without having part of the light go directly through the unsilvered windows. The light source and lens had to be mounted separately from the table on which the shock tube was mounted in order to avoid vibrations which led to erroneous oscillograms. Since the laboratory was not large enough to mount the light 200 cm. to one side of the shock tube, it was suspended from the ceiling about 150 cm. down the axis of the tube and reflected at 90° into the shock tube ports. After passing through the shock tube and through 1-mm. collimating slits on both sides of the tube, the light went through a Bausch and Lomb 33-86-40 monochromator and into a 1P28 photomultiplier. The rest of the detection system has been described previously.[5] The lighting alignment was fairly critical, but within experimental error of about 1% all the light entering the monochromator had passed through 30 cm. of gas, and none through only 10 cm. For a few of the shocks, used only for the measurement of extinction coefficients at lower temperatures, a single pass (10 cm.) of light was used rather than a triple pass; the results agreed with those from triple pass measurements.

Chemicals. Fluorine from the General Chemical Division of Allied Chemical Corp. was purified by passing it through a sodium fluoride trap to remove HF. A sample of gas that was allowed to react with mercury showed, within an experimental error of 0.2%, no unreacted gas after 3 days. This same method of purification was used by Shields,[20] who then fractionally distilled the fluorine and could detect no difference in vibrational relaxation times in the first and last fractions. Since it seems likely that any impurity that would have a large effect on the dissociation rate would also have an effect on the vibrational relaxation rate, we believe the method of purification to be adequate. In particular, we believe that the amount of HF present is completely negligible.

Matheson Co. argon was used without further purification. Oxygen from the Air Reduction Co. was further purified by a bulb-to-bulb distillation at liquid nitrogen temperature on the vacuum line, with the middle fraction being used. Carbon dioxide from the Ohio Chemical and Manufacturing Co. was purified by repeated partial condensation in the vacuum line.

Calculations. The methods of calculation for incident and reflected shock parameters as well as for high temperature extinction coefficients and rate constants have all been described previously.[5,8] The thermodynamic data were taken from the JANAF tables[21] and need no comment, with the exception of the heat of dissociation of F_2. This heat, which was long thought to be 60–70 kcal./mole of F_2, has recently been reconsidered and remeasured. The pertinent literature references are given in the JANAF tables, and we have used their value of 36.7 kcal./mole at 0°K. If this were in error by 10%, it would lead to a 5% error in the measured value of the rate constants in incident shocks in 5% F_2–95% Ar mixtures. For our purposes, therefore, any remaining uncertainty in this value can be ignored.

Those calculations which were too tedious to do by hand, mainly the calculation of shock wave parameters, were made using FORTRAN programs on the control data 1604 computer of the Numerical Analysis Center of the University of Minnesota.

Results

Introduction. Two kinds of experimental measurements were made. First we studied the disappearance of F_2 behind reflected shock waves in 5% F_2–95% Ar, 5% F_2–1% CO_2–94% Ar, and 5% F_2–2.5% O_2–92.5% Ar mixtures. Second, we studied the disappearance of F_2 behind incident shock waves in F_2–Ar mixtures with 5, 10, and 20% F_2. Originally we had thought that the limitations of the apparatus would preclude the use of incident shocks—that the highest pressure of F_2–Ar mixture that could be used safely in the existing shock tube would not be concentrated enough to allow us to measure the changes in F_2 concentration with reasonable accuracy nor to cause large enough schlieren signals for triggering. In view of this we studied[8] the measurement of rate constants behind reflected shock waves in a known system, Br_2, and then proceeded to the study of F_2. As will be seen below, the results did not seem reliable, although we cannot offer a good explanation for their invalidity. Therefore,

(19) The PEK-109 power supply gave d.c. current with a.c. ripple sufficient to cause 10% ripple in the light intensity. This was reduced to 1% by the addition of two more LC sections, each with L = 0.02 h. and C = 500 $\mu\mu$f. The power supply had adequate reserves so that, even with this additional filtering, the lamp could be run at the rated power.

(20) F. D. Shields, *J. Acoust. Soc. Am.*, **34**, 271 (1962).

(21) "JANAF Thermochemical Tables," The Dow Chemical Co., Midland, Mich., June, 1960.

it was decided to make observations behind incident shock waves, starting at the lowest pressures that allowed triggering and observation of the F_2 concentration, and at a rather low temperature in the incident shock wave, and to increase the temperature, *i.e.* the drive gas pressure, as long as the apparatus held together. To our surprise we finished all the experiments that seemed necessary without any mishap; no windows broke nor even leaked. The results behind the incident shock waves showed no anomalies, and we believe they are reliable. The details of both sets of experiments follow.

Extinction Coefficients. The extinction coefficient of F_2 has been measured at room temperature as a function of wave length by three groups.[22-24] These are in general agreement; the most recent[24] seemed to us the most reliable, and we have used their values at room temperature. The observations in the shock tube were all made at 313 mμ. Except that the extinction coefficient, ϵ, is lower, which is somewhat critical in our experiments, this is a better wave length for observations than the maximum because the change in ϵ with temperature is less. The spectrum of F_2 at room temperature has been analyzed in detail,[25] and it is clear that the simple theory of Sulzer and Wieland,[26] which was useful in predicting the temperature dependence of the extinction coefficients of Br_2 and Cl_2, should not work here. Nevertheless, it should give a rough idea of the temperature dependence to be expected, and, accordingly, we have fit the experimental curve to a single peak, gaussian with respect to wave number, and from this peak calculated ϵ *vs.* T at 313 mμ.

High temperature extinction coefficients were measured in the various shock waves, each incident shock wave experiment giving one point on each oscillogram, and each reflected shock wave experiment giving one point in the incident wave and another higher temperature value in the reflected wave. The results for all the incident shock waves are given in Fig. 1, and for all the reflected shock waves in Fig. 2. The high temperature values for the incident shocks were fit to a straight line by a least-squares calculation, and this line was used to calculate $d \ln \epsilon / dT$, which is needed in the rate constant calculations. It can be seen that the results in reflected shock waves in F_2–Ar are consistently lower and slightly more scattered than in the incident shock waves. The results in the F_2–O_2–Ar and F_2–CO_2–Ar mixtures show that something anomalous is happening in these mixtures. We regard only the incident shock wave measurements as reliable. The agreement (see Fig. 1) between the extinction coefficients measured in shock waves and those measured in a static experiment at room temperature[24] indicates that no significant amount of F_2 has disappeared in the period between making up the mixture and running the shock. As mentioned previously, there was no slow disappearance after putting the mixture in the shock tube. The extinction coefficient measurements indicate that there was no unobservably rapid disappearance when the

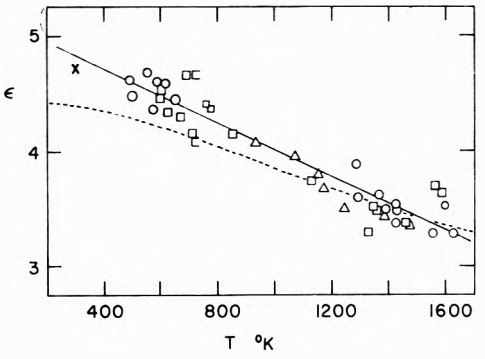

Figure 1. Extinction coefficient for F_2 *vs.* temperature at 313 mμ (incident shock waves): cross, room temperature value (ref. 24); squares, 5% F_2 in Ar; circles, 10% F_2 in Ar; triangles, 20% F_2 in Ar; heavy line, least squares fit to $\epsilon = 5.20 - 0.00118T$; dotted line, prediction from the approximate theory of Sulzer and Wieland.

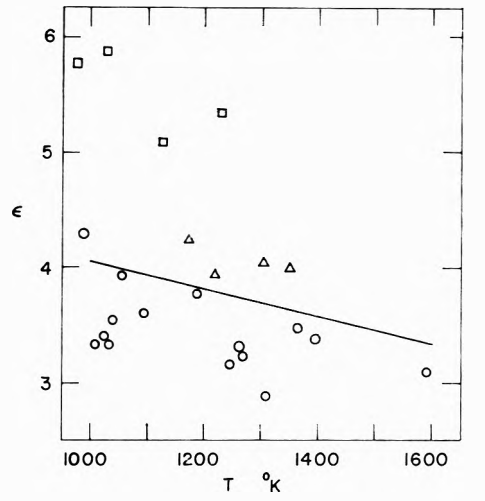

Figure 2. Extinction coefficient for F_2 *vs.* temperature at 313 mμ (reflected shock waves): heavy line, heavy line from Fig. 1; circles, 5% F_2 in Ar; triangles, 5% F_2–2.5% O_2 in Ar; squares, 5% F_2–1% CO_2 in Ar.

(22) H. von Wartenburg, G. Sprenger, and J. Taylor, *Z. physik. Chem., Bodenstein Festband*, 31 (1931).

(23) M. Bodenstein and H. Lockusch, *Z. anorg. allgem. Chem.*, **231**, 24 (1937).

(24) R. Stuenberg and R. Vogel, *J. Am. Chem. Soc.*, **78**, 901 (1956).

(25) A. L. G. Rees, *J. Chem. Phys.*, **26**, 1567 (1957).

(26) P. Sulzer and K. Wieland, *Helv. Phys. Acta*, **25**, 653 (1952).

tube was first filled. The reaction of a few per cent of the total F_2 would not have been detected in either case.

Emission. In the Br_2 and Cl_2 work[4,5,10] emission from two-body recombination of Br and Cl atoms was appreciable at the higher temperatures. Two experiments were run in 5% F_2–95% Ar incident shocks with initial temperatures near 1650°K., with the light source turned off. In neither case could any emission be detected. Since this was hotter than any of the experiments where the rate constants were measured, it was assumed that no emission correction was necessary.

Vibrational Relaxation. Shields[20] has measured the vibrational relaxation times for F_2 at 28 and 102°. If these results are extrapolated to high temperatures by the method of Millikan and White,[27] they indicate that vibrational relaxation would require only a few microseconds under the conditions of our experiments, so that we can assume the F_2 always to be vibrationally relaxed. This assumption is borne out by the extinction coefficient values that are measured at the shock front; these values fall off with temperature in the fashion that would be expected for vibrationally equilibrated F_2.

Reflected Shock Waves in F_2–Ar Mixtures. A series of 11 reflected shock waves was run in 5% F_2–95% Ar at temperatures between 1000 and 1600°K. The dissociation rate constants measured in these shocks are shown in Fig. 3. These rate constants were calculated assuming that the degree of dissociation at the end plate was zero. This introduces a small error into the calculated temperature and density, but it would not significantly alter the temperature dependence. These experiments give the untenable result that there is no activation energy for the dissociation reaction. Primarily for this reason it was decided to run a series of experiments in incident shock waves if possible.

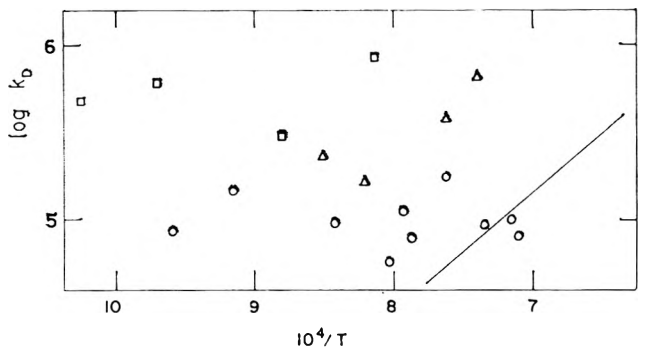

Figure 3. Log k_D *vs.* $1/T$ (reflected shock waves): line, incident shock wave result; see Fig. 4; circles, 5% F_2 in Ar; triangles, 5% F_2–2.5% O_2 in Ar; squares, 5% F_2–1% CO_2 in Ar.

Reflected Shock Waves in F_2–Ar Mixtures with Added O_2 or CO_2. In order to test whether small amounts of air as an impurity could lead to serious errors in measured rate constants some experiments with added O_2 or CO_2 were run in reflected shock waves before it was realized that the reflected shock wave results were unsatisfactory. . Four shock waves were run with a 5% F_2–1% CO_2–94% Ar mixture with temperatures between 1100 and 1200°K. with the results shown in Fig. 3. The apparent rate of dissociation is about ten times greater than in the absence of CO_2 for all the points. An inspection of Fig. 2 indicates that these shocks are suspect, and in any event we would not attribute the increased rate of dissociation simply to a greater efficiency for CO_2 as a third body. Clearly some reaction between CO_2 and F_2 is occurring. However, it is also reasonably clear that traces of CO_2 due to air leaks would not lead to serious errors in the dissociation rate measurements in the presence of argon. If air leaked in to the unlikely extent that 1% of a mixture were air, only approximately 0.01% of the total would be CO_2. This could lead to a 10% error in the rate constants if the reaction were a chain reaction and proceeding as in these mixtures. If the reaction were a simple nonchain reaction, leading perhaps to stable products such as fluorophosgene, then the error would be even less.

Four experiments in 5% F_2–2.5% O_2–92.5% Ar mixtures at temperatures between 1200 and 1350°K. led to the apparent dissociation rate constants shown in Fig. 3. The rate constants are about three to four times larger than the corresponding values in argon. Again in a 1% air leak the O_2 concentration would be about 0.2%, and this would lead to at most a 5% error in the rate constant. It is apparent that both O_2 and CO_2 are acting as more than simple third bodies, and it would be of interest to determine the actual reactions and rate constants. For the purpose of this study it was sufficient to know that these conceivable impurities would not lead to a significant error in the rate constants being studied. It was not felt necessary to test the effect of added N_2.

In spite of the uncertainties in the reflected shock wave results, we did not feel it was necessary to repeat these tests with added CO_2 and O_2 in incident shock experiments.

Incident Shock Waves in F_2–Ar Mixtures. A series of six incident shock waves was run in 5% F_2–95% Ar, a series of nine in 10% F_2, and a series of five in 20% F_2. The high drive pressure required (up to 200 p.s.i.)

(27) R. C. Millikan and D. R. White, *J. Chem. Phys.*, 39, 3209 (1963).

limited the range of initial low pressures to 0.07–0.2 atm., but otherwise the series covered a reasonable range of experimental conditions. The results of the experiments are shown in Fig. 4. Lines fit to the equation $\log k_D = A + B/T$ by least squares give for the three series

$$5\%\ F_2 \quad \log k_D = 9.85 - 6520/T$$

$$10\%\ F_2 \quad \log k_D = 8.54 - 4520/T$$

$$20\%\ F_2 \quad \log k_D = 6.61 - 2410/T$$

The slopes correspond to activation energies of 29.9 ± 3.7, 20.7 ± 5.6, and 11.0 ± 7.6 kcal./mole of F_2, respectively. We regard the 5% F_2 results as most reliable for two reasons: first, the scatter is less; second, the correction for changing density and temperature behind the shock front is smallest here, and so subject to the least uncertainty. This correction term, (1

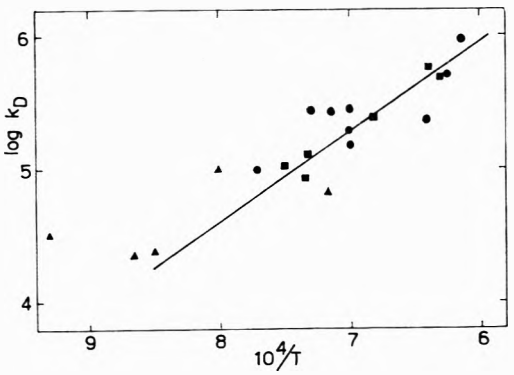

Figure 4. Log k_D *vs.* $1/T$ (incident shock waves): line, least-squares fit to the 5% data; squares, 5% F_2 in Ar; circles, 10% F_2 in Ar; triangles, 20% F_2 in Ar.

$- \mathrm{d} \ln \epsilon/\mathrm{d}\alpha - \mathrm{d} \ln \Delta/\mathrm{d}\alpha)^{-1}$, has an average value of 1.25, 5.0, and −2.0 for the 5, 10, and 20% series, respectively, and in the last two cases changes appreciably with the shock temperature. An error of 10% in $\mathrm{d} \ln \epsilon/\mathrm{d}T$ would cause errors of 1, 10, and 8%, respectively, in the correction terms of the 5, 10, and 20% shocks. Also it should be recognized that the measurement of the initial slope is more uncertain in the mixtures with the larger percentages of F_2, either because the slope is smaller than in the more dilute mixture, or because it is changing more rapidly with the degree of the reaction, and it is, in fact, a slope near the shock front, rather than the slope at the shock front, that is measured.

As can be seen from Fig. 4 the data are not good enough to draw significant conclusions about the relative effectiveness of F_2 and Ar as third bodies. The most we could say is that F_2 is between 1 and 20 times as effective as Ar.

Equilibrium Constants. As a check on the validity of our experiments the equilibrium constant for the reaction $F_2 = 2F$ was calculated in many of those experiments where the observation time was sufficiently long that equilibrium was reached. Since the density and temperature can be calculated as a function of the degree of dissociation behind a shock wave, it is possible to construct a plot of light intensity *vs.* degree of dissociation with no approximations and, by measuring the equilibrium light intensity, to calculate the equilibrium degree of dissociation. From the known initial concentration and a knowledge of the density as a function of the degree of dissociation for the particular shock, it is then possible to calculate the equilibrium constant. The calculated equilibrium constants agreed with the JANAF values[21] within a factor of 2, and for the 10% and 20% were scattered around them. The values of the constants from the 5% experiments were all low, but still within the experimental scatter of the 10 and 20% points. As these measurements are made 200–500 μsec. behind the shock front, and as the scatter was large, this is not strong evidence, but, such as it is, it suggests that these shocks are normal.

Discussion

Comparison with Other Halogens. With this study dissociation rates for all the halogens, including hydrogen, have been determined at high temperatures behind shock waves in the presence of argon as a third body. If one assumes that $k_D = A \exp(-H/RT)$ with no temperature dependence in the pre-exponential

Table I: Apparent Activation Energies for the Reaction $Ar + X_2 = Ar + 2X$

X_2	ΔH_{act}[a]	Ref:	D_0^0	Difference
I_2	30.8 ± 0.3	2	35.4	4.6
Br_2	43.8 ± 3.7	3	45.4	1.6
	38.2	4		7.2
	39.0 ± 0.8	5		6.4
	37.7 ± 1.0	8		7.7
Cl_2	51.3 ± 11.7	7	57.1	5.8
	48.5 ± 2.9	9		8.6
	47.2 ± 2.2	10		9.9
F_2	29.9 ± 3.7	This work	36.7	6.8
H_2	95–97[b]	12, 14, 15	103.6	7–9

[a] The measured rate constants were fit to an equation $k_D = A \exp(-\Delta H/RT)$. [b] The H_2 results in these references have been reported in the form $k_D = AT^{-1} \exp(-D_0^0/RT)$. If these had been fit to the form $k_D = A \exp(-\Delta H/RT)$, then ΔH would have been lower by about RT = 7–9 kcal./mole. An RT correction will not account for the discrepancy in any of the other halogens, however.

term, then in every case the apparent activation energy for dissociation is less than the dissociation energy of the halogen. These activation energies are summarized in Table I. The hydrogen results can be accounted for by using D_0^0 in the exponential term and including a pre-exponential temperature dependence of T^{-1}. For all of the others the power of the temperature in the pre-exponential term would have to be considerably greater than this.

Since the dissociation energies are quite different for the several halogens a more meaningful comparison of the differences among them can be made by comparing recombination rate constants, $k_R = k_D/K_{eq}$. The high temperature results converted to this form are shown in Fig. 5 along with the low temperature

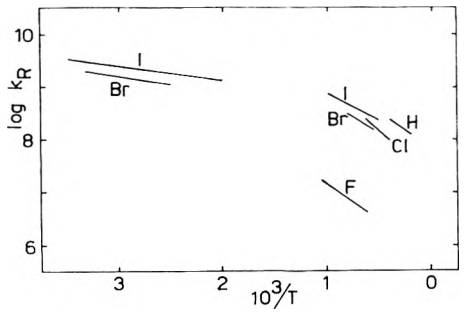

Figure 5. Log k_R *vs.* $1/T$ for the various halogens: F_2, this research; Cl_2, ref. 9, 10; Br_2, ref. 8, 28; I_2, ref. 2, 27; H_2, ref. 15.

results for I_2[28] and Br_2.[29] It would appear that the shock wave results uniformly show a greater temperature dependence than the low temperature results. This large temperature dependence is another way of viewing the low activation energy of the dissociation reaction. Three explanations for this temperature dependence come to mind: first, that there is a systematic experimental error in the shock wave work; second, that the shock wave rate constants are measured too far from equilibrium to be converted meaningfully to recombination rate constants; third, that the effect is real and the temperature dependence of the three body recombination rate constant is highly unusual. The first of these is probably ruled out by the spectrophotometric shock wave studies of the hydrogen–bromine reaction,[30] where the high temperature results showed the same temperature dependence as the low temperature results. Pritchard[31,32] has given theoretical reasons for preferring the second alternative, reasons that have been disputed by Rice.[33,34] In support of the third alternative it should be noted that Phillips and Sugden[35] have found similar large negative temperature dependences for the reactions occurring in flames

$$H + X + M = HX + M^*$$

where X is H, Cl, or Br and M is Tl or Pb.

It can be seen in Fig. 5 that F_2 dissociates more slowly than might be expected by comparison with the other halogens. It can also be seen that I_2, Br_2, Cl_2, and H_2 all show about the same recombination rate constants at high temperatures. If species as different as I atoms and H atoms recombine at roughly the same rate, it is surprising that F atoms should recombine only one-tenth as fast. This would lead us to suspect the results presented here except that there is no conceivable way that the reaction could be slowed down. Any small amount of impurity must either be less efficient than argon as a third body, in which case it would have an effect on the observed rate constant only as large as its relative concentration, or else it must be more efficient than argon, in which case the apparent rate constant is too large.

The Possibility of ArF or ArF_2. It is possible that the observed rate constants appear low because another colored species is being formed, and the observed color change is due to more than the disappearance of F_2. It is not to be expected that the F atoms absorb at 313 mμ, but the possibility that argon fluorides, such as ArF or ArF_2, are being formed must be considered.

The formation of ArF_2 alone (or any higher fluoride) could not explain any apparent anomaly in the initial slopes, since the formation must involve some sort of recombination reaction, although if the species were stable they could affect the apparent equilibrium positions. An effect on the initial rates would have to lie in the formation of ArF according to

$$Ar + F_2 \xrightarrow{k_1} ArF + F$$

$$ArF + M \xrightarrow{k_2} Ar + F + M$$

Since we are considering the initial reaction, only the forward rates will be considered. If $k_2 \leq k_1$, then the change in light intensity interpreted as $d[F_2]/dt$ would really be due to $d([F_2] + \epsilon_{ArF}[ArF]/\epsilon_{F_2})/dt$,

(28) D. L. Bunker and N. Davidson, *J. Am. Chem. Soc.*, **80**, 5085 (1958).

(29) W. G. Givens, Jr., and J. E. Willard, *ibid.*, **81**, 4773 (1959).

(30) D. Britton and R. M. Cole, *J. Phys. Chem.*, **65**, 1302 (1961).

(31) H. O. Pritchard, *ibid.*, **65**, 504 (1961).

(32) H. O. Pritchard, *ibid.*, **66**, 2111 (1962).

(33) O. K. Rice, *ibid.*, **65**, 1972 (1961).

(34) O. K. Rice, *ibid.*, **67**, 1733 (1963).

(35) L. F. Phillips and T. M. Sugden, *Intern. Congr. Pure Appl. Chem., 18th, Montreal*, 35 (1961).

where ϵ refers to the extinction coefficient of the species in question. Since the ArF is formed at the same rate as the F_2 disappears and its rate of disappearance is low, the apparent rate of disappearance of F_2 is lower than the actual rate by a factor of $(1 - \epsilon_{ArF}/\epsilon_{F_2})$, and the apparent rate constant is lower than the true one. If the ratio $\epsilon_{ArF}/\epsilon_{F_2}$ were independent of temperature, the activation energy measured would be that associated with the first reaction and k_1. It is this last factor which tells against this possibility. One would expect the activation energies of both these reactions to be roughly equal to their enthalpy changes, but $k_2 \leq k_1$ implies that E_2 is of the order of E_1, which is measured to be 30 kcal./mole, while $E_1 + E_2$ is known to be 36 kcal./mole.

The observed activation energy is that expected for the dissociation of F_2, as was discussed earlier, or at most it is a few kcal./mole lower. A lowering of, say, 5 kcal./mole would imply that the second reaction above had an energy of approximately 5 kcal./mole and an activation energy of the same order or lower. This would mean, however, that the second reaction should be many times faster than the first, in which case no appreciable concentration of ArF could form, and that which did form would be related to the F_2 concentration by the steady-state approximation so that $[ArF] \sim (k_1/k_2)[F_2]$, and the apparent rate would not be affected, or would be *increased* slightly, if anything.

This has been discussed at some length because in other experiments in this laboratory[36] we have found that when xenon is present in the shock mixture a definite effect attributable to the formation of a xenon fluoride can be observed. We recognize that the experiments described here cannot be regarded as conclusively settling this interesting question in Ar–F_2 shocks—this would require observations at more than one wave length—but we report our results at this time because circumstances required the dismantling of the fluorine handling system, and we do not foresee the possibility of further experimental work in the near future.

Reflected Shock Waves. A comparison of the results of the F_2–Ar experiments in incident and reflected shock waves shows clearly the anomalously high rate constants in the reflected shock waves at the lower end of the temperature range studied. At about 1400°K. the two methods give the same results, but at lower temperatures the reflected shock wave results deviate more and more from what might be considered normal. We cannot explain this result. Our work on the dissociation of Br_2 in reflected shock waves[8] gives us a general confidence in reflected shock wave results. The only suggestion we can offer is that some impurity with a remarkably high catalytic effect is produced behind the incident shock wave, and when the reflected shock wave comes back, the composition of the mixture has been subtly changed (no significant amount of F_2 has disappeared), and the impurity catalyzes the decomposition. The effectiveness of any given catalyst would be expected to decrease with increasing temperature so that the decreasing deviation from normal with increasing temperature is an argument for the presence of a catalyst. The presence of this catalyst in the incident shock wave is unlikely, for the rate constants measured behind the incident shock waves seem unusually low.

Acknowledgments. We thank the U. S. Army Research Office (Durham) for support of this work. C. D. J. thanks the Shell Oil Company and the Procter and Gamble Company for fellowship support.

(36) D. J. Seery and D. Britton, unpublished work.

The Heats of Formation of Zirconium Diboride and Dioxide[1]

by Elmer J. Huber, Jr., Earl L. Head, and Charles E. Holley, Jr.

University of California, Los Alamos Scientific Laboratory, Los Alamos, New Mexico *(Received June 11, 1964)*

The heat of formation of zirconium diboride as determined by oxygen bomb calorimetry on two samples of the material was $\Delta H_f°_{298} = -77.2 \pm 1.2$ kcal./mole. The heat of formation of zirconium dioxide from the combustion of the metal in oxygen was $\Delta H_f°_{298} = -263.1 \pm 0.5$ kcal./mole.

Introduction

Because of their use in high temperature applications, refractory-type compounds such as zirconium diboride with a melting point of *ca.* 3000°[2] are becoming increasingly important. Values in the literature for heat of formation of this compound[3-6] vary from -60 to <-78 kcal./mole. Recently, Johnson and co-workers[7] have reported a tentative value of -73 kcal./mole based upon fluorine bomb calorimetry.

This paper describes the determination of the heat evolved from the combustion of two different samples of zirconium diboride in an oxygen bomb calorimeter at a known initial pressure of oxygen. Zirconium metal was also burned. The method has been described.[8] The energy equivalent of the calorimeter as determined by the combustion of standard benzoic acid was 2383.5 ± 0.6 cal./deg. for sample A and 2386.5 ± 0.8 cal./deg. for sample B and the zirconium metal.

Experimental

Zirconium Diborides. In Table I are listed the results of the analyses which were performed in this laboratory on the two samples of the material. Sample A was obtained from the Varlacoid Chemical Co., New York 4, N. Y. Sample B was made by J. M. Leitnaker, formerly of this laboratory.

No N or H was detected. The Zr, B, C, O, and Hf were determined chemically; the other metallic impurities, by spectrochemical methods. Sample A was 96.1 mole % ZrB_2; sample B was 99.2 mole % $ZrB_{1.99}$. Because of the larger amounts of inpurities, the stoichiometry of sample A is not accurately known.

Combustion of Zirconium Diborides. The samples were burned in oxygen at 25 atm. pressure on sintered disks of the monoclinic form of ZrO_2 containing a small amount of the cubic form. Ignition was effected by passing an electrical current through a 10-mil diameter fuse wire. A magnesium fuse wire was used for sample A, and a zirconium fuse wire for sample B. Each sample was in a finely divided form, but no weight increase was observed upon exposure to the oxygen pressure for a 1-hr. period. The average initial temperature was 25.0° and the average temperature rise, 1.266°.

Table I: Analyses of Zirconium Diborides (wt. %)

	Sample A	Sample B
Zr	78.5	80.8
B	18.6	18.9
C	...	0.01
O	0.80	0.20
Si	...	0.05
Mo	...	0.03
Hf	1.80	...
Na	0.02	...
Al	0.02	...
Ca	0.11	...
Fe	0.09	...
Ti	0.05	...

(1) Work done under the auspices of the U. S. Atomic Energy Commission.

(2) F. W. Glaser and B. Post, *Trans. AIME*, **197**, 1117 (1953).

(3) G. V. Samsonov, *Zh. Fiz. Khim.*, **30**, No. 9, 2057 (1956).

(4) G. V. Samsonov, *Zh. Prikl. Khim.*, **28**, 919 (1955).

(5) V. A. Epel'baum and M. I. Starostina, *Bor, Tr. Konf. po Khim. Bora i Ego Soedin.*, 1955, 97 (1958).

(6) L. Brewer and H. Haraldsen, *J. Electrochem. Soc.*, **102**, 399 (1955).

(7) G. K. Johnson, E. Greenberg, J. L. Margrave, and W. N. Hubbard, to be published.

(8) E. J. Huber, Jr., C. O. Matthews, and C. E. Holley, Jr., *J. Am. Chem. Soc.*, **77**, 6493 (1955).

The completeness of combustion was determined by dissolving the combustion products in 25 g. of molten KOH and measuring the amount of hydrogen evolved. The reaction vessel was a nickel tube with a standard taper joint which fitted into a water-cooled Pyrex joint attached to a gas measuring apparatus. The KOH was outgassed at 400°, the sample and 4 ml. of H_2O were added, and the temperature was raised to 180° for 1 hr. At this temperature the KOH–H_2O mixture is liquid and most of the reaction occurs. The gas was then pumped into the measuring system through a cold trap and the temperature raised to 400° for another hour. The total volume of gas was measured and then the percentage of hydrogen was determined with a mass spectrograph.

The reaction of NaOH with nickel has been studied by Williams, *et al.*,[9] and at 400° the rate is very low. This is also true for KOH as was determined by blank runs on the system which gave negligible gas evolution and negligible nickel dissolved in the KOH. On a known sample of ZrB_2 weighing 0.1 g. the amount of hydrogen evolved was 99.9% of the theoretical amount.

The reaction with the combustion products was not complete with one treatment presumably because of the large amounts of material to be dissolved, which included several grams of ZrO_2 from the disk. A grayish residue frequently remained. Most of the combustion products had to be run twice, and a few of them three times.

As determined in this manner, the completeness of combustion varied from 89.80 to 100.00%. The completeness of combustion was higher when the ZrB_2 was spread in a thinner layer over a greater area of the disk.

Only lines of monoclinic ZrO_2 were found on the X-ray pattern of the combustion products. A microscopic examination of a combustion product showed grains of ZrO_2, measuring from 1–5 μ across, set in an optically isotropic phase of variable refractive index near 1.46, which presumably was B_2O_3 glass. No other constituents were observed.

The possibility of a reaction between the two combustion products, ZrO_2 and B_2O_3, was investigated[10] by taking an equimolar mixture of the two compounds and heating in air at 1465°. The fused mass was pulverized and subjected to X-ray analysis. The diffractometer scan was identical with that of the unheated mixture. Up to the temperature employed there was no reaction.

The specific heats of ZrO_2 and B_2O_3 were taken as 0.109 and 0.216 cal./g./deg., respectively. Seven runs were made on sample A, and nine runs on sample B. They are listed in Table II.

Table II: The Heat of Combustion of Zirconium Diboride

Mass burned, g.	Wt. fuse wire, mg.	Wt. ZrO_2, g.	Energy equiv., cal./degree, total	ΔT, °K.	Energy from Firing, cal.	Energy from ZrB_2, cal./g.	Dev. from mean, cal./g.
			Sample A				
0.8103	6.82	26.6	2389.8	1.4266	4.4	4152.3	7.4
0.7687	5.89	35.2	2390.7	1.3479	2.7	4143.3	1.6
0.7400	6.74	37.3	2391.0	1.2990	2.7	4139.7	5.2
0.7505	6.80	35.3	2390.7	1.3204	3.0	4148.7	3.8
0.7600	6.87	31.2	2390.3	1.3340	2.7	4138.7	6.2
0.7847	5.98	31.1	2390.3	1.3764	2.5	4144.5	0.4
0.7613	6.05	32.3	2390.4	1.3370	2.9	4147.4	2.5
					Av.	4144.9	3.9
					Std. dev.		1.85
			Sample B				
0.6650	24.87	25.2	2392.7	1.2122	2.1	4251.4	12.2
0.6382	25.18	25.4	2392.8	1.1594	2.0	4251.0	8.2
0.6303	25.28	25.1	2392.7	1.1508	1.7	4251.2	12.0
0.6497	21.62	25.2	2392.7	1.1841	1.8	4262.9	23.7
0.6481	24.90	25.5	2392.8	1.1776	1.8	4235.1	4.1
0.6208	24.57	25.6	2392.8	1.1223	1.6	4209.9	29.3
0.6482	23.91	25.8	2392.8	1.1785	1.7	4242.2	3.0
0.6384	25.63	23.1	2392.5	1.1563	1.6	4216.0	23.2
0.6790	24.96	22.8	2392.5	1.2375	1.5	4253.0	13.8
					Av.	4239.2	14.4
					Std. dev.		5.9

Zirconium Metal. The metal was in the form of 15-mil sheet. The analyses showed 0.019% C, 0.008% H, and 0.006% O, with no N or foreign metals detected.

Combustion of Zirconium Metal. The combustions were carried out under the same conditions used for the diborides. A zirconium fuse wire was used for ignition. No oxygen pick-up was observed. Twelve runs were made. The average initial temperature was 24.9° with a 1.250° average temperature rise.

The completeness of combustion was determined by the KOH method described above on five of the combustion products and by heating to constant weight at 1025° in oxygen on the other seven. Completeness of combustion varied from 99.30 to 99.95%.

X-Ray examination of a combustion product showed only the monoclinic form of ZrO_2. Another combustion product, ignited at 1000° in oxygen, gave a similar powder pattern but indicated some crystal growth.

(9) D. D. Williams, J. A. Grand, and R. R. Miller, *J. Am. Chem. Soc.*, **78**, 5150 (1956).

(10) C. P. Kempter, private communication.

It was thought that an oxygen-deficient ZrO_2 combustion product might be revealed by this method. The metal evidently burns completely to stoichiometric ZrO_2. Listed in Table III are the results.

Table III: The Heat of Combustion of Zirconium Metal

Mass burned, g.	Wt. ZrO_2, g.	Energy equiv., cal./deg., total	ΔT, °K.	—Energy from— Firing, cal.	Zr, cal./g.	Dev. from mean, cal./g.
1.1476	27.1	2392.9	1.3787	2.9	2872.3	4.8
0.9949	36.9	2393.9	1.2033	2.0	2893.4	16.3
1.0297	26.5	2392.8	1.2397	2.5	2878.4	1.3
1.0136	39.1	2394.2	1.2250	2.8	2890.8	13.7
0.9826	25.4	2392.7	1.1812	2.4	2873.9	3.2
1.0456	31.8	2393.4	1.2573	2.8	2875.3	1.8
1.0408	28.2	2393.0	1.2486	2.7	2868.2	8.9
0.9515	28.8	2393.0	1.1445	2.8	2875.5	1.6
1.1015	43.0	2394.6	1.3302	2.9	2889.2	12.1
1.1304	31.8	2393.4	1.3552	2.5	2867.1	10.0
0.9792	34.0	2393.6	1.1761	2.4	2872.4	4.7
1.0474	34.2	2393.6	1.2562	2.5	2868.3	8.8
				Av.	2877.1	7.3
			Std. dev.			5.3

Calculations

Each of the metallic impurities in sample A was assumed to be present as the oxide with the exception of Hf. The Hf was calculated as the diboride with a heat of combustion equivalent to that of the zirconium diboride on a molar basis. The combustion value, corrected for impurities, derived in this manner was 4292.2 cal./g., or 3.55% higher than the uncorrected value. The correction for impurities contributed an uncertainty of an estimated 0.28% in the corrected value which, combined with the uncertainty in the determination of the energy equivalent of the calorimeter and the random errors, gave a final value of 4292.2 ± 12.7 cal./g. for the heat of combustion of ZrB_2 under the conditions stated. This is equivalent to 484.4 ± 1.4 kcal./mole. Reduction to unit fugacity of oxygen and conversion to a constant pressure process yielded a value of $\Delta H_f°_{298} = -486.1 \pm 1.4$ kcal./mole. The combination of this value with the heat of formation of ZrO_2, −263.1 ± 0.5 (see below), and with the heat of formation of amorphous B_2O_3, −300.0 ± 0.7 kcal./mole,[11] yielded a value for the heat of formation of ZrB_2, $\Delta H_f°_{298} = -77.0 \pm 1.6$ kcal./mole.

For the calculations in this paper the 1961 atomic weights[12] are used; it was necessary to correct the older heat of formation values.

The calculations for sample B were done similarly. The small amount of carbon was assumed to be combined as ZrC, with a heat of combustion of 3010 cal./g.[13] After correction for impurities, the value for the heat of combustion became 4267.9 cal./g., or 0.67% larger. In this case the correction for the impurities introduced an uncertainty of 0.08%, which, combined with the other uncertainties, resulted in an over-all uncertainty of 0.29%, or 12.5 cal./g. The formula for this material was $ZrB_{1.985\pm0.003}$. The ΔH for the reaction

$$ZrB_{1.985} + 2.49O_2 = ZrO_2 + 0.992B_2O_3(amor.)$$

was −483.55 ± 1.41 kcal. After combination with the necessary auxiliary reactions as done above, a value of −77.3 ± 1.6 kcal./mole was obtained for the heat of formation of $ZrB_{1.985}$.

These two values, −77.0 ± 1.6 and −77.3 ± 1.6 kcal./mole for the heat of formation of ZrB_2, give an average of −77.2 ± 1.2 kcal./mole, a value near the more negative end of the range of earlier work.[3-6]

The impurities in the zirconium metal were assumed to be present as the carbide, dihydride, and dioxide. A value of 3110 cal./g. was taken as the heat of combustion of the hydride.[14] The heat of combustion value, corrected for impurities, was 2877.0 cal./g. or 0.003% smaller than the uncorrected value. An uncertainty of 0.03% was introduced in this correction, which contributed to an over-all uncertainty of 5.4 cal./g. The conversion of this figure to the heat of formation of ZrO_2 yields a value, $\Delta H_f°_{298} = -263.1 \pm 0.5$ kcal./mole, or 1.6 kcal. more negative than Humphrey's value.[15]

Acknowledgments. Valuable assistance was rendered by F. H. Ellinger, X-ray analysis; O. Simi, spectrochemical analysis; L. Gritzo, O. Kriege, and Helen Cowan, chemical analysis; and R. M. Douglass, microscopic examination.

(11) This value is a weighted mean of the values of W. D. Good, M. Månsson, and J. P. McCullough, "Thermochemistry of Boron and Some of Its Compounds," presented at the Symposium on Thermodynamics and Thermochemistry, Lund, Sweden, July 18, 1963; E. J. Prosen, W. H. Johnson, and F. Y. Pergiel, *J. Res. Natl. Bur. Std.*, **62**, 43 (1959); and G. L. Gal'chenko, A. N. Kornilov, B. I. Timofeev, and S. M. Shuratov, *Dokl. Akad. Nauk SSSR*, **127**, 1016 (1959).

(12) A. E. Cameron and E. Wichers, *J. Am. Chem. Soc.*, **84**, 4175 (1962).

(13) A. D. Mah and B. J. Boyle, *ibid.*, **77**, 6512 (1955).

(14) D. R. Fredrickson, R. L. Nuttall, H. E. Flotow, and W. N. Hubbard, *J. Phys. Chem.*, **67**, 1506 (1963).

(15) G. L. Humphrey, *J. Am. Chem. Soc.*, **76**, 978 (1954).

Electromotive Force Studies in Aqueous Solutions at Elevated Temperatures. V. The Thermodynamic Properties of DCl Solutions[1]

by M. H. Lietzke and R. W. Stoughton

Chemistry Division, Oak Ridge National Laboratory, Oak Ridge, Tennessee *(Received June 12, 1964)*

Measurements of the e.m.f. of the cell, Pt–$D_2(p)$|DCl(m)|AgCl, Ag, have been used to determine the thermodynamic properties of DCl solutions in D_2O as well as the standard potential of the cell to 225°. The standard potential was found to be lower in the deuterated system than in the corresponding protonated system and the difference became greater the higher the temperature. Activity coefficient behavior in the two systems is consistent with a lower value of the dielectric constant of D_2O at all temperatures. As judged from the variation of activity coefficients with temperatures and concentration the difference in the dielectric constant values appears to go through a minimum at about 100°.

Previous papers in this series have described the determination of the standard potential of the Ag, AgCl electrode[2] and the thermodynamic properties of HCl solutions[3] to 275°. In the present work, measurements of the e.m.f. of the cell, Pt–$D_2(p)$|DCl(m)|AgCl, Ag, have been used to determine the thermodynamic properties of DCl solutions in D_2O as well as the standard potential of the cell to 225°. In addition, the original e.m.f. data obtained in HCl solutions have been used to recalculate the properties of these solutions in a manner consistent with that used in the present calculations of the properties of DCl solutions. Thus a direct comparison can be made of the thermodynamic properties of HCl and DCl solutions over a wide range of concentration and temperature.

Experimental

The experimental apparatus and the preparation of electrodes were the same as described previously.[2,4]

The e.m.f. measurements were made on DCl solutions (in D_2O) of 0.0102, 0.0196, 0.0502, 0.0735, 0.1004, 0.1983, 0.495, and 1.127 m concentration at temperatures of about 25, 60, 90, 125, 150, 175, 200, and 225°. The DCl was purchased from Merck Sharp and Dohme of Canada Limited in 50-g. ampoules containing 38% by weight DCl solution in D_2O. The mass spectrographic assay of the DCl indicated 97.3% DCl by weight; because of the rapid exchange of H^+ with the D_2O in the final solution, the isotopic composition of the DCl under the experimental conditions is determined by that of the D_2O. The D_2O was prepared by twice distilling nominally 99.7% D_2O under an atmosphere of nitrogen that had been dried over $Mg(ClO_4)_2$. The first distillation was made from a 1 m D_2SO_4 and 0.5 m $K_2Cr_2O_7$ solution and the second from 2% $KMnO_4$ and 0.04 m NaOD. Extreme precautions were taken at all times to exclude any contamination by H_2O. Final mass spectrographic assay of the D_2O indicated 99.4% D_2O by weight. The D_2 gas was obtained in a cylinder from the Y-12 plant of the Nuclear Division of Union Carbide Corporation. Mass spectrographic analysis indicated an assay of 99.84% D_2 by weight.

Results and Discussion

In treating the results, the deuterium pressure was calculated by subtracting the vapor pressure of the solution from the observed total pressure, while the vapor pressure of the solution was obtained by taking the vapor pressure of pure D_2O[5] at the tempera-

(1) Research sponsored by the U. S. Atomic Energy Commission under contract with the Union Carbide Corporation.

(2) R. S. Greeley, W. T. Smith, Jr., R. W. Stoughton, and M. H. Lietzke, *J. Phys. Chem.*, **64**, 652 (1960).

(3) R. S. Greeley, W. T. Smith, Jr., M. H. Lietzke, and R. W. Stoughton, *ibid.*, **64**, 1445 (1960).

(4) M. B. Towns, R. S. Greeley, and M. H. Lietzke, *ibid.*, **64**, 1861 (1960).

(5) E. H. Riesenfeld and T. L. Chang, *Z. physik. Chem.*, **333**, 120 (1936).

Table I: Observed Values of the E.m.f. in Volts for the Cell, Pt–$D_2(p)$|DCl(m)|AgCl, Ag, and Deviations[a] of the E.m.f. Values Calculated from Smoothed Activity Coefficients

	t, °C.							
m	25	60	90	125	150	175	200	225
0.0102	0.4505	0.4529	0.4481	0.4359	0.4215			
	−3	0	0	5	−6			
0.0196	0.4195	0.4175	0.4092	0.3922				
	7	2	−3	−13				
0.0502	0.3760	0.3685	0.3552	0.3350	0.3161	0.2954	0.2718	0.2435
	22	13	−1	2	−2	6	11	−8
0.0735	0.3576	0.3478	0.3345	0.3119	0.2923	0.2706	0.2464	0.2164
	18	7	10	5	5	11	18	−12
0.1004	0.3417	0.3315	0.3148	0.2913	0.2719	0.2499	0.2248	0.1940
	6	8	−11	−12	−2	8	11	−23
0.1983	0.3100	0.2974	0.2742	0.2538	0.2328			
	10	26	−30	26	34			
0.495	0.2621	0.2451	0.2229	0.1915	0.1677			
	−22	1	−6	−19	−12			
1.127	0.2174	0.1933	0.1680					
	7	−13	15					

[a] The deviations are given below each e.m.f. as observed e.m.f. values less the value calculated from smoothed activity coefficients. Thus, a positive deviation indicates that the e.m.f. reported here is algebraically larger. These deviations have been computed on an equal-moles-of-solvent basis (with HCl).

ture of measurement and correcting for the presence of DCl in solution by Raoult's law. Each e.m.f. value was corrected to 1.00 atm. of deuterium pressure by subtracting $(RT/2F)$ ln f_{D_2}, where the deuterium fugacity f_{D_2} was taken equal to the deuterium pressure in atmospheres. The solubility of AgCl was neglected, and the ionic strength was taken to be equal to the DCl molality. The corrected e.m.f. values E at each ionic strength were plotted as a function of temperature and the values corrected to the round values of the temperature 25, 60, 90, 125, 150, 175, 200, and 225°. The temperature of measurement was usually no more than 1° from the corresponding round temperature. These corrected values are given in Table I. At the higher temperatures, the e.m.f. values were considered unreliable at the lowest acidities because of hydrolysis of the AgCl and at the highest acidities because of corrosion of the bomb. Hence these values are not given in the table.

The e.m.f. values for the cell, Pt–$H_2(p)$|HCl(m)|AgCl, Ag, which were reported in a previous paper in this series,[2] had been smoothed with respect to temperature variation by the method of least squares. For the purposes of the present study the original data on HCl were replotted and the values of the e.m.f. at round temperatures were read from the curves. These values, which differ slightly from those smoothed by least squares, are presented in Table Ia.

For the purpose of determining the E^0 of the cell, values of $E^{0\prime\prime}$, defined by eq. 1, were calculated for each data point. In this equation, E is the e.m.f.

$$E^{0\prime\prime} = E + \frac{2RT}{F} \ln m - \frac{2RT}{F} \frac{S\rho^{1/2}\sqrt{m}}{1 + A\sqrt{m}} \quad (1)$$

at 1 atm. of D_2 at temperature T, m is the molality of the DCl solution (which equals the ionic strength), F is the Faraday constant, S is the Debye–Hückel limiting slope (at temperature T), and A was assigned a constant value of 1.5 in all the present calculations. Multiplication by the square root of the density ρ of the solvent approximately corrects the molality term to one in volume concentration as required by the Debye–Hückel equation.

In computing the values of $S\rho^{1/2}$ at temperature T, it is necessary to know the density and dielectric constant of D_2O as a function of temperature. Values of the density of D_2O from 30 to 250° are given by Heiks, *et al.*,[6] while the dielectric constant from 4 to 100° has been measured by Malmberg.[7] Above 100°

(6) J. R. Heiks, M. K. Barnett, L. V. Jones, and E. Orban, *J. Phys. Chem.*, **58**, 488 (1954).

Table Ia: Values of the E.m.f. in Volts for the Cell, Pt-$H_2(p)$|HCl(m)|AgCl, Ag, and Deviations[a] of the E.m.f. Values Calculated from Smoothed Activity Coefficients

	t, °C.							
m	25	60	90	125	150	175	200	225
0.005	0.4983	0.5057	0.5065					
	3	−4	−4					
0.0075	0.4778	0.4826	0.4814	0.4759				
	−1	−11	−11	11				
0.01	0.4640	0.4675	0.4654	0.4578	0.4477	0.4350	0.4171	0.3982
	3	−4	0	17	20	29	11	−41
0.025	0.4198	0.4181	0.4108	0.3983	0.3855	0.3691	0.3493	0.3252
	10	0	−6	10	20	25	0	−3
0.05	0.3861	0.3798	0.3706	0.3545	0.3396	0.3212	0.2984	0.2716
	9	−12	−7	8	22	31	19	−9
0.075	0.3662	0.3584	0.3473	0.3288	0.3131	0.2934	0.2708	0.2452
	7	−10	−7	4	23	32	36	32
0.1	0.3519	0.3436	0.3312	0.3112	0.2945	0.2730	0.2460	0.2224
	3	−5	−4	5	25	25	−5	20
0.2	0.3187	0.3062	0.2905	0.2685	0.2497	0.2267	0.2021	0.1747
	11	−10	−16	6	26	35	50	58
0.5	0.2721	0.2546	0.2357	0.2085	0.1870	0.1631	0.1305	0.0928
	13	−19	−24	−17	3	27	−14	−44
1.0	0.2335	0.2125	0.1908	0.1620	0.1385	0.1129	0.0852	
	4	−6	−5	6	9	11	4	

[a] See footnote *a*, Table I.

the dielectric constant of H_2O was used in preference to extrapolating the D_2O values, since the experimental values for the two solvents tended to merge at 100° and since different expressions for D_2O gave widely different values on extrapolating to higher temperatures (some higher and some lower than the H_2O values). The H_2O values used were computed at each temperature using the equation given by Åkerlof and Oshry.[8]

By the use of the Nernst equation and the assumption that the logarithm of the activity coefficient of DCl can be expressed at each temperature as the sum of a Debye–Hückel term and a linear term in ionic strength Bm (at least to 0.1 m), one obtains the relation $E^{0\prime\prime} = E^0 - (2RT/F)Bm$. With the further assumption that ΔC_p for the cell reaction is independent of temperature, the temperature-dependent equation for $E^{0\prime\prime}$ becomes

$$E^{0\prime\prime} = a_0 + a_1T + a_2T \ln T - \frac{2RT}{F}(a_3/T + a_4 + a_5 \ln T)m \quad (2)$$

The values of $E^{0\prime\prime}$ in the range 0.0102 to 0.1004 m were fitted by the method of least squares using eq. 2 to determine the six coefficients a_0, a_1, . . . a_5. The three terms involving a_0, a_1, and a_2 give the value of E^0 for the cell at any temperature T, while the terms involving a_3, a_4, and a_5 give the linear term B in the expression for the logarithm of the activity coefficient of DCl. In carrying out the least-squares determination each data point was assigned a weight equal to the reciprocal of the product of the absolute temperature and the molality (the two independent variables) associated with the point. This scheme of weighting effectively equalized the contribution of each data point to the over-all fit. The values of E^0 were calculated both on a molal basis and on an equal-moles-of-solvent basis (*i.e.*, moles of solute/55.51 moles of solvent rather than 1000 g. of solvent) and are presented in Table II, while the coefficients for eq. 2 are given in Table III.

The values of $E^{0\prime\prime}$ for DCl were also fitted to an equation in which T^2 was used instead of $T \ln T$. In this case the standard error of fit was slightly larger than

(7) C. G. Malmberg, *J. Res. Natl. Bur. Std.*, **60**, 609 (1958).

(8) G. C. Åkerlof and H. J. Oshry, *J. Am. Chem. Soc.*, **72**, 2844 (1950).

Table II: Values of the Standard Potentials E^0, in v., of the Cells: Ag, AgCl *vs.* Hydrogen and *vs.* Deuterium Electrodes

	D_2–DCl (molal basis)		D_2–DCl (equal-moles-of-solvent basis)	H_2–DCl		ΔE^0 (HCl–DCl) in m.v. (molal basis)		ΔE^0 in m.v. (equal-moles-of-solvent basis)
t, °C.	This work	Ref. 9		This work	Ref. 9	This work	Ref. 9	
25	0.2094	0.2127	0.2146	0.2220	0.2224	12.6	9.7	7.4
50	(0.1913)	0.1931		(0.2052)	0.2046	(13.9)	11.5	
60	0.1828		0.1886	0.1973		14.5		8.7
90	0.1531		0.1594	0.1699		16.8		10.5
125	0.1111		0.1180	0.1313		20.2		13.3
150	0.0766		0.0838	0.0998		23.2		16.0
175	0.0386		0.0462	0.0650		26.4		18.8
200	−0.0027		0.0053	0.0274		30.1		22.1
225	−0.0471		−0.0388	−0.0131		34.0		25.7

Table III: Parameters of Eq. 2

	DCl (molal basis)	DCl (equal-moles-of-solvent basis)	HCl
a_0	−0.308117	−0.310350	−0.235985
a_1	0.0151850	0.0152514	0.0136202
a_2	−0.00236052	−0.00236780	−0.00212092
a_3	−16.4883	−14.7245	−4.17975
a_4	113.631	101.579	27.9216
a_5	−5979.35	−5355.82	−1161.13
σ_f[a]	1.3×10^{-8}	1.3×10^{-8}	1.6×10^{-8}

[a] Standard error of fit.

when the $T \ln T$ term was used (2.6×10^{-8} *vs.* 1.3×10^{-8}). Since eq. 2 is based on the thermodynamic assumption that ΔC_p is constant while the equation involving T^2 is purely empirical and since the standard error of fit is smaller when the $T \ln T$ term is used, only the coefficients and E^0 values obtained in the former case are tabulated. Attempts were also made to fit an equation like (2) in which quadratic terms in T were added to the expression for E^0 and BT; such expressions would be consistent with a linear dependence of ΔC_p on T. However the least-squares procedure (on a computing machine) would not converge, presumably because the data are not sufficiently precise to evaluate the coefficients of both $T \ln T$ and T^2 terms.

For comparison purposes values of $E^{0\prime\prime}$ were also computed for HCl and fitted using eq. 2. The values of E^0 so obtained as well as the coefficients of eq. 2 for HCl are also given in Tables II and III. It is interesting to note that the value of E^0 for the cell involving DCl and D_2O is lower than that of the corresponding protonated system and that this difference becomes larger the higher the temperature.

The standard e.m.f. of the cell, Pt–$D_2(p)$|DCl(m)|AgCl, Ag, has recently been determined from 5 to 50° by Gary, Bates, and Robinson.[9] In Table II their E^0 and ΔE^0 ($E^0_{HCl} - E^0_{DCl}$) values at 25 and 50° are compared with ours (our calculated values at 50° being enclosed in parentheses). The difference between the two values of E^0 for the deuterated system at each temperature appears to be larger than expected. The difference may in part result from the methods of smoothing as to temperature and concentration.

After the E^0 values for the cells had been determined, eq. 3 was used to calculate an activity coefficient value

$$E = E^0 - \frac{2RT}{F} \ln m - \frac{2RT}{F} \ln \gamma \qquad (3)$$

γ for each experimental concentration at each round temperature to 225° over the entire concentration range 0.0102 to 1.127 m for DCl and 0.005 to 1.0 m for HCl. These activity coefficients were then fitted by the method of least squares using

$$\log \gamma = \frac{-S\rho^{1/2}\sqrt{m}}{1 + 1.5\sqrt{m}} + Bm + Cm^2 \qquad (4)$$

where B and C were taken as

$$B = b_0/T + b_1 + b_2 \log T$$

and

$$C = c_0/T + c_1 + c_2 \log T$$

consistent with ΔC_p equal to a constant.

The values of the parameters b_0, b_1, b_2, c_0, c_1, and c_2 which were obtained in the fits to eq. 4 are given in Table IV. For concentrations below 0.1 m, the parameters in Table III should give more nearly correct values for the activity coefficients.

Values of the e.m.f. E were calculated from the E^0 values and the smoothed values of the activity co-

(9) R. Gary, R. G. Bates, and R. A. Robinson, *J. Phys. Chem.*, **68**, 1186 (1964).

Table IV: Parameters of Eq. 4 Which May Be Used to Calculate the Activity Coefficients of DCl and HCl

	DCl (molal basis)	DCl (equal-moles-of-solvent basis)	HCl
b_0	−1935.96	−1637.96	1165.04
b_1	39.9021	33.7150	−20.7158
b_2	−13.4953	−11.3949	6.85004
c_0	2505.34	1834.31	−1381.23
c_1	−51.6705	−37.7763	25.9846
c_2	7.60646	12.8003	−8.64215
σ_f	2.3×10^{-6}	2.1×10^{-6}	8.5×10^{-6}

efficients for the experimental conditions in both DCl and HCl solutions by the use of eq. 3 and 4. The algebraic differences between the observed E values and those calculated with the smoothed coefficients are given below the observed E values in Tables I and Ia.

By the use of the parameters in Table IV values of log γ for both HCl and DCl (on an equal-moles-of-solvent basis) *vs.* $\sqrt{m}$ at 25, 90, and 200° were calculated; these are shown in Fig. 1.

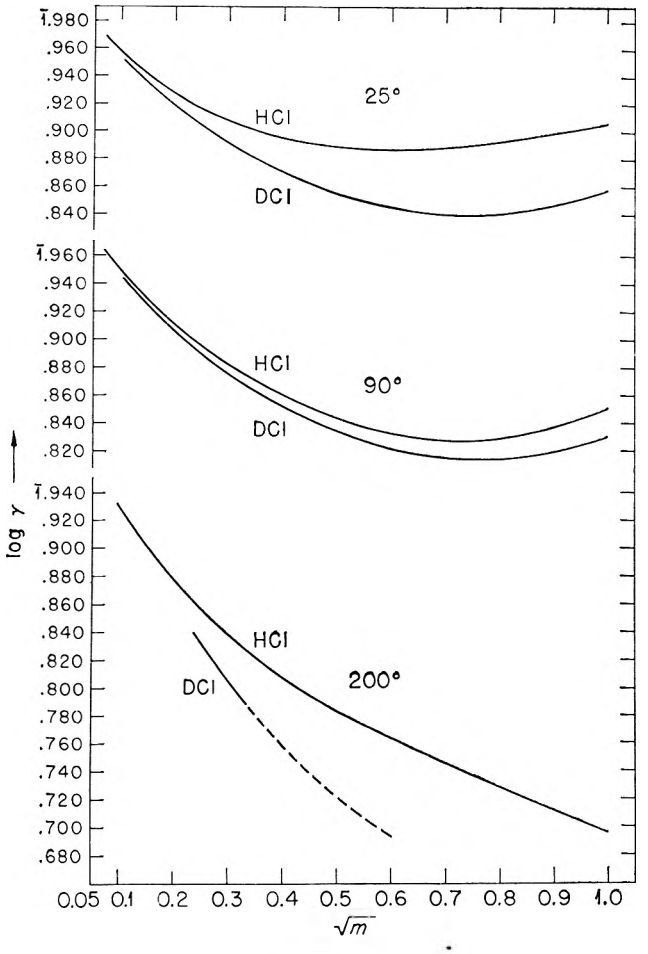

Figure 1. Plots of log γ *vs.* $\sqrt{m}$ for HCl and DCl solutions at 25, 90, and 200°.

As seen in Fig. 1, (a) the activity coefficient of DCl (in D_2O) is lower than that of HCl in H_2O at all temperatures and concentrations; (b) the difference between the two activity coefficients is greater at 25° and at 200° than at 90°; and (c) for any curve the lower the minimum value of the activity coefficient (*vs.* $\sqrt{m}$) the higher the value of m at the minimum. The fact that the DCl curves at 25 and 90° lie below the HCl curves is consistent with a lower dielectric constant for D_2O at each temperature. The fact that the two curves are closer together at 90 than at 25° is consistent with a smaller difference in dielectric constant at the higher temperature. Interestingly enough, the difference at 200° is consistent with a greater difference in dielectric constant at that temperature than at 90°. This would imply that values of the two dielectric constants become closer together at about 100° and then diverge again at the higher temperature with that of D_2O always remaining lower than that of H_2O. It is to be hoped that accurate measurements may be made of the dielectric constant of D_2O above 100° in order to check this suggestion.

The partial molal free energy $\bar{G}$, entropy $\bar{S}$, and enthalpy $\bar{H}$ for either DCl or HCl may be expressed in terms of the standard values and the parameters in Table IV by the equations

$$\bar{G} - \bar{G}^0 = 4.606RT\left[\log m - \frac{S\rho^{1/2}\sqrt{m}}{1 + 1.5\sqrt{m}} + \left(\frac{b_0}{T} + b_1 + b_2 \log T\right) m + \left(\frac{c_0}{T} + c_1 + c_2 \log T\right) m^2\right] \quad (5)$$

$$\bar{S} - \bar{S}^0 = 4.606R\left[-\log m + \left(\frac{\sqrt{m}}{1 + 1.5\sqrt{m}}\right) \times \frac{\partial}{\partial T}(TS\rho^{1/2}) - \left(b_1 + b_2 \log T + \frac{b_2}{2.303}\right) m - \left(c_1 + c_2 \log T + \frac{c_2}{2.303}\right) m^2\right] \quad (6)$$

and

$$\bar{H} - \bar{H}^0 = 4.606RT\left\{-\frac{\sqrt{m}}{1 + 1.5\sqrt{m}}\left[S\rho^{1/2} - \frac{\partial}{\partial T}(TS\rho^{1/2})\right] + \left(\frac{b_0}{T} - \frac{b_2}{2.303}\right) m + \left(\frac{c_0}{T} - \frac{c_2}{2.303}\right) m^2\right\} \quad (7)$$

where S is the value consistent with eq. 4, *i.e.*, on a common logarithm basis.

Acknowledgments. The authors wish to express their sincere appreciation to W. D. Armstrong, John Byrnes, Walter Stevens, and Ralph Whitfield who performed the experimental e.m.f. measurements.

The Kinetics of the Decarboxylation of Malonic Acid and Other Acids—A General Relationship

by Louis Watts Clark

Department of Chemistry, Western Carolina College, Cullowhee, North Carolina *(Received June 22, 1964)*

Kinetic data are reported for the following decarboxylation reactions: malonic acid in benzoic acid, pivalic acid, octanoic acid, heptanoic acid, and *dl*-2-methylpentanoic acid; *n*-butylmalonic acid in hexanoic acid and octanoic acid; *n*-hexylmalonic acid in *o*-cresol; and oxanilic acid in *o*-cresol, octanoic acid, benzoic acid, and decanol. The activation parameters for these reactions were calculated and compared with corresponding data obtained previously. A general kinetic relationship was indicated.

A plot of enthalpy *vs.* entropy of activation for a series of related reactions often yields a straight line, the slope of which is designated as the isokinetic temperature. This is the temperature at which the rate of reaction is equal for all the reactions conforming to the line.[1]

In the case of the decarboxylation of oxanilic acid in the molten state and in a dozen polar solvents (ethers and amines) the isokinetic temperature determined graphically was found to be 423°K.[2] For the decarboxylation of malonic acid in the molten state and in 11 polar solvents (acids, cresols, nitro compounds) the isokinetic temperature was found graphically to be 407°K.[3] These values corresponded closely to the melting points of the two reactants (oxanilic acid melts at 150°, which is 423°K., malonic acid at 135.6°,[4] which is 409°K.)

It was subsequently pointed out by a referee that the isokinetic temperatures for these two reaction series, calculated by the method of least squares, were slightly different from those reported, namely, 418°K. for the oxanilic acid reaction and 414°K. for the malonic acid reaction. These revised values still did not differ appreciably from the melting points of the two reactants. In view of these circumstances it was decided to perform additional experiments in order to try to establish more accurate values for the two isokinetic temperatures. Accordingly, the following experiments were carried out in this laboratory: (1) The decarboxylation of malonic acid in benzoic acid, pivalic acid, octanoic acid, heptanoic acid, isovaleric acid, and *dl*-2-methylpentanoic acid; (2) the decarboxylation of *n*-butylmalonic acid in hexanoic acid and in octanoic acid; (3) the decarboxylation of *n*-hexylmalonic acid in *o*-cresol; and (4) the decarboxylation of oxanilic acid in *o*-cresol, octanoic acid, benzoic acid, and *n*-decyl alcohol. The data obtained in this research were com-

(1) S. L. Friess, E. S. Lewis, and A. Weissberger, Ed., "Technique of Organic Chemistry," Vol. VIII, Part I, "Investigations of Rates and Mechanisms of Reactions," 2nd Ed., Interscience Publishers, Inc., New York, N. Y., 1961, p. 207.

(2) L. W. Clark, *J. Phys. Chem.*, 66, 1543 (1962).

(3) L. W. Clark, *ibid.*, 67, 526 (1963).

(4) T. Salzer, *J. Prakt. Chem.*, 61, 66 (1900).

bined with others obtained previously revealing an unexpected general relationship. The results of this investigation are reported herein.

Experimental

Reagents. (*a*) *Reactants.* The four reactants, malonic acid, *n*-butylmalonic acid, *n*-hexylmalonic acid, and oxanilic acid, assayed at least 99% pure by neutralization equivalents. This degree of purity also was verified by measuring the volume of CO_2 evolved on complete reaction. Their melting points agreed with those cited in the literature.

(*b*) *Solvents.* Reagent grade benzoic acid, 100% assay, was used directly from the container without further treatment. The other solvents were reagent grade or highest purity chemicals. A fresh sample of each liquid was distilled off at atmospheric pressure immediately before use.

Apparatus and Technique. The apparatus and technique have been described in detail previously.[5] The use of a completely transistorized temperature control unit enabled the temperature of the oil bath to be kept constant to ±0.005°. The evolved CO_2 was collected in a 50-ml. buret calibrated by the U. S. Bureau of Standards. The temperature of the water surrounding the buret was controlled by ±0.05°, using a water circulator, heater, mercury thermoregulator, and electronic relay.

In each decarboxylation experiment a sample of reactant was weighed out in a fragile glass capsule. The weight of sample was that required to furnish 40.0 ml. of CO_2 at STP on complete reaction, calculated on the basis of the actual molar volume of CO_2 at STP, namely, 22,267 ml. About 60 ml. of solvent was used in each experiment.

Results

The decarboxylation reactions of all the reactants in all the liquids studied in this research gave good first-order kinetics over the greater part of the reaction. Each reaction was generally studied over a 20° range of temperature, at three or four different temperatures. Two experiments were ordinarily carried out at each temperature. Variations between the two values of the rate constant as measured in the same solvent at the same temperature were usually no more than 1%. The average values of the rate constants for the reactions in the various solvents at the different temperatures studied are shown in Table I. The apparent first-order rate constants were calculated from the slopes of the experimental logarithmic plots. Table II shows the parameters of the absolute reaction rate equation[6] calculated from the data in Table I.

Table I: Apparent First-Order Rate Constants for the Decarboxylation of Several Reactants in Various Solvents

Reactant	Solvent	Temp., °C. (cor.)	$k \times 10^4$, sec.$^{-1}$
Malonic acid	Benzoic acid	137.11	2.12
		145.78	4.68
		154.66	10.16
	Pivalic acid	142.06	2.23
		151.21	6.26
		160.50	17.15
	Octanoic acid	139.69	2.83
		150.06	8.10
		159.84	22.5
	Heptanoic acid	139.09	2.98
		149.70	7.58
		159.11	16.7
	dl-2-Methylpentanoic acid	139.94	3.35
		149.70	7.18
		159.32	14.9
	Isovaleric acid	139.94	3.17
		150.75	8.93
		159.67	20.3
n-Butylmalonic acid	Octanoic acid	137.87	2.32
		147.78	5.98
		157.77	12.9
	Hexanoic acid	135.61	1.94
		147.78	6.40
		155.49	13.25
n-Hexylmalonic acid	*o*-Cresol	135.11	3.79
		136.75	4.37
		144.05	7.63
		151.36	13.6
		155.70	18.8
Oxanilic acid	*o*-Cresol	128.63	0.705
		138.91	2.62
		148.13	7.98
	Octanoic acid	140.73	2.78
		150.34	7.22
		159.46	18.67
	Decanol	130.66	1.21
		140.72	3.71
		150.45	10.44
	Benzoic acid	131.32	0.94
		140.97	2.53
		151.76	7.23

Activation parameters for the decarboxylation of various reactants in a wide variety of solvents, based upon previously reported results, are brought together in Table III. All the data in Tables II and III are shown graphically in Fig. 1.

(5) L. W. Clark, *J. Phys. Chem.*, **60**, 1150 (1956).

(6) S. Glasstone, K. J. Laidler, and H. Eyring, "The Theory of Rate Processes," McGraw-Hill Book Co., Inc., New York, N. Y., 1941, p. 14.

Table II: Activation Parameters for the Decarboxylation of Several Reactants in Various Solvents Based on Present Research

Reactant	Solvent	ΔH^*, kcal./mole	ΔS^*, e.u./mole
Malonic acid	Octanoic acid	34.8	+8.9
	Benzoic acid	30.4	−1.8
	Heptanoic acid	29.7	−3.4
	Isovaleric acid	32.56	+3.57
	dl-2-Methylpentanoic acid	26.45	−11.1
	Pivalic acid	38.7	+18.3
n-Butylmalonic acid	Hexanoic acid	33.2	+5.1
	Octanoic acid	32.7	+3.8
n-Hexylmalonic acid	*o*-Cresol	25.9	−11.4
Oxanilic acid	Benzoic acid	33.3	+4.7
	o-Cresol	41.0	+23.9
	Hexanoic acid	36.73	+13.3
	n-Decyl alcohol	36.3	+12.8

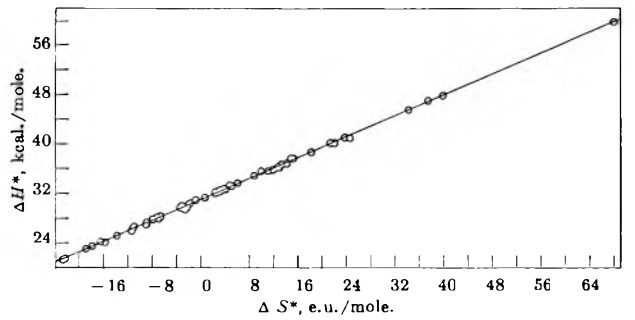

Figure 1. Enthalpy–entropy of activation plot for the decarboxylation of oxanilic acid, oxamic acid, malonic acid, *n*-butylmalonic acid, *n*-hexylmalonic acid, and benzylmalonic acid in the molten state and in solution.

Discussion

It is surprising to note that all the points representing the reactions shown in Tables II and III lie on the same isokinetic temperature line (see Fig. 1). These include parameters for the decarboxylation of oxamic acid in five solvents, of oxanilic acid in the molten state and in 16 solvents, of malonic acid in the molten state and in 21 solvents, of *n*-butylmalonic acid in the molten state and in six solvents, of *n*-hexylmalonic acid in the molten state and in one solvent, and of benzylmalonic acid in the molten state and in two solvents—a total of 56 reactions, representing six reactants, and covering a wide range of solvent types. These results are based upon more than 500 kinetic experiments, carried out by a single investigator, extending over a period of approximately 8 years.

The fact that all these reactions conform to the same isokinetic temperature line is strong evidence that they all take place according to the same mechanism.[7]

Table III: Activation Parameters for the Decarboxylation of Several Reactants in Various Solvents—Previously Reported Results

Reactant	Solvent	ΔH^*, kcal./mole	ΔS^*, e.u./mole
Oxanilic acid	Bis(2-chloroethyl) ether[a]	21.4	−22.4
	n-Butyl ether[a]	25.1	−13.9
	n-Amyl ether[a]	28.3	−6.6
	β-Chlorophenetole[a]	31.3	+0.7
	Phenetole[a]	32.6	+4.0
	Anisole[a]	32.6	+11.1
	Dibenzyl ether	36.8	+14.2
	N,N-Dimethylaniline[a]	37.6	+15.3
	Melt[a]	40.1	+21.4
	n-Hexyl ether[a]	40.1	+22.1
	o-Ethylaniline[a]	45.5	+34.3
	o-Toluidine[a]	47.8	+39.9
	8-Methylquinoline[b]	35.6	+10.0
Oxamic acid	Aniline[c]	59.7	+68.0
	Quinoline[d]	47.0	+37.5
	8-Methylquinoline[d]	36.0	+12.2
	Dimethyl sulfoxide[e]	37.7	+14.9
	Triethyl phosphate[e]	40.9	+24.7
Malonic acid	Melt[f]	35.8	+11.9
	Propionic acid[f]	33.6	+6.1
	Hexanoic acid[f]	32.5	+3.2
	m-Cresol[f]	32.3	+3.2
	n-Butyric acid[f]	32.3	+2.5
	n-Valeric acid[f]	32.2	+2.4
	β-Mercaptopropionic acid[f]	30.3	−9.9
	p-Cresol[f]	29.8	−2.4
	Nitrobenzene[f]	28.1	−7.2
	Phenol[f]	27.3	−8.9
	Decanoic acid[f]	26.6	−11.0
	o-Cresol[f]	24.2	−16.5
	o-Nitrotoluene[f]	23.5	−17.9
	2-Nitro-*m*-xylene[g]	30.0	−3.12
	Benzaldehyde[h]	27.9	−7.0
	β-Chlorophenetole[i]	27.8	−7.9
Benzylmalonic acid	Melt[j]	29.4	−2.6
	n-Butyric acid[j]	23.0	−18.9
	Decanoic acid[j]	26.9	−9.0
n-Hexylmalonic acid	Melt[k]	32.0	+2.4
n-Butylmalonic acid	Melt[l]	32.2	+2.9
	Phenol[l]	36.2	+13.0
	m-Cresol[l]	29.7	−2.3
	p-Cresol[l]	24.0	−15.8
	o-Cresol[l]	21.3	−22.8

[a] See ref. 2. [b] L. W. Clark, *J. Phys. Chem.*, **65,** 542 (1961). [c] L. W. Clark, *ibid.*, **65,** 180 (1961). [d] L. W. Clark, *ibid.*, **65,** 659 (1961). [e] L. W. Clark, *ibid.*, **65,** 1651 (1961). [f] See ref. 3. [g] L. W. Clark, *J. Phys. Chem.*, **62,** 368 (1958). [h] L. W. Clark, *ibid.*, **64,** 677 (1960). [i] L. W. Clark, *ibid.*, **65,** 2271 (1961). [j] L. W. Clark, *ibid.*, **67,** 1481 (1963). [k] L. W. Clark, *ibid.*, **67,** 2602 (1963). [l] L. W. Clark, *ibid.*, **68,** 587 (1964).

This mechanism has been shown to consist of the formation of an activated complex, a carbonyl carbon atom of the reactant coordinating with a pair of unshared electrons on one of the nucleophilic atoms of the solvent, facilitating cleavage.[8]

An interesting feature of the results shown in Fig. 1 is the large variety of reactions composing a single reaction series. These include: (1) the decarboxylation of oxamic acid and oxanilic acid (and presumably their derivatives) in the molten state and in a wide variety of polar solvents (ethers, amines, alcohols, acids, cresols, triethyl phosphate, dimethyl sulfoxide, etc.), and (2) the decarboxylation of malonic acid and of all monoalkylated derivatives of malonic acid in the molten state and in several types of polar solvents (acids, cresols, nitro compounds, ethers, aldehydes, etc.).

Inasmuch as oxamic acid and oxanilic acid belong to the type of α-keto acids, and malonic acid and its derivatives belong to the type of β-keto acids, it may be expected that the decarboxylations of α- and β-keto acids in the molten state and in many polar solvents likewise belong to this reaction series.

It has been found that the decarboxylation of malonic acid in alcohols forms a new reaction series as shown by the fact that the isokinetic temperature line for this group of reactions lies below and parallel to that for the reactions in acids, nitro compounds, cresols, etc.[3] A third parallel line is formed by the group of reactions in aniline derivatives,[9] a fourth for the reaction in picolines.[10] (Compare ref. 7, p. 1208). On the other hand, the decarboxylation of oxamic and oxanilic acids in all types of polar solvents apparently constitutes only a single reaction series, all points lying on the same isokinetic temperature line. It may be expected that other α-keto acids will follow the same pattern as oxamic and oxanilic acids, and other β-keto acids that of malonic acid.

The equation of the line in Fig. 1, obtained by the method of least squares, is

$$\Delta H^* = 422.0\Delta S^* + 31{,}000$$

The slope of the line, which is designated as the isokinetic temperature, is thus 422.0°K. or 149°C. It is now evident that the fact that this value is within 1° of the melting point of oxanilic acid is only a coincidence.

The free energy of activation at the isokinetic temperature for all the reactions belonging to this reaction series is given by the last constant in the above equation, namely, 31,000 cal. The specific reaction velocity constant for all the reactions in the series at the isokinetic temperature may be calculated by substituting this value of ΔF^* in the absolute reaction rate equation[6]

$$k = \frac{\kappa T}{h} e^{-\Delta F^*/RT}$$

The rate constant thus calculated turns out to be 8.55×10^{-4} sec.$^{-1}$.

In the case of a reaction taking place at a temperature *below* 149°, the reaction having the *lowest* enthalpy of activation will have the highest rate, whereas, *above* 149°; the reaction having the *highest* enthalpy of activation will have the *highest* rate.

Petersen, *et al.*,[11] have analyzed the effect of experimental errors on the validity of an observed linear enthalpy–entropy of activation relationship, and they reached the conclusion that "the positive demonstration of such a phenomenon is extremely difficult due to the inherent nature and magnitude of experimental errors." They applied their method of evaluation to many published examples but failed to find a single clearly valid case. They thought that the major part of any observed linear enthalpy–entropy of activation relationship is very likely the result of experimental error in most, if not all, previously published examples.

In view of this sweeping indictment one is prone to ask whether or not the results shown in Fig. 1 may be considered valid.

Petersen, *et al.*, pointed out that only unless the observed range of ΔH^* values in a given series is greater than twice the maximum possible error in ΔH^* can any validity be assumed in the observed ΔH^*–ΔS^* relationship, and only unless the range is much greater than this can any details of the relationship be inferred. Now the range of ΔH^* values represented by the reactions in Fig. 1 is nearly 40.0 kcal./mole. The error in ΔH^* of the reactions included in Fig. 1 can be readily calculated by recourse to the formula proposed by Petersen and co-workers[11]

$$\delta = 2R \frac{T'T}{T' - T} \alpha$$

where δ is equal to the maximum possible error in ΔH^*, α is the maximum fractional error in the rate constants, R is the gas constant in calories, and T'

(7) J. E. Leffler, *J. Org. Chem.*, **20**, 1202 (1955).

(8) G. Fraenkel, R. L. Belford, and P. E. Yankwich, *J. Am. Chem. Soc.*, **76**, 15 (1954).

(9) L. W. Clark, *J. Phys. Chem.*, **62**, 79 (1958).

(10) L. W. Clark, *ibid.*, **60**, 1583 (1956).

(11) R. C. Petersen, J. H. Markgraf, and S. D. Ross, *J. Am. Chem. Soc.*, **83**, 3819 (1961).

and T are the upper and lower temperatures, respectively, at which the rate constants were determined.

What is α, the maximum fractional error in the rate constants, of the 56 reactions represented by the points in Fig. 1? This we can only estimate. Each reaction has been carried out at least twice at each temperature, and often five or more temperatures have been studied for one reaction. Every effort has been made to reduce experimental error to a minimum. Reagents of the highest purity have been used. Temperature control has been $\pm 0.1°$ in the earlier experiments, and about $\pm 0.005°$ in the later ones. Reproducibility of the experiments has been of the order of about 1%. In view of these factors, an assumed value of α of 0.05 should not be too small. We may exaggerate this value and set α equal to 0.1 or 10 times the reproducibility of k for the sake of removing any question as to the reliability of the calculations. If we let typical values of T' and T be 423 and 413°K., respectively, and set α equal to 0.1, the value of δ turns out to be 7 kcal./mole. Twice this amount is 14 kcal./mole, as compared with 40 kcal./mole for the range of ΔH^* values. Since the range of ΔH^* values covered by the reactions in Fig. 1 is very much greater than twice the maximum fractional error in ΔH^*, the linear relationship represented by the data in Fig. 1 must be considered valid.

Acknowledgments. Acknowledgment is made to the donors of The Petroleum Research Fund, administered by the American Chemical Society, for support of this research. Thanks are due also to Western Carolina College for the use of its punch card equipment and computer facilities, and to William Cowan, the programmer, who wrote the Fortran program used in this research.

The Entropy of $NH_3 \cdot 2H_2O$. Heat Capacity from 15 to 300°K.[1]

by J. P. Chan and W. F. Giauque

Low Temperature Laboratory, Departments of Chemistry and Chemical Engineering, University of California, Berkeley, California *(Received June 30, 1964)*

The heat capacity of $NH_3 \cdot 2H_2O$ has been determined from 15 to 300°K. The melting point was found to be 176.16 ± 0.05°K. and the ice–$NH_3 \cdot 2H_2O$ solution peritectic point is 176.09 ± 0.05°K. The $NH_3 \cdot 2H_2O$–NH_4OH eutectic temperature is 175.42 ± 0.05°K. The heat of fusion at the melting point is 1673 cal./mole. For the reaction $2H_2O(l) + NH_3(sat.\ l) = NH_3 \cdot 2H_2O(sat.\ l)$, we find, from available data, $\Delta F_{25°} = 2123$ cal./mole, $\Delta H_{25°} = 2842$ cal./mole, and $\Delta S_{25°} = -2.413$ gibbs/mole. Similarly for the reaction $2H_2O(l) + NH_3(g, f = 1) = NH_3 \cdot 2H_2O(sat.\ l)$, $\Delta F_{25°} = -825$ cal./mole, $\Delta H_{25°} = -7874$ cal./mole, and $\Delta S_{25°} = -23.643$ gibbs/mole. From these results and other available data the entropy of $NH_3 \cdot 2H_2O(sat.\ l)$ is found to be 55.81 gibbs/mole at 298.15°K. The more accurate entropy value calculated from the present calorimetric data is 55.67 gibbs/mole and the small difference is within the limits of error of the various experiments which have enabled the comparison. This result indicates that no disorder such as that involving hydrogen bonds is present at limiting low temperatures. Tables of C_p, S, $(F° - H°_0)/T$ and $(H° - H°_0)/T$ are included.

Low temperature calorimetric studies of NH_3,[2] H_2O,[3] and their compounds $(NH_4)_2O$[4] and NH_4OH[4] have previously been completed in this laboratory. More recently Rollet and Vuillard[5] found another hydrate, $NH_3 \cdot 2H_2O$. Ice has disordered hydrogen bonding and since hydrogen bonds must play an important role in bonding[6] $NH_3 \cdot 2H_2O$, an investigation of this substance designed to show whether its hydrogen bonds become ordered at low temperatures was of interest. We may say at once that $NH_3 \cdot 2H_2O$ has been found to approach zero entropy and thus attains perfect crystalline order, at limiting low temperatures.

Preparation and Purity of $NH_3 \cdot 2H_2O$. NH_3 was prepared from NH_4Cl and KOH as described by Overstreet and Giauque.[2] This was combined with distilled water, boiled to eliminate CO_2, to make the hydrate. The sample was purposely made with an excess concentration of NH_4OH to avoid the presence of ice at temperatures below the peritectic point of the dihydrate. This is undesirable because it would not be possible to use the calorimetric measurements on the $NH_3 \cdot 2H_2O$–NH_4OH eutectic for analytical purposes and also because the presence of excess ice would be certain to trigger the separation of $NH_3 \cdot 2H_2O$ into ice and solution when the peritectic point was reached. Actually, it was found that this almost always occurred, even without excess ice.

When the composition is on the NH_4OH side of $NH_3 \cdot 2H_2O$ the heat of fusion of the small amount of their eutectic mixture serves as a quantitative means of adjusting the composition by guiding the removal of measured amounts of the more volatile NH_3 gas from the system. These were condensed in a bulb of known volume by means of liquid nitrogen and measured approximately by gas pressure at ordinary temperatures. The amount of ammonia removed was finally measured accurately by the difference in the initial and final weights of the material in a closed container and thus as *in vacuo*.

Apparatus and Temperature Scale. The measurements were made in Gold Calorimeter V as described

(1) This work was supported in part by the National Science Foundation.

(2) R. Overstreet and W. F. Giauque, *J. Am. Chem. Soc.*, **59**, 254 (1937).

(3) W. F. Giauque and J. W. Stout, *ibid.*, **58**, 1144 (1936).

(4) D. L. Hildenbrand and W. F. Giauque, *ibid.*, **75**, 2811 (1953).

(5) A. P. Rollet and G. Vuillard, *Compt. rend. Acad. Sci. Paris*, **243**, 383 (1956); G. Vuillard, *Publ. Sci. Univ. Alger.*, **B3**, 80 (1957).

(6) L. Pauling, *J. Am. Chem. Soc.*, **57**, 2680 (1935).

previously[7] except that copper–constantan standard thermocouple No. 102, used previously, was replaced because of its accidental breakage. A new thermocouple calibrated at the triple (13.94°) and boiling (20.36°) points of hydrogen, the triple (63.15°) and boiling (77.34°) points of nitrogen, and also at 176°K., through comparison with standard No. 102 before it was broken, was installed. A gold resistance thermometer–heater of about 260 ohms at room temperature was used for high precision in obtaining temperature drifts. A value of 0°C. was taken as 273.15°K., and 1 defined cal. as 4.1840 absolute joules.

Heat Capacity Measurements. The heat capacity data are given in Table I. The measurements for the solid were made on a sample which contained less ($1.8687H_2O$) than 2 moles of water/mole of ammonia for the reason given above. When we attempted to use the analytical procedure based on the heat of fusion of the $NH_3 \cdot 2H_2O$–NH_4OH eutectic in a manner similar to that described by Hildenbrand and Giauque[4] for the lower hydrates, the fact that the peritectic point, 176.09°, of $NH_3 \cdot 2H_2O$ is only 0.67° above the eutectic temperature, which was measured at 175.42°K., made this procedure difficult. Heat effects along the short melting line between the eutectic point and the melting point were practically inseparable from the heat of fusion and heat capacity until the amount of eutectic was reduced to a very small value by approaching the $NH_3 \cdot 2H_2O$ over-all composition. As mentioned above this was done by removing small amounts of ammonia gas, under conditions such that the relative partial pressure of water was trivial. This was followed by extensive thermal stirring of the residual sample by heat introduction in the lower portion of the calorimeter.

When the composition corresponded to $NH_3 \cdot 1.9991H_2O$, the heat of fusion of the eutectic and the heat capacity along the melting curve became clearly separable from the main heat of fusion. Aqueous ammonia solutions supercool readily, as had been noted by Vuillard,[5] and we made use of this fact in crystallizing the dihydrate by the following procedure. The ammonia dihydrate was cooled as glass to the temperature of boiling nitrogen and was then slowly warmed while the heavy metal block surrounding the calorimeter remained cold. At approximately 157°K., about 19° below the peritectic point, crystallization started and hydrogen gas was admitted to the space between the cold block and the calorimeter to remove some of the heat evolved during the crystallization. The heat capacity of the substance and the calorimeter were important in absorbing heat. The procedure was evidently effective, for although the evolved heat may have raised the temperature within the calorimeter to the peritectic point for a brief period, there was no evidence of composition dislocation, and subsequent cooling completed the crystallization. In the case of $NH_3 \cdot 1.8687H_2O$, the excess ammonia was crystallized as NH_4OH. The heat capacity of the solid was measured on this material and the result corrected for the known heat capacity of the amount of NH_4OH present. As a check several heat capacity measurements were made on solid $NH_3 \cdot 1.9991H_2O$, and agreement with the values based on the corrected mixture

Table I: Heat Capacity of $NH_3 \cdot 1.8687H_2O$ and $NH_3 \cdot 1.9991H_2O$[a]

$T_{av.}$, °K.	C_{measd}
$NH_3 \cdot 1.8687H_2O$ sample	
Series 1	
14.40	0.729
15.90	0.880
17.84	1.176
19.99	1.571
22.14	2.031
24.55	2.505
27.22	3.050
30.09	3.610
32.93	4.229
35.91	4.775
39.19	5.326
42.48	5.927
45.98	6.538
50.15	7.234
Series 2	
157.69	22.01
164.14	22.93
170.35	23.78
Series 3	
40.83	5.659
44.60	6.292
48.30	6.910
51.90	7.521
55.39	8.089
59.18	8.700
63.50	9.374
68.15	10.10
73.11	10.90
78.24	11.57
84.10	12.36
90.49	13.24
96.94	14.06
103.63	14.93
110.32	15.85
117.24	16.85
124.34	17.80
131.49	18.70
138.35	19.56
145.32	20.45
152.52	21.36
159.58	22.30
166.66	23.24
$NH_3 \cdot 1.9991H_2O$ sample	
Series 4	
183.72	38.03
192.28	38.94
200.07	40.21
208.11	41.45
215.90	42.66
223.49	43.87
230.93	45.10[b]
238.48	46.24
245.97	47.41
253.07	48.40
259.93	49.24
266.98	50.41
274.34	51.20
281.63	52.10
288.15	52.82
Series 5	
141.43	19.92
148.37	20.81
155.63	21.74

[a] 0°C. = 273.15°K.; mol. wt. NH_3 = 17.0306, H_2O = 18.0153; 108.337 g. of $NH_3 \cdot 1.8687H_2O$ or 105.963 g. of $NH_3 \cdot 1.9991H_2O$ in the calorimeter (wt. *in vacuo*). 1 gibbs = 1 defined cal./defined degree. Heat capacity in gibbs/mole of NH_3. [b] This and succeeding runs of series 4 corrected for NH_3 vaporization.

(7) J. B. Ott and W. F. Giauque, *J. Am. Chem. Soc.*, 82, 1308 (1960).

was found to be within the limit of error of the measurements.

The heat capacities were measured continuously and the temperature increments may be estimated by the separation of the measurements.

The Melting and Peritectic Points. The $NH_3 \cdot 2H_2O$–ice solution peritectic point was observed by measuring the temperature as a function of the fraction of the heat of melting. The values are given in Table II, along with the value of the true peritectic temperature obtained by means of a plot of T *vs.* $1/f$, where f = fraction melted. This plot was extrapolated as usual to the hypothetical value $1/f = 0$. The slope of the curve indicated a liquid soluble–solid insoluble impurity of 8 parts in 100,000 on a molal basis. The relative $H_2O:NH_3$ proportions will not alter the peritectic temperature. This small amount of impurity was based on the high precision slope of the resistance thermometer data given in Table II. The impurity probably consisted of 3 parts of $(NH_4)_2CO_3$ in 100,000 of hydrated ammonia. The sample was handled in a closed system or under an atmosphere of carbon dioxide-free nitrogen to avoid this possibility. However, it was cooled in a convenient CO_2 bath to reduce the vapor pressure (about 1 atm. at 25°) before it was transferred to the calorimeter and probably absorbed the 0.7 cc. NTP of CO_2/mole of ammonia dihydrate needed to explain the observed impurity. In any case 0.003% carbonate should have a trivial effect on the results.

Table II: Peritectic Temperature of $NH_3 \cdot 2H_2O$–Ice Solution[a]

Fraction melted	T, °K., by resistance therm.	T, °K., by thermocouple
0.096	176.060	176.08
0.302	176.076	176.09
0.588	176.085	176.10
Extrap.	176.088	

[a] Accepted peritectic point = 176.09 ± 0.05°K.

The melting point appears to be 0.07 ± 0.01° above the peritectic point. This value is based on a single observation made with a preliminary sample which was believed to be nearly of dihydrate composition and, after remaining isothermal for a few minutes following partial melting, suddenly dropped in temperature. The drop of 0.07° is presumed to correspond to the appearance of the ice phase which would reduce the temperature to that of the peritectic. While the above observation is somewhat uncertain, it seems quite consistent with the extrapolation of the melting point diagram of Rollet and Vuillard.[5] Thus, the thermodynamically unstable melting point is taken as 176.16 ± 0.05°K.

The Heat of Fusion of $NH_3 \cdot 2H_2O$. The heat of fusion of ammonia dihydrate was measured as usual by starting heat input somewhat below the peritectic point and continuing until the calorimeter was well above the ice melting curve immediately above the melting point of $NH_3 \cdot 2H_2O$. Measuring the heat of fusion of a substance which temporarily forms a peritectic presents a problem caused by the fact that the first equilibrium liquid produced is of a somewhat different composition than that of the original compound. In this case the equilibrium liquid composition is near that of $NH_3 \cdot 2H_2O$, and there is no reason to believe that much composition dislocation occurred during the process of complete melting to form liquid dihydrate. We have assumed that the finely divided ice, which may have existed for a short period during the melting, stayed on location in the somewhat viscous liquid until melting was complete. However, in order to eliminate any cumulative effect from possible composition dislocation the sample was always thermally stirred by heating it nearly to ordinary temperatures several times before recrystallization for another heat of fusion or other measurements. This precaution was especially indicated after the lengthy melting needed for a study of the peritectic temperature. The heat of fusion data are given in Table III where they are corrected for the $\int C_p dT$ above and below the melting point.

The phase diagram of Rollet and Vuillard[5] indicates that the eutectic composition is about 73 mole % $NH_3 \cdot 2H_2O$ and 27 mole % NH_4OH. In a series of short runs it was found that the heat capacity returned to a normal value after the eutectic region had been passed. The heat of fusion of the eutectic in the sample used for the heat of fusion at the melting point was 10.1 (two values, 10.3 and 9.9) cal./mole of NH_3 in the sample. The fact that the eutectic point and the peritectic point were only 0.67° apart made it very difficult to determine the heat of fusion per mole of eutectic, but it cannot be far from 1600 cal./mole, which was assumed. Thus we conclude that the sample actually melted in the calorimeter had an over-all composition of $NH_3 \cdot 1.9991H_2O$ and represented 1.9959 moles of $NH_3 \cdot 2H_2O$ and 0.0017 mole of NH_4OH. The eutectic melting heat of 10.1 cal./mole corresponded to the melting of 0.0046 mole of $NH_3 \cdot 2H_2O$ + 0.0017 mole of NH_4OH, leaving 1.9913 moles of $NH_3 \cdot 2H_2O$ to be melted above the $NH_3 \cdot 2H_2O$–NH_4OH eutectic tem-

Table III: Heat of Fusion of $NH_3 \cdot 2H_2O$[a]

Expt. no.	T_1, °K. (initial)	T_2, °K. (final)	Total cal./mole	$\int_{T_1}^{T_2} C_p dT$	ΔH_F, cal./mole
1	175.805	180.663	1845.0	175.3	1670
2	175.869	182.569	1919.8	245.2	1675
			Accepted value		1673

[a] There were 1.9976 moles in calorimeter; 1.9913 moles melted at m.p., 176.16°K.

perature. The data are placed on a molal basis in Table III.

The Thermodynamic Properties of $NH_3 \cdot 2H_2O$. The heat capacity of solid ammonia dihydrate was obtained by correcting the observations on $NH_3 \cdot 1.8687H_2O$ for the presence of 0.1313 mole of NH_4OH/mole of total NH_3, using the data of Hildenbrand and Giauque.[4]

The measurements on the liquid were made after the determination of the heat of fusion and following adjustment to an over-all composition of $NH_3 \cdot 1.9991H_2O$. There were 1.9976 moles of ammonia in the solution of the above composition in the calorimeter during the measurements on the liquid. It was assumed that the heat capacity/gram was the same for the dihydrate as for $NH_3 \cdot 1.9991H_2O$ in obtaining the molal values of $NH_3 \cdot 2H_2O$. Minor corrections were applied to the heat capacity measurements on the liquid for the heat effect due to vaporization into the small gas volume above the liquid sample. The heat per mole of NH_3 was estimated with sufficient accuracy for this purpose by means of the approximation $\Delta H_{vap} = RT^2 \, d \ln P/dT$, where P is the vapor pressure over $NH_3 \cdot 2H_2O$ as given by the tables of Scatchard, *et al.*[8] Smoothed values of the heat capacity and related thermodynamic properties are given in Table IV.

The extrapolation over the region 0–15°K. was made by means of a plot of C/T *vs.* T^2 and also by extrapolating Debye equation θ values. The two methods agreed closely in giving the entropy at 15°K. as 0.27 gibbs/mole.

The Entropy of $NH_3 \cdot 2H_2O$. The entropy and free energy values given in Table IV for $NH_3 \cdot 2H_2O$ were calculated on the assumption that this substance attained a perfectly ordered structure in approaching 0°K. and thus had no residual entropy. To test the truth of this assumption we may use the data of Scatchard, Epstein, Warburton, and Cody[4] on the thermodynamic properties of aqueous ammonia, in combination with the well known entropies of liquid water and ammonia gas taken as 16.71 and 46.03 gibbs/mole, respectively.

Table IV: Thermodynamic Properties of Ammonia Dihydrate (gibbs/mole)[a]

T, °K.	C_p	S	$-(F^\circ - H^\circ_0)/T$	$(H^\circ - H^\circ_0)/T$
15.0	0.784	0.270	0.073	0.197
20.0	1.583	0.592	0.159	0.432
25.0	2.612	1.057	0.290	0.767
30.0	3.638	1.623	0.464	1.159
35.0	4.607	2.259	0.674	1.584
40.0	5.498	2.931	0.914	2.017
45.0	6.364	3.629	1.177	2.452
50.0	7.205	4.344	1.458	2.886
55.0	8.028	5.069	1.753	3.316
60.0	8.833	5.802	2.060	3.742
70.0	10.399	7.282	2.700	4.582
80.0	11.845	8.767	3.366	5.401
90.0	13.175	10.239	4.048	6.192
100.0	14.459	11.694	4.740	6.954
110.0	15.824	13.135	5.438	7.698
120.0	17.232	14.573	6.139	8.434
130.0	18.516	16.004	6.843	9.161
140.0	19.761	17.422	7.548	9.874
150.0	21.033	18.828	8.253	10.575
160.0	22.354	20.228	8.958	11.270
170.0	23.725	21.624	9.662	11.962
176.16(s)	24.569	22.483	10.095	12.388
176.16(l)	37.029	31.980	10.095	21.885
180.0	37.496	32.784	10.571	22.213
190.0	38.762	34.845	11.794	23.050
200.0	40.192	36.868	12.997	23.871
210.0	41.742	38.866	14.182	24.685
220.0	43.329	40.845	15.349	25.496
230.0	44.940	42.806	16.500	26.306
240.0	46.495	44.752	17.637	27.115
250.0	47.975	46.681	18.760	27.921
260.0	49.356	48.589	19.871	28.719
270.0	50.666	50.477	20.969	29.508
273.15	51.058	51.062	21.311	29.754
280.0	51.892	52.342	22.056	30.285
290.0	53.029	54.183	23.133	31.050
298.15	53.871	55.665	24.002	31.663
300.0	54.048	55.977	24.203	31.797

[a] Molecular weight = 53.0612; 1 gibbs = 1 defined cal./defined deg.

From the tables of Scatchard, *et al.*,[8] we find, by graphical interpolation, the following data for the reaction

$$2H_2Ol + NH_3(\text{sat. l}) = NH_3 \cdot 2H_2O(\text{sat. l})$$

$$\Delta F_{25^\circ} = -2123 \text{ cal./mole}$$

$$\Delta H_{25^\circ} = -2842 \text{ cal./mole} \qquad (1)$$

$$\Delta S_{25^\circ} = -2.413 \text{ gibbs/mole}$$

(8) G. Scatchard, L. F. Epstein, J. Warburton, and P. J. Cody, *Refrig. Eng.*, **53**, 413 (1947).

In converting the units in the tables of Scatchard, *et al.*, we have taken 1 b.t.u. = 252.196 defined cal. We believe these tables to be most accurate near ordinary temperature but they evidently contain serious errors at lower temperatures. For example, they appear to have been prepared on the assumption that the heat capacity was 1 cal./g. at all lower temperatures and all compositions. The heat capacities of $(NH_4)_2O$, NH_4OH, and $NH_3 \cdot 2H_2O$ are now available and it has become evident that the heat capacities are very much less than the values assumed by Scatchard, *et al.*,[8] for extrapolation purposes.

From the calculations of Hildenbrand and Giauque[4] for the reaction

$$NH_3(g, f = 1) = NH_3(\text{sat. l}) \qquad (2)$$

$$\Delta F_{25^\circ} = +1298 \text{ cal./mole}$$

$$\Delta H_{25^\circ} = -5032 \text{ cal./mole}$$

$$\Delta S_{25^\circ} = -21.230 \text{ gibbs/mole}$$

Combining the data for reactions 1 and 2

$$2H_2O(l) + NH_3(g, f = 1) = NH_3 \cdot 2H_2O(\text{sat. l}) \qquad (3)$$

$$\Delta F_{25^\circ} = -825 \text{ cal./mole}$$

$$\Delta H_{25^\circ} = -7874 \text{ cal./mole}$$

$$\Delta S_{25^\circ} = -23.643 \text{ gibbs/mole}$$

$$S, NH_3 \cdot 2H_2O(\text{sat. l}) = 2S, H_2O(l) + S, NH_3(g, f = 1) - 23.643$$

$$= 2 \times 16.71 + 46.03 - 23.643$$

$$= 55.81 \text{ gibbs/mole at } 298.15^\circ K.$$

and this value may be compared with the more accurate result $\int_0^T C_p \, d \ln T = 55.67$ gibbs/mole obtained in the present research.

The agreement is within the limits of the experimental error of the present data and the experiments on which the tables of Scatchard, *et al.*,[8] are based, and indicates that the hydrogen bonding in $NH_3 \cdot 2H_2O$ attains perfect order at limiting low temperatures.

Acknowledgment. We thank P. R. Siemens and G. V. Calder for assistance with the measurements.

NOTES

Evidence for the Existence of the Crystalline Phase $BeSO_4 \cdot H_2O$

by D. R. Petersen, H. W. Rinn, and S. T. Sutton

Chemical Physics Research Laboratory, The Dow Chemical Company, Midland, Michigan
(Received April 20, 1964)

The extensive investigations, summarized by Pascal,[1] of the crystalline hydrates of beryllium sulfate have been marked by disagreement over the existence of various postulated phases. For example, while the dehydration sequence of $BeSO_4 \cdot 4H_2O$—the form found under conventional temperature and pressure conditions—is commonly reported to be *tetrahydrate* to *dihydrate* to *monohydrate* to *anhydrate*, Campbell[2] and his colleagues, in refuting some conclusions of Rohmer[3] on the nature of the dihydrate, were led to reject the monohydrate as a distinct species.

The present note describes definite evidence for the existence of the disputed phase $BeSO_4 \cdot H_2O$ through the joint application of the methods of differential thermal analysis (hereafter DTA), mass spectrometric thermal analysis (MTA), and X-ray diffraction (XRD). The study has verified that the normal dehydration sequence of the tetrahydrate is through the dihydrate and the monohydrate to the anhydrous form. Each of the members of this series was found to be crystalline and sufficiently stable to allow the photographic recording of its powder diffraction pattern.

(1) P. Pascal, Ed., "Nouveau Traité de Chimie Minérale," Vol. 4, Masson et Cie., Paris, 1958, pp. 75–80.

(2) A. N. Campbell, A. J. Sukava, and J. Koop, *J. Am. Chem. Soc.*, **73**, 2831 (1951).

(3) R. Rohmer, *Bull. soc. chim.*, [5] **10**, 468 (1943).

Experimental

The starting material for the DTA and the MTA experiments was "beryllium sulfate, purified," Fisher Chemical Co., catalog No. B-311. No contaminants of consequence were found by either X-ray fluorescence or optical emission spectroscopy. Gravimetric analysis gave 40.7 ± 0.1 wt. % water (calculated for the tetrahydrate: 40.68%).

The DTA apparatus used was that of the R. L. Stone Co., Model 12AC. A 10-mg. portion of the starting material, diluted with alumina, was compared with an alumina reference over the temperature range from 25 to 925°, at a uniform heating rate of 10°/min. The experiment was carried out in air at atmospheric pressure. Four such runs were made on as many sample portions; in each case the DTA trace was as shown in Fig. 1.

The MTA equipment is based upon a modified Bendix time-of-flight mass spectrometer[4,5] which allows the collection and identification through mass analysis of volatile reaction products obtained when a substance is heated close to the ion source of the spectrometer. In our particular experiment, a 4-mg. portion of the starting material was held under 2×10^{-6} torr for 17 hr. and then introduced into the sample heating furnace within the mass spectrometer. It was heated from room temperature to 750° at a rate of 10°/min. The experiment was repeated at a higher heating rate and gave results substantially the same as shown in Fig. 1 for the first run.

Sample portions for XRD were prepared from the starting material by heating it to its several stages of dehydration either in the DTA equipment or in a standard laboratory furnace for various times at temperatures suggested by the DTA trace. For samples made in the furnace, the loss in weight at each stage was noted. A total of six separate dehydrations was made over the full range from tetrahydrate to anhydrate; all gave comparable results, both in weight loss and XRD experiments. In the latter, the individual portions were ground in a dry nitrogen atmosphere and loaded into a wedge holder, protected from atmospheric moisture by a 0.25-mil Mylar cover. Powder data were recorded on photographic film in a GE camera of diameter 143.2 mm., using Cu Kα X-radiation, with an exposure time of 3 hr. The XRD pattern ascribed by us to the monohydrate was obtained on nine separate exposures, all properly predicted. We had no difficulty in securing uncontaminated XRD patterns of any of the phases mentioned above, except that the monohydrate was observed to revert almost immediately to the dihydrate if not protected from moisture in the air.

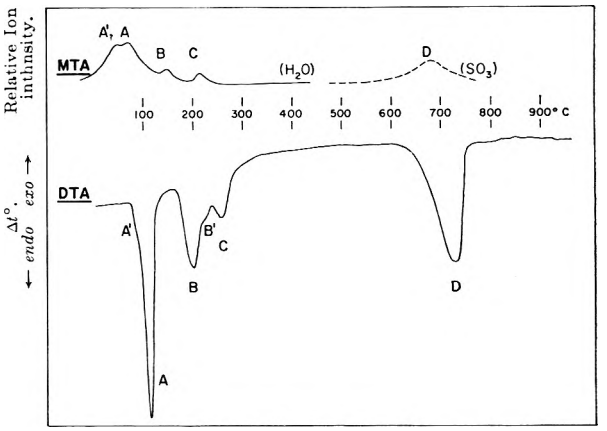

Figure 1. Correspondence between the MTA and the DTA traces of the thermal dehydration and decomposition of $BeSO_4 \cdot 4H_2O$. The four principal reactions are: (A) $BeSO_4 \cdot 4H_2O \rightarrow BeSO_4 \cdot 2H_2O + 2H_2O$; (B) $BeSO_4 \cdot 2H_2O \rightarrow BeSO_4 \cdot H_2O + H_2O$; (C) $BeSO_4 \cdot H_2O \rightarrow BeSO_4 + H_2O$; (D) $BeSO_4 \rightarrow BeO + SO_3$.

Results and Discussion

The DTA and MTA results are combined in Fig. 1; endotherms and total-mass peaks which we believe correspond are indicated. The phase change at A is the transformation of the tetrahydrate to the dihydrate. We found, for example, the residue after the starting material (tetrahydrate) was held for 16 hr. at 110° to weigh 79.4% of the original, with 79.66% calculated for the dihydrate. The transition is said[2] to occur at 88–90°, approximately where the reaction begins in our DTA trace. The analogous total-mass peak in the MTA record appears at a lower temperature, presumably because of the much different sample environment. The very small shoulder A′ on the low-temperature side of the DTA endotherm A is of unknown origin; note that the corresponding feature in the MTA record is more pronounced.

The transition at B is from the dihydrate to the monohydrate. Thus, the dihydrate held for 0.75 hr. at 210° gave a residue weight of 87.4%, with 87.23% calculated for the monohydrate. Both the dihydrate and the monohydrate were found to revert completely to the tetrahydrate if exposed to atmospheric moisture for more than an hour or two. The small shoulder B′ in the DTA pattern if reproducible, but unexplained.

The change from the monohydrate to the anhydrate is shown at *C*. Various experiments in which the dihydrate was held at temperatures in the range from

(4) R. S. Gohlke, "Uses of a Total Ionization Monitor for Time-of-Flight Mass Spectrometry," presented before the Tenth Annual Meeting of ASTM Committee E-14 on Mass Spectrometry, New Orleans, La., June 3–8, 1962.

(5) H. G. Langer and R. S. Gohlke, *Anal. Chem.*, **35**, 1301 (1963).

250 to 500° showed a mean residue weight of 75.3%, against 74.47% calculated for $BeSO_4$. This transition may be that observed at 270° by Campbell, Sukava, and Koop,[2] but attributed by them to a different reaction.

The MTA record shows that no water remains in the system above 300°, in agreement with the DTA results. In the range 600–800°, reaction D, the evolved gas is SO_3; the residue was identified as BeO by XRD. The single endotherm in the DTA trace and the single MTA peak make unlikely the formation of an intermediate oxysulfate of beryllium analogous to, say, dolerophanite, $CuO \cdot CuSO_4$.[6]

Table I: X-Ray Powder Data for $BeSO_4 \cdot 2H_2O$

d, obsd., Å.	I/I_1, obsd.
4.95	20
4.80	70
4.09	5
3.92	2
3.55	100
3.33	6
2.87	12
2.79	12
2.61	3
2.47	1
2.38	4
2.16	5
2.11	1
2.045	2
1.925	6
1.830	1
1.815	1
1.770	2
1.651	1
1.500	2
1.439	1
1.389	1
1.353	1
1.324	1

Our XRD data for $BeSO_4 \cdot 4H_2O$ were found to match very closely those in the X-Ray Powder Data File,[7] and so are not reproduced here. The crystal structure of the tetrahydrate is known[8]; it conforms to the tetragonal space group $I\bar{4}c2$, with $a = 8.04$ Å., $c = 10.77$ Å.

The powder data obtained by us for the dihydrate appear to be somewhat better resolved than the previously published data[9] and are given in Table I. Our data for the monohydrate are found in Table II; earlier listings for "$BeSO_4$ (10.80% H_2O)" and for "$BeSO_4$" in the X-Ray Powder Data File[10] show similarities to those in Table II, but the correspondence is not complete. Unit cells have not been assigned by us to either $BeSO_4 \cdot 2H_2O$ or $BeSO_4 \cdot H_2O$.

Table II: X-Ray Powder Data for $BeSO_4 \cdot H_2O$

d, obsd., Å.	I/I_1, obsd.
5.25	84
4.00	2
3.85	30
3.77	2
3.55	100
3.43	3
3.18	2
3.01	2
2.795	10
2.625	8
2.525	1
2.470	1
2.285	18
2.180	8
2.090	7
1.960	5
1.915	2
1.846	2
1.761	3
1.717	2
1.665	1
1.595	1
1.488	3
1.465	3
1.432	1
1.391	2
1.347	2
1.315	2
1.278	2
1.241	1
1.190	1
1.177	1
1.136	1
1.112	1
1.087	1

Our XRD data for $BeSO_4$ in Table III show some minor improvement over previous work[11] and are here indexed on the basis of the cell proposed by Grund[12]

(6) H. J. Borchardt and F. Daniels, *J. Phys. Chem.*, **61**, 917 (1957).

(7) American Society for Testing Materials, X-Ray Powder Data File, Set 12, Special Technical Publication 48-L, 1962, card 12-71.

(8) C. A. Beevers and H. Lipson, *Z. Krist.*, **82**, 297 (1932).

(9) American Society for Testing Materials, X-Ray Powder Data File, Sets 1–5 (Revised), Special Technical Publication 48-J, 1960, card 5-0407. See also ref. 2.

(10) Ref. 9, cards 5-0350 and 5-0358, respectively, and ref. 2.

(11) See ref. 9, card 1-0495.

(12) A. Grund, *Tschermaks mineral. petrog. mitt.*, **5**, 227 (1955); *Chem. Abstr.*, **50**, 4579*d* (1956).

Table III: X-Ray Powder Data for $BeSO_4$

d, obsd., Å.	I/I_1, obsd.	d, calcd., Å.	hkl
3.77	100	3.760	101
3.48	3	3.450	002
3.18	3	3.171	110
2.34	18	2.335	112
		2.243	200
2.03	1	2.047	103
1.926	6	1.926	211
1.876	3	1.880	202
		1.725	004
1.585	1	1.586	220
		1.515	114
1.509	5	1.512	213
		1.461	301
1.441	1	1.441	222
1.412	1	1.418	310
1.369	2	1.367	204
		1.319	105
1.308	2	1.312	312
1.250	1	1.253	303
1.220	2	1.224	321
1.164	1	1.167	224
		1.150	006
1.132	1	1.137	215
		1.121	400
1.093	1	1.096	314
		1.094	323
		1.081	116
1.073	1	1.075	411
1.063	1	1.066	402

and by Kokkoros.[13] The anhydrate was found by them to be related structurally to cristobalite and to conform to the tetragonal space group $I\bar{4}$, with $a = 4.485$ Å., $c = 6.90$ Å.

The powder data[14] and structure of BeO are well known and need no comment.

We may conclude that the thermal dehydration and decomposition sequence of $BeSO_4 \cdot 4H_2O$ leads through the stages: tetrahydrate to dihydrate to monohydrate to anhydrate to oxide. The rejection[2] of $BeSO_4 \cdot H_2O$ as a true phase thus is shown to be unfounded.

Acknowledgment. Thanks are due to Drs. H. G. Langer and R. S. Gohlke of the Eastern Research Laboratory of The Dow Chemical Co. for executing the MTA experiment; this method, coupled with DTA and XRD, is seen to provide a useful and convenient tool for the study of phase relationships.

(13) P. Kokkoros, *Tschermaks mineral. petrog. mitt.*, **6**, 116 (1956); *Chem. Abstr.*, **50**, 14,307 (1956).

(14) See ref. 9, card 4-0843.

The Structure of Ammonium Hexanitratocerate(IV) in Solution[1a]

by Russell D. Larsen[1b] and Glenn H. Brown

Department of Chemistry, Kent State University, Kent, Ohio *(Received April 30, 1964)*

A question of interest is posed in the chemical literature concerning the structure of ammonium hexanitratocerate(IV) (common name: ceric ammonium nitrate) both in the solid state and in solution. No direct structural evidence exists on this compound in either state. The question of interest to chemists is whether the $Ce(NO_3)_6^{-2}$ ion exists either in the salt or in solution. For years[2] it was felt that no appreciable complex ion formation occurred between cerium(IV) and nitrate ion in solution. Other evidence[3] suggests the existence of a nitrate complex; however, this question was not answered by definitive structural studies. Smith, Sullivan, and Frank,[3] in proposing this salt as a primary standard for oxidimetry, indicated that, on the basis of its chemical behavior in solution, the salt is a complex salt in contrast to a "double" salt such as cerium(IV) ammonium sulfate. This chemical evidence consists of: the lack of hydrolysis of the nitrate to give insoluble cerium(IV) salts; solutions of the complex in nitric acid are salted out with ammonium nitrate but not with nitric acid; the nitrate salt is cleanly separated from solutions of cerium group metals (except thorium) without double salt formation in contrast to the more common double salt behavior. A nitrate complex of this type is somewhat unique, however, in that bidentate nitrate complexes are known for only a few atoms. Thorium, uranium, and silver ions are also thought to form such complexes.[2,4,4a]

In this note results of an X-ray diffraction study of an aqueous solution of ammonium hexanitratocerate-

(1) (a) Abstracted in part from the Ph.D. dissertation of R. D. Larsen, Kent State University, Kent, Ohio, 1964; (b) Frick Chemical Laboratory, Princeton University, Princeton, N. J.

(2) D. M. Yost, H. Russell, and C. S. Garner, "The Rare-Earth Elements and Their Compounds," John Wiley and Sons, Inc., New York, N. Y., 1947, p. 61.

(3) G. F. Smith, V. R. Sullivan, and G. Frank, *Ind. Eng. Chem., Anal. Ed.*, **8**, 449 (1936).

(4) Discussion of G. E. Walrafen indicates that Raman spectral evidence on molten silver nitrate by G. E. Walrafen and D. E. Irish, *J. Chem. Phys.*, **40**, 911 (1964), allows for a structural configuration in which Ag^+ ions are probably nearest neighbors to two oxygens of a single nitrate ion; however, the O–Ag–O linkage is probably not covalent.

(4a) NOTE ADDED IN PROOF.—Recently results have been reported for the existence of an eight-coordinate complex of the tetranitratocobaltate(II) ion in which each nitrate is bidentate; *cf.* F. A. Cotton and J. G. Bergmann, *J. Am. Chem. Soc.*, **86**, 2941 (1964).

(IV) are reported in which evidence is presented for the existence of hexanitratocerate(IV) ion in solution.

Experimental

Method. The radial distribution method of analysis of X-ray diffraction data as applied to polyatomic liquids was used in this study.[5] Radial distribution functions were calculated using the formalism of Waser and Schomaker[6] as extensively applied by Levy[7] and Kruh[8] to other systems.

Materials. The samples (53.7% by weight in water) were prepared by direct weight of reagent grade ammonium hexanitratocerate(IV) purchased from the G. Fredrick Smith Chemical Co.

Apparatus. X-Ray diffraction data were collected using a Picker X-ray unit with a horizontal-axis diffractometer and a flat sample holder; the radiation was 35 kv. and 20 ma. Mo $K\alpha$ which was monochromatized by filters and a pulse height analyzer. The time–count–diffraction angle data were recorded from a digital print-out for $^4/_{15}°$ 2θ increments up to 30°, 2θ, and for 2° 2θ increments up to 90°, 2θ.

Procedure. The time–count–diffraction angle data were converted to a common basis of counts per minute. Replicate samples were averaged and corrected for the sample-container contribution and for polarization. The coherent scattering factors for cerium were corrected for dispersion. The incoherent scattering factors for cerium were calculated by the method of Bewilogua.[9] The corrected experimental intensity data were normalized to the total theoretical intensities using the methods of Krogh-Moe[10] and Norman.[11]

The Waser–Schomaker formalism involves the convolution of a modification function with the intensity function. The particular modification function that was used in this study was of the general form employed by Levy[7]

$$M(s) = [f_x(0)/f_x(s)]^2 \qquad (1)$$

where f_x is the coherent scattering factor of an atom x (*i.e.*, cerium ion) chosen as the unit of composition to which the other atoms in the polyatomic liquid are stoichiometrically related. A convergence factor was not employed in calculating the areas under the radial distribution maxima. Of the various distribution functions that were calculated the following function was used in evaluating the areas under the maxima

$$D(r) = 4\pi r^2 g_1 + 2r/\pi \int_0^{s_m} si(s)M(s) \sin rs\, ds \qquad (2)$$

where g_1 is the average electron density in units of electrons^2/Å.^{3}; s_m is the upper limit of integration. The intensity function $si(s)$ is

$$si(s) = s[I_{e.u.} - \Sigma f_m^2] \qquad (3)$$

where $I_{e.u.}$ is the corrected and normalized experimental coherent intensity in electron units. The Σf_m^2 term is the theoretical coherent data summed over a stoichiometric unit consisting of 1 mole of water to 0.03813 mole of solute. $D(r)$ is a superposition of modified pair distribution functions,[7] the transforms of each being the so-called "shape functions"

$$T_{mn}(r) = 1/\pi \int_0^{s_m} f_m f_n M(s) \cos rs\, ds \qquad (4)$$

where f_m and f_n are the coherent scattering factors of atoms m and n, respectively. $M(s)$ is the mocification function defined by eq. 1.

Results and Discussion

Radial distribution curves for 53.7% ammonium hexanitratocerate(IV) solution show that interactions occur at 1.35, 2.15, 2.85, 3.60, 4.30, and 5.10 Å. and at other higher radial distances that cannot be interpreted as simple pair interactions. Above 5.0 Å. there is little deviation from the bulk scattering indicating that the short-range order is restricted to a rather small range of interaction. The 1.35- and 2.15-Å. distances are readily attributable to N–O and O–O interactions, respectively, within a nitrate ion. The 2.85-Å. peak can be attributed to Ce–O interactions. There is good agreement of 106.6% for 12 Ce–O interactions in comparing the area for this number of "pure" interactions to the experimentally determined area. Figure 1 shows the shape function for 12 Ce–O interactions compared with the experimental radial distribution peak at 2.85 Å.

This agreement presents strong evidence for 12-coordination of oxygen around cerium. This can be interpreted as corresponding to six bidentate nitrate ions coordinated to a central cerium(IV) ion. It is postulated on the basis of the evidence afforded by this work that the nitrate configuration about cerium is in the approximate geometrical shape of an icosahedron. An icosahedral configuration economically allows for a 12-coordination of bidentate ligands.

(5) A summary of the pertinent theory and general procedure is given in the Ph.D. dissertation of R. D. Larsen.

(6) J. Waser and V. Schomaker, *Rev. Mod. Phys.*, **25**, 671 (1953).

(7) H. A. Levy, P. A. Agron, M. A. Bredig, and M. D. Danford, *Ann. N. Y. Acad. Sci.*, **79**, 762 (1960); H. A. Levy and M. D. Danford in "Molten Salt Chemistry," M. Blander, Ed., Interscience Publishers, New York, N. Y., 1964, p. 109.

(8) R. F. Kruh, *Chem. Rev.*, **62**, 319 (1962).

(9) L. Bewilogua, *Physik. Z.*, **32**, 740 (1931).

(10) J. Krogh-Moe, *Acta Cryst.*, **9**, 951 (1956).

(11) N. Norman, *ibid.*, **10**, 370 (1957).

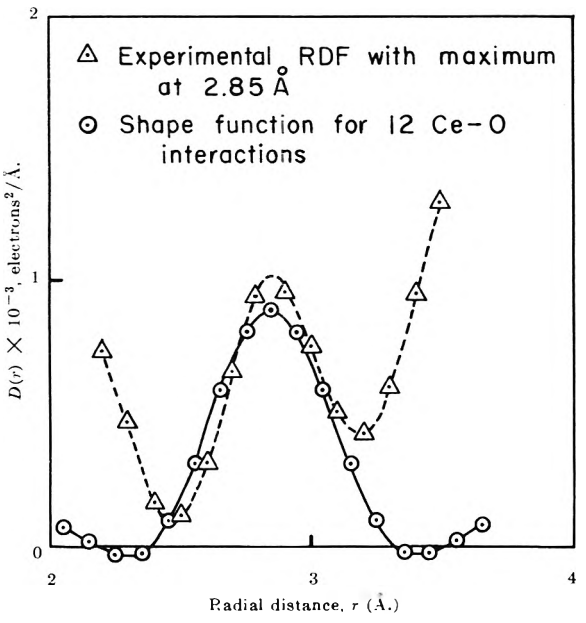

Figure 1. The shape function for 12 Ce–O interactions compared with the experimental radial distribution peak at 2.85 Å.

Favorable support for an icosahedral arrangement is afforded by consideration of the critical radius ratios of cerium(IV) with surrounding ions.

A similar geometric arrangement has been reported for another rare earth salt. Martin, Rundle, and Golden[12] found a 12-coordinate arrangement around one of the lanthanum ions in $La_2(SO_4)_3 \cdot 9H_2O$ for which they proposed an icosahedral configuration as the most favorable. Their argument is based upon considerations of critical radius ratios and upon the geometry of the atoms established by X-ray analysis of the solid.

It might be expected that thorium(IV) or cerium(IV) ions, which are of comparable size, will be surrounded by equal numbers of complexing species. The striking difference between cerium(IV) and thorium(IV) nitrate complexes, however, is the coordination number of 11.2 (experimental)[13] found for cerium(IV) contrasted to the coordination number of 8.5 (average experimental value for four different solutions) found for thorium(IV) in aqueous and acidic media in a similar diffraction study.[14]

In this study as well as the thorium nitrate study, no evidence is indicated for metal ion–metal ion interactions in solution. The absence of a marked distribution function maximum and the internal consistency of radial distances, "peak shapes," and coordination numbers all preclude the existence of Ce–Ce or Th–Th interactions. Consequently, with the apparent absence of metal ion–metal ion interactions, the evidence for hydrolysis and polymerization of Ce(IV) and Th(IV) found in other studies at lower concentrations[15,16] cannot be supported at these higher concentrations. If the hydrolytic and polymeric species are present, their concentrations are probably so low that they are not able to be detected in these concentrated solutions. These results are, however, consistent with those found in dilute, strongly acidic solutions. It would be of considerable interest to know at what point anion penetration predominates over solvation in the first coordination sphere surrounding a tetrapositive heavy metal ion.

Acknowledgment. The authors wish to thank Dr. Richard J. DeSando of Monsanto Research Corp., Miamisburg, Ohio, for his helpful discussions and interest in this work. Acknowledgment is also extended to the B. F. Goodrich Computer Center for kind use of the IBM 7074.

(12) D. S. Martin, R. E. Rundle, and S. A. Golden, *J. Chem. Phys.*, **24**, 1114 (1956).

(13) Figure 1 shows the agreement between the experimental coordination number of 11.2 and the assumed 12-coordinate shape function for six Ce–O interactions. These areas agree within 106.6%. An 11.2-coordinate shape function gives even better agreement with the experimental curve but does not, of course, correspond to a simple integral geometrical configuration.

(14) R. D. Larsen and G. H. Brown, to be published.

(15) K. A. Kraus and R. W. Holmberg, *J. Phys. Chem.*, **58**, 325 (1954).

(16) S. Hietanen and L. G. Sillén, *Acta Chem. Scand.*, **13**, 533 (1959).

Recalculated Values for the Diffusion Coefficients of Several Aqueous Ternary Systems at 25°[1]

by Peter J. Dunlop[2]

Institute for Enzyme Research, University of Wisconsin, Madison, Wisconsin 53706 *(Received May 7, 1964)*

There exist in the literature some accurate ternary diffusion data[3-5] which were obtained several years

(1) This work was supported, in part, by research grants from the U. S. National Science Foundation (GP-179) and from the National Institute of Arthritis and Metabolic Diseases (U.S.P.H.S.) (AM-05177).

(2) Department of Physical and Inorganic Chemistry, Adelaide University, South Australia.

(3) P. J. Dunlop and L. J. Gosting, *J. Am. Chem. Soc.*, **77**, 5238 (1955).

(4) P. J. Dunlop, *J. Phys. Chem.*, **61**, 994 (1957).

(5) P. J. Dunlop, *ibid.*, **61**, 1619 (1957).

ago with the Gouy diffusiometer and which have been interpreted in terms of previously described flow equations.[6] These flow equations are characterized by four diffusion coefficients, which may be computed from experimental diffusion data for each composition of a ternary system. Diffusion coefficients for the above systems have already been computed and reported,[3-5] but the analytical procedures available at that time either were not of a general nature or were known to be relatively inaccurate. Since the data were published, Fujita and Gosting have provided a general analytical method[7] for computing these four diffusion coefficients using data obtained with the Gouy diffusiometer. This method utilizes the concentrations of the upper and lower solutions used in each Gouy experiment, the reduced height–area ratios, $\mathfrak{D}_A$,[3] the areas, Q,[7] under the deviation graphs obtained by plotting the relative fringe deviations, Ω_j,[3] *vs.* the reduced fringe number, $f(\zeta_j)$,[3] and also the total number of interference fringes, J, obtained in each diffusion experiment. Their procedure and the others used previously to analyze the data cited above have already been described in detail.[3-5,7,8] By the method of Fujita and Gosting new values of the diffusion coefficients have been computed[9] for all the above systems. It is the purpose of this paper simply to report these new values and to compare them with those obtained earlier; in addition, the density data obtained for the diffusion experiments have been analyzed to yield data for partial specific volumes. It is not intended to give a description of the calculations since explicit details have already been published.

Results and Discussion

The only data, in addition to those already published, which are required for the calculations are the Q values for each experiment performed with the Gouy diffusiometer. For each system considered, S-I, S-II, etc., these have been computed from the original experimental data by numerical integration and are given in Table I as Q_{exptl}. The Q value for each experiment is reported with the corresponding value of the refractive index fraction of solute component 1, α_1,[3] in the diffusion boundary. Thus Q values in Table I may be correlated with the diffusion data previously reported. Also included in Table I are values of Q_{calcd} computed from the new values of the four diffusion coefficients. Comparison of the Q_{exptl} and Q_{calcd} values gives some idea of how accurately the computed values of the diffusion coefficients for the volume fixed reference frame,[10] $(D_{ij})_V$, represent the experimental data. It is believed that each experimental value of Q is accurate to better than $\pm 2 \times 10^{-4}$.

Table II gives the new values for the four diffusion coefficients for each of the five systems. The numbers in parentheses underneath each value of the $(D_{ij})_V$ are the diffusion coefficients previously reported. It is seen that the new values for systems I and II differ, sometimes quite considerably, from the old ones but that the values for systems IIIA, IIIB, and IV remain essentially unchanged. This seems to indicate that the initial method used to compute the $(D_{ij})_V$ values for these latter systems is essentially as accurate as the method of Fujita and Gosting. However, because the previous method can only be accurately used when the magnitudes of the fringe deviation graphs are quite sensitive to changes in the value of α, it is by no means as general and hence the procedure of Fujita and Gosting is to be preferred. It is believed that the new data for systems I and II are more accurate than those previously reported. These new $(D_{ij})_V$ values may be used to compute the reduced-height area ratios with an average deviation for all systems of $\pm 0.05\%$ and a maximum deviation of 0.09%.

The original articles[3-5] also reported the densities, d, of the solutions used in the various diffusion experiments. These sets of data have been fitted by the method of least squares to series expanded about the mean solute concentrations for each system. The following equations were obtained

$$\text{S-I: } d = 1.012469 + 0.023971(C_1 - \bar{C}_1) - 0.046088(C_2 - \bar{C}_2) \text{ (av. dev. } = \pm 0.001\%)$$

$$\text{S-II: } d = 1.011303 + 0.023922(C_1 - \bar{C}_1) + 0.040099(C_2 - \bar{C}_2) \text{ (av. dev. } = \pm 0.0007\%)$$

$$\text{S-IIIA: } d = 1.004732 + 0.003896(c_1 - \bar{c}_1) + 0.006295(c_2 - \bar{c}_2) \text{ (av. dev. } = \pm 0.0009\%)$$

$$\text{S-IIIB: } d = 1.023178 + 0.003894(c_1 - \bar{c}_1) + 0.006118(c_2 - \bar{c}_2) \text{ (av. dev. } = \pm 0.001\%)$$

$$\text{S-IV: } d = 1.007964 + 0.003896(c_1 - \bar{c}_1) + 0.002638(c_2 - \bar{c}_2) \text{ (av. dev. } = \pm 0.001\%)$$

(6) R. L. Baldwin, P. J. Dunlop, and L. J. Gosting, *J. Am. Chem. Soc.*, **77**, 5235 (1955).

(7) H. Fujita and L. J. Gosting, *J. Phys. Chem.*, **64**, 1256 (1960).

(8) L. A. Woolf, D. G. Miller, and L. J. Gosting, *J. Am. Chem. Soc.*, **84**, 317 (1962).

(9) These computations were performed with a Bendix G-15 computer using programs written by R. P. Wendt, *J. Phys. Chem.*, **63**, 1287 (1959).

(10) G. J. Hooyman, H. Holtan, Jr., P. Mazur, and S. R. de Groot, *Physica*, **19**, 1095 (1953).

Table I[a,b]: Experimental and Computed Areas of the Fringe Deviation Graphs

S-I: 0 = H_2O; 1 = LiCl; 2 = KCl
($\bar{C}_1$ = 0.25; $\bar{C}_2$ = 0.20) ($\bar{v}_1$ = 0.4358; $\bar{v}_2$ = 0.3830)

α_1	0.0008	0.1002	0.8303	0.8309	0.9999
$Q_{exptl} \times 10^4$	0.00	10.01	36.31	36.00	31.01
$Q_{calcd} \times 10^4$	0.32	9.89	35.60	35.59	31.93

S-II: 0 = H_2O; 1 = LiCl; 2 = NaCl
($\bar{C}_1$ = 0.25; $\bar{C}_2$ = 0.20) ($\bar{v}_1$ = 0.4370; $\bar{v}_2$ = 0.3150)

α_1	0.0002	0.2654	0.6995	0.9997
$Q_{exptl} \times 10^4$	−4.43	0.00	8.03	12.50
$Q_{calcd} \times 10^4$	−5.23	0.90	8.45	11.98

S-IIIA: 0 = H_2O; 1 = raffinose; 2 = KCl
($\bar{c}_1$ = 0.75; $\bar{c}_2$ = 0.75) ($\bar{v}_1$ = 0.6122; $\bar{v}_2$ = 0.3716)

α_1	−0.0005	0.0027	1.0001	1.0057
$Q_{exptl} \times 10^4$	−4.60	2.14	5.46	0.48
$Q_{calcd} \times 10^4$	−4.12	1.66	5.46	0.48

S-IIIB: 0 = H_2O; 1 = raffinose; 2 = KCl
($\bar{c}_1$ = 0.75; $\bar{c}_2$ = 3.73) ($\bar{v}_1$ = 0.6122; $\bar{v}_2$ = 0.3892)

α_1	0.0003	0.0040	1.0002	1.0247
$Q_{exptl} \times 10^4$	−6.85	−1.57	21.28	−2.63
$Q_{calcd} \times 10^4$	−7.52	−0.83	19.78	−1.19

S-IV: 0 = H_2O; 1 = raffinose; 2 = urea
($\bar{c}_1$ = 0.75; $\bar{c}_2$ = 3.00) ($\bar{v}_1$ = 0.6122; $\bar{v}_2$ = 0.7383)

α_1	0.0010	0.0233	1.0004	1.0198
$Q_{exptl} \times 10^4$	1.16	23.97	7.71	−4.90
$Q_{calcd} \times 10^4$	1.04	24.10	7.26	−4.47

[a] The mean solute concentrations for systems I and II are in moles/l., $\bar{C}_i$, and the mean solute concentrations for systems IIIA, IIIB, and IV are in g./100 ml., $\bar{c}_i$. [b] The partial specific volumes are expressed in ml./g.

Table II[a]: Recalculated Diffusion Coefficients $(D_{ij})_V$ for the Volume Frame of Reference[b]

System	$(D_{11})_V \times 10^5$	$(D_{12})_V \times 10^5$	$(D_{21})_V \times 10^5$	$(D_{22})_V \times 10^5$
S-I[c]	1.1309	−0.0017	0.2196	1.8120
	(1.145)	(−0.007)	(0.204)	(1.817)
S-II	1.1048	0.0985	0.1928	1.3520
	(1.069)	(0.141)	(0.225)	(1.316)
S-IIIA	0.4303	0.0023	0.0095	1.8274
	(0.4303)	(0.0022)	(0.0094)	(1.828)
S-IIIB	0.4300	0.0056	0.0357	1.8179
	(0.4309)	(0.0066)	(0.0327)	(1.815)
S-IV	0.4206	0.0000	0.0114	1.3207
	(0.4210)	(0.0000)	(0.0106)	(1.321)

[a] All diffusion coefficients have units of cm.^{2} sec.$^{-1}$. [b] See ref. 10. [c] The data for the first two systems are for concentrations expressed in moles/l.; the data for last two systems are for concentrations expressed in g./100 ml. It should be noted that the values of the *cross-term* diffusion coefficients depend on the concentration scale used.

Using the coefficients in these equations and an expression[11] derived in a previous publication, partial specific volumes, $\bar{v}_i$, for the solute components in each of the five systems were computed. These values, together with the corresponding solute concentrations, are listed in Table I.

(11) P. J. Dunlop and L. J. Gosting, *J. Phys. Chem.*, **63**, 86 (1959).

Irradiation Effects in the Platinum-Catalyzed Deuterium Exchange of Water with Benzene and Other Substances[1]

by W. G. Brown, J. L. Garnett,[2] and O. W. VanHook

Chemistry Division, Argonne National Laboratory, Argonne, Illinois *(Received May 25, 1964)*

In the process of initiating deuterium exchange between water and an organic material, *e.g.*, benzene, by heating with platinum oxide, recently reported[3] and described as "self-activation," the hydrogen required for the generation of active sites must be supplied by C–H dissociative mechanisms. It could be anticipated, therefore, that the activation process, and hence the scope of this technique for isotopic labeling, might be extended by ionizing radiation whether supplied externally, perhaps by γ-irradiation, or internally as in the production of tritium-labeled materials. With the deuterium oxide–benzene–platinum oxide as a test system of good reproducibility, an accelerating effect of exposure to γ-rays prior to heating is actually found. Prior irradiation with ultraviolet light is also effective in facilitating activation of the catalyst and this finding has practical as well as theoretical interest. Preliminary experiments indicate, for example, that photoactivation will initiate deuterium exchange in pyridine, a substance otherwise immune to exchange by the "self-activation" technique.

Reaction mixtures, consisting typically of 1.7 g. of benzene, 1.6 g. of deuterium oxide, and 0.02 g. of platinum oxide, were outgassed, sealed in appropriate ampoules, irradiated, and heated as shown in Tables I and II. The products analyzed by low-voltage mass spectrometry.

(1) Based on work performed under the auspices of the U. S. Atomic Energy Commission.

(2) School of Chemistry, University of New South Wales, Kensington, N. S. W., Australia.

(3) J. L. Garnett and W. A. Sollich, *J. Phys. Chem.*, **68**, 436 (1964).

Table I: Exchange of Deuterium between Benzene and Deuterium Oxide under "Self-Activation" Conditions

Temp.	Time, hr.	Isotope distribution d_0	d_1	d_2	d_3	d_4	d_5	d_6
114	12	99.7	0.30					
	16	99.6	0.40	0.03	0.03	0.03	0.03	0.05
	21	97.6	0.90	0.40	0.20	0.20	0.20	0.40
	24	94.7	1.30	0.50	0.50	0.50	0.80	1.60
	41	86.9	2.20	1.30	1.00	1.40	2.00	5.30
	51	71.0	7.30	2.40	2.20	3.50	6.30	7.20
	66	23.9	23.3	15.3	10.6	10.7	10.4	5.90
134	0.5	100	...					
	1.5	99.7	0.30					
	2.5	99.0	0.27	0.09	0.09	0.09	0.09	0.09
	Equil., calcd.[a]	1.56	9.37	23.5	31.2	23.5	9.37	1.56

[a] Calculated statistical distribution of deuterium at exchange equilibrium.

Table II: Effect of Radiation on Catalyst Activity in the Exchange of Benzene with Deuterium Oxide

Irradiation[a] Source	Exposure	Heating period Temp., °C.	Time, hr.	Isotope distribution[b] d_0	d_1	d_2	d_3	d_4	d_5	d_6
Co^{60}	0.1 Mrad	134	1.5	99.7	0.20	0.04	0.02	0.01	0.01	0.02
	10 Mrads	134	2.5	67.5	18.7	6.40	3.11	1.70	1.55	1.13
	3 Mrads	114	21.7	93.6	2.64	0.86	0.50	0.46	0.68	1.23
High pressure	1 hr.	134	2.5	91.0	3.50	0.90	0.60	0.60	1.20	2.40
arc	1 hr.	114	21.7	57.4	16.9	7.40	5.70	7.20	2.90	2.60
c	1 hr.	114	21.7	77.7	14.5	3.80	1.64	0.93	0.76	0.80
Low pressure	1 hr.	134	1.5	80.6	12.6	3.30	1.40	0.76	0.67	0.71
arc	0.25 hr.	114	21.7	80.4	9.70	2.60	1.70	1.50	1.90	2.20
	1 hr.	114	21.7	15.8	20.6	18.7	15.5	16.1	9.50	3.80
d	1 hr.	114	21.7	28.0	26.0	16.0	10.0	7.50	6.50	4.00
e	1 hr.	114	21.7	96.9	2.10	0.40	0.18	0.11	0.09	0.18
f	1 hr.	114	21.7	29.2	25.4	16.0	11.2	8.90	6.40	3.00

[a] Cobalt-60 γ-ray exposures in Mrads at a dose rate of 4×10^6 rads (room temperature). Low pressure arc exposures made at a distance of 40 mm. from a coiled mercury arc (Nester–Faust UV-300). High pressure arc exposures with sample, forced air-cooled, at 60 mm. from a high pressure arc (Engelhard Industries 673A-36). [b] Benzene–deuterium oxide ratio such as to provide a statistical deuterium distribution 55:45. [c] Benzene–deuterium oxide mixture irradiated; platinum oxide introduced subsequently. [d] Vycor ampoule, all others quartz. [e] Benzene–platinum oxide mixture irradiated; deuterium oxide introduced subsequently. [f] Deuterium oxide–platinum oxide irradiated, benzene introduced subsequently.

Apart from any radiation effects, the rate of deuterium exchange with benzene and the distribution of deuterated species may vary with the degree of agitation and the particular batch of platinum oxide. Under the conditions employed, and with all experiments done on one lot of platinum oxide, the behavior is reproducible and the onset of exchange under self-activation after a period of incubation, approximately 12 hr. at 114° or a much shorter time at 134°, can be seen clearly in the data of Table I. These results illustrate quite strikingly, in the early buildup of highly deuterated species, the relative importance of sites favorable for multiple exchange,[4,5] in this mode of activation. The accelerating effect of preirradiation appears in the data of Table II relating to experiments under conditions identical otherwise with those pertaining to Table I.

Since benzene absorbs strongly in the wave length region most effective in photoactivation, it is a plausible postulate that a photochemical product derived from benzene is an active reducing agent for platinum oxide. However, irradiation of a benzene–platinum oxide mixture to which deuterium oxide is added subsequently does not produce an appreciable effect. But the ir-

(4) (a) J. L. Garnett and W. A. Sollich, *J. Catalysis*, 2, 350 (1963); (b) *ibid.*, 2, 359 (1963).

(5) J. R. Anderson and C. Kemball, *Advan. Catalysis*, 9, 51 (1957).

radiation of a deuterium oxide–platinum oxide mixture, with subsequent addition of benzene, is effective, and so also is the irradiation of a benzene–deuterium oxide mixture with subsequent addition of platinum oxide. The acceleration due to irradiation is not simulated by hydrogen peroxide which, added in concentrations up to 3×10^{-2} *M*, has very little effect. It appears therefore that photochemical excitation in platinum oxide and a resultant interaction with water may be involved in the generation of active centers that grow or multiply during the subsequent heat incubation. The photochemical activation is reminiscent of the photochemical reduction of zinc oxide[6] and of mercuric sulfide[7] in aqueous suspensions.

Cyclohexane responded poorly to the self-activation exchange technique with deuterium uptake to the extent of 0.1% after 68 hr. at 134°; prior exposure under the low pressure mercury lamp brought about a modest twofold increase in deuterium content. Exposure of a mixture containing pyridine, deuterium oxide, and platinum oxide to the low pressure source for 1 hr., followed by heating to 134° for 17 hr., effected deuteration to the extent of 0.8%; without the ultraviolet exposure and heated for 60 hr. at 134° there was no detectable exchange.

The distribution of label in the benzene, cyclohexane, and pyridine, deuterated on irradiation-activated catalyst, indicates concurrent multiple and stepwise exchange. There is an indication, to be tested in future studies, that with benzene at least, ultraviolet irradiation is somewhat more effective in activating sites on which stepwise exchange occurs.

(6) J. G. Calvert, K. Theurer, G. T. Rankin, and W. M. MacNevin, *J. Am. Chem. Soc.*, **76**, 2575 (1954).

(7) L. I. Grossweiner, *J. Phys. Chem.*, **59**, 742 (1955).

Electron Spin Resonance Studies of Radical Reactions in Irradiated Alkyl Halides at Low Temperatures

by P. B. Ayscough and H. E. Evans[1]

Department of Physical Chemistry, The University, Leeds 2, England *(Received September 2, 1963)*

The behavior of organic radicals trapped in solid matrices at low temperatures may often be studied by electron spin resonance methods. In many cases the radicals disappear on standing without significant change in the form of the hyperfine spectra, suggesting a simple recombination or disproportionation reaction. There are, however, a few examples of systems in which the occurrence of secondary reactions is indicated by changes in the hyperfine structure of the e.s.r. spectra. For instance, the addition of phenyl radicals to olefins at −196° has been observed by Bennett and Thomas,[2] while the isomerization of *n*-propyl, *n*-butyl, and isobutyl radicals at −196° has been reported by Ayscough and Thomson.[3,4] Attempts to extend the observations on *n*-propyl and *n*-butyl radicals to higher temperatures (−180 to −150°) were largely unsuccessful because the rate of disappearance of the radicals increases so much that the change from a six-line to an eight-line spectrum (corresponding to the formation of isopropyl or *sec*-butyl radicals) cannot be followed readily. Furthermore, the asymmetry of the spectra, suggesting the presence of another radical, possibly halogenated, becomes more pronounced as the temperature increases. It was therefore decided to confine further studies of isomerization reactions to irradiated isobutyl halides in which these problems are much less serious.

Experimental

Commercial samples of alkyl halides were dried over calcium chloride, distilled through a 20-cm. column packed with Fenske helices, exhaustively degassed ($<10^{-5}$ mm. pressure), and distilled under vacuum before being sealed into sample tubes and frozen by quenching in liquid nitrogen. The special high purity isobutyl bromide was purified using a Perkin–Elmer fractometer gas chromatography unit which permits the preparation of 0.5-ml. samples. Isobutene was supplied by I.C.I. Ltd., and isobutane was taken from a standard sample supplied by the National Physical Laboratory. *t*-Butyl bromide-d_1 was prepared by ultraviolet-catalyzed addition of deuterium bromide (produced by the action of deuterium oxide on phosphorus tribromide) to isobutene.

A Varian e.p.r. spectrometer using 100 kc./sec. modulation and a Mullard 25-cm. electromagnet were used. Samples approximately 0.2 ml. in volume were irradiated in tubes of high purity quartz ("Spectrosil") using a 1750-c. Co^{60} source. The dose rate was about 5×10^{17} e.v. ml.$^{-1}$ min.$^{-1}$; the time of irradiation

(1) Berkeley Nuclear Laboratories of the Central Electricity Generating Board, Gloucestershire.

(2) J. E. Bennett and A. Thomas, Sixth International Symposium on Free Radicals, Cambridge, England, 1963.

(3) P. B. Ayscough and C. Thomson, *Trans. Faraday Soc.*, **58**, 1477 (1962).

(4) P. B. Ayscough, K. J. Ivin, J. H. O'Donnell and C. Thomson, Fifth International Symposium on Free Radicals, Uppsala, Sweden, 1961.

5–30 min. Irradiated samples were examined at −196° using a dewar vessel inside the cavity and at higher temperatures using a nitrogen flow system. For accurate temperature control between −196 and 165° an external thermostat was constructed. This enabled the temperature to be preset and maintained within ±1° for long periods.

Results

(1) *Reactions in Isobutyl Halides.* When samples of γ-irradiated isobutyl halides are maintained at −196° for several days, the original five-line spectrum of isobutyl radicals with an average hyperfine splitting of 21 gauss changes to the ten-line spectrum of *t*-butyl radicals with an average hyperfine splitting of 22 gauss (see Fig. 1). (The two outer lines of the *t*-butyl spectrum are observed only at higher gain.) At −196° the change corresponds, apparently, to a first-order process, suggesting the intramolecular isomerization reaction[4] shown in eq. 1.

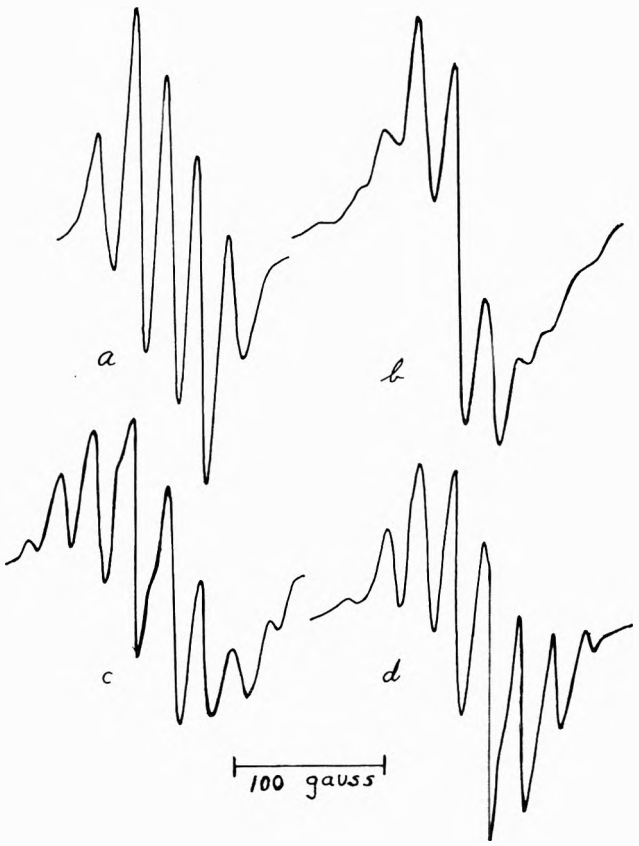

Figure 1. E.s.r. spectrum of γ-irradiated alkyl bromides at −196°: (a) isobutyl bromide immediately after irradiation; (b) isobutyl bromide with 0.1% *t*-butyl bromide after 20 days at −196°; (c) isobutyl bromide with 1% *t*-butyl bromide after 20 days at −196°; (d) *t*-butyl bromide.

$$(CH_3)_2\dot{C}HCH_2 \longrightarrow (CH_3)_3\dot{C} \qquad (1)$$

This interpretation was supported by the observation that in irradiated isobutyl chloride the net loss of radicals is negligible.

While further study showed the change to be qualitatively reproducible, its rate was greatly affected by the degree of crystallinity of the sample and by the radiation dose. At higher temperatures (−177, −172, and −167°) the reaction in isobutyl bromide did not follow the simple first-order kinetics observed at −196° in the preliminary experiments and was not reproducible in rate. These observations suggested that reactions with some of the products of the radiolysis might also be involved. These products include hydrogen bromide, bromine, *t*-butyl bromide and other isomeric butyl bromides, isobutene, and other hydrocarbons.[5] It should be noted that the products of the reactions

$$(CH_3)_2CH\dot{C}H_2 + (CH_3)_3CBr \longrightarrow (CH_3)_2CHCH_2Br + (CH_3)_3\dot{C} \qquad (2)$$

$$(CH_3)_2CH\dot{C}H_2 + (CH_3)_2C{=}CH_2 \longrightarrow (CH_3)_2\dot{C}CH_2CH_2CH(CH_3)_2 \qquad (3)$$

would each give ten-line spectra. (In alkyl halide matrices the hyperfine splittings of methylene protons in the β-position relative to the unpaired electron are in the ratio 2:1 because of the unsymmetrical configuration of the radical.[3]) Further experiments were therefore carried out to study the effect of these additives.

(2) *Reactions in Isobutyl Bromide with Various Additives.* Experiments were carried out in which known amounts (2–10%) of various of the radiolysis products were added to the isobutyl bromide before irradiation. The amounts added were greatly in excess of the yield from the irradiation itself, so any effect of one or more of these additives on the subsequent reactions of the trapped isobutyl radicals must be large to be significant. It was therefore not necessary to attempt precise measurements of the rates. Samples were observed for several days while maintained at −196°. The rate of isomerization was determined approximately by measuring the rate of growth, under standard experimental conditions, of the ten-line spectrum attributed to *t*-butyl radicals. This rate was compared with that observed using distilled commercial samples of isobutyl bromide. As these samples are known to contain about 1% *t*-butyl bromide, this procedure involves, in effect, measurement of a series

(5) W. S. Wilcox, *Radiation Res.*, **10**, 112 (1959).

of competition reactions. These experiments are briefly summarized as follows.

(1) Added bromide, hydrogen bromide, butene-1 or isobutene cause no change in the observed rate of isomerization though the over-all rate of decay of the spectrum is increased slightly.

(2) Added *t*-butyl bromide and *t*-butyl bromide-d_1 cause an increase in the rate of isomerization. For instance, the rate is doubled by the addition of about 6% of *t*-butyl bromide. However, in both cases a ten-line spectrum is produced, whereas the $(CH_3)_3\dot{C}CH_2D$ radical gives a nine-line spectrum.

(3) Irradiation of a 1:1 mixture of isobutyl bromide and *t*-butyl bromide-d_1 gives a mixture of five-line and nine-line spectra initially; on standing, the ten-line spectrum of the *t*-butyl radical appears, but there is no increase in the size of the nine-line spectrum.

(4) The removal of traces of *t*-butyl bromide by repeated gas chromatographic separation (*i.e.*, to less than 0.1%) caused the rate of the observed reaction to decrease by a factor of 50 to 100.

(5) The rate of isomerization was shown to be insensitive to changes in surface area by adding powdered quartz before irradiation.

(6) Continuous irradiation with visible light has no effect on the rate.

These results are to be compared with observations on γ-irradiated isobutene and isobutane which gave mixtures of five- and ten-line spectra (attributed to isobutyl and *t*-butyl radicals) but provide no evidence for isomerization.

Discussion

One of the special problems encountered when applying e.s.r. methods to the study of reactions in solid matrices is associated with the necessarily low activation energy of processes occurring in solids at low temperatures. Because of this, the rate of, for instance, recombination of trapped species is likely to be greatly influenced by variations in the local environment which affect the rate of diffusion through the matrix. Reactions occurring in the trapping site, *e.g.*, intramolecular isomerization, should not be so sensitive to such environmental factors. The evidence presented in this paper appears to contradict this view if this is indeed the observed reaction. Apart from recombination, the three most likely reactions of isobutyl radicals in this system are (1) isomerization, (2) bromine abstraction, and (3) addition to olefin. The experiments using monodeuterated *t*-butyl bromide show that bromine abstraction is negligible, and addition to olefin is eliminated by the negligible effect of added butene-1 and isobutene. On the other hand, if the observed reaction is simply intramolecular isomerization, it is difficult to account for the extraordinary sensitivity toward traces of *t*-butyl bromide. The effect is certainly not chemical, so it must result from modification of the trapping sites of the isobutyl radicals. Without much further study one can only speculate about the nature of such a modification. It may be a simple physical distortion resulting in greater mobility for the trapped radical, or it may be a change in the local crystal fields which reduces the activation energy of the isomerization step. Perhaps more likely is the production of metastable domains on rapid quenching of the doped samples: the increased mobility of the radicals during the consequent slow phase change, together with the release of energy during this process, may allow isomerization to occur in these systems but not in a very pure sample. Some earlier observations made in this laboratory indicate a relationship between phase changes in solid chloroform and carbon tetrachloride and slow, reversible changes in the e.s.r. spectra following γ-irradiation.[6]

Acknowledgment. We wish to acknowledge generous financial support from D.S.I.R. in the form of maintenance and capital grants. We are also grateful to Professor F. S. Dainton, F.R.S., for permitting the use of radiation facilities presented to him by the Rockefeller Foundation.

(6) A. P. McCann, Ph.D. Thesis, University of Leeds, England, 1961.

Thermal Reactions of Organic Nitrogen Compounds. III. 1-Isopropylpyrrole

by I. A. Jacobson, Jr., and H. B. Jensen

Laramie Petroleum Research Center, Bureau of Mines, U. S. Department of the Interior, Laramie, Wyoming
(*Received November 4, 1963*)

This is the third and final publication of a series dealing with the thermal reactions of alkylpyrroles. Only a limited amount of the literature on thermal reactions of organic nitrogen compounds deals with pyrrolic compounds,[1-7] and the majority of the perti-

(1) G. Ciamician and P. Maghaghi, *Ber.*, **18**, 1828 (1885).

(2) G. Ciamician and P. Silber, *ibid.*, **20**, 698 (1887).

(3) P. Crespieux and A. Pictet, *ibid.*, **28**, 1904 (1895).

(4) A. Pictet, *ibid.*, **37**, 2792 (1904); **38**, 1946 (1905).

(5) A. G. Oosterhuis and J. P. Wibaut, *Rec. trav. chim.*, **55**, 348 (1936).

(6) W. Reppe, *et al.*, *Ann.*, **596**, 80 (1955).

nent papers appeared more than 50 years ago. The first paper[8] of the Bureau's study of pyrrolic shale oil compounds described the thermal reactions of 1-methylpyrrole and the second[9] dealt with 1-*n*-butylpyrrole. To obtain information on the thermal reactions of other types of alkyl-substituted pyrroles, 1-isopropylpyrrole was selected as a representative branched-chain alkyl member.

Experimental

Materials. 1-Isopropylpyrrole was synthesized by the thermal decomposition of the diisopropylamine salt of mucic acid[10] and was purified by distillation, refluxing with calcium hydride, and redistillation. The final product was more than 98 mole % pure as determined by a freezing-point method.

2-Isopropylpyrrole and 3-isopropylpyrrole were prepared for use in some flow studies and for g.l.c. calibrations. A silver nitrate solution (0.25 mole in 50 ml. of water) was stirred into an equimolar mixture of pyrrole (0.25 mole), 2-iodopropane, and sodium bicarbonate in 50 ml. of toluene. The heterogeneous mixture was heated and stirred at 65° for 6 hr.[11] The 2- and 3-isopropylpyrrole were separated from the reaction mixture and distilled. G.l.c. studies on selected fractions indicated a purity of about 97% for the 3-isopropylpyrrole, and a purity of about 72% for the 2-isopropylpyrrole. The principal contaminant in each case was the other isomer.

Apparatus. The experimental work was performed using both a flow system and a static system. The equipment has been previously described.[9] The flow system's collection train was modified so that a representative sample of the liquid and of the gaseous products could be collected after conditions had stabilized.

Procedure. Flow studies were performed using the general procedure previously described.[9] Flow runs were made on 1-isopropylpyrrole at selected temperatures between 465 and 575°; several residence times were used at each temperature studied. The flow runs were made using combinations of the following conditions: empty reaction tube, packed reaction tube, presence of a diluent gas (purified nitrogen), absence of a diluent gas, and presence of nitric oxide. For all runs, the products were vented until steady-state conditions were obtained. This was assumed to be after 1 ml. of sample had been introduced into the reaction system. The product flow then was directed through a liquid nitrogen trap. The material that did not condense was collected in an evacuated gas bulb. After the completion of a run, the material that had condensed in the liquid nitrogen trap was warmed to room temperature and the gases that evolved were collected in the same gas bulb.

Flow runs on 2- and 3-isopropylpyrrole were made in the same manner. These compounds were studied at selected temperatures in the range of 500 to 550°.

Static thermal runs were made on 1-isopropylpyrrole in the manner previously described.[9] These runs were made between 340 and 400° with several residence times used at each temperature.

Analysis. Relative concentrations of the various compounds in the liquid products were determined by g.l.c., and the composition of the gaseous products was determined by mass spectral analysis.

Results and Discussion

It was found that 1-isopropylpyrrole isomerized irreversibly to 2-isopropylpyrrole which in turn isomerized reversibly to 3-isopropylpyrrole. These isomerization reactions were not affected by changes in the area-to-volume ratio, by presence or absence of an inert diluent gas, or by addition of nitric oxide. These data indicate that these isomerization reactions are homogeneous, nonchain, and unimolecular.

There were decomposition reactions in conjunction with the various isomerization reactions. The decomposition products from the 1-isopropylpyrrole work consisted of 3-methylpyridine, pyrrole, 2-methylpyrrole, 3-methylpyrrole, 2-ethylpyrrole, 3-ethylpyrrole, and hydrocarbons. The absence of 1-substituted pyrroles in the decomposition products demonstrated that the alkyl group had isomerized to the 2-position of the pyrrole ring before any decomposition took place. The relative concentrations of the decomposition products were affected by changes in the area-to-volume ratio, by absence or presence of any inert diluent gas, and by addition of nitric oxide. These data indicate that these decomposition reactions were heterogeneous, free-radical reactions.

Samples of 2-isopropylpyrrole and 3-isopropylpyrrole were also thermally studied. When either of these compounds was the starting material, the reaction products consisted of a mixture of 2-isopropylpyrrole and 3-isopropylpyrrole and of decomposition materials. No 1-isopropylpyrrole was found in the reaction products, thus demonstrating the irreversibility of the 1-

(7) J. M. Patterson and F. Drenchko, *J. Org. Chem.*, **27**, 1650 (1962).

(8) I. A. Jacobson, Jr., H. H. Heady, and G. U. Dinneen, *J. Phys. Chem.*, **62**, 1563 (1958).

(9) I. A. Jacobson, Jr., and T. B. Jensen, *ibid.*, **66**, 1245 (1962).

(10) L. C. Craig and R. M. Hixon, *J. Am. Chem. Soc.*, **53**, 187 (1931).

(11) The authors thank Dr. C. A. VanderWerf of the University of Kansas for suggesting this synthesis method.

to 2- isomerization and the reversibility of the 2- to 3-isomerization.

The preceding data demonstrated that the only route by which 1-isopropylpyrrole disappeared was by an irreversible isomerization to 2-isopropylpyrrole. First-order rate equations were used for the kinetic calculation of the isomerization of 1-isopropylpyrrole to 2-isopropylpyrrole based on the disappearance of the 1- isomer. The specific reaction rate constant was calculated for each temperature studied for both the static and the flow work. From these specific reaction rate constants, activation energies were calculated for the flow work and for the static work. These two activation energies showed no significant difference; therefore, the data from both the flow work and from the static work were used to evaluate the Arrhenius equation for the isomerization of 1-isopropylpyrrole to the 2-isopropylpyrrole isomer. In the temperature range studied, 340 to 575°, this equation was found to be

$$k_{12} = 1.10 \times 10^{13} e^{-(55{,}500 \pm 2600/RT)} \text{ sec.}^{-1}$$

The two previous papers of this series[8,9] have reported the isomerization reactions of 1-methylpyrrole and 1-*n*-butylpyrrole. From these results and those reported for 1-isopropylpyrrole in this paper, it was found that in each case the alkyl group isomerized by the route

1-alkylpyrrole → 2-alkylpyrrole ⇆ 3-alkylpyrrole

Therefore, a total of nine isomerization reactions have been studied—three for each compound.

Table I: Entropies and Heats of Activation for the Isomerization Reactions of Alkylpyrroles at 500°

Reaction[a]	ΔS^*, e.u.	ΔH^*, kcal./mole[b]
	Methylpyrrole	
k_{12}	−1.3	56.8 ± 1.6
k_{23}	−29	34.5 ± 3.9
k_{32}	−10	48.1 ± 2.7
	n-Butylpyrrole	
k_{12}	−0.7	56.4 ± 0.2
k_{23}	−15	44.0 ± 1.5
k_{32}	−8.9	48.3 ± 1.7
	Isopropylpyrrole	
k_{12}	−2.7	54.0 ± 0.6
k_{23}	−14	44.7 ± 3.7
k_{32}	−12	45.2 ± 3.8

[a] For the reaction: 1 alkylpyrrole $\xrightarrow{k_{12}}$ 2-alkylpyrrole $\underset{k_{32}}{\overset{k_{23}}{\rightleftharpoons}}$ 3-alkylpyrrole. [b] The plus or minus values are for one standard deviation.

Entropies and heats of activation were calculated for all nine of the pyrrole isomerizations studied. These calculated values are presented in Table I. When the heat of activation was plotted against the entropy of activation, a straight line resulted. The slope of this line, as determined by a least-squares method, weighing each point in proportion to its variance, gave the isokinetic temperature. This temperature was found to be 860°K. and had a correlation index of 0.92. The existence of this linear relationship indicates that either the reaction mechanism or the transition state is similar for all nine isomerization reactions.[12] The studies were all carried out below the isokinetic temperature; therefore, the isomerization reactions were enthalpy controlled.

Acknowledgment. Thanks are extended to API Research Project 52 for purification and purity determination of 1-isopropylpyrrole. The work reported in this note was done under a cooperative agreement between the University of Wyoming and the Bureau of Mines, U. S. Department of the Interior.

(12) J. E. Leffler, *J. Org. Chem.*, **20**, 1202 (1955).

Resistance–Pressure Relation of the Reaction Product of Pyromellitic Anhydride and Pyrene

by J. H. Lupinski, C. M. Huggins, and H. G. Pfeiffer

General Electric Research Laboratory, Schenectady, New York
(Received January 10, 1964)

Electrically conducting powders exhibiting a strong pressure dependence have long been known as, for example, in the carbon microphone. These materials have not been overly successful as pressure-measuring devices because of drift and hysteresis in the pressure–conductivity relationship. In several recent publications,[1-3] a new family of pressure-sensitive compounds has been reported. Some theoretical arguments were presented which correlated the pressure–conductivity relation with their intrinsic molecular properties rather than with the area and quality of contact between the

(1) J. J. Brophy and J. W. Buttrey, "Organic Semiconductors," The Macmillan Company, New York, N. Y., 1962, p. 143.

(2) H. A. Pohl and E. H. Engelhardt, *J. Phys. Chem.*, **66**, 2085 (1962).

(3) H. A. Pohl, A. Rembaum, and A. Henry, *J. Am. Chem. Soc.*, **84**, 2699 (1962).

powder grains. The pressure dependence reported by Pohl and co-workers was of the form, $\log \sigma = kp^{1/2}$, where σ is the conductivity and p the pressure. Because of the possible significance in pressure-measuring devices and for theoretical considerations, it was decided to investigate one of these materials over a wider range of pressure.

Experimental

A mixture of 20.2 g. of pyrene, 11.8 g. of pyromellitic anhydride, and 13.6 g. of zinc chloride was ground in a mortar and placed in a test tube which was suspended in a 2-l. round-bottomed flask in which a temperature of 300° was maintained by refluxing benzophenone. The reactants were protected from oxygen by an atmosphere of nitrogen. After being heated for 24 hr., the black reaction mixture was removed and ground in a mortar. It was then washed five times with 1 *N* HCl and then once with water. The washed product was extracted with water in a Soxhlet extractor for 35 hr. Still in the Soxhlet extractor, the material was treated with boiling ethyl alcohol for 18 hr. and finally was extracted for 36 hr. with toluene. Each extraction was considered complete when the solvent remained colorless. The product was removed from the extractor thimble and dried under reduced pressure at 50° for 30 hr. The yield was 19.5 g.

The material was pressed into pellets under a pressure of 12,000 kg./cm.^{2} for 5 min. For resistivity measurements under pressure, the pellets were placed in a die provided with a bakelite lining having the same diameter as the pellet and both electrodes covered the sample completely. Low pressures (up to 600 kg./cm.^{2}) were applied with a heavy-duty C-clamp; the die and a pressure gauge were placed in the clamp. For higher pressures (600–12,000 kg./cm.^{2}) a hydraulic press was used. Pellets were also pressed at 50,000 atm. and 100 and 200°; no thermoplastic behavior was found; the materials were still obviously compacted powders; the samples were brittle and disintegrated into powders when rubbed.

In the course of the electrical measurements (see Fig. 1), it was found that there is a marked sample–electrode "contact" effect. Therefore, some of the pellets were provided with evaporated gold electrodes (about 1 μ thick). Especially at low pressures (up to 50 kg./cm.^{2}), there is a significant difference between the coated and uncoated pellets. When plotted on an expanded scale, the resistivity is virtually independent of pressure in these gold-coated samples at pressures up to 50 kg./cm.^{2} (insert in Fig. 1). At higher pressures, the behaviors of the coated and uncoated samples are convergent. Since the pellets are exposed to fairly high pressures they do change their dimensions. Measurements of these changes in the samples are complicated by the fact that the steel pistons also change under pressure. By investigating the pistons only, it was found that the changes in the pellets are small compared to those in the pistons. The resistivity data in Fig. 1 have not been corrected for dimension changes in the sample; however, we estimate the changes to be about 10% at 12,000 kg./cm.^{2}. Dimension changes of a sample under high pressure were also reported by Chapman and co-workers.[4]

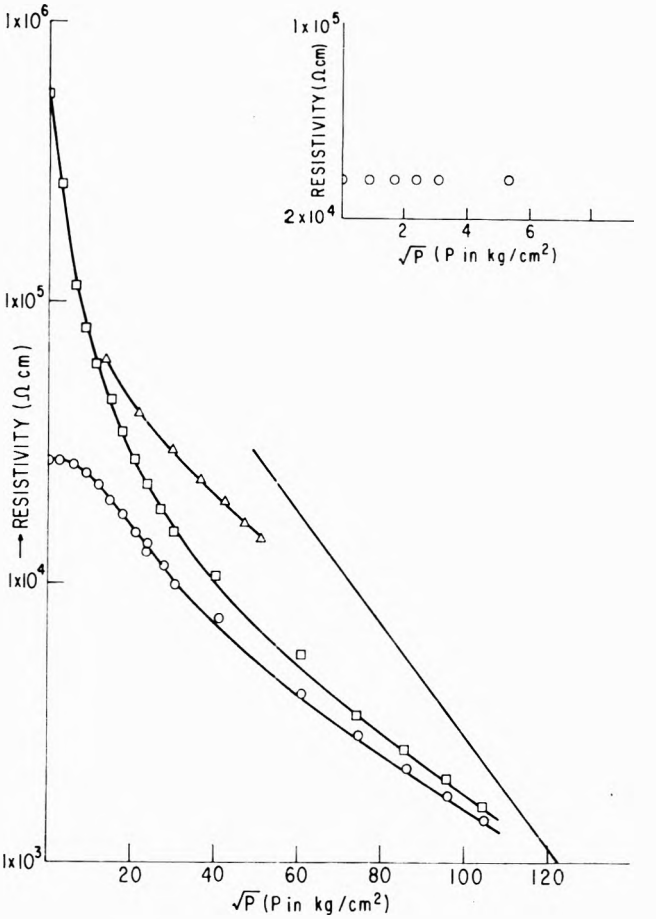

Figure 1. Experimental details showing electrical behavior of condensation product of pyrene and pyromellitic acid dianhydride: ●, our data on uncoated sample; ⊙, our data on gold-coated sample; Δ, data from ref. 2 (Fig. 1, sample 39); —, data from ref. 3 (Fig. 4, Sample 71). Only the slope of this line can be represented, since resistance rather than resistivity was reported. Insert: gold-coated sample; expanded scale of low pressure range.

(4) D. Chapman, R. J. Warn, A. G. Fitzgerald, and A. D. Yoffe, *Trans. Faraday Soc.*, **60**, 294 (1964).

In the pressure-resistance relation, hysteresis effects larger than would be tolerable in a sensitive pressure transducer were observed. After a pressure cycle of 0–12,000 kg./cm.^{2} one sample showed a 10% reduction in thickness.

Discussion

From our data (Fig. 1), it can be seen that in these samples, the log of the resistivity is not a strict linear function of $p^{1/2}$. If only that part of the curve between $p^{1/2} = 50$ and $p^{1/2} = 100$ is considered, one might argue whether the points form a straight line. However, if a larger range of pressure and the changes in the sample dimensions are considered, it is clear that the resistivity–pressure relation is not that required by the proposed theory[3] and is leveling off with increasing pressure.

It is now accepted[5] that results obtained from measurements on compacted powders do not represent the bulk properties of the material under investigation. The "sample-electrode" effect, discussed in this note, clearly demonstrates that other factors in addition to the bulk resistivity contribute to the observed resistance. The results obtained in these experiments indicate again[6] that electrical characteristics observed on compacted powders are a complex function of the bulk properties, electrode contacts, and intergrain effects, and simple interpretations based only on the intrinsic properties of materials can be misleading.

Acknowledgment. We wish to express our thanks to J. R. Ladd for the preparative work and to F. P. Bundy for help with the high pressure work.

(5) D. D. Eley and J. D. Parfitt, *Trans. Faraday Soc.*, **51**, 1529 (1955)

(6) C. M. Huggins and A. H. Sharbaugh, *J. Chem. Phys.*, **38**, 393 (1963).

The Frenkel Approximation in the Thermodynamic Theory of Surfaces

by H. Saltsburg[1]

Department of Chemistry, Boston University, Boston, Massachusetts
(Received February 3, 1964)

The thermodynamic equilibrium between a droplet and its vapor is of fundamental importance in theories of vapor nucleation.[2] It is the purpose of this note to demonstrate that the thermodynamic potential employed by Frenkel[2b] to examine this equilibrium is an approximation[3] and, as commonly employed, ignores the distinction between the two usual Gibbs dividing surfaces, the surface of tension (SOT) and the "$\Gamma=0$" surface (Γ).[3,4]

In particular, the Frenkel potential Φ for the two-phase system liquid (2) and vapor (1) is given by

$$\Phi \equiv N_1\mu_1(T,P_1) + N_2\mu_2(P_1,T) + \sigma A \quad (1)$$

where N, μ, P, T, σ, and A have their usual significance. It will be shown that a specific choice of dividing surface is required to make Φ a thermodynamic potential consistent with the equilibrium condition

$$(\partial\Phi)_{T,P_1,N_{\text{total}}} = 0 \quad (2)$$

and that this choice is not consistent with commonly employed experimental techniques for the determination of σ.

From the Gibbs theory, in the form prior to a choice of dividing surface, for a spherical interface[5]

$$dU_{\text{total}} = TdS_{\text{total}} - P_1dV_1 - P_2dV_2 + \mu_1(P_1,T)dN_1 + \mu_2(P_2,T)dN_2 + \mu_s dN_s + \sigma dA + Cd_c \quad (3)$$

Integrating in the usual fashion[3] at constant curvature

$$U_t = TS_t - P_1V_1 - P_2V_2 + N_1\mu_1 + N_2\mu_2 + \mu_s N_s + \sigma A \quad (4)$$

For an incompressible droplet

$$\mu_2(P_2,T) = \mu_2(P_1,T) + \bar{V}_2(P_2 - P_1) \quad (5)$$

whence Φ may be written

$$\Phi = U_t - TS_t + P_1V_1 + P_2V_2 - \mu_s N_s \quad (6)$$

Combining (6) with dU_t from (3) and noting the equilibrium condition

$$\mu_1(P_1,T) = \mu_2(P_2,T) = \mu_s = \mu$$

one obtains

$$d\Phi = -S_t dT + (P_1 - P_2)dV_2 + V_t dP_1 - N_s d\mu_s + \mu(dN_1 + dN_2) + \sigma dA + Cdc \quad (7)$$

The conditions $dT = 0$, $dP_1 = 0$, and $dN_t = 0$ require that

$$(P_1 - P_2)dV_2 - d(N_s\mu_s) + \sigma dA + Cdc = 0 \quad (8)$$

and thus (8) is at variance with the result of the exact

(1) General Dynamics/General Atomic, San Diego, Calif.

(2) (a) M. Volmer, "Kinetik der Phasenbildung," Theodor Steinkopff, Ed., Dresden and Leiden, 1934; (b) J. Frenkel, "Kinetic Theory of Liquids," Clarendon Press, Oxford, 1946, p. 368.

(3) (a) F. P. Buff, *J. Chem. Phys.*, **19**, 1591 (1951); (b) "Handbuch der Physik," Vol. X, Springer-Verlag, Berlin, 1960, p. 281.

(4) J. W. Gibbs, "Collected Works," Vol. I, Longmans Green and Co., New York, N. Y., 1931, p. 219.

(5) J. W. Gibbs, *ibid.*, p. 225.

Gibbs theory unless $d(\mu_s N_s) \equiv 0$. This is equivalent to the choice of the Γ surface.

If however one makes this choice of dividing surface then the equilibrium condition is correctly given by

$$(P_1 - P_2)dV_2 + \sigma dA + C dc = 0 \qquad (9)$$

and if the theoretically or experimentally determined values of σ are calculated from such an equation, no modification of the thermodynamic theory is required, curvature dependence having already been included. If the defining equation for σ is the more commonly employed form

$$(P_1 - P_2)dV_2 + \sigma dA = 0 \qquad (10)$$

which refers to the SOT then one cannot simply include curvature corrections to σ in the Frenkel theory. To do so is to neglect the distinction between the SOT and the Γ surface.

Consequently, the explicit inclusion of curvature terms in the formal thermodynamic framework must be done to make Φ a potential but the value of σ and C must be appropriate to the Γ surface, a consideration usually overlooked. This difficulty in the usual Becker–Döring type nucleation theory was first pointed out by Buff and Kirkwood.[6] The present analysis demonstrates explicitly that this difficulty is inherent in the Frenkel approach without considering the logical difficulty of choosing a dividing surface unless one can clearly have particles in either one phase or the other, a difficulty in the operational definition of droplet radius in nucleation theories.

(6) F. P. Buff and J. Kirkwood, *J. Chem. Phys.*, **18**, 991 (1950).

The Electronegativity of Perhalo Groups

by James E. Huheey

Division of Chemistry, Worcester Polytechnic Institute, Worcester, Massachusetts *(Received February 3, 1964)*

Recently, Ettinger[1] has discussed the electronegativity of the difluoramino group and arrived at a value of 3.25–3.30 (Pauling's scale) by three independent methods. He also pointed out that if partial charge is neglected, this is the orbital electronegativity of nitrogen hybridized to give 84% p-character as calculated by Jaffé.[2] However, neglect of ionic character in fluorine compounds is often a serious oversimplification. Fortunately, the orbital electronegativity method of Jaffé allows the effect of partial charge on electronegativity to be estimated. This simplifies the problem of calculation of group electronegativities.[3]

The orbital electronegativity of nitrogen containing 80% p-character[4] is (Mulliken's scale)

$$\chi_N = 10.71 + 14.44\delta_N$$

where δ is the partial charge on the atom ($\delta = 0$ corresponds to the singly occupied orbital of Jaffé, and the value of χ when $\delta = 0$ may be considered the "inherent electronegativity" of the atom). The electronegativity of fluorine is

$$\chi_F = 12.18 + 17.36\delta_F$$

Combining[3] these equations gives the group electronegativity

$$\chi_{NF_2} = 11.63 + 5.42\delta$$

or in Pauling units

$$\chi_{NF_2} = 3.70 + 1.82\delta$$

Since the inherent electronegativity (3.70) is somewhat higher than that proposed by Ettinger, other perhalo groups were checked.

Trichloromethyl Group. From the infrared absorption of the phosphoryl group in diethyl trichloromethylphosphonate (7.83 μ),[5] the electronegativity of this group may be estimated by the method of Bell and coworkers.[6] This method yields an estimate of 2.68. From the orbital electronegativity method[2] one obtains an estimate of 2.84.

Trifluoromethyl Group. From the phosphoryl group infrared absorption on tris(trifluoromethyl)phosphine oxide (7.53 μ),[7] the group electronegativity can be calculated[6] to be 3.29. The orbital electronegativity method gives a value of 3.45.

Fluoroxy Group. Although the calculations for this group are far more uncertain than for the previous

(1) R. Ettinger, *J. Phys. Chem.*, **67**, 1558 (1963).

(2) (a) J. Hinze and H. H. Jaffé, *J. Am. Chem. Soc.*, **84**, 540 (1962); (b) J. Hinze M. A. Whitehead, and H. H. Jaffé, *ibid.*, **85**, 148 (1963); (c) J. Hinze and H. H. Jaffé, *J. Phys. Chem.*, **67**, 1501 (1963).

(3) Jaffé and co-workers[2b] described a method for the calculation of group electronegativities from orbital electronegativities. In the present work, a modification of Jaffé's method was used utilizing two premises: (1) the orbital electronegativities of all of the atoms in the group become (and remain) equal; (2) the sum of partial charges residing in the orbitals must equal zero for a neutral group, plus one for a monovalent cation, etc. The complete method and results for several groups will be published in the near future.

(4) Estimated from bond angle in NF_3. Small changes in p-character do not change the results appreciably.

(5) C. E. Griffin, *Chem. Ind.* (London), 1058 (1960).

(6) J. V. Bell, J. Heisler, H. Tannenbaum, and J. Goldenson, *J. Am. Chem. Soc.*, **76**, 5185 (1954).

(7) R. C. Paul, *J. Chem. Soc.*, 574 (1955).

groups, it is included to indicate the trend of the fluoro derivatives of carbon, nitrogen, and oxygen.

In the absence of data on a compound containing both the fluoroxy and phosphoryl groups, the method of Bell cannot be used. However, the infrared spectrum of FSO_3F[8] is virtually the same as that of sulfuryl fluoride[9] for the sulfuryl group stretching frequencies. Although the relationship between substituent electronegativity and absorption frequency does not appear to be as precise as for the phosphoryl group, compounds with less electronegative groups such as sulfuryl chloride, methyl phenyl sulfone, and diphenyl sulfone[10] exhibit considerably lower frequencies. The electronegativity of the fluoroxy group can therefore be estimated to be very nearly that of fluorine.

Calculation of the electronegativity of the fluoroxy group by the orbital electronegativity method[3] is imprecise because of uncertainties as to the nature of the hybridization of the oxygen and fluorine. Using 81% p-character for oxygen (estimated from the bond angle in oxygen difluoride) and pure p-orbitals for the fluorine, an estimate of 3.40 can be obtained. This should be considered as a minimum since any s-character in the bonding orbitals of the fluorine will tend to increase the electronegativity.

Clifford's Method. Clifford[11] has shown that the electronegativity of negative groups often approximates the average of the individual electronegativities of the constituent atoms. Values obtained by this method are listed in Table I and compared with the other methods.

Discussion

From Table I it will be seen that the infrared-derived values and orbital electronegativity values of trichloromethyl and trifluoromethyl groups parallel each other with a difference of about 0.15. The agreement for the fluoroxy groups is poorer. The values determined by the method of Clifford show no regularity, but approximate those obtained by the other two methods.

One significant difference should be pointed out between the trihalomethyl groups on the one hand and the difluoramino and fluoroxy groups on the other. All of these groups will cause a highly polar σ-bond, raising the electronegativity of the attached moiety. In the case of the nitrogen- and oxygen-containing groups, this may enhance back-bonding if suitable vacant orbitals are available. Thus the net partial charge and apparent electronegativity would be lower than if σ-bonding alone were involved.

In summary, it would appear that the electronegativity of the difluoramino group is somewhat higher than previously estimated. It should be emphasized that assignment of a single value for the electronegativity of a group is no more valid than assigning a single value for the electronegativity of a single atom. The calculated orbital electronegativities for these groups given above is for the neutral group, *i.e.*, when bonded to another group or atom of equal electronegativity. For any other case, the electronegativity will vary as a function of partial charge.[2,3]

The excellent agreement of the three methods of Ettinger would appear, therefore, to be fortuitous, a phenomenon not unknown in previous electronegativity calculations.

Table I: Methods of Estimating Group Electronegativity

Group	Infrared data	Orbital electronegativity	Method of Clifford
Trichloromethyl	2.68	2.84	2.83
Trifluoromethyl	3.29	3.45	3.55
Difluoramino	...	3.70	3.60
Fluoroxy	3.9	3.40	3.73

(8) F. B. Dudley, G. H. Cady, and D. F. Eggers, Jr., *J. Am. Chem. Soc.*, **78**, 290 (1956).
(9) R. N. Haszeldine and J. M. Kidd, *J. Chem. Soc.*, 2901 (1955).
(10) D. Barnard, J. M. Fabian, and H. P. Koch, *ibid.*, 2442 (1949).
(11) A. F. Clifford, *J. Phys. Chem.*, **63**, 1227 (1959).

The System Li_2SiF_6–$(NH_4)_2SiF_6$–H_2O at 25°

by John A. Skarulis, Vincent N. Darnowski, William P. Kilroy, and Thomas Milazzo

Department of Chemistry, St. John's University, Jamaica, New York
(*Received March 17, 1964*)

Curiosity as to why lithium hexafluorosilicate was not included in studies of the thermal decomposition equilibria of alkali metal hexafluorosilicates[1,2] led us to study its dissociation pressures and its solubilities in hydrofluorosilicic acid solutions and in other aqueous systems, including the system Li_2SiF_6–$(NH_4)_2SiF_6$–H_2O at 25°. This report deals mainly with the last mentioned system and the discovery of a new double salt, $LiNH_4SiF_6$.

(1) G. Hantke, *Z. angew. Chem.*, **39**, 1065 (1926).
(2) R. Caillat, *Ann. chim.*, **20**, 267 (1945).

Experimental

The equipment used in the preparation and storage of the component salts was made of either polyethylene, polypropylene, or Teflon.

The ammonium hexafluorosilicate, which was obtained through the courtesy of Davison Chemical Corp., was recrystallized from water by cooling a filtered, saturated solution at 50° to room temperature. The crystals were air-dried, pulverized, and finally stored over either concentrated sulfuric acid or phosphorus pentoxide. They were 99.9% $(NH_4)_2SiF_6$ as determined by three analyses: ammonia distillation, loss on ignition at 400°, and titration of the hydrofluorosilicic acid obtained by cation exchange.

In a typical preparation of lithium hexafluorosilicate, 85 g. of Mallinckrodt reagent lithium chloride was added slowly to 370 ml. of Baker 30% reagent hydrofluorosilicic acid; the mixture was cooled in ice and treated with an equal volume of 95% ethanol added dropwise with stirring. To purify the salt, a cold saturated solution of the crude material in 10% hydrofluorosilicic acid was filtered and then treated with ethanol as before. The crystals were washed with small amounts of cold ethanol, air-dried, and stored in a desiccator over either concentrated sulfuric acid or phosphorus pentoxide. The final product, a white powder, was 99.9% Li_2SiF_6 based on decomposition to lithium fluoride at 400° and also on conversion to lithium sulfate. However, assays of only 98.6% were obtained when solutions of the salt were titrated hot with standard base either directly or after being passed through a cation exchanger. Also, values as high as 99.3% were obtained by the titration procedures with samples of the salt which had been permitted to stand in an atmosphere of dry silicon tetrafluoride for several weeks. Therefore, it was concluded that the chief impurity in the preparation was lithium fluoride which was present not to the extent of 1.4% as indicated by the 98.6% assay but somewhere in the neighborhood of 0.5%. The low assay was attributed partially to a loss of titratability because of hydrolysis.

Known complexes of the component salts and water were mixed in polyethylene test tubes at 25 ± 0.02° over periods ranging from 6 to 20 days. The saturated solutions were analyzed for lithium ion and total lithium, ammonium, and hexafluorosilicate ions. In the first analysis, samples were evaporated to dryness and ignited to lithium fluoride at 400°. In the second, samples were weighed directly in 100-ml. flasks, made up to volume immediately; 10- or 20-ml. aliquots were passed through an Amberlite IR 120 cation-exchange resin bed which extended to the 15-ml. mark in a 25-ml. buret, then eluted with 60 ml. of distilled water, and the fluorosilicic acid eluate was titrated hot with standard 0.1 *N* base with phenolphthalein as indicator. A check of the ion-exchange procedure on known mixtures proved that it was capable of accuracy and precision within 5 parts per 1000 when assay values of 98.6% Li_2SiF_6 and 99.9% $(NH_4)_2SiF_6$ were used for the component salts. Therefore, the compositions of the known complexes were based on these assays in order to minimize the error arising from the loss of titratability referred to earlier.

When it became evident that a double salt was formed in the system, steps were taken to prepare crystals of it for an X-ray study. An equal volume of 95% ethanol was layered on an undersaturated solution which contained 4.25 g. of lithium hexafluorosilicate, 2.00 g. of ammonium hexafluorosilicate, and 18.75 g. of water, and allowed to diffuse spontaneously over a period of 5 days. The crystals which were formed were filtered, washed with ethanol, and then air-dried. They consisted mainly of platelets with a smaller proportion of larger pendant-like forms and a negligible proportion of rods. Several grams of the platelets were hand-picked for chemical and X-ray analysis. The crystals were analyzed for lithium by ignition to lithium fluoride at 400°, for ammonium ion by ammonia distillation from alkaline solution, and for hexafluorosilicate ion by titration with base of the filtered and washed potassium hexafluorosilicate which had been precipitated by the addition of excess potassium nitrate in ice-cold solution. Also, the density of the crystals was determined by use of a pycnometer with benzene as the displacing liquid.

Results and Discussion

In the preparation of lithium hexafluorosilicate, temperatures higher than room temperature were avoided to minimize the uncertain effects of hydrolytic decomposition. The procedure used was adopted because the differences in the solubilities of the salt in water as well as in hydrofluorosilicic acid solutions at 0 and 25° proved to be too small for recrystallization purposes by temperature changes in the range between the two temperatures. Since little solubility data on lithium hexafluorosilicate appear in the literature, the solubilities in hydrofluorosilicic acid solutions at 0 and 25° are given in Table I and plotted in Fig. 1.

The temperature of 400° which was used to decompose lithium hexafluorosilicate to lithium fluoride in the method of analysis for lithium was selected on the basis of the data given in Table II. The maximum dissociation pressures were measured with essentially the same apparatus that was used for the other alkali metal hexafluorosilicates in the earlier work cited.[2]

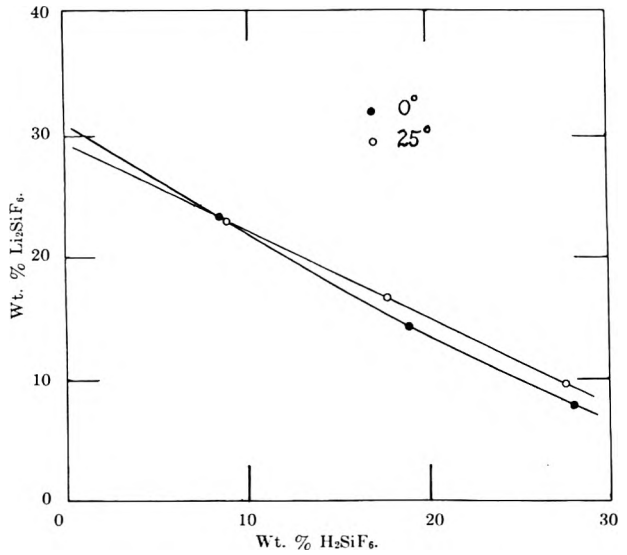

Figure 1. Solubilities of lithium hexafluorosilicate in hydrofluorosilicic acid solutions.

Table I: The System Li_2SiF_6–H_2SiF_6–H_2O[a]

0°		25°	
% Li_2SiF_6	% H_2SiF_6	% Li_2SiF_6	% H_2SiF_6
7.83	28.24	9.61	27.70
14.40	18.98	16.34	17.81
23.26	8.49	22.86	8.86
31.0[b]	0.00	29.2[b]	0.00

[a] V. N. Darnowski, Master's Dissertation, St. John's University, 1958. [b] Extrapolated.

The temperature at which the dissociation pressure of lithium hexafluorosilicate is 1 atm. is in the neighborhood of 310°. Incidentally, a fit of the data in Table II to $\log p = A/T + B$ by the method of least squares yields 34.9 kcal. mole^{-1} as the heat of dissociation of the lithium salt.

Table II: Maximum Dissociation Pressures of Li_2SiF_6 by the Static Method[a]

t, °C.	p, mm.
203	1.2
232	6.1
272	108.6
300	576.8
316	1062.8

[a] See footnote *a* in Table I.

The problem of hydrolysis in aqueous systems of lithium hexafluorosilicate was considered. It was felt that the presence of ammonium hexafluorosilicate, which is acidic in character, would repress the hydrolysis. Moreover, an investigation of the system Li_2SiF_6–LiF–H_2O at 25° as part of a study of the quaternary system Li_2SiF_6–HF–H_2O[3] gave information as to the extent of hydrolysis which was to be expected. Data pertaining to the invariant solution saturated with respect to lithium hexafluorosilicate and lithium fluoride are given in Table III. The mixtures cover the whole range of solid phases and are treated as quaternary, ignoring any silicon dioxide which may have formed as a solid phase by hydrolysis. The degree of hydrolysis of lithium hexafluorosilicate in the presence of lithium fluoride is of the order of 3% and the amount of lithium fluoride in the saturated solution very small.

Table III: The System Li_2SiF_6–LiF–H_2O at 25°. Compositions of Invariant Solution Treated as Quaternary Ignoring SiO_2 Formed by Hydrolysis

Wt. % solution				Mole % solute			
H^+	Li^+	SiF_6^{-2}	F^-	$(H^+)_2$	$(Li^+)_2$	SiF_6^{-2}	$(F^-)_2$
0.014	2.644	26.93	0.30	1.8	48.25	48.00	2.0
0.015	2.644	26.87	0.33	1.9	48.14	47.79	2.2
0.0088	2.653	26.87	0.24	1.1	48.90	48.37	1.6
0.014	2.644	26.88	0.30	1.7	48.29	47.95	2.1
0.010	2.618	26.59	0.24	1.3	48.73	48.34	1.7

The results of the analyses of the saturated solutions in the system Li_2SiF_6–$(NH_4)_2SiF_6$–H_2O are given in

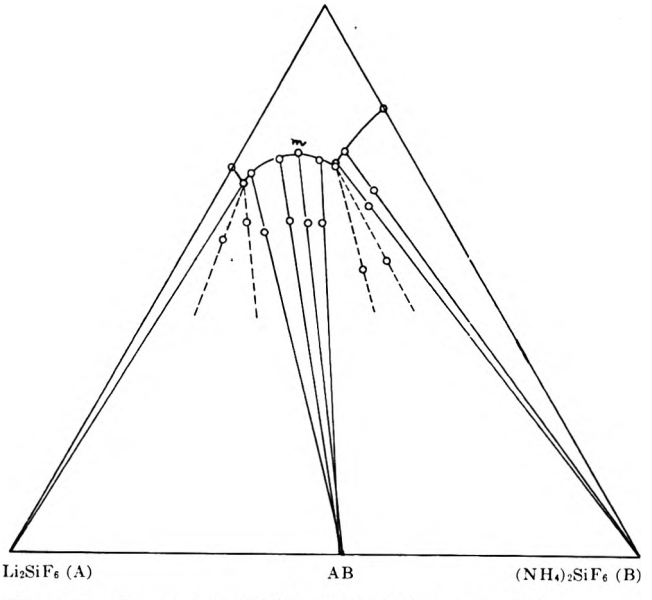

Figure 2. The system Li_2SiF_6–$(NH_4)_2SiF_6$–H_2O at 25°.

(3) W. P. Kilroy, Master's Dissertation, St. John's University, 1962.

Table IV and plotted in Fig. 2. The convergence of the tie lines of mixtures 4 to 7, inclusive, indicates a solid phase with the composition $LiNH_4SiF_6$. Mathematical extrapolation to per cent $(NH_4)_2SiF_6$ at 0% H_2O yields values of 52.6, 53.2, 54.6, and 52.9, respectively, which agree well with 53.3, the theoretical percentage of $(NH_4)_2SiF_6$ in the double salt. Similar extrapolation of mixtures 10 and 11 gives values of 100.8 and 101.4, respectively, clearly indicating ammonium hexafluorosilicate as the solid phase. Lithium hexafluorosilicate, though not established as a solid phase in this study, is undoubtedly anhydrous as in the system Li_2SiF_6–H_2SiF_6–H_2O[3] and other systems at 25°.[4] It is noted that the line from W to AB in Fig. 2 does not intersect the solubility curve of the double salt at the point of maximum water content, m, even though the salt is congruently soluble. Without doubt, this is an effect of hydrolysis. Analysis of individual crystals which were isolated by alcohol precipitation confirmed the existence of the double salt.

Table IV: The System Li_2SiF_6(A)–$(NH_4)_2SiF_6$(B)–H_2O(W) at 25°

	Complex		Solution		Solid phase
	% A	% B	% A	% B	
1	...	...	29.48	0.00	A
2	37.50	5.33	29.07	3.07	A + AB
3	32.08	7.30	29.28	3.13	A + AB
	Average		29.18	3.10	AB
4	30.18	11.12	27.14	3.77	AB
5	25.24	14.19	21.19	6.86	AB
6	22.62	17.08	17.81	9.21	AB
7	20.06	19.55	15.08	13.41	AB
8	18.19	28.17	13.10	16.52	B + AB
9	13.63	32.73	13.10	16.47	B + AB
	Average		13.10	16.50	B + AB
10	11.24	25.47	12.71	16.27	B
11	9.02	24.85	10.13	16.70	B
12	...	...	0.00	18.70	B

Anal. Calcd. for $LiNH_4SiF_6$: Li^+, 4.15; NH_4^+, 10.80; SiF_6^{-2}, 85.0. Found: Li^+, 4.17; NH_4^+, 10.81; SiF_6^{-2}, 84.1.

Duplicate determinations of the density of the solid at 25° gave values of 2.316 and 2.319 g./ml. The results of the X-ray study of the crystals will be presented in a subsequent report.[5]

(4) J. A. Skarulis, unpublished data. The dihydrate is the solid phase at 0°.

(5) The powder data have been submitted for inclusion in the ASTM X-ray Powder Data File.

Diffusion in Defect Crystalline Solutions in the Systems CaF_2–YF_3 and NaF–LiF–MgF_2[1]

by James M. Short and Rustum Roy

Materials Research Laboratory, The Pennsylvania State University, University Park, Pennsylvania *(Received April 4, 1964)*

Phase diagrams of the systems CaF_2–YF_3[2,3] and LiF–MgF_2[4] indicate that crystalline CaF_2 and LiF can, by solution of YF_3 or MgF_2, respectively, incorporate unusually high concentrations of defects by a suitable charge balance mechanism for the altervalent ions Y^{3+} and Mg^{2+}. That interstitial F^- ions are the predominant defect in solutions of YF_3 in CaF_2 has been confirmed by density[2] and conductivity measurements.[5] It is likely[6] that addition of Mg^{2+} to LiF produces cation vacancies. The effect of these gross concentrations of defects on cation diffusion rates in CaF_2 and LiF has been investigated. The species studied were: (a) the self-diffusion of Ca^{2+} in polycrystalline CaF_2 and solutions of YF_3 in CaF_2 containing up to 40 mole % YF_3; (b) the interdiffusion of Na^+ from NaF into polycrystalline LiF and into a solution of 6 mole % MgF_2 in LiF.

The rate of self-diffusion of Ca^{45} was measured in polycrystalline pellets, which were pretreated under nitrogen and compacted in a pellet mold. A thick layer of otherwise identical radioactive CaF_2–YF_3 solution was pressed at 10 kbars onto an inert pellet, and one-dimensional diffusion was carried out at temperatures in the range 700–1100° for periods of 100–500 hr. Sections of 10–50 μ were ground off the pellet onto abrasive paper with a specially constructed precision grinder. A Geiger–Muller counter served to measure the activity, which was corrected for dead-time and absorption losses. A microbalance was used to determine the weights and corresponding thicknesses of the sections. The relative rates of diffusion from NaF of Na^+ into pure LiF and into a 6 mole % solution of MgF_2 in LiF were also measured. The concentration–distance curve was determined by milling and flame photometric analysis.

(1) Based on a Ph.D. Thesis (1961) by J. Short. The Pennsylvania State University, University Park, Pa., which was presented at the Annual Meeting of the American Association for the Advancement of Science, Denver, Colo., December, 1961.

(2) J. Short and R. Roy, *J. Phys. Chem.*, **67**, 1860 (1963).

(3) T. Vogt, *Neues Jahrb. Mineral.*, 11, 9 (1914).

(4) W. E. Counts, R. Roy, and E. F. Osborn, *J. Am. Ceram. Soc.*, **36**, 15 (1953).

(5) R. W. Ure, *J. Chem. Phys.*, **26**, 1363 (1957).

(6) Y. Haven, *Rec. trav. chim.*, **69**, 1259 (1950).

Table I gives the measured diffusion coefficients and the calculated values of D_0 and Q in the expression $D = D_0e^{-Q/kT}$. While the increases in the diffusion coefficients in the defect crystalline solutions are highly significant, the values of D_0 and Q must be considered only approximate. In LiF–MgF_2 at these temperatures association between Mg^{2+} and cation vacancies is insignificant.[7] Even so, it is probably not possible to state simple quantitative relations between the changes in D, D_0, and Q and the concentration of MgF_2 or cation vacancies, since the diffusion took place in a nonbinary two-phase system which need not move directly toward equilibrium.[8]

Table I: Measured Diffusion Coefficients and Values of D_0 and Q in $D = D_0e^{-Q/kT}$

Solution compn.	Temp., °C.	D, cm.²/sec.	D_0, cm.²/sec.	Q, e.v.
CaF_2 (Ca^{45} self-diffusion)	700	2.5×10^{-13}	1×10^{-4}	1.7
CaF_2 (Ca^{45} self-diffusion)	900	8.3×10^{-12}	1×10^{-4}	1.7
CaF_2 (Ca^{45} self-diffusion)	1100	8.6×10^{-11}	1×10^{-4}	1.7
20% YF_3–80% CaF_2	900	1.8×10^{-11}	3×10^{-4}	1.7
20% YF_3–80% CaF_2	1100	1.9×10^{-10}	3×10^{-4}	1.7
40% YF_3–60% CaF_2	1100	1.6×10^{-9}	2×10^{-8}	(1.7)
LiF (Na^+ diffusion)	522	1.9×10^{-10}	4.1×10	1.8
LiF (Na^+ diffusion)	626	4.0×10^{-9}	4.1×10	1.8
6% MgF_2–94% LiF	522	3.3×10^{-9}	7.6×10^{-2}	1.2
6% MgF_2–94% LiF	626	2.4×10^{-8}	7.6×10^{-2}	1.2

In the system CaF_2–YF_3 D_0 was roughly proportional to the YF_3 content, while Q did not show measurable variation. The increase in the diffusion rates of Ca^{2+} is most simply explained if the mass-action equilibria[9] for Schottky and anti-Frenkel defects are written

$$[V_{Ca^{2+}}][V_{F^-}]^2 = K_S \quad (1)$$

$$[F_{in.}^-][V_{F^-}] = K_{a.F} \quad (2)$$

The law of mass action implies that increasing the concentration of interstitial F^-, $[F_{in}^-]$, will increase the concentration of cation vacancies, $[V_{Ca^{2+}}]$. If Ca^{2+} diffused *via* cation vacancies, an increase in its diffusion rate would be expected. However, if Ca^{2+} diffuses through the largest interstitial sites ($^1/_2$00), (0$^1/_2$0), (00$^1/_2$), ($^1/_2{}^1/_2{}^1/_2$), which are also in eightfold coordination with respect to F^-, the introduction of F^- into these sites should then decrease the concentration of any interstitial Ca^{2+} (Frenkel defects) and the self-diffusion rate of Ca^{2+}. The observed increase in the diffusion rate makes the mechanism of cation vacancy diffusion probable.

Further evidence for the cation vacancy diffusion mechanism for Ca^{2+} was found in the observation that the self-diffusion rate at 760° of Ca^{45} in a 3 mole % NaF–97% CaF_2 solution was 0.7 of that in pure CaF_2. This is explainable by eq. 1 and 2 in terms of an increase in $[V_{F^-}]$ and a corresponding decrease in $[V_{Ca^{2+}}]$ in the crystalline solution.

Acknowledgment. This research was supported by a grant from the Bausch and Lomb Optical Company for work on substantially defective ionic materials.

(7) P. Berge, *Bull. Soc. Franc. Mineral. Crist.*, **83**, 57 (1960).

(8) J. Short and R. Roy, *J. Am. Ceram. Soc.*, **47** [3], 149 (1964).

(9) F. A. Kroger and H. J. Vink, "Solid State Physics," Vol. 3, F. Seitz and D. Turnbull, Academic Press, New York, N. Y., 1956, p. 307.

Structural Study of the Complex Barium Citrate by Ultrasonic Waves

by Satya Prakash, Firoze Maneckji Ichhaporia, and Jata Dhari Panday

Department of Chemistry, University of Allahabad, Allahabad, India
(Received April 27, 1964)

One of the purposes of investigations in sonochemistry is to determine and correlate certain of the molecular properties of fluids from experimental measurements on sound velocity and attenuation. Data covering wide ranges of temperature, pressure, and concentration for aqueous solutions of acids, bases, and salts and their mixtures are now available. From such results it is possible to deduce general laws with regard to the acoustic and molecular properties of ions and molecules in aqueous solutions. Sette[1] has given discussion and reviews on the use of ultrasonic velocities in the determination of molecular structure and the structure of liquids. Work on complex ions has been carried out by Subrahmanyam.[2] With the latter object in view, the composition of the soluble complex barium citrate has been studied ultrasonically by the determination of velocity and compressibility. The velocity measurements have been made by the optical method as devised by Debye and Sears.[3,4] The probable errors involved in the measurements of ultrasonic velocity and compressibility are 0.15 and 0.4 %, respectively.

(1) D. Sette, *Ric. Sci.*, **20**, 102 (1950).

(2) T. Satyavati, P. J. Reddy, and S. V. Subrahmanyam, *J. Phys. Soc. Japan.*, **17**, 1061 (1962).

(3) P. Debye, *Ber.*, **84**, 125 (1932).

(4) P. Debye and F. W. Sears, *Proc. Natl. Acad. Sci. U. S.*, **18**, 410 (1932).

Experimental

Standard solutions of barium chloride and citric acid were prepared using B.D.H. Analar grade reagents in doubly distilled water. The acid solution was always freshly prepared to avoid the growth of fungus. Its pH was measured and found to be 1.8. The pH of the barium chloride solution was brought down to 1.8 by the addition of a few drops of hydrochloric acid, before the volume was made up.

Various mixtures were then prepared of the two according to Job's[5,6] method of continuous variation and the mole ratio method. In Job's method, the two are so mixed that the volume of one increases as that of the other decreases proportionately, the total volume being constant. In the mole ratio method, the volume of the acid is kept constant at twice the concentration of the other. The volume of barium chloride is slowly increased as the total volume is kept constant with the addition of water. These mixtures were allowed to stand for 30 min. to attain equilibrium, and the velocity of each was then measured by the optical diffraction method. The density of each mixture was also measured immediately after the velocity measurement. From the velocity and density data, the adiabatic compressibility was determined. Subtracting the compressibility values from the compressibility value of water, which is 44.67 cm.^{2}/dyne $\times$ 10^{12}, and taking the velocity of water as 1500 m./sec. and the density as 0.9951 g./ml., we get the compressibility lowerings. Curves showing the variation of velocity and compressibility lowerings with the composition variation are shown in Fig. 1 to 6.

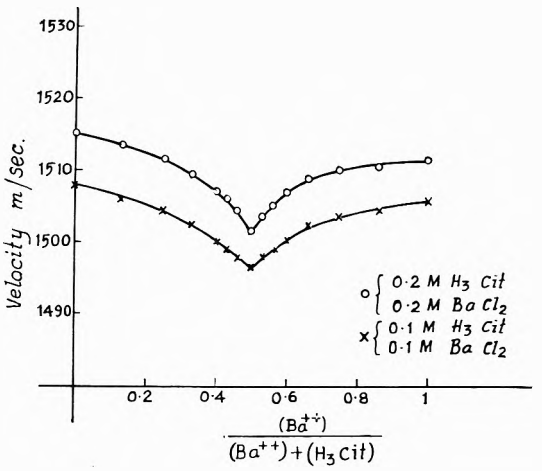

Figure 1. Variation of ultrasonic velocity with composition according to Job's method, at fixed pH and when the two mixed are equimolecular.

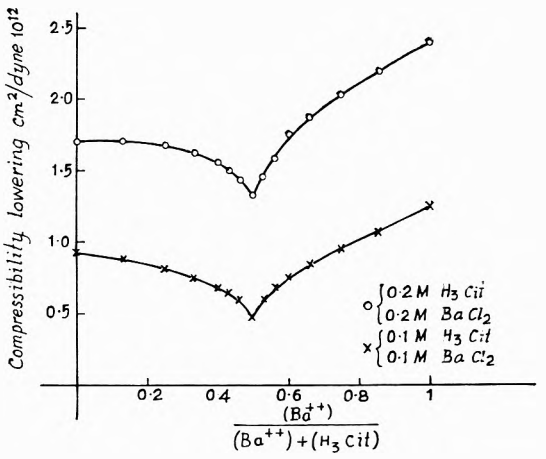

Figure 2. Variation of compressibility lowering with composition according to Job's method, at fixed pH and when the two mixed are equimolecular.

Results and Discussion

From Fig. 1 and 2, where both barium chloride and citric acid are equimolecular, we find that the ultrasonic velocity and compressibility lowering gradually decreases, reaches a minimum, and then increases again. The minimum occurs at the point 0.5 of the ratio $(Ba^{+2})/[(Ba^{+2}) + (H_3Cit)]$, *i.e.*, at the composition 1:1. This indicates the formation of maximum complex ions at this point. Had there been no interaction between the molecules of the two, the curve would have been linear. When the two are nonequimolecular, the velocity and compressibility lowering (see Fig. 3 and 4) reach a minimum at 0.33 (1:2 citric acid:barium chloride) and at 0.66 (2:1 citric acid:barium chloride) again showing the composition as 1:1. In the mole ratio method, (Fig. 5 and 6) the depression in velocity and compressibility lowering is more gradual, but all the same, it reaches its least value at the point where the number of moles of Ba^{+2} is equal to the number of moles of citric acid. This method also clearly indicates the formation of complex ions of the composition 1:1. The composition is in accordance with the results obtained by Mathur[7] who studied the complex by potentiometric and solubility methods.

When an electrolyte is dissolved in water, the compressibility of water is decreased. The decrease is due to the electrostatic field of the ions on the surrounding water. For any particular electrolyte, the decrease in the compressibility of water can be taken as a measure of the number of free ions in the solution. When two

(5) P. Job, *Ann. Chim.*, **9**, 113 (1928).

(6) P. Job, *ibid.*, **6**, 97 (1936).

(7) K. C. Mathur, Ph.D. Thesis, Allahabad University, Allahabad, 1959.

electrolytic solutions are mixed, we should expect the compressibility to vary linearly between the values corresponding to the individual electrolytic solution if there were no interaction between the two components (see Subrahmanyam[2]). In such a case, the compressibility of water minus the compressibility of the solution, *i.e.*, compressibility lowerings, should also vary linearly. From the compressibility data of the complex barium citrate, we find that where the number of free ions is greater, the compressibility values are lower. As the mixture approaches the ratio 1:1, the compressibility value is at a maximum, for here the number of free ions is at a minimum. The curves drawn between compressibility lowerings and composition variations all show a minimum at maximum complex formation.

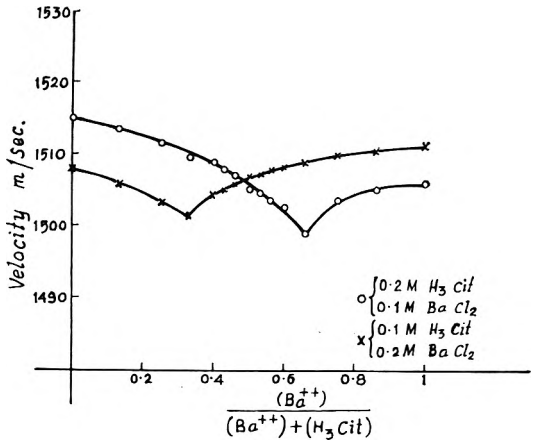

Figure 3. Variation of ultrasonic velocity with composition according to Job's method, at fixed pH and when the two mixed are nonequimolecular.

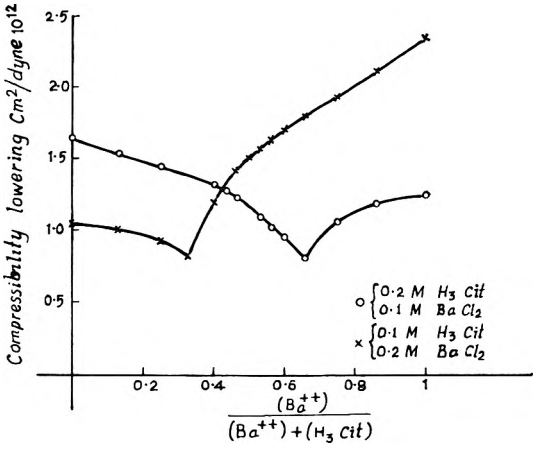

Figure 4. Variation of compressibility lowering with composition according to Job's method, at fixed pH and when the two mixed are nonequimolecular.

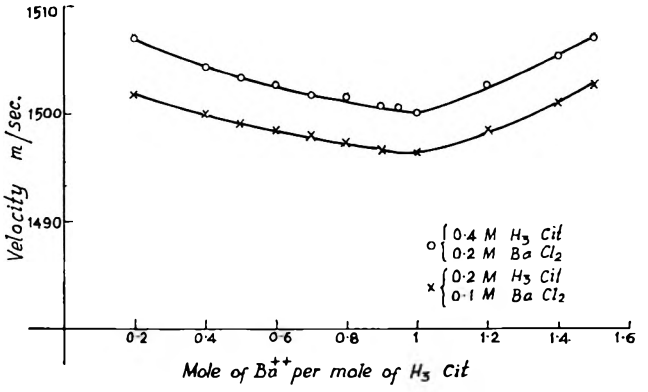

Figure 5. Variation of ultrasonic velocity with composition according to the mole ratio method at fixed pH.

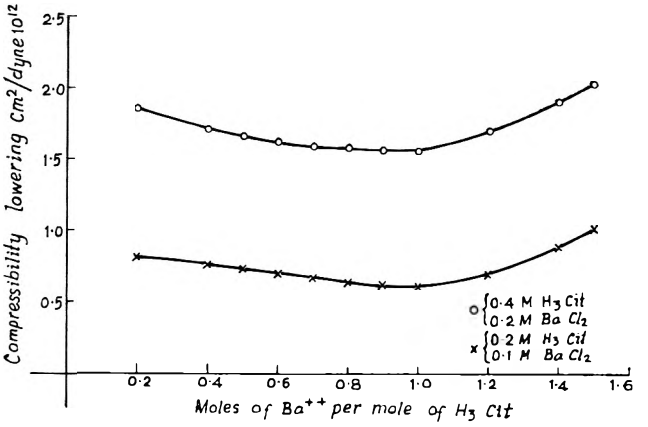

Figure 6. Variation of compressibility lowering with composition according to the mole ratio method at fixed pH.

Thus, we see that the nonlinear curves obtained from the study of the variation of the velocity and compressibility not only indicate the formation of the complex but also the composition at which maximum complex formation takes place.

Acknowledgment. This work has been supported by a scholarship from Sir Ratan Tata Trust to F. M. I. and by a senior fellowhip from the Council of Scientific and Industrial Research to J. D. P.

On the Mechanism of Benzene Formation in the Radiolysis of Acetylene

by Yves Rousseau[1] and Gilbert J. Mains

Department of Chemistry, Carnegie Institute of Technology, Pittsburgh, Pennsylvania 15213 *(Received May 4, 1964)*

Many mechanisms have been suggested to explain the formation of benzene in the radiation induced polymerization of acetylene. Some of these involve ionic intermediates,[2] some propose excited electronic states of acetylene,[3] and still others suggest free radicals.[4] Recently this laboratory presented evidence for a free radical mechanism[5] based mainly upon data obtained from studies of the radiolysis and mercury-sensitized photolysis of a 1:1 acetylene-acetylene-d_2 mixture. The X-ray dose independent distribution of isotopically substituted benzenes found by these authors was: C_6H_6, 7.2%; C_6H_5D, 6.6%; $C_6H_4D_2$, 24.2%; $C_6H_3D_3$, 12.0%; $C_6H_2D_4$, 28.7%; C_6HD_5, 8.6%; C_6D_6, 12.9%. The relatively large yields of benzene molecules containing odd numbers of deuterium atoms provided strong evidence against a totally excited state mechanism and for a mechanism which could effect the randomization of deuterium. A mechanism, involving carbon–hydrogen scission to form the chain initiating intermediates C_2H and H, was suggested.

While scission of the C–H bond was proposed by Mains, Niki, and Wijnen,[5] an alternate mechanism involving scission of the carbon–carbon triple bond could also explain their observations. Although such a mechanism was deemed unlikely, sufficient energy is available in radiolysis to effect scission of the carbon–carbon triple bond and the possibility of a chain initiation involving CH has never been ruled out directly. The research reported here specifically considers this alternate mechanism for benzene formation.

Irradiation of acetylene enriched in C^{13} should permit a decision to be reached as to whether carbon–carbon triple bond scission contributes significantly to benzene formation, provided, of course, the C^{13} isotope is not distributed randomly among the C_2H_2 molecules. If no carbon–carbon triple bond scission occurs, the distribution of C^{13} among the product benzenes will reflect the nonrandom distribution in the original acetylene. On the other hand, if carbon–carbon triple bond scission occurs, the distribution of C^{13} among the product benzenes will be random. These alternatives represent limiting cases in which the distribution of C^{13} among the benzene products may be easily predicted, provided kinetic isotope effects may be ignored (a good first approximation).

If a sample of enriched acetylene contains x fraction C^{13} atoms and y fraction C^{12} atoms, the isotopic distribution of benzenes arising from complete randomization of C^{13} is given by the terms in the expansion of $(x + y)^6$. This would be the extreme case for carbon–carbon triple bond scission. If no carbon–carbon scission occurs, the carbon atoms enter into benzene production in groups of two, and the distribution of benzenes is given by the sums of the appropriate terms in the expansion of $(a - b + c)^3$ where a is the fraction of $HC^{13}C^{13}H$, b is the fraction of $HC^{12}C^{13}H$, and c is the fraction of $HC^{12}C^{12}H$ in the mixture. These benzene distributions clearly differ so long as the distribution of C^{13} in the original acetylene is not random, *i.e.*, $a \neq x^2$, $b \neq 2xy$, and $c \neq y^2$. If a competition exists between a carbon–carbon triple bond scission mechanism and one involving no such scission, the observed benzene production should fall between the calculated extremes.

In order to verify the accuracy of the predicted results, the nonrandomly C^{13} enriched acetylenes can be subjected to mercury photosensitization. It is generally accepted that no carbon–carbon triple bond scission occurs in mercury photosensitization because insufficient energy is available. In this case the observed relative abundance of isotopic benzenes should match the values predicted from the expansion of $(a + b + c)^3$.

Experimental

Acetylene enriched in C^{13} was obtained from Merck Sharp and Dohme of Canada, Ltd., and was found to contain 56 atom % C^{13} by analysis using a Consolidated Electrodynamics Corporation Model 21-103C mass spectrometer. This analysis was performed by neglecting C^{13} isotope effects in the calculated standard patterns for $HC^{13}C^{13}H$ and $HC^{13}C^{12}H$, an assumption justified by the absence of significant residuals in analysis of the mass spectrum of the enriched sample. The distribution of C^{13} in the acetylene as received was random, and, therefore, an almost equal amount of $HC^{12}C^{12}H$ acetylene was added to the enriched material. The composition of the resultant mixture was:

(1) Postdoctoral Fellow, U.S.A.E.C. Contract No. AT(30-1)2007, 1963–1964.

(2) S. C. Lind, D. C. Bardwell, and J. H. Perry, *J. Am. Chem. Soc.*, **48**, 1556 (1926).

(3) L. M. Dorfman and F. J. Shipko, *ibid.*, **77**, 4723 (1955).

(4) C. Rosenblum, *J. Phys. Chem.*, **52**, 474 (1948).

(5) G. J. Mains, H. Niki, and M. H. J. Wijnen, *ibid.*, **67**, 11 (1963).

(6) R. Kuntz and G. J. Mains, *J. Am. Chem. Soc.*, **85**, 2219 (1963).

$HC^{13}C^{13}H$, 13.69%; $HC^{13}C^{12}H$, 23.90%; and $HC^{12}C^{12}H$, 62.41%.

The mercury-photosensitized experiments were performed at room temperature (23 ± 1°) using a quartz cylindrical cell, 5 cm. in diameter and 10 cm. long. The light source employed was a low pressure mercury lamp described previously.[6] A Vycor filter to absorb any 1849 Å. radiation and a neutral density filter to reduce the intensity were inserted between the lamp and the reaction vessel. The incident intensity, as measured by N_2O–propane actinometry,[7] was found to be 0.17 μeinstein/min. under these conditions. Conversions were kept below 0.5% in view of the large quenching cross section of benzene.[8] The benzene product was recovered in a trap at −131° (*n*-pentane slush) and analyzed by mass spectrometry, neglecting C^{13} isotope effects in the mass spectral patterns of the benzenes.

In the radiolysis experiments, Pyrex cells fitted with in-blown windows described previously[5] were immersed up to the windows in a water bath at room temperature and irradiated by a 20-μa. beam of 5-Mev. electrons from a Van de Graaff accelerator. Bombardment times were kept low (5–10 sec.) to avoid secondary reactions. Conversions were 1% or less.

The acetylene pressure used in both photolysis and radiolysis was 30 mm. Each experiment was performed in duplicate for both types of radiation.

Results and Discussion

Table I compares the predicted and observed distribution of C^{13} in the benzene product for both photolysis and radiolysis. Neglecting for the moment the large apparent yields of $C^{13}{}_6H_6$ and $C^{13}{}_5C^{12}H_6$, it may be readily seen that both the photolysis results and the radiolysis results conform very closely to that predicted for a mechanism involving no carbon–carbon bond cleavage. The deviations in the yields of benzene containing two or less C^{12} atoms are almost certainly due to small amounts of other products, such as C_6H_8, which are also formed and which exhibit mass spectral patterns which overlap those of the benzene products. These minor products will not significantly affect the analysis of the benzenes obtained in larger yields and the agreement between the yields calculated, assuming no carbon–carbon cleavage, and the experimental results may be readily seen.

The results reported here preclude any radiolysis mechanism resulting in randomization of C^{13} as might be expected from carbon–carbon triple bond cleavage. Any such process must play a minor role in the mechanism of benzene formation.

Table I: Relative Abundance of the Isotopic Benzenes in %

	Predicted		Observed	
Benzene	C≡C bond cleavage	No C≡C bond cleavage	5-Mev. (e^-) irradiation	Hg 6 ($^3P_1$) sensitization
$C^{13}{}_6H_6$	0.03	0.26	0.4	1.2
$C^{13}{}_5C^{12}H_6$	0.49	1.35	1.6	2.3
$C^{13}{}_4C^{12}{}_2H_6$	3.56	5.76	5.8	6.3
$C^{13}{}_3C^{12}{}_3H_6$	13.89	13.61	13.4	13.4
$C^{13}{}_2C^{12}{}_4H_6$	30.16	26.66	26.3	25.0
$C^{13}C^{12}{}_5H_6$	34.97	27.99	28.0	27.2
$C^{12}{}_6H_6$	16.90	24.37	24.5	24.6

Acknowledgments. This research was supported by the U. S. Atomic Energy Commission under Contract No. AT(30-1)2007, and grateful acknowledgment is made thereto. The authors wish to thank Mr. S. Wrbican for careful determination of the mass spectra, and Dr. T. Hardwick, Gulf Research and Development Co., for the use of the Van de Graaff accelerator.

(7) Y. Rousseau and H. E. Gunning, *Can. J. Chem.*, **41**, 465 (1963).
(8) J. R. Bates, *J. Am. Chem. Soc.*, **54**, 569 (1932).

Change in the Heat Capacity of Boron Trioxide during the Glass Transformation

by S. S. Chang and A. B. Bestul

National Bureau of Standards, Washington, D. C. 20234
(Received April 2, 1964)

For 41 glass-forming substances, Wunderlich[1] compiled values for the difference, Δc_p, in heat capacity at the glass transformation temperature, T_g, between the glass and the equilibrium supercooled liquid. These values should represent the configurational heat capacities of the equilibrium supercooled liquids. With the exception of two extreme variations, Wunderlich gives for Δc_p the "universal" value of 2.7 ± 0.5 cal. deg.$^{-1}$ per specially defined "bead." For polymers, these beads are the equivalent of molecular chain links. One of the exceptions was B_2O_3, for which a value of 0.55 cal. deg.$^{-1}$ was quoted. We have examined the original publication[2] from which the values for B_2O_3 were taken. It appears that the values compiled for B_2O_3 in ref. 1 should be multiplied by a factor of five. The heat capacity values in the original

(1) B. Wunderlich, *J. Phys. Chem.*, **64**, 1052 (1960).
(2) S. B. Thomas and G. S. Parks, *ibid.*, **35**, 2091 (1931).

reference were listed in one column in units of calories per (mean) gram-atom, as was the fashion at that time. Apparently, in computing the data in ref. 1 the mean gram-atom was taken for the gram molecular weight, which contains 5 mean g.-atoms. Application of this factor gives a value of 2.75 cal. deg.$^{-1}$ for Δc_p per bead for B_2O_3. This value is well within the stated limit of uncertainty of Wunderlich's "universal" value. In addition to any inherent variation between the configurational heat capacities for the different substances, the applicable uncertainty includes any contributions associated with any inadequacies in the treatment of measurement and interpretation problems such as: (1) heat effects arising from potentially isothermal configurational equilibration during the course of a heat capacity measurement, (2) the specification of the value of T_g to which the heat capacity values are extrapolated, and (3) the specification of the "bead" unit in the case of molecules usually considered as monomers. Without attention to such problems, the several different curves given in ref. 2 can lead to values of Δc_p for B_2O_3 varying at least from 2.3 to 4.4 cal. deg.$^{-1}$. The selection of the (here corrected) value in ref. 1 represents the application of current understanding of the nature of the glass transformation process in order to treat the above-mentioned problems in such a way as to evaluate at T_g the heat capacity of the equilibrium supercooled liquid (including configurational heat capacity) and of the glass in a configurational state of *fixed* deviation from equilibrium (thus excluding configurational heat capacity). The original curve thus selected for use happens to be the same as that designated (without detailed explanation) by Thomas and Parks as "the normal or standard values for a carefully annealed boron trioxide." The above correction changes the conclusion from Wunderlich's original compilation that B_2O_3 is an exceptional substance in the above respect. It is now shown to behave exactly like other glass-forming substances investigated in this respect.

We have also examined the original reference[3] for $H_2SO_4 \cdot 3H_2O$, the other exception in Wunderlich's original tabulation. No tabulation errors were found.

In ref. 1 the universality of Δc_p was discussed in terms of glass transformation based on the theory of Hirai and Eyring for molecular rearrangement in liquids, and reference was made to the desirability of a solution to the heat capacity equation based on the second-order thermodynamic transition theory of Gibbs and DiMarzio for glass transformation. According to Gibbs and DiMarzio,[4] this theory does also lead to universality of Δc_p at T_2, the temperature at which they predict that an equilibrium supercooled liquid should lose all its configurational entropy on cooling in equilibrium.

(3) J. E. Kunzler and W. F. Giauque, *J. Am. Chem. Soc.*, **74**, 797 (1952).

(4) J. H. Gibbs and E. A. DiMarzio, private communication.

The Wetting of Gold Surfaces by Water[1]

by Malcolm L. White

Bell Telephone Laboratories, Incorporated, Allentown, Pennsylvania
(Received May 7, 1964)

Past work on the wetting of metal surfaces by water has yielded some apparently conflicting results. For example, Harkins[2] reported that water does not spread on clean mercury. Bartell and Smith,[3] however, found that water had a low contact angle on vacuum-evaporated films of gold and silver. Trevoy and Johnson[4] found that a number of different metal surfaces could be made hydrophilic if properly cleaned, but this cleaning involved vigorous chemical and electrochemical oxidation, so that the metal surfaces were undoubtedly covered with an unknown amount of oxide. Bewig and Zisman[5] obtained low contact angles of water on gold and platinum by an HNO_3–H_2SO_4 etching treatment which would result in oxide formation, even on these noble metals.

Some recent observations in this laboratory have indicated that the oxide on metal surfaces has a very striking effect on the wettability of the metal by water, an oxide-free metal surface being hydrophobic and the oxidized surface hydrophilic.

Gold is a metal of particular interest in surface studies, because it is the only metal which does not form an oxide on heating in air or oxygen. This is apparent not only from thermodynamic data,[6] but also from experimental studies in which gold was heated in air and oxygen to 900° with no evidence of oxide formation as determined by X-ray and electron diffraction techniques.[7,8]

(1) Presented at the 145th National Meeting of the American Chemical Society, New York, N. Y., September, 1963.

(2) W. D. Harkins, "Physical Chemistry of Surface Films," Reinhold Publishing Co., New York, N. Y., 1952, p. 12.

(3) F. E. Bartell and J. T. Smith, *J. Phys. Chem.*, **57**, 165 (1953).

(4) D. J. Trevoy and H. Johnson, Jr., *ibid.*, **62**, 833 (1958).

(5) K. W. Bewig and W. A. Zisman, Advances in Chemistry Series, No. 33, American Chemical Society, Washington D. C., 1961.

(6) A. Glassner, "The Thermodynamic Properties of the Oxides, Fluorides and Chlorides to 2500°K.," Argonne National Laboratory Report ANL-5750.

Due to the instability of gold oxide it is possible to clean gold surfaces by thermal or chemical techniques that will remove organic contamination, but will not oxidize the gold, so that a clean oxide-free metal surface can be obtained.

An all-Pyrex and metal system was built so that a sample of gold foil could be placed in it, heated to 500° in clean air, and then cooled to about 5° without removing it from the system. Air, saturated with water at room temperature, was then passed over the sample and condensed on the surface. By observing the appearance of the condensed water under 50–100× magnification, it was possible to determine the wettability of the surface. Water condensing on a completely hydrophilic surface, such as clean glass, spreads immediately so that a thin film of water is formed which gradually builds up in thickness, as evidenced by a continually changing pattern of interference colors. When a thick enough film of water is formed, the interference colors disappear, and the sample surface is seen through a transparent film of water. With a less wettable surface the water does not spread as completely, this being easily detected by the lack of broad interference colors and the appearance of nonwetting areas. Strongly hydrophobic surfaces show droplets formed from the condensation.

A very effective technique for obtaining clean air was to pass it through a stainless steel tube (packed with stainless steel wool) heated to 550–600°. This heating treatment served to oxidize organic contaminants, presumably to CO_2 and H_2O which were then condensed in a Dry Ice–alcohol trap following the furnace. The cleanness of the system was checked as follows: a piece of polished aluminum (99.0+%) was oxidized at 500° in air for 10 min. in the apparatus to give a completely hydrophilic surface. The sample was kept in the system with the cleaned air flowing over it and the wettability periodically checked. It was found that the oxidized aluminum surface stayed completely hydrophilic for a period of at least 23 hr., showing that no hydrophobic contaminants were present in the air. When the oxidized aluminum surface was removed from the clean system and exposed to the laboratory air for 5 min., a detectable change in wettability was seen, so the gas system used can be considered as very clean.

The gold used was 0.010-in. foil of 99.99% purity which was degreased with trichloroethylene and acetone before using. The samples were polished with 0.3-μ particle size alumina on billiard cloth and then ultrasonically agitated to remove any adhering abrasive particles. The vacuum-evaporated gold films were prepared on cleaned microscope glass cover slips by evaporation of 99.99% gold from a tungsten filament in a Varian VI-4 unit at a pressure of 10^{-7} mm. to give about a 1000-Å. film of gold. This is considered to be a grease-free system, because no lubricants are used.

In order to test the contamination associated with the polishing process, a microscope cover slip was polished in the same way as the gold samples. It was found that the surface was slightly hydrophobic after the polishing, but could be made completely hydrophilic by heating in clean air in the apparatus at 250° or higher for 10 min., showing that the contaminants picked up during the polishing are easily removed by thermal oxidation.

The polished gold surface was found to be strongly hydrophobic, showing drop-type condensation of water vapor. Heating the gold to 500° for 30 min. in the clean air in the apparatus caused no change in the wettability of the surface. The gold could even be heated to 950° for 2 hr. in a muffle furnace with no change in wetting characteristics, showing that organic contamination was not causing the hydrophobic character of the surface, since any organic material would be burned off at this temperature.

The gold can also be cleaned by a wet oxidation procedure using hot 30% hydrogen peroxide, this treatment having previously been shown to be very effective for removing all traces of oxidizable impurities without leaving any metallic or inorganic residues.[9] After 20–30 min. boiling in 30% hydrogen peroxide, the gold surface remained strongly hydrophobic, confirming the results of the thermal treatments that organic contamination cannot account for the hydrophobic character of the gold. It is known that gold is not oxidized by hydrogen peroxide.[10]

These results were checked on gold surfaces that were degreased, but not polished, and on vacuum-evaporated films to make sure that the surface preparation techniques were not affecting the results. In all cases the gold remained hydrophobic.

It was found, however, that the gold could be made hydrophilic by anodically oxidizing it in an acid solution. When the gold was made an anode in 1 N HNO_3 (with another piece of gold as the cathode) and a potential was applied at a current density of about 5 ma./cm.^{2} for 5–10 min., the surface became hydrophilic, although complete spreading was not observed. The gold that was used as the cathode, however, remained strongly hydrophobic. During the anodization a color change

(7) D. Dlark, T. Dickinson, and W. N. Mair, *Trans. Faraday Soc.*, **55**, 1937 (1959).

(8) D. Clark, T. Dickinson, and W. N. Mair, *J. Phys. Chem.*, **65**, 1470 (1961).

(9) D. O. Feder and D. E. Koontz, ASTM STP 246, 1958, p. 41.

(10) M. C. Sneed, J. L. Maynard, and R. C. Brasted, "Comprehensive Inorganic Chemistry," Vol. 2, D. Van Nostrand, Princeton, N. J., 1954.

on the gold anode confirmed the presence of (hydrated) gold oxide.[11]

When the oxidized hydrophilic gold surface was heated to 250° in clean air in the apparatus, the oxide disproportionated to free gold and oxygen, as evidenced by the disappearance of the oxide color, and the surface again became strongly hydrophobic. This experiment was repeated using different methods of surface preparation, always with the same result that the oxidized surface was hydrophilic and the oxide-free surface hydrophobic. When the oxidized gold was kept in clean air in the apparatus at room temperature, it also became strongly hydrophobic after 5–10 hr., with an attendant disappearance of the oxide color.

All of the above experimental evidence leads to the conclusion that it is the oxide on a gold surface which makes it hydrophilic. It seems likely that there would be more interaction of water (and therefore more wetting) with a metal oxide than with a free metal surface because of dipole–dipole effects and hydrogen bonding of water with the oxide, these effects not being present on a free metal surface. It is also very likely that other metals are similar to gold in their wettability by water, the oxide-free metal surfaces being hydrophobic, with the formation of oxide causing the surface to become hydrophilic.

These observations have been confirmed by some recent calculations of Fowkes,[12] who has shown that water should not spread on oxide-free metal surfaces because of the large relative contributions of metallic bond forces and London dispersion forces to the total surface energy, these forces not contributing significantly to any interaction with water.

(11) L. Young, "Anodic Oxide Films," Academic Press, New York, N. Y., 1961.

(12) F. M. Fowkes, 66th ASTM Meeting, Atlantic City, N. J., June, 1963.

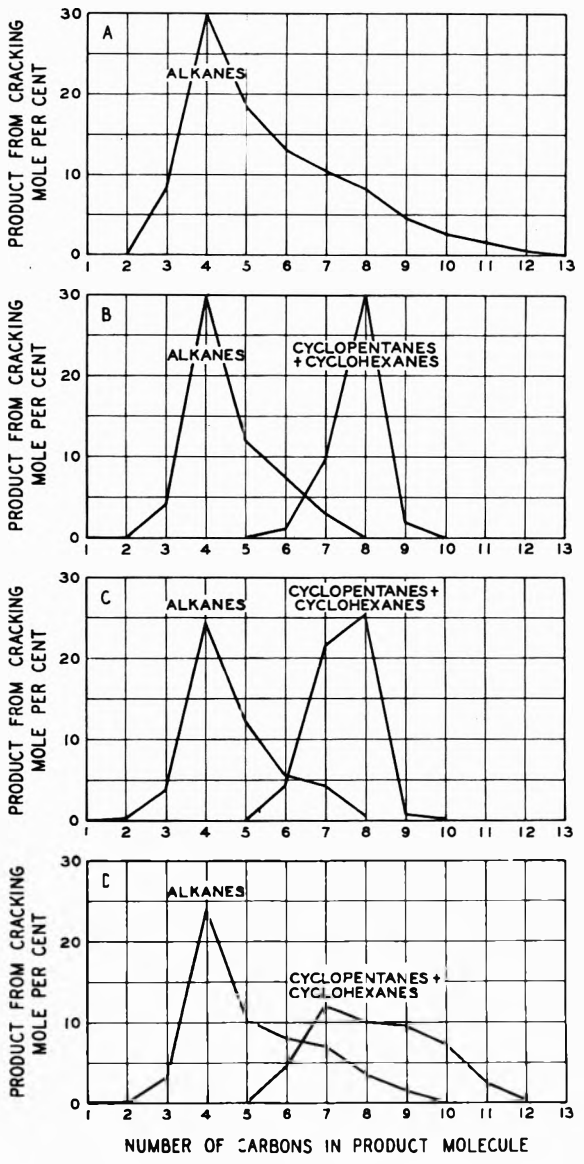

Figure 1. Product distribution from hydrocracking:
A, *n*-hexadecane, 48.7% cracking at 290°;
B, hexamethylcyclohexane, 87.5% cracking at 234°;
C, cyclododecane, 91.0% cracking at 296°;
D, cyclopentadecane, 94.9% cracking at 291°.

Reactions of Large Cycloalkane Rings in Hydrocracking

by R. J. White, Clark J. Egan, and G. E. Langlois

California Research Corporation, Richmond, California
(Received June 17, 1964)

It was shown previously[1] that alkylcyclohexanes having four or more carbons in alkyl side chains undergo the paring reaction. In this selective cracking reaction the cycloalkane character of the reactant is preserved (both alkylcyclopentanes and alkylcyclohexanes of lower molecular weight are formed), and the predominant alkane product from cracking is isobutane. In this paper the behavior of cyclododecane and cyclopentadecane under similar cracking conditions is reported. These large ring hydrocarbons having no side chain conceivably could either undergo the paring reaction after contraction of the ring or could undergo

(1) C. J. Egan, G. E. Langlois, and R. J. White, *J. Am. Chem. Soc.*, **84**, 1204 (1962).

ring opening and crack as alkanes, which give essentially no cyclic products.

Figure 1 shows the distribution by carbon number of the products from cracking an alkane, *n*-hexadecane,[2] and three cycloalkanes of increasing ring size, hexamethylcyclohexane, cyclododecane, and cyclopentadecane. Table I shows the reaction conditions and product composition. The product distribution from cyclododecane and cyclopentadecane, as determined from a combination of gas chromatographic and mass spectrometric analyses, is unusual in that: (1) the moles of cycloalkanes in the product from cracking equal the moles of cycloalkane that cracked—thus, no rings are lost in the cracking process; (2) the predominant cyclic products are alkylcyclopentanes and alkylcyclohexanes having seven or eight carbons; (3) the predominant alkane products are isobutane and isopentane; (4) no evidence for cycloheptanes through cycloundecanes is found in the mass spectrometric analysis of the product from cracking; (5) essentially no methane, no ethane, and only a small amount of propane are produced in cracking.

This product distribution is quite similar to that obtained from the paring reaction of hexamethylcyclohexane (Fig. 1B). This suggests that cyclododecane and cyclopentadecane undergo a rapid ring contraction on the surface of the catalyst to form alkylcyclopentanes and alkylcyclohexanes. Some of these cycloalkanes are desorbed before they crack and appear as isomers as shown in Table I. The remaining isomers undergo selective cracking at a slower rate. The mechanism of this cracking reaction has been described previously.[1]

Table I: Reaction Conditions and Product Composition

	Reactant			
	n-Hexadecane	Hexamethylcyclohexane	Cyclododecane	Cyclopentadecane
Temp., °C.	290	234	296	291
Pressure, atm.	82	82	82	82
Residence time, sec.[a]	7.6	14.6	16.6	15.5
First-order rate constant (cracking only), sec.$^{-1}$	0.088	0.125	0.164	0.192
Conversion, total %	51.4	100	97.4	98.5
Conversion, cracking %	48.7	87.5	91.0	94.9
Product (moles/100 moles of reactant)				
C_1–C_3 alkanes	12.1	1.7	7.1	8.4
C_4–C_7 isoalkanes	89.2	91.5	67.3	86.5
C_4–C_7 unbranched alkanes	13.1	1.4	8.9	9.9
C_8–C_{13} alkanes	26.2	...	...	11.2
i-C_{16} alkanes	2.7			
C_6–C_{11} cycloalkanes	...	82.1	96.4	97.7
C_{12} cycloalkanes	...	12.5	6.2[b]	
C_{15} cycloalkanes	...			3.6[b]
Reactant	48.6	...	2.6	1.6

[a] Apparent time of hydrocarbon in volume occupied by catalyst; calculated assuming no conversion and perfect gas law for hydrogen and vapor. [b] Mainly cyclopentane and cyclohexane rings.

The behavior of the cyclopentadecane is of interest because the ring strain present in medium-size rings containing 8–14 carbons has largely disappeared in rings containing 15 or more carbons ("Rings containing 15 or more carbons are folded in nearly random stacks and resemble open-chain compounds[3]").

It is concluded that as the ring size is increased, cycloalkanes containing up to 15 ring carbons still behave as cycloalkanes rather than as unbranched alkanes in hydrocracking.

Experimental

The apparatus, procedure, and methods of analysis used have been discussed previously.[1] In the present experiments, the catalyst was nickel sulfide (5.3% Ni) on commercial silica-alumina, the pressure was 82 atm., and the molal ratio of hydrogen to reactant was ~10. Most of the experiments were performed in duplicate or triplicate with reproducibility within 10%.

Chemicals. *n*-Hexadecane was obtained from Humphrey–Wilkinson (99% pure). Only one peak was observed in gas chromatographic analysis.

The cyclododecane contained no impurities detectable by gas chromatographic analysis. The boiling point was 160° at 100 mm; n^{20}D 1.4504.

Cyclopentadecane was obtained by reduction of cyclopentadecanone (Aldrich) 98.6% pure by gas chromatographic analysis. The melting point was 62.8–63.4°.

Acknowledgments. The authors gratefully acknowledge the contributions of Mr. C. F. Spencer in the mass spectrometric analysis of the products and of Mr. J. Abell for assistance in obtaining the cyclododecane and cyclopentadecane.

(2) Data from R. F. Sullivan of this laboratory.

(3) D. J. Cram and G. S. Hammond, "Organic Chemistry," 2nd Ed., McGraw-Hill Book Co., New York, N. Y., 1964, p. 161.

Diffusion Potential in Molten Salt Systems

by I. G. Murgulescu and D. I. Marchidan

Institute of Physical Chemistry, Bucharest 9, Romania

(Received June 1, 1964)

In our previous works[1-3] we have shown that the diffusion potential is nil in the concentration cells of the type

$$Me_1|Me_1X_n||Me_1X_n(x_1) + Me_2X_m(x_2)|Me_1$$

for the following binary melts: AgCl + KCl, AgBr + KBr, AgBr + NaBr, AgBr + LiBr, AgBr + $PbBr_2$, $AgNO_3$ + $LiNO_3$, $PbCl_2$ — KCl.

At the separation limit between the molten salts, no use of diaphragms was made. For the diffusion potential, we have taken as valid the relation, used for aqueous electrolytes,[4] of the form

$$\epsilon = -\frac{RT}{nF}\int_A^B (t_1 \, d \ln a_1 + t_2 \, d \ln a_2) \quad (1)$$

By substituting the activity a_2 as a function of a_1, with the aid of the Gibbs–Duhem equation, there results

$$\epsilon = -\frac{RT}{nF}\int_A^B \left(\frac{x_2 t_1 - x_1 t_2}{x_2}\right) d \ln a_1 \quad (2)$$

In virtue of the fact that the diffusion potential ϵ is nil, we can write

$$x_2 t_1 - x_1 t_2 = 0 \quad (3)$$

From relation 3 there results that the transport numbers of the two cations are variable and proportional to the molecular fractions of the corresponding salts.

In a note published in this journal,[5] Berlin and his collaborators ascribe to us the statement that the mobilities or the transport numbers should remain constant all along the concentration range as used in the cell.

This statement is not to be found in our works, and on the other hand the fact that the diffusion potential vanishes does not imply any direct conclusion as to the individual mobilities of the ions.

(1) I. G. Murgulescu and D. I. Marchidan, *Zh. Fiz. Khim.*, **34**, 2534 (1960).

(2) I. G. Murgulescu and D. I. Marchidan, *Rev. Chim. Acad. Rep. Populaire Roumaine*, **5**, 17 (1960).

(3) I. G. Murgulescu and D. I. Marchidan, *ibid.*, **5**, 299 (1960).

(4) (a) K. Jellinek, "Lehrbuch der physikalischen Chemie," III Band, Stuttgart, 1930, p. 780; (b) E. A. Guggenheim, "Thermodynamics," 1957, p. 396.

(5) A. Berlin, F. Měněs, S. Forcheri, and C. Monfrini, *J. Phys. Chem.*, **67**, 2505 (1963).

Low Pressure Flow of Gases

by H. J. M. Hanley and W. A. Steele

Whitmore Laboratory, Department of Chemistry, The Pennsylvania State University, University Park, Pennsylvania
(Received June 4, 1964)

The isothermal flow of gases at low pressures has been a subject of interest, both theoretically and experimentally, for some time.[1-3] Theoretical equations are well known for flow in cylindrical tubes in the limit of low pressures (Knudsen flow) and of high pressures (Poiseuille flow); however, the intermediate (slip flow) region is not well understood.[4] In many of the recent theoretical treatments, the authors make use of Knudsen's original data[5] to relate their results to experiments. In this note, further experiments of this kind are reported; it will be seen that these data show features not present in previous work.

Flow experiments were performed by measuring the time dependence of the pressure differences between two containers of known volume connected by twenty-five stainless steel tubes of length 10.000 cm. and i.d. 0.015 cm. The pressure differences were read to an accuracy of 3×10^{-5} mm. by means of a differential capacitance manometer coupled to a chart recorder. Data have been obtained for helium, neon, and argon at a number of temperatures and at pressures corresponding to a tube diameter to mean free path ratio ranging from 0.002 to 15. Flow rates are given in terms of the number of molecules passing through unit area of the tube in unit time, for unit gradient in the gas density. If this quantity is denoted by D, one can calculate a dimensionless flow rate $D^* = D/av$, where a = tube radius and v = average molecular speed. These rates are plotted in Fig. 1–3 as a function of a/λ, where λ = kinetic theory mean free path. It is most convenient to compute λ from the viscosity of the gas

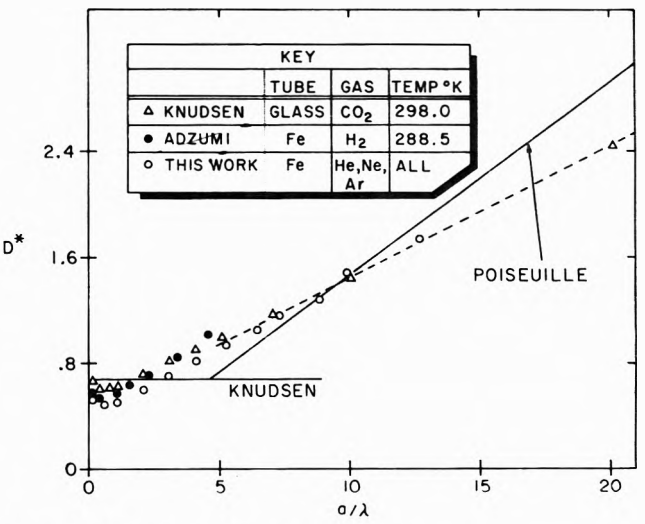

Figure 1. Flow data for various workers.

(1) W. G. Pollard and R. D. Present, *Phys. Rev.*, **73**, 762 (1948).

(2) D. S. Scott and F. A. L. Dullien, *A.I.Ch.E. J.*, **8**, 293 (1962).

(3) O. Gherman, *Soviet Phys JETP*, **34**, 1016 (1958).

(4) S. A. Schaaf, "Handbuch der physik," Band VIII/2, Springer-Verlag, Berlin, 1963.

(5) M. Knudsen, *Ann. Physik*, **28**, 75 (1909).

$$\lambda = 3\eta kT/\bar{p}\bar{v}m \qquad (1)$$

where $\bar{p}$ is the average pressure of the flowing gas.

In terms of the parameters defined here, the Knudsen equation leads to the result that

$$\lim_{a/\lambda \to 0} D^* = {}^2/_3 \qquad (2)$$

and the Poiseuille equation becomes

$$\lim_{a/\lambda \to \infty} D^* = (3\pi/64)(a/\lambda) \qquad (3)$$

In Fig. 1, the data obtained in the present investigation are compared with the predictions of eq. 2 and 3 and with some experimental results of other workers in this field.[5,6] It is seen that there is little difference between the various sets of data and, when viewed on a scale such as that used in Fig. 1, the flow rates seem to go rather smoothly from those characteristic of a Knudsen gas to those for a Poiseuille gas. However, Fig. 2 and 3 show some of the data plotted on an expanded scale. It can now be seen that the experimental data shown in the figures exhibit several interesting features: the minima in the flow rates are much sharper than those observed previously, particularly at higher temperatures and with the lower boiling gases (*i.e.*, the substances with the weaker intermolecular interactions); also, the limiting low pressure data do not agree with the prediction of the Knudsen equation, but vary with temperature and with the gas (this result is in qualitative agreement with the earlier work of Lund and Berman[7]). A theoretical explanation of these effects will necessarily involve a consideration of the dynamics of the molecular collisions between molecules in the gas and between a gas molecule and the wall of the tube. Since the nature of these collisions is determined by the intermolecular forces, the observed differences in flow properties of the various gases are undoubtedly due to the differences in the gas–gas and gas–surface interactions. However, a quantitative treatment of this effect is lacking at present.

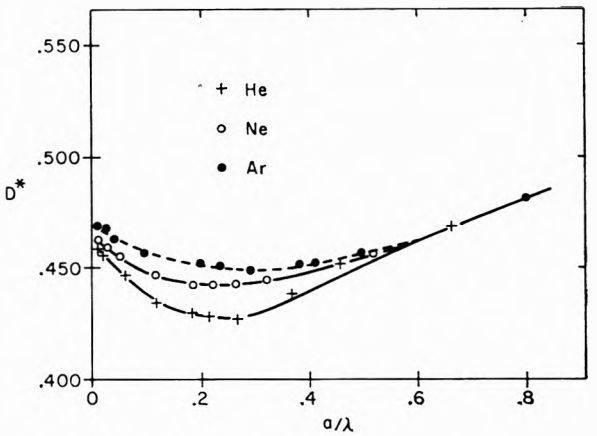

Figure 2. Flow rates at 273°K.

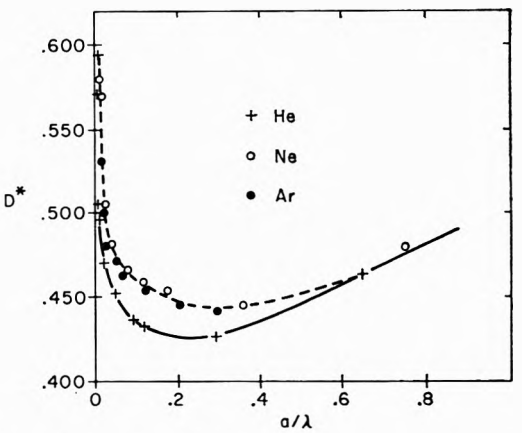

Figure 3. Flow rates at 386°K.

Acknowledgment. This work was supported by the National Science Foundation.

(6) H. Adzumi, *Bull. Chem. Soc. Japan*, **14**, 343 (1939).

(7) L. M. Lund and A. S. Berman, *J. Chem. Phys.*, **28**, 363 (1958).